

NASA Contractor Report 3247

NASA
CR
3246-
pt.2
c.1

LOAN-CONFERE
AFWL TECH
KIRTLAND AFB

0062018



TECH LIBRARY KAFB, NM

Rotary Balance Data for a Typical Single-Engine General Aviation Design for an Angle-of-Attack Range of 8° to 90°

*II - Influence of Horizontal
Tail Location for Model D*

Billy Barnhart

CONTRACT NAS1-16205
NOVEMBER 1982

NASA



NASA Contractor Report 3247

Rotary Balance Data for a Typical Single-Engine General Aviation Design for an Angle-of-Attack Range of 8° to 90°

*II - Influence of Horizontal
Tail Location for Model D*

Billy Barnhart
Bihrlle Applied Research, Inc.
Jericho, New York

Prepared for
Langley Research Center
under Contract NAS1-16205



National Aeronautics
and Space Administration

**Scientific and Technical
Information Branch**

1982

SUMMARY

The influence of horizontal tail location on the rotational flow aerodynamics is discussed for a 1/6-scale general aviation airplane model. The model was tested using various horizontal tail positions, with both a high and a low-wing location and for each of two body lengths. Data were measured, using a rotary balance, over an angle-of-attack range of 8° to 90° , and for clockwise and counter-clockwise rotations covering an $\frac{\Omega b}{2V}$ range of 0 to 0.9.

The relative positions of the wing and horizontal tail had a large effect on the static pitching moment characteristics, as anticipated. Rotation produced an appreciable nose-down pitching moment increment that increased non-linearly with increasing rotation. The effect of rotation was relatively less for a T-tail configuration.

For the model tested, horizontal tail location had no influence on the rotational yaw characteristics below 35° angle of attack. Above 35° , low horizontal tail locations reduced or eliminated the damping contribution of the vertical tail. The T-tail configurations tested did not interfere with the vertical tail contribution. All the T-tail configurations examined were damped in yaw throughout the test angle-of-attack range, as was one of three low horizontal tail locations. Two low tail configurations exhibited autorotative yawing moments in the flat spin region (i.e., 80° to 90° angle of attack).

INTRODUCTION

The NASA Langley Research Center is conducting a broad general aviation stall/spin research program, which includes spin-tunnel and free-flight radio-control model tests, as well as full-scale flight tests for a number of configurations typical of light, general aviation airplanes. As a part of this effort, rotary balance tests were conducted in the Langley Spin Tunnel to establish a rotational flow aerodynamic base for analysis of model and full-scale flight results.

Rotary balance data were obtained for a representative, single-engine, general aviation model, referred to as model D. The test results were divided into three areas, each of which is discussed in a separate report. The aerodynamic effectiveness of the controls and their influence on predicted spin modes are discussed in reference 1. Reference 2 discusses the influence of each airplane component, as well as body length and wing location, on the rotational aerodynamic characteristics. This report presents the effect of horizontal tail location in the presence of each of two wing locations and two body lengths. The Appendix in the above references contains all data measured during the subject studies.

SYMBOLS

The units for physical quantities used herein are presented in the International System of Units (SI) and U.S. Customary Units. The measurements were made in the U.S. Customary Units; equivalent dimensions were determined by using the conversion factors given in reference 3.

b	wing span, m (ft)
\bar{c}	mean aerodynamic chord, cm (in.)
C_L	lift-force coefficient, $\frac{\text{Lift force}}{qS}$
C_N	normal-force coefficient, $\frac{\text{Normal force}}{qS}$
C_A	axial-force coefficient, $\frac{\text{Axial force}}{qS}$
C_Y	side-force coefficient, $\frac{\text{Side force}}{qS}$
C_l	rolling-moment coefficient, $\frac{\text{Rolling moment}}{qSb}$
C_m	pitching-moment coefficient, $\frac{\text{Pitching moment}}{qSc}$
C_n	yawing-moment coefficient, $\frac{\text{Yawing moment}}{qSb}$
q	free-stream dynamic pressure, N/m ² (lb/ft ²)
S	wing area, m ² (ft ²)
V	free-stream velocity, m/sec (ft/sec)
α	angle of attack, deg

Ω angular velocity about spin axis, rad/sec
 $\frac{\Omega b}{2V}$ spin coefficient, positive for clockwise spin

Abbreviations:

cg center of gravity
SR spin radius

TEST EQUIPMENT

A rotary balance measures the forces and moments acting on a model while it is subjected to rotational flow conditions. Historical background for this testing technique is discussed in reference 4. A photograph and sketch of the rotary balance apparatus installed in the Langley Spin Tunnel are shown in figures 1 and 2, respectively. The system's rotary arm, which rotates about a vertical axis at the tunnel center, is supported by a horizontal boom and is driven by a motor mounted external to the test section.

A NASA six-component strain gauge balance, affixed to the bottom of the rotary balance apparatus and mounted inside the model, is used to measure the normal, lateral, and longitudinal forces, and the yawing, rolling and pitching moments acting about the model body axis. Controls located outside of the tunnel are used to activate motors on the rotary rig, which position the model to the desired attitude. The angle-of-attack range of the rig is 0° to 90° , and the sideslip angle range is $\pm 15^\circ$. Spin radius and lateral displacement motors are used to position the moment center of the balance on, or at a specific distance from, the spin axis. (This is done for each combination of angle of attack and sideslip angle.) It is customary to mount the balance to the model such that its moment center is at the location about which the aerodynamic moments are desired. Electrical currents from the balance and to the motors on the rig are conducted through slip rings. Figure 2 shows how the rig is positioned in angle of attack and sideslip.

The system is capable of rotating up to 90 rpm in either direction. A range of $\frac{\Omega b}{2V}$ values can be obtained by adjusting rotational speed and/or tunnel air flow velocity. (Static aerodynamic forces and moments are obtained when $\Omega = 0$.)

The data acquisition, reduction, and presentation system is composed of a 12-channel scanner/voltmeter, a mini-computer with internal printer, a plotter, and a CRT display. This equipment permits data to be presented via on-line digital print-outs and/or graphical plots.

TEST PROCEDURES

Rotary aerodynamic data are obtained in two steps. First, the inertial forces and moments (tares) acting on the model at different attitudes and rotational speeds must be determined. Ideally, these inertial terms would be obtained by rotating the model in a vacuum, thus eliminating all aerodynamic forces and moments. As a practical approach, this is approximated closely by enclosing the model in a sealed spherical structure, which rotates with the model without touching it, such that the air immediately surrounding the model is rotated with it. As the rig is rotated at the desired attitude and rate, the inertial forces and moments generated by the model are measured and stored on magnetic tape for later use.

The second step is to record force and moment data with the air on and with the enclosure removed. The tares, measured in step one, are then subtracted from these data, leaving only the aerodynamic forces and moments, which are converted to coefficient form and stored on magnetic tape.

MODEL

A 1/6-scale model, representing a single-engine general aviation airplane, was constructed from foam/fiberglass and aluminum. A photograph of the model installed on the rotary balance is shown in figure 1. A three-view drawing of the low-wing, short body model is shown in figure 3. The model was constructed such

that the body could be lengthened by using an alternate aft fuselage section (figure 4). For the long-body configuration, the vertical tail was moved aft and the fuselage was faired smoothly to the rudder, whose span was increased to the bottom of the fuselage, as shown in figure 4. It was possible to mount the wing in either a low position, as shown in figure 3, or a high position, as shown in figure 5. Also, six different horizontal tail locations could be tested (figure 6). Dimensional characteristics of the model are given in Table I.

TEST CONDITIONS

The tests were conducted in the spin tunnel at a tunnel velocity of 7.62 m/sec (25 ft/sec), which corresponds to a Reynolds number of 128,000 based on the model mean aerodynamic chord. All the configurations were tested through an angle-of-attack range of 8° to 90° , at a zero sideslip angle. For angles of attack above 30° , the spin axis passed through the cg, and for angles of attack up to 35° 91.4 cm (36 in.) forward (full-scale) of the cg. Consequently, data were obtained for both a 0 and 91.4 cm spin radius at 30° and 35° angles of attack. At each spin attitude, measurements were obtained for nominal $\frac{\Omega b}{2V}$ values of 0.1, 0.2, 0.3, 0.4, 0.5, 0.6, 0.7, 0.8, and 0.9, in both clockwise and counter-clockwise directions, as well as for $\frac{\Omega b}{2V} = 0$ (static value).

DATA PRESENTATION

All data measured for this study are presented in the Appendix. Table II identifies the configurations tested and their corresponding appendix figure numbers. The body-axis aerodynamic coefficients, plotted as functions of $\frac{\Omega b}{2V}$, are presented for each configuration in six sequentially numbered figures in the following order: C_n , C_l , C_m , C_N , C_Y , C_A . Each figure, in turn, consists of four pages, which present the subject aerodynamic coeffi-

cient vs. $\frac{\Omega b}{2V}$ for the following angles of attack and spin radii:

- a) $\alpha=8, 10, 12, 14, 16$ deg SR=91.4cm (36 in.) full scale
- b) $\alpha=18, 20, 25, 30, 35$ deg SR=91.4cm (36 in.) full scale
- c) $\alpha=30, 35, 40, 45, 50$ deg SR=0
- d) $\alpha=55, 60, 70, 80, 90$ deg SR=0

All moment data are presented for a cg position of $0.25\bar{c}$.

DISCUSSION

The influence of horizontal tail location on this configuration's aerodynamic moments was examined because these moments determine the existence and the nature of spin modes. Furthermore, since rolling moment characteristics were shown to be determined almost entirely by the wing (reference 2), this discussion covers only pitching and yawing moments.

Static Pitching Moment Characteristics

Short Body, Low Wing:

The horizontal tail location obviously affects an airplane's static pitching moment characteristics. The pitching moment contributed by the horizontal tail is a function of the tail lift curve slope, arm, and angle of attack; the latter two being influenced by tail position. The horizontal tail location's effect on the static pitching moment coefficient can be seen in figure 7 for the short body model configured with a low wing.

For the low tail positions (1 and 3), the pitching moment becomes increasingly more nose-down with increasing angle of attack throughout the 8° to 90° range. Tail-1, having the shortest tail arm, has the least nose-down moment throughout the angle-of-attack range. Whereas the low tail C_m 's always become more nose-down with increasing α , the T-tail configuration (tail A) has a pitch instability after wing stall that extends over a 12° angle-of-attack range. Apparently, the tail is immersed in the reduced dynamic pressure wing wake, beginning at 16° angle of attack. (Wing stall occurs at 12° angle of attack at the Reynolds number

of these tests. Higher R_e would, of course, delay the stall and this phenomenon to a higher angle of attack.)

Short Body, High Wing:

The high wing's effect on the low tails is generally to make the pitching moment coefficients somewhat more nose-down than those for the low wing (figure 8). It was also noted that the high-wing position decreases the nose-down break at stall for tail 3. A significant effect of wing location was observed for the T-tail static pitching moment in the post-stall angle-of-attack region. No loss of stability was observed for the high wing, T-tail airplane, whereas instability occurred with the low wing. Instability was avoided in the post-stall angle-of-attack region because the wing and T-tail's relative positions more nearly approximated those of the low-wing, low-tail configuration.

Long Body:

Static pitching moment data for the long body configurations are presented in figures 9 and 10 for the low and high-wing airplanes, respectively. Lengthening the fuselage has little effect on the C_m variation with angle of attack for tail 3, except that the nose-down moments are amplified by the longer tail arm. Tail 1 shows a similar amplification; however, with the low wing, the longer body produces a sharper nose-down break at wing stall (figure 9).

The longer body improves the T-tail C_m versus α characteristics for both wing locations: with the high wing, it produces a sharper nose-down break beginning at 16° angle of attack. With the low wing, the longer body results in less pitch instability than was observed for the short body configuration. As was noted for the other tails, the pitching moment for the long body model is, overall, more nose-down throughout the angle-of-attack range due to the increased tail arm.

As noted above, the relative positioning of the wing and horizontal tail determines the pitching moment characteristics at

stall. The length of the tail arm and/or the wing location determines the magnitude of the nose-down break at stall for the low tails. For a T-tail, the relative wing-tail positioning can eliminate or lessen a post-stall pitch instability.

There was very little difference in pitching moment between the three T-tail positions (tails A, B, and C), except for that produced by the small difference in tail arm (see figure 11).

Rotational Pitching Moment Characteristics

Rotation, both clockwise and counter clockwise, produces an appreciable non-linear increase in the nose-down pitching moment coefficients from the static values for all tail positions, as shown in figure 12. Evidently this is a characteristic of most airplanes in a rotational flow environment (reference 4). Rotation produces an increase in the dynamic pressure at the tail, which is apparently partly responsible for this effect. The increase in tail dynamic pressure becomes significant for large angles of attack and high rotation rates. In addition, a radial pressure gradient is postulated to exist above a stalled rotating surface (reference 5) that would also increase the nose-down pitching moment, as observed. At most angles of attack, the T-tail configurations have a smaller increase in nose-down C_m due to rotation than do the low tail configurations, as shown in figure 12. In fact, reference 4 shows that a T-tail configuration has the least increase in nose-down moment with rotation.

In most cases, the increase in nose-down pitching moment due to rotation becomes greater with increasing angle of attack. An exception to this occurs for the low-wing T-tail configurations, which show the largest increase in nose-down C_m due to rotation occurring at 25° to 35° angle of attack (e.g., see Appendix figure A3. This is the angle-of-attack range where the C_m versus angle-of-attack curve regains stability following the loss of pitch stability observed for these configurations in the post-stall region.

Yawing Moment Characteristics

When plotted as functions of $\frac{\Omega b}{2V}$, the yawing moment coefficients are damped in the second and fourth quadrants and propelling in the first and third. Typical yawing moment coefficient versus $\frac{\Omega b}{2V}$ plots for this airplane are presented in Appendix figure A1 for an angle-of-attack range of 8° to 90° for a short body, low-wing, T-tail configuration.

Below stall ($\alpha=12^\circ$), the yawing moment is damped, although a decrease in damping occurs when the rotation rate is sufficient to increase the angle of attack above stall over a major portion of the inboard wing. Between 12° and 18° angle of attack, propelling yawing moments occur for $\frac{\Omega b}{2V}$ magnitudes less than 0.2. As demonstrated in reference 2, this is caused by wing stall. From 20° to 90° angle of attack, the yawing moment coefficients are damped for all $\frac{\Omega b}{2V}$'s, although the damped slope through zero rotation rate is slight for the 20° to 30° angle-of-attack range.

The influence of horizontal tail location on these yawing moment characteristics was determined by comparing the yawing moment coefficient plots found in the Appendix; e.g., figures A1, A7, and A13 present data for tails A, 1, and 3, respectively for the short-body, low-wing airplane. Similar figures for the long body and/or high-wing configurations can be determined from Table II. To simplify the discussion, however, sample comparison plots are included with the text to illustrate the analysis.

Below 35° angle of attack, the yawing moment characteristics are not influenced by horizontal tail location, as demonstrated by figure 13 at $16^\circ \alpha$. Furthermore, this was true regardless of wing location and body length. By approximately 40° angle of attack, however, the T-tails start to provide greater damping than do the low tails (figure 14). Generally, this characteristic continues through 90° angle of attack due to the low horizontal tails' adverse influence on the vertical

tail. This is demonstrated by figures 15a and 15b, which present yawing moment coefficients at $80^\circ \alpha$ for a T-tail and three low-tail configurations, as well as for the horizontal tail-off configuration. Reference 4 shows that the pressure field associated with the outboard low horizontal tail is responsible for degrading the damping contribution of the vertical tail. For the T-tail configuration, the horizontal tail is above the vertical and, as shown in figures 15a and 15b, its yawing moment closely approximates the horizontal tail-off data.

Although the low horizontal tail locations result in less damping than the T-tail for angles of attack between 40° and 70° , the data are generally damped for the airplane configurations studied (figure 14). In the 80° to 90° angle-of-attack range, however, low tail positions 2 and 3 show neutral or propelling yawing moments up to approximately $\pm 0.5 \frac{\Omega b}{2V}$ (figure 15). The T-tail and low-tail position 1 both are damped at these angles of attack. For this configuration, at least, it is possible to find a low-tail position that eliminates a propelling yawing moment, present for other low-tail positions, at flat spin angles of attack. In this case, it is not necessary to move the horizontal tail to the T-tail position to retain most of the damping of the horizontal tail-off configuration.

Although tail 1 provides almost as much damping as the T-tail configuration in the 80° to 90° angle-of-attack region regardless of body length or wing location, its effectiveness at steeper angles of attack is dependent on wing location. In the 40° to 70° angle-of-attack range, tail 1 provides the greatest damping of the low tails tested for the low-wing airplane (figure 16). However, for the high-wing configuration, it provides the least (figure 17).

There was no difference in the yaw damping characteristics between the three T-tail positions investigated (see figures A37, A43, and A49 in the Appendix).

Examination of the available data can provide insight into possible spin characteristics with the various horizontal tail locations. All of the tail positions result in large nose-down pitching moment coefficients in the flat spin angle-of-attack region. This indicates that very fast rotation rates would be required at these angles of attack to generate sufficient nose-up inertial moment to provide pitch equilibrium. Of the horizontal tail positions examined, only tails 2 and 3 could possibly have flat spins, since only they exhibit propelling yawing moment coefficients at 80° to 90° angle of attack out to relatively high values of $\frac{\Omega b}{2V}$ (figure 15). The T-tails and tail position 1, being damped in yaw at these angles of attack, should not exhibit flat spins. Steeper spin modes, however, may be experienced with pro-spin controls. This is indeed the case for the T-tail, as shown in reference 1.

CONCLUDING REMARKS

The following observations pertaining to general aviation Model D are based on the results of the present investigation:

- o The relative positioning of the wing and horizontal tail determined the static pitching moment characteristics, as would be expected.
- o A post-stall pitch instability exhibited by the T-tail configuration could be eliminated by a high-wing location or minimized by increasing the tail arm. Moving the horizontal tail to a low position also eliminated the instability.
- o Rotation produced an appreciable nose-down pitching moment increment that increased non-linearly with increasing rotation. This is evidently caused, in part, by increased dynamic pressure at the tail and by radial pressure gradients above the stalled rotating surfaces. The nose-down increment was generally less for a T-tail configuration.

- o Horizontal tail location had no influence on the rotational yaw characteristics for angles of attack less than 35° .
- o For angles of attack greater than 35° , low horizontal tails reduced or eliminated the damping contributed by the vertical tail; T-tails, being above the vertical, did not.
- o One of the low-tail positions examined provided yaw damping approaching that of the horizontal tail-off and T-tail configurations in the 80° to 90° angle-of-attack range, where the other low tails were autorotative.

REFERENCES

1. Ralston, John N. and Barnhart, Billy P.: Rotary Balance Data for a Typical Single-Engine General Aviation Design for an Angle-of-Attack Range of 8° to 90° . III- Influence of Control Deflection on Predicted Model D Spin Modes. NASA CR-3248, 1983.
2. Ralston, John N.: Rotary Balance Data for a Typical Single-Engine General Aviation Design for an Angle-of-Attack Range of 8° to 90° . I- Influence of Airplane components for Model D. NASA CR-3246, 1983.
3. Standard for Metric Practice. E 380-79, American Society for Testing and Materials, c.1980.
4. Bihrlle, W., Jr. and Bowman, J.S., Jr.: Influence of Wing, Fuselage, and Tail Design on Rotational Flow Aerodynamics Beyond Maximum Lift, Journal of Aircraft, Volume 18, Number 11, November 1981.
5. McCormick, Barnes W.: The Prediction of Normal Force and Rolling Moment Coefficients for a Spinning Wing. NASA CR-165680, 1981.

TABLE I.- DIMENSIONAL CHARACTERISTICS

Overall length, short fuselage, m (ft) . . .	1.3	(4.3)
Overall length, long fuselage, m (ft) . . .	1.425	(4.675)
Wing:		
Span, m (ft)	1.8	(5.91)
Area, m ² (ft ²)	0.448	(4.825)
Root chord, cm (in.)	26.7	(10.5)
Tip chord, cm (in.)	17.9	(7.03)
Mean aerodynamic chord, cm (in.)	24.5	(9.64)
Leading edge of \bar{c} , distance rearward of		
leading edge of root chord, cm (in.) . .	5.44	(2.14)
Aspect ratio		7.24
Taper ratio		0.67
Dihedral, low wing, deg		7
Dihedral, high wing, deg		1.5
Incidence:		
Root, deg		2.0
Tip, deg		-1.0
Airfoil section:		
Root		NASA 65 ₂ 415
Tip		NASA 65 ₂ 415 mod
Horizontal tail		
Span, m (ft)	0.508	(1.67)
Area, m ² (ft ²)	0.065	(0.696)
Aspect ratio		4.0
Airfoil section		NACA 0012
Vertical tail		
Area, m ² (ft ²)	0.03	(0.328)
Sweep at leading edge		33.9
Aspect ratio		1.47
Airfoil section		NASA 63A012

TABLE II.- CONFIGURATIONS TESTED AND FIGURE INDEX

(All configurations tested through $\alpha=8^\circ$ to 90° at $\beta=0^\circ$ and controls neutral)

FIGURE NO.	PAGE NO.	FUSELAGE	WING POSITION	HORIZONTAL TAIL LOCATION
A1-A6	A2-A25	Short ↓	Low ↓	A
A7-A12	A26-A49			1
A13-A18	A50-A73			3
A19-A24	A74-A97	High ↓	High ↓	A
A25-A30	A98-A121			1
A31-A36	A121-A145			3
A37-A42	A146-A169	Long ↓	Low ↓	A
A43-A48	A170-A193			B
A49-A54	A194-A217			C
A55-A60	A218-A241	High ↓	High ↓	1
A61-A66	A242-A265			2
A67-A72	A266-A289			3
A73-A78	A290-A313	High ↓	High ↓	A
A79-A84	A314-A337			1
A85-A90	A338-A361			2
A91-A96	A362-A385			3

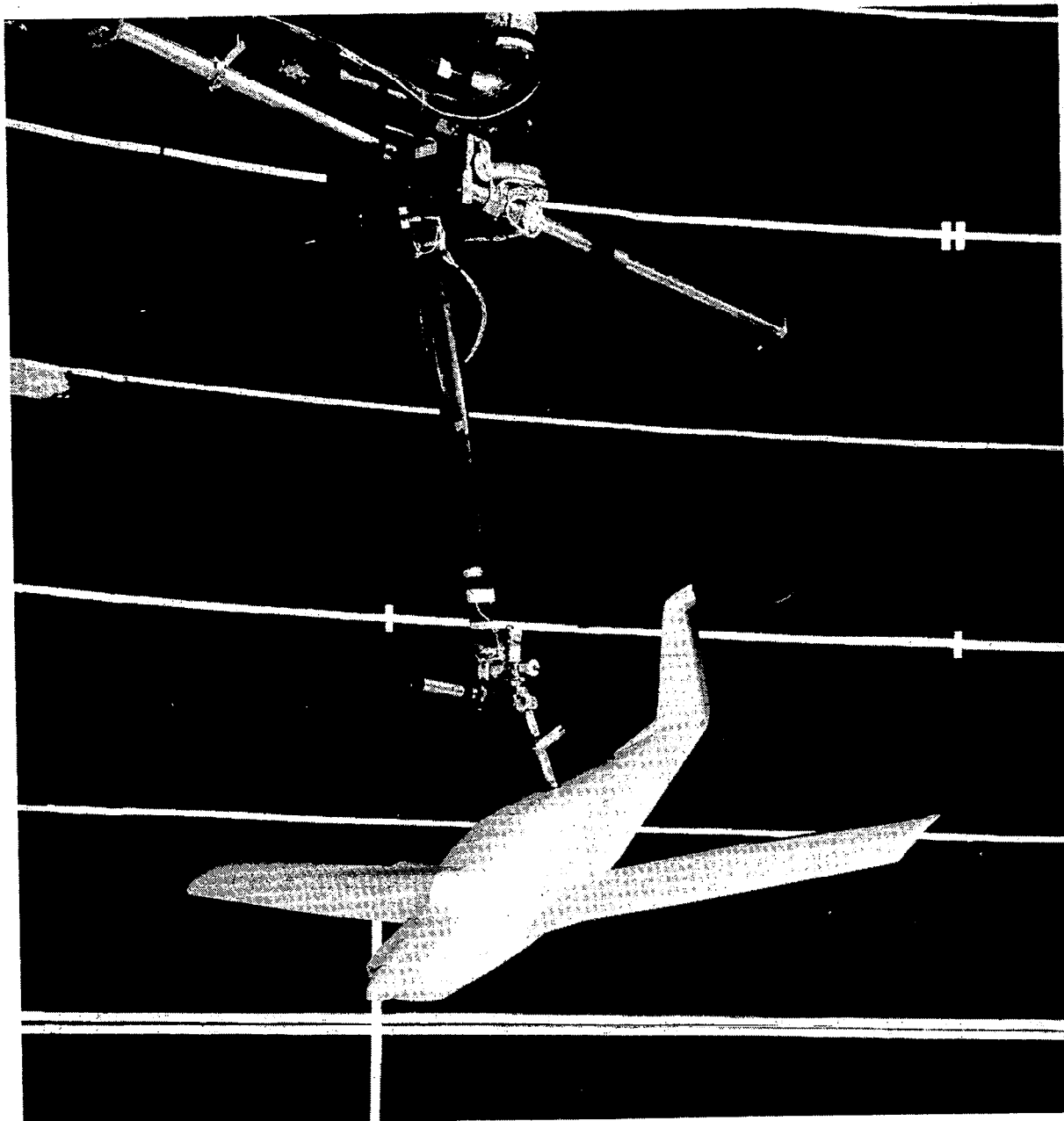
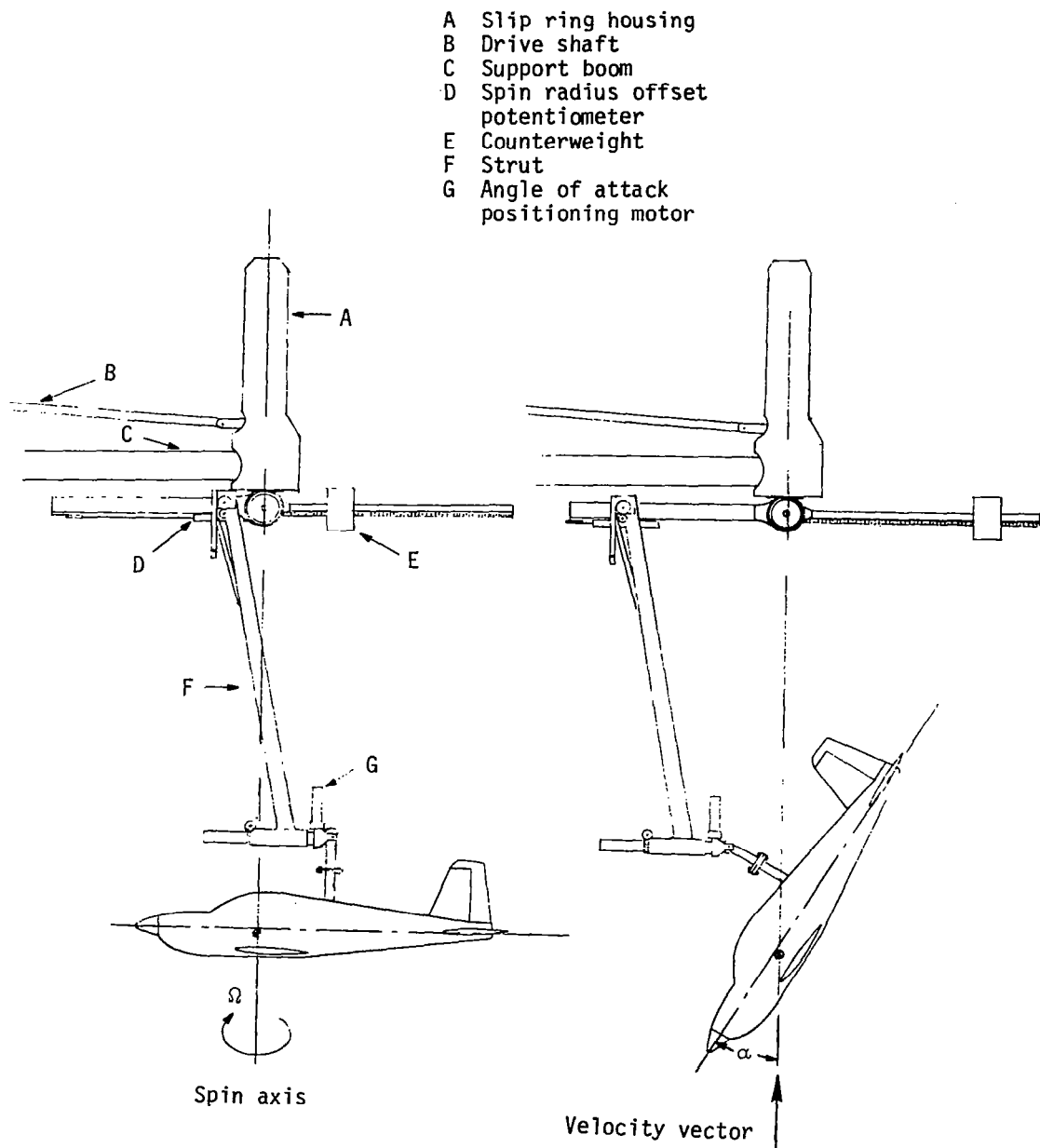
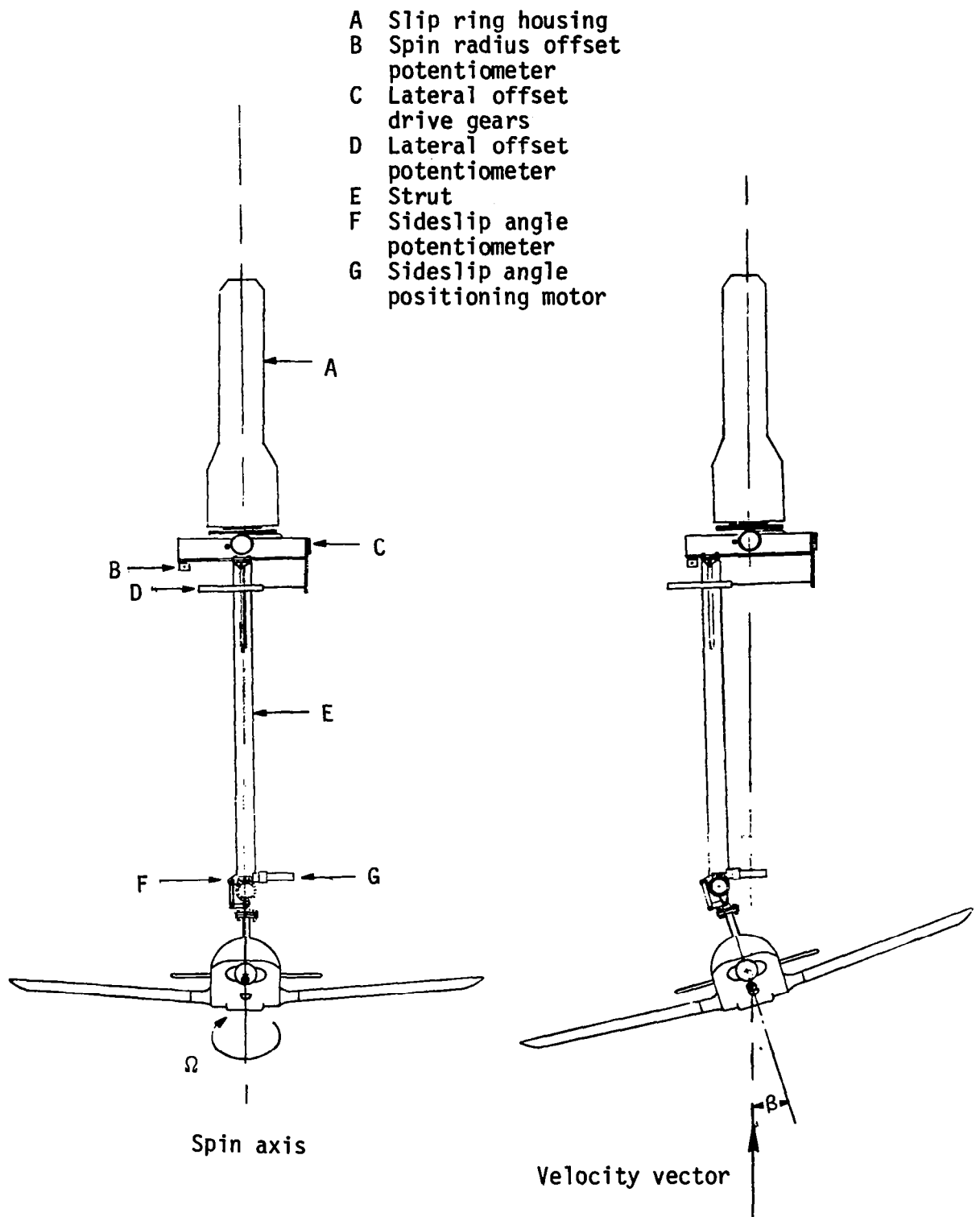


Figure I. - Photograph of 1/6 scale model installed on rotary balance apparatus.

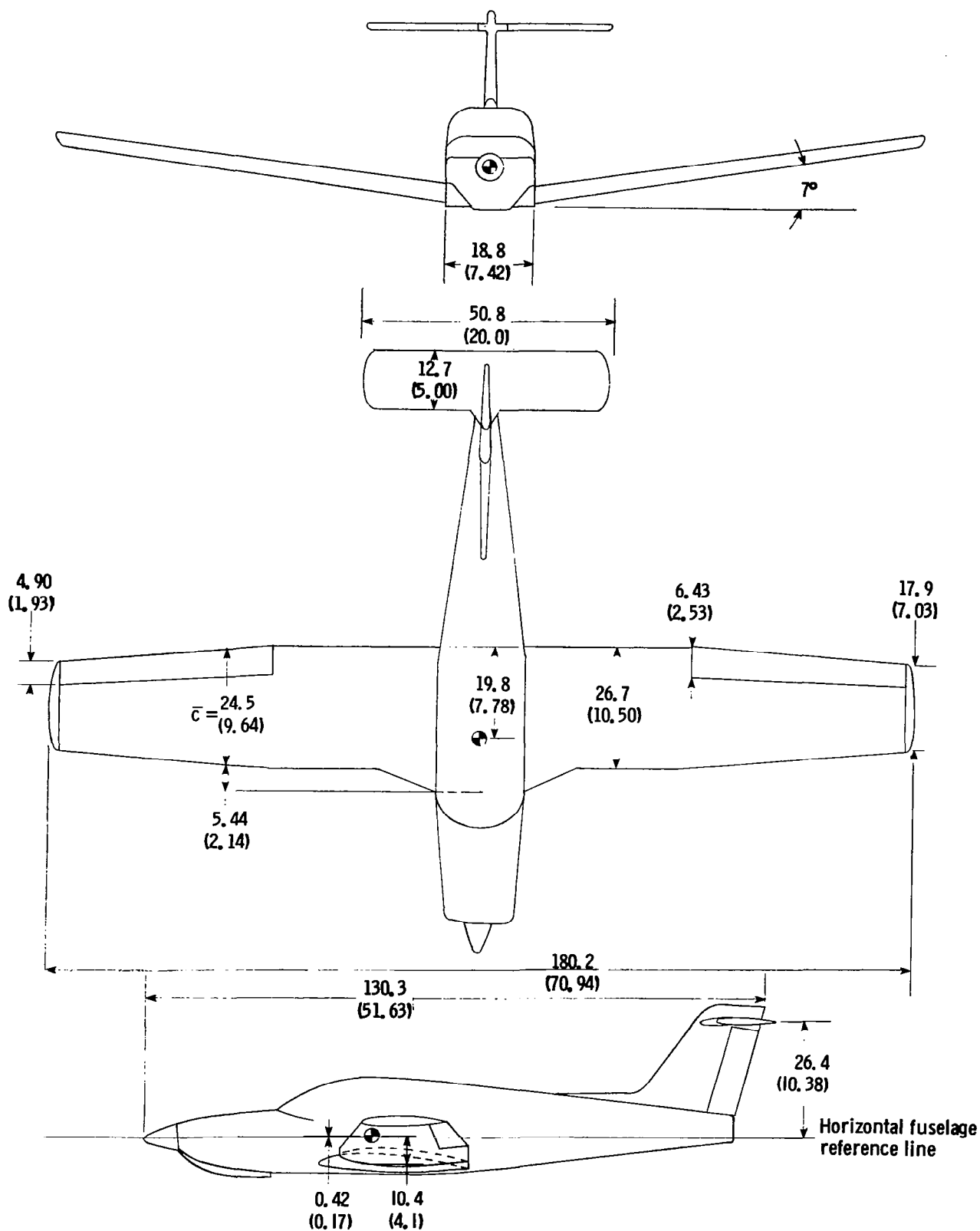


(a) Side view of model.

Figure 2.- Sketch of rotary balance apparatus.



(b) Front view of model.



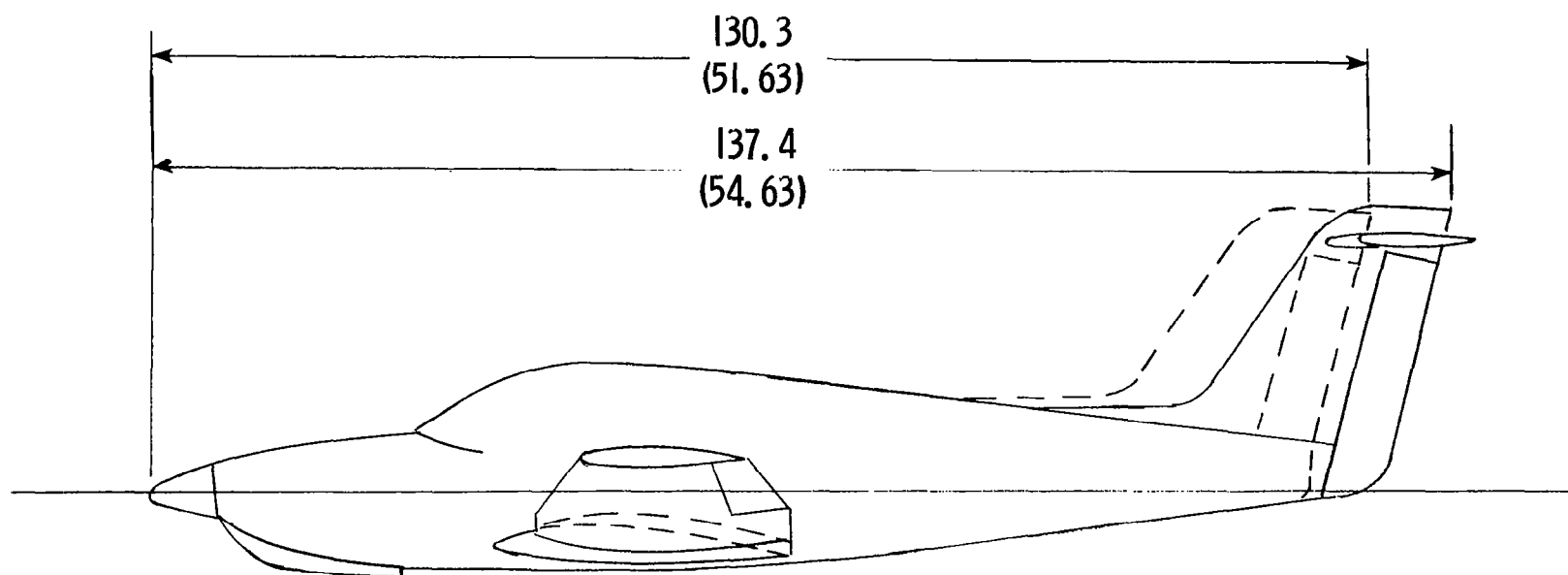


Figure 4.- Comparison of 1/6-scale long and short body configurations.
Dimensions are given in centimeters (inches), model scale.

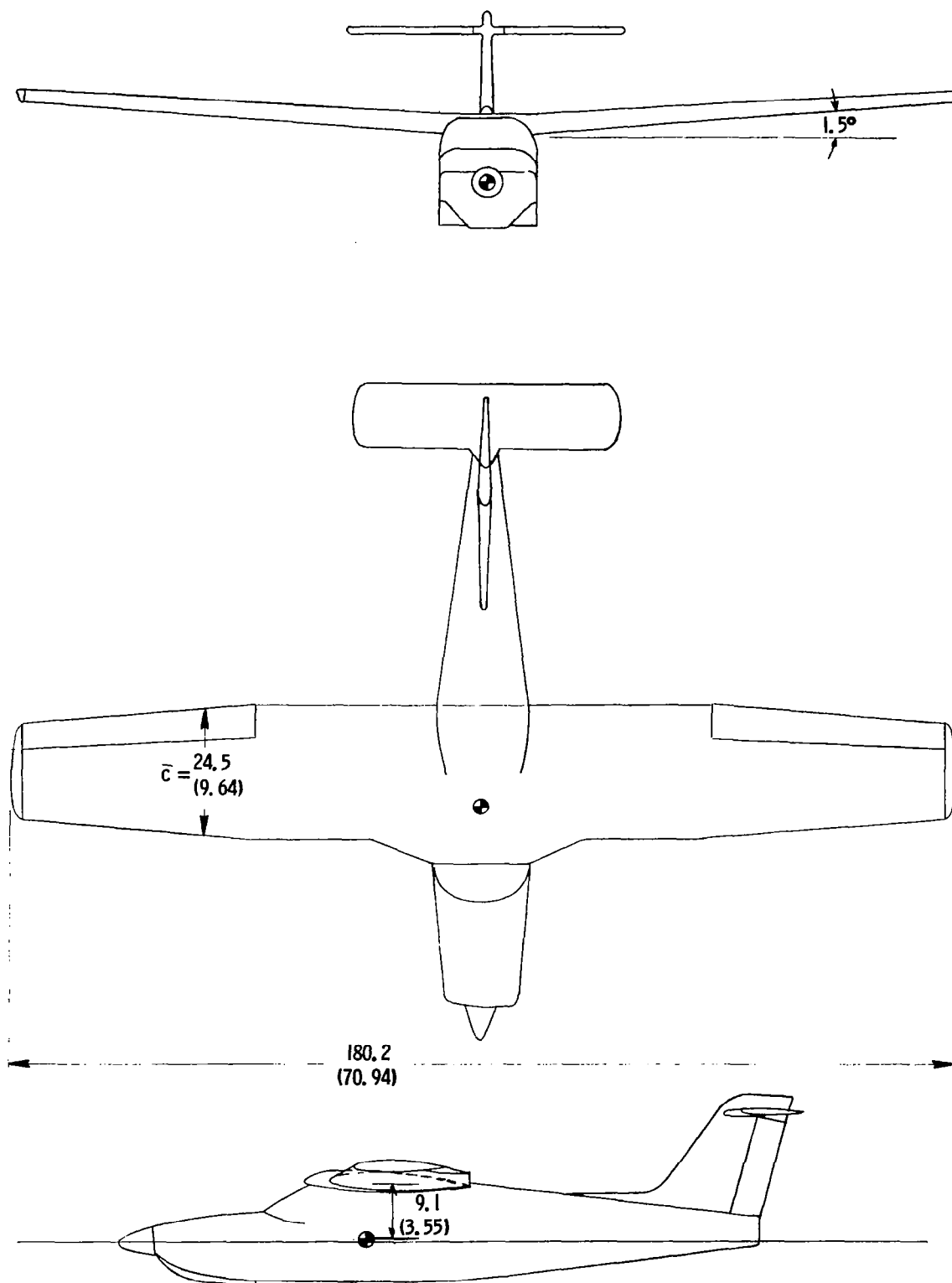
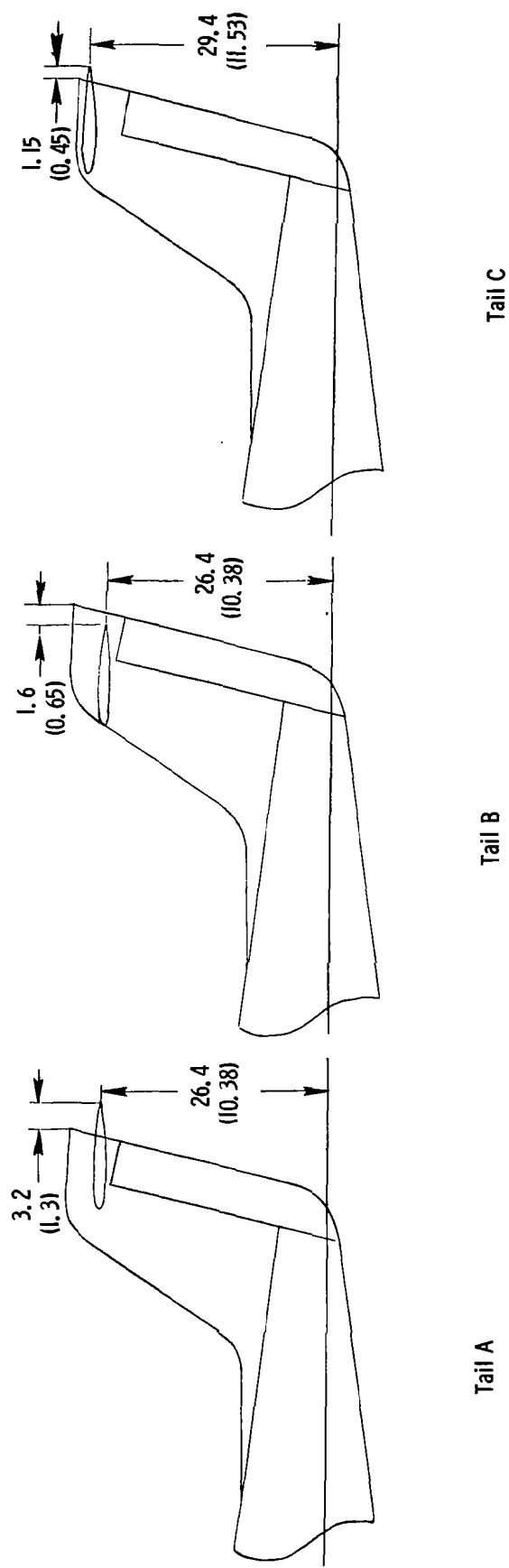
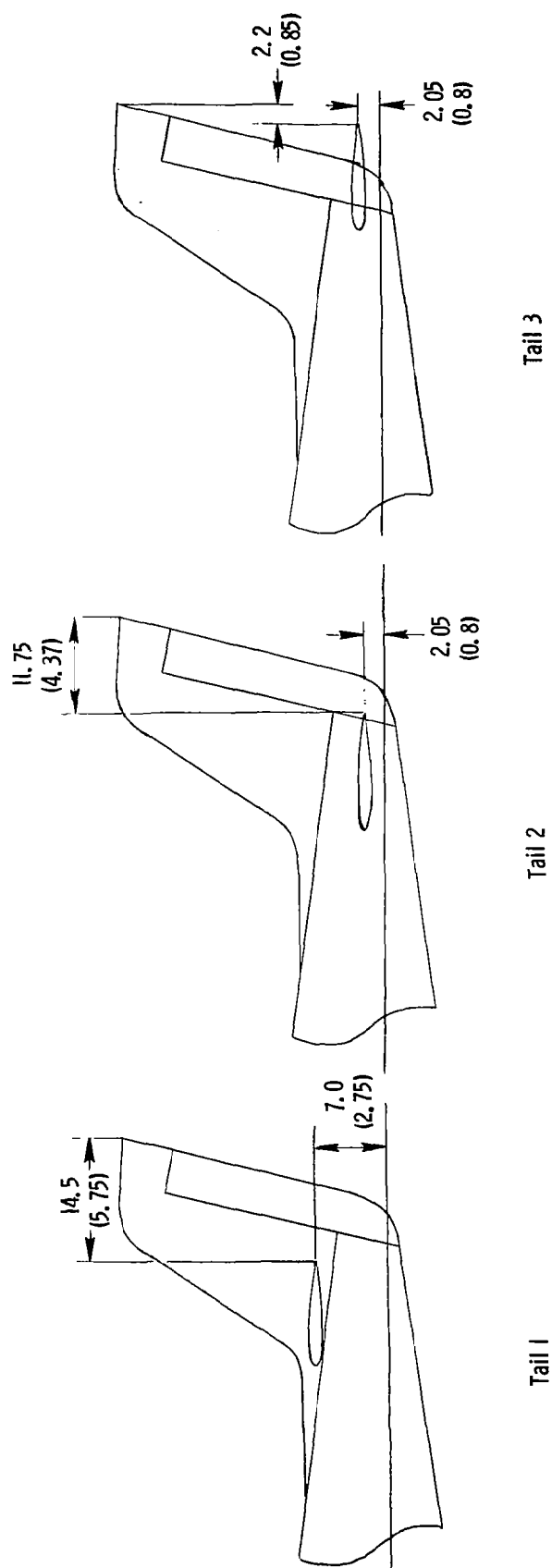


Figure 5.- Three-view of 1/6-scale high wing, short body configuration. Center of gravity positioned at $0.25\bar{c}$. Dimensions are given in centimeters (inches), model scale.



(a) T-tail locations.

Figure 6. - Alternate horizontal tail locations. Dimensions are given in centimeters (inches), model scale.



(b) Low tail locations.

Figure 6. - Concluded.

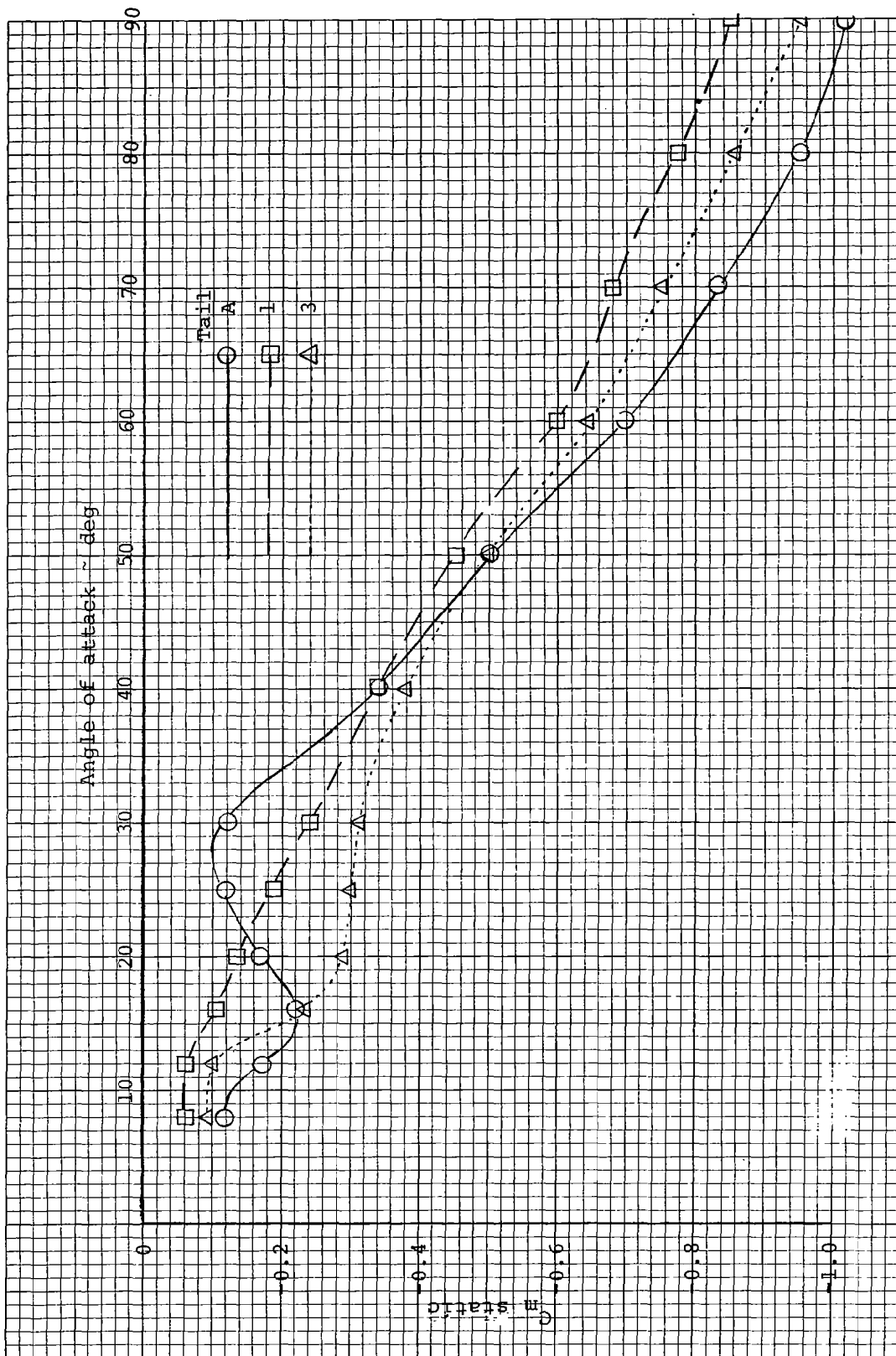


Figure 7.- Effect of horizontal tail location on the static pitching moment coefficient for the short body, low wing model D.

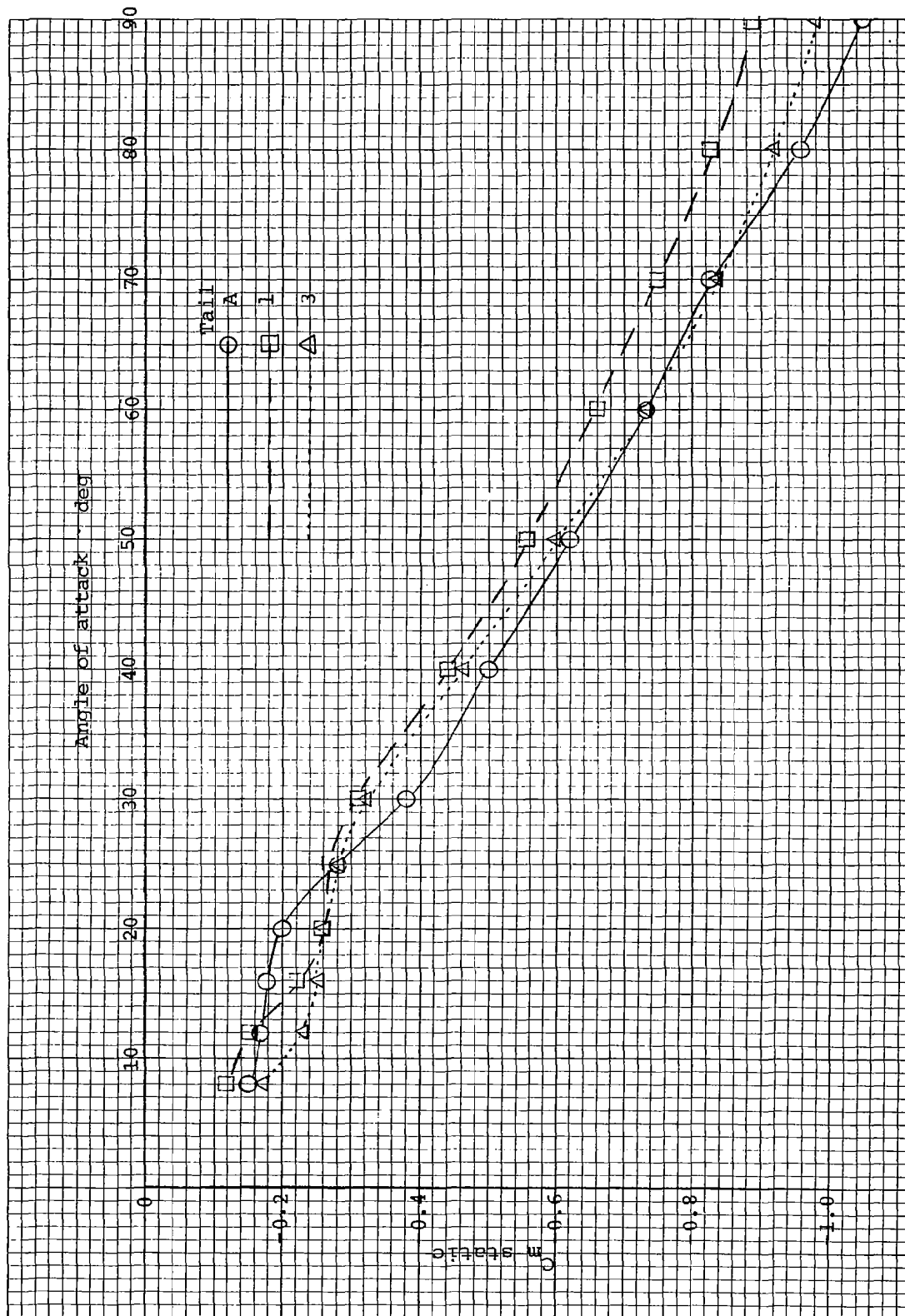


Figure 8.- Effect of horizontal tail location on the static pitching moment coefficient for the short body, high wing model D.

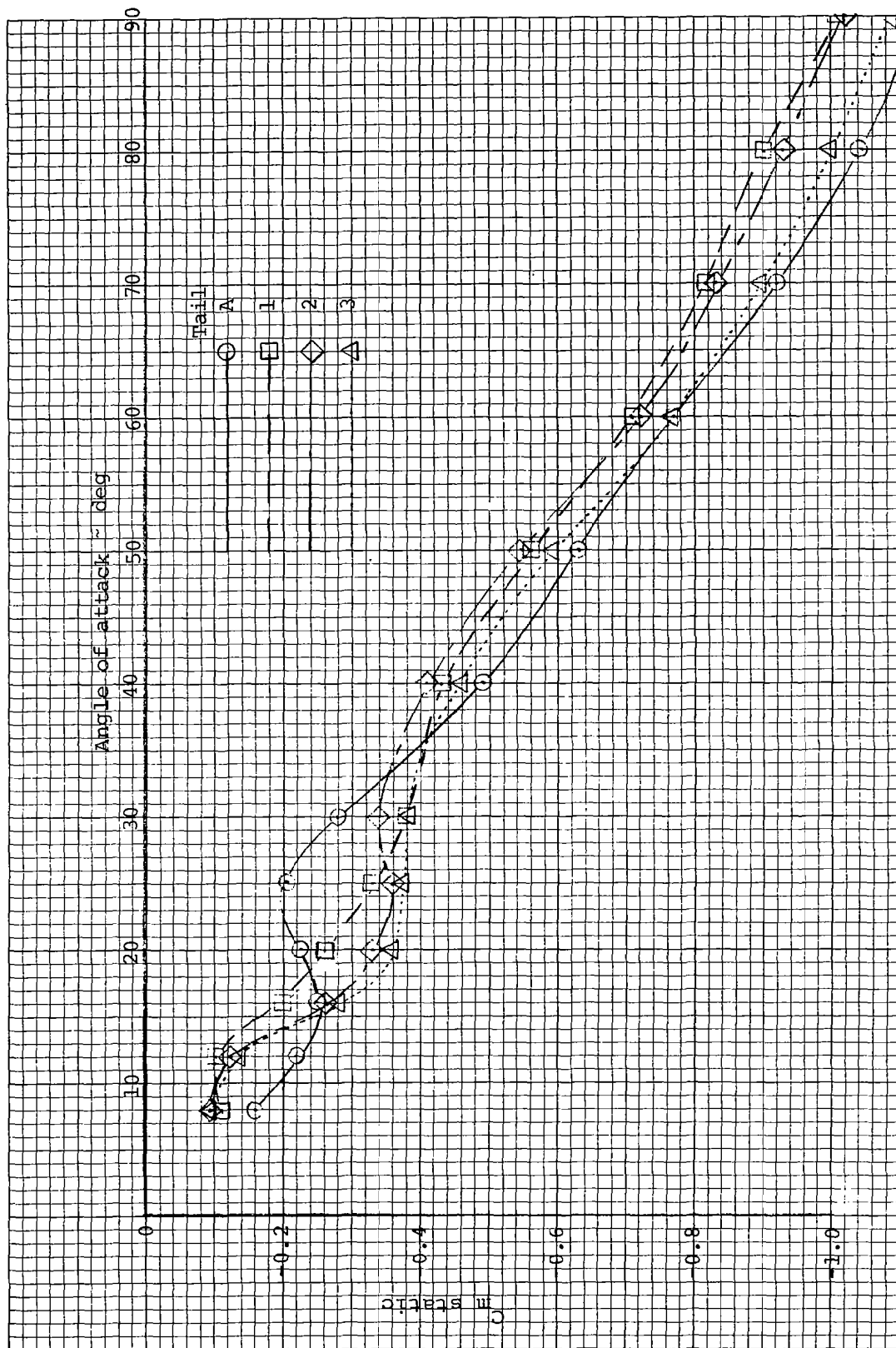


Figure 9.- Effect of horizontal tail location on static pitching moment coefficient for the long body, low wing model D.

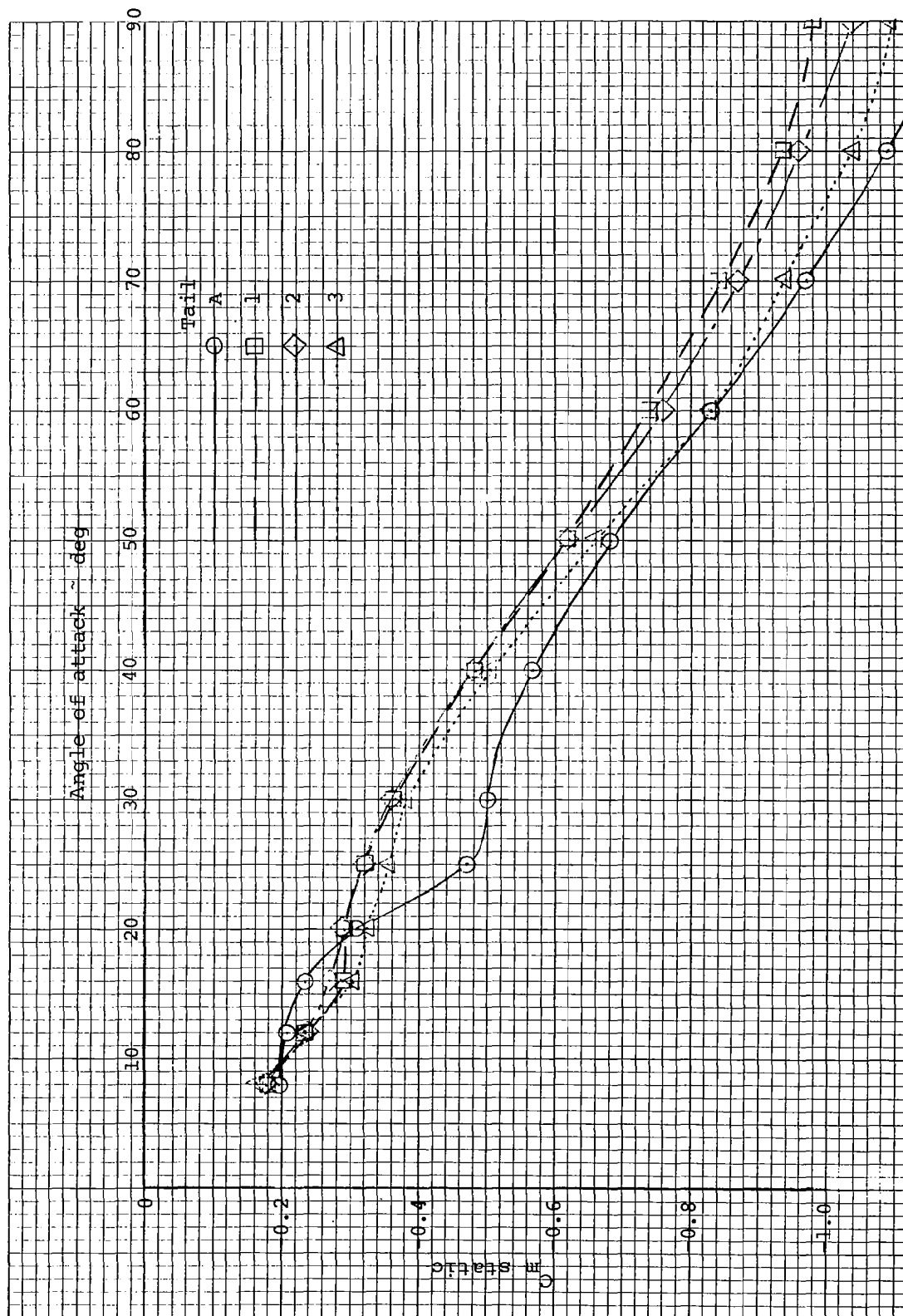


Figure 10.- Effect of horizontal tail location on the static pitching moment coefficient for the long body, high wing model D.

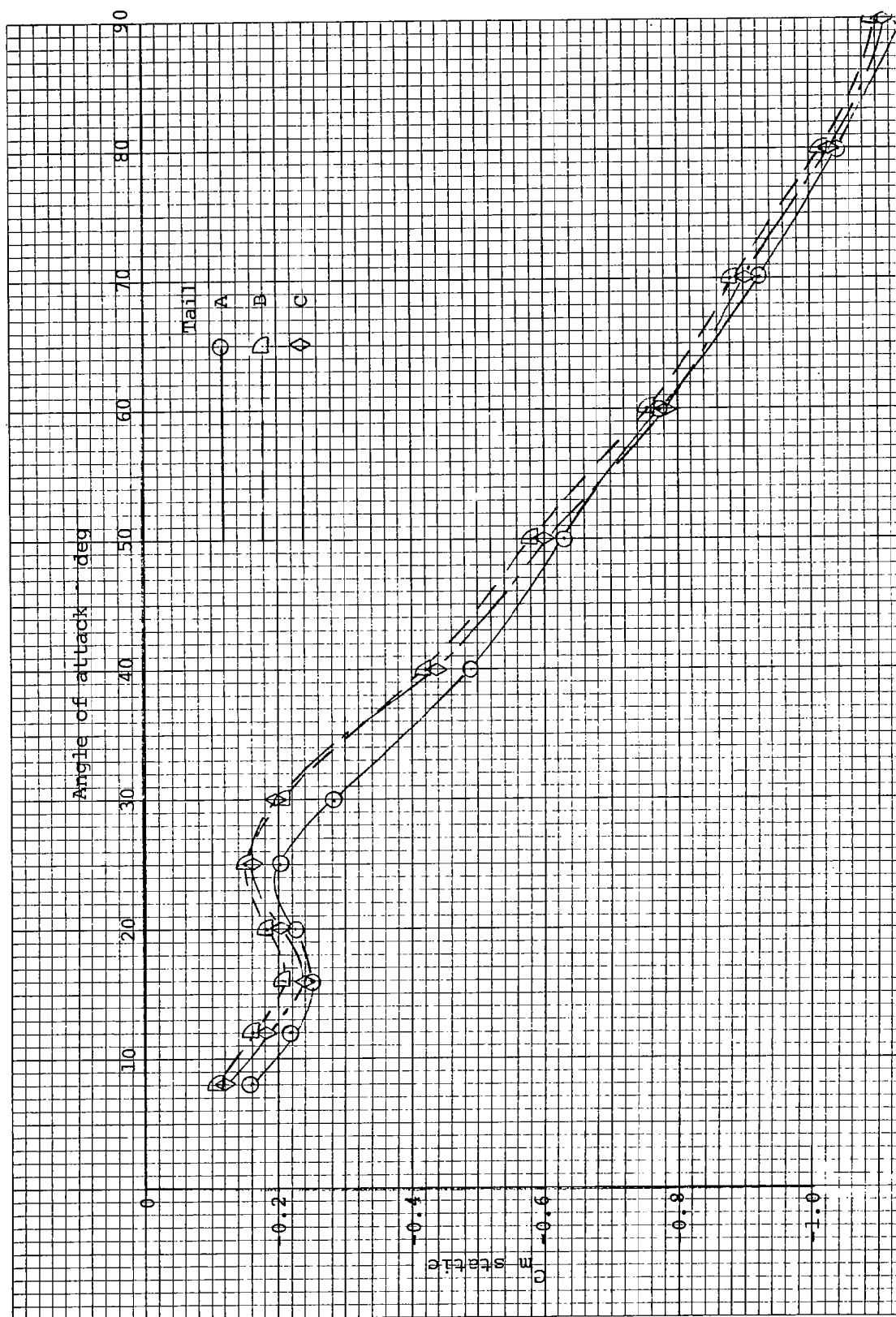
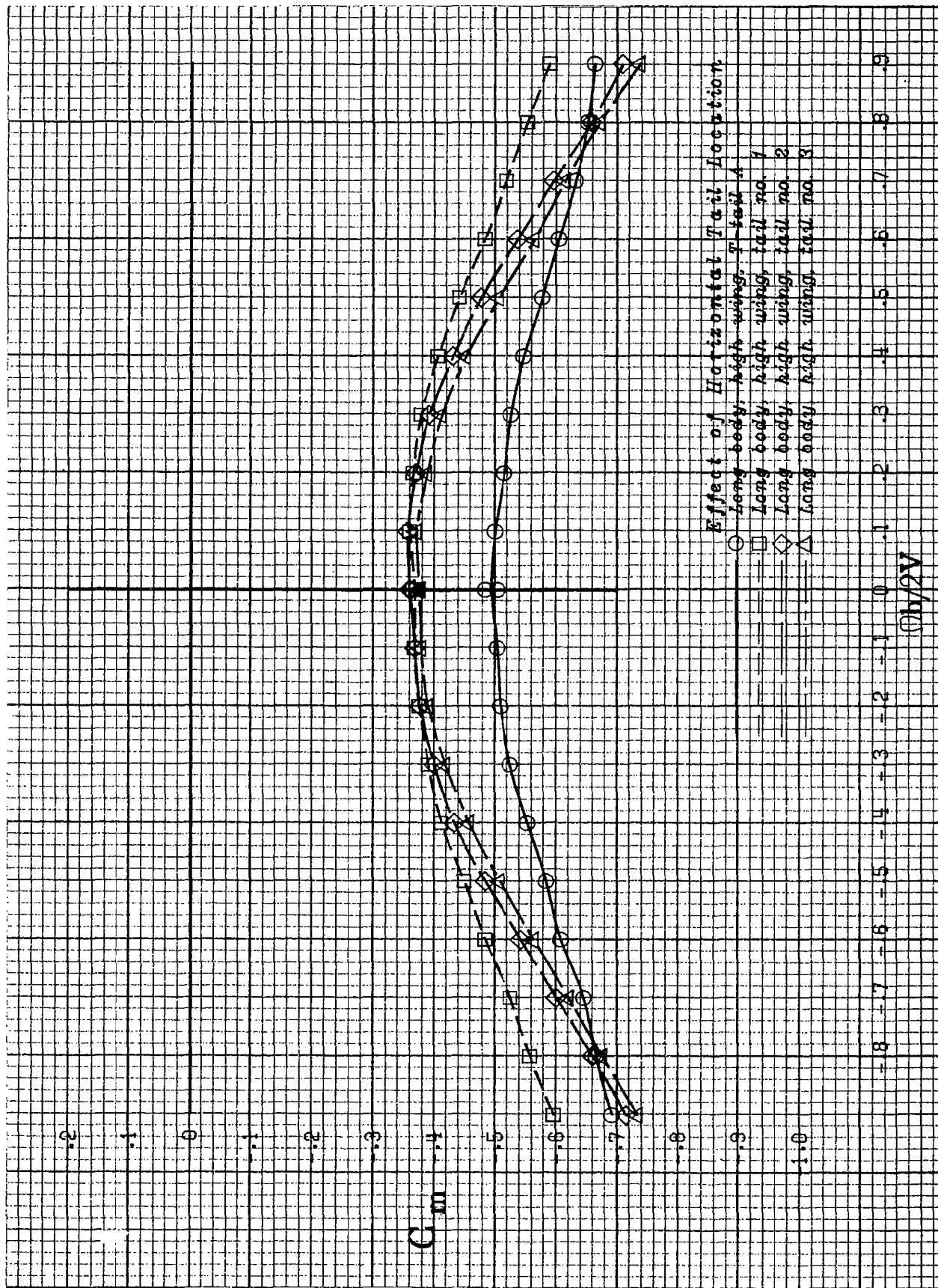
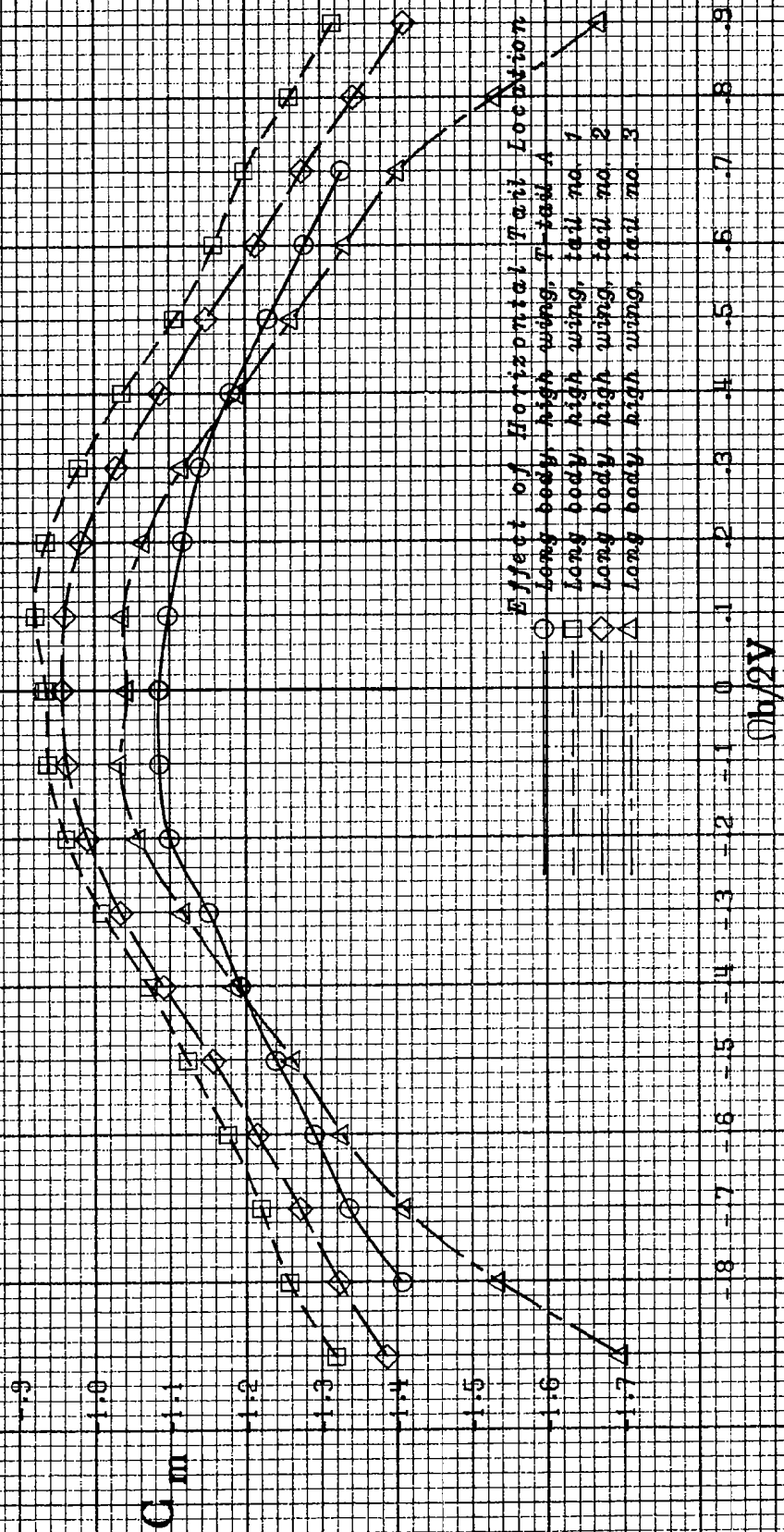


Figure 11.- Effect of T-tail location on the static pitching moment coefficient for the long body, low wing model D.



(a) 30° angle of attack.

Figure 12.- Effect of horizontal tail location on the pitching moment coefficient for the long body, high wing model D.



(b) 80° angle of attack.
Figure 12.- Concluded.

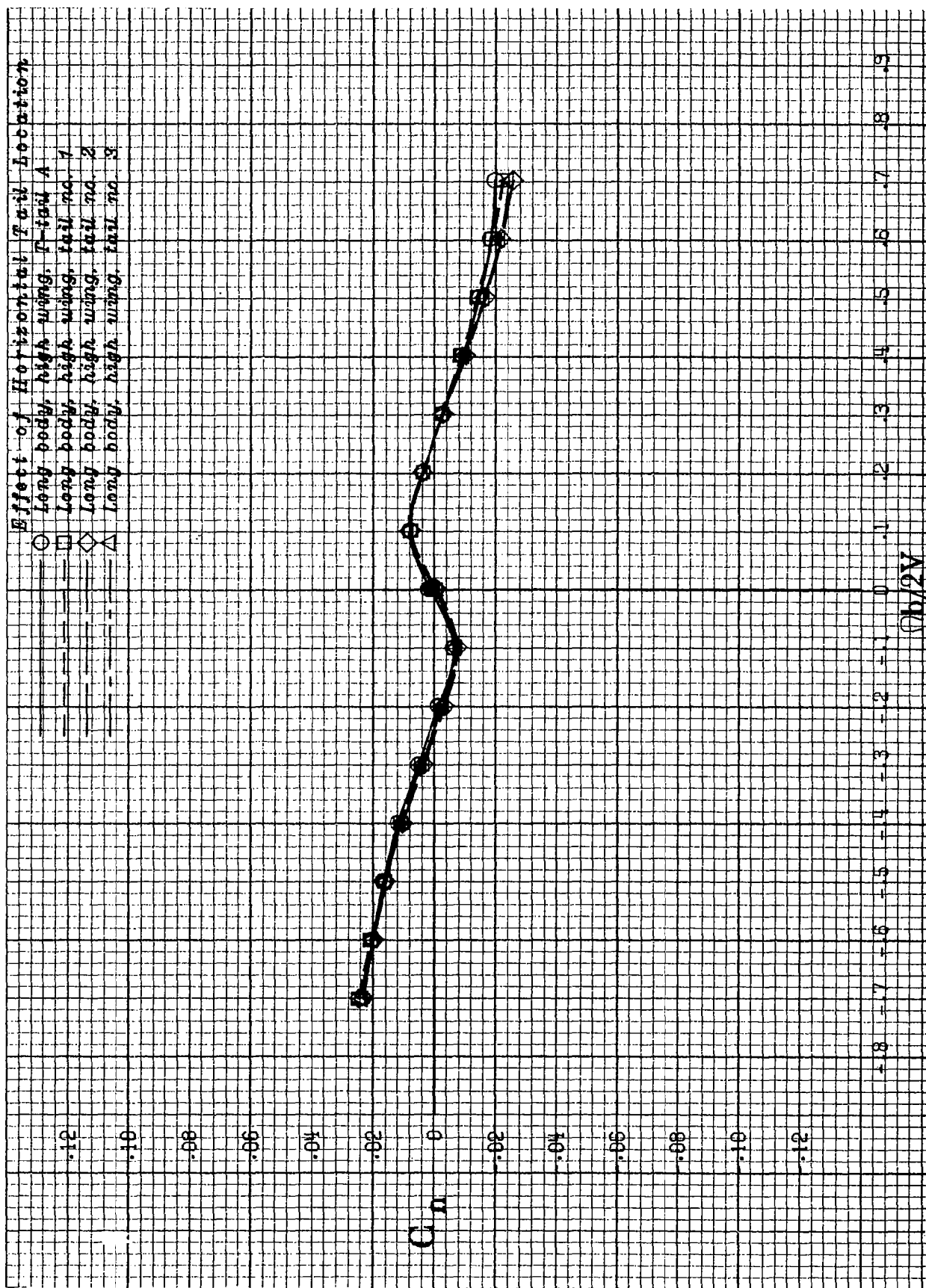


Figure 13.- Effect of horizontal tail location on yawing moment coefficient at 16° angle of attack for the long body, high wing model D.

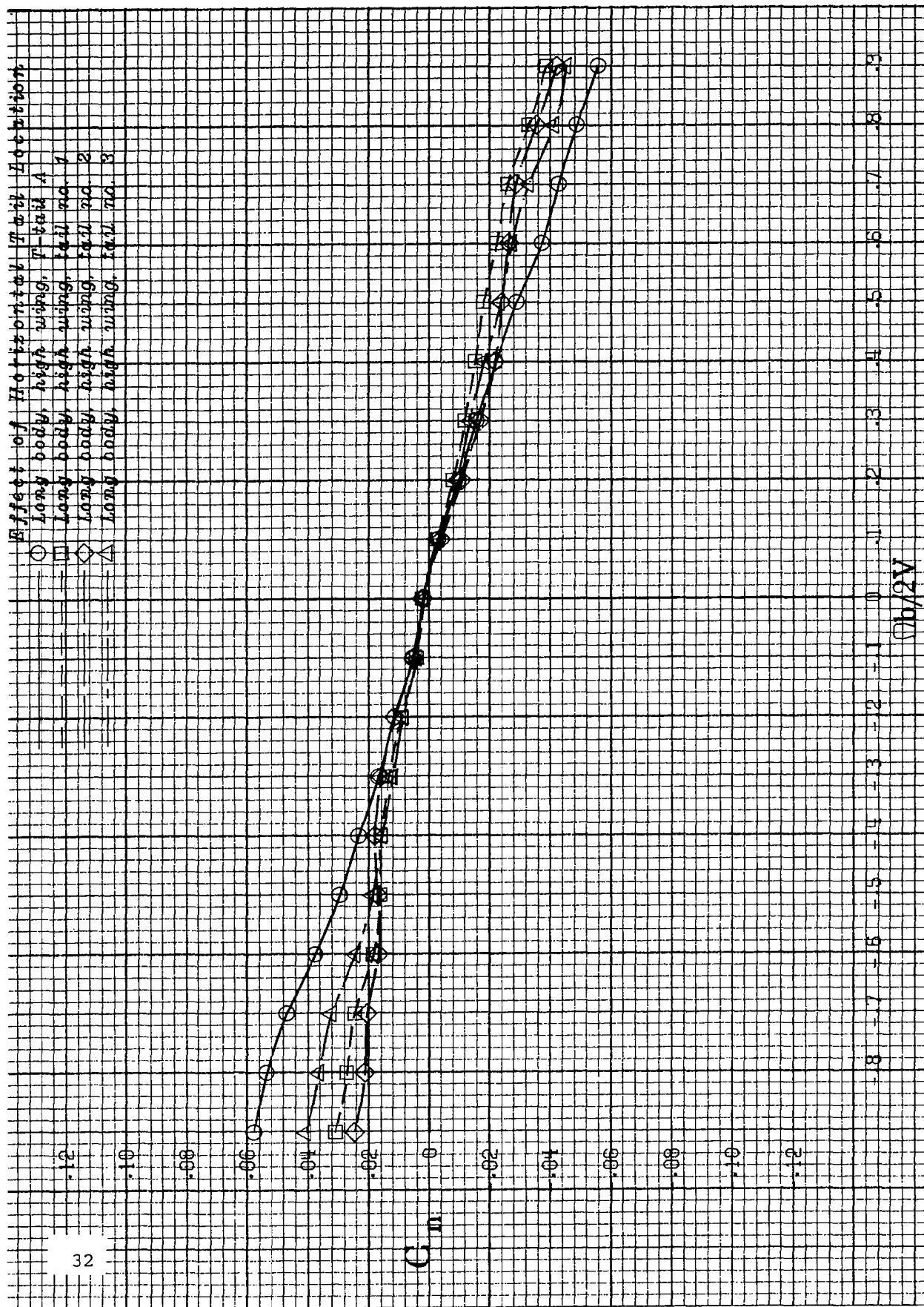
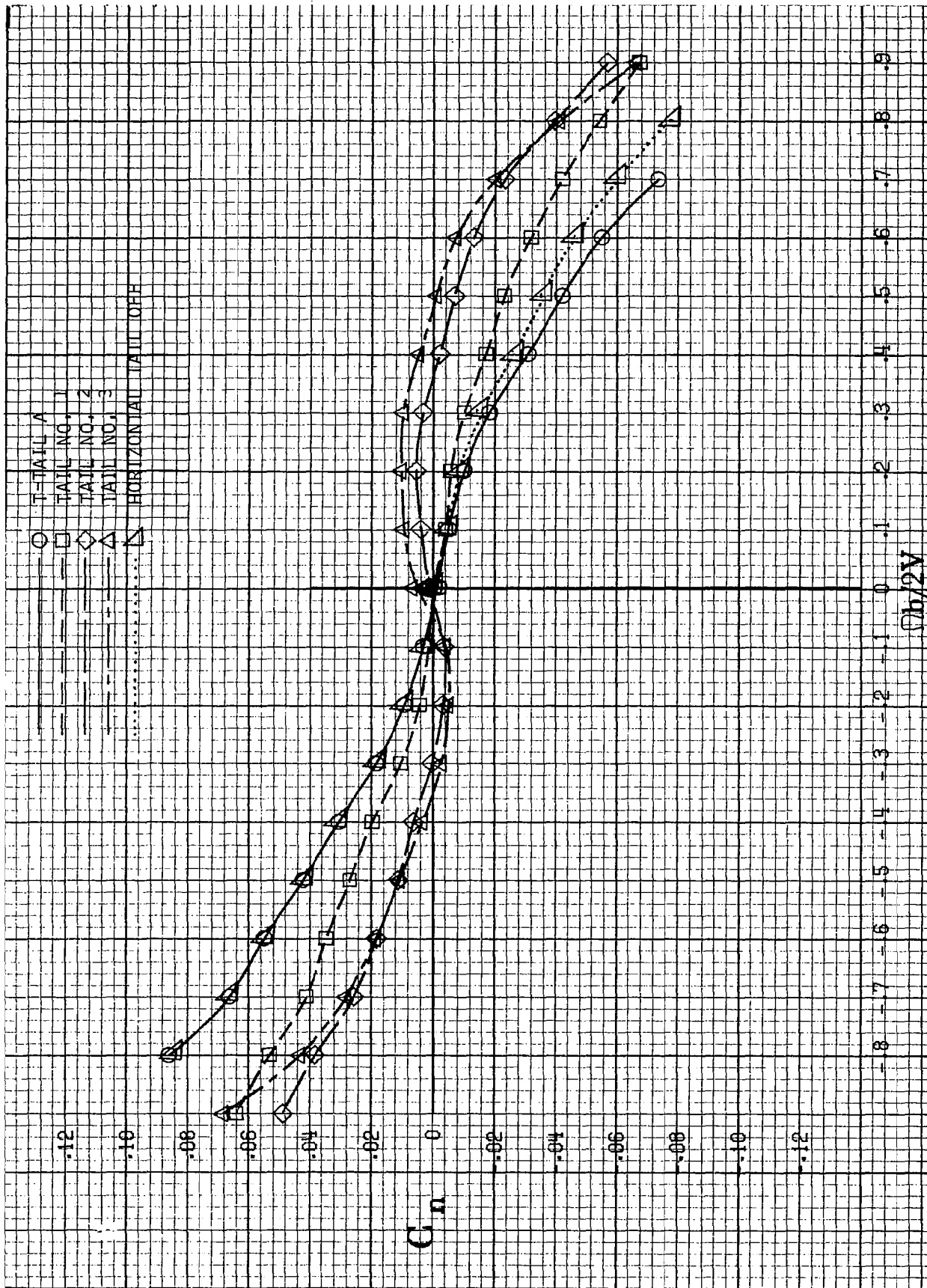
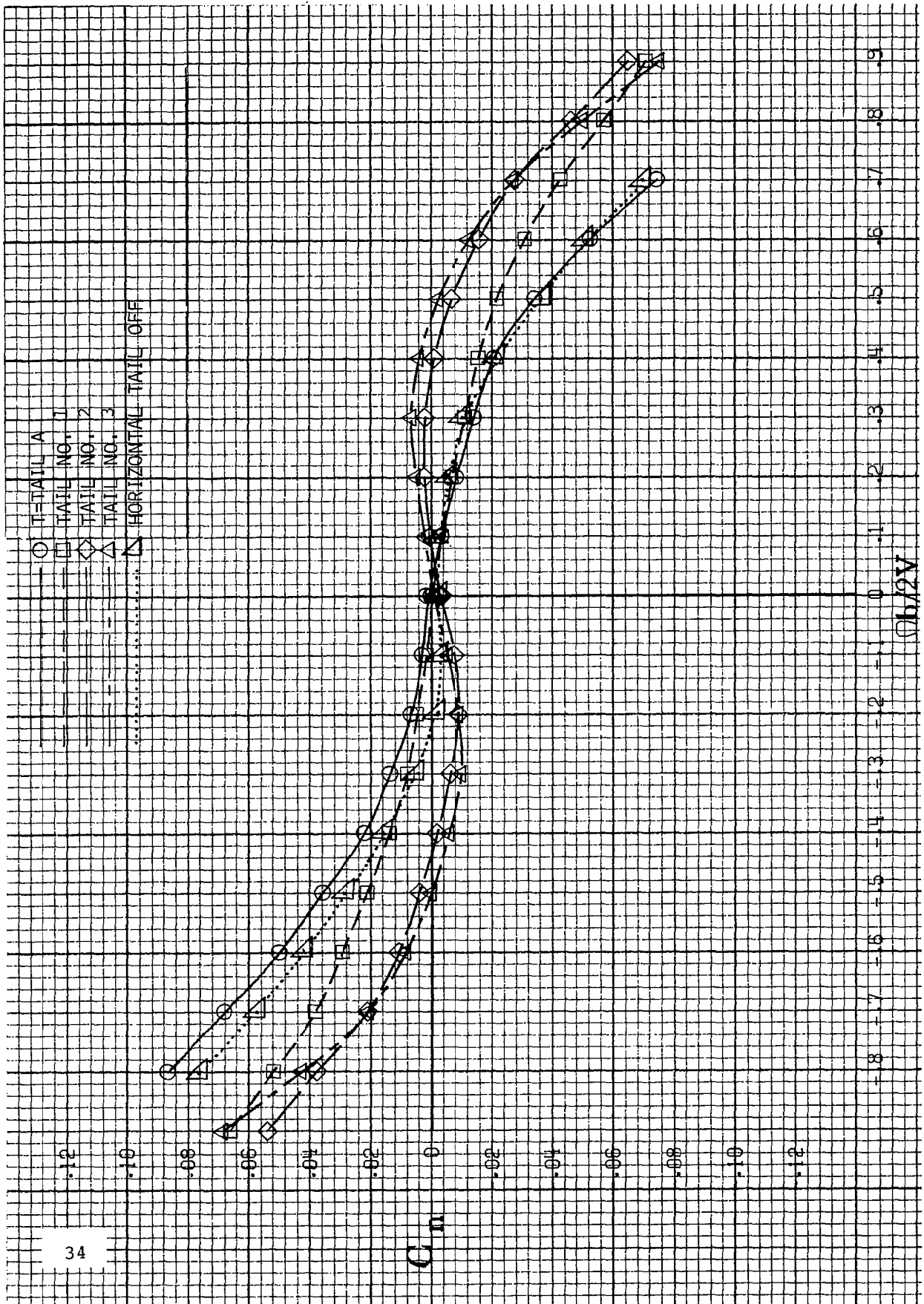


Figure 14.- Effect of horizontal tail location on the yawing moment coefficient at 400 angle of attack for the long body, high wing model D.



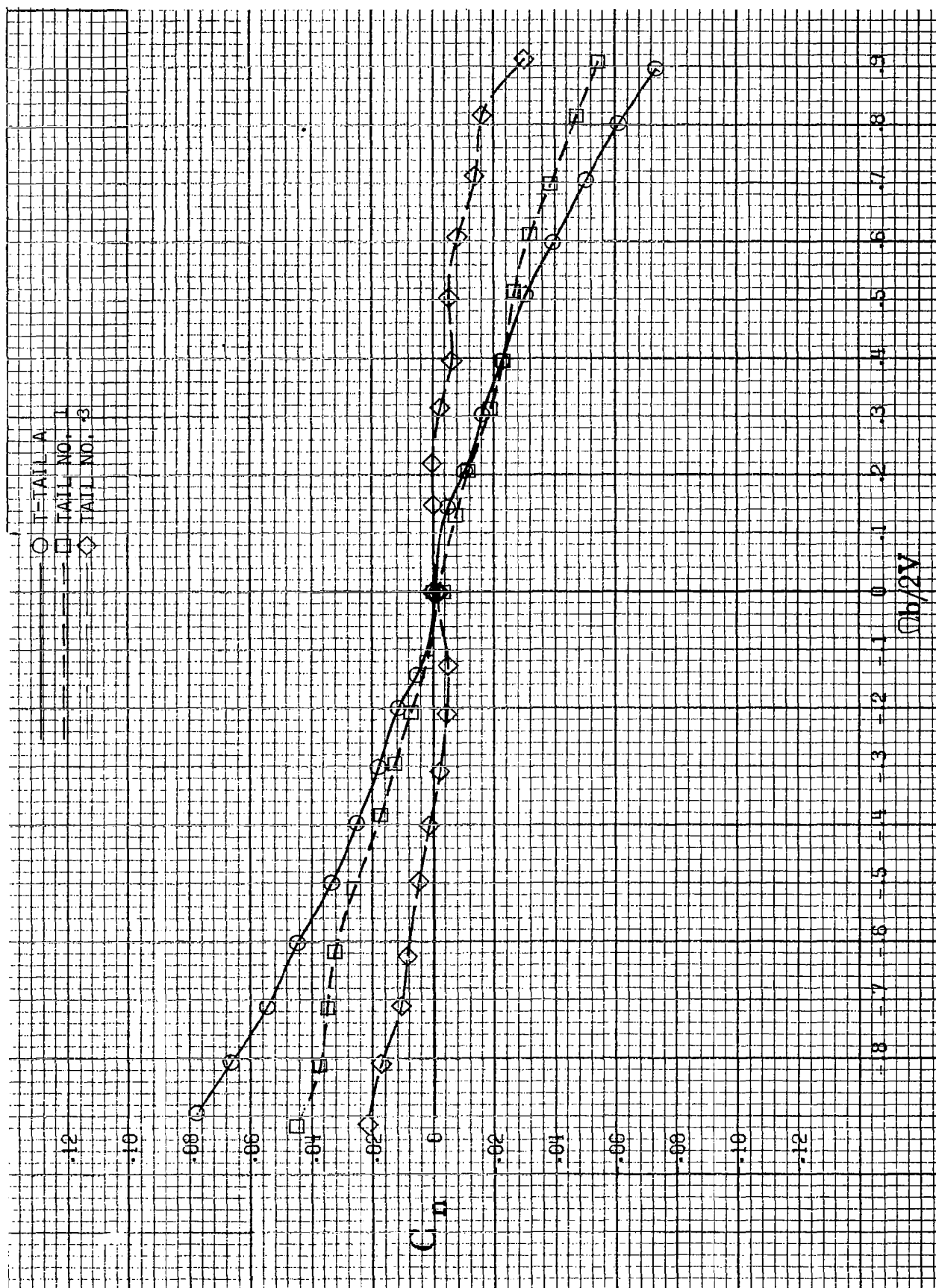
(a) Long body, low wing configuration.

Figure 15.- Effect of horizontal tail location on the yawing moment coefficient at 80° angle of attack for model D.



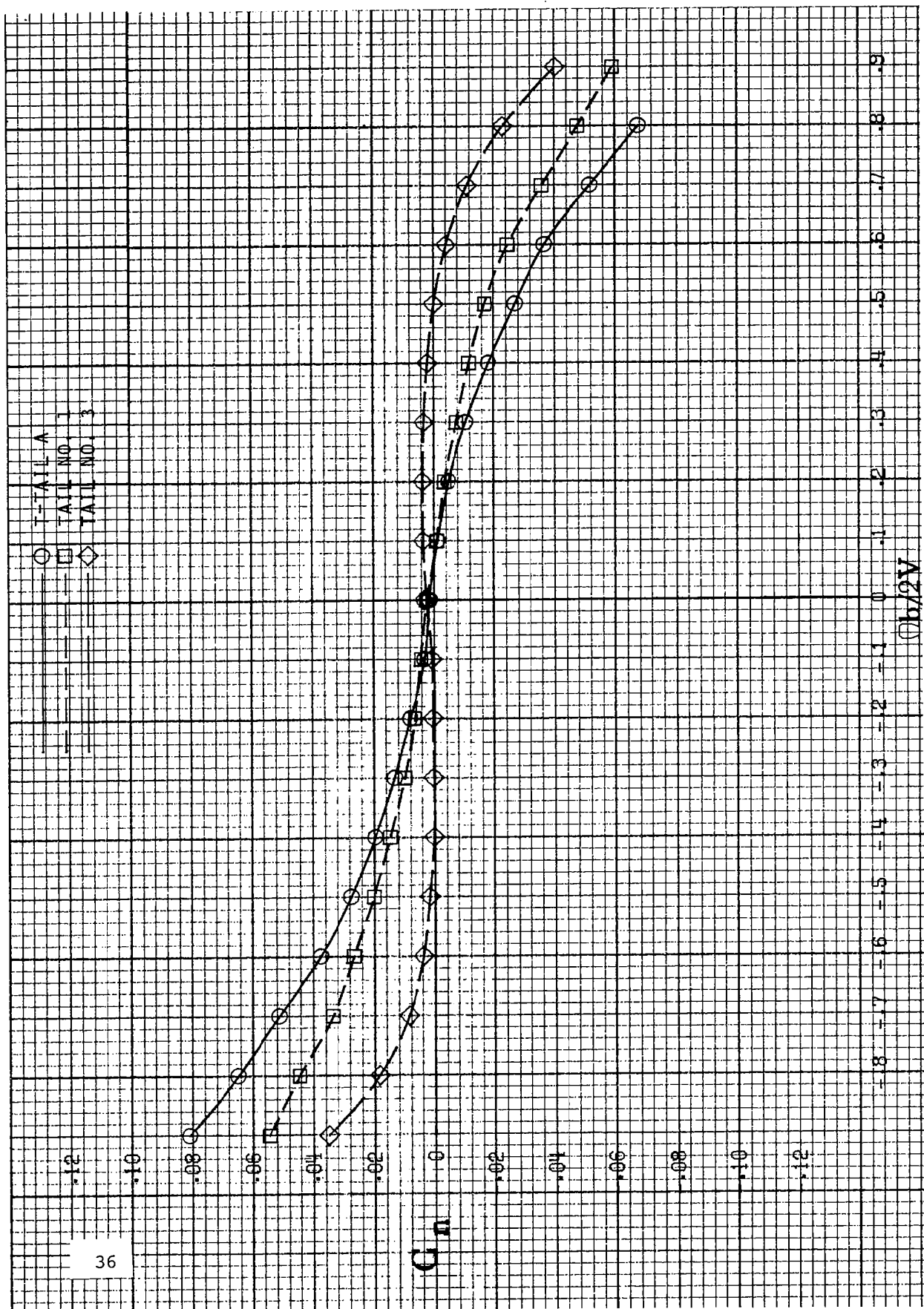
(b) Long body, high wing configuration.

Figure 15.- Continued.



(c) Short body, low wing configuration.

Figure 15.- Continued.



(d) Short body, high-wing configuration.

Figure 15.- Concluded.

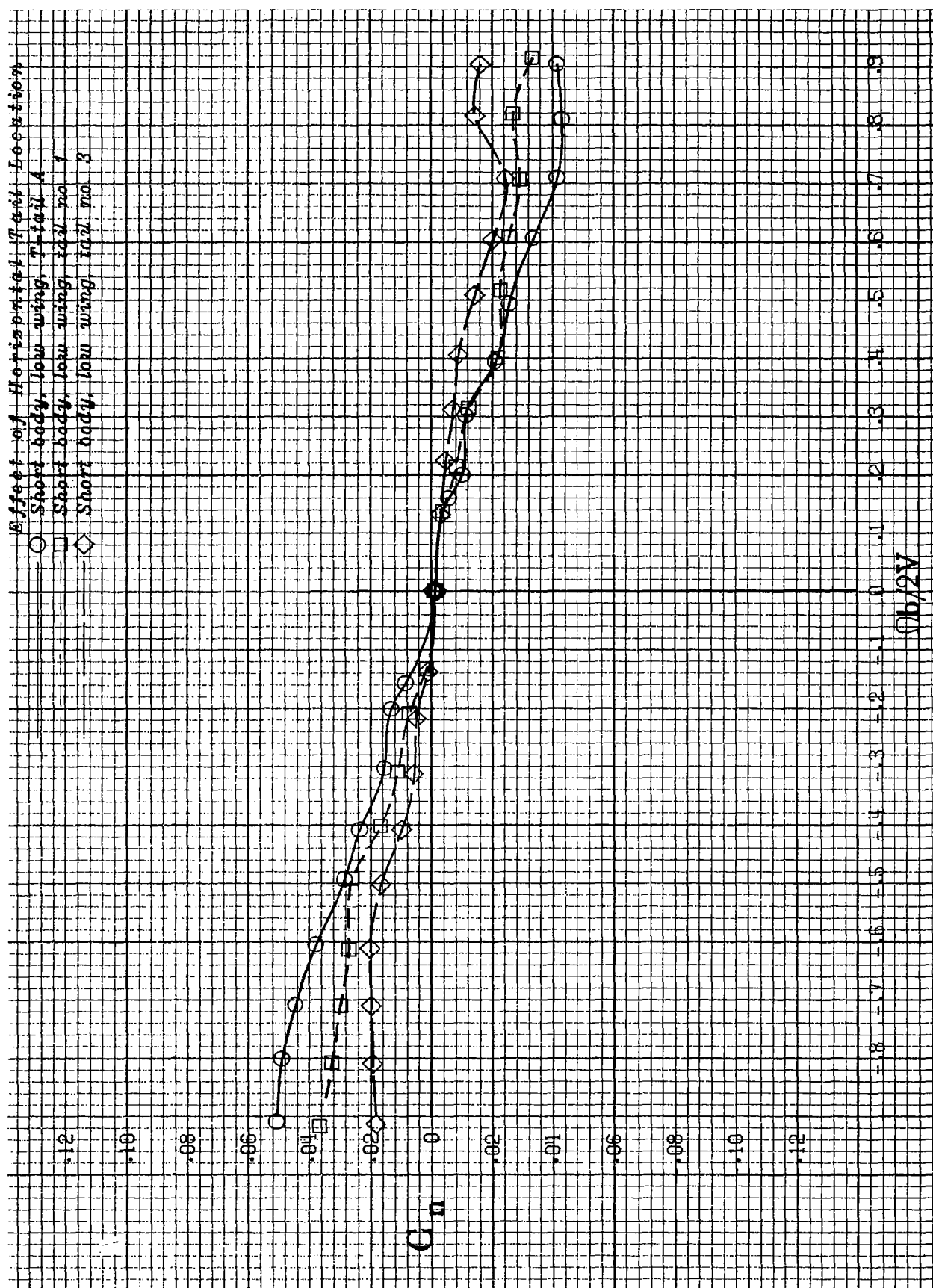


Figure 16.- Effect of horizontal tail location on the yawing moment coefficient at 60° angle of attack for the short body, low wing model D.

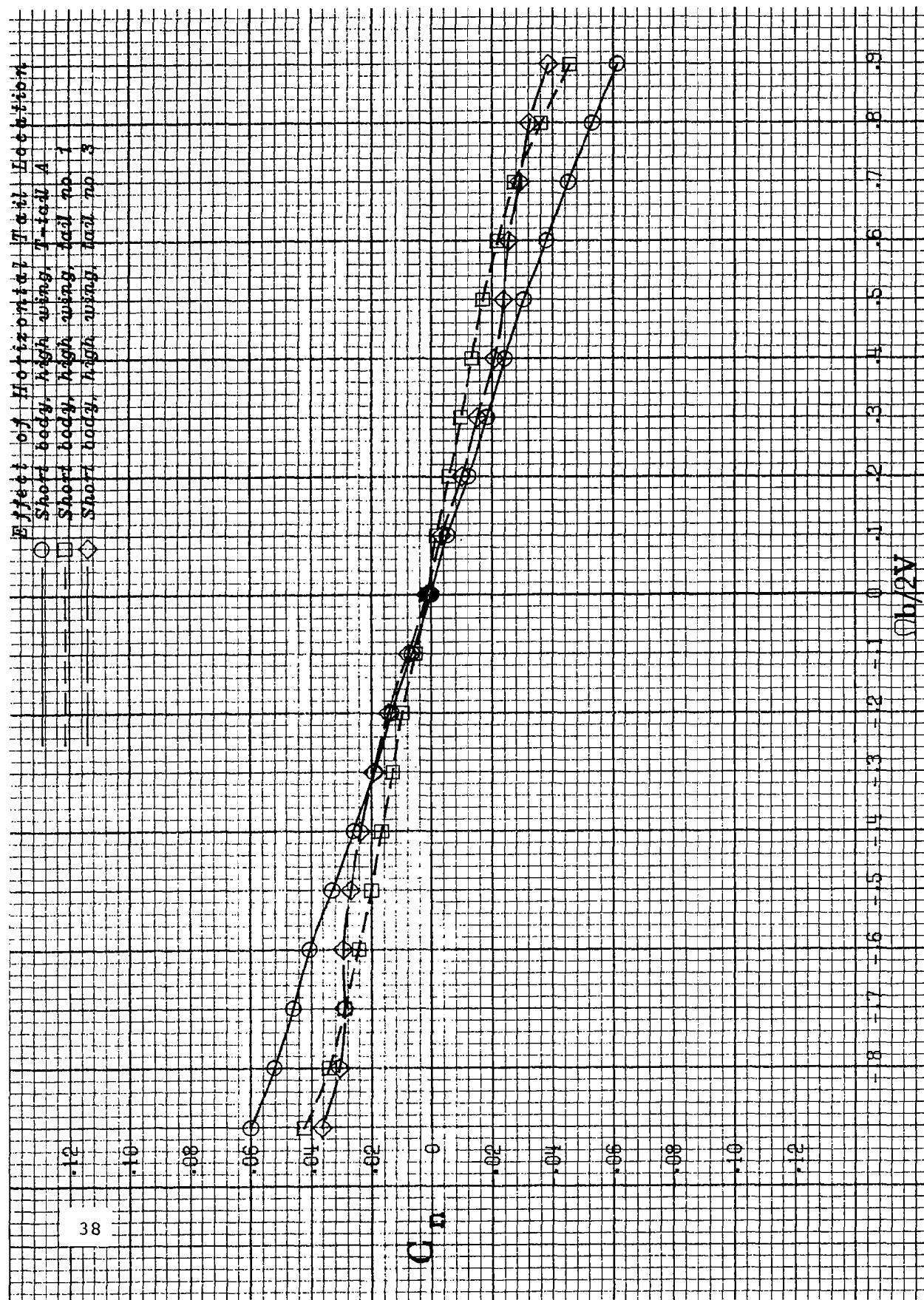
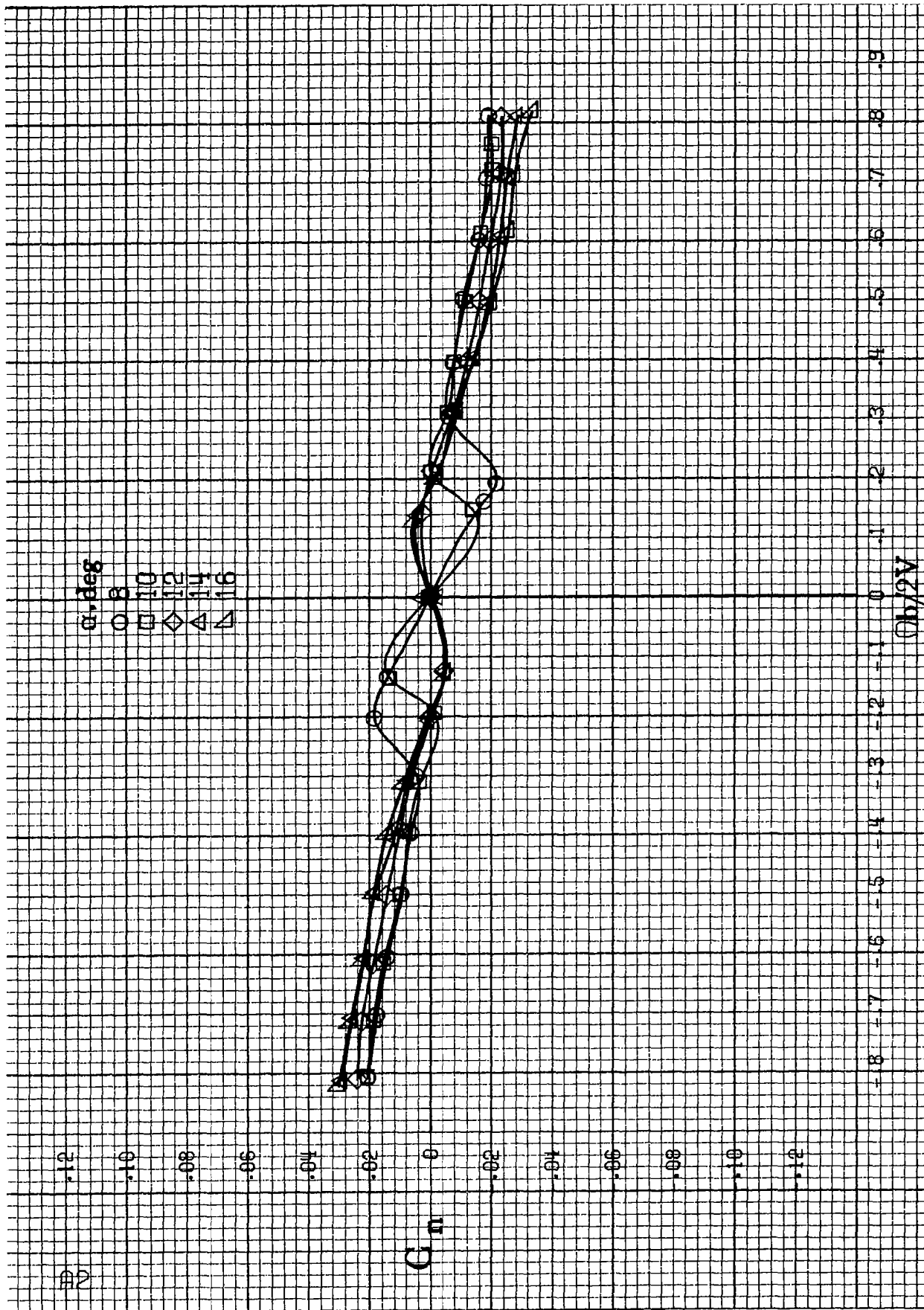


Figure 17.- Effect of horizontal tail location on the yawing moment coefficient at 60° angle of attack for the short body, high wing model D.

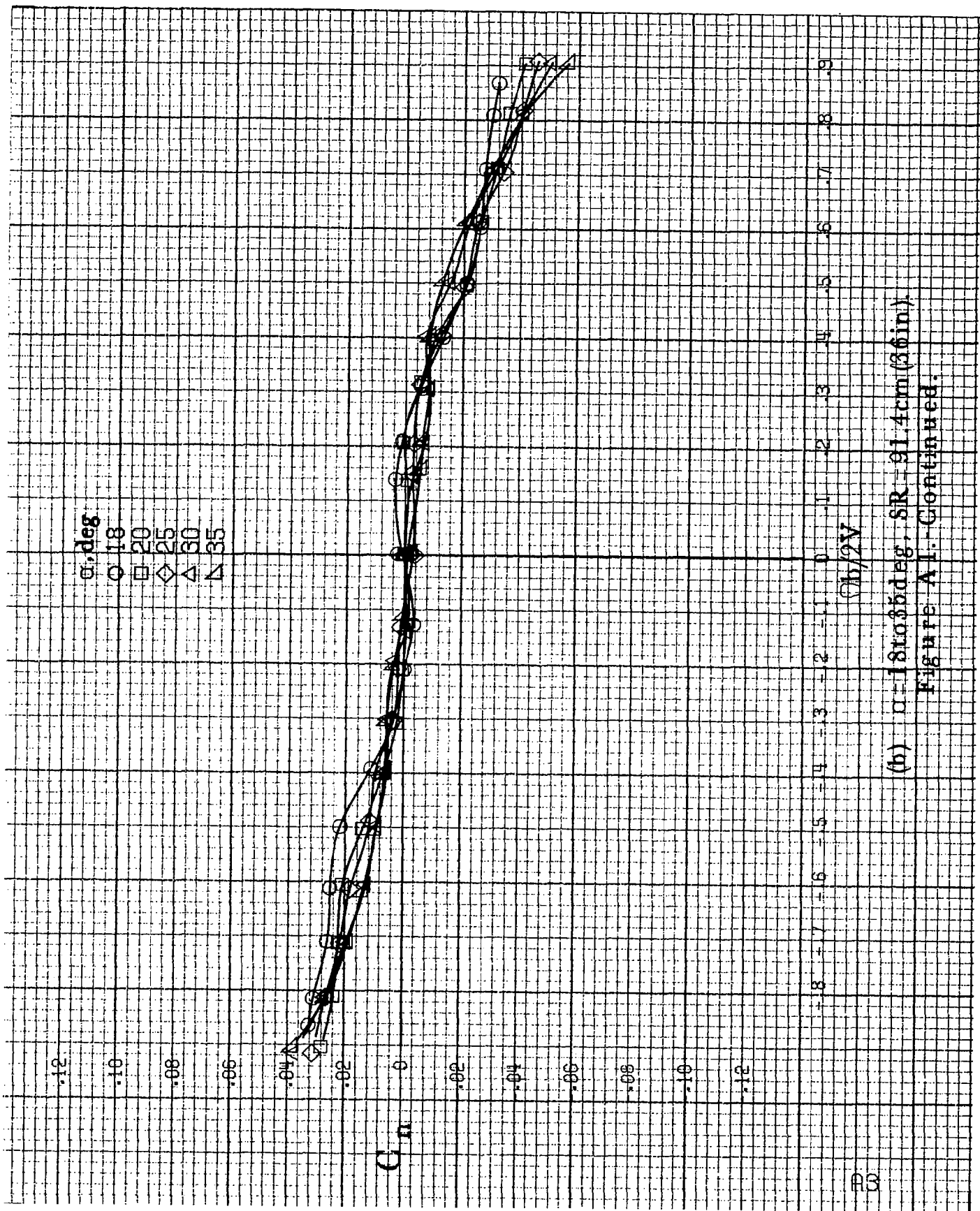
APPENDIX



(a) $\alpha = 8$ to 16° , $SR = 91.4 \text{ cm (36 in)}$.

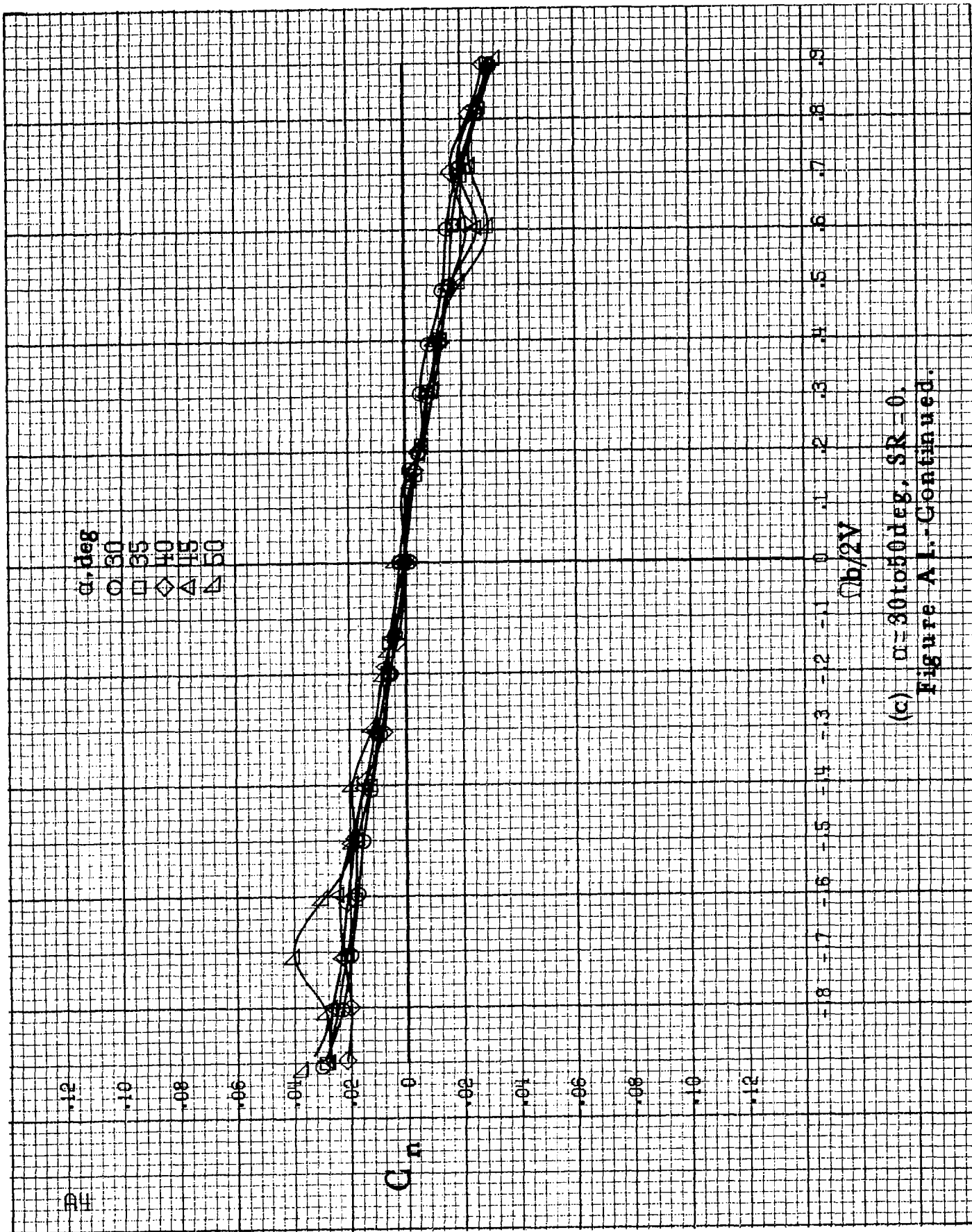
$\Omega/2V$

Figure A1. Effect of rotation rate and angle of attack on yawing-moment coefficient for short body, low wing, horizontal T-tail A configuration. $\delta_a = 0^\circ$, $\delta_r = 0^\circ$, $\beta = 0^\circ$.

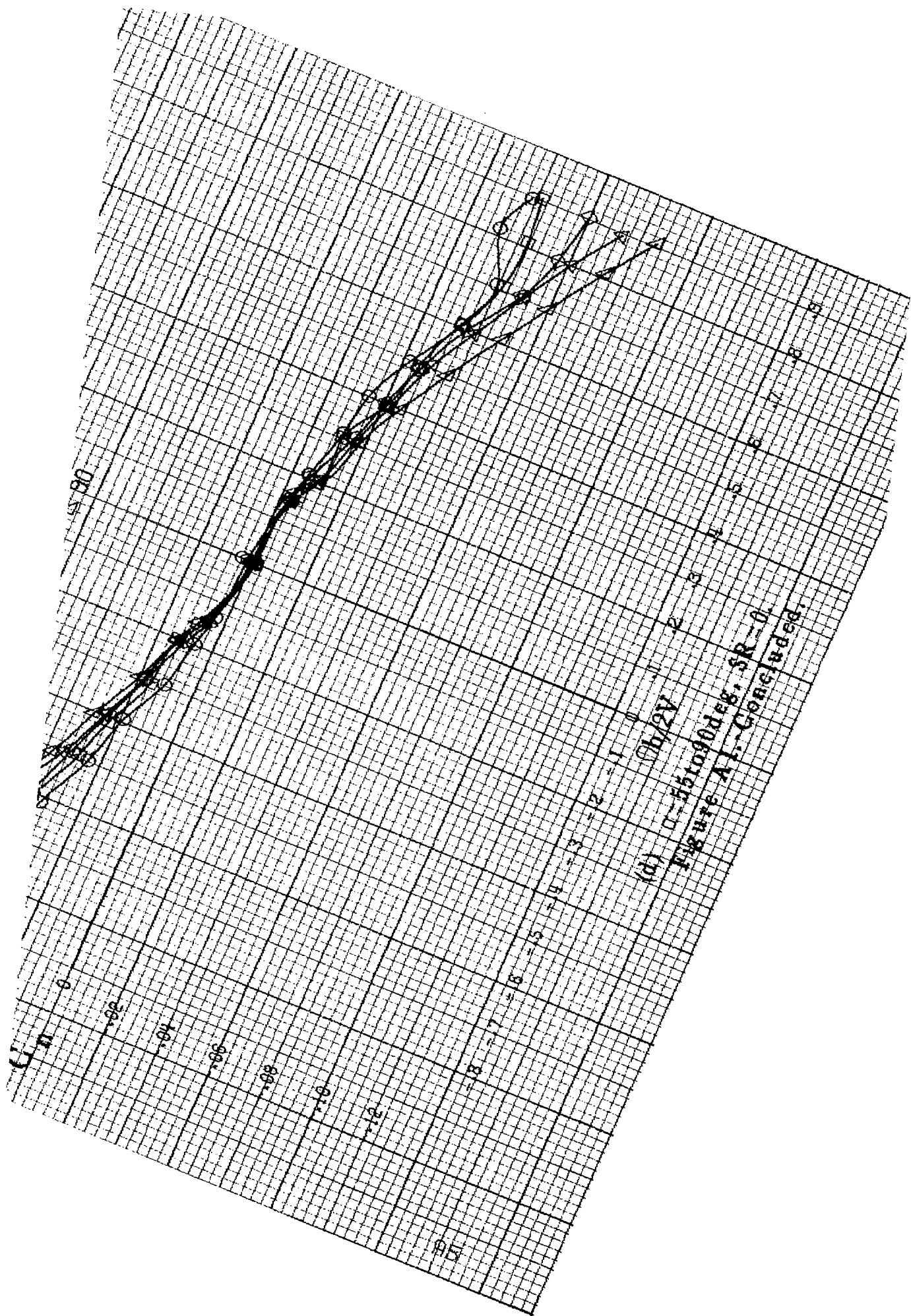


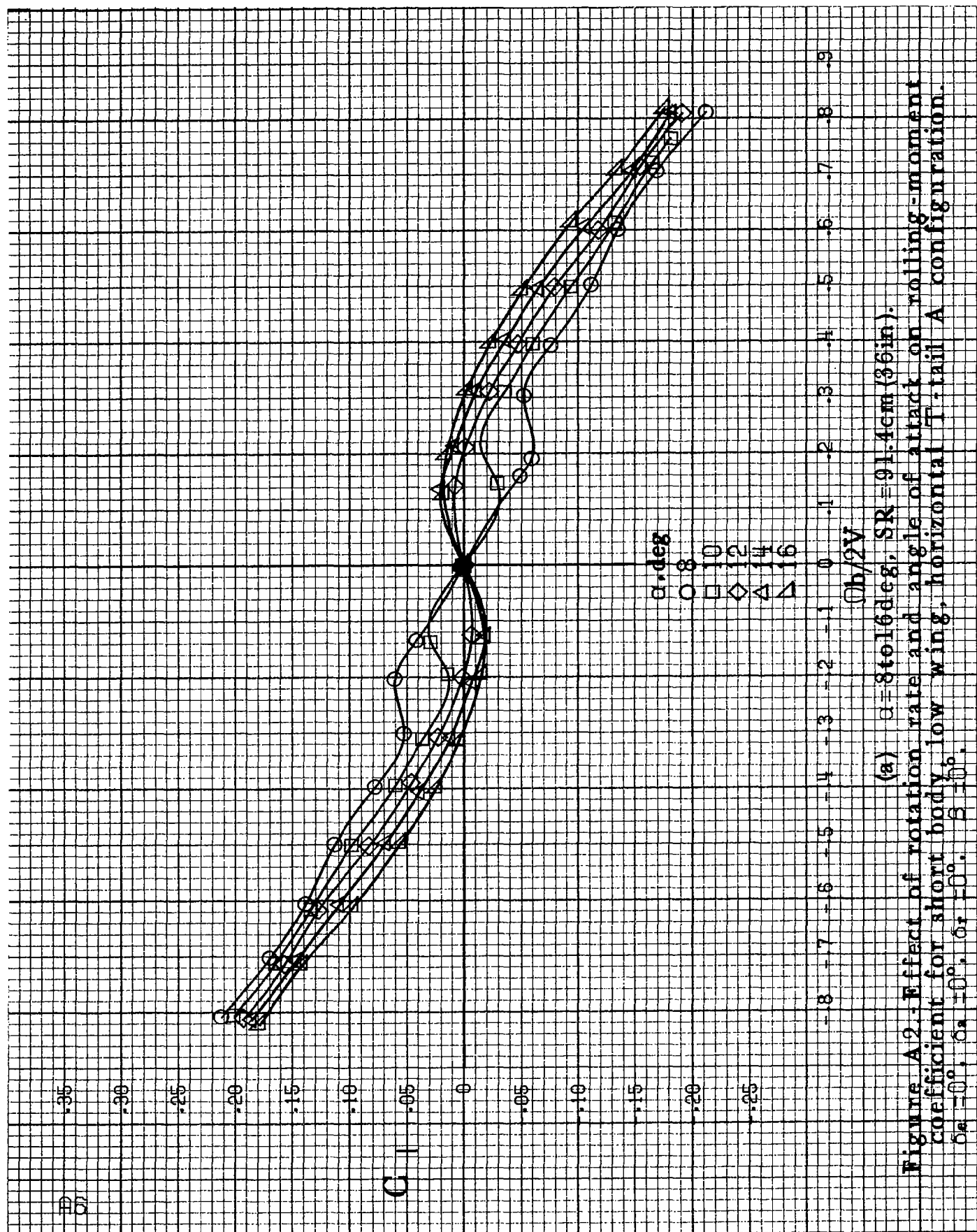
(b) $\alpha=18$ to 35 deg, $SR=91.4$ cm (36 in).

Figure A1. Continued.



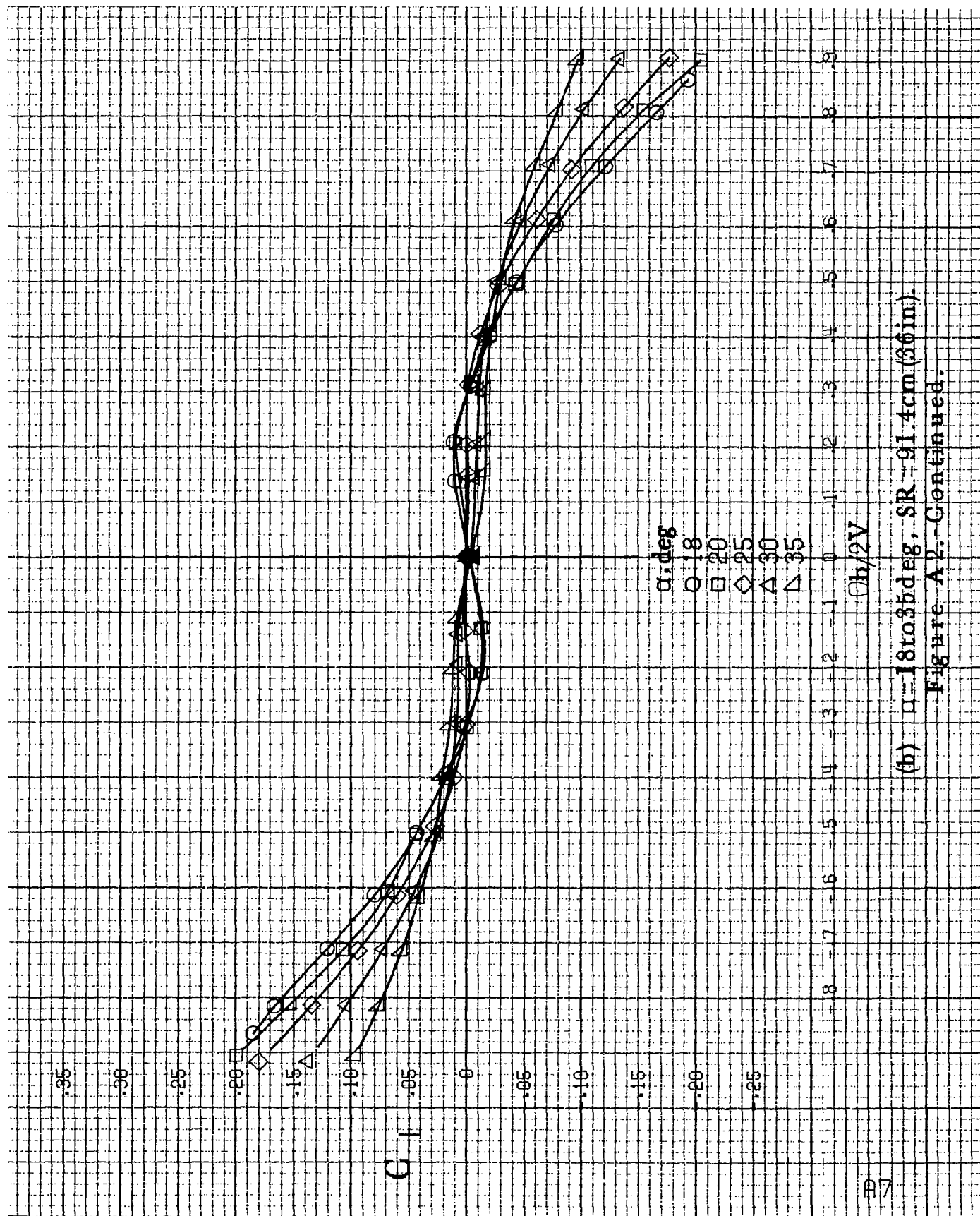
(c) $\alpha = 30$ to 50° , $SR = 0$.
Figure A I.-Continued.





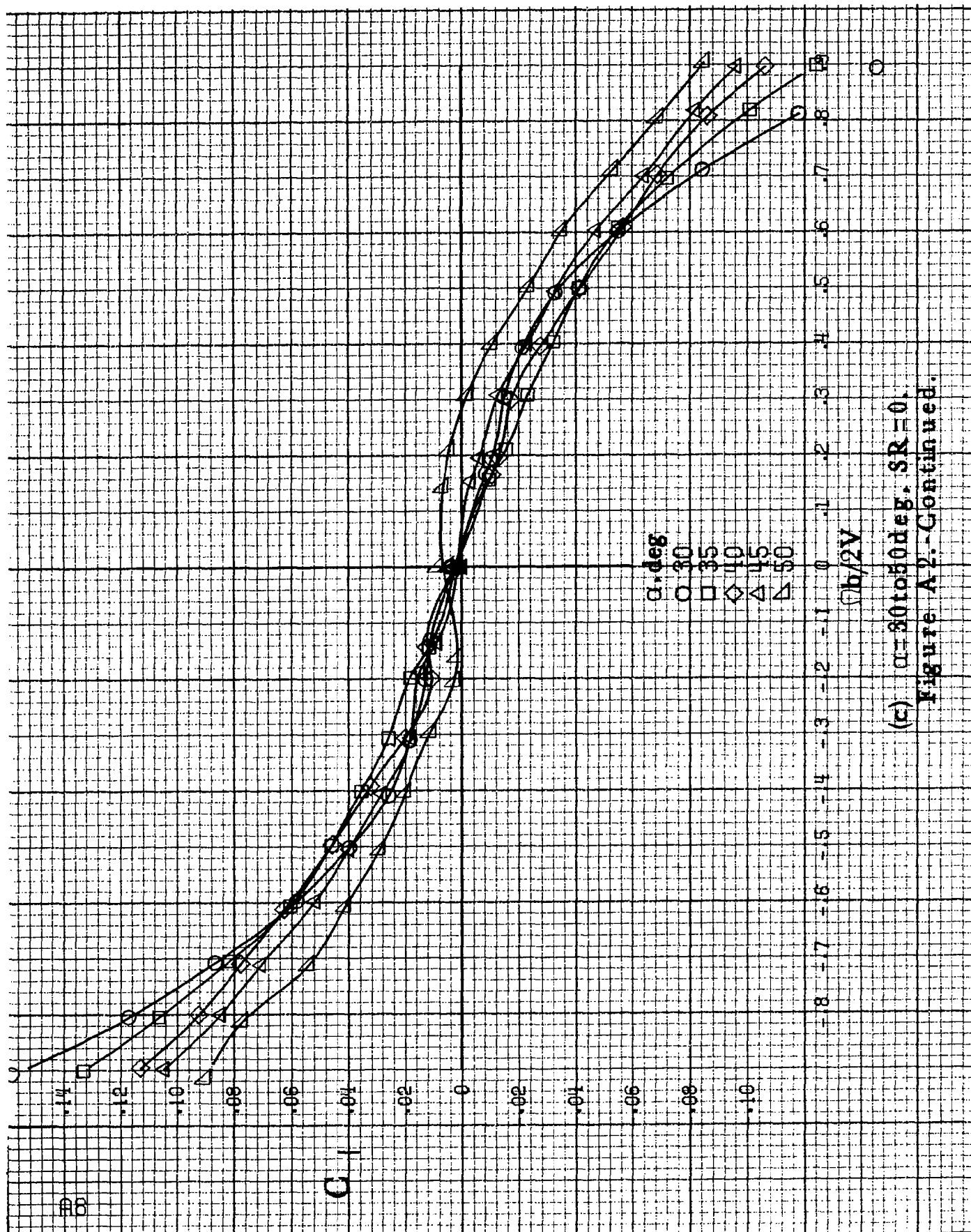
(a) $\alpha=8$ to 16 deg, $SR=91.4$ cm (36 in).

Figure A2.-Effect of rotation rate and angle of attack on rolling-moment coefficient for short body, low wing, horizontal T-tail A configuration. $\delta_a=0^\circ$, $\delta_s=0^\circ$, $\delta_r=0^\circ$, $\beta=10^\circ$.

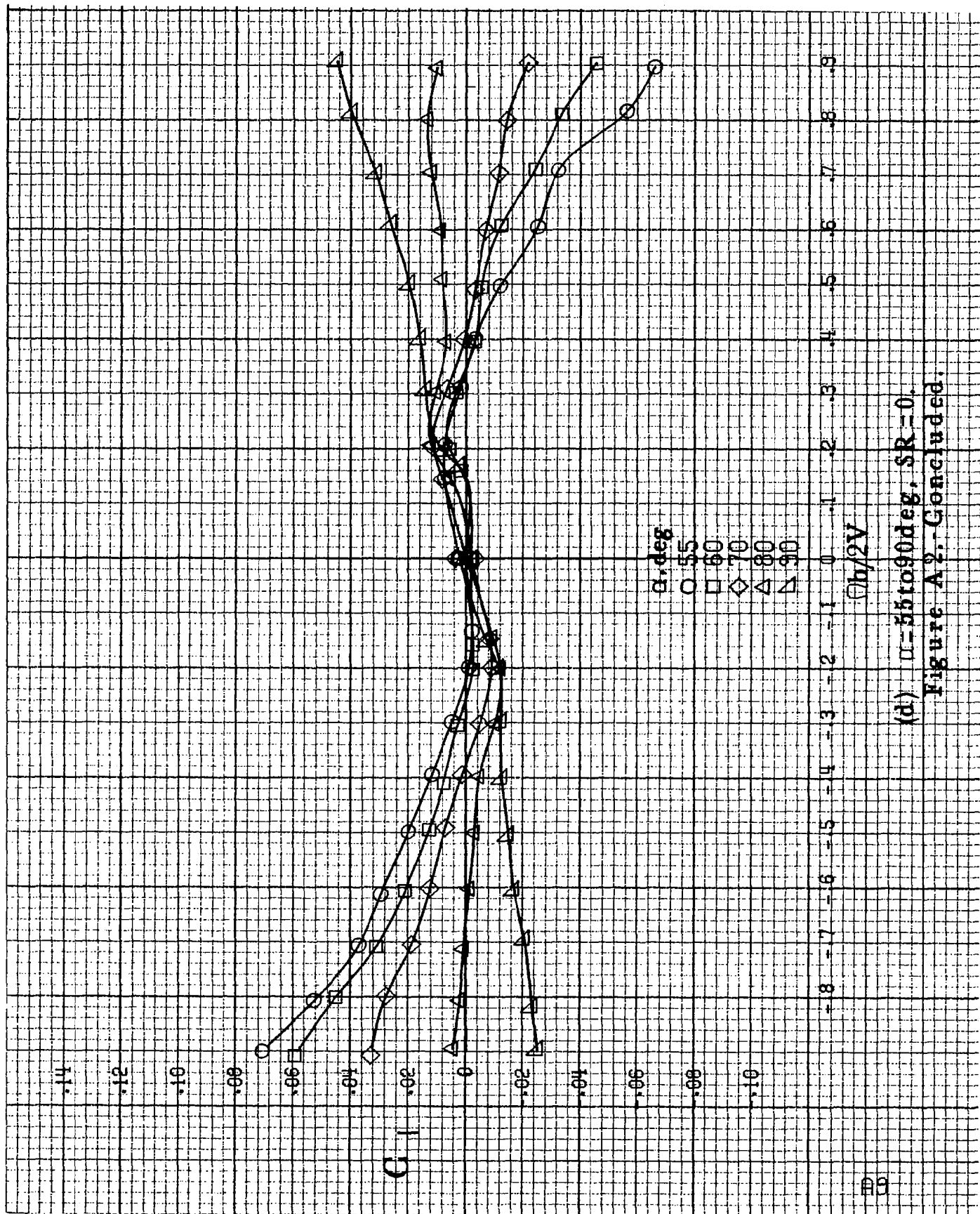


(b) $\alpha=18$ to 35° , $SR=91.4\text{cm}$ (36in).

Figure A 2.-Continued.



(c) $\alpha = 30$ to 50 deg., $SR = 0$.
Figure A 2.-Continued.



(d) $\alpha = 55$ to 90° , $SR = 0$.
Figure A2.-Concluded.

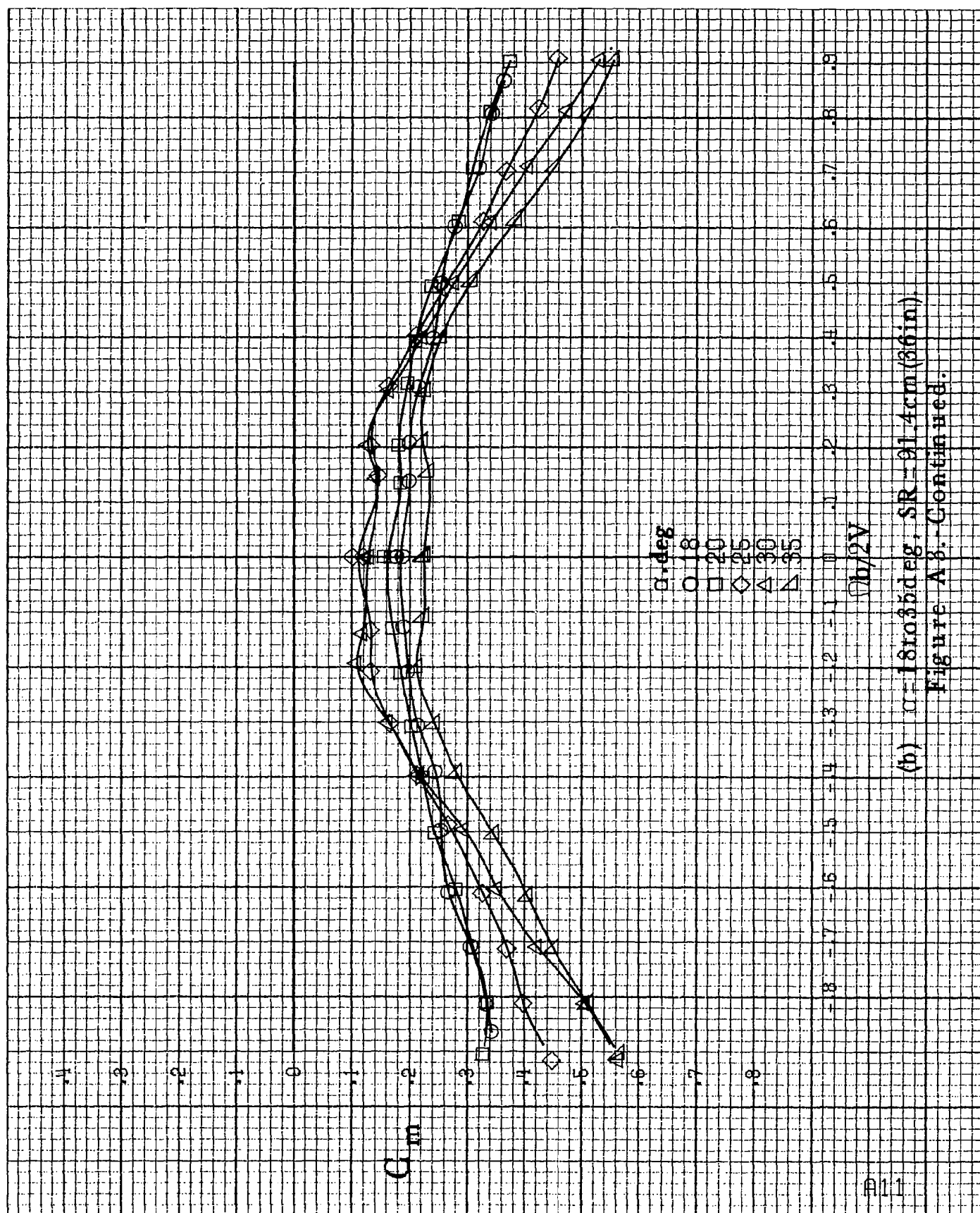
C_m

α, deg
 $\circ 8$
 $\square 10$
 $\diamond 12$
 $\triangle 14$
 $\nabla 16$

$\Omega b/2V$

(a) $\alpha = 8 \text{ to } 16 \text{ deg}$, $SR = 91.4 \text{ cm (36 in.)}$.

Figure A.3: Effect of rotation rate and angle of attack on pitching-moment coefficient for short body, low wing, horizontal T-tail A configuration. $\delta_e = 0^\circ$, $\delta_s = 0^\circ$, $\delta_r = 0^\circ$, $\beta = 0^\circ$.



(b) $\alpha = 18$ to 35 deg. SR = 91.4 cm (36 in).
Figure A 3. - Continued.

G_m

α, deg

○ 30

□ 35

◇ 40

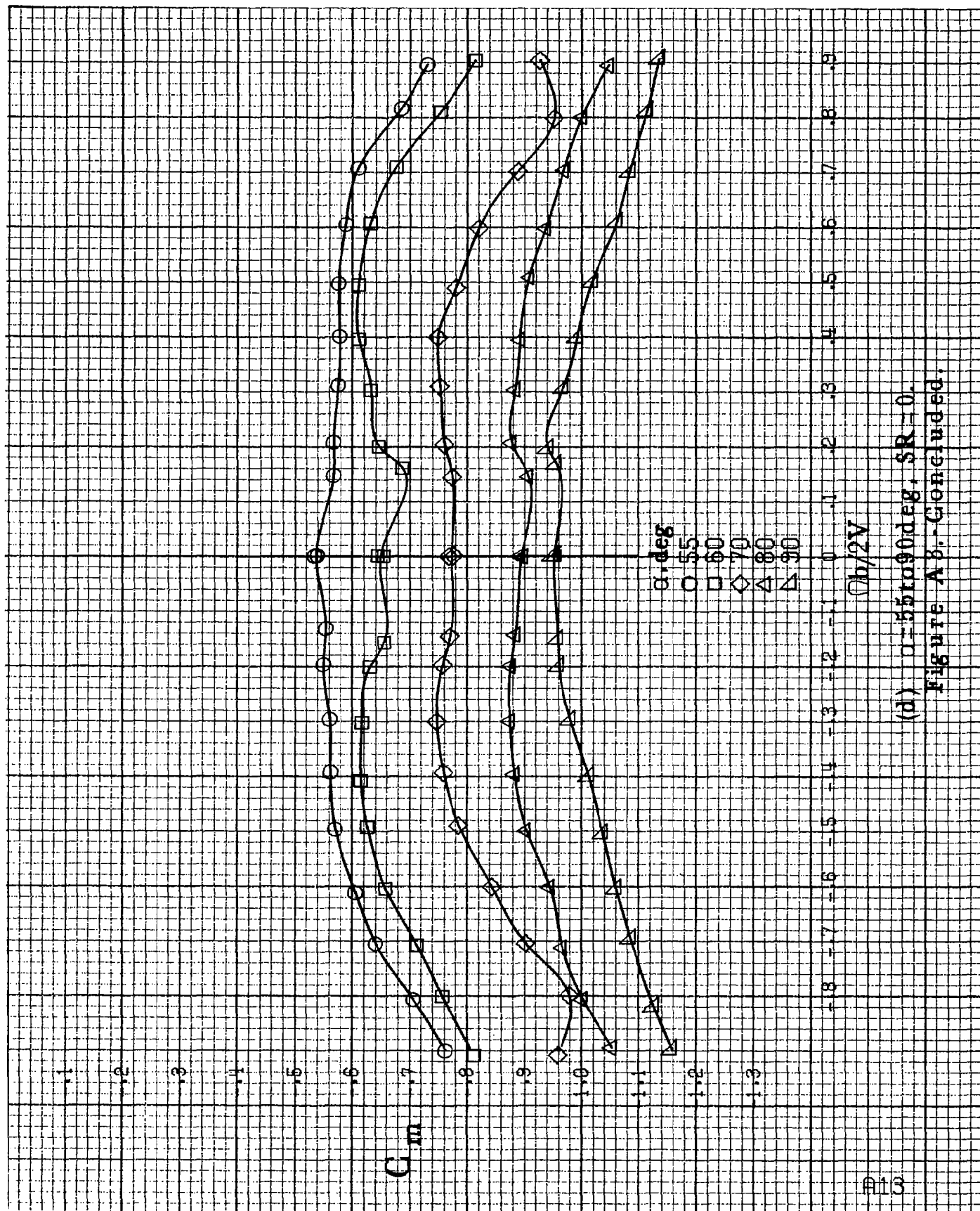
△ 45

▽ 50

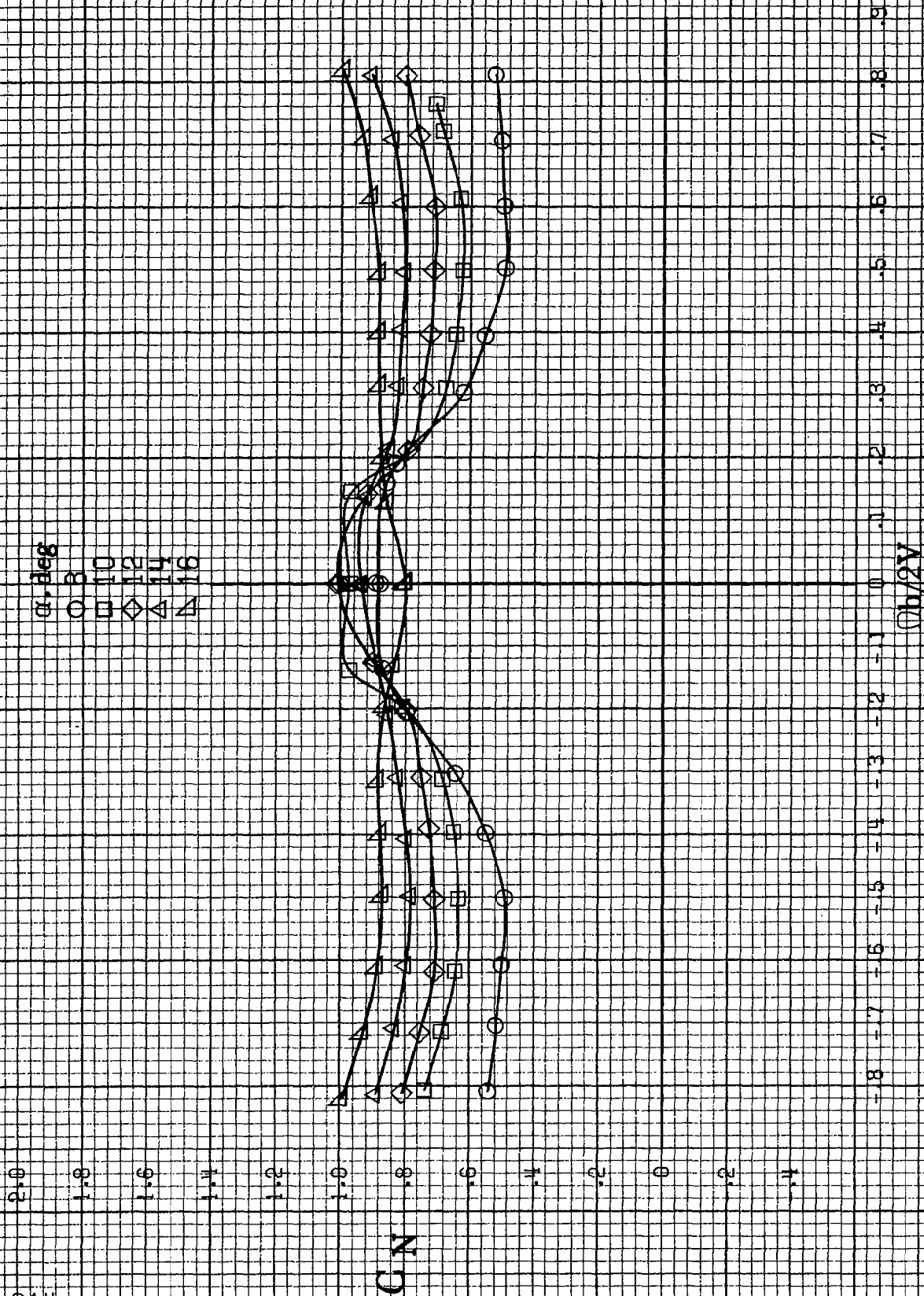
$\mu h/2V$

(c) $\alpha = 30 \text{ to } 50 \text{ deg}, SR = 0$

Figure A3. Continued.



(d) $\alpha=55$ to 90° , $SR=0$.
Figure A 8.- Concluded.



(a) $\alpha = 8$ to 16° , $SR = 91.4 \text{ cm (36 in.)}$.
 Figure A.4. Effect of rotation rate and angle of attack on normal-force coefficient for short body, low wing, horizontal T-tail A configuration.
 $\delta_e = 0^\circ$, $\delta_s = 0^\circ$, $\delta_r = 0^\circ$, $\beta = 0^\circ$.

α, deg
 ○ 18
 □ 20
 ◇ 25
 △ 30
 ▲ 35

C/N

$\phi_b/2V$

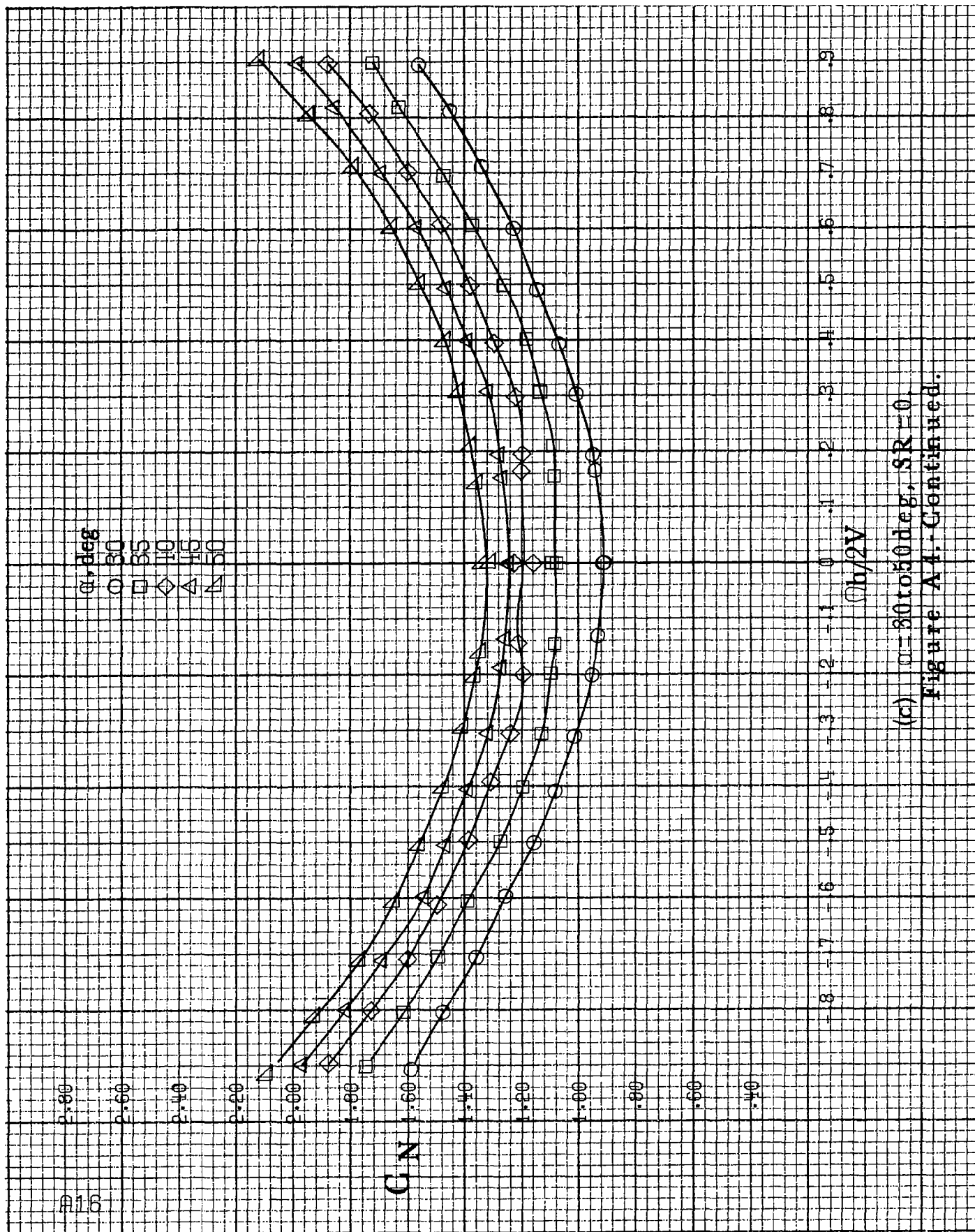
(b) $\alpha=18$ to 35 deg, SR = 91.4 cm (36 in).
 Figure A4.-Continued.

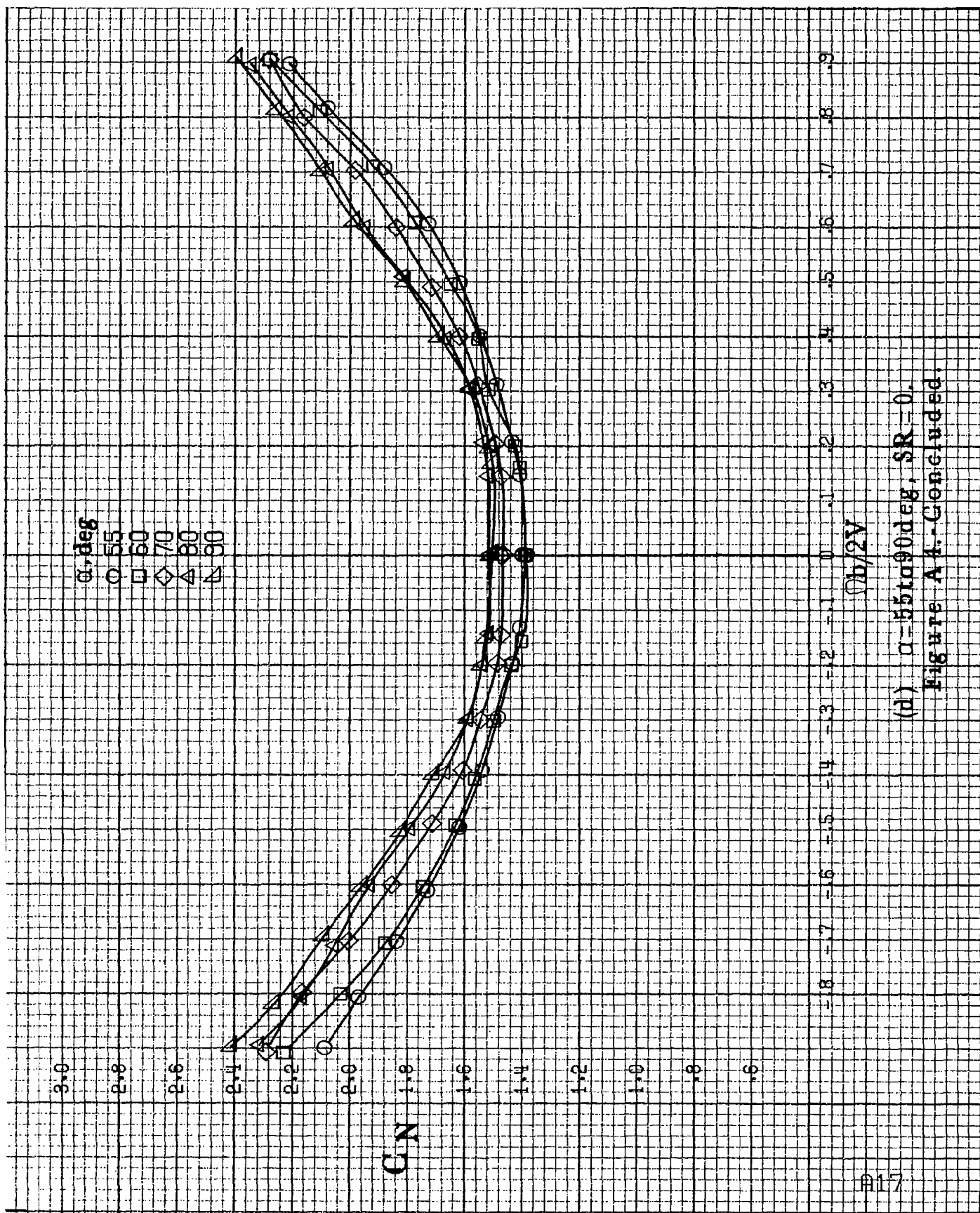
α, deg
 O 30
 □ 35
 ◇ 40
 △ 45
 ▽ 50

CN

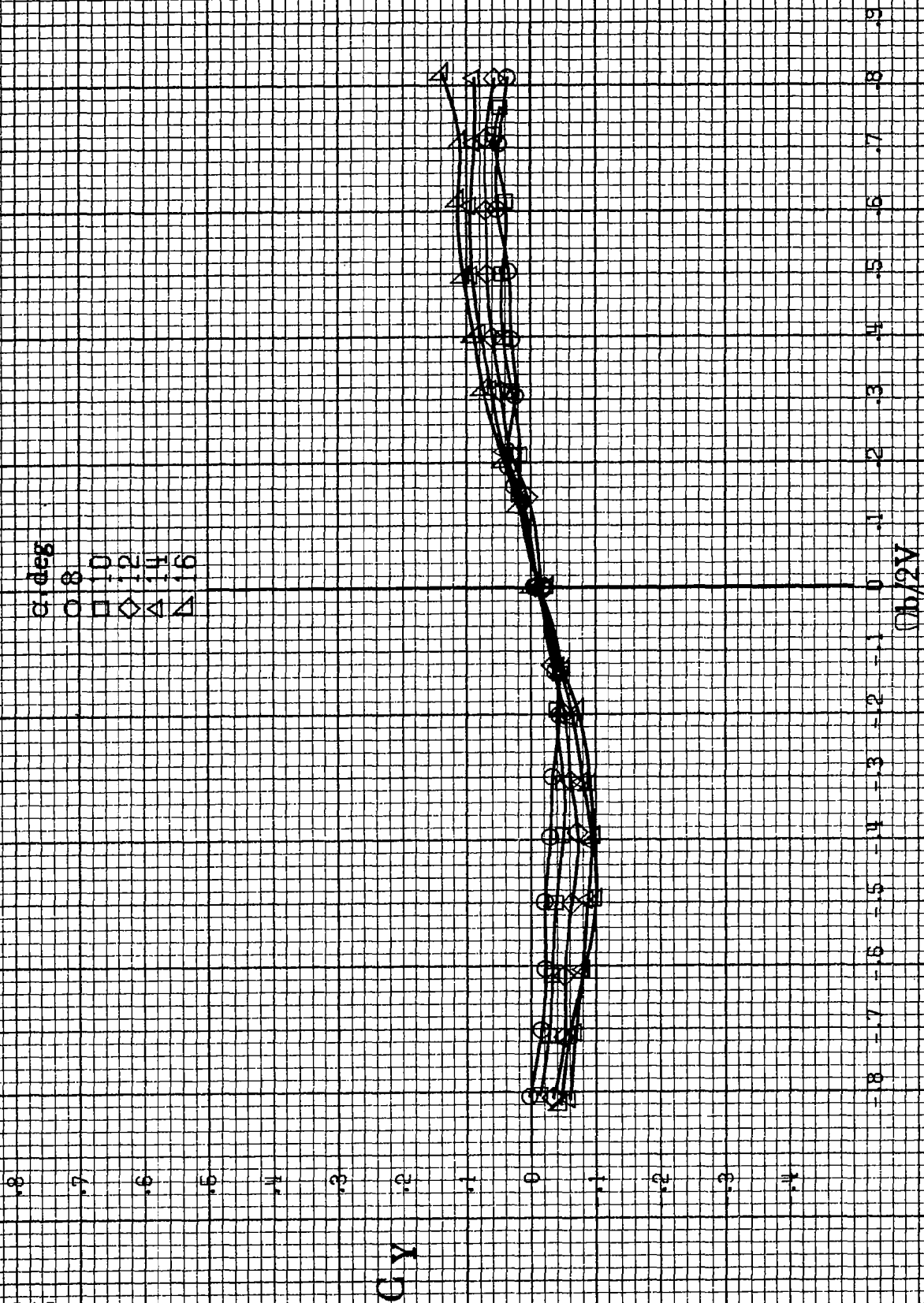
$\phi h/2V$

(c) $\alpha=30$ to 50 deg, $SR=0$.
 Figure A4.-Continued.



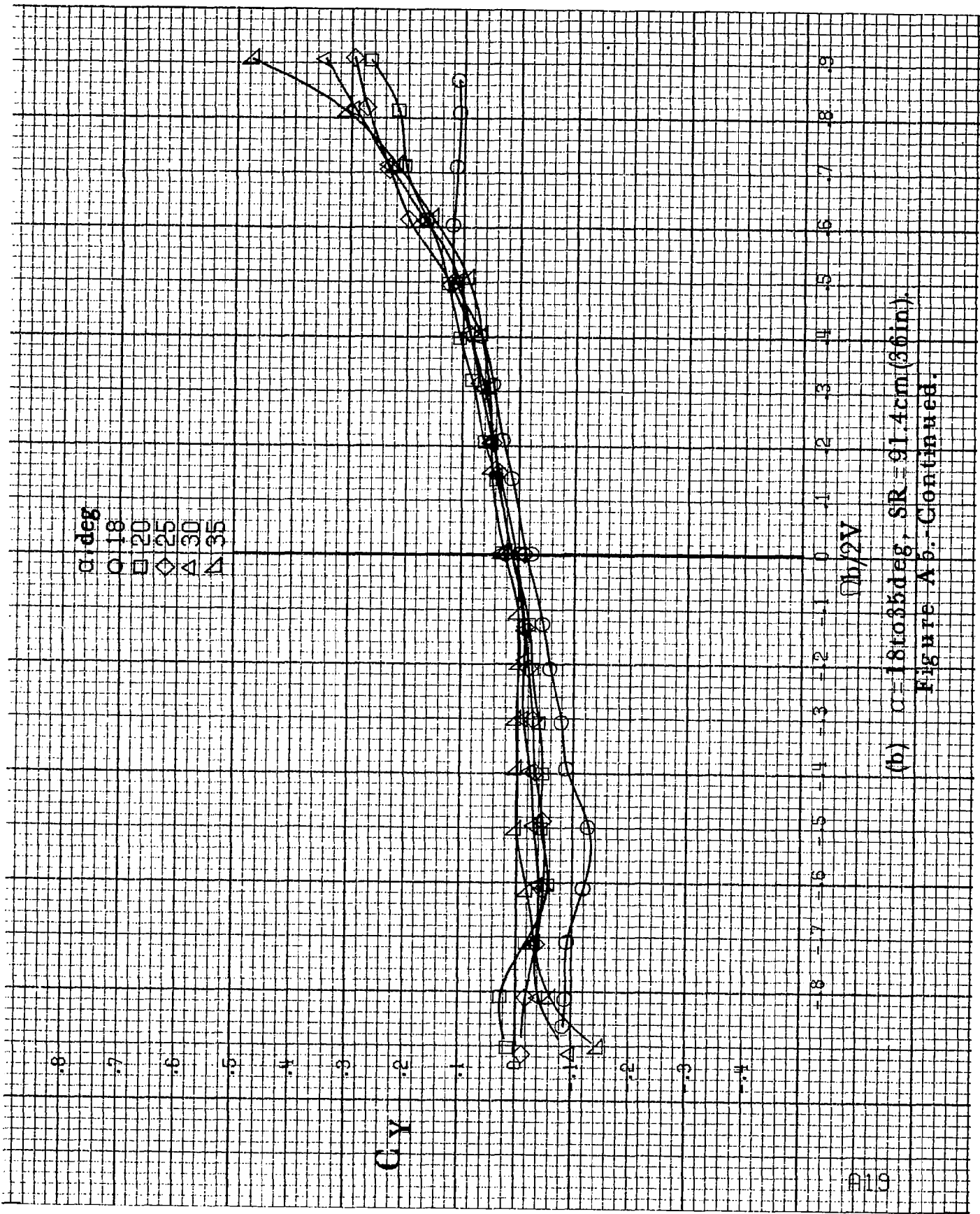


(d) $\alpha = 55$ to 90° , $SR = 0$.
Figure A4.-Concluded.

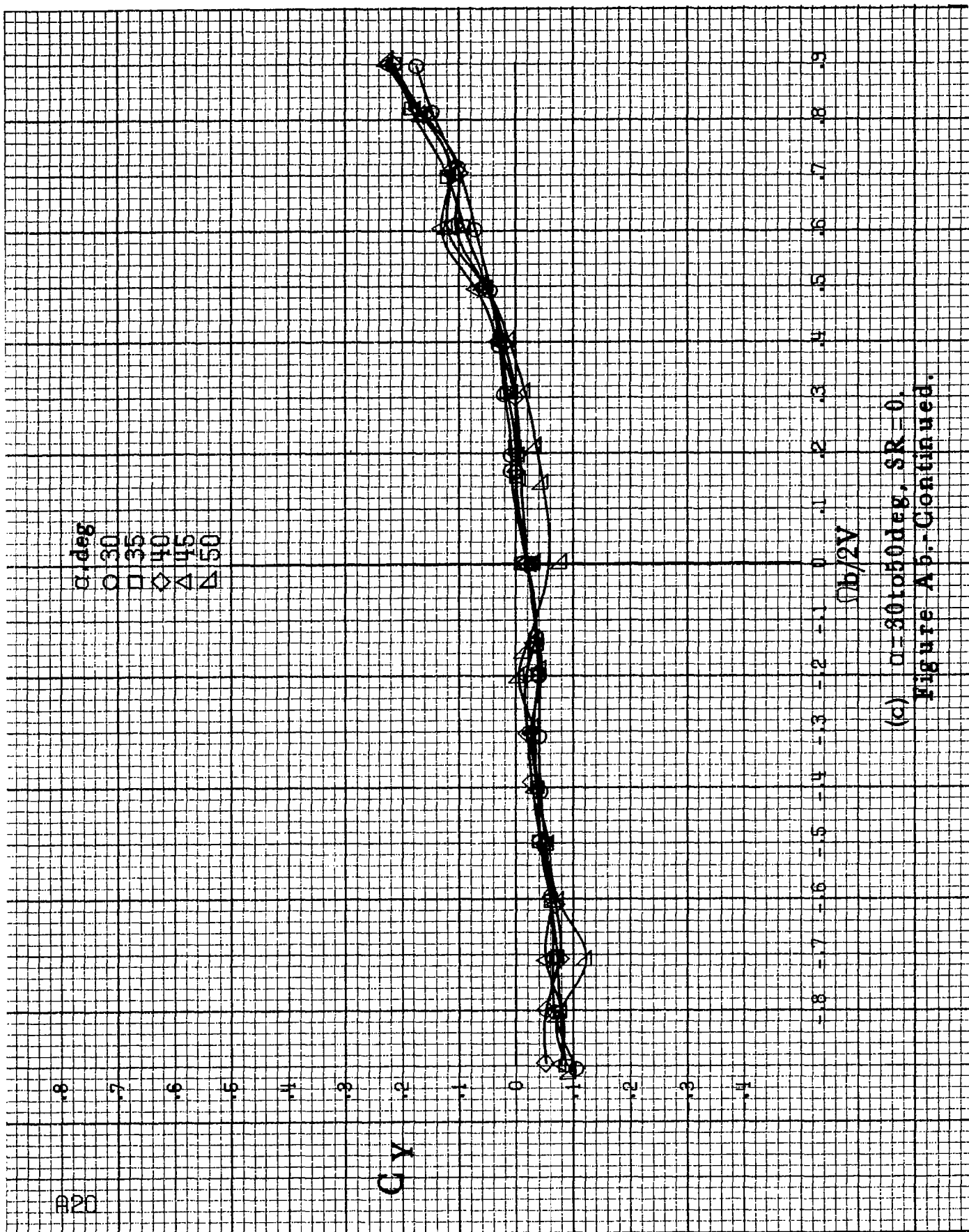


(a) $\alpha=8$ to 16° , $SR=91.4\text{cm}(36\text{in})$.

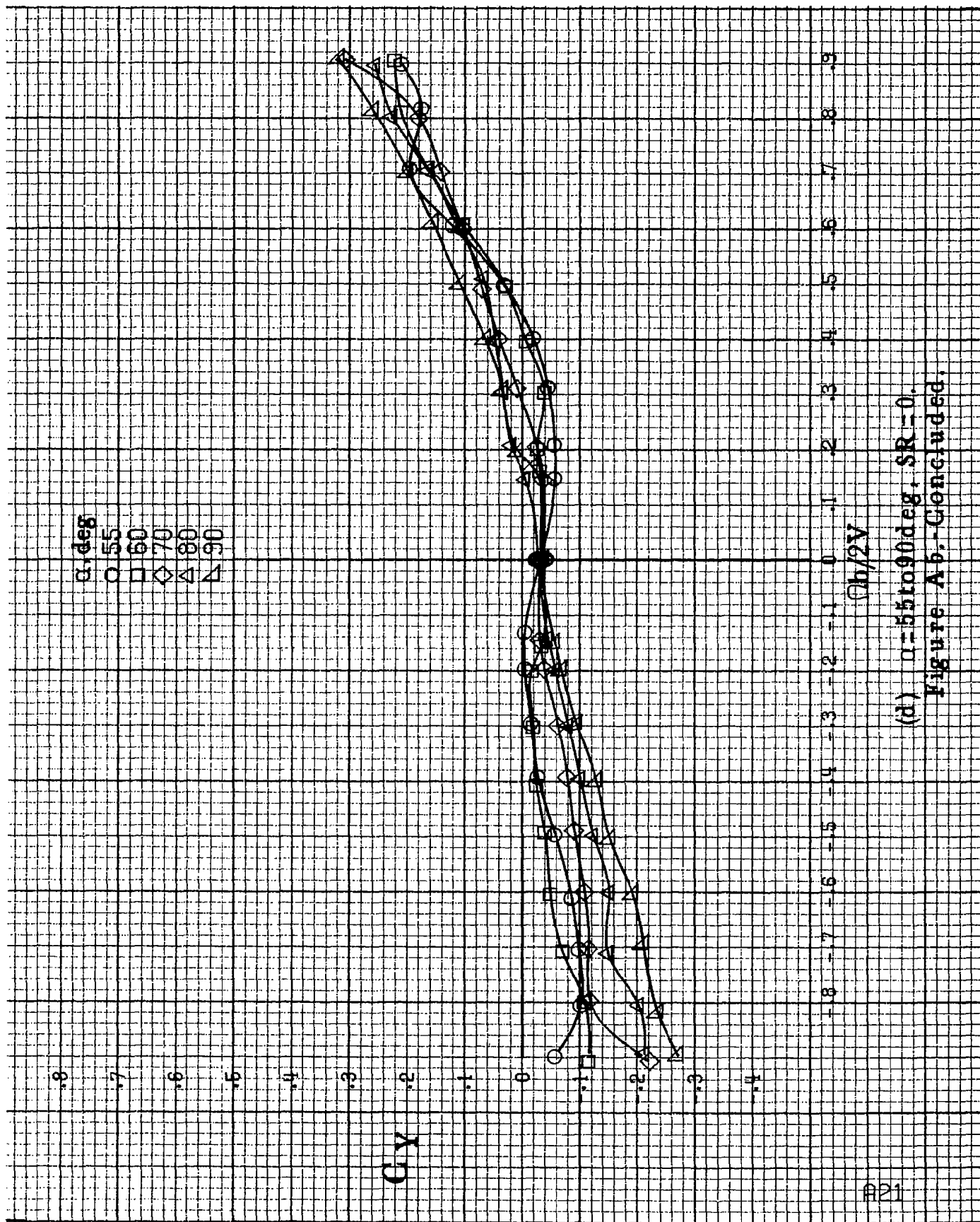
Figure A5. Effect of rotation rate and angle of attack on side-force coefficient for short body, low wing, horizontal T-tail A configuration. $\delta a=0^\circ$, $\delta r=0^\circ$, $\delta \tau=0^\circ$.



(b) $\alpha = 18$ to 35° , $SR = 91.4 \text{ cm (36 in.)}$.
 Figure A 6.-Continued.



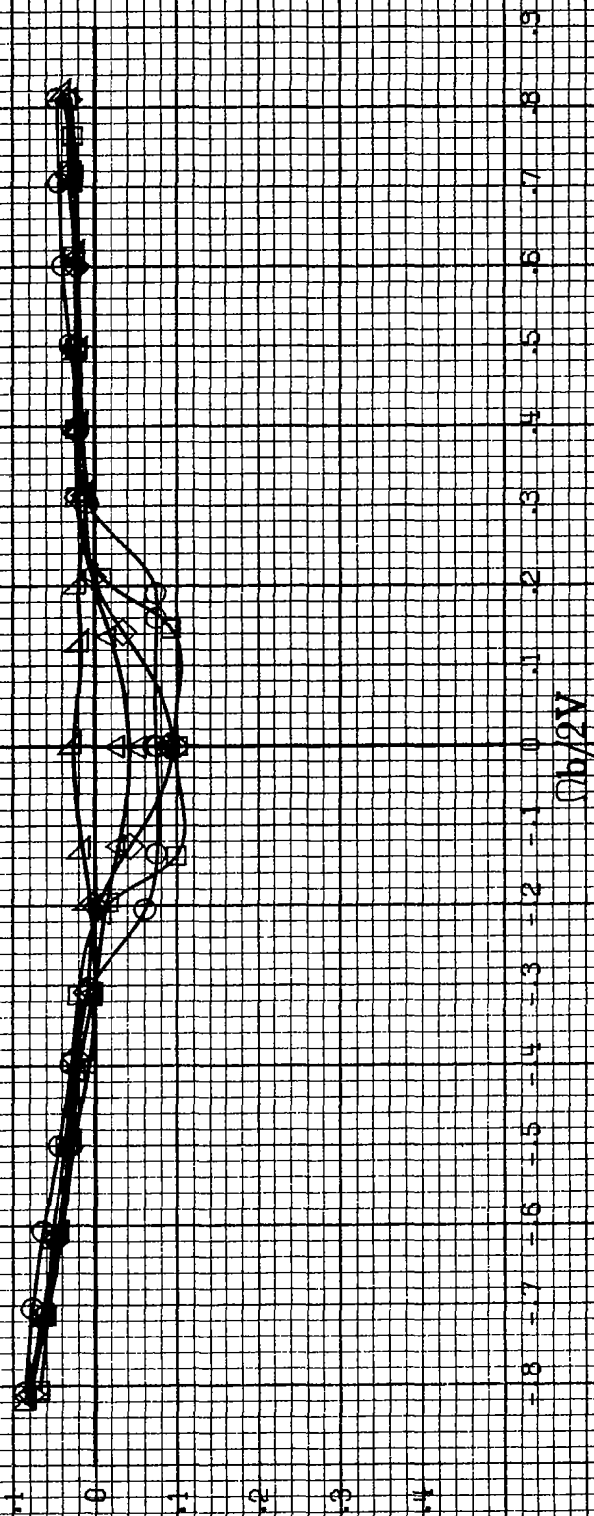
(c) $\alpha = 30$ to 50 deg, $SR = 0$.
Figure A5.-Continued.



(d) $\alpha=55$ to 90 deg. $SR=0$.
Figure A 6. - Concluded.

C_A

α, deg
 O 8
 □ 10
 ◇ 12
 △ 14
 ▽ 16



(a) $\alpha=8$ to 16° , $SR=91.4\text{cm}$ (36in).

Figure A6. Effect of rotation rate and angle of attack on axial-force coefficient for short body, low wing, horizontal T-tail A configuration. $\delta_a = 0^\circ$, $\delta_s = 0^\circ$, $\delta_r = 0^\circ$, $\delta = 0^\circ$.

CA

α , deg
 ○ 18
 □ 20
 ◇ 25
 △ 30
 ▲ 35

$\phi_b/2V$

(b) $\alpha = 18$ to 35 deg, $SR = 91.4$ cm (36 in.)

Figure A 6.-Continued.

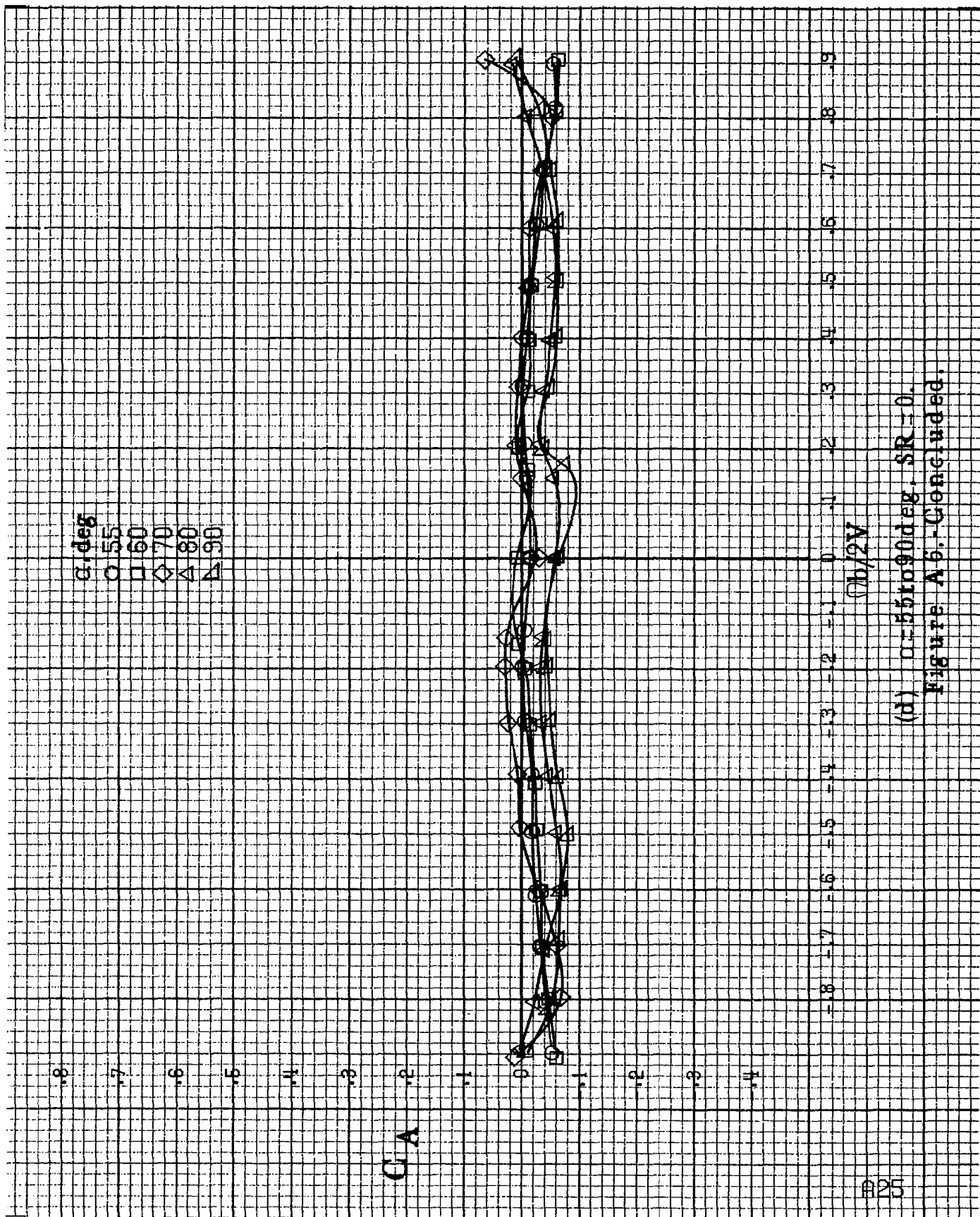
A24

α, deg
 ○ 30
 □ 35
 ◇ 40
 △ 45
 ▽ 50

C A



(c) $\alpha = 30 \text{ to } 50 \text{ deg}$, $SR = 0$.
 Figure A 6. - Continued.



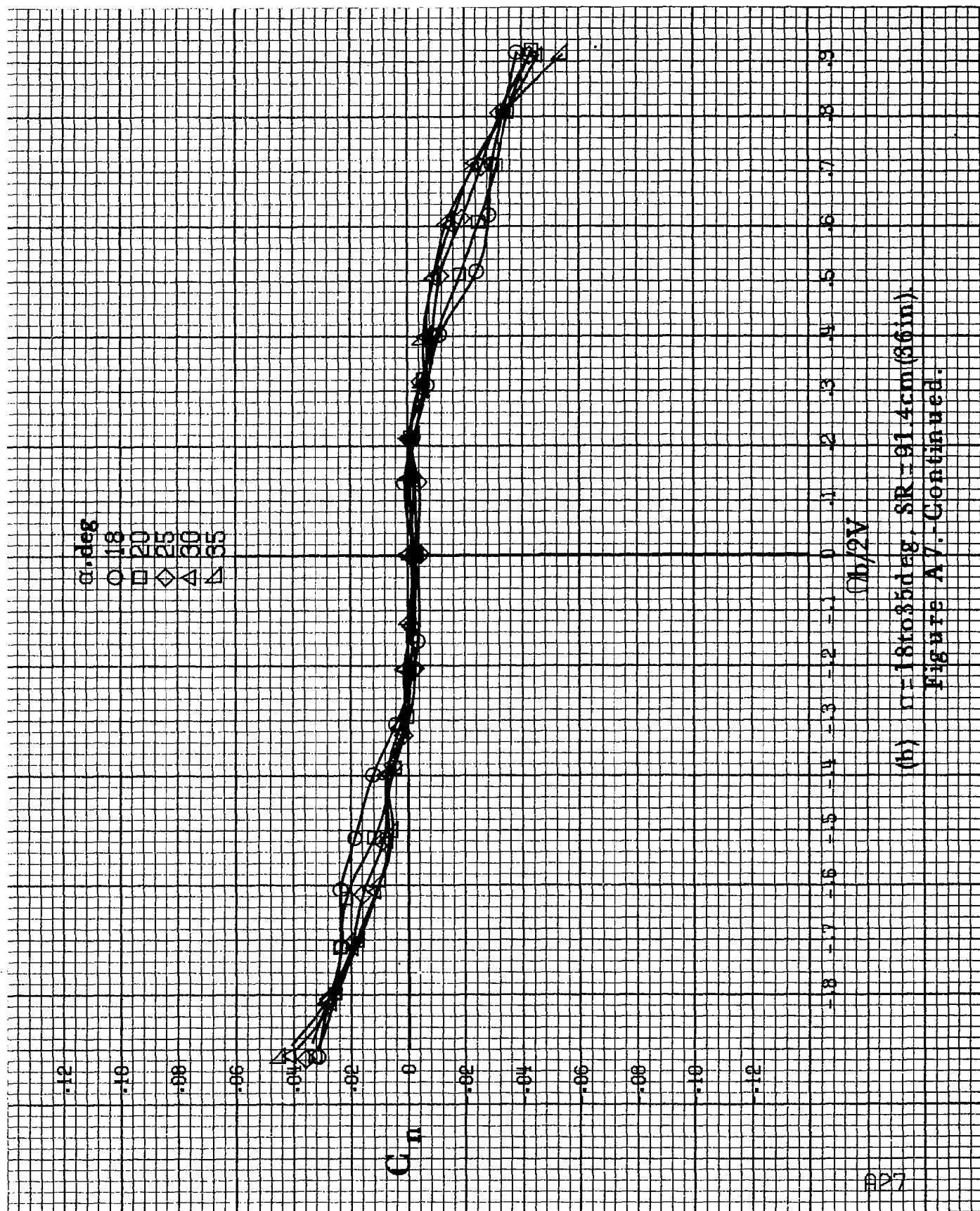
(d) $\alpha = 55$ to 90° , $SR = 0$.
Figure A 6.-Concluded.

α, deg

\circ 8
 \square 10
 \diamond 12
 \triangle 14
 ∇ 16

 C_n C_n $Qb/2V$ (a) $\alpha = 8$ to 16 deg, $SR = 91.4 \text{ cm (36 in.)}$.

Figure A7. Effect of rotation rate and angle of attack on yawing-moment coefficient for short body, low wing, horizontal tail no. 1 configuration. $\delta_a = 0^\circ$, $\delta_e = 0^\circ$, $\delta_r = 0^\circ$, $B = 10^\circ$.



(b) $\alpha = 18$ to 35° , $SR = 91.4 \text{ cm (36 in.)}$
Figure A7.-Continued.

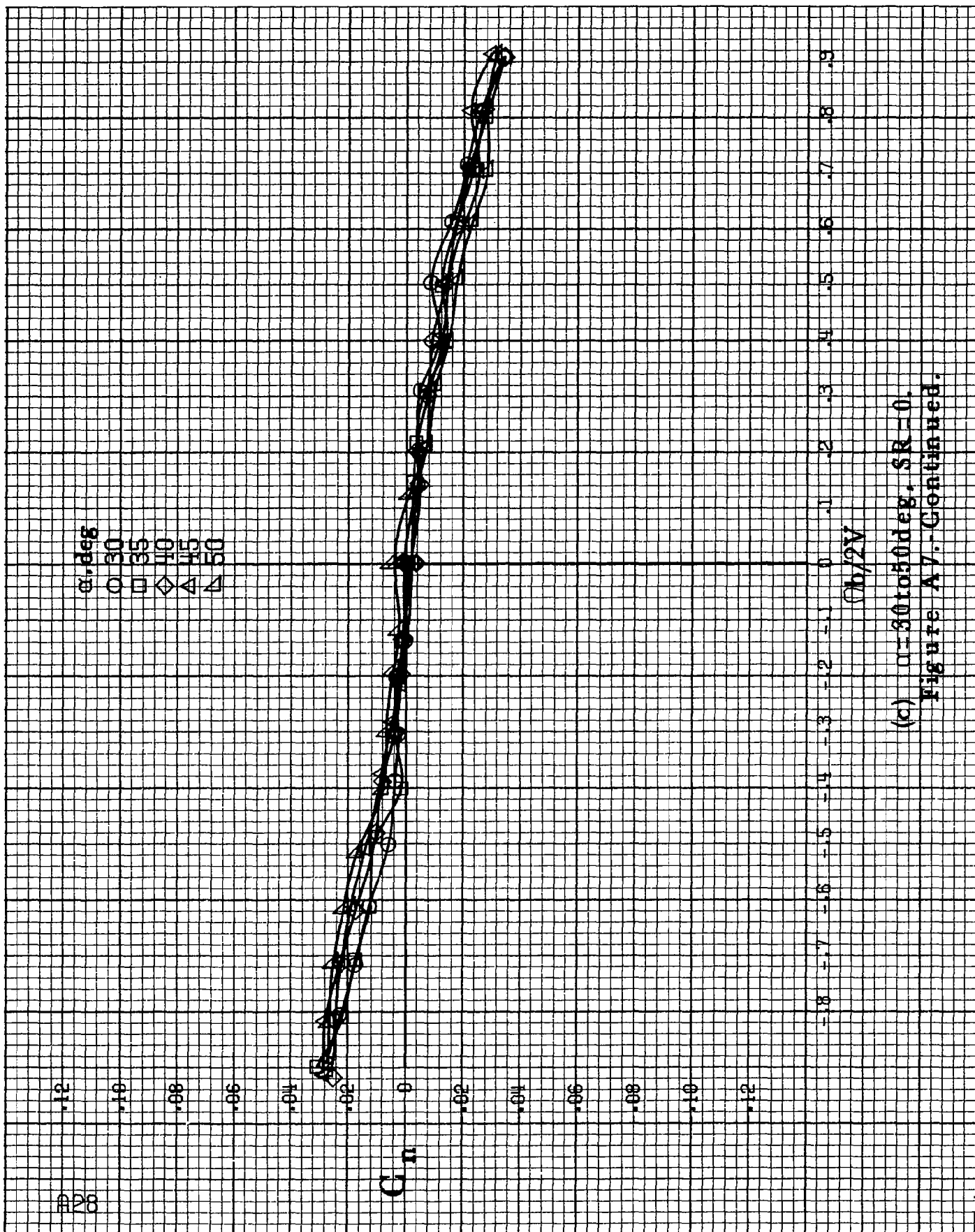
α, deg
 ○ 30
 □ 35
 ◇ 40
 ▲ 45
 ▴ 50

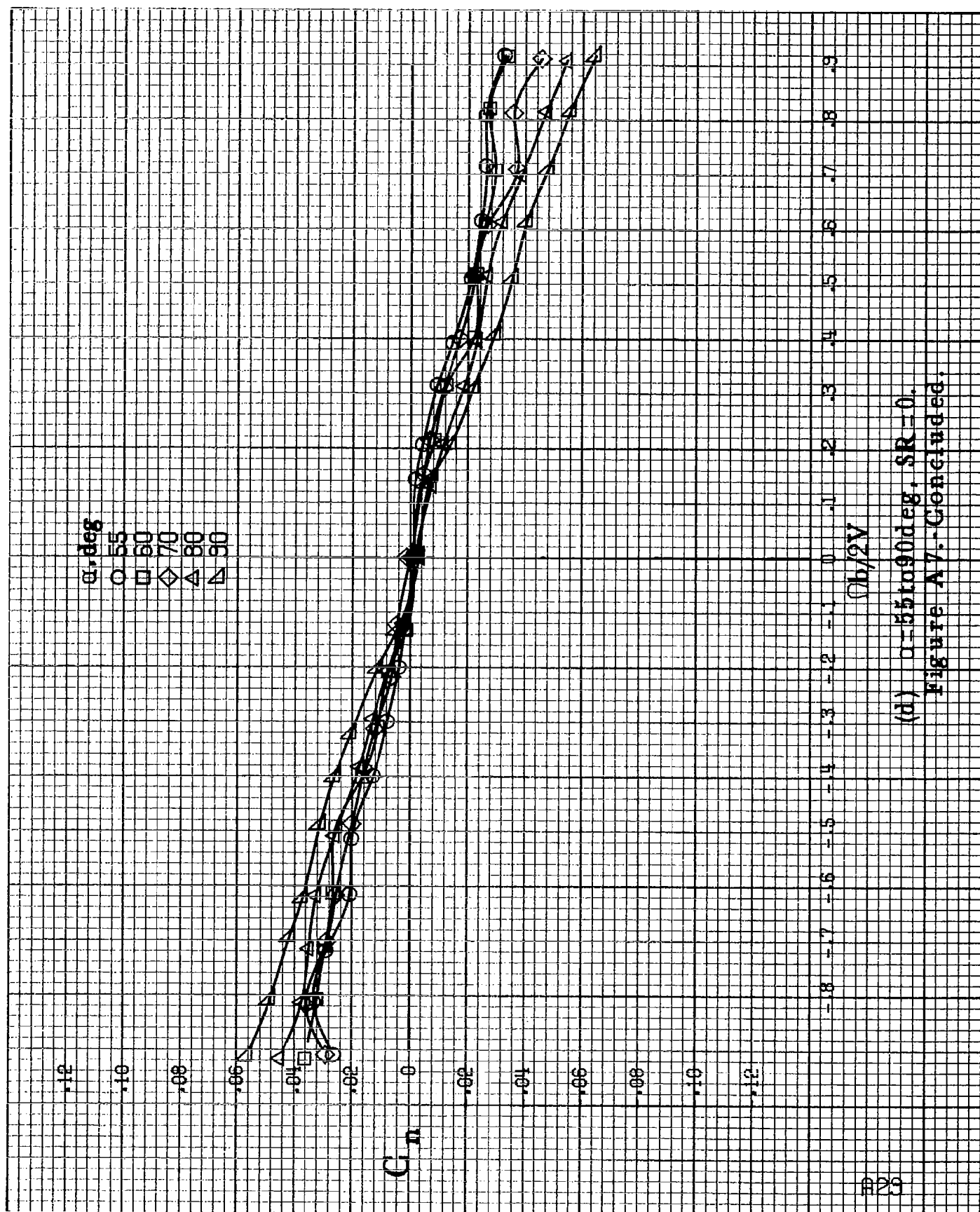
G_n

$\Phi_b/2V$

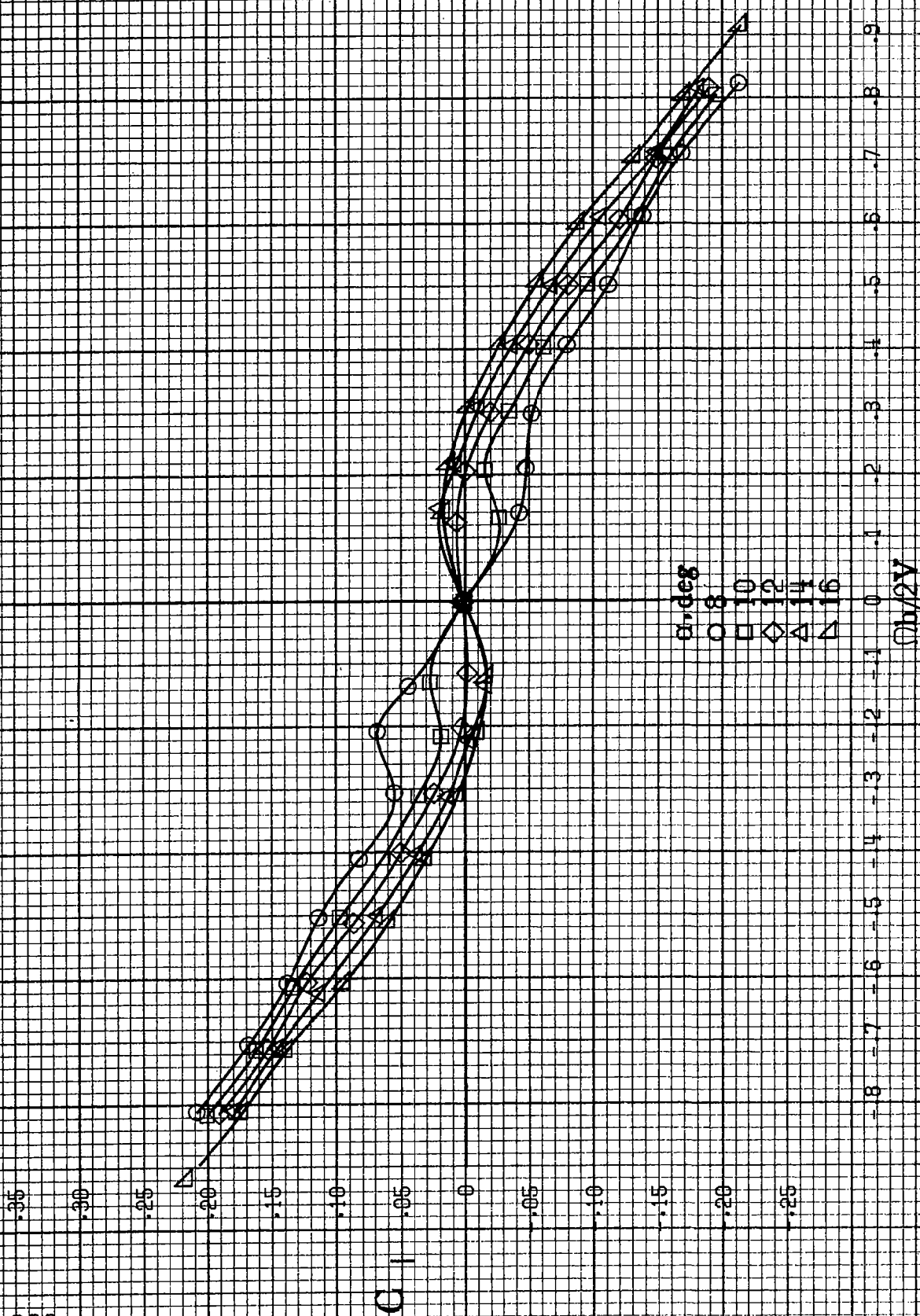
(c) $\alpha=30$ to 50 deg, $SR=0$.

Figure A7.-Continued.



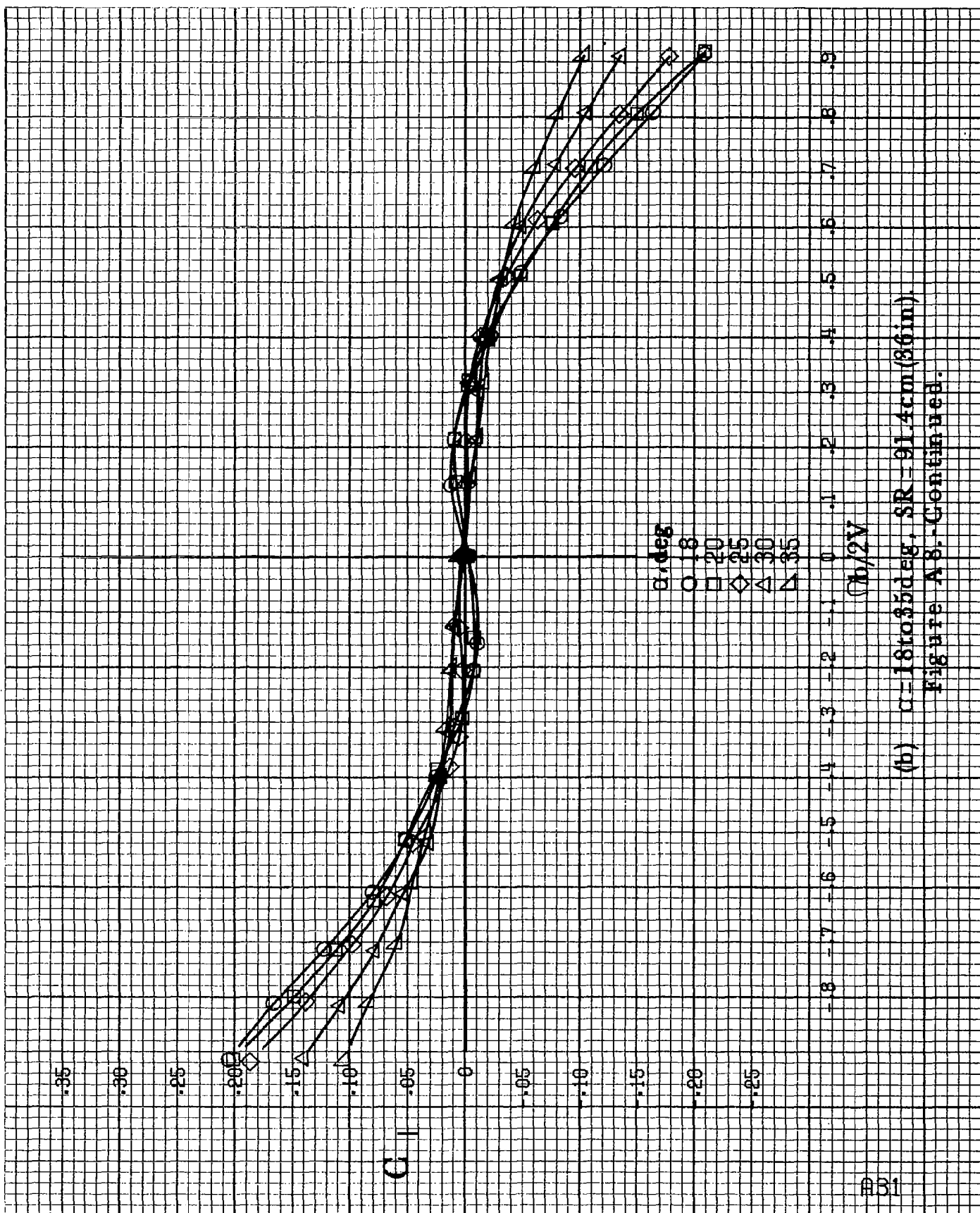


(d) $\alpha=55$ to 90° deg. $SR=0$.
Figure A7.-Concluded.



(a) $\alpha=8$ to 16° , $SR=91.4\text{cm}(36\text{in})$.

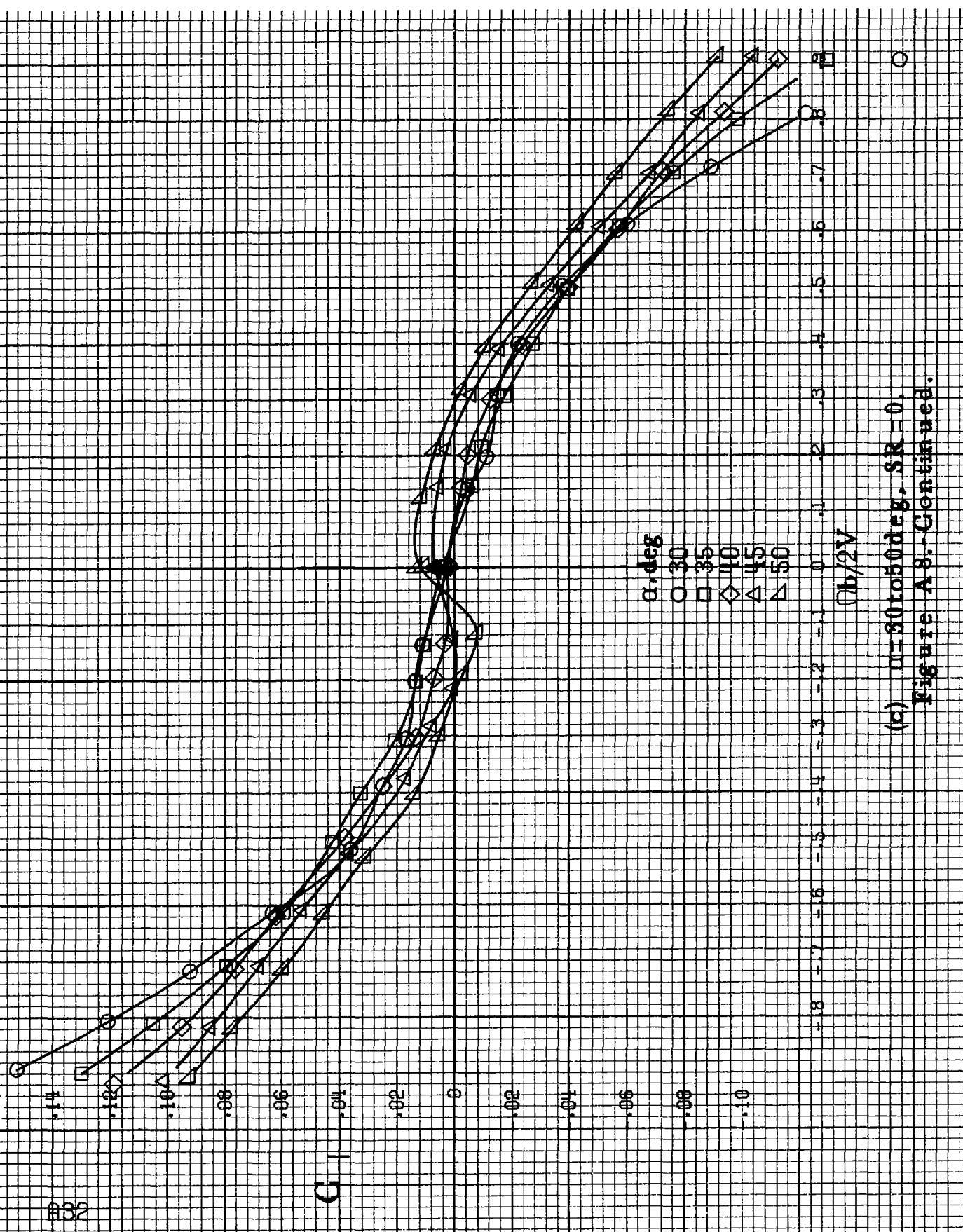
Figure A8.-Effect of rotation rate and angle of attack on rolling-moment coefficient for short body, low wing, horizontal tail no. 1 configuration. $\delta_e=0^\circ$; $\delta_a=0^\circ$; $\delta_r=10^\circ$; $\beta=10^\circ$.



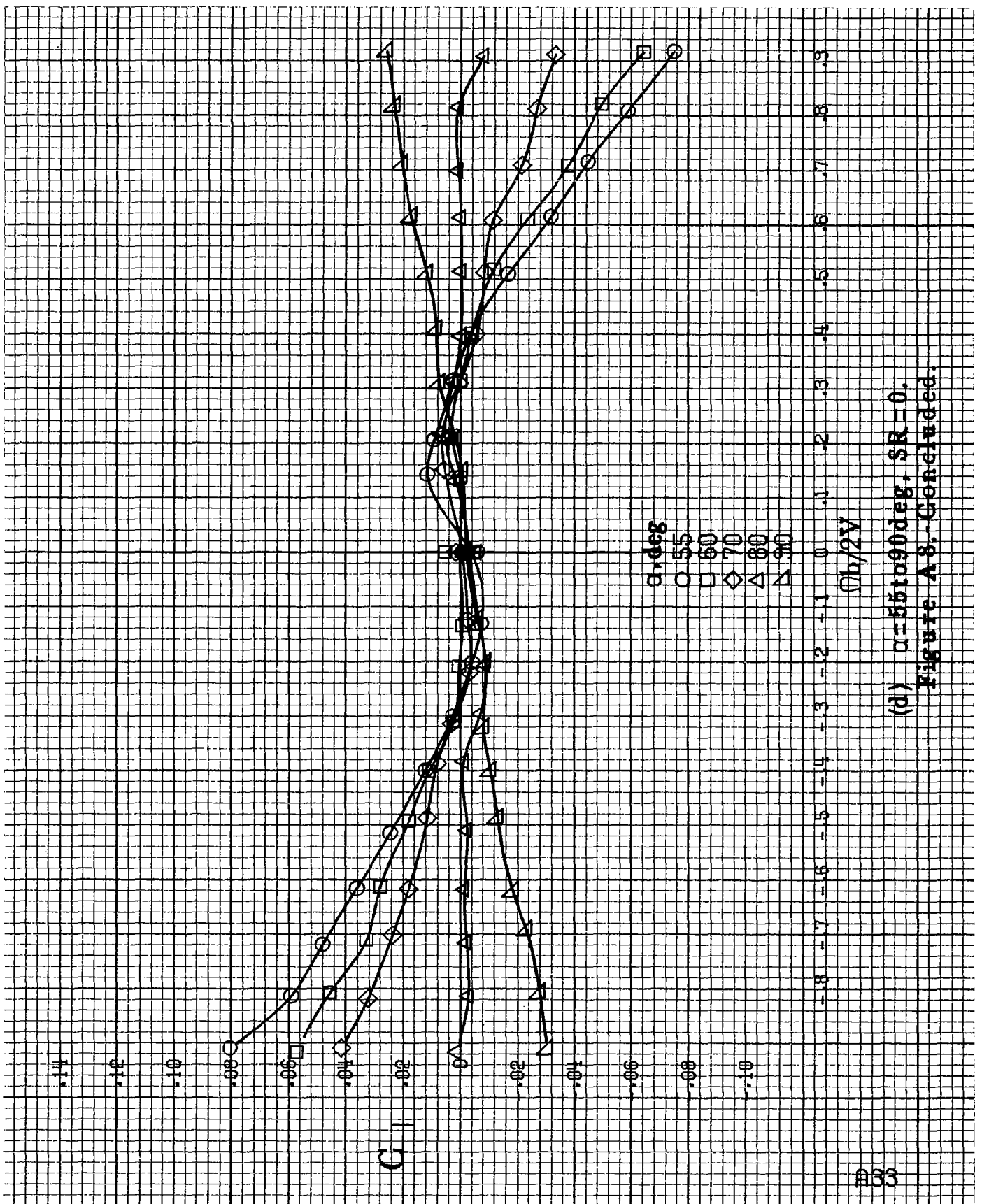
(b) $\alpha=18$ to 35° , $SR=91.4\text{cm}(36\text{in})$.
Figure A8.-Continued.

A32

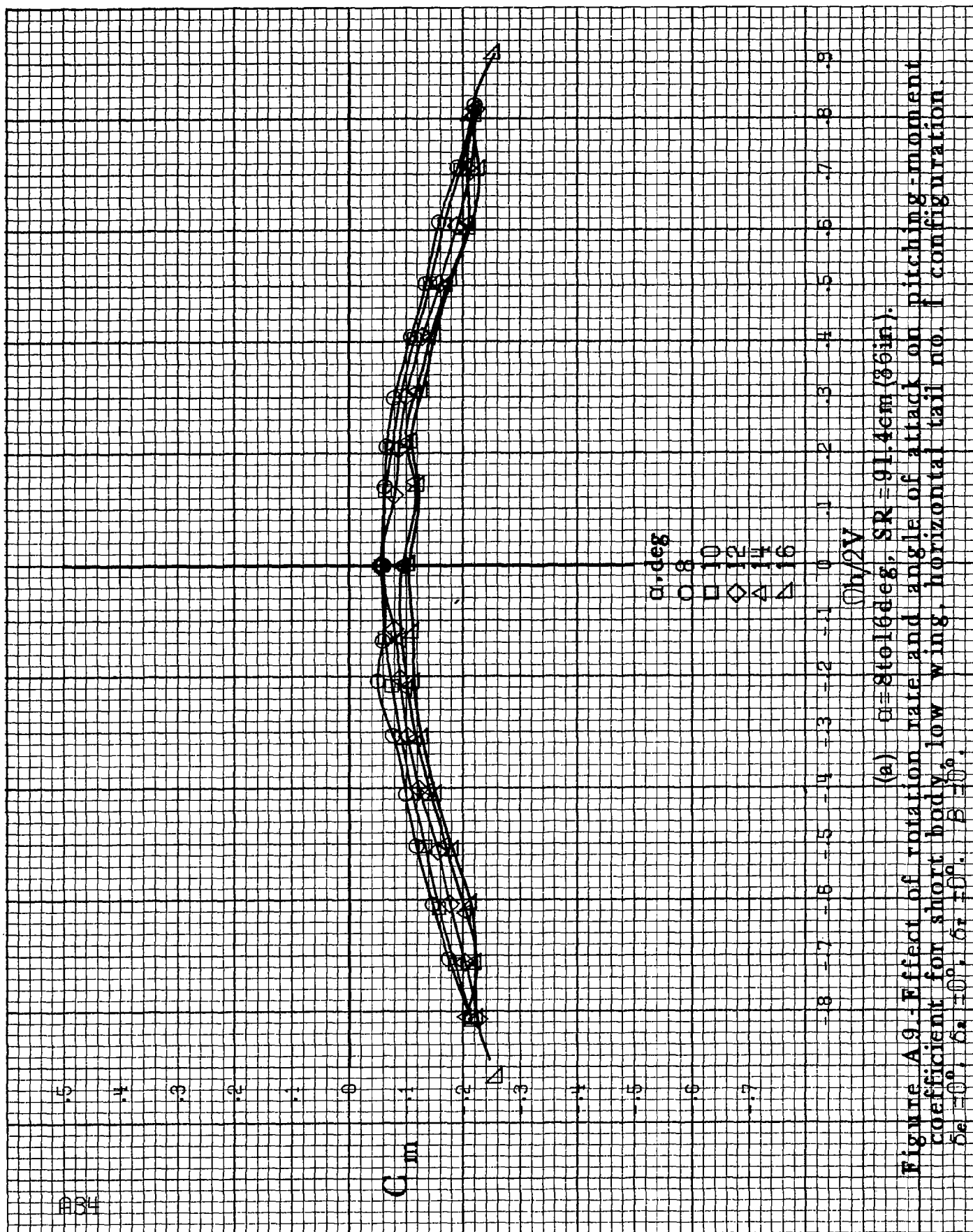
C



(c) $\alpha = 30$ to 50° , $SR = 0$.
Figure A8.-Continued.

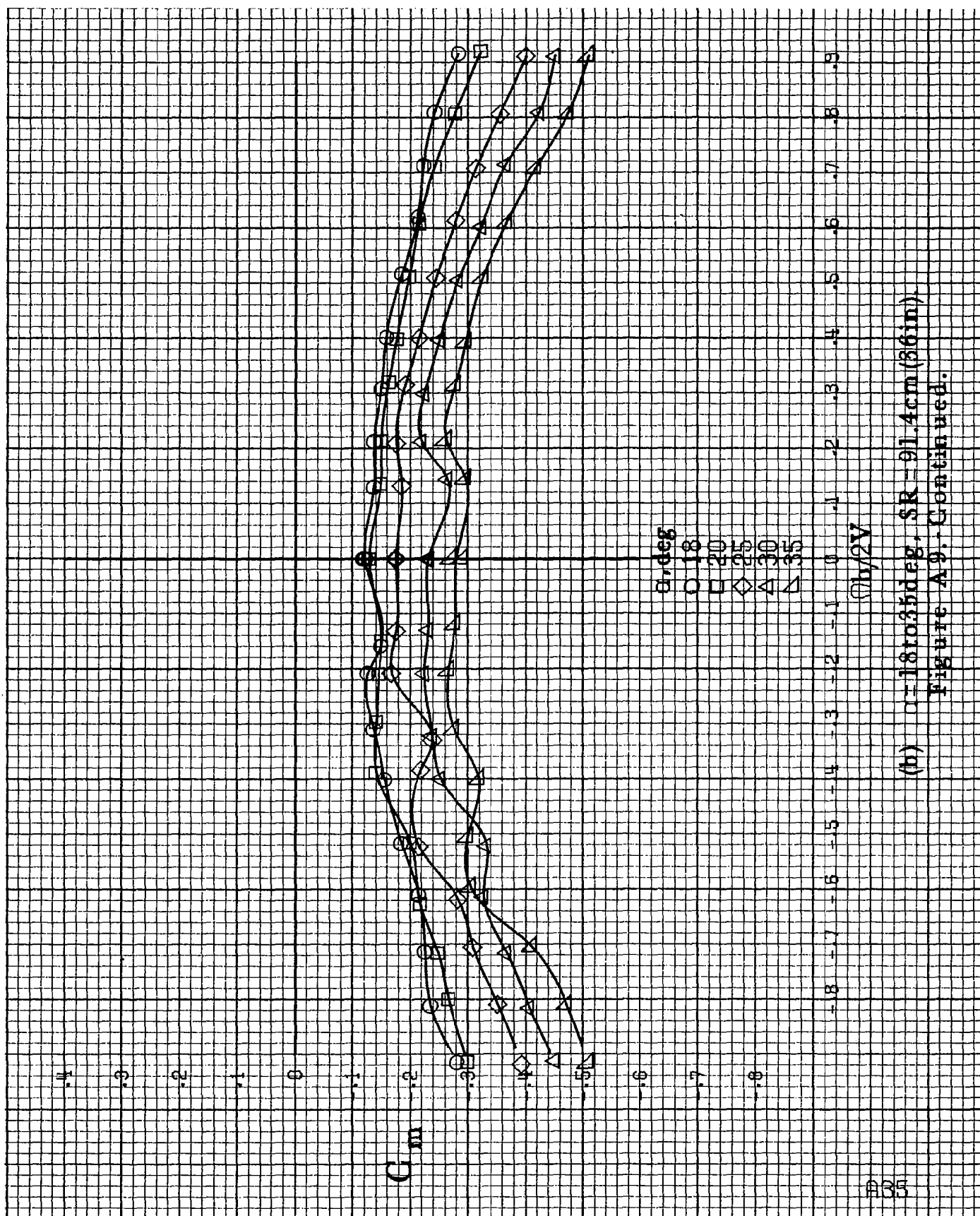


(d) $\alpha=55$ to 90° deg. $SR=0$.
Figure A8. Concluded.

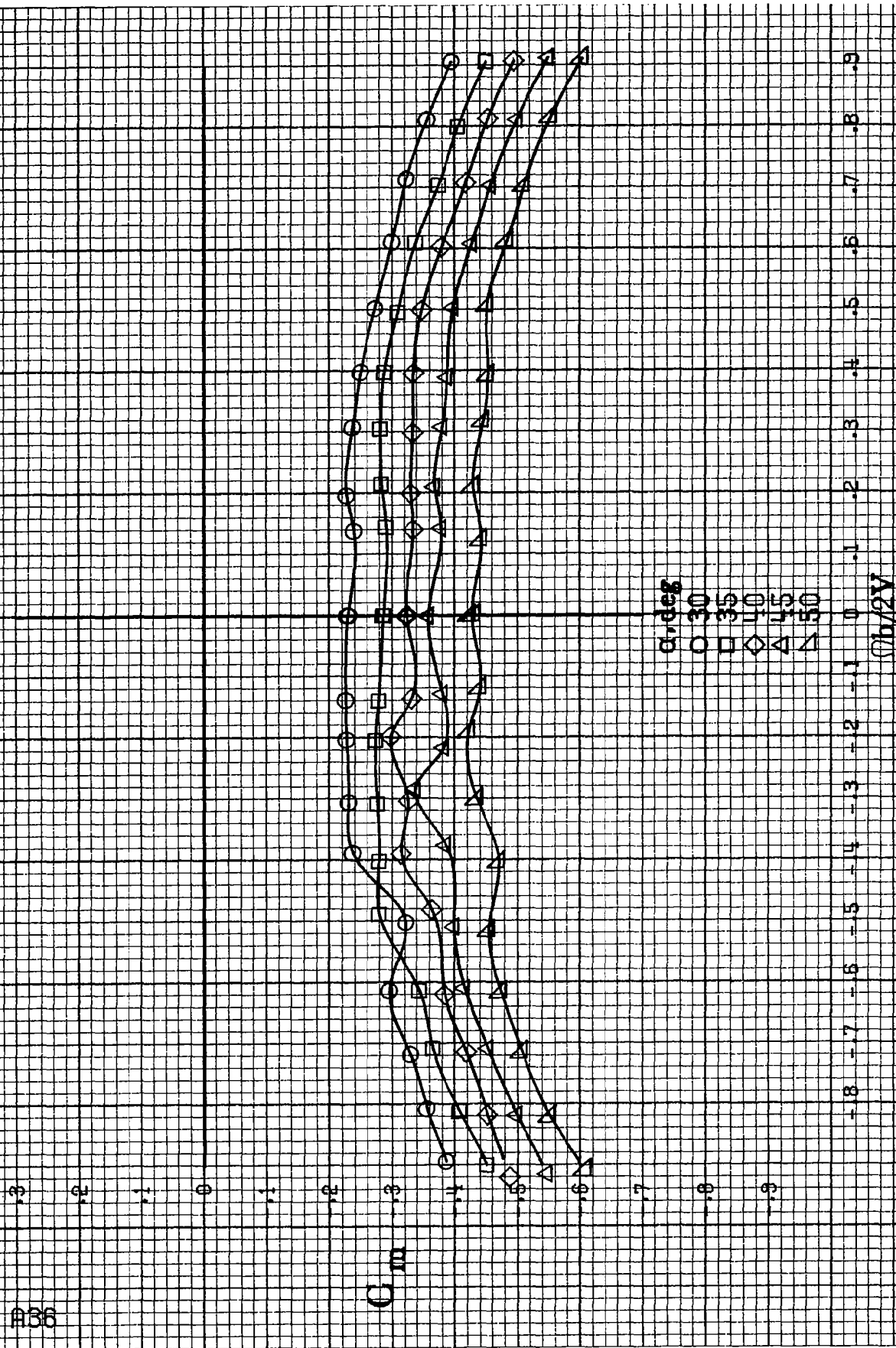


(a) $\alpha = 8$ to 16 deg, $SR = 91.4$ cm (36 in).

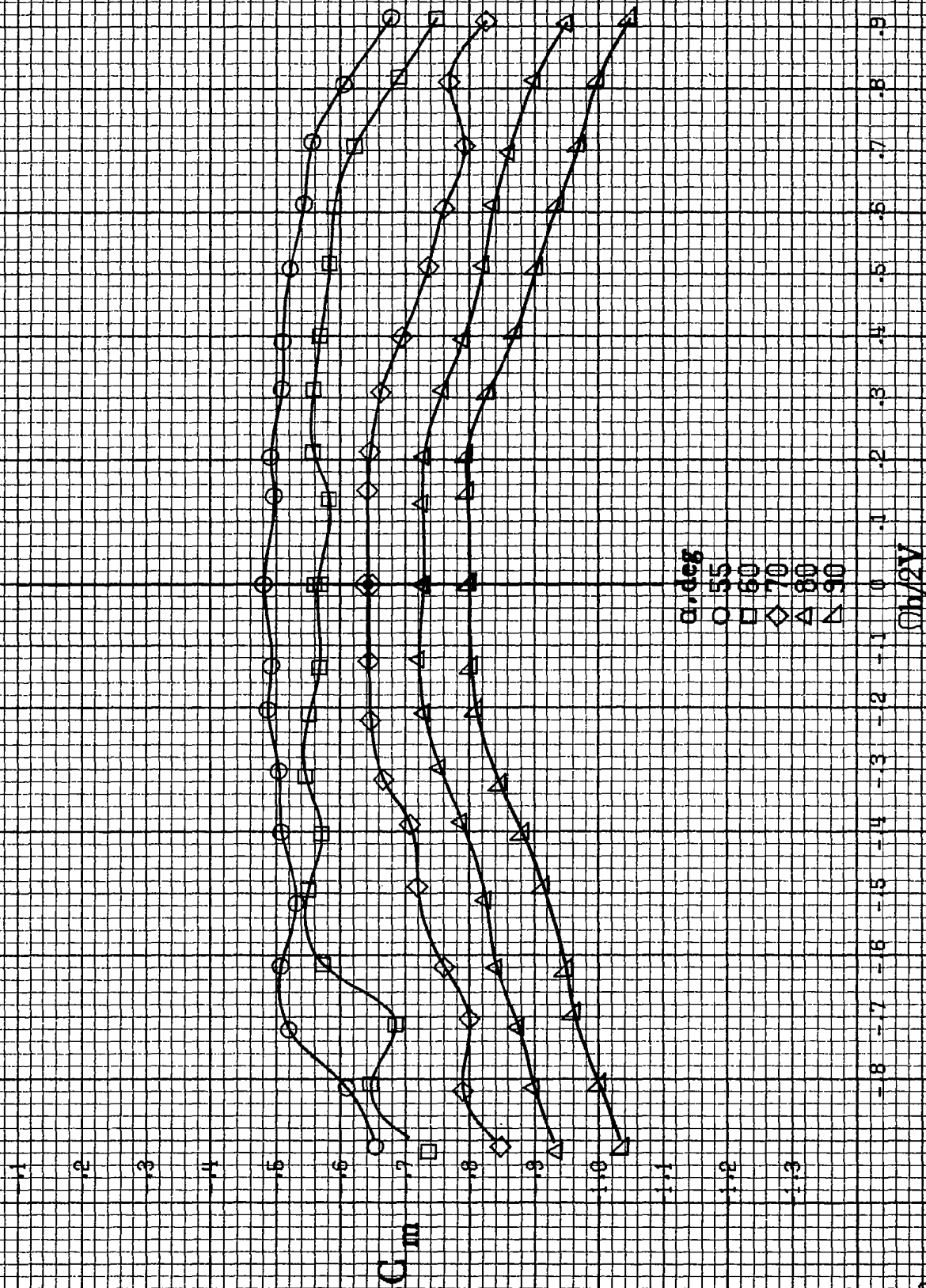
Figure A.9. Effect of rotation rate and angle of attack on pitching-moment coefficient for short body, low wing, horizontal tail no. 1 configuration. $\delta_e = 0^\circ$, $\delta_s = 0^\circ$, $\delta_r = 0^\circ$, $\beta = 0^\circ$.



(b) $\alpha = 18$ to 35 deg. SR-91.4cm (36in).
Figure A9. Continued.



(c) $\alpha=30$ to 50 deg, $SR=0$.
Figure A9.-Continued.



(d) $\alpha = 55$ to 90° , $SR = 0$.
Figure A9. Concluded.

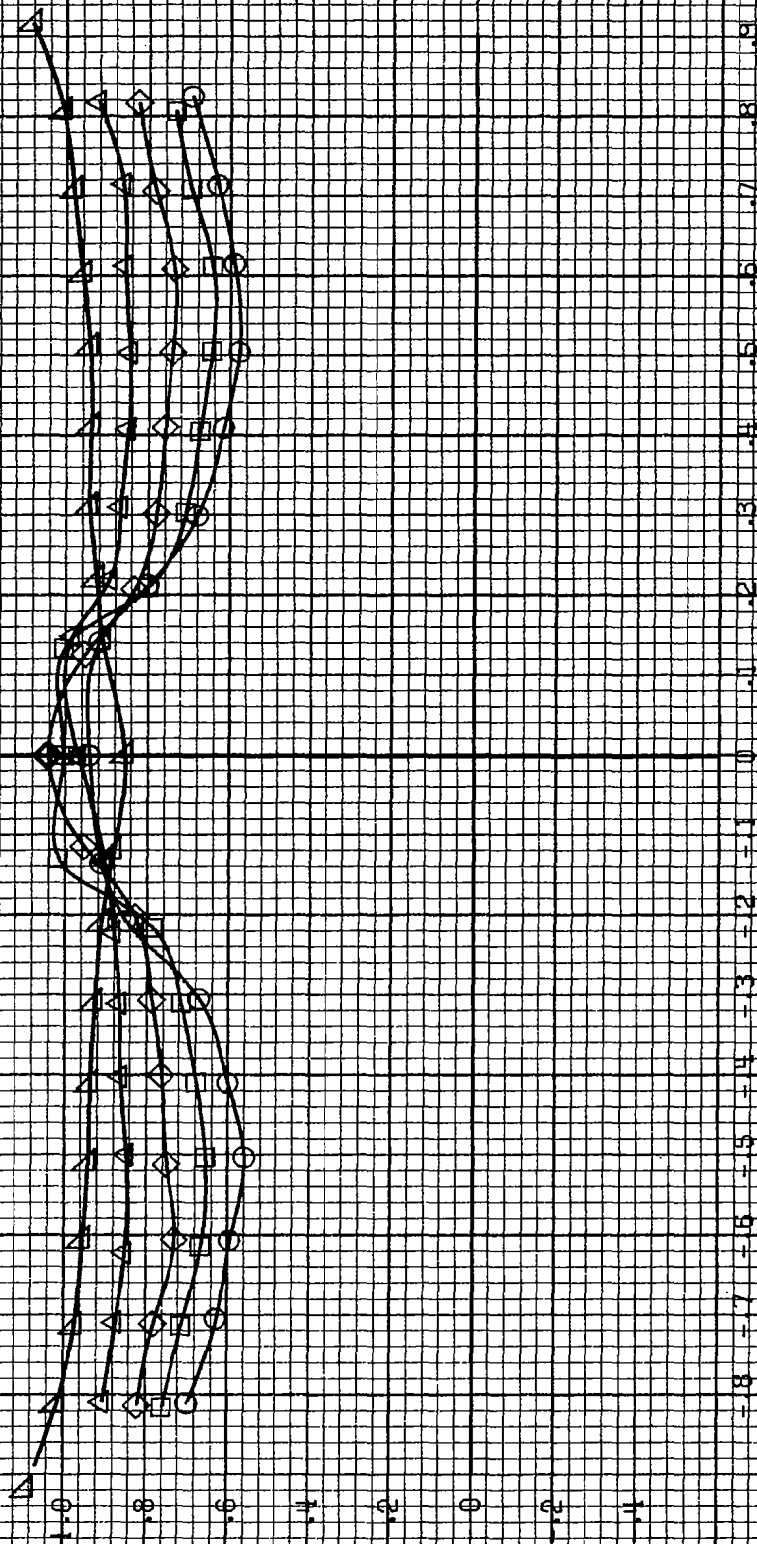
α, deg
 8
 10
 12
 14
 16

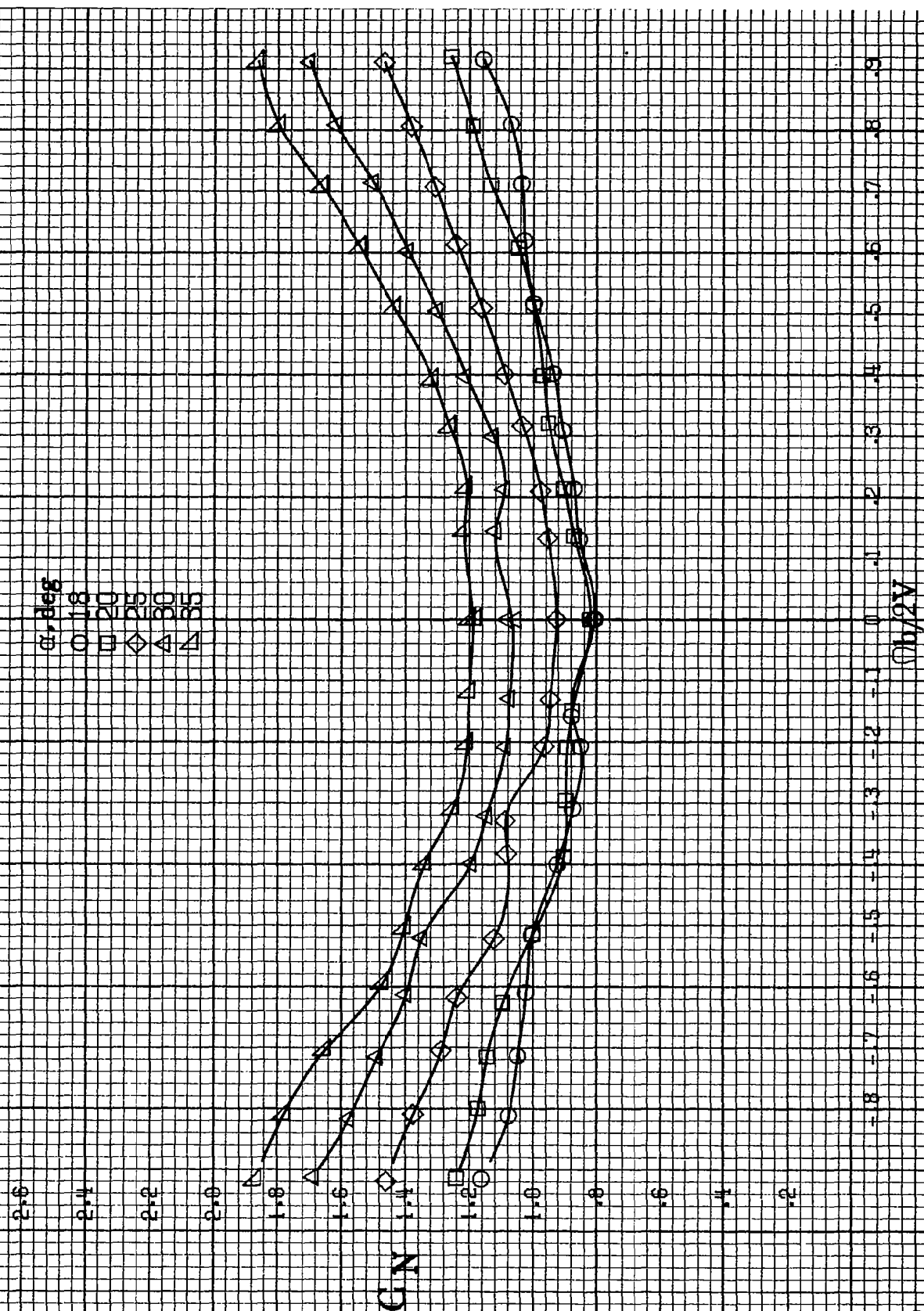
C_N

$b/2V$

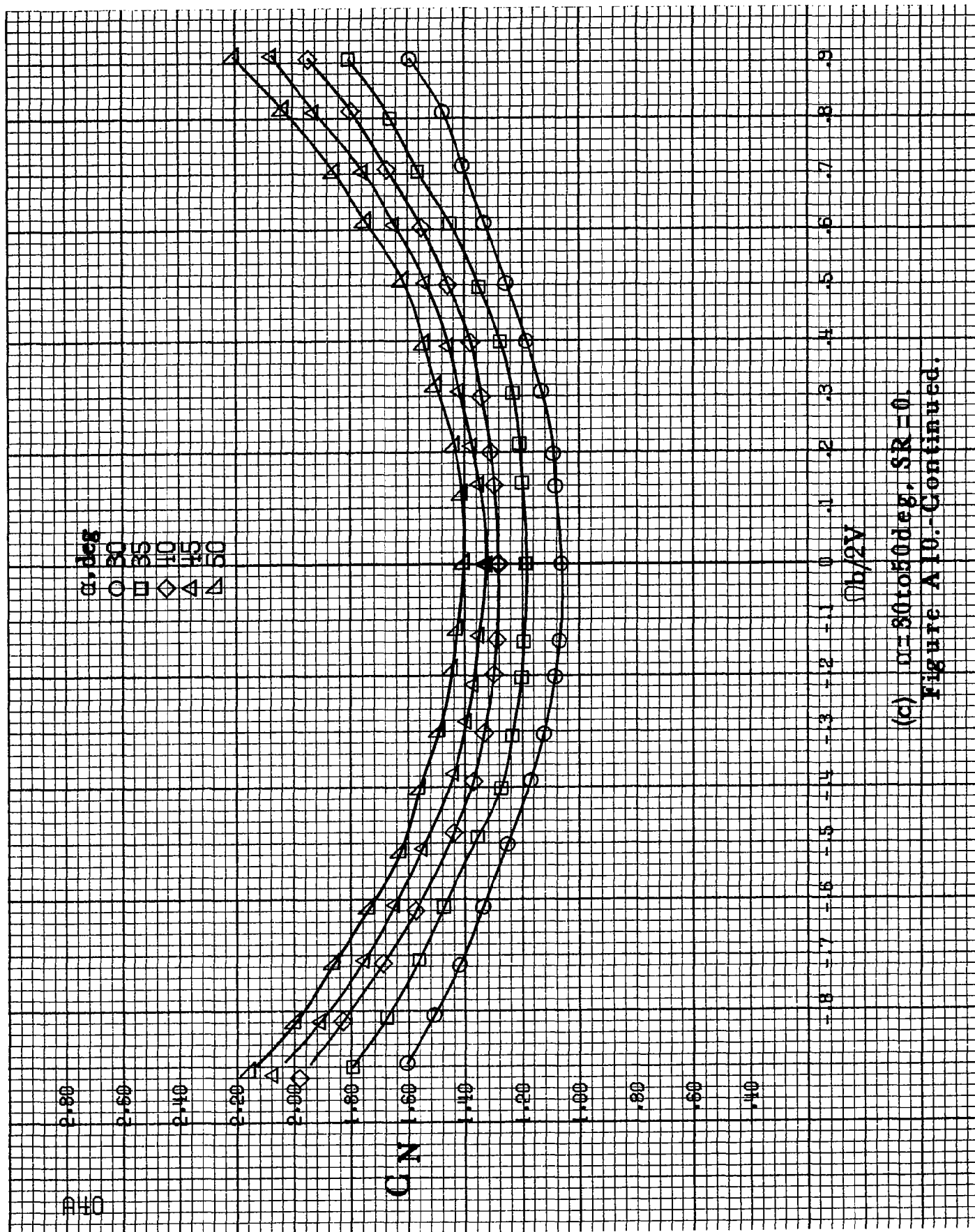
(a) $\alpha=8$ to 16 deg, $SR=91.4\text{cm}$ (36in).

Figure A10.-Effect of notation rate and angle of attack on normal-force coefficient for short body, low wing, horizontal tail no. 1 configuration. $\delta_e=0^\circ$, $\delta_a=0^\circ$, $\delta_r=0^\circ$, $\beta=0^\circ$.

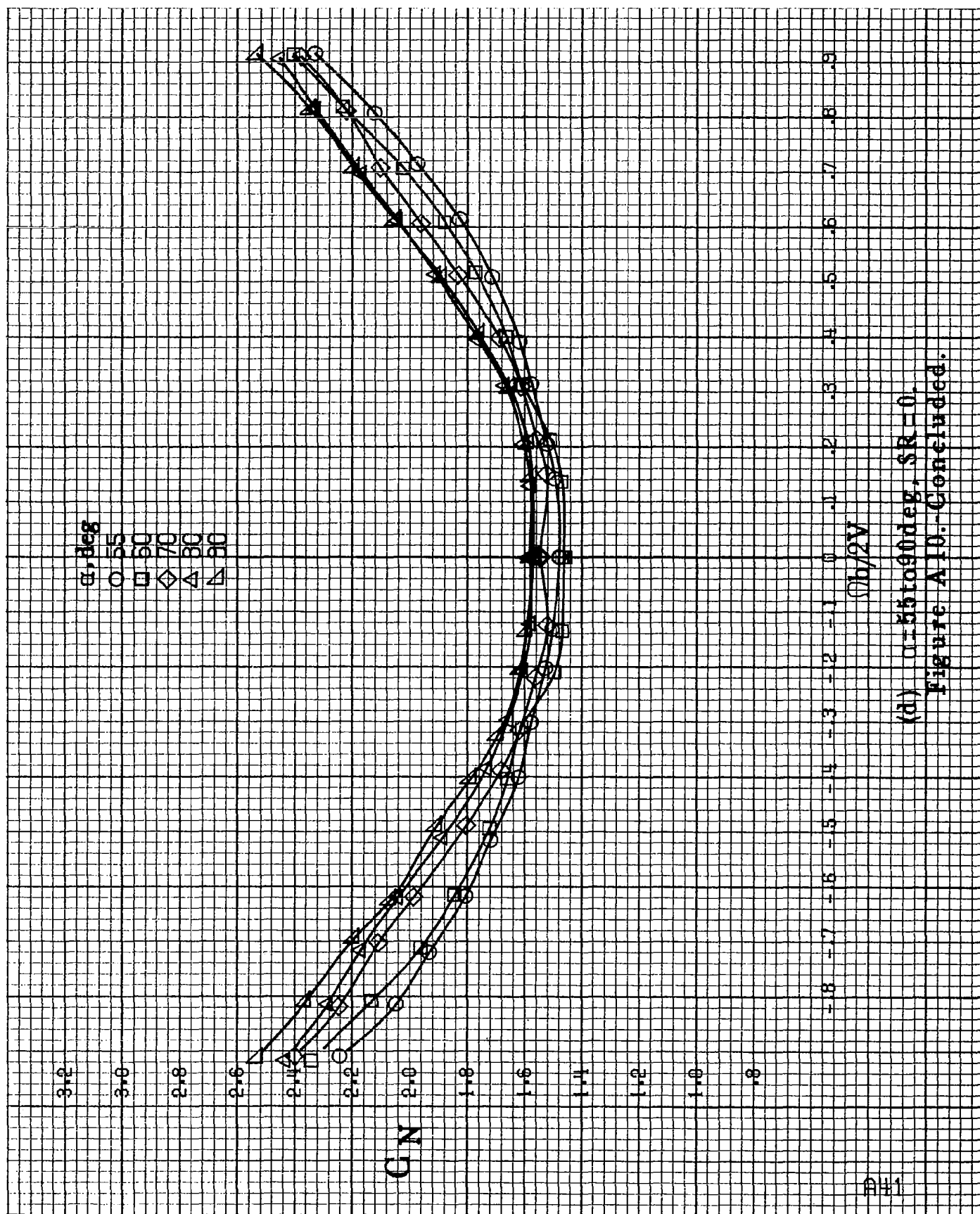




(b) $\alpha = 18$ to 35° , SR = 91.4 cm (36 in.)
Figure A10.-Continued.



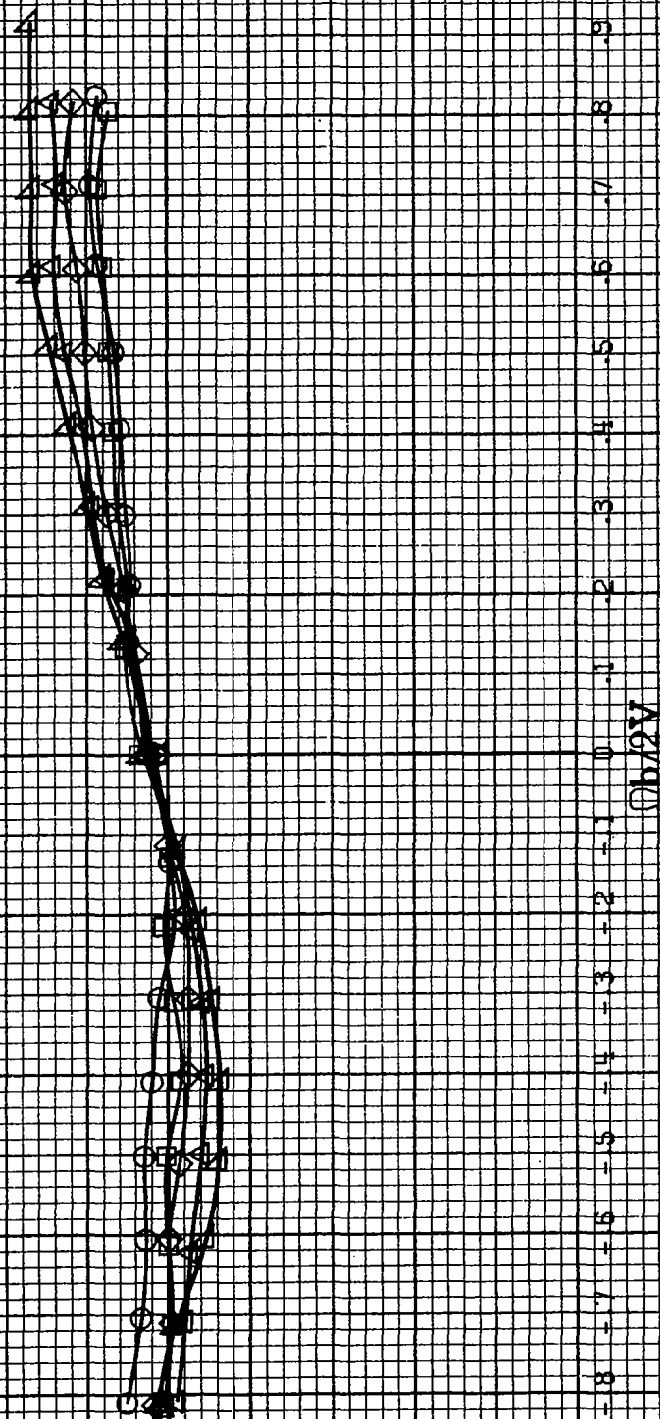
(c) $\alpha = 30$ to 50° , $SR = 0$.
Figure A10.-Continued.



(d) $\alpha=55$ to 90° , $SR=0$.
Figure A10.-Concluded.

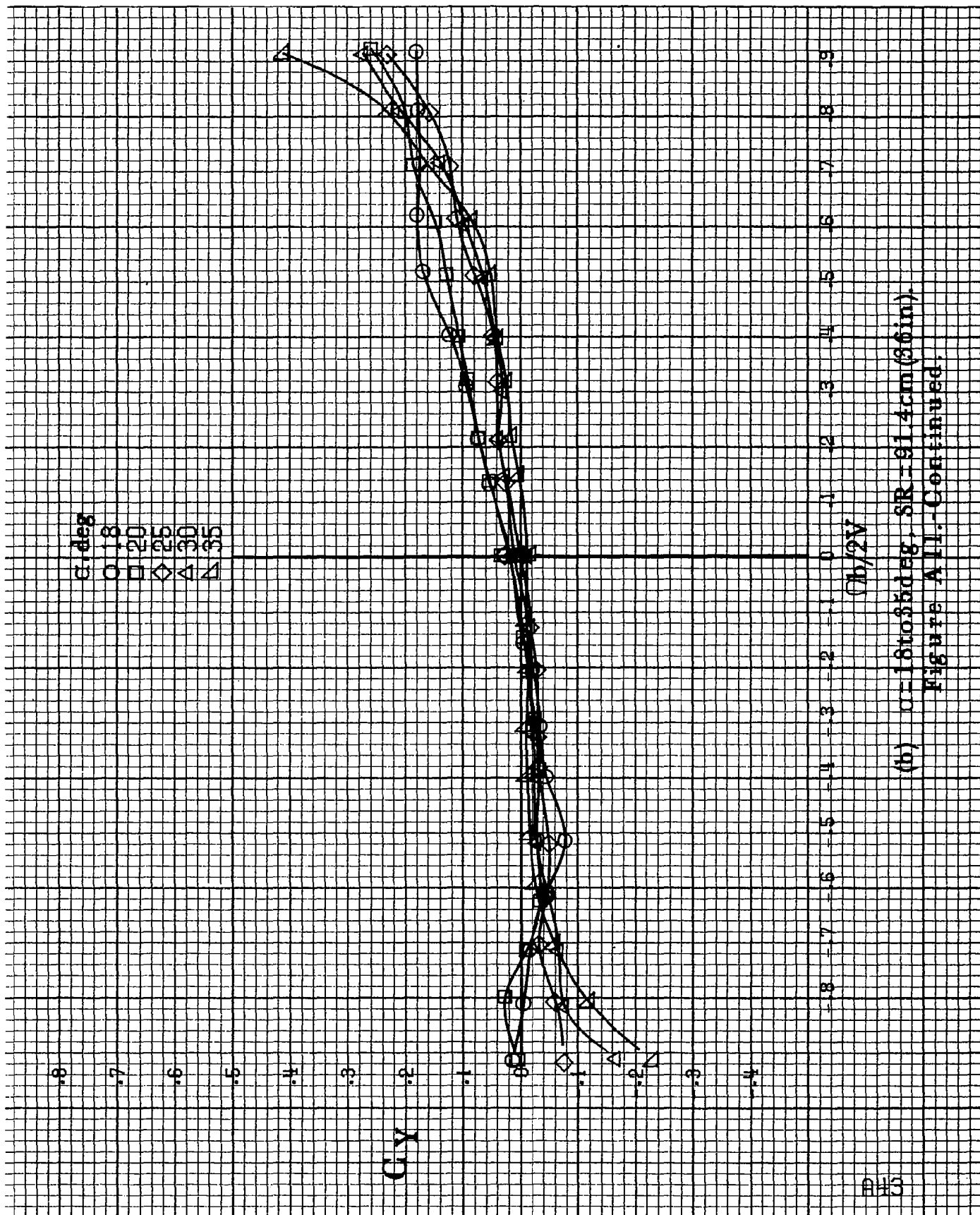
α, deg
 O 8
 □ 10
 ◇ 12
 △ 14
 ▽ 16

C_Y



(a) $C = 8 \text{ to } 16 \text{ deg}$, $SR = 91.4 \text{ cm (35 in)}$.

Figure A11.-Effect of rotation rate and angle of attack on side-force coefficient for short body, low wing, horizontal tail no. 1 configuration. $\delta_a = 0^\circ$, $\delta_s = 0^\circ$, $\delta_r = 0^\circ$.



(b) $\alpha = 18$ to 35° , SR = 91.4 cm (36 in).
Figure A11. Continued.

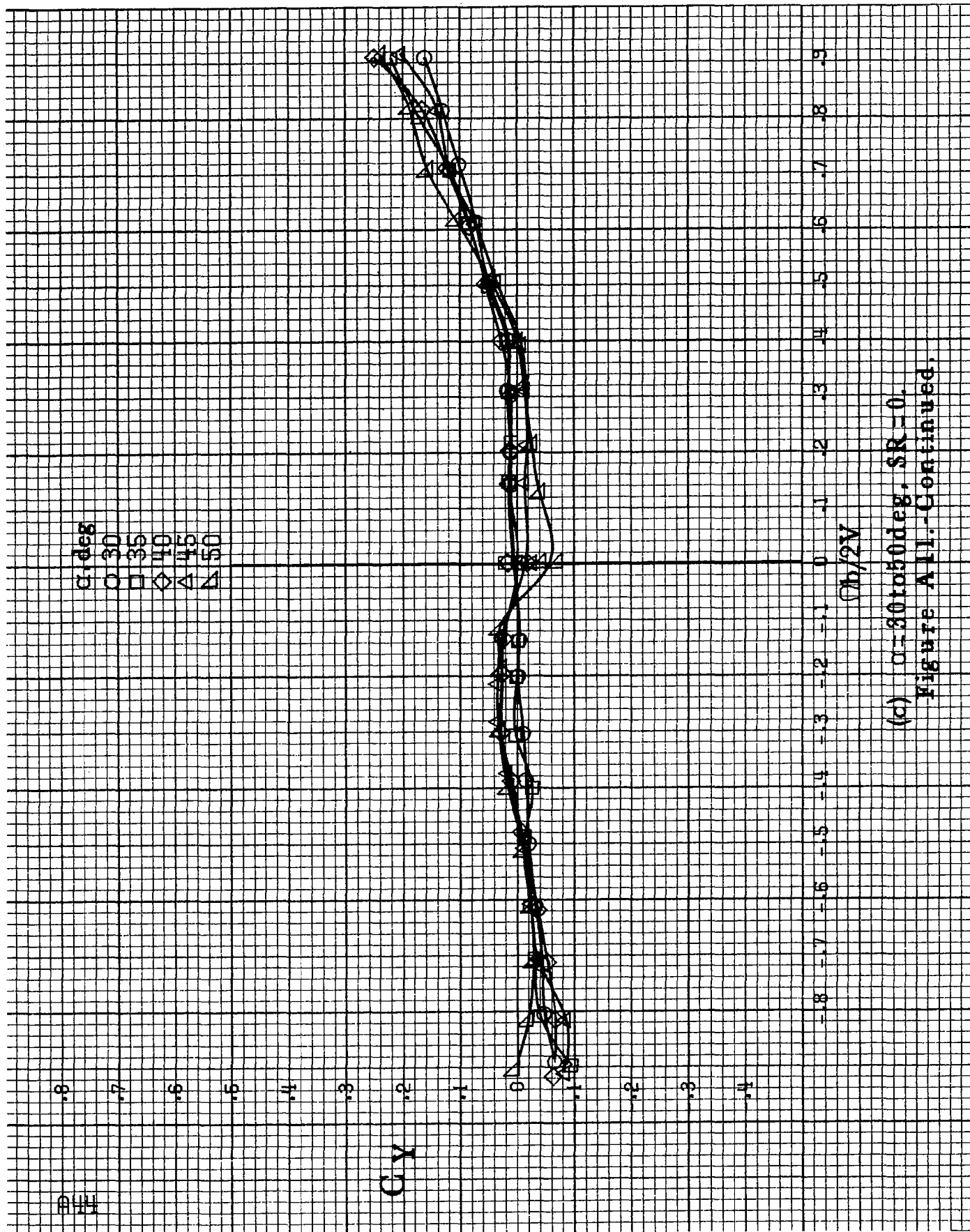
PHI

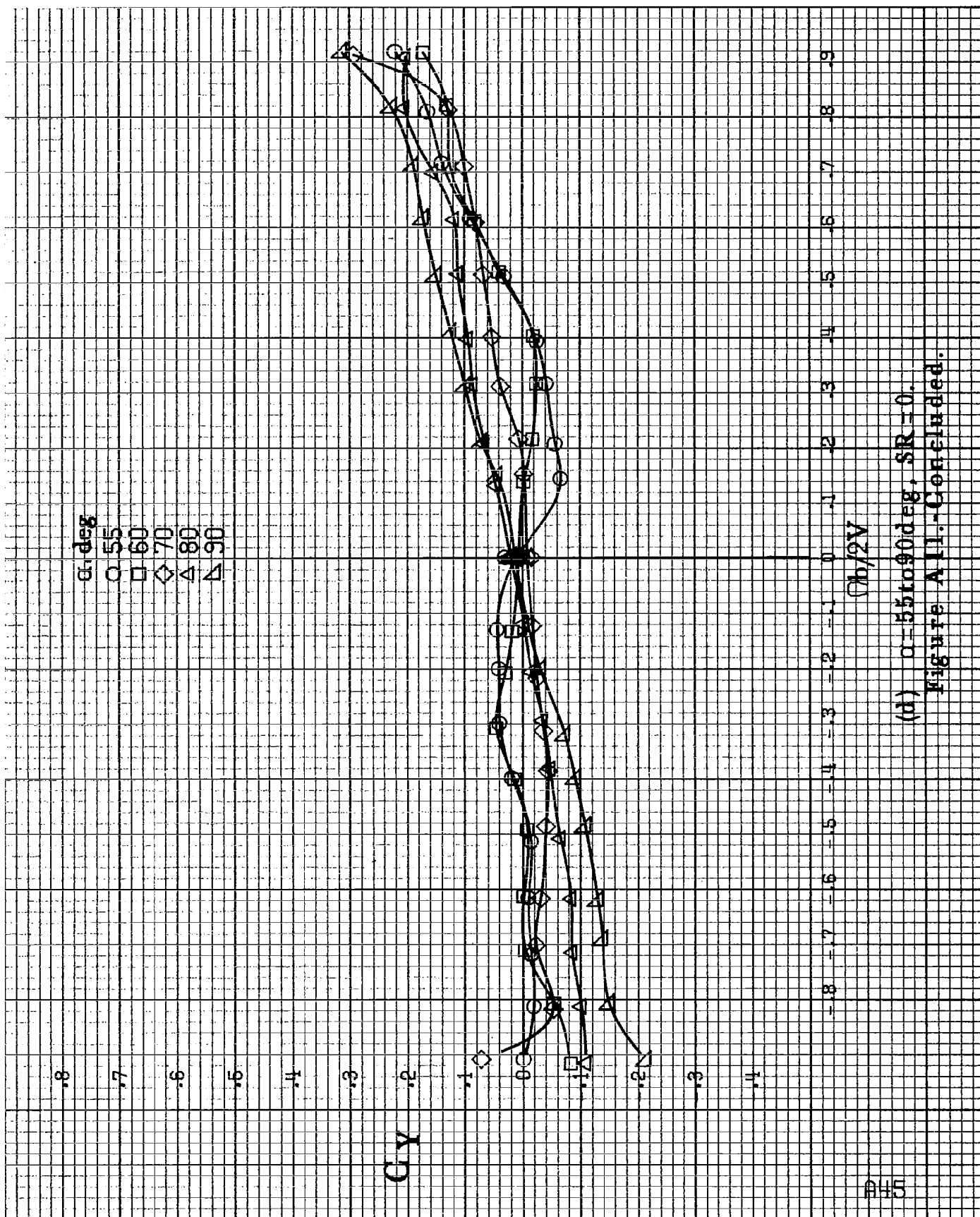
α , deg
 ○ 30
 □ 35
 ◇ 40
 △ 45
 ▽ 50

Cy

$\Omega_b/2V$

(c) $\alpha=30$ to 50 deg, $SR=0$.
 Figure A11.-Continued.





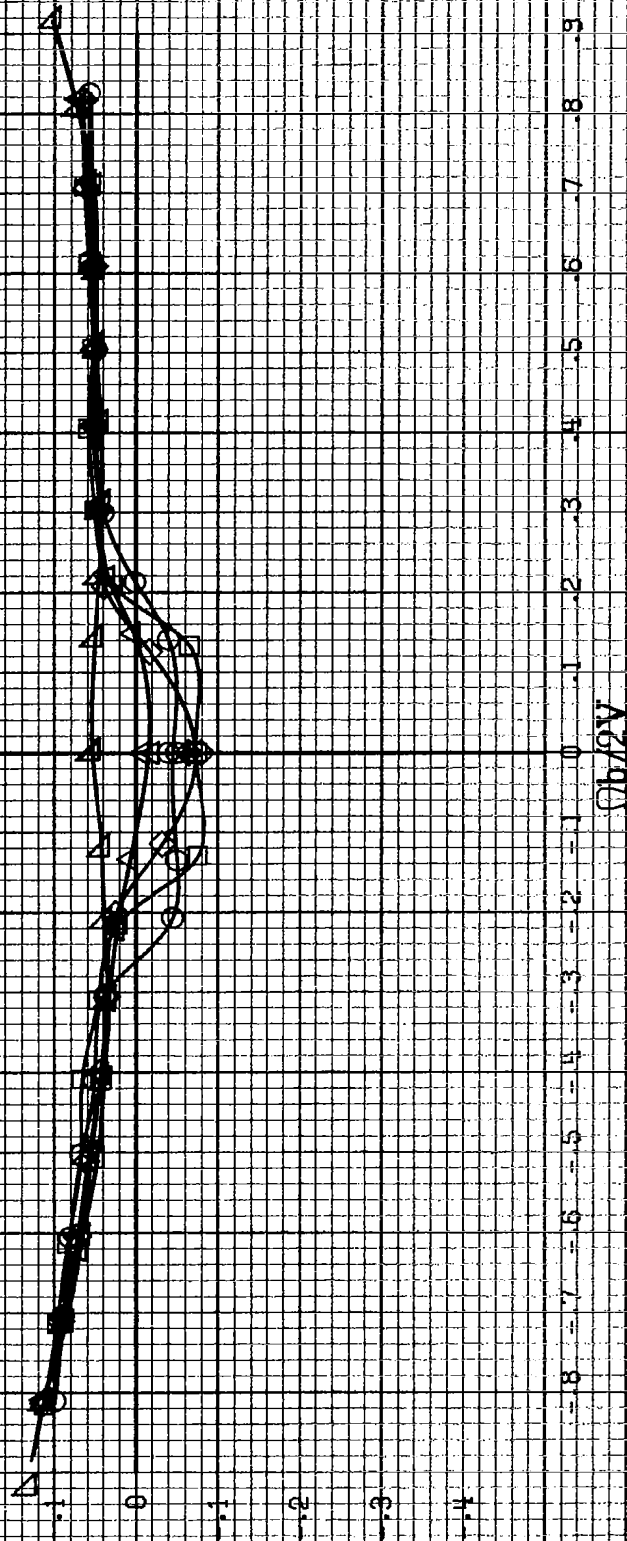
(d) $\alpha=55$ to 90 deg, $SR=0$.

Figure A11.-Concluded.

8-6

α, deg
 $\circ 8$
 $\square 10$
 $\diamond 12$
 $\triangle 14$
 $\nabla 16$

C_A



(a) $\alpha = 8$ to 16 deg, $SR = 91.4 \text{ cm (36 in.)}$.

Figure A.12.-Effect of rotation rate and angle of attack on axial-force coefficient for short body, low wing, horizontal tail no. 1 configuration. $\delta_e = 0^\circ$, $\delta_a = 0^\circ$, $\delta_r = 0^\circ$, $\beta = 0^\circ$.

GA

α , deg
 ○ 18
 □ 20
 ◇ 25
 △ 30
 ▲ 35

-0.8 -0.7 -0.6 -0.5 -0.4 -0.3 -0.2 -0.1 0 0.1 0.2 0.3 0.4 0.5 0.6 0.7 0.8 0.9
 $(h/2V)$

(b) $C=18$ to 35 deg, $SR=91.4$ cm (36 in.)
 Figure A12.-Continued.

α, deg
 30
 35
 40
 45
 50

C A

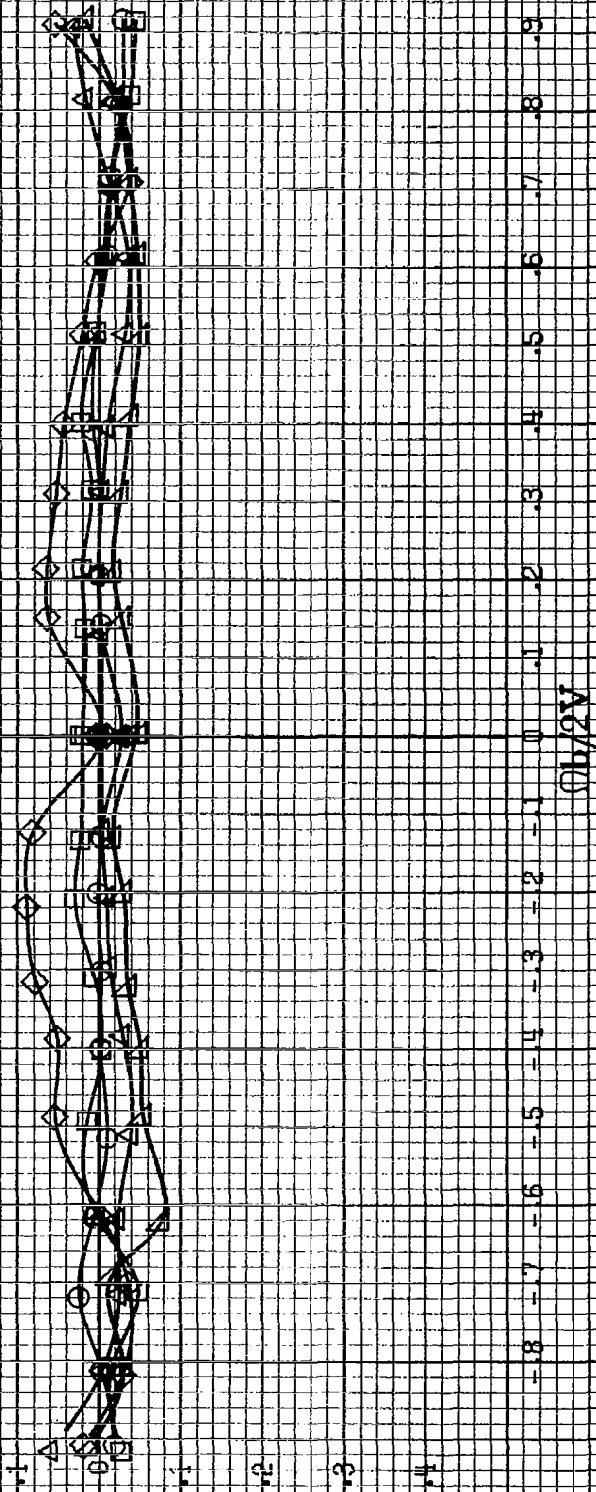


Ob/2V

(c) $u=80$ to 50 deg , $SR=0$.
 Figure A12.-Continued.

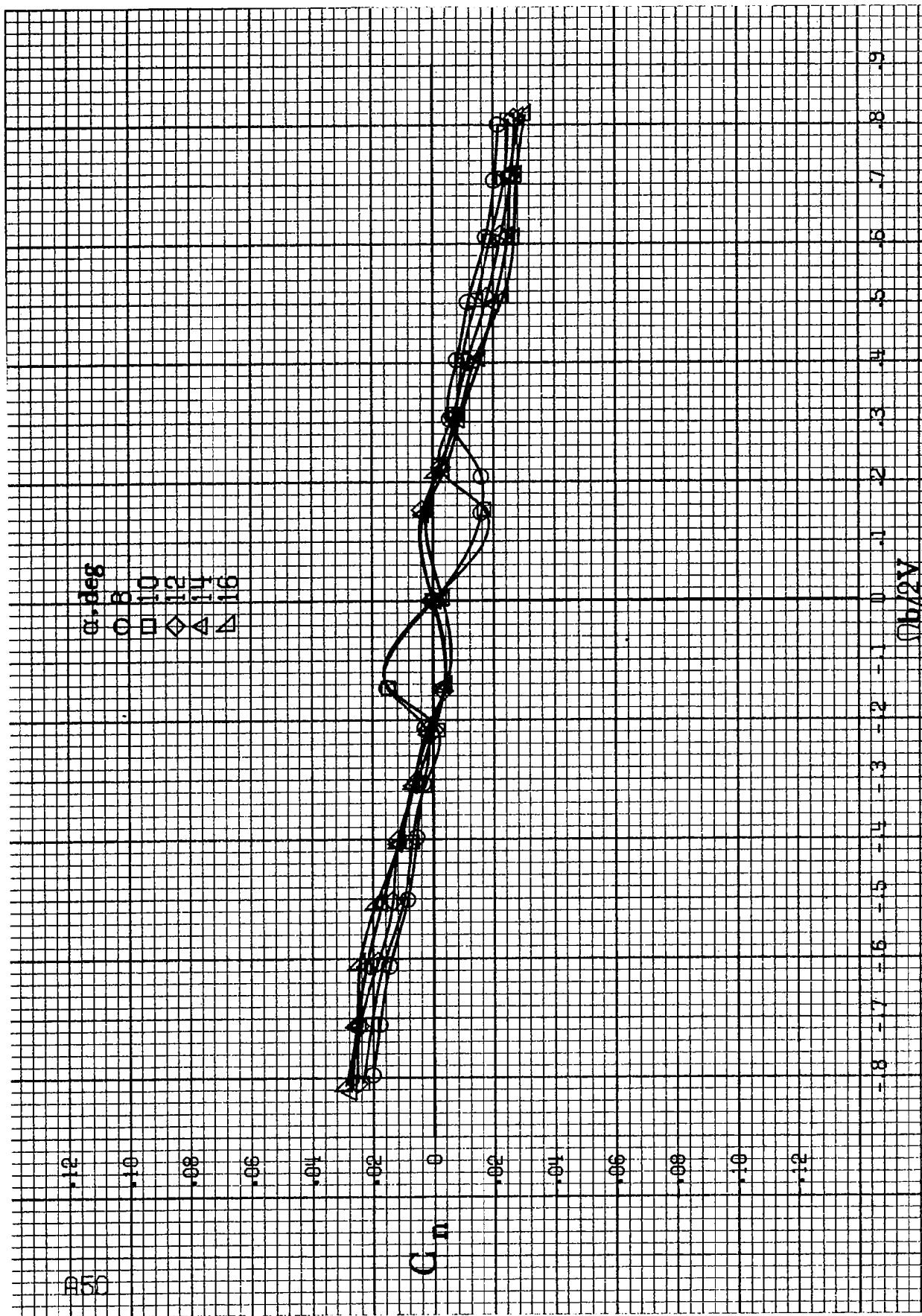
GA

α , deg
 O 55
 □ 60
 ◇ 70
 △ 80
 ▽ 90



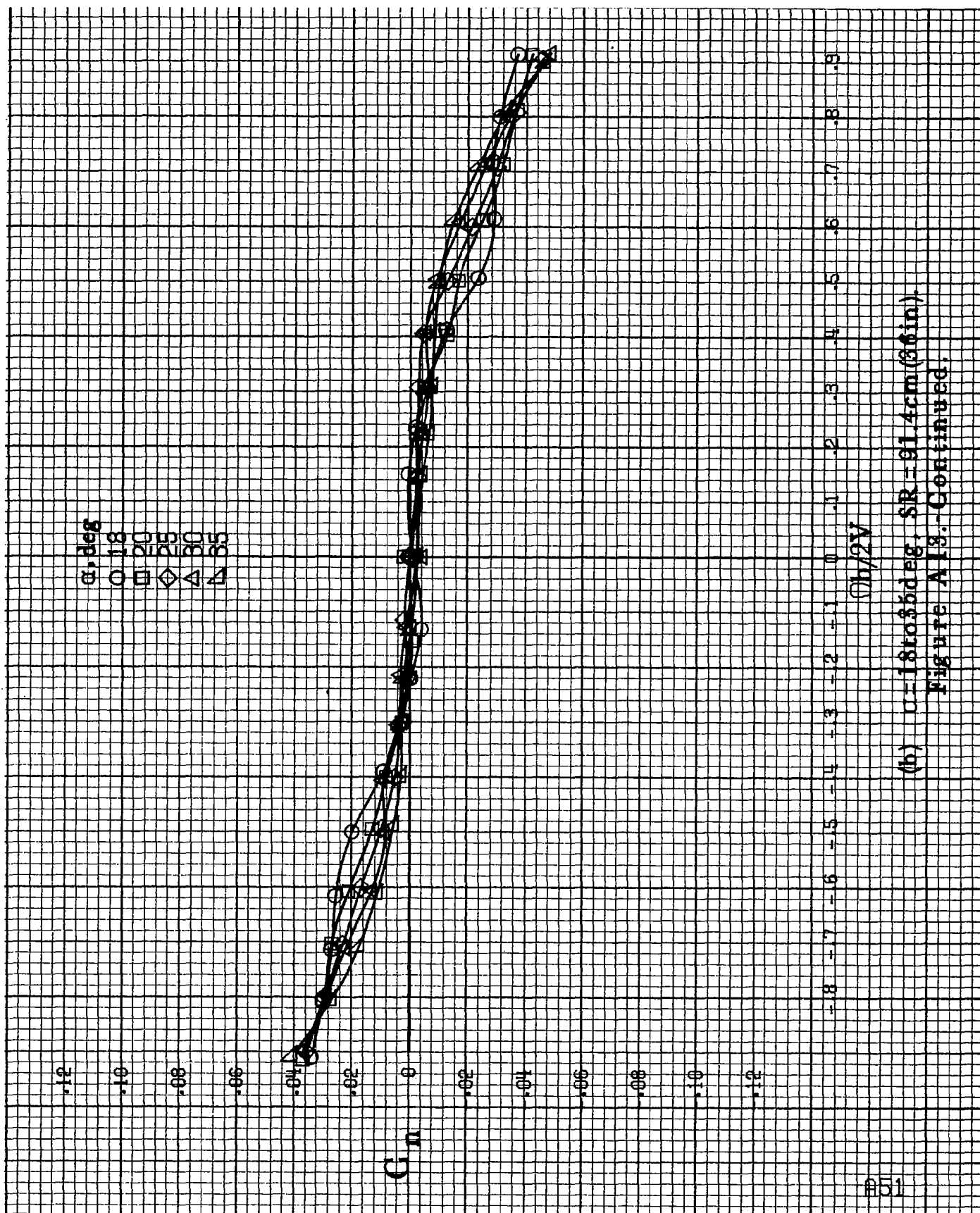
(d) $\alpha = 55$ to 90 deg, $SR = 0$.

Figure A12.-Concluded.

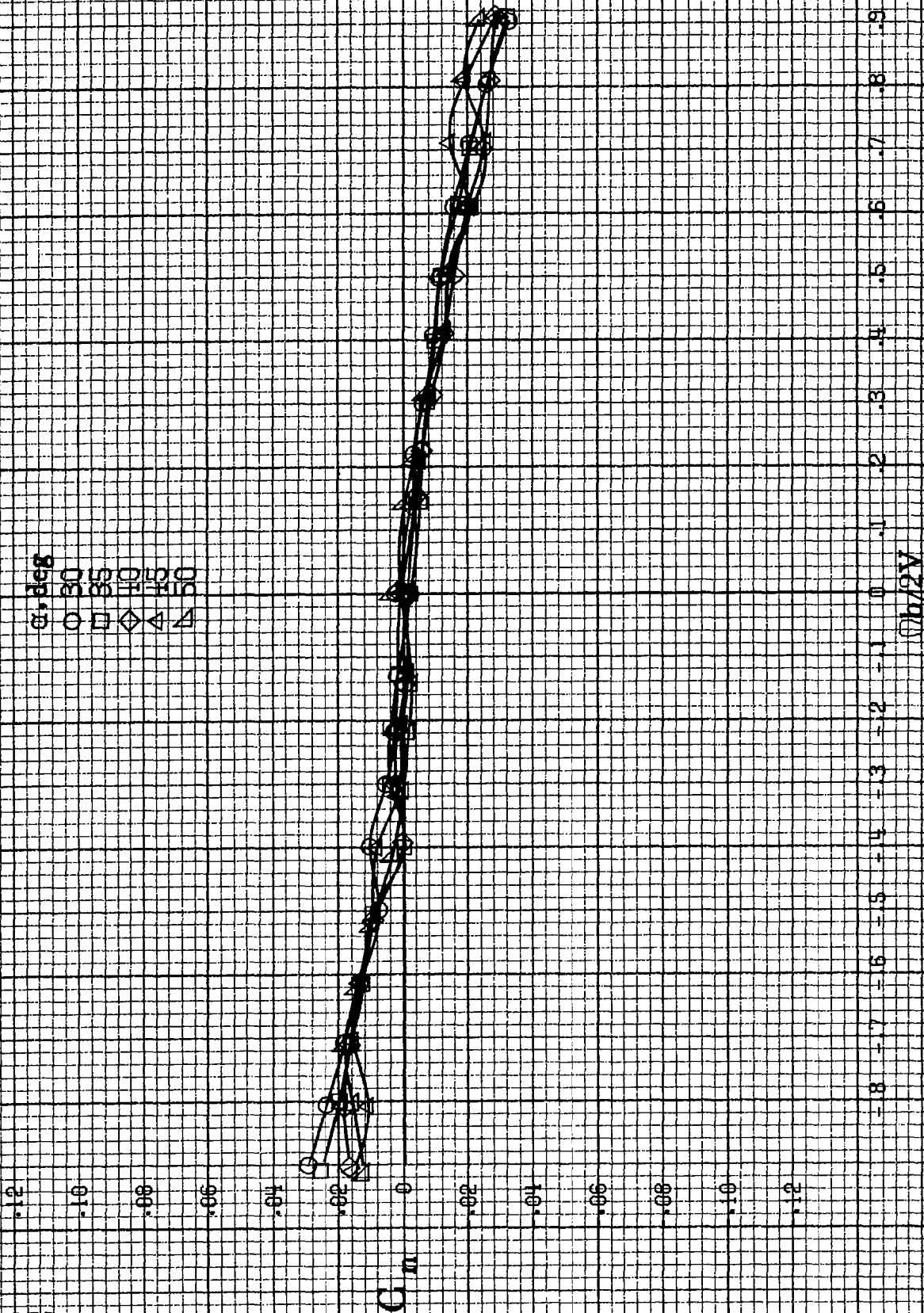


(a) $\alpha = 8$ to 16° , $SR = 91.4 \text{ cm (36 in.)}$

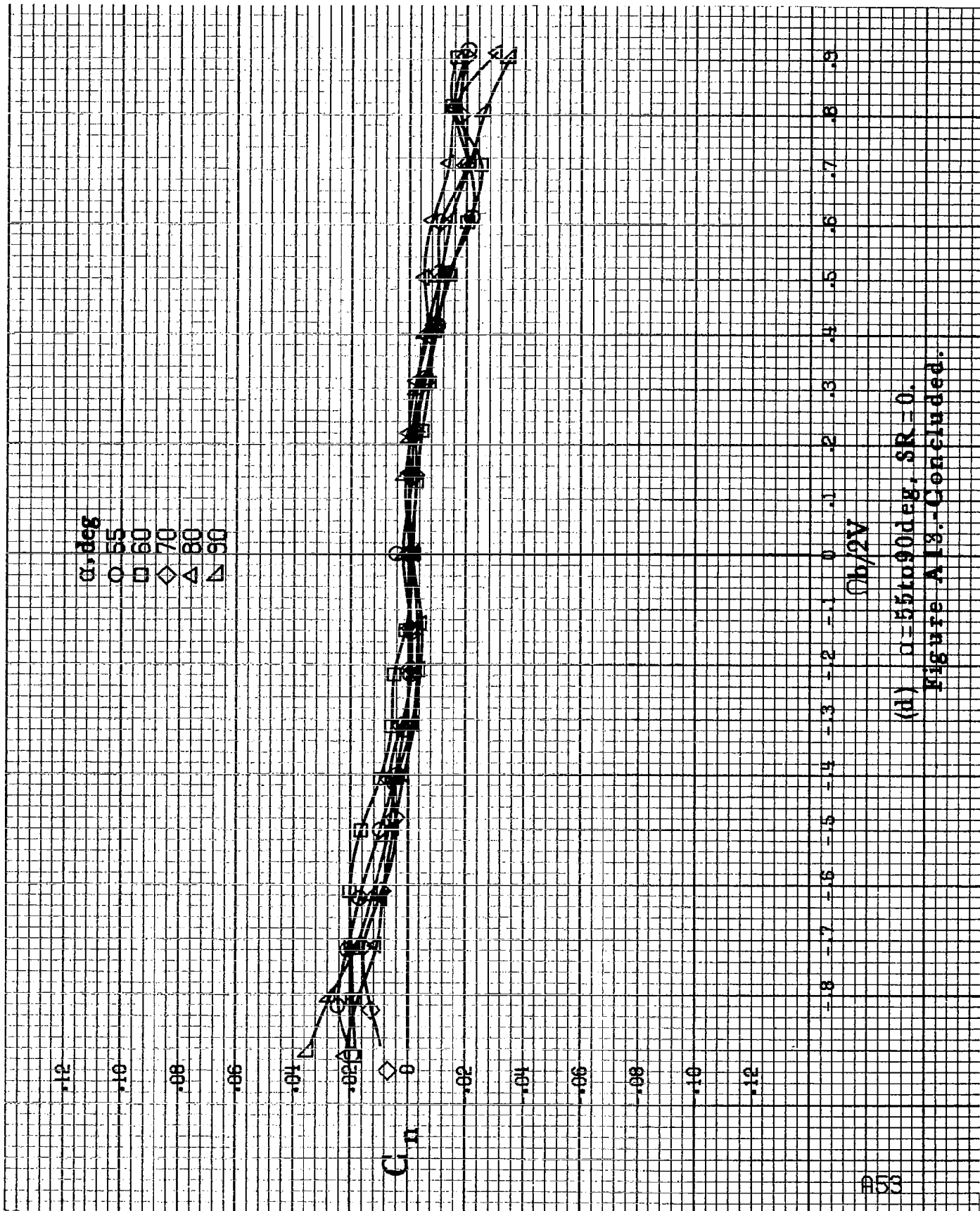
Figure A13.-Effect of rotation rate and angle of attack on yawing-moment coefficient for short body, low wing, horizontal tail no. 3 configuration. $\delta_e = 0^\circ$, $\delta_a = 0^\circ$, $\delta_r = 0^\circ$.



(b) $\alpha=18$ to 35 deg; $SR=91.4$ cm (36 in).
Figure A13.-Continued.



(c) $\alpha = 30$ to 50 deg. $SR = 0$.
Figure A18.-Continued.



(d) $\alpha=55$ to 90° , $SR=0$.
Figure A13.-Concluded.

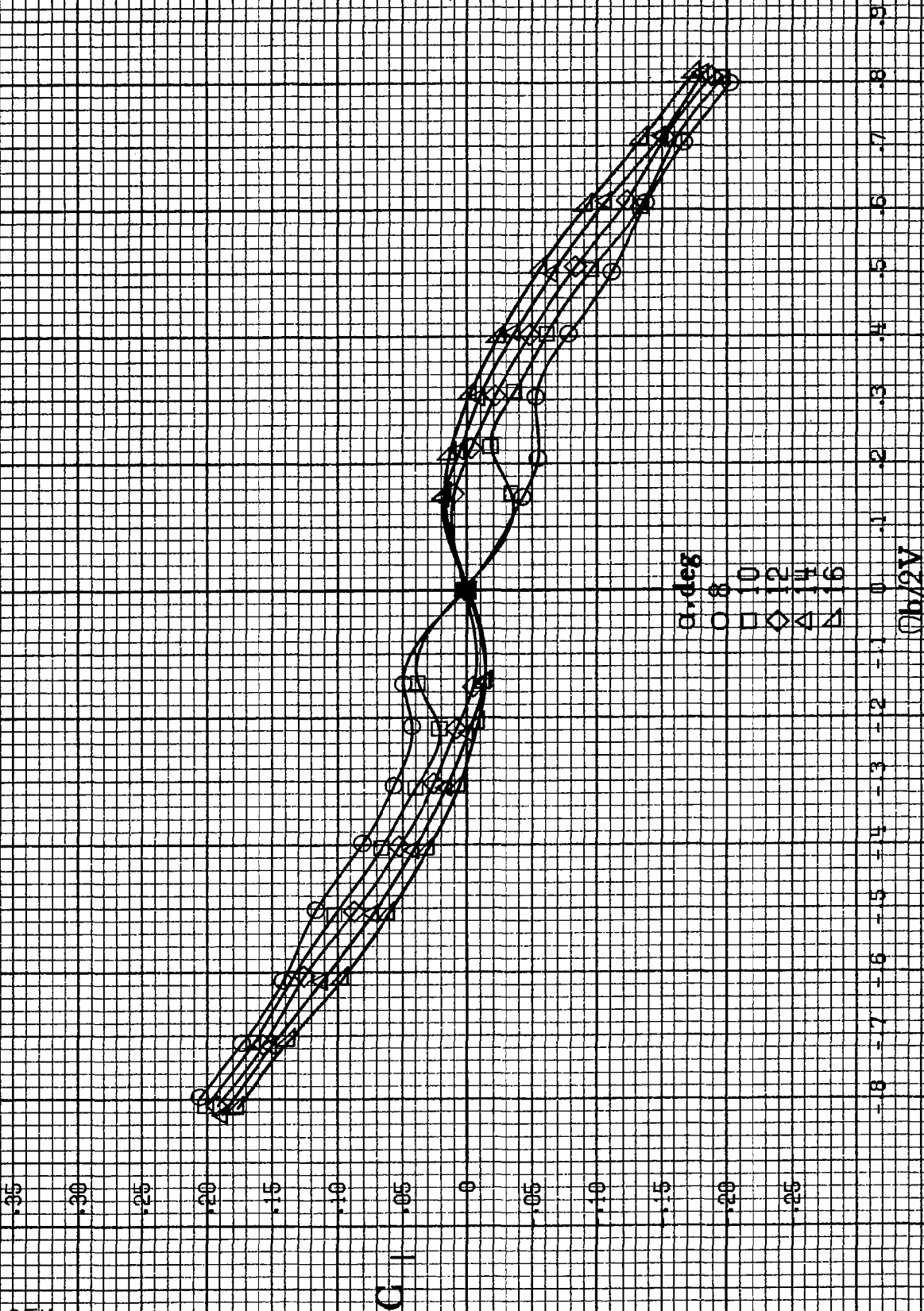
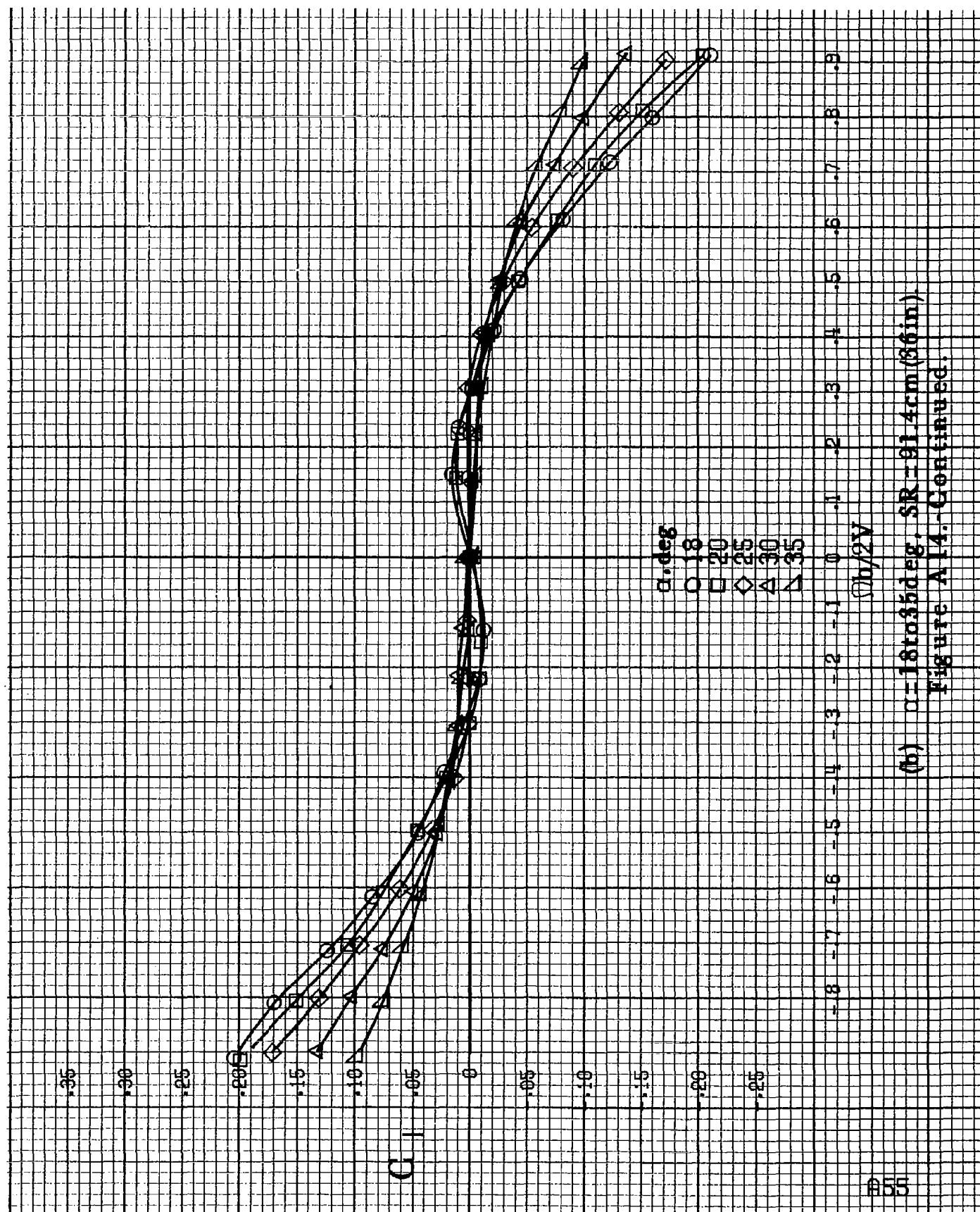
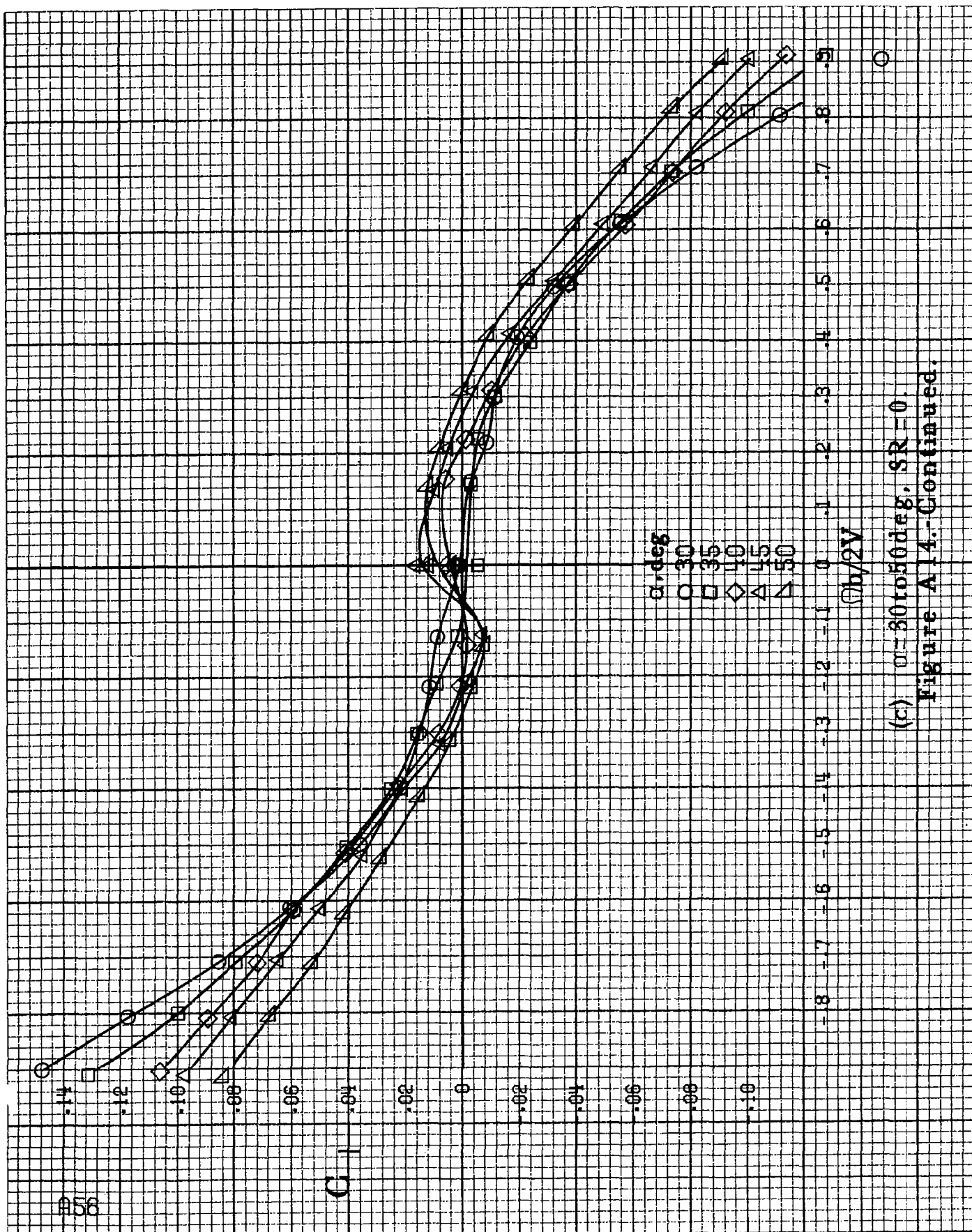


Figure A14.-Effect of rotation rate and angle of attack on rolling-moment coefficient for short body, low wing, horizontal tail no. 3 configuration. $\delta_e = 0^\circ$, $\delta_a = 0^\circ$, $\delta_r = 0^\circ$, $\beta = 0^\circ$.

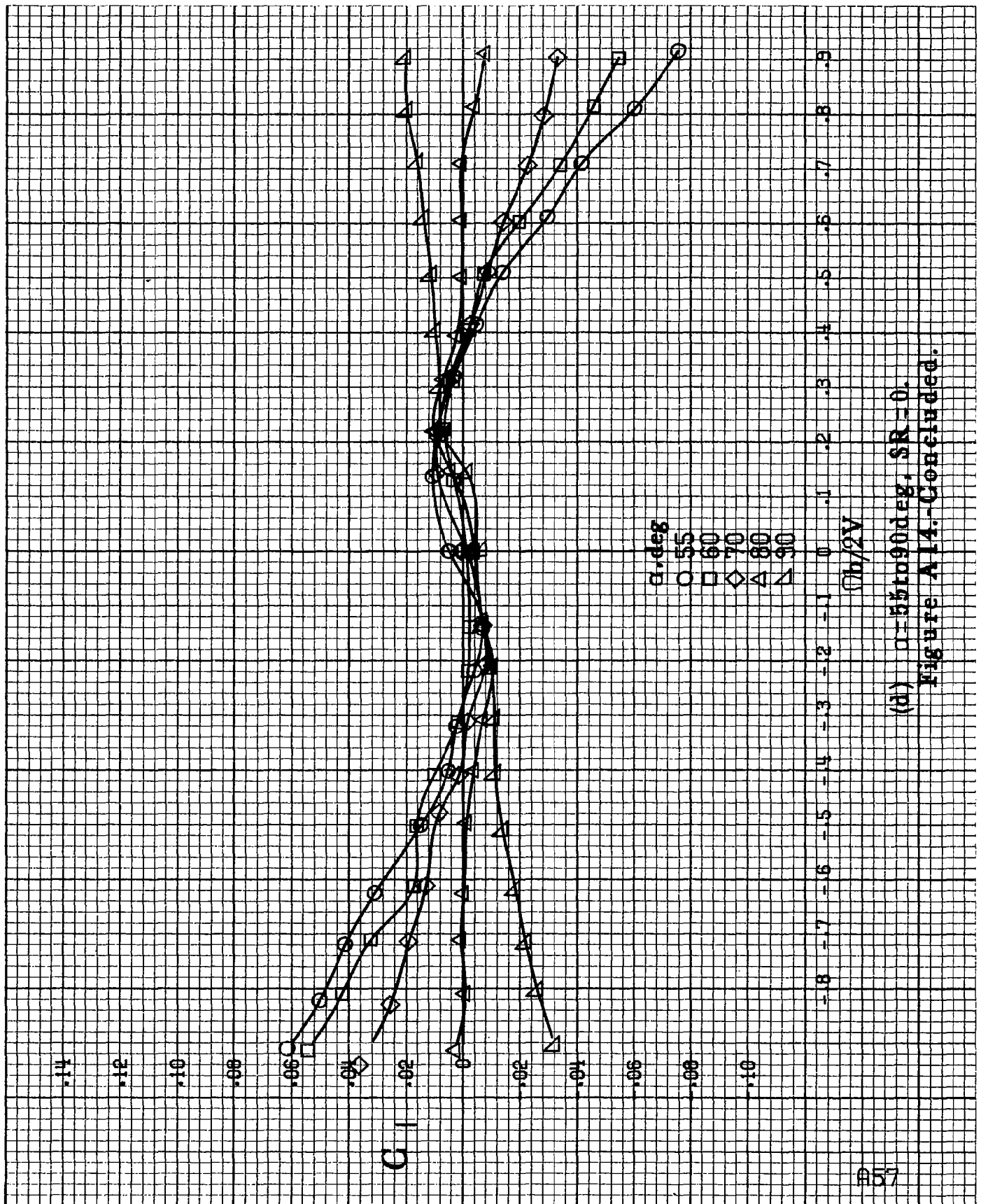


(b) $\alpha=18$ to 35° , $SR=91.4\text{cm}(36\text{in})$.
Figure A14.-Continued.



(c) $\alpha=30$ to 50° , $SR=0$.

Figure A14-Continued.



(d) $\alpha=55$ to 90° , $SR=0$.
Figure A 14.-Concluded.

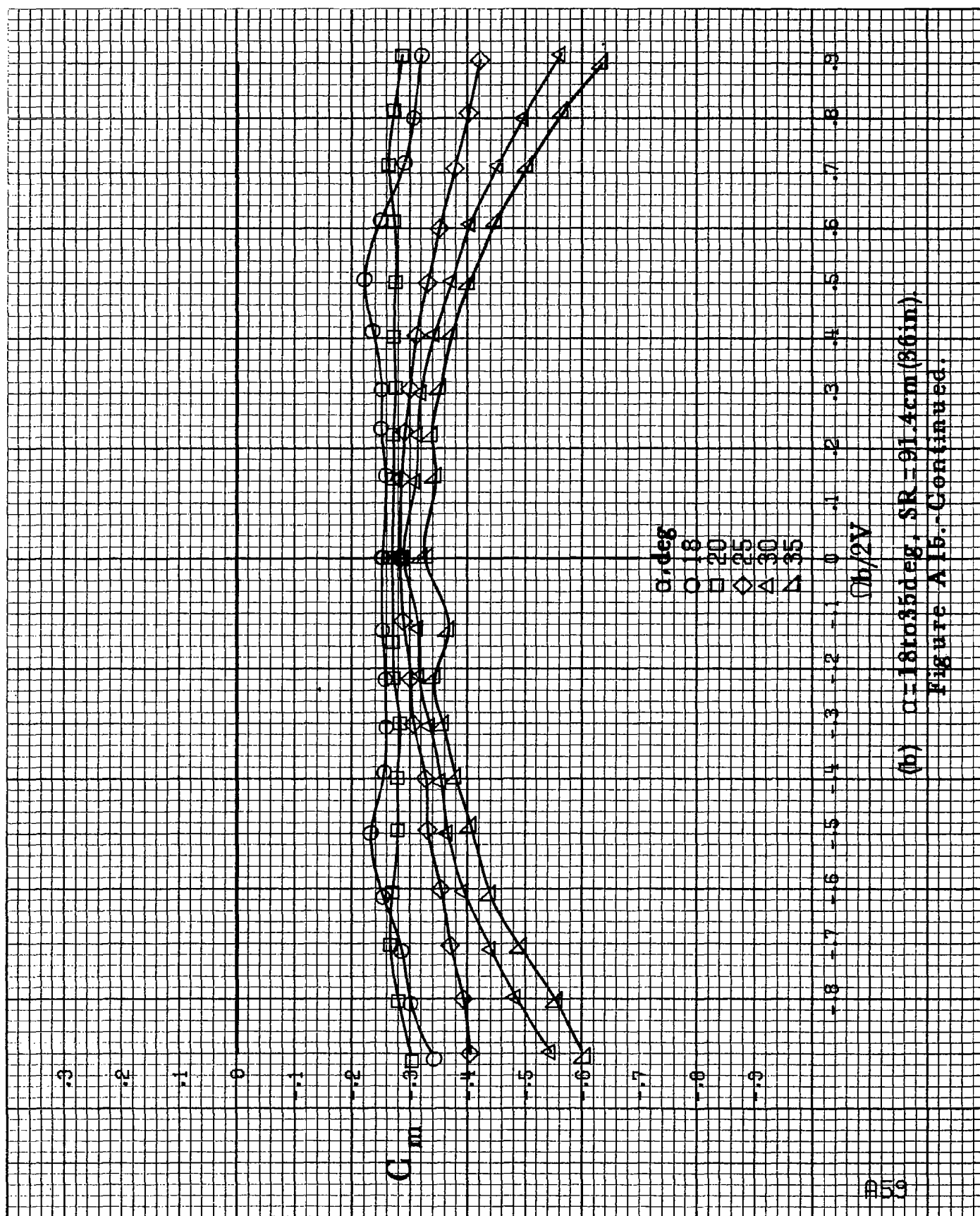
C_m α, deg

\circ 8
 \square 10
 \diamond 12
 \triangle 14
 ∇ 16

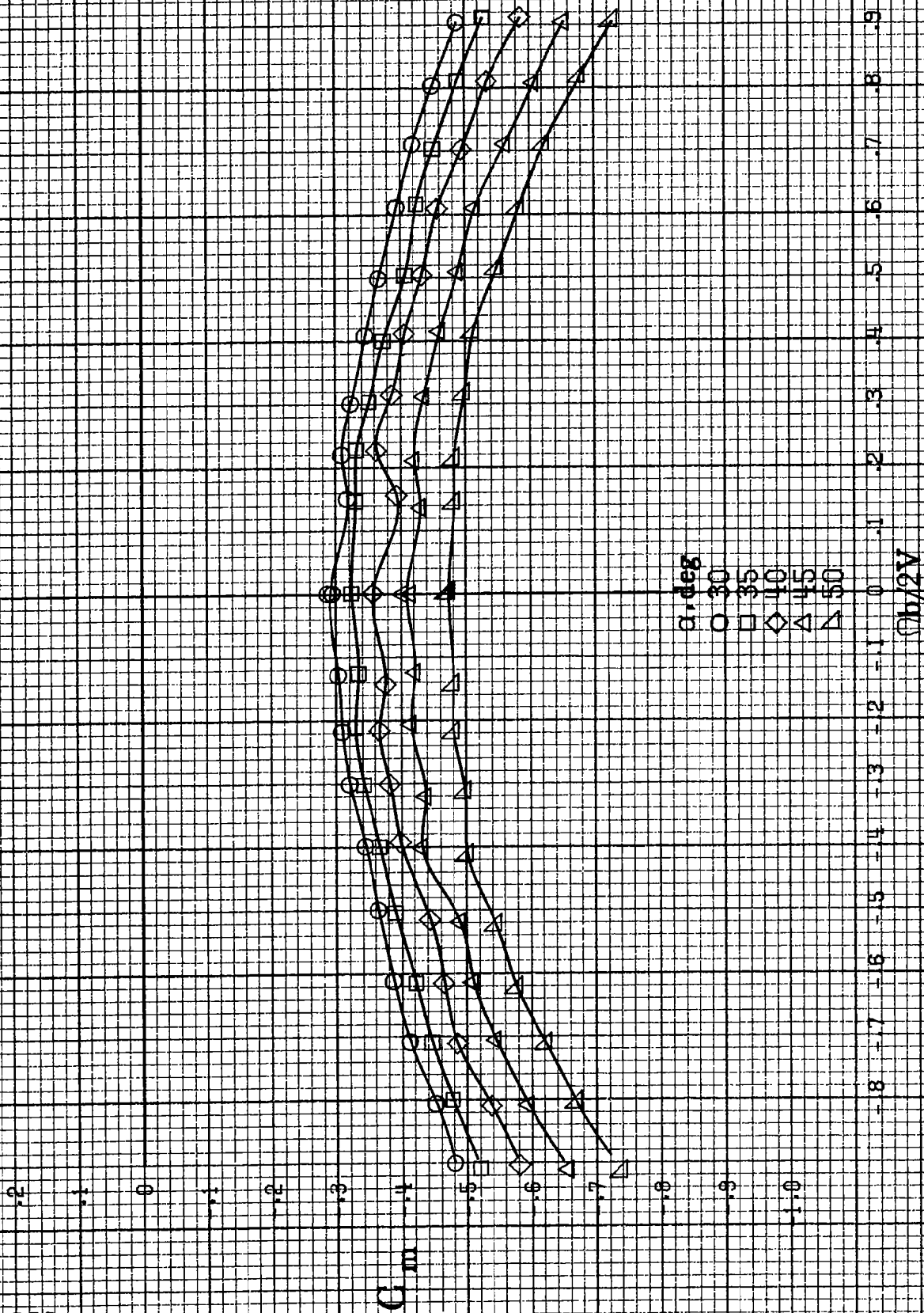
 $b/2V$ (a) $\alpha = 8$ to 16° , $SR = 91.4 \text{ cm (36 in.)}$.

Figure A15.-Effect of rotation rate and angle of attack on pitching-moment coefficient for short body, low wing, horizontal tail no. 3 configuration.

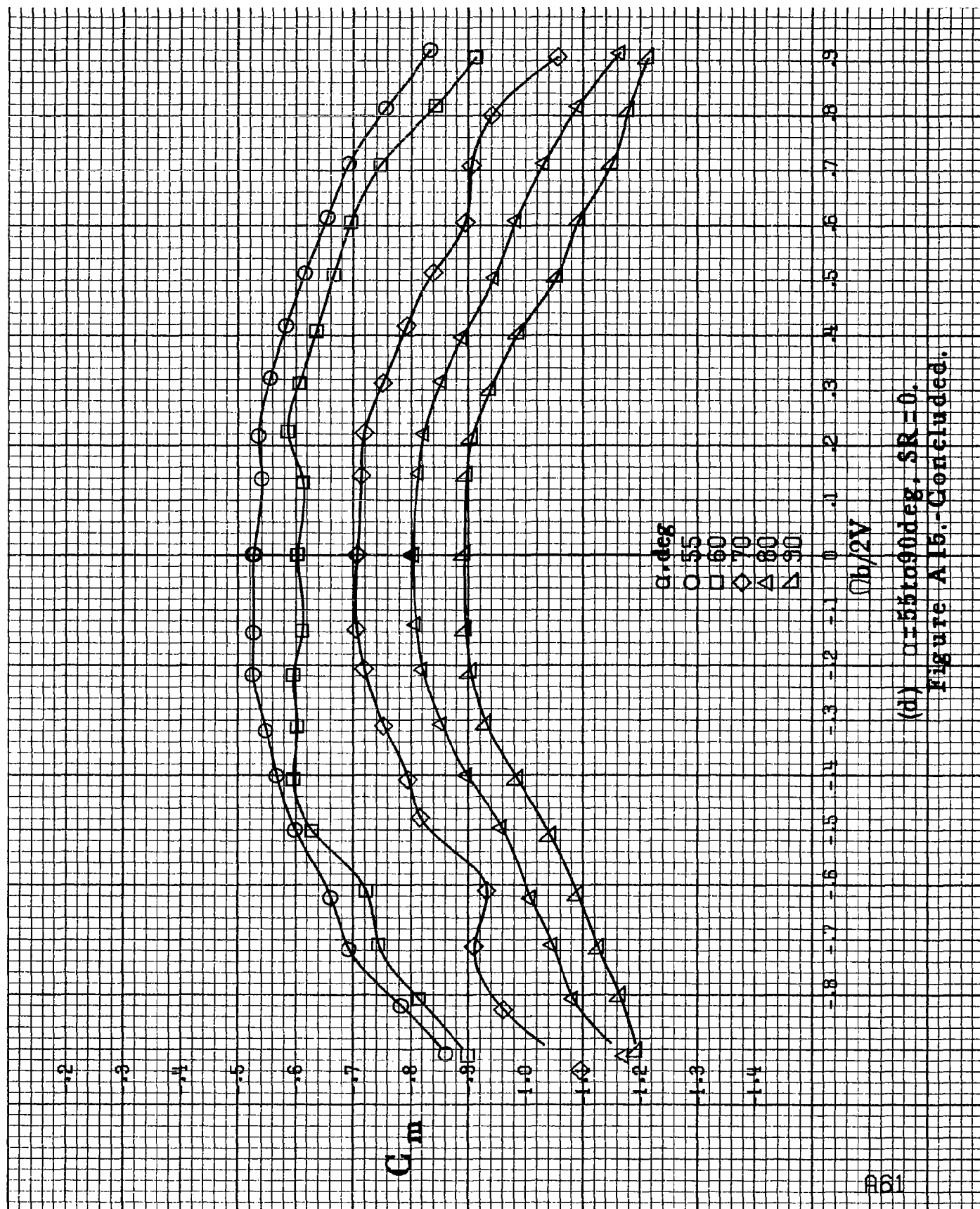
$\delta_\alpha = 0^\circ$, $\delta_\beta = 0^\circ$, $\delta_\gamma = 0^\circ$, $\beta = 0^\circ$.



(b) $\alpha = 18$ to 35 deg, $SR = 91.4 \text{ cm} (86 \text{ in})$.
Figure A15.-Continued.



(c) $n=30$ to 50° , $SR=0$.
Figure A15.-Continued.

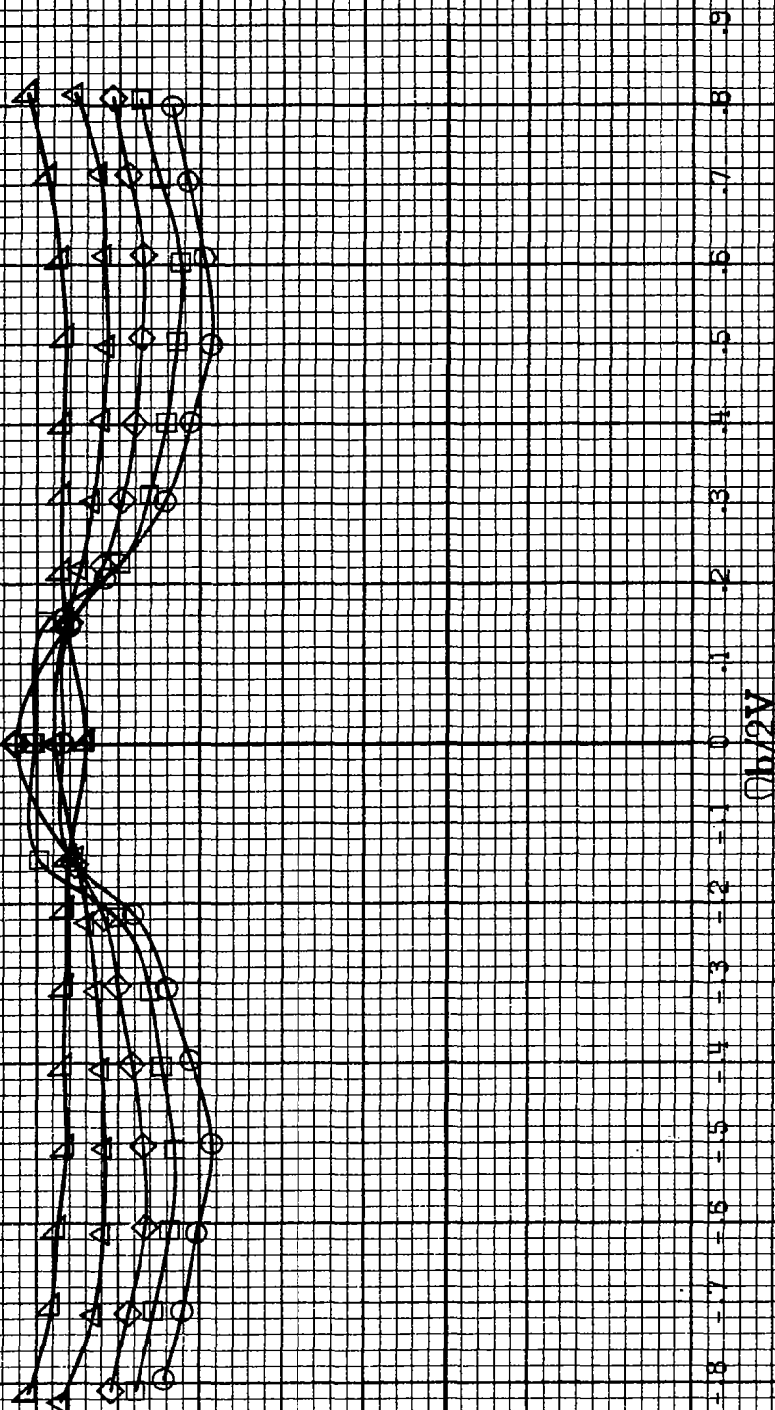


(d) $\alpha = 55$ to 90° , $SR = 0$.
Figure A15.-Concluded.

α, deg

○ 8
□ 10
◇ 12
△ 14
▽ 16

C_N



(a) $\alpha = 8$ to 16° , $SR = 91.4 \text{ cm (36 in.)}$.

Figure A16.-Effect of rotation rate and angle of attack on normal-force coefficient for short body, low wing, horizontal tail no. 3 configuration. $\delta a = 0^\circ$, $\delta r = 0^\circ$, $\delta \tau = 0^\circ$, $S = 10^\circ$.

α, deg
 ○ 18
 □ 20
 ◇ 25
 △ 30
 ▲ 35

2.6

2.4

2.2

2.0

1.8

1.6

1.4

1.2

1.0

.8

.6

.4

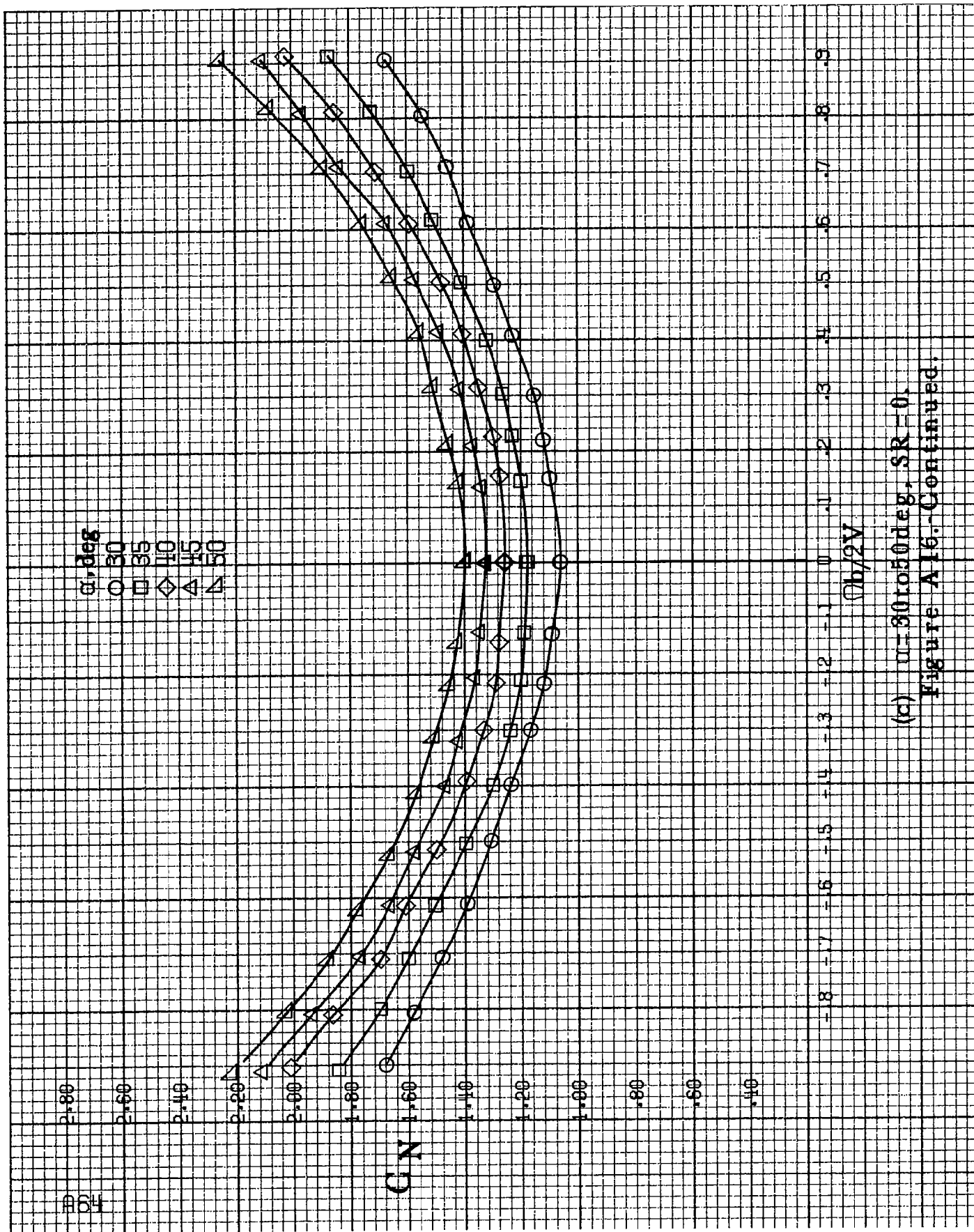
.2

GN

-8 -7 -6 -5 -4 -3 -2 -1 0 .1 .2 .3 .4 .5 .6 .7 .8 .9

$(b/2V)$

(b) $\alpha=18$ to 35 deg, SR=91.4cm(36in).
 Figure A16.-Continued.



(c) $\alpha = 30$ to 50 deg, $SR = 0$,
Figure A16.-Continued.

α, deg
 O 55
 □ 60
 ◇ 70
 △ 80
 ▽ 90

3.2

3.0

2.8

2.6

GN

2.0

1.8

1.6

1.4

1.2

1.0

.8

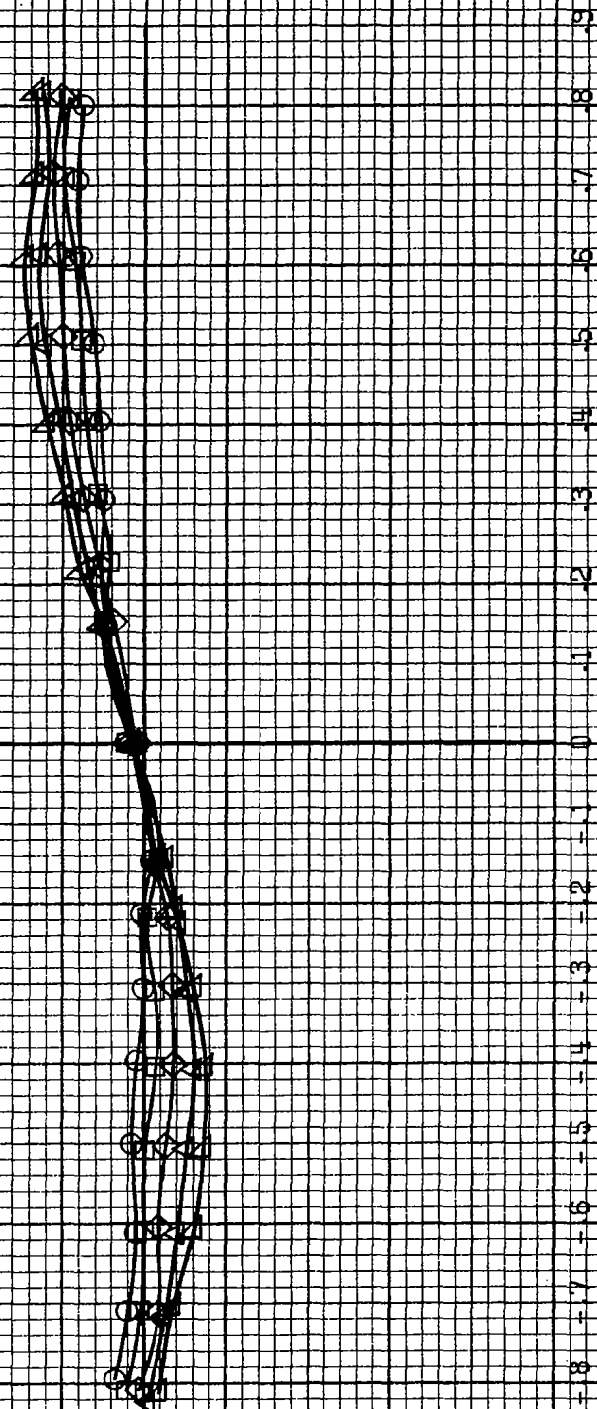
.9

$(h/2V)$

(d) $\alpha=55$ to 90 deg, $SR=0$.
 Figure A16.-Concluded.

α, deg
 O 8
 □ 10
 ◇ 12
 △ 14
 ▲ 16

C_Y



$\Omega b / 2V$

(a) $\alpha = 8$ to 16 deg, $SR = 91.4 \text{ cm (36 in)}$.

Figure A17.-Effect of rotation rate and angle of attack on side-force coefficient for short body, low wing, horizontal tail no. 3 configuration. $\delta_e = 0^\circ$, $\delta_a = 0^\circ$, $\delta_r = 0^\circ$.

α, deg
 O 18
 □ 20
 ◇ 25
 △ 30
 ▽ 35

C_Y

$h/2V$

(b) $\alpha=18$ to 35 deg, $SR=91.4\text{cm}(36\text{in})$.

Figure A17.-Continued.

α, deg

○ 30

□ 35

◇ 40

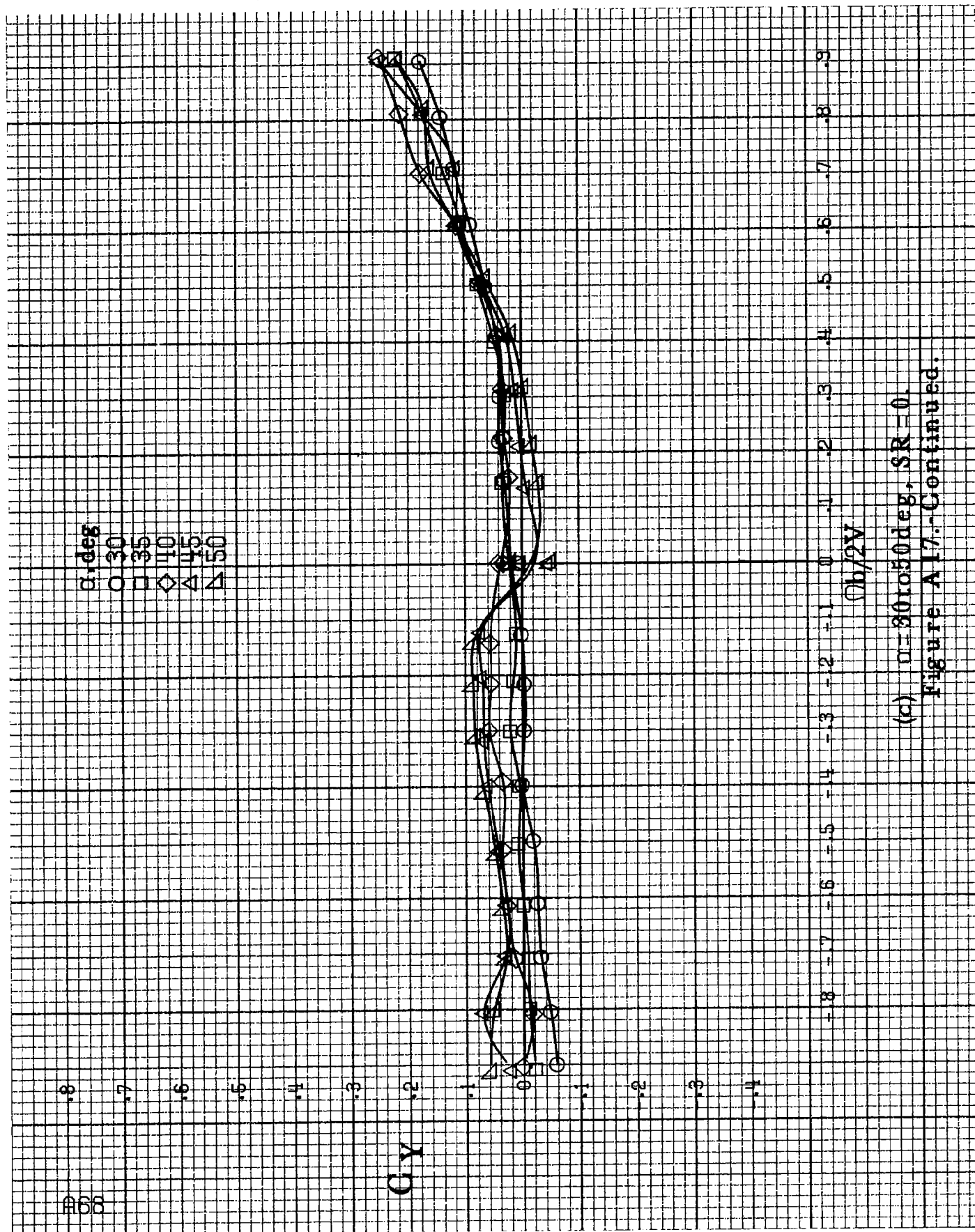
△ 45

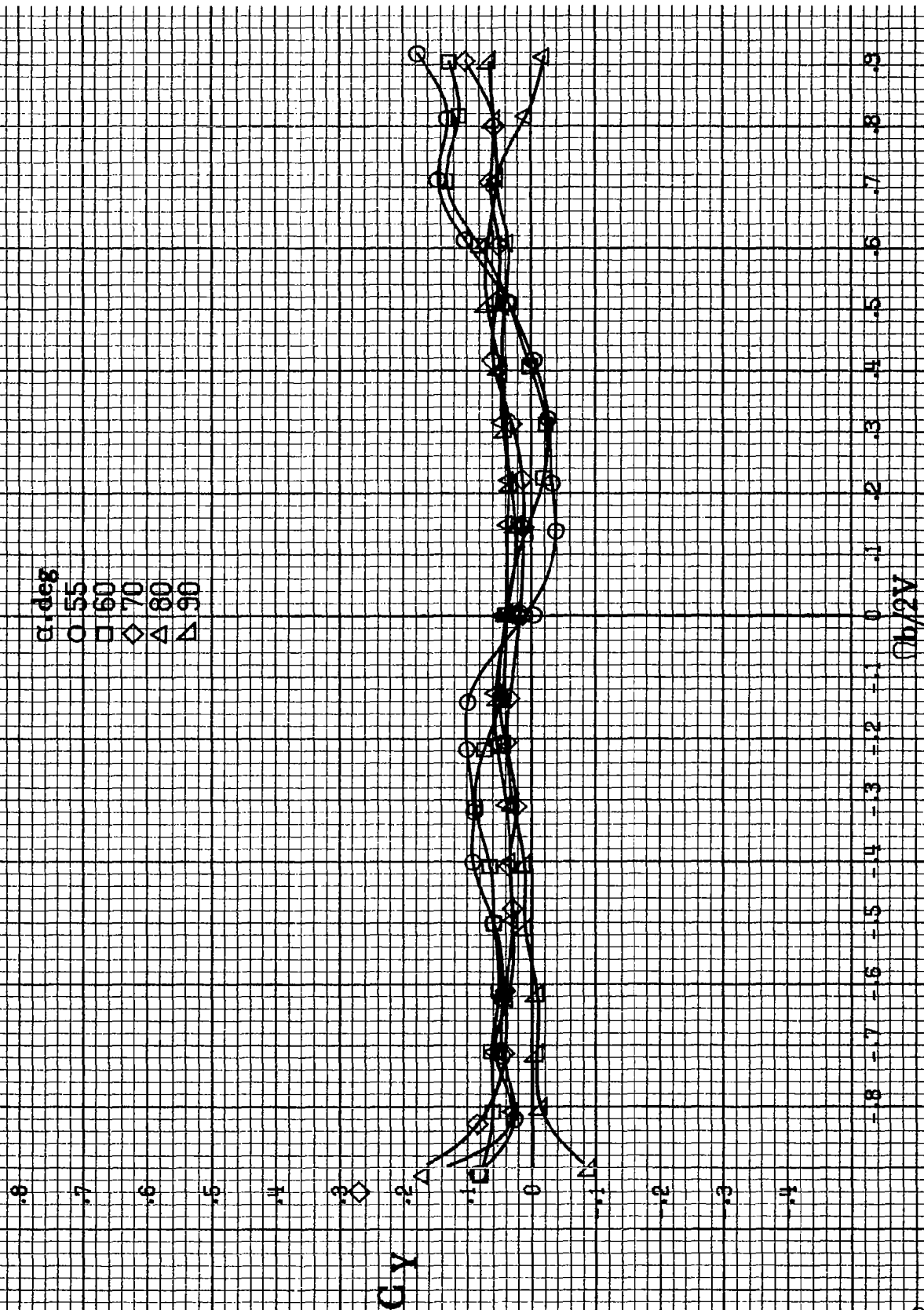
▽ 50

Cy

 $\phi_b/2V$ (c) $\alpha = 30 \text{ to } 50 \text{ deg}$, $SR = 0$.

Figure A17.-Continued.

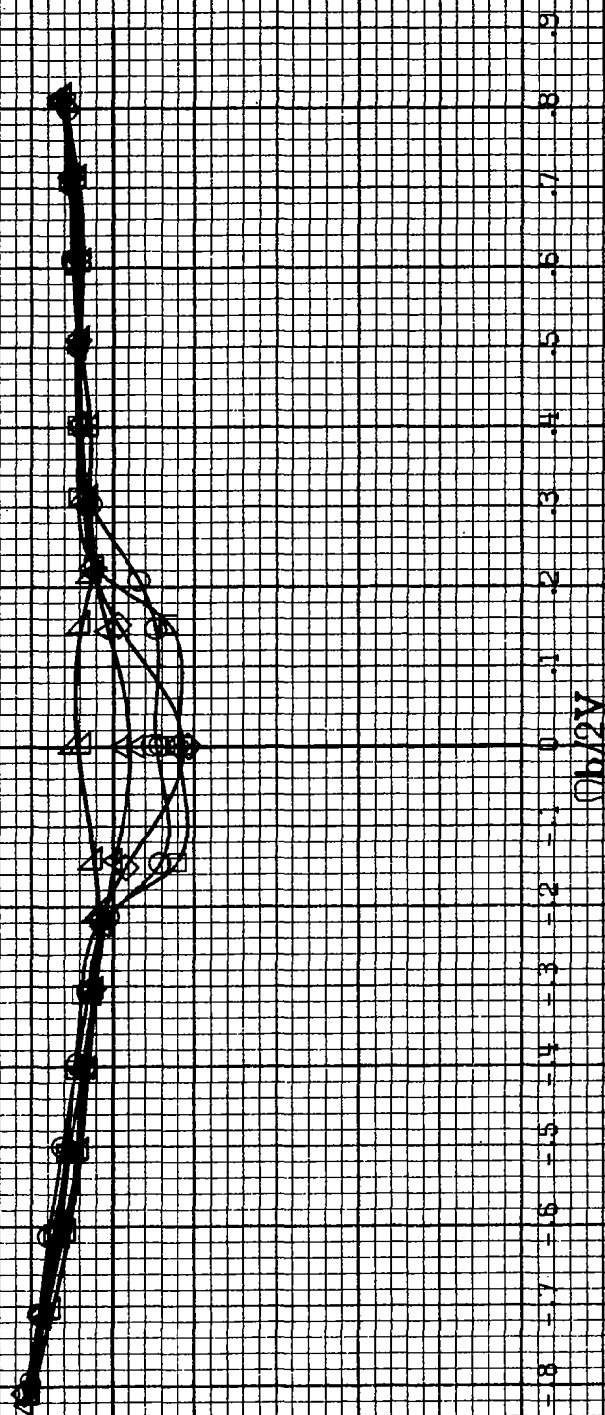




(d) $\alpha=55$ to 90 deg, $SR=0$.
Figure A17.-Concluded.

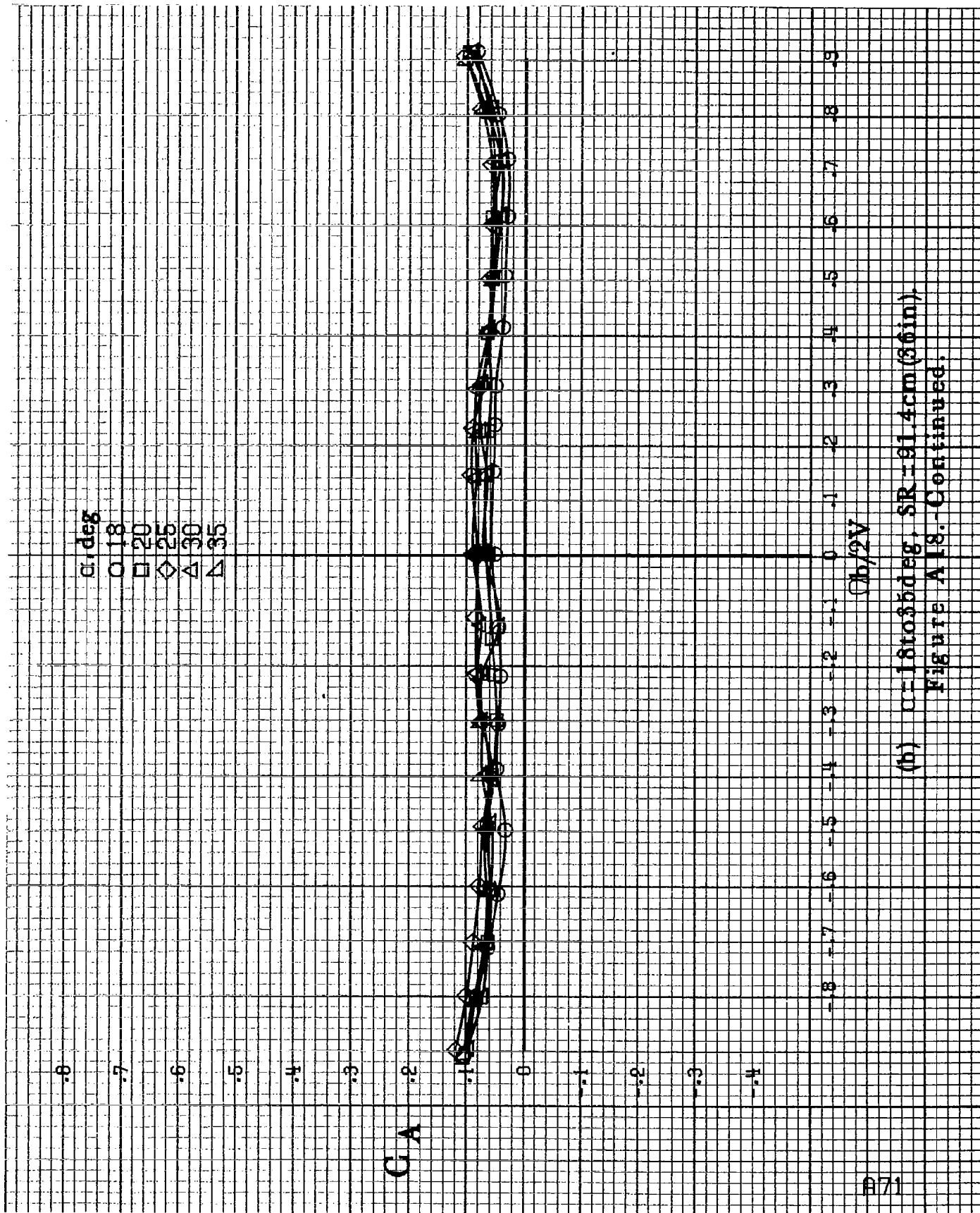
α, deg
 O 8
 □ 10
 ◇ 12
 △ 14
 ▲ 16

C.A



(a) $\alpha=8$ to 16° , $SR=91.4$ cm (36 in).

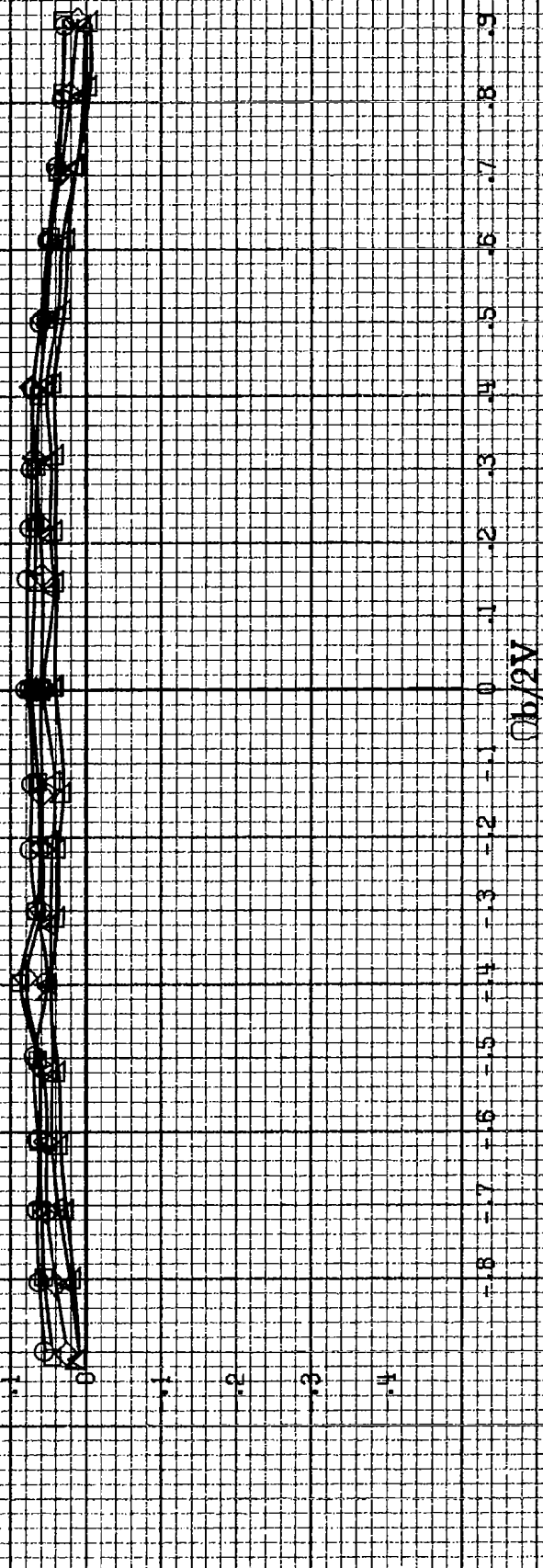
Figure A.18.-Effect of notation rate and angle of attack on axial-force coefficient for short body, low wing, horizontal tail no. 3 configuration. $\delta_a=0^\circ$, $\delta_w=0^\circ$, $\delta_r=0^\circ$, $\delta=10^\circ$.



(b) $\alpha=18$ to 35 deg, $SR=91.4$ cm (36 in).
Figure A18.-Continued.

α, deg
 \circ 30
 \square 35
 \diamond 40
 \triangle 45
 ∇ 50

C_A



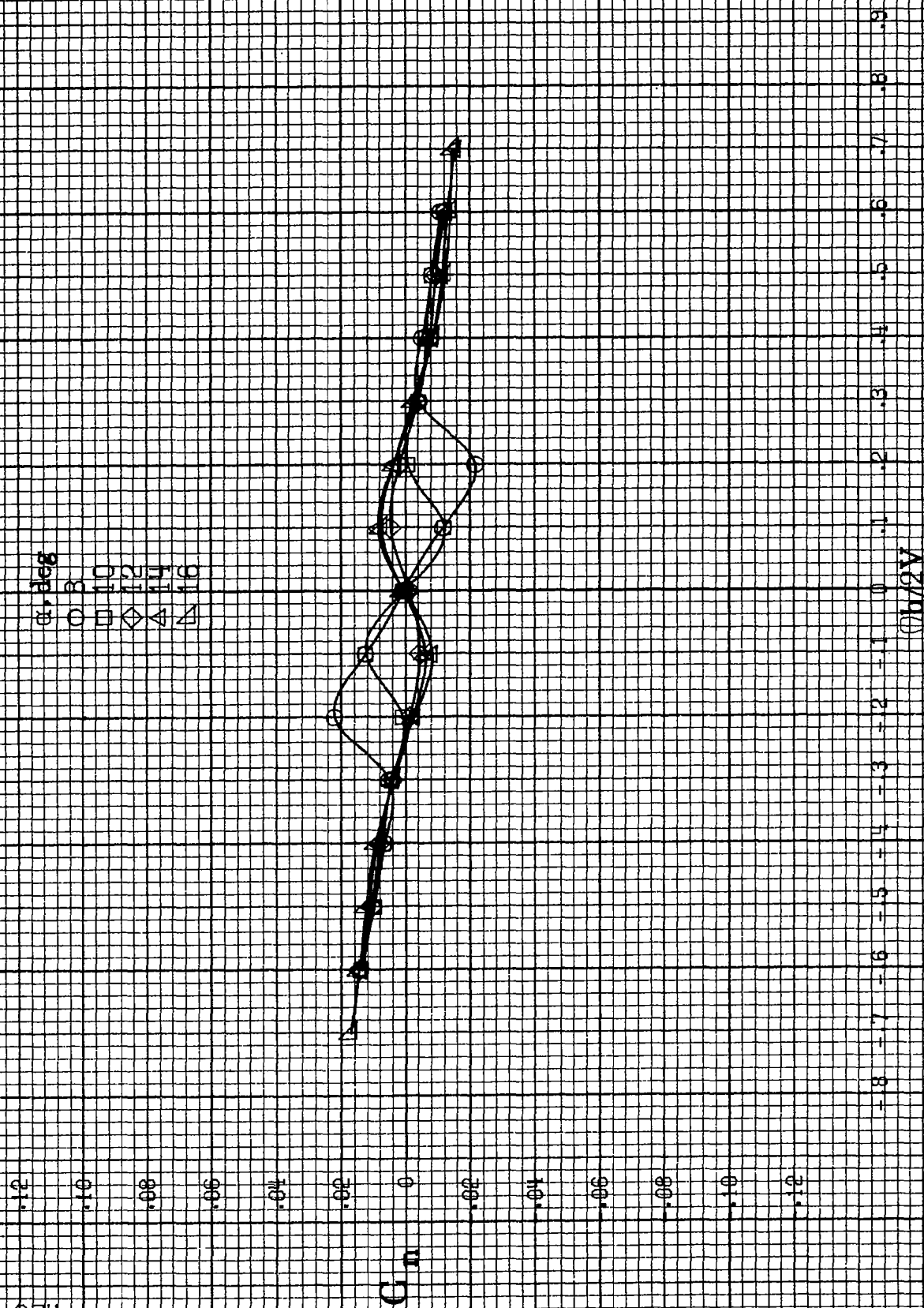
(c) $\alpha=30$ to 50° , $SR=0$.
 Figure A18.-Continued.

α , deg
 ○ 55
 □ 60
 ◇ 70
 △ 80
 ▴ 90

C_A

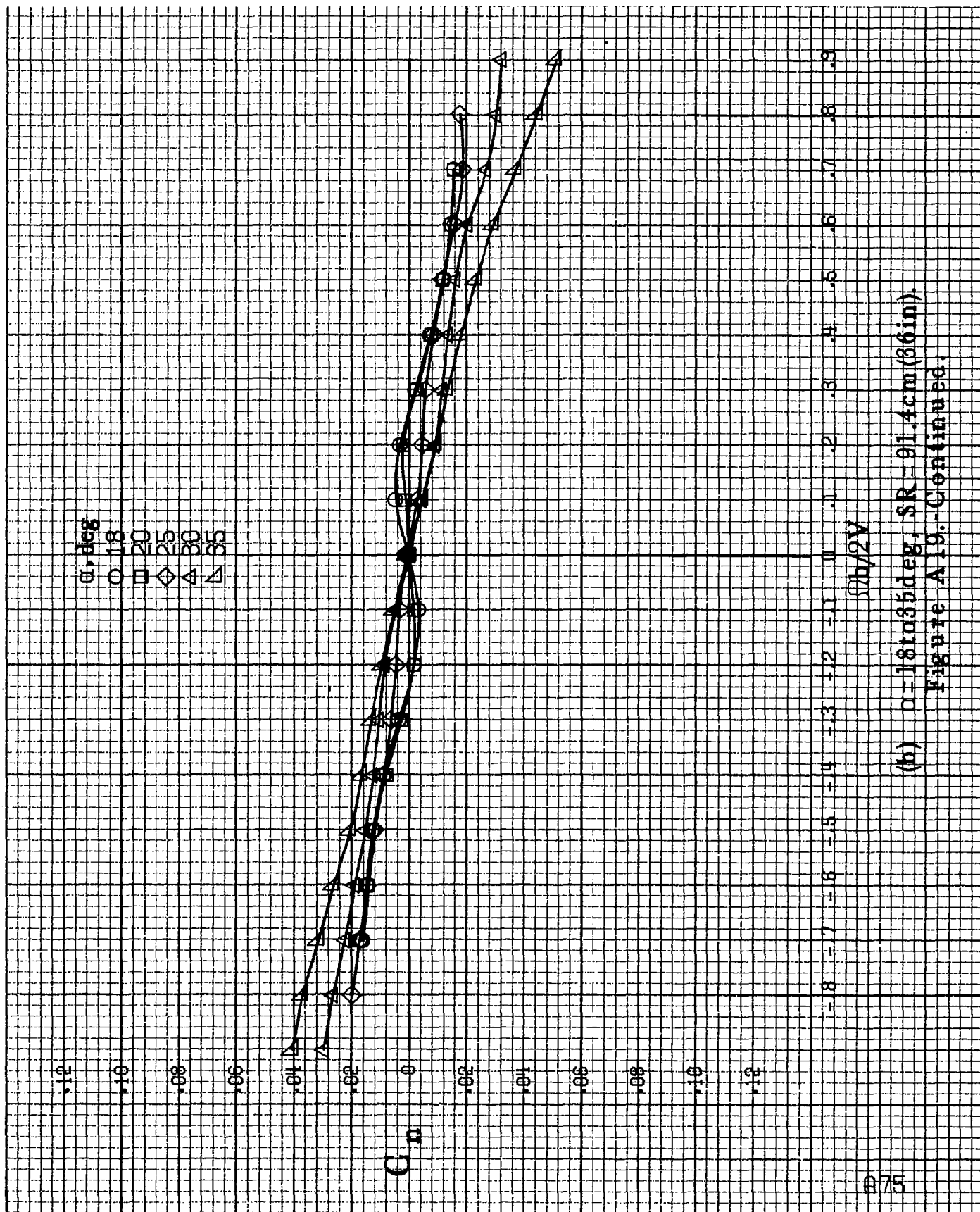
$b/2V$

(d) $\alpha=55$ to 90 deg, $SR=0$.
 Figure A18.-Concluded.



(a) $\alpha = 8$ to 16° , $SR = 91.4$ cm (35 in).

Figure A19 - Effect of rotation rate and angle of attack on yawing-moment coefficient for short body, high wing, horizontal T-tail A configuration.



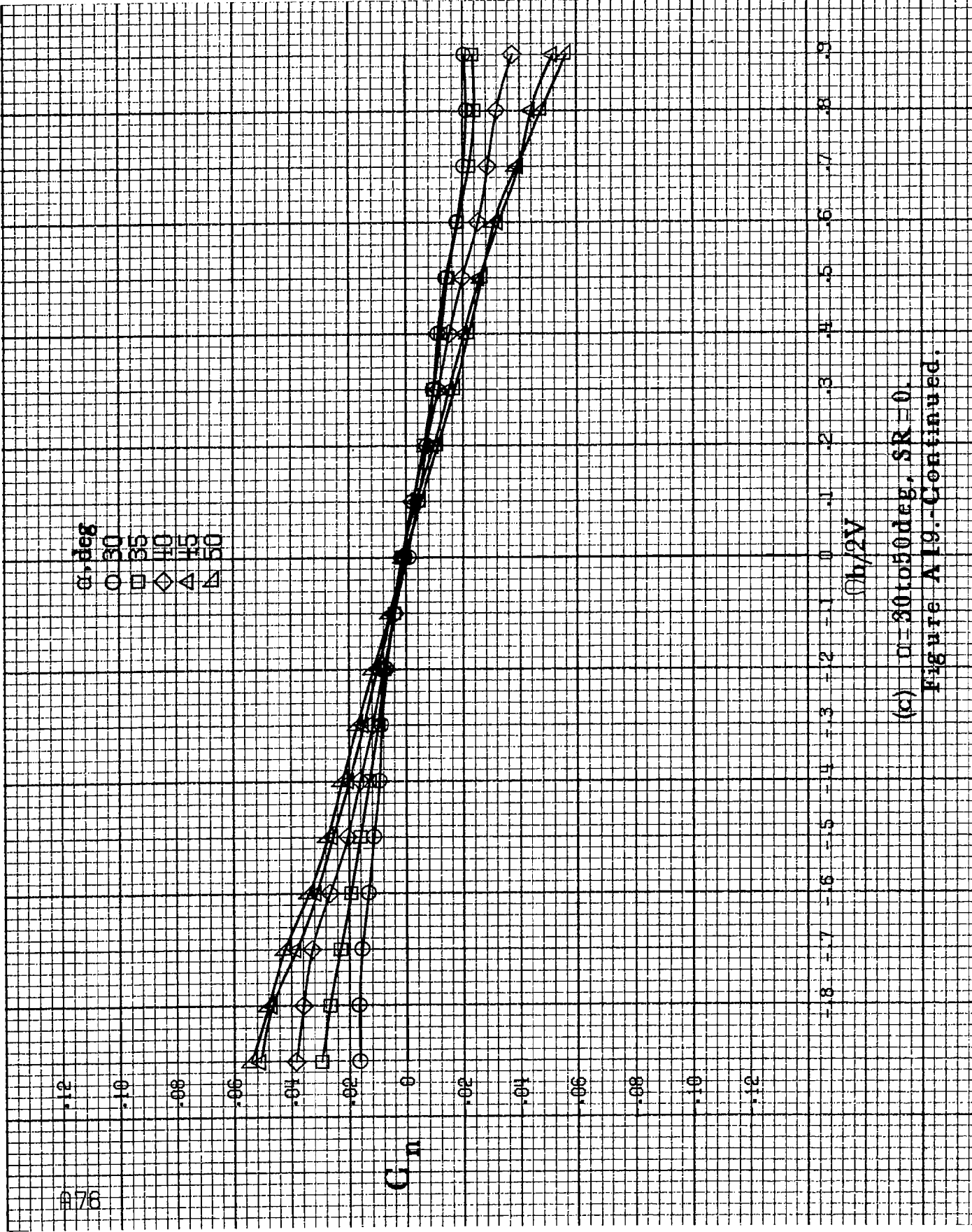
(b) $\alpha=18$ to 35° , SR=91.4cm (36in).
Figure A19.-Continued.

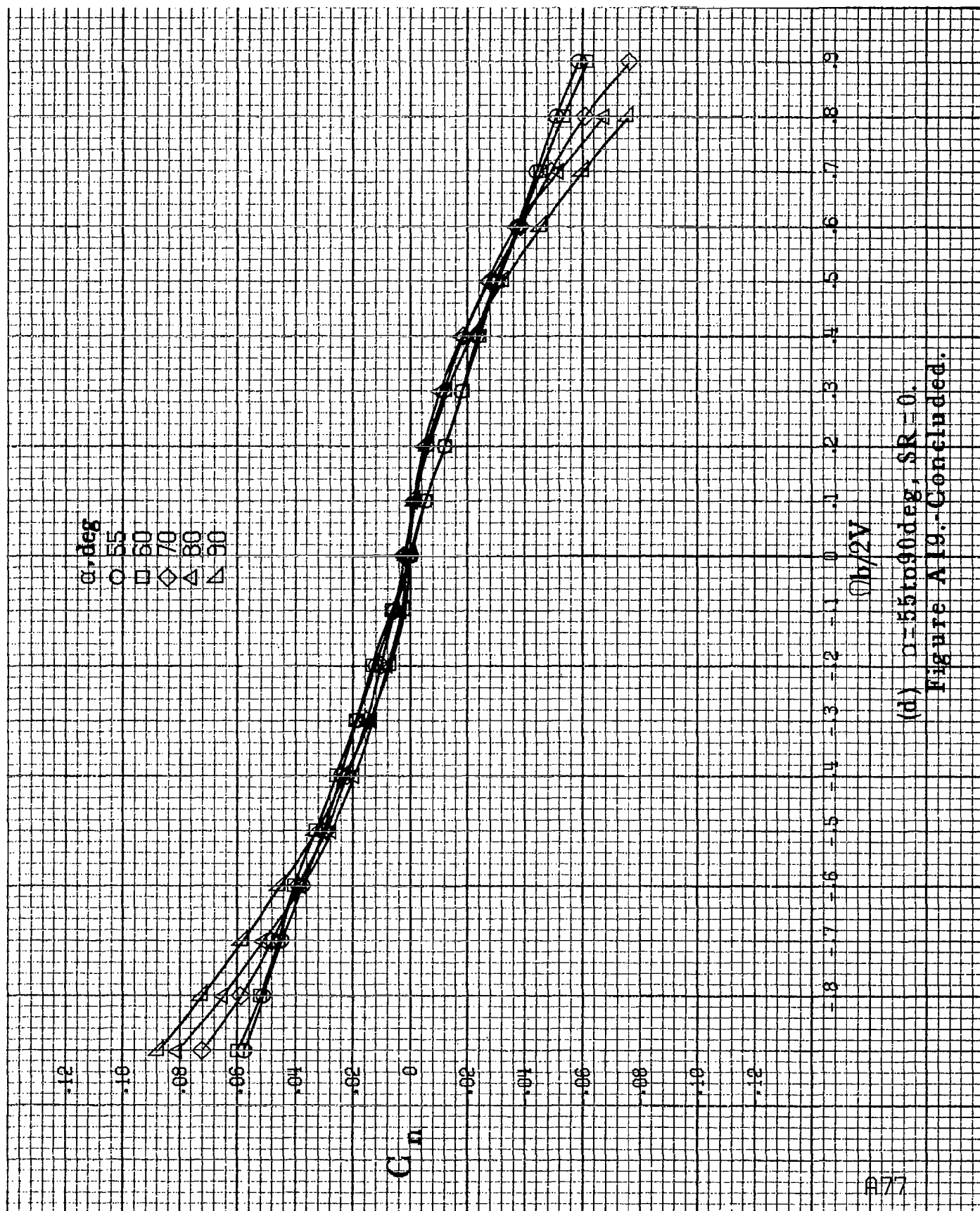
α , deg
 ○ 30
 □ 35
 ◇ 40
 △ 45
 ▽ 50

G_m

$\phi_b/2V$

(c) $\alpha = 30$ to 50 deg, $SR = 0$.
 Figure A19.-Continued.

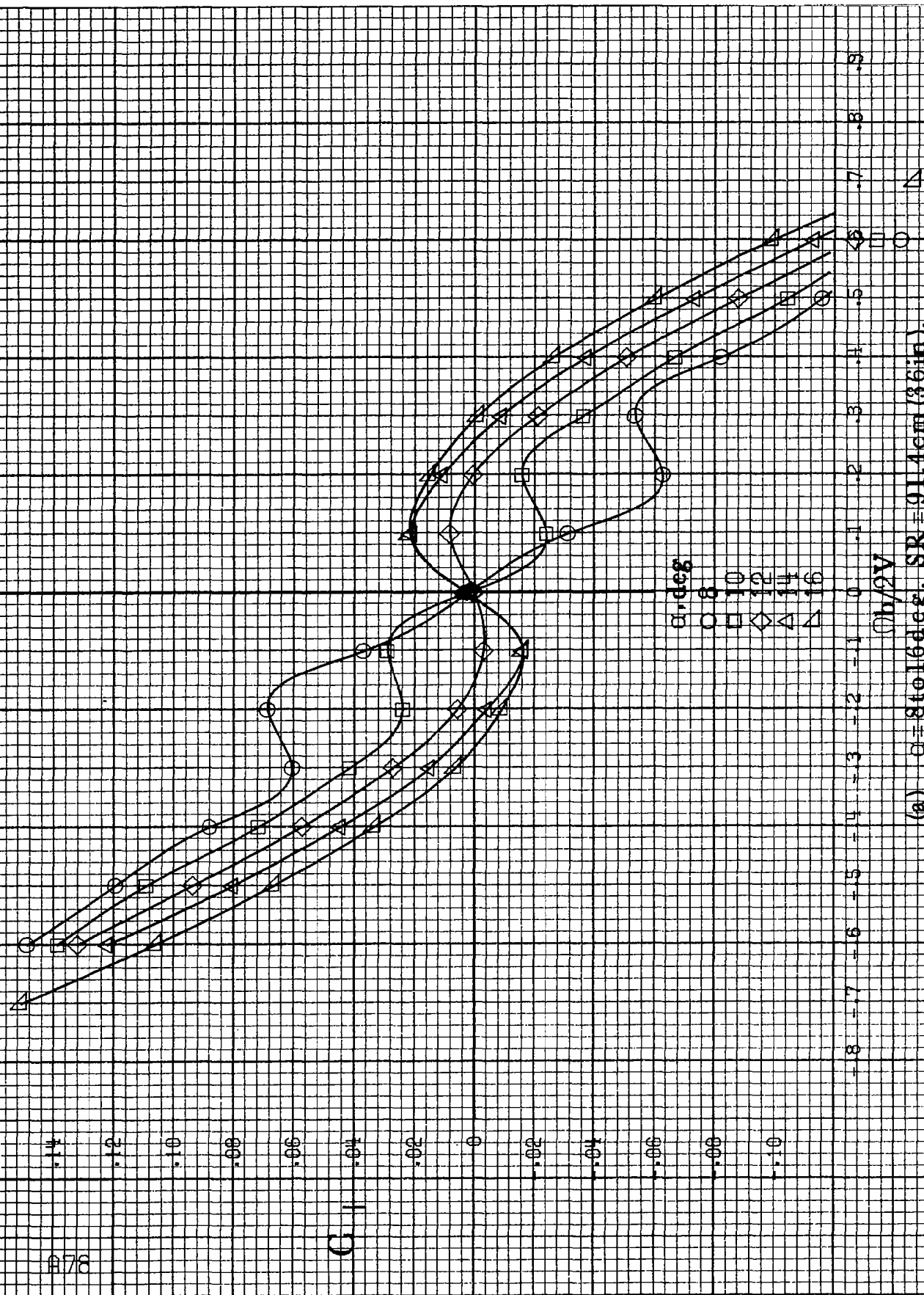




(d) $\alpha = 55$ to 90° , $SR = 0$.

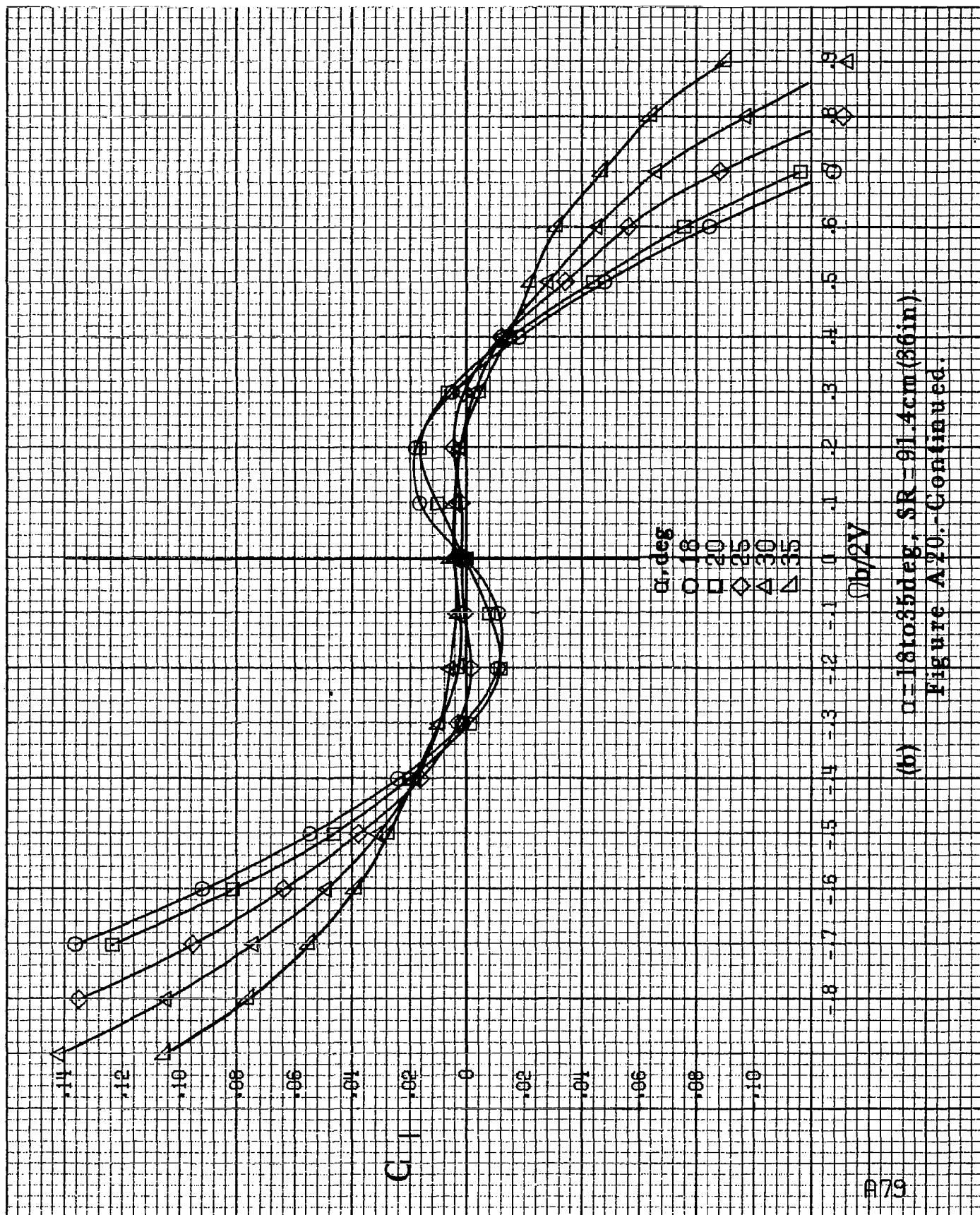
Figure A19.-Concluded.

C_L



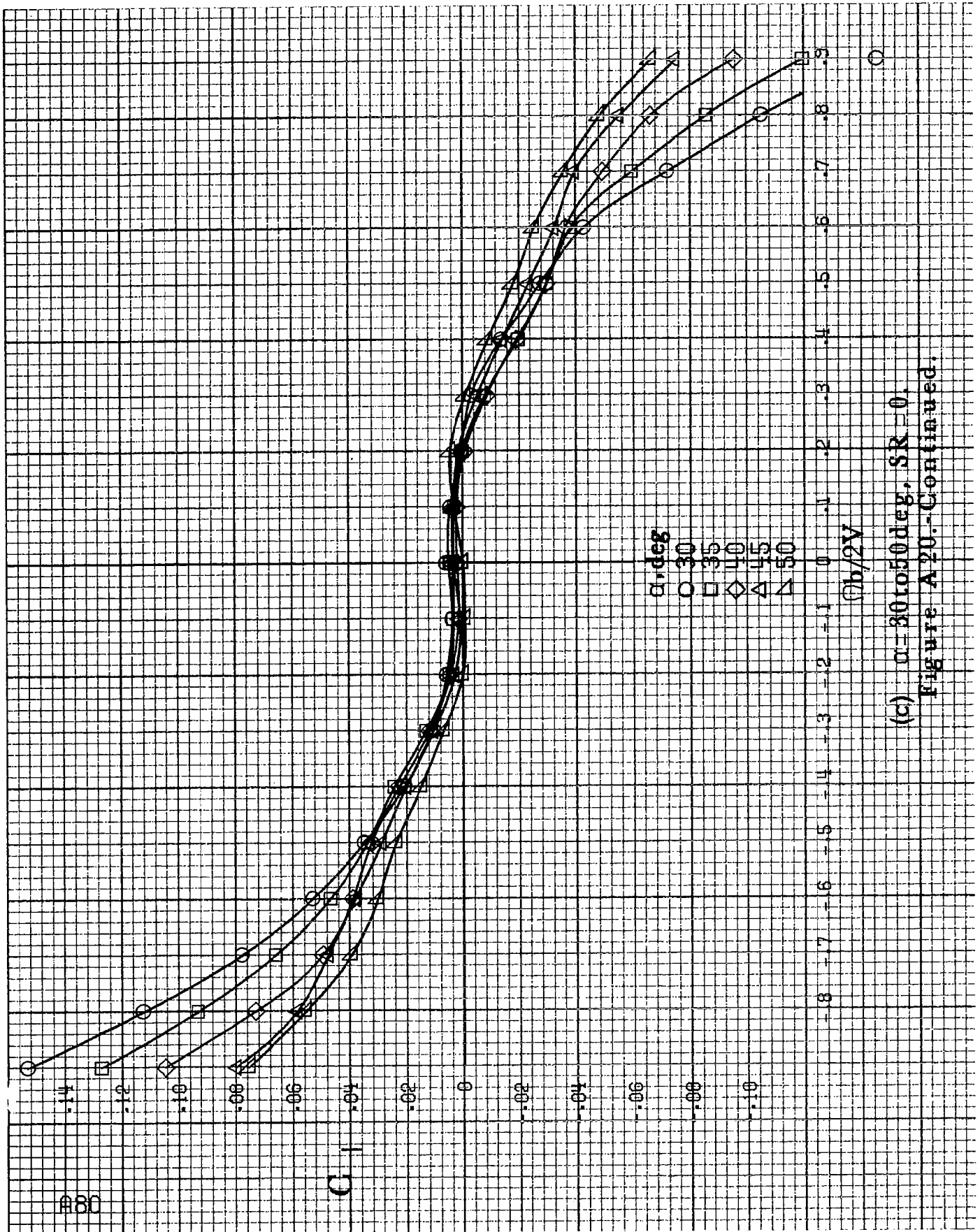
(a) $\alpha = 8$ to 16° , $SR = 91.4 \text{ cm (36 in.)}$.

Figure A20.-Effect of rotation rate and angle of attack on rolling-moment coefficient for short body, high wing, horizontal T-tail A configuration.

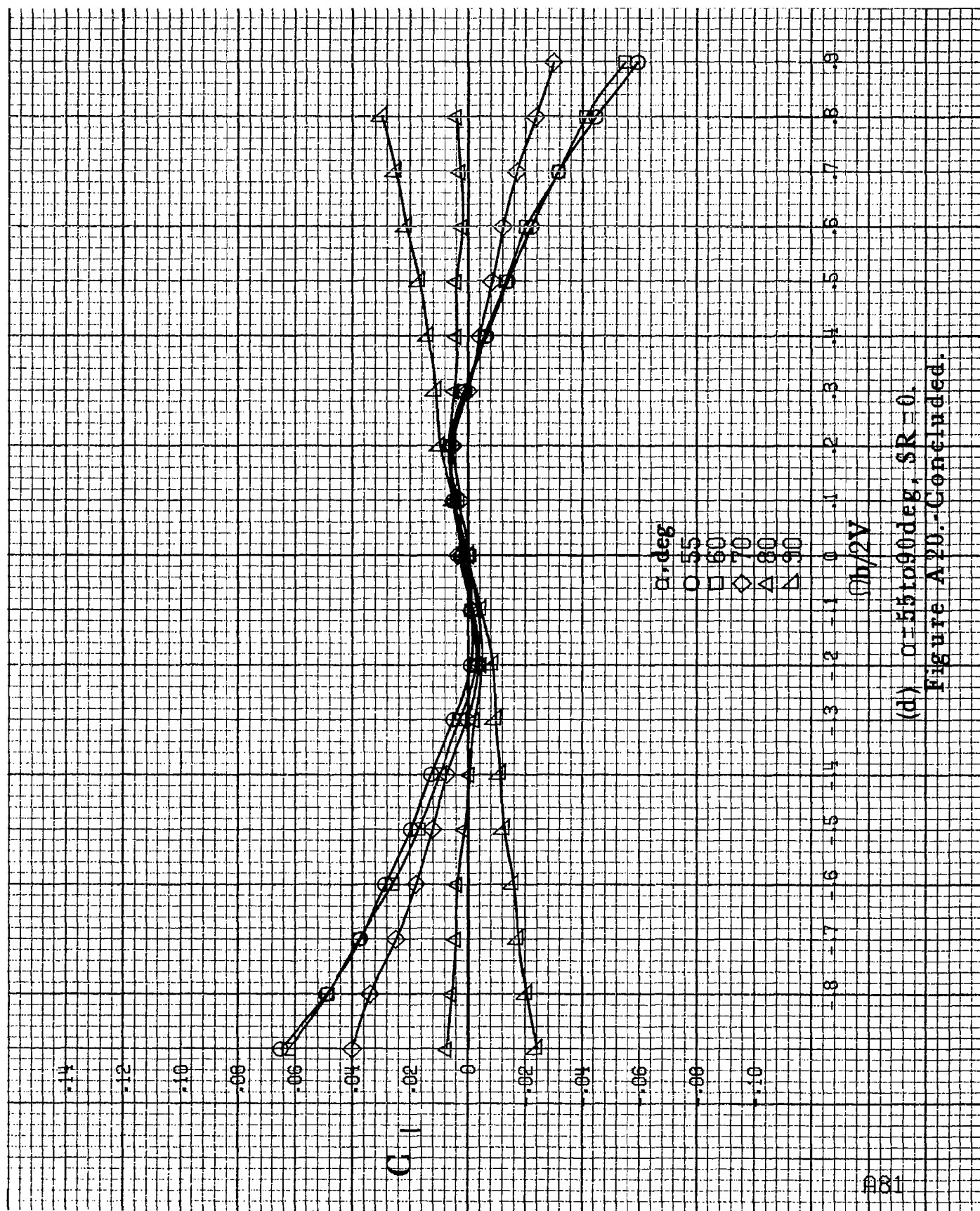


(b) $\alpha=18$ to 35° , $SR=91.4\text{cm}(86\text{in})$.

Figure A20.-Continued.

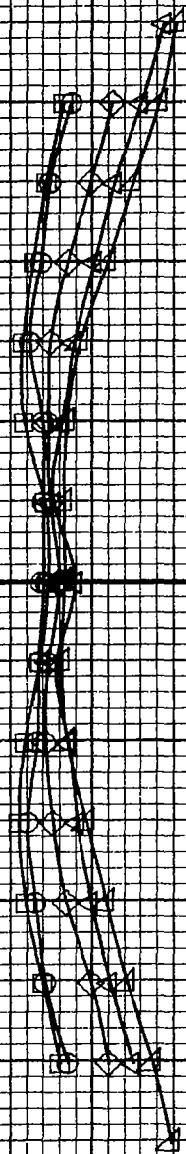


(c) $\alpha=30$ to 50 deg, $SR=0$.
Figure A20.-Continued.



(d) $\alpha = 55$ to 90° , $SR = 0$.
Figure A20.-Concluded.

C_m



α, deg

$h/2V$

8

10

12

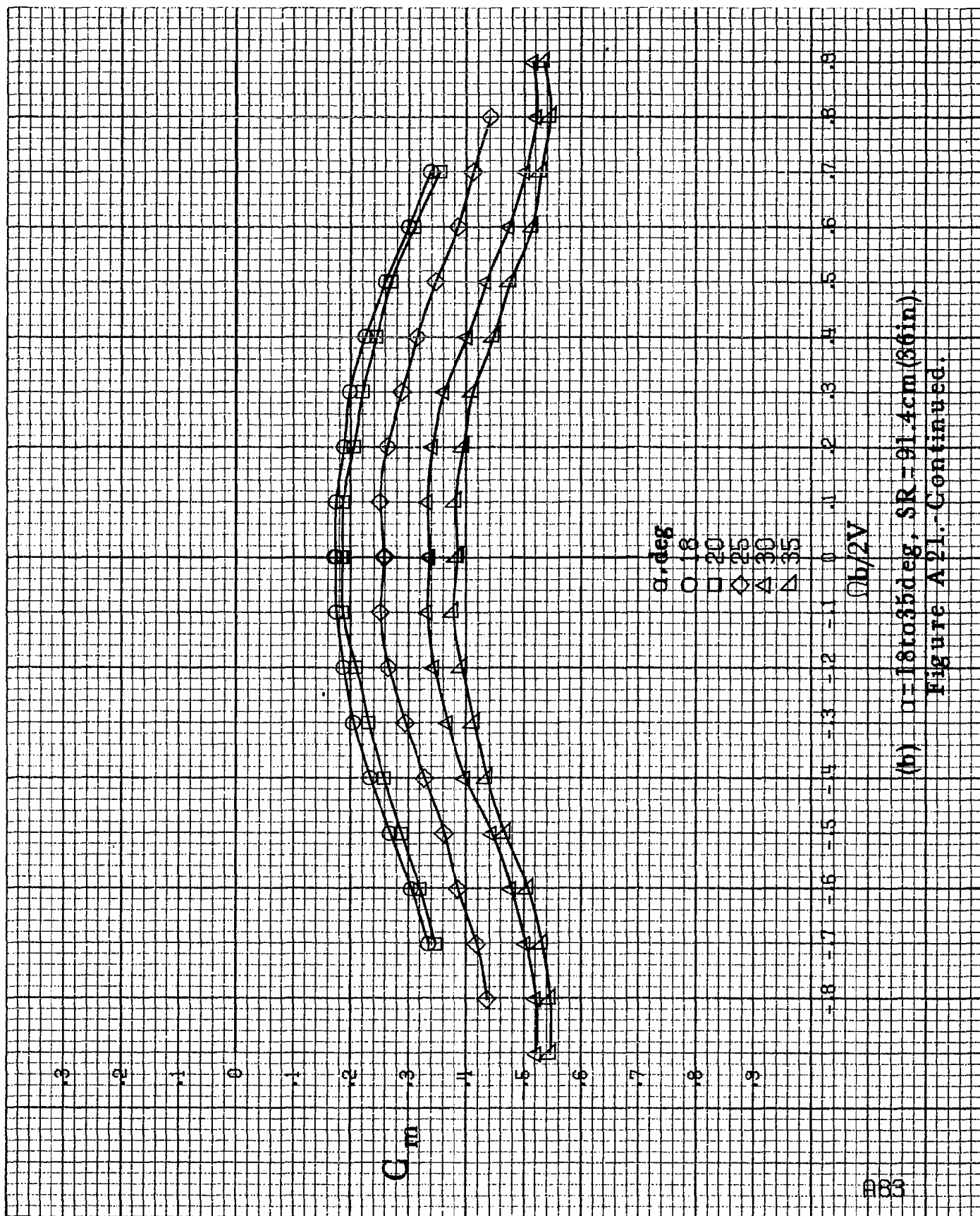
14

16

$h/2V$

(a) $\alpha = 8$ to 16 deg, $SR = 91.4$ cm (36 in).

Figure A21. Effect of rotation rate and angle of attack on pitching-moment coefficient for short body, high wing, horizontal T-tail A configuration.



(b) $\alpha = 18$ to 35° , $SR = 91.4 \text{ cm (36 in.)}$.

Figure A21.-Continued.

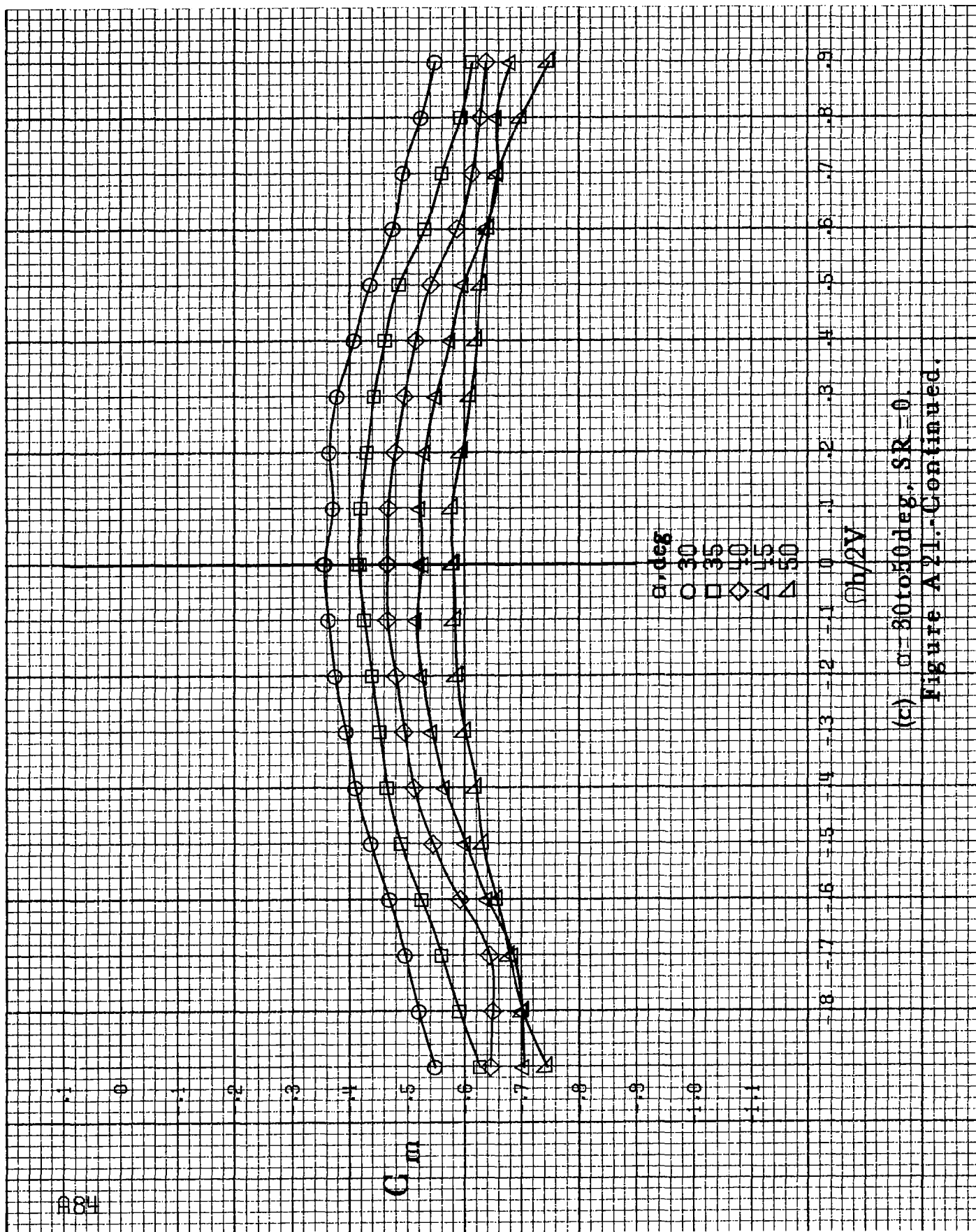
C_m

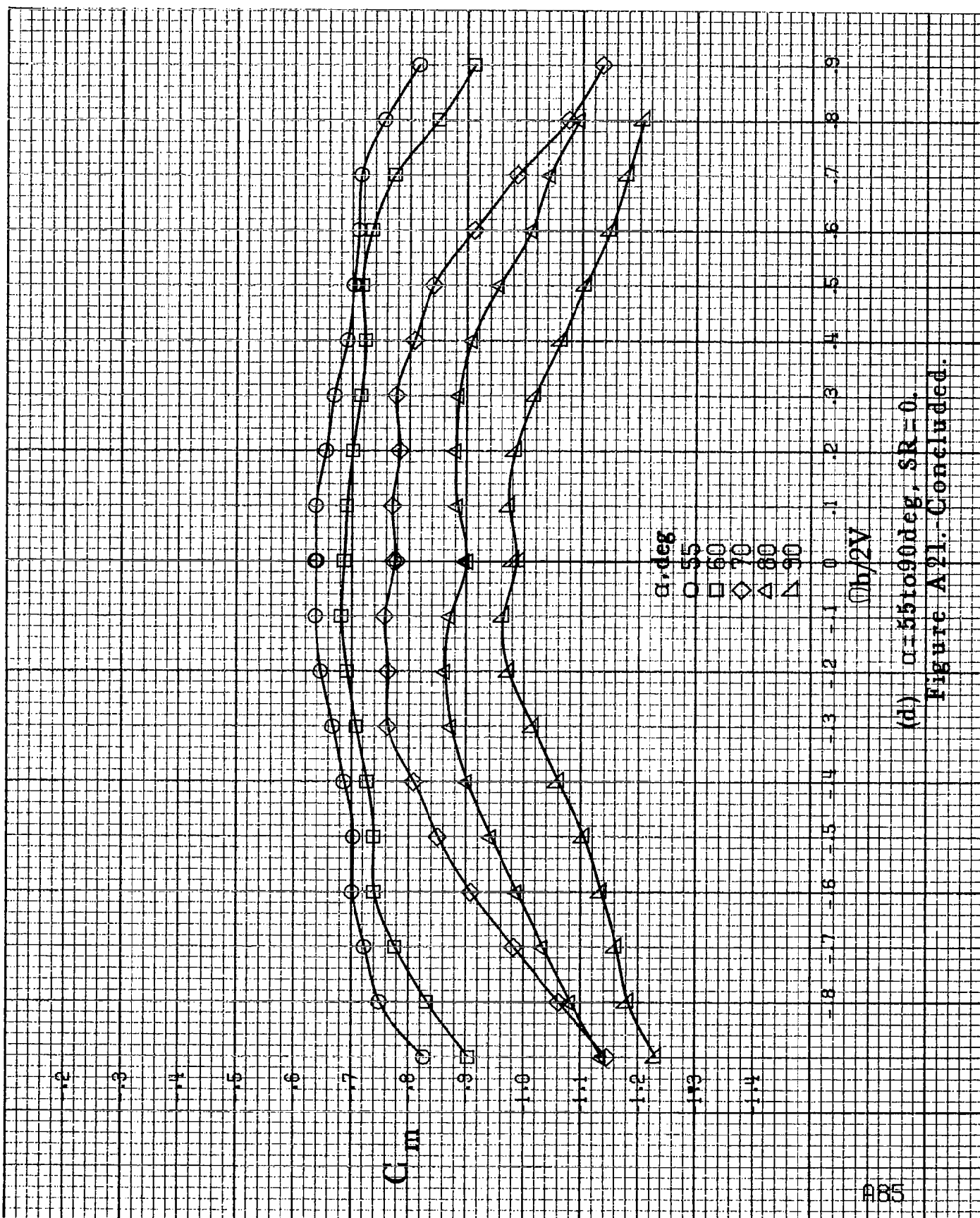
α, deg
 \circ 30
 \square 35
 \diamond 40
 \triangle 45
 ∇ 50

$\phi_b/2V$

(c) $\alpha=30$ to 50 deg, $SR=0$.

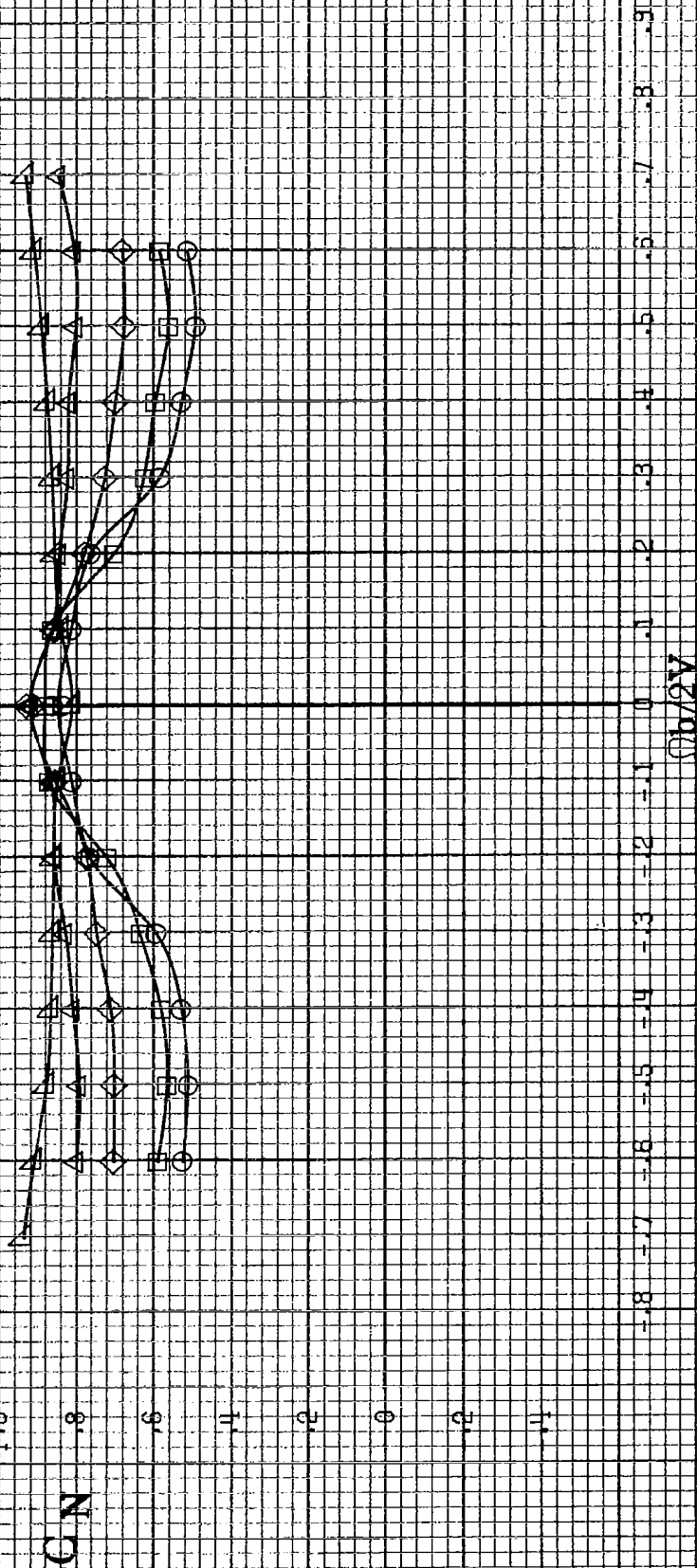
Figure A21.-Continued.





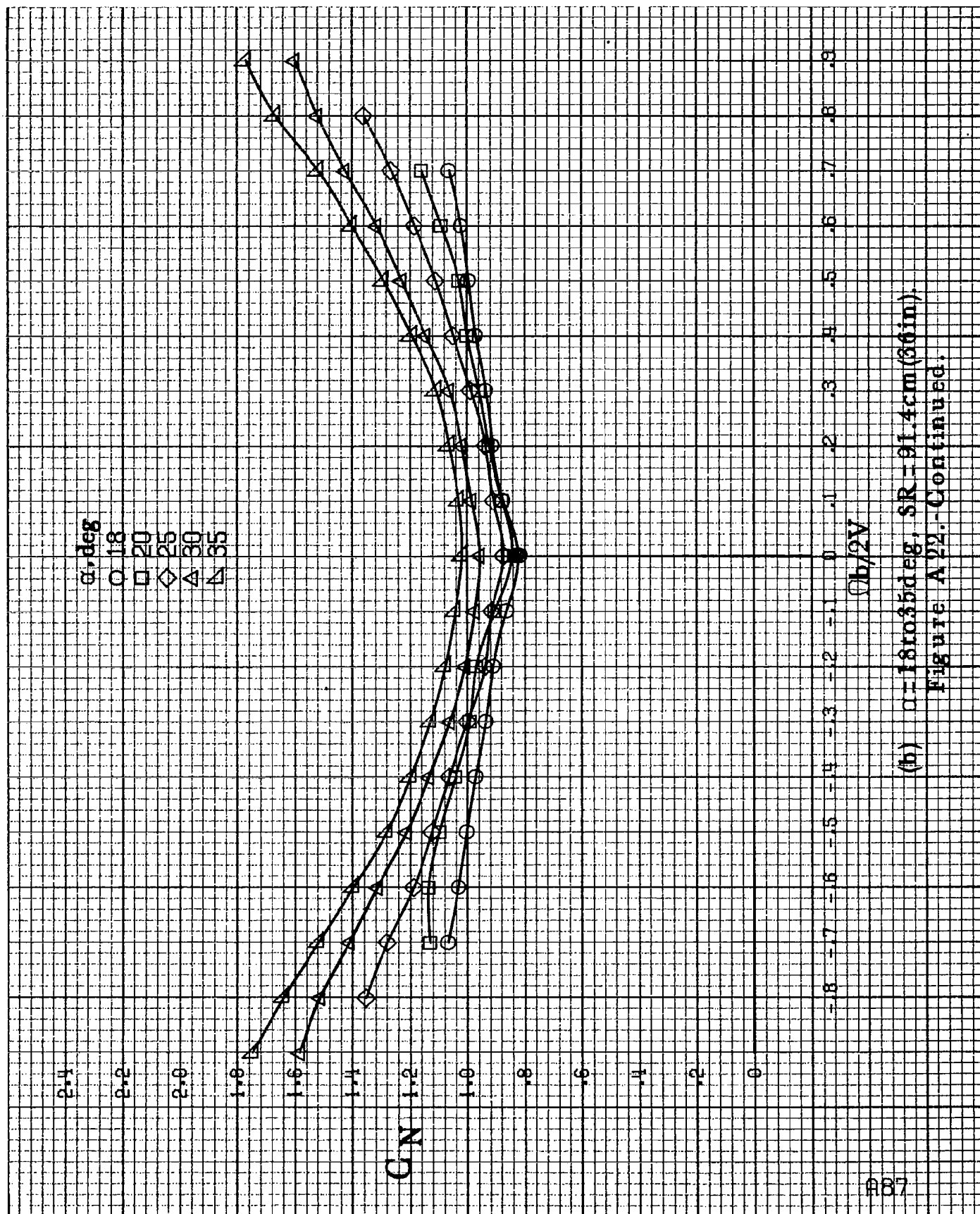
(d) $\alpha=55$ to 90° , $SR=0$.
 Figure A21. Concluded.

α , deg
 8
 10
 12
 14
 16



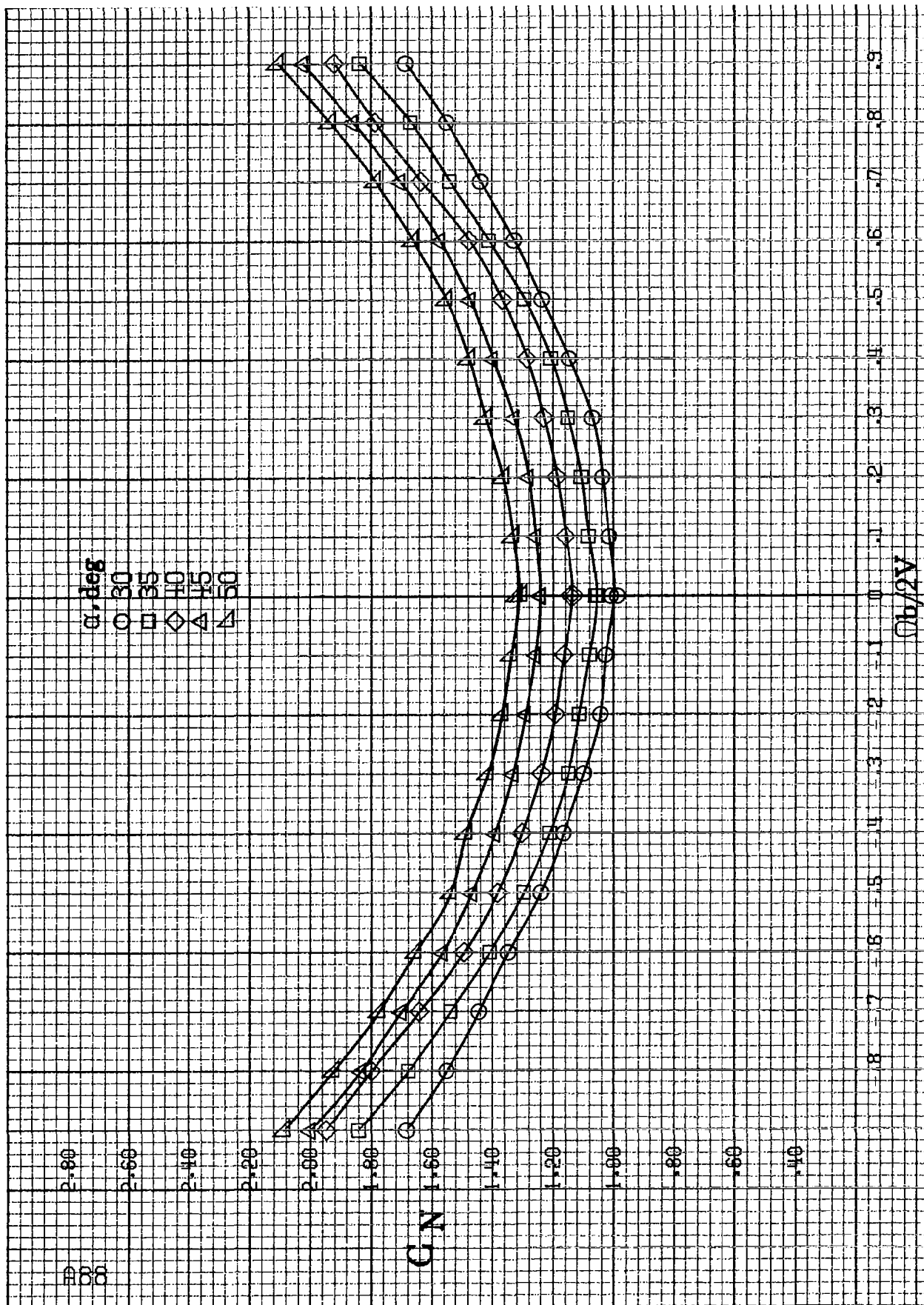
(a) $\alpha = 8$ to 16 deg, $SR = 91.4$ cm (36 in).

Figure A22.-Effect of rotation rate and angle of attack on normal force coefficient for short body, high wing, horizontal T-tail A configuration.



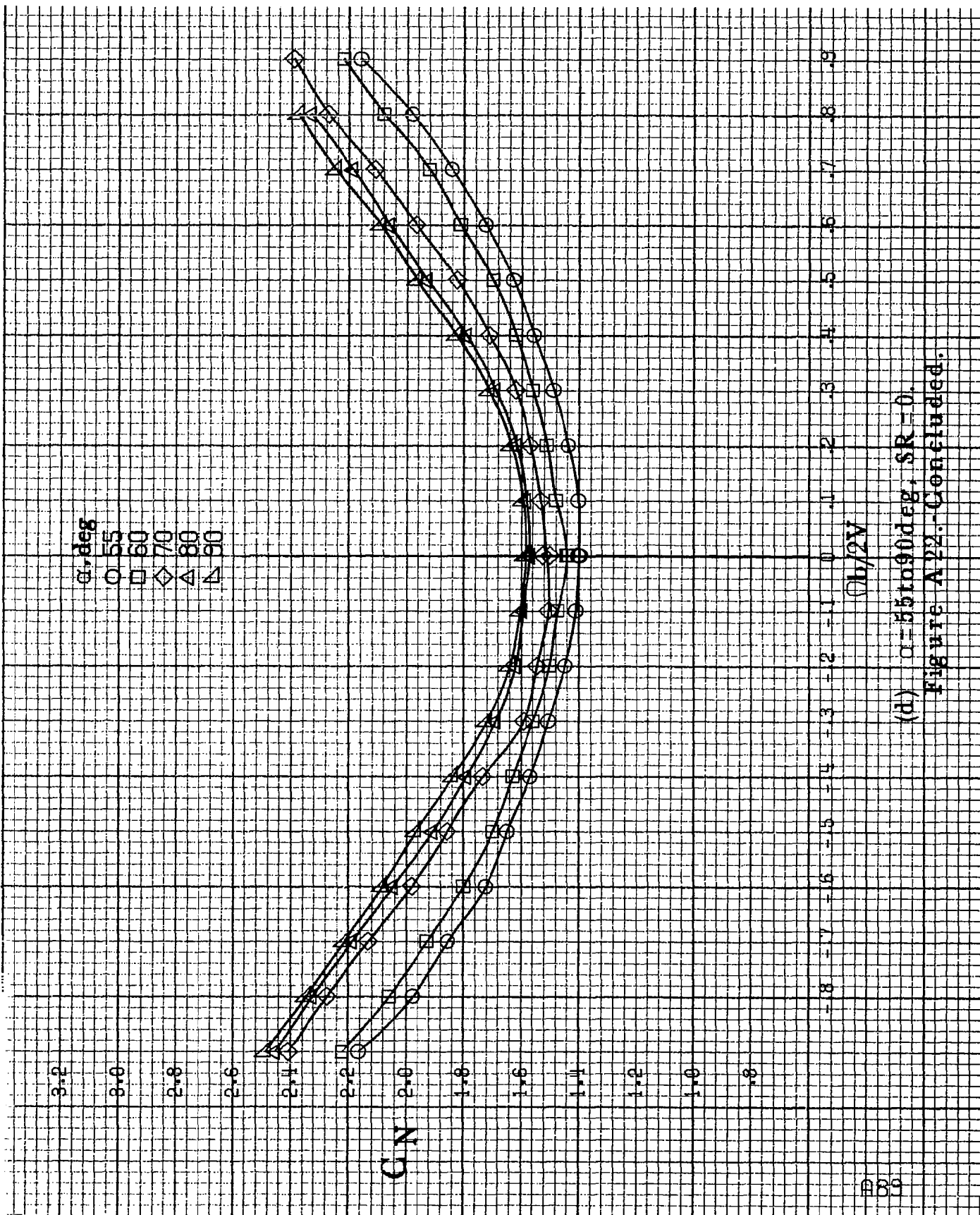
(b) $\alpha=18$ to 35° deg, $SR=91.4\text{ cm (36 in.)}$

Figure A22.-Continued.



(c) $\phi = 30$ to 50 deg, $SR = 0$.

Figure A 22.-Continued.



(d) $\alpha = 55$ to 90° , $SR = 0$.
Figure A22.-Concluded.

800

α, deg

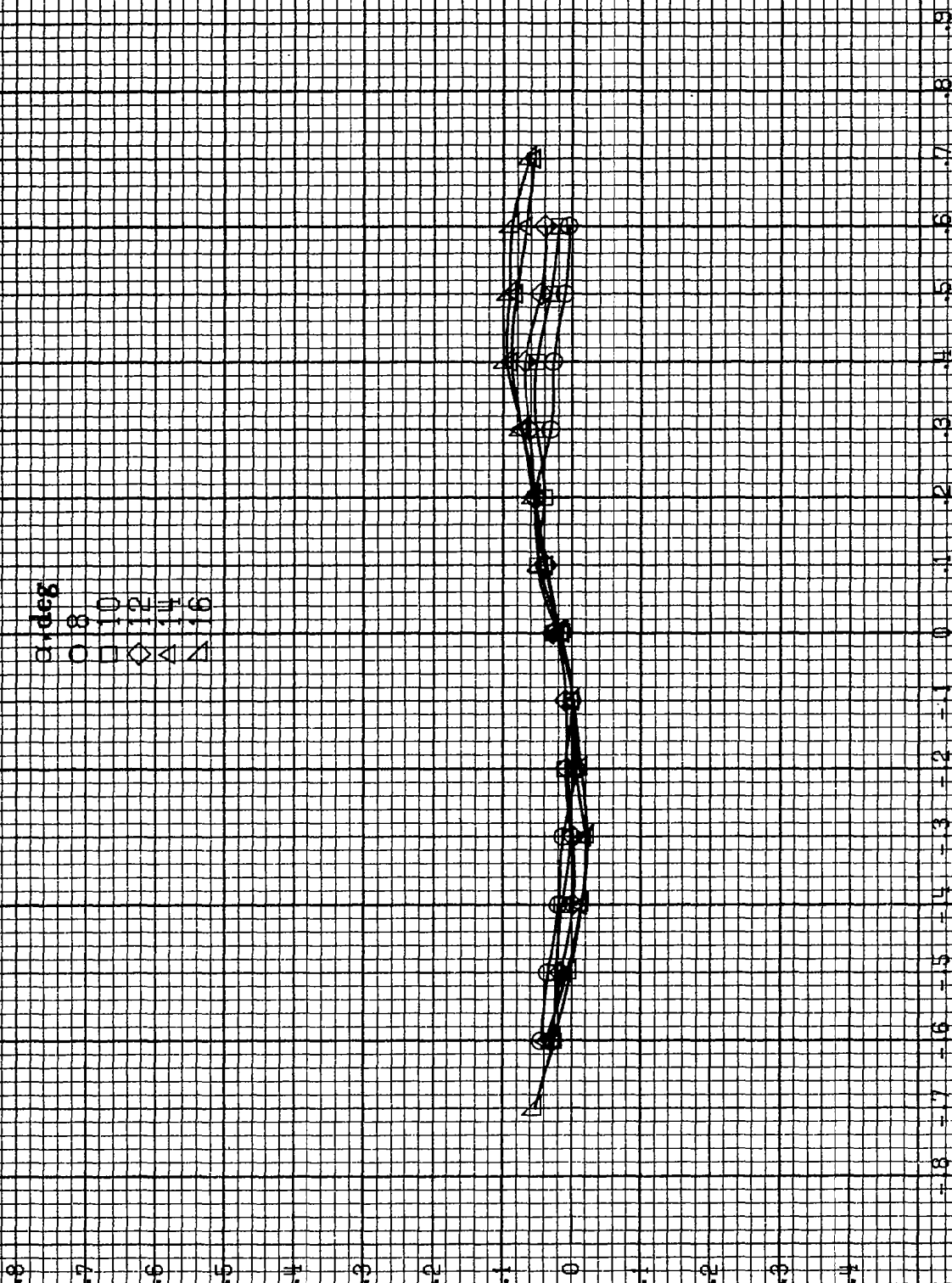
○ 8
□ 10
△ 12
△ 14
△ 16

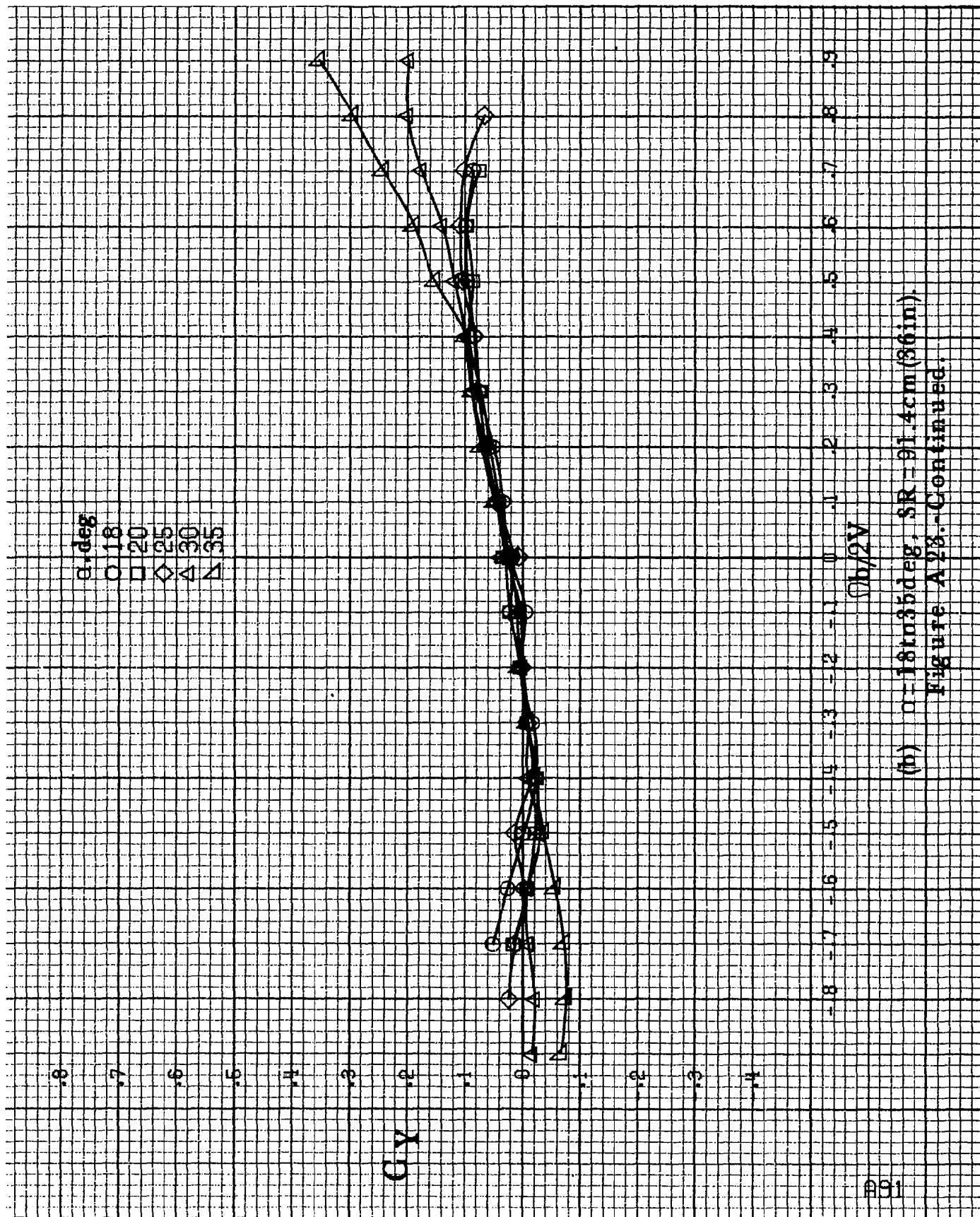
C_Y

$Q_b/2V$

(a) $\alpha = 8 \text{ to } 16 \text{ deg}$, $SR = 91.4 \text{ cm (36 in)}$.

Figure A28 - Effect of rotation rate and angle of attack on side-force coefficient for short body, high wing, horizontal T-tail A configuration.





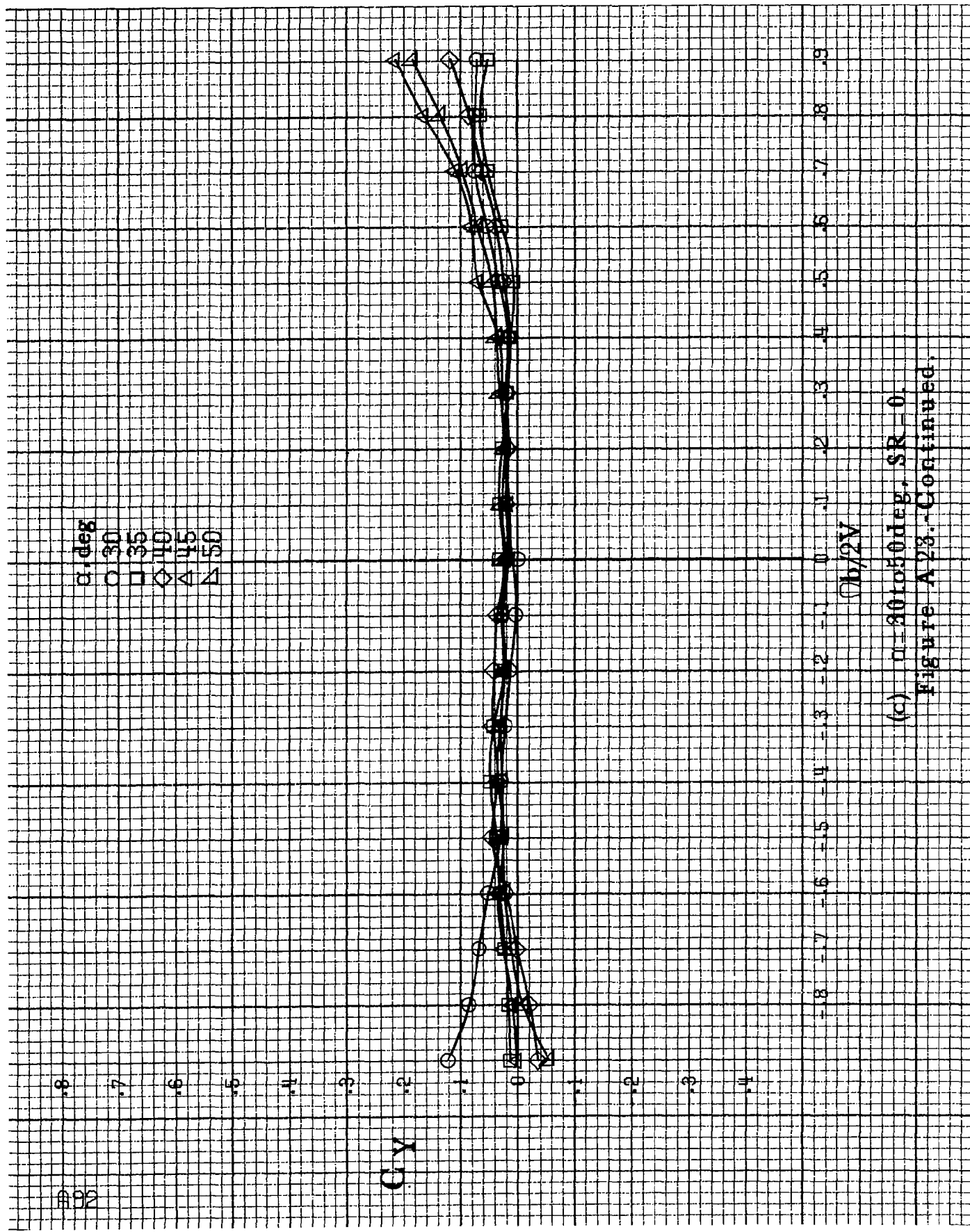
(b) $\alpha = 18$ to 35° , $SR = 91.4 \text{ cm (36 in.)}$.
Figure A23. Continued.

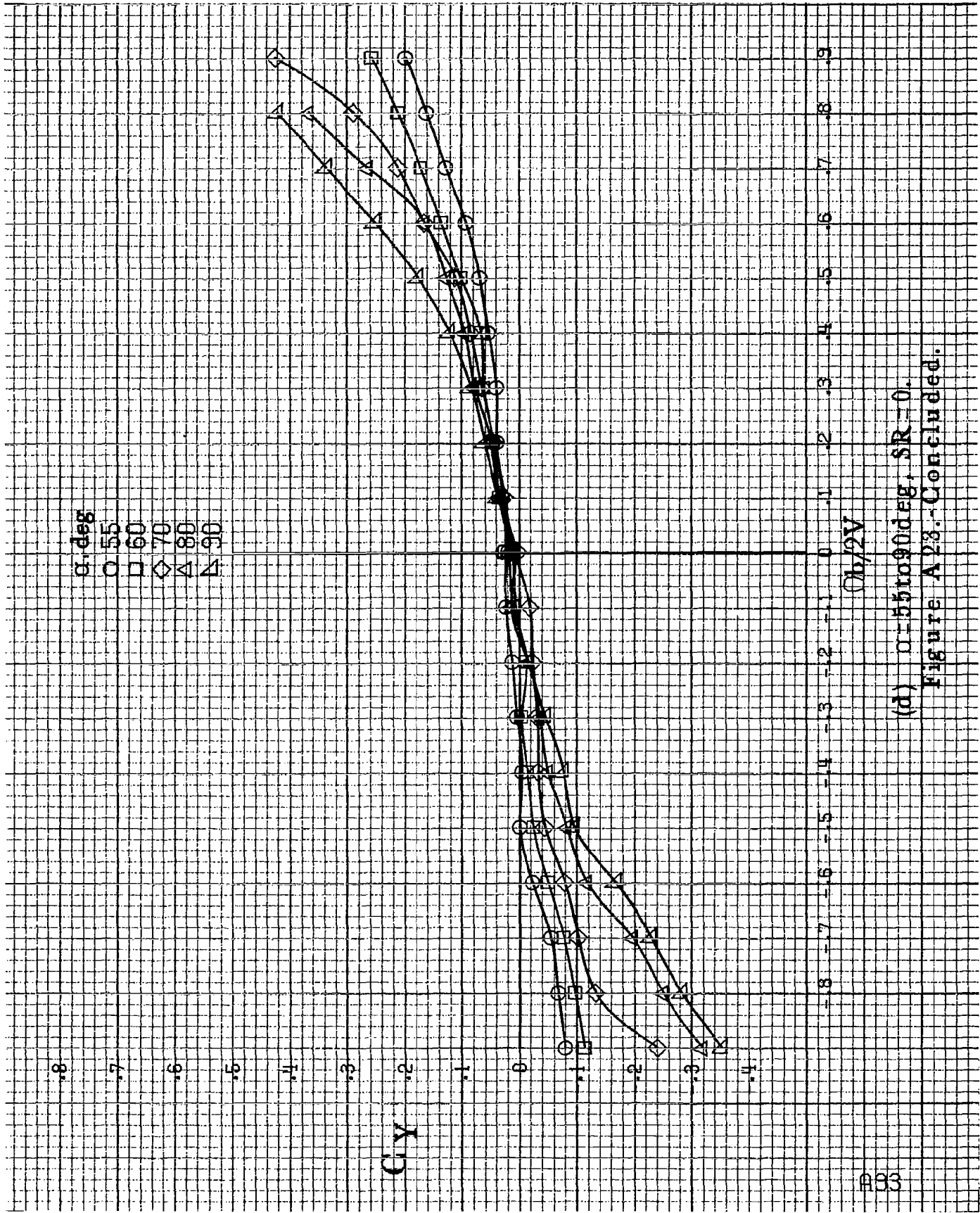
α, deg
 \circ 30
 \square 35
 \diamond 40
 \triangle 45
 ∇ 50

Cy

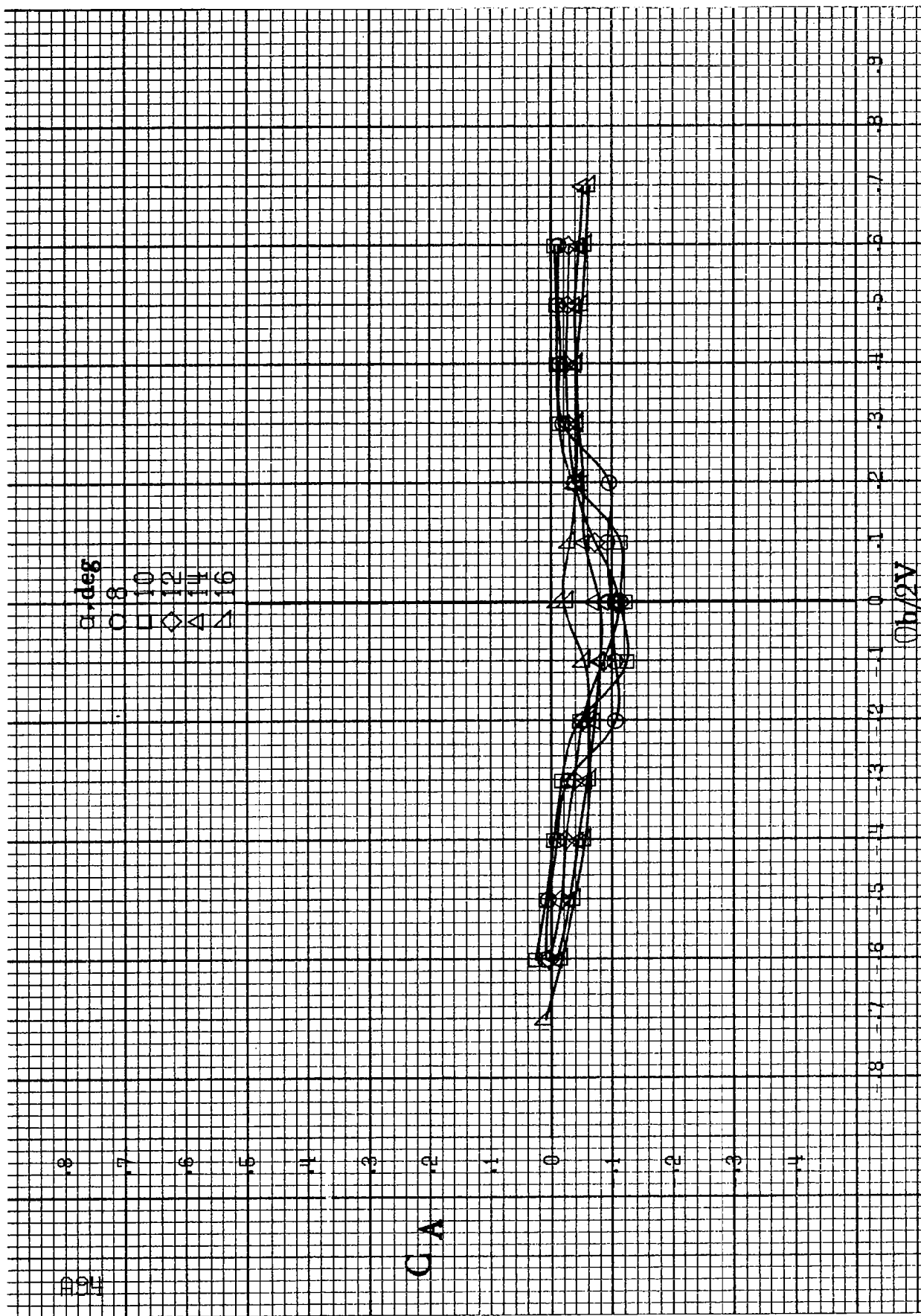
$\phi_b/2V$

(c) $\eta=30$ to 50deg , $SR=0$.
 Figure A23.-Continued.





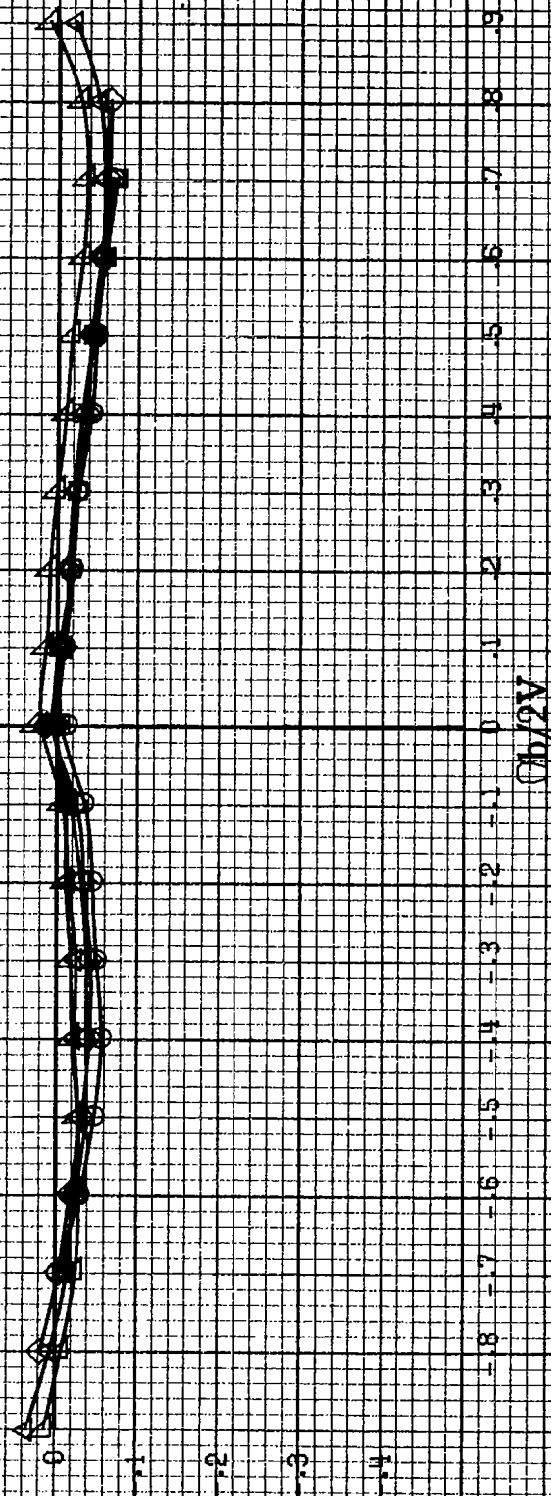
(d) $\alpha=55$ to 90° , $SR=0$.
 Figure A23.-Concluded.



(a) $\alpha = 8$ to 16° , $SR = 91.4 \text{ cm (36 in)}$.
 Figure A24. Effect of rotation rate and angle of attack on axial-force coefficient for short body, high wing, horizontal T-tail A configuration.

α , deg
 □ 18
 ○ 20
 ◇ 25
 △ 30
 ▴ 35

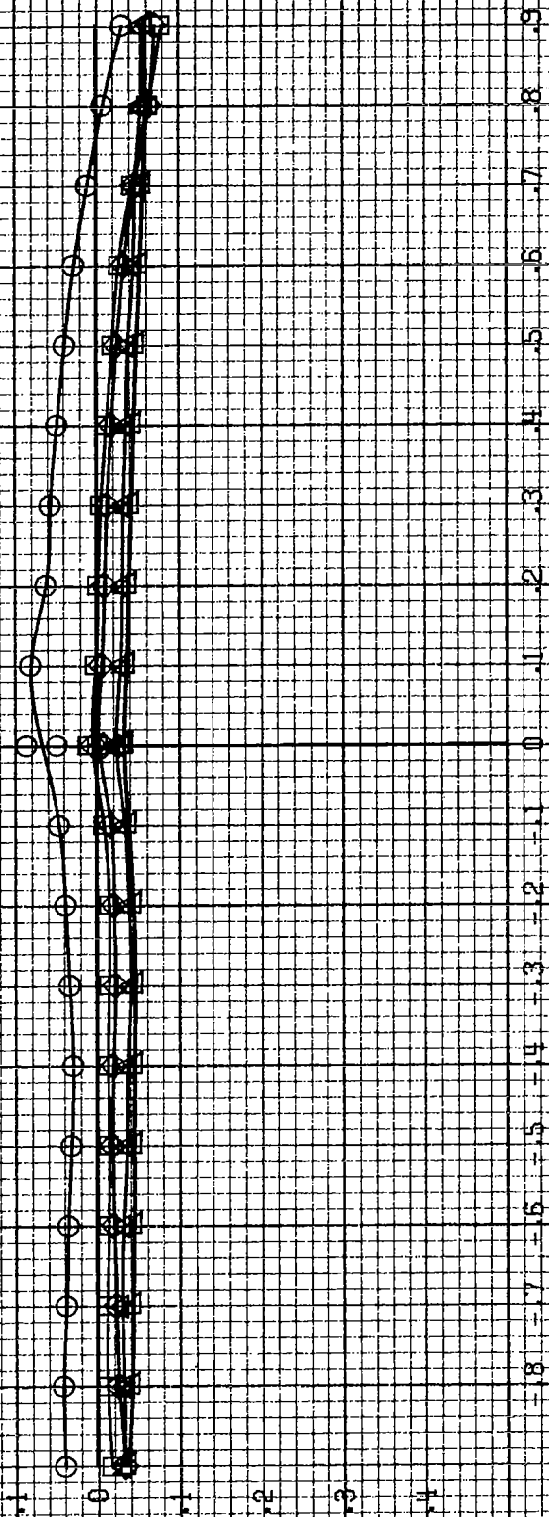
CA



(b) $\alpha = 18$ to 35° , $SR = 91.4 \text{ cm (36 in.)}$
 Figure A24.-Continued.

α, deg
 ○ 30
 □ 35
 ◇ 40
 △ 45
 ▽ 50

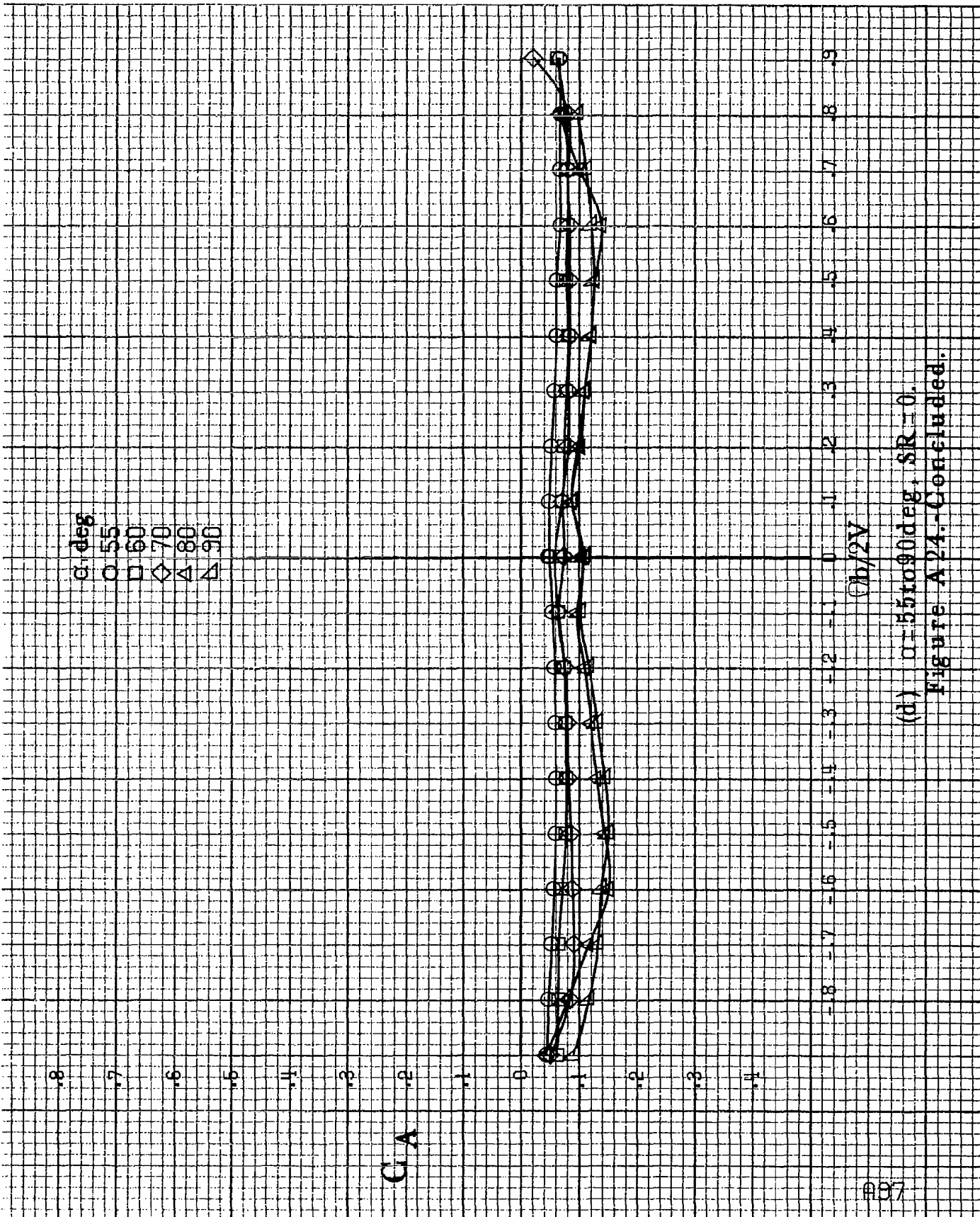
C_A



$b/2V$

(c) $\alpha=30$ to 50° , $SR=0$.

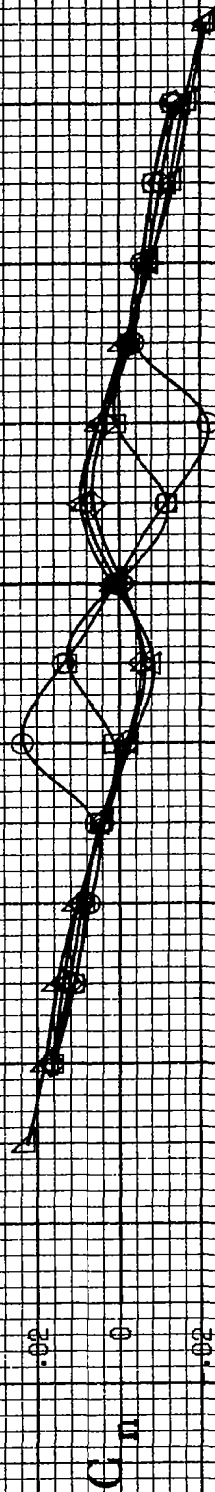
Figure A24.-Continued.



(d) $\alpha=55$ to 90 deg, $SR=0$.

Figure A 24.-Concluded.

α , deg
 3
 10
 12
 14
 16



$Qb/2V$

(a) $\alpha = 8$ to 16 deg, $SR = 91.4$ cm (36 in).

Figure A25. Effect of rotation rate and angle of attack on yawing-moment coefficient for short body, high wing, horizontal tail no. 1 configuration. $\delta_e = 0^\circ$, $\delta_r = 0^\circ$, $\delta_z = 0^\circ$.

α, deg
 O 18
 □ 20
 ◇ 25
 △ 30
 ▽ 35

-12
-10
-08
-06
-04
-02
0
-02
-04
-06
-08
-10
-12

C_m

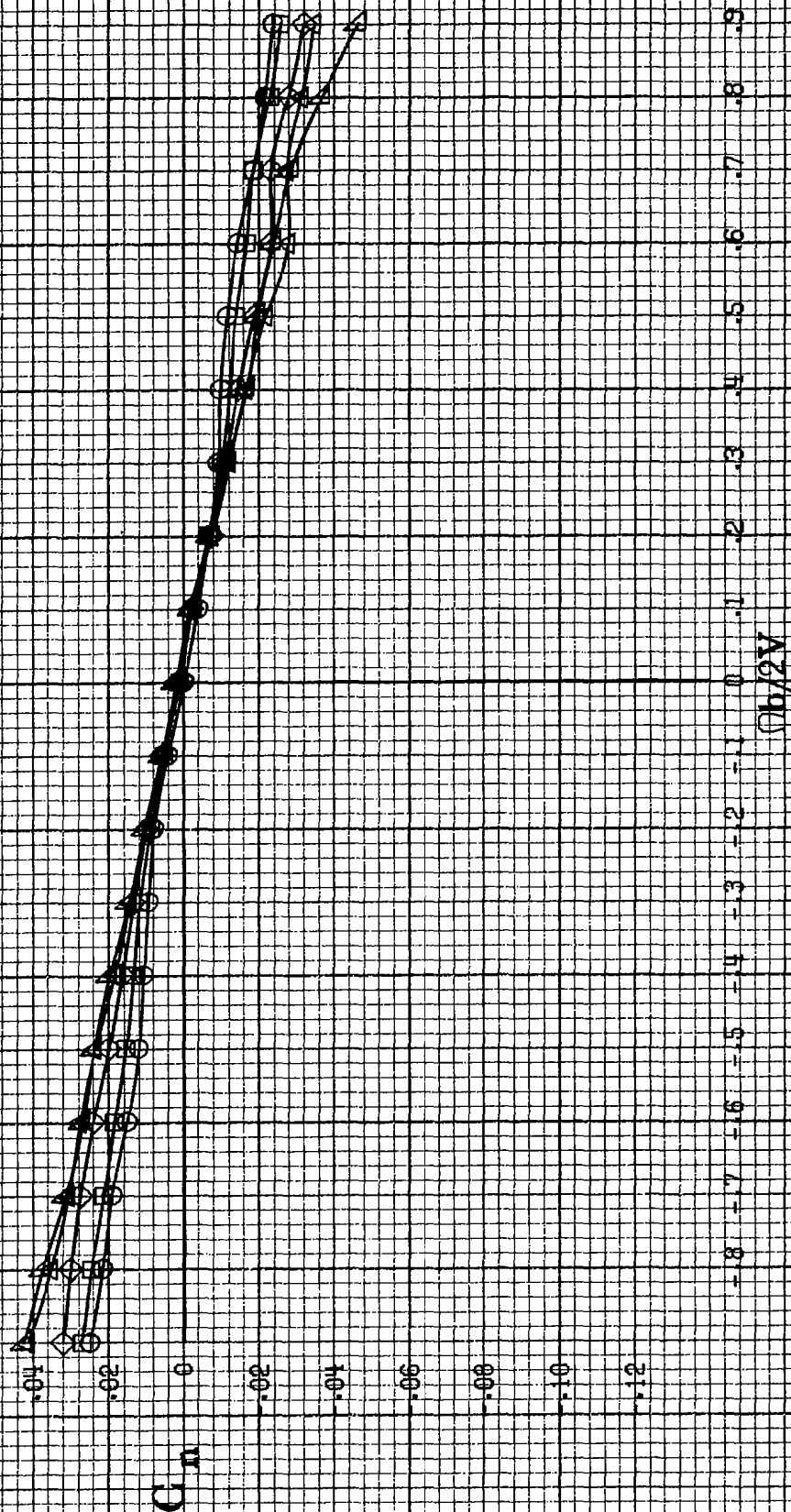
-18 -17 -16 -15 -14 -13 -12 -11 -10 -9 -8 -7 -6 -5 -4 -3 -2 -1 0 .1 .2 .3 .4 .5 .6 .7 .8 .9

$U_b/2V$

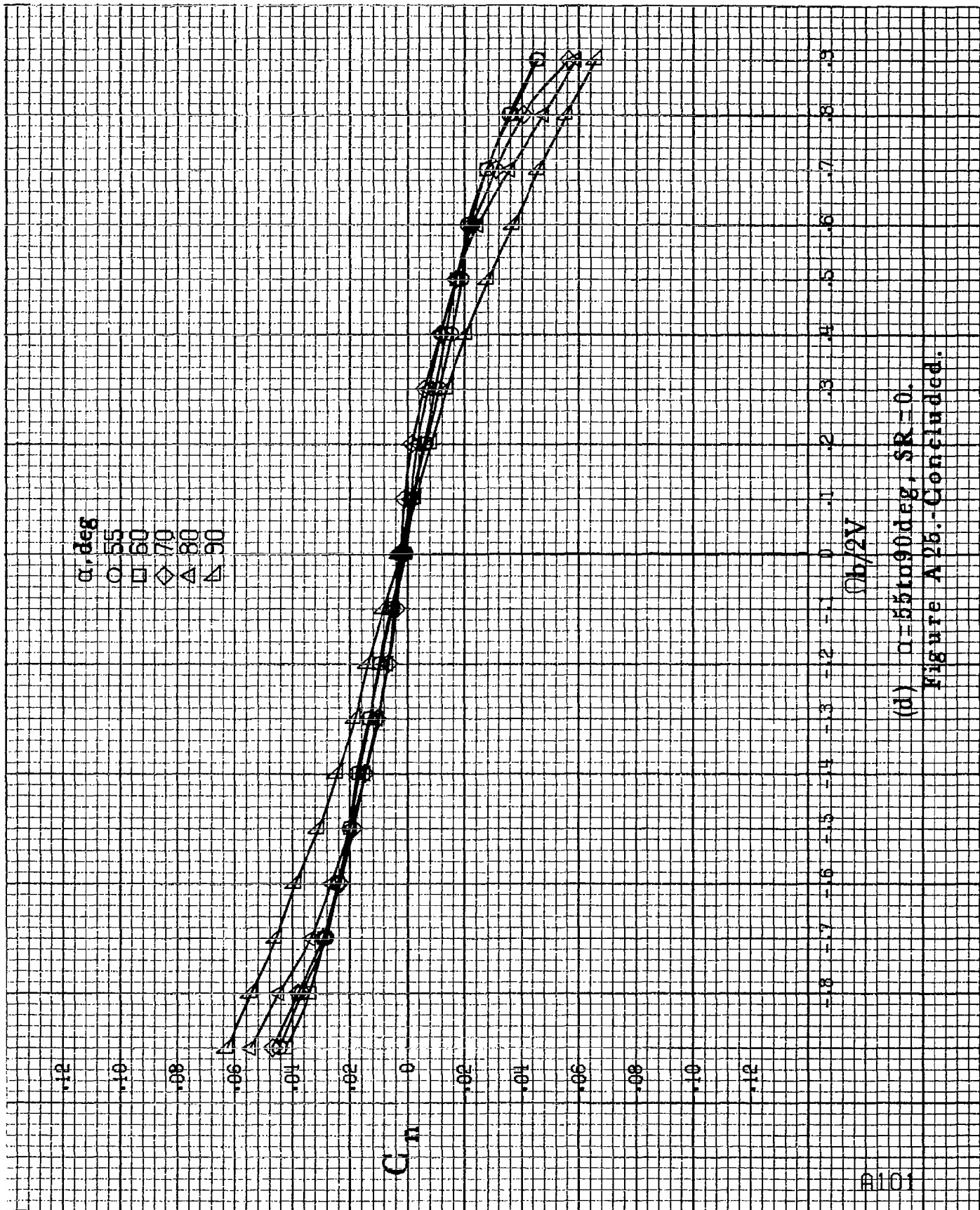
(b) $\alpha=18$ to 35 deg, $SR=91.4 \text{ cm (36 in.)}$
 Figure A25.-Continued.

B100

α, deg
 ○ 30
 □ 35
 ◇ 40
 ▲ 45
 ▽ 50



(c) $\alpha=30$ to 50° , $SR=0$,
 Figure A25.-Continued.



(d) $\alpha=55$ to 90° , $SR=0$.
Figure A25.-Concluded.

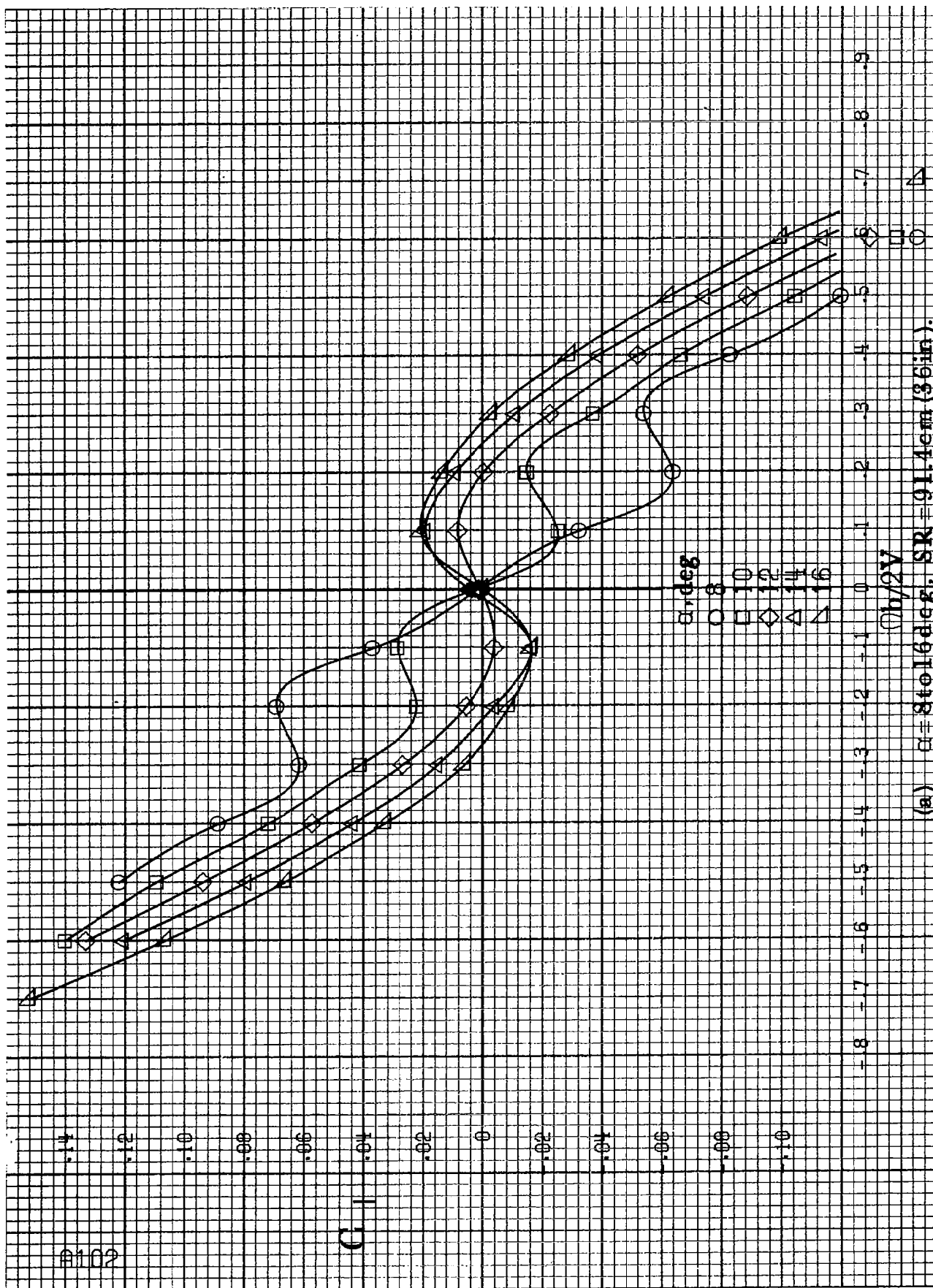
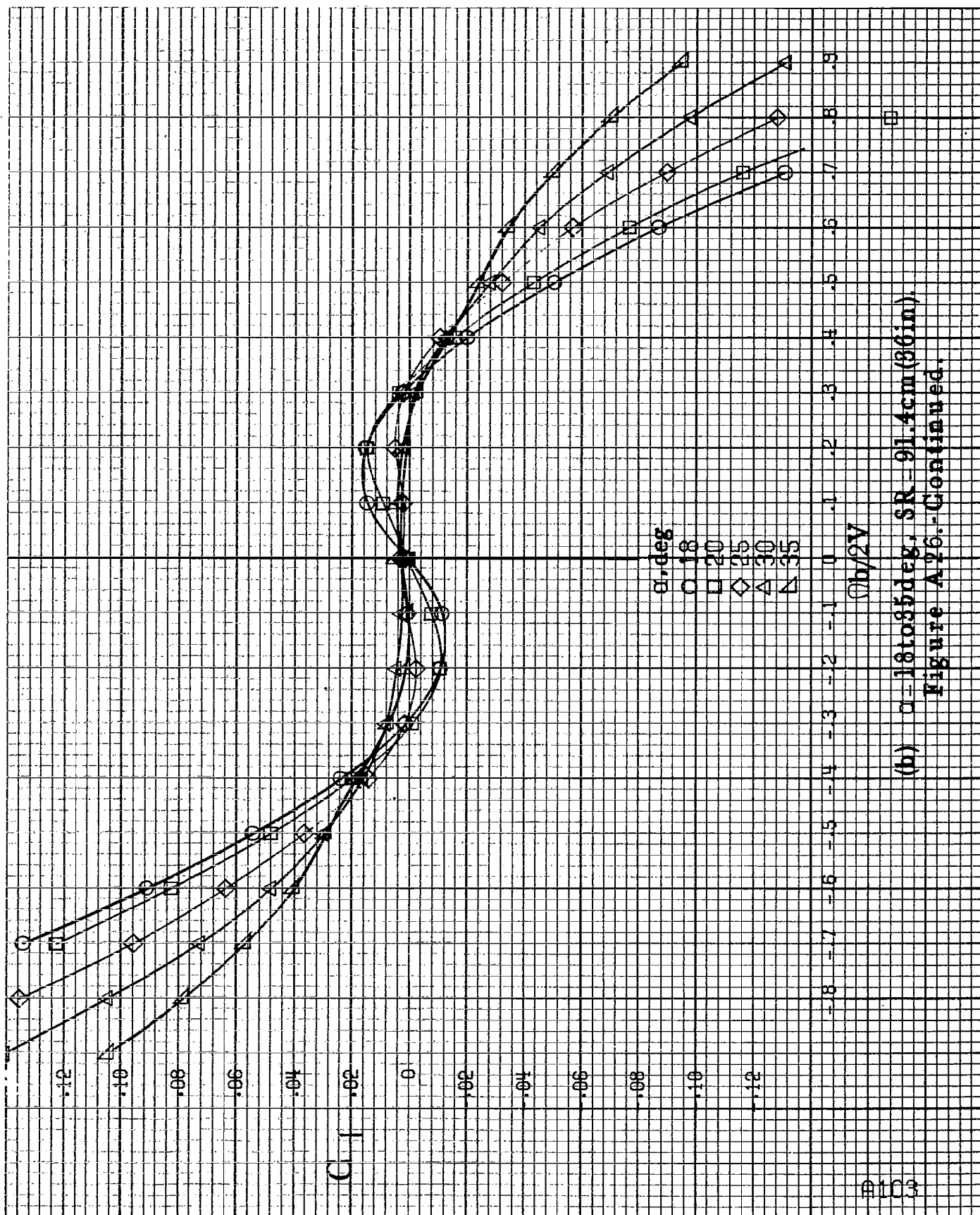
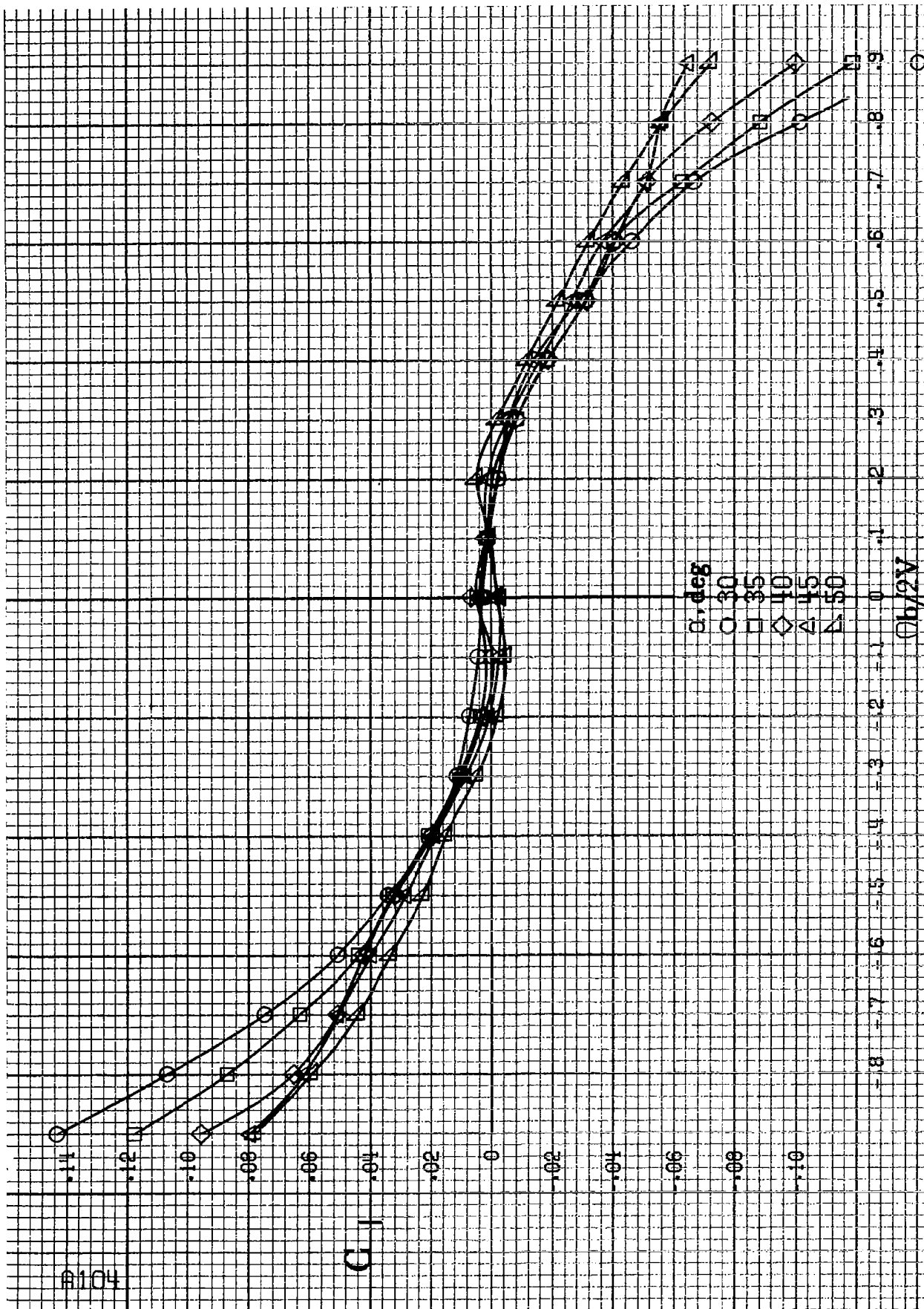


Figure A26.-Effect of notation rate and angle of attack on rolling-moment coefficient for short body, high wing, horizontal tail no. 1 configuration. $\delta_c = 0^\circ$, $\delta_s = 0^\circ$, $\delta_r = 0^\circ$, $\beta = 10^\circ$.

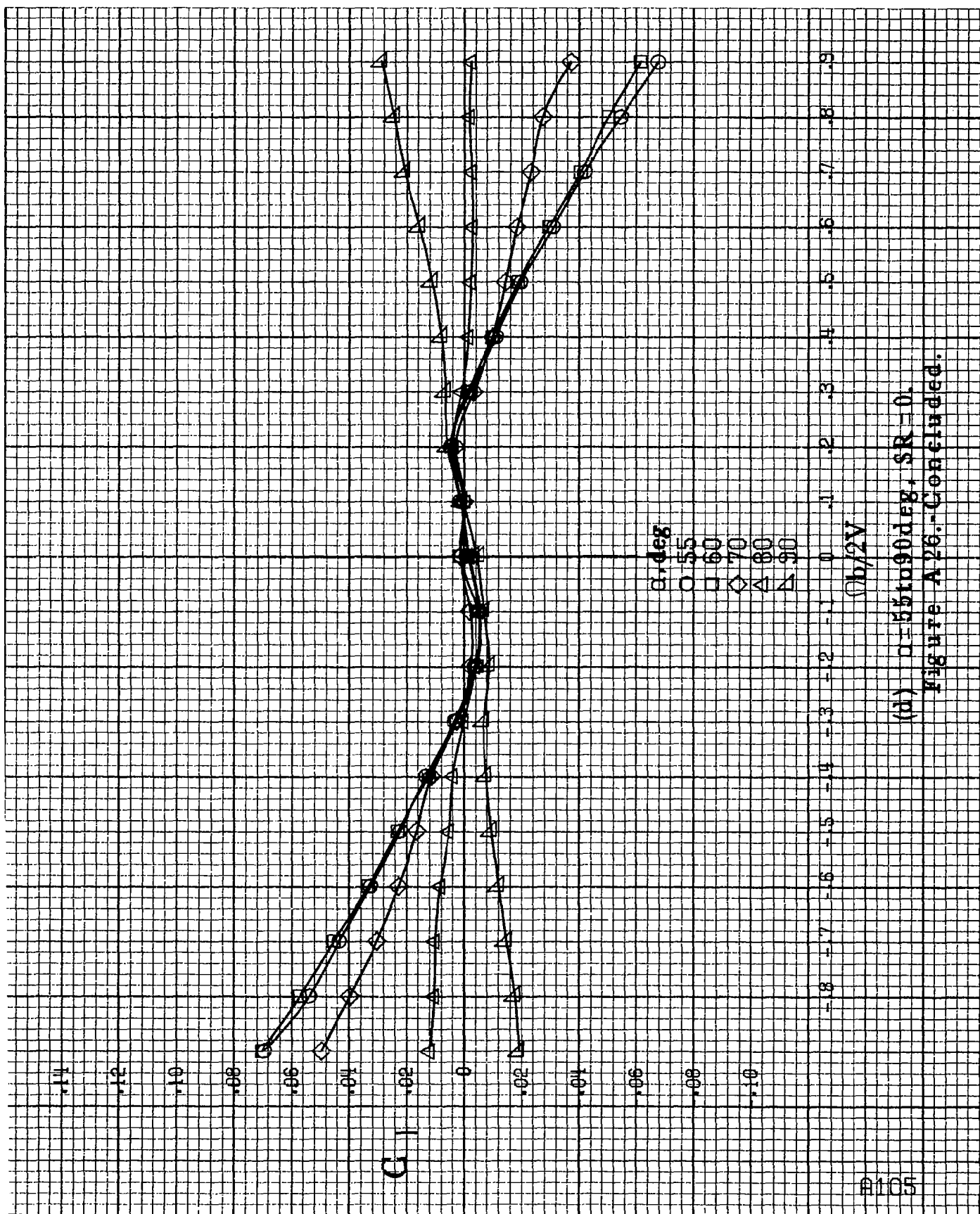


(b) $\alpha = 18$ to 35° , $SR = 91.4\text{cm}(36\text{in})$
Figure A 26.-Continued.



(c) $\alpha=30$ to 50° , $SR=0$.

Figure A26.-(Continued).



(d) $\alpha = 55$ to 90° , $SR = 0$.
Figure A26.-Concluded.

C_m α, deg

0 8

1 12

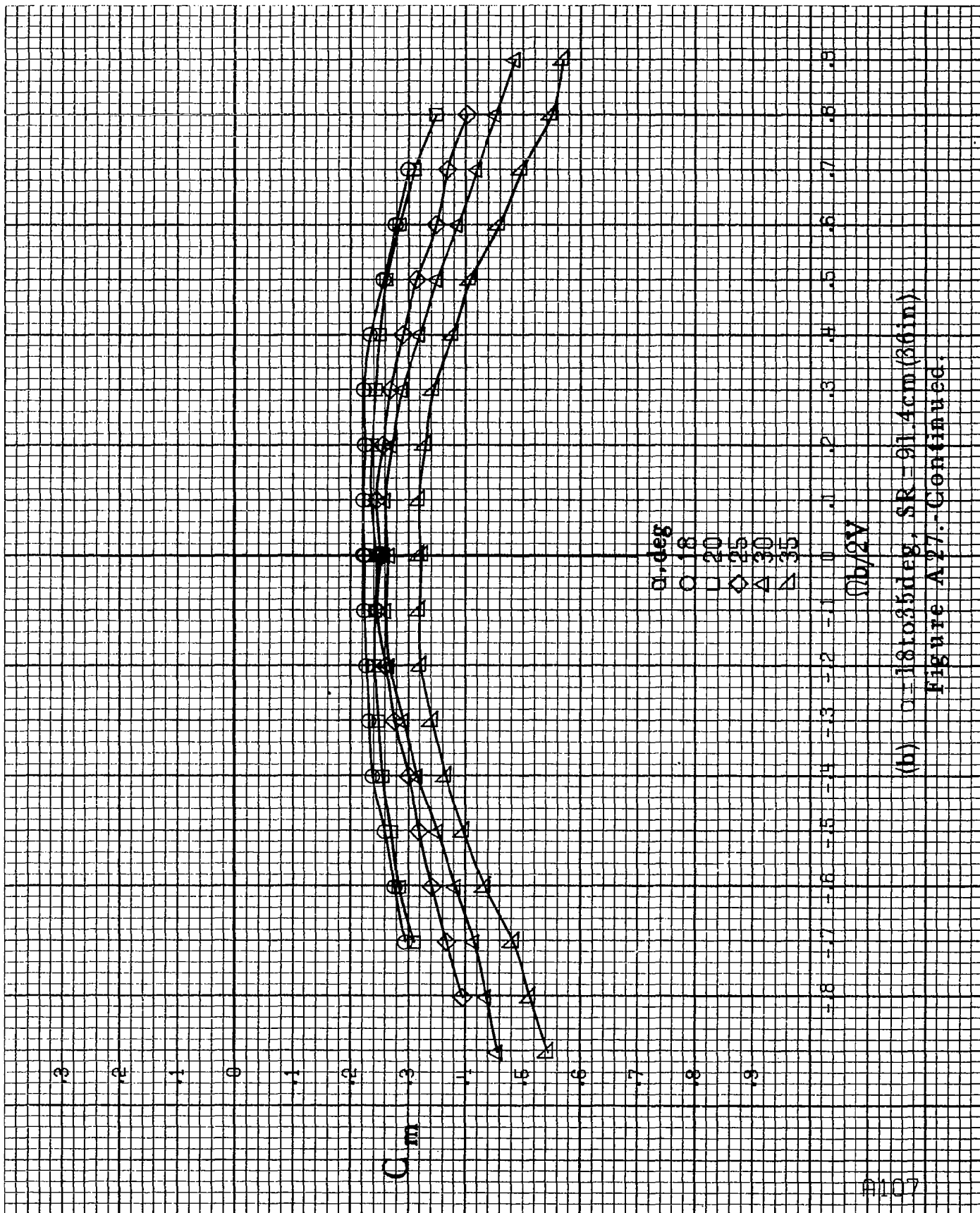
2 14

3 16

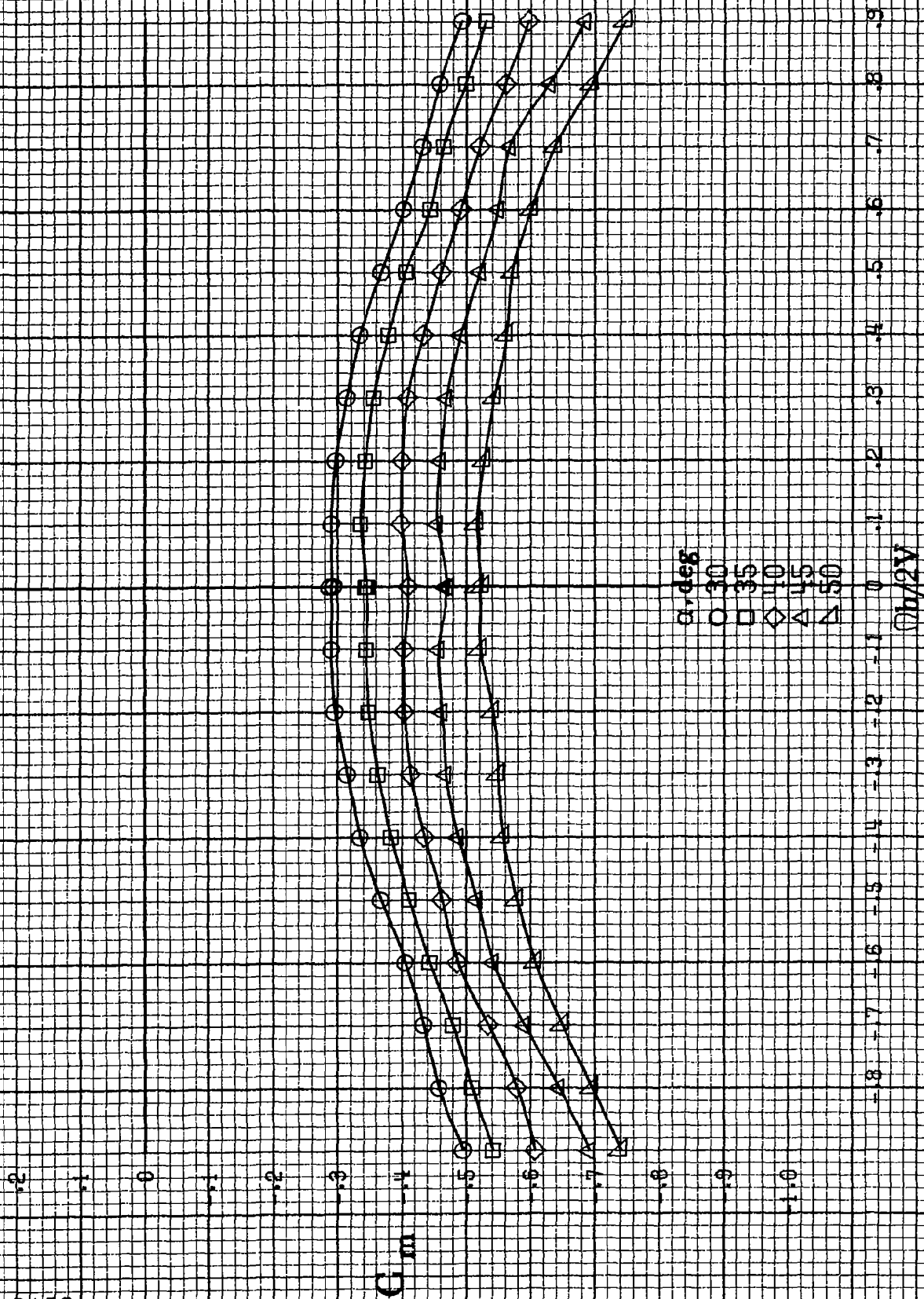
 $Qb/2V$ (a) $\alpha = 8$ to 16 deg, $SR = 91.4 \text{ cm (36 in.)}$.

Figure A27 - Effect of rotation rate and angle of attack on pitching-moment coefficient for short body, high wing, horizontal tail α_o of configuration.

$\delta_a = 10^\circ$, $\delta_s = 0^\circ$, $\delta_r = 10^\circ$, $\beta = 0^\circ$.

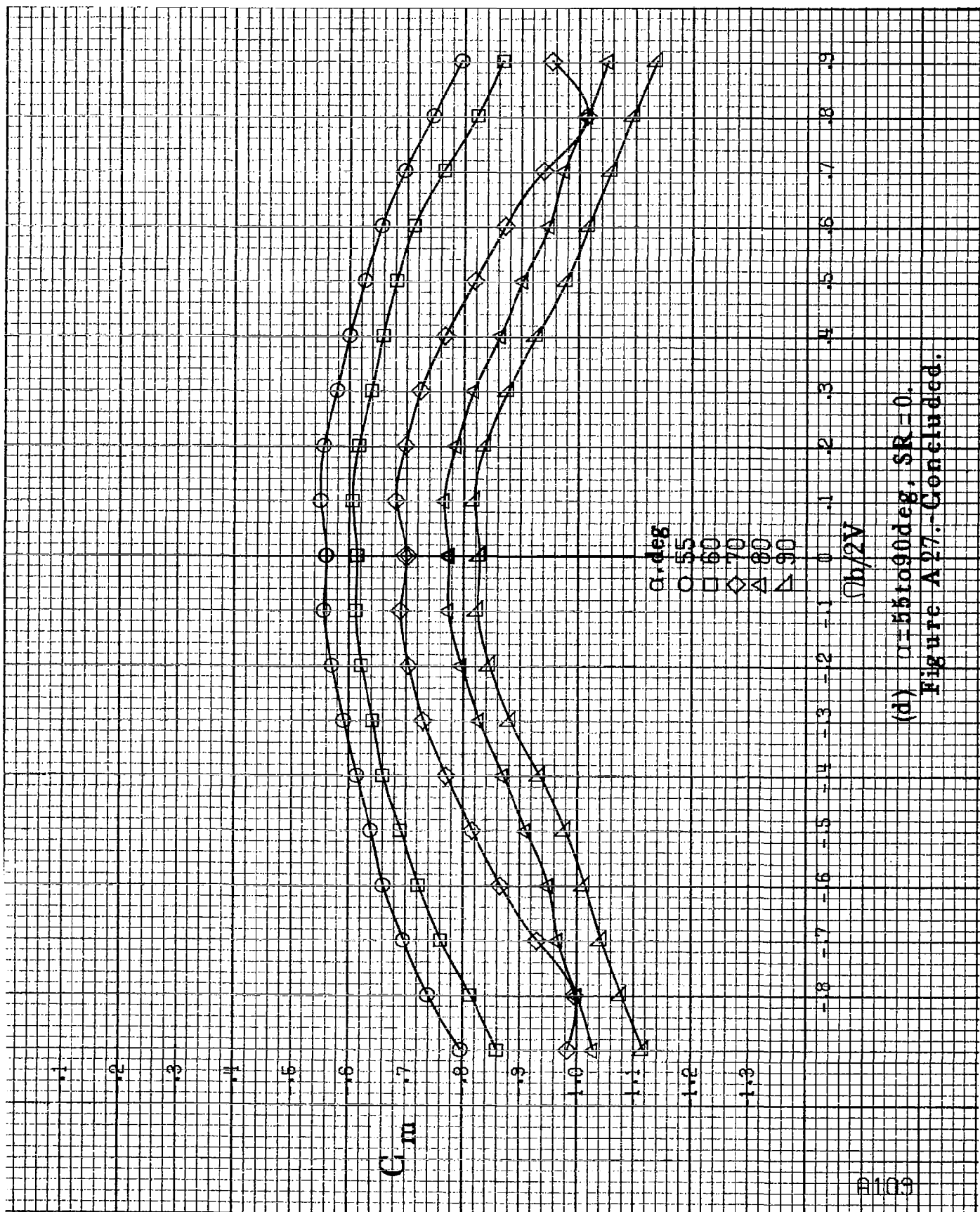


(b) $\alpha = 18$ to 35 deg, $SR = 91.4 \text{ cm (36 in)}$
 Figure A 27.-Continued.



(c) $\alpha = 30$ to 50° , $SR = 0$.

Figure A27.-Continued.



(d) $\alpha = 55$ to 90° , $SR = 0$.
Figure A 27.-Concluded.

α, deg

8

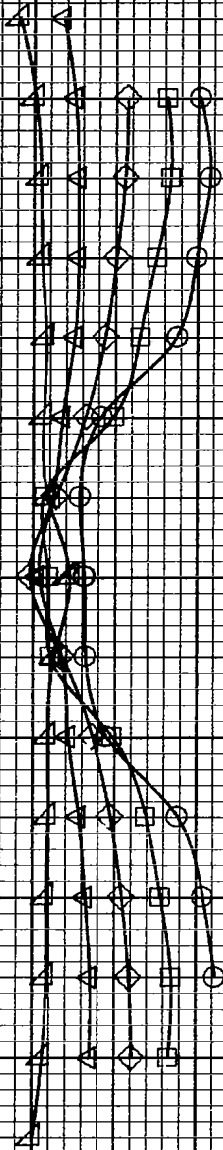
10

12

14

16

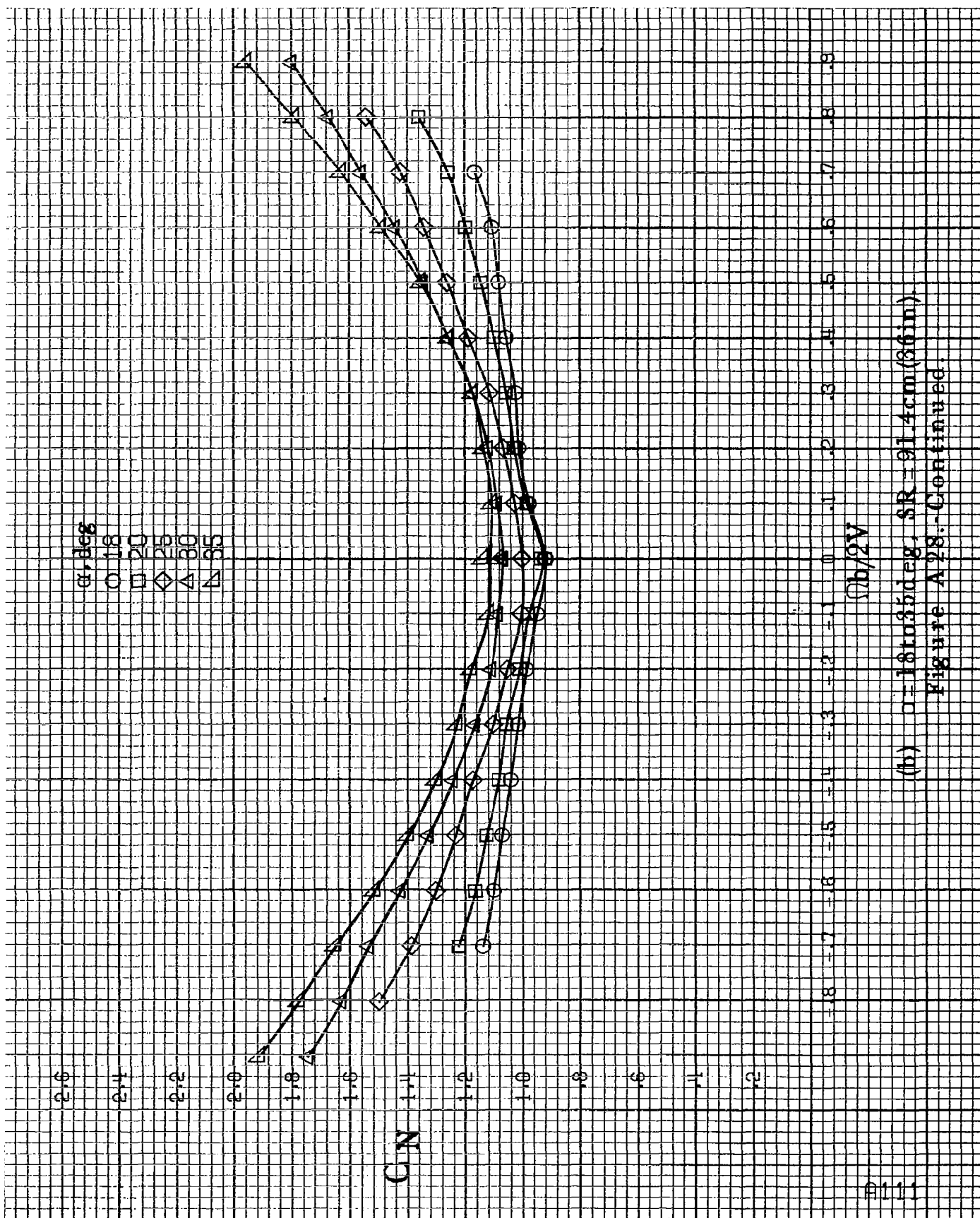
C_N



$\Omega b/2V$

(a) $\alpha=8$ to 16° , $SR=91.4\text{cm}$ (36in).

Figure A28.-Effect of rotation rate and angle of attack on normal-force coefficient for short body, high wing, horizontal tail no. 1 configuration. $\delta a=0^\circ$, $\delta s=0^\circ$, $\delta r=0^\circ$.



(b) $\alpha = 18$ to 35° , $SR = 0.14 \text{ cm (36 in.)}$
Figure A28.-Continued.

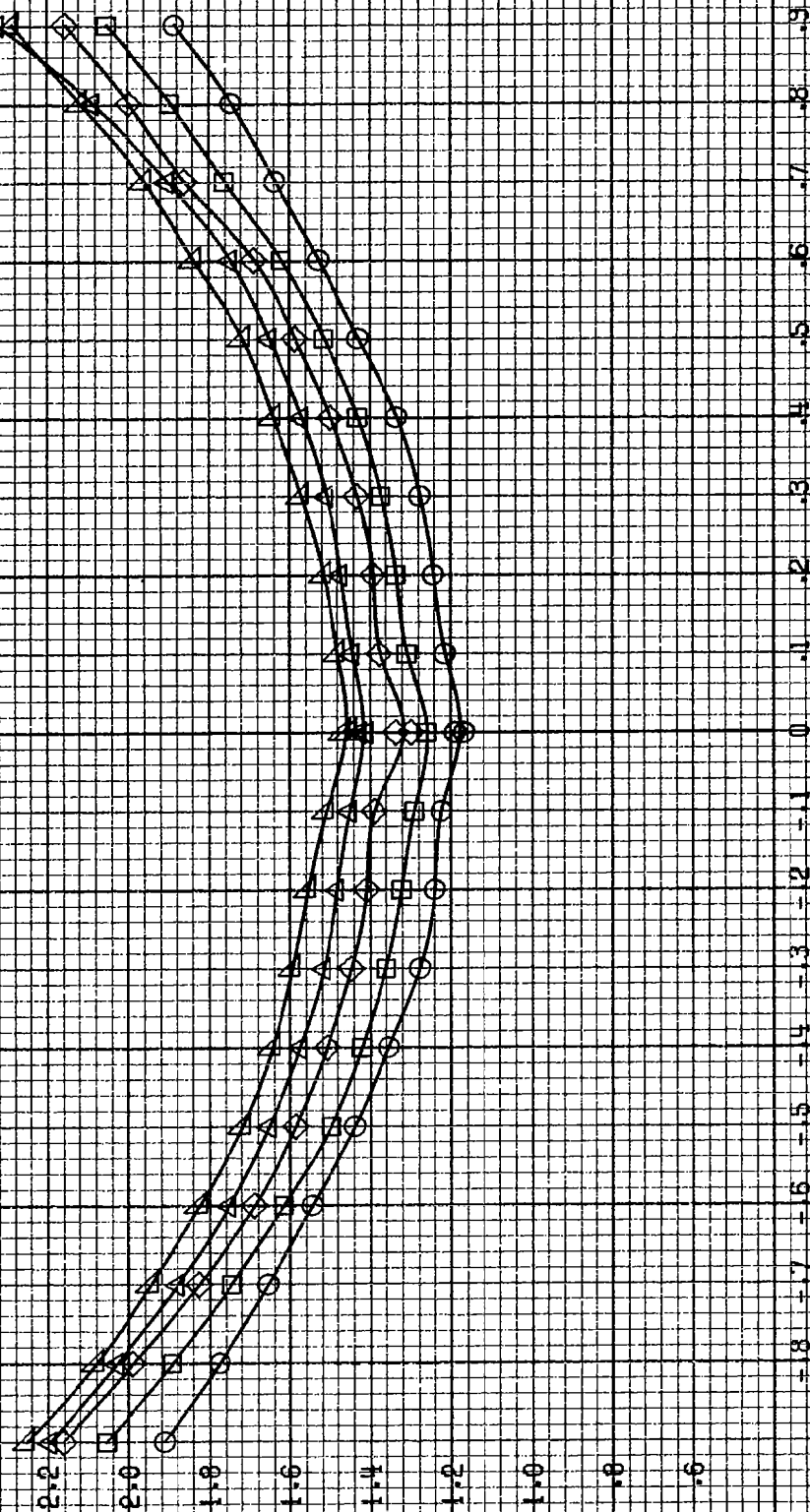
1112

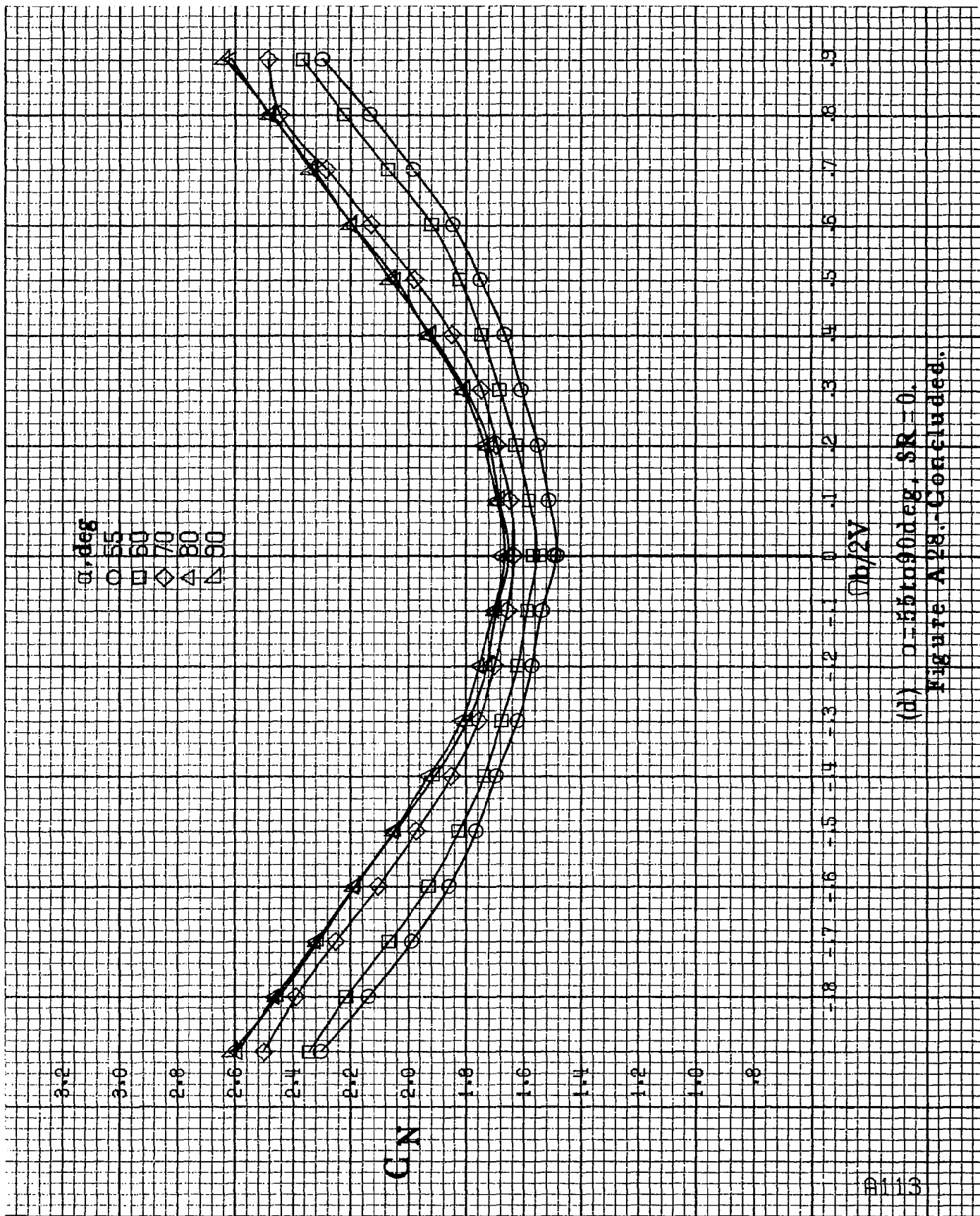
α , deg
 ○ 30
 □ 35
 ◇ 40
 △ 45
 ▽ 50

C_N

$\phi h/2V$

(c) $\alpha=30$ to 50 deg, $SR=0$.
 Figure A28.-Continued.



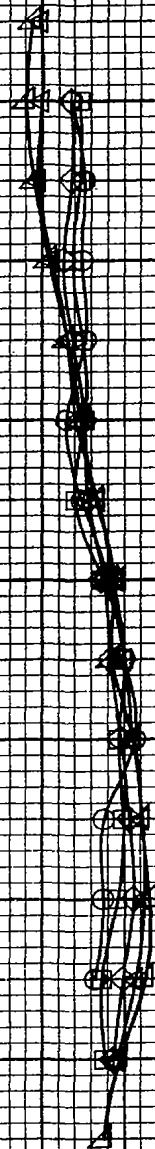


(d) $\alpha = 55$ to 90° , $SR = 0$.
 Figure A28. Concluded.

1114

α , deg
 8
 10
 12
 14
 16

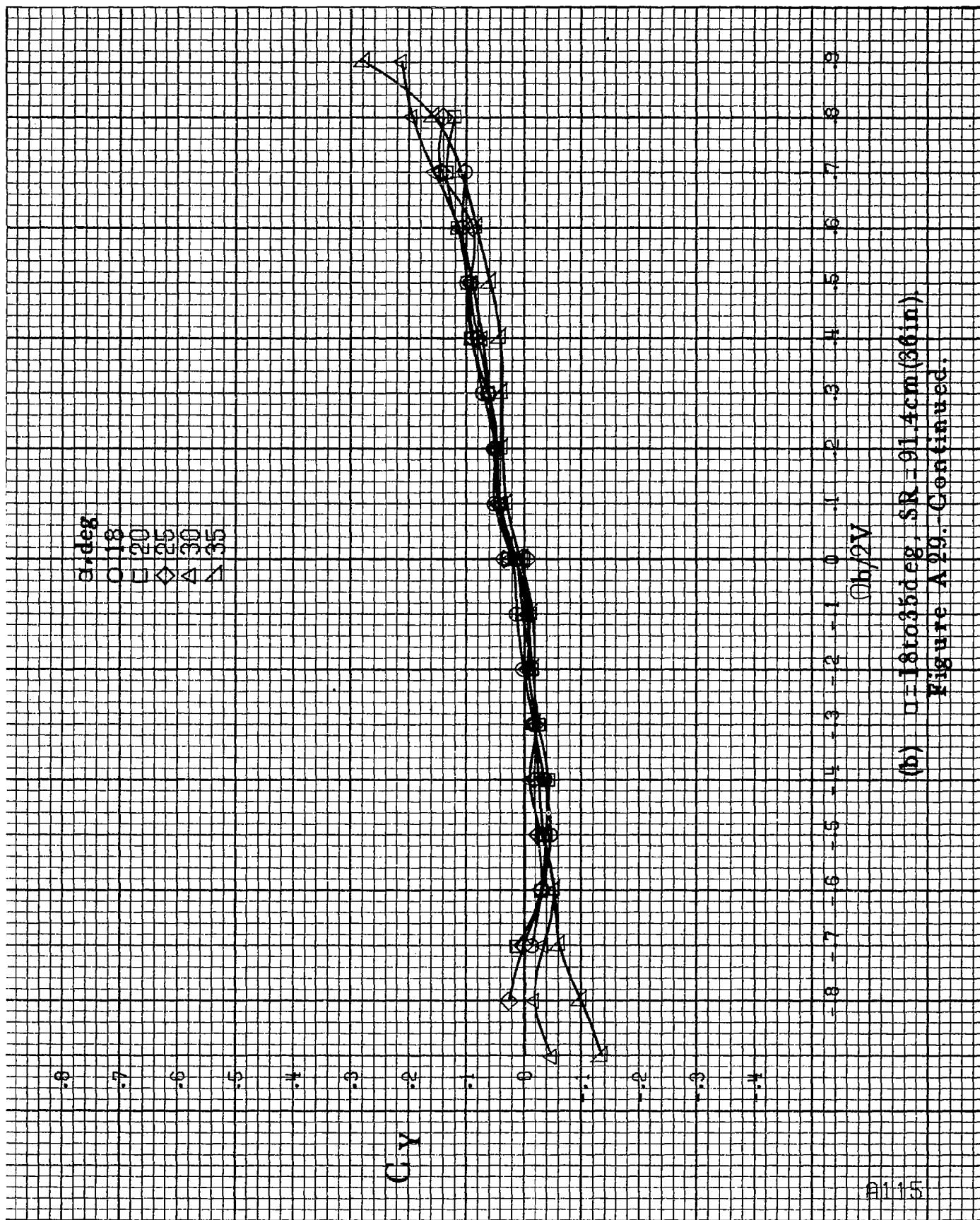
C_Y



$C_b/2V$

(a) $\alpha = 8$ to 16 deg, $SR = 91.4$ cm (36 in).

Figure A29.-Effect of rotation rate and angle of attack on side-force coefficient for short body, high wing, horizontal tail no. 1 configuration. $\delta a = 0^\circ$, $\delta r = 0^\circ$, $\delta \beta = 0^\circ$.



(b) $\alpha=18$ to 35° , $SR=91.4\text{cm}(36\text{in})$.

Figure A29. Continued.

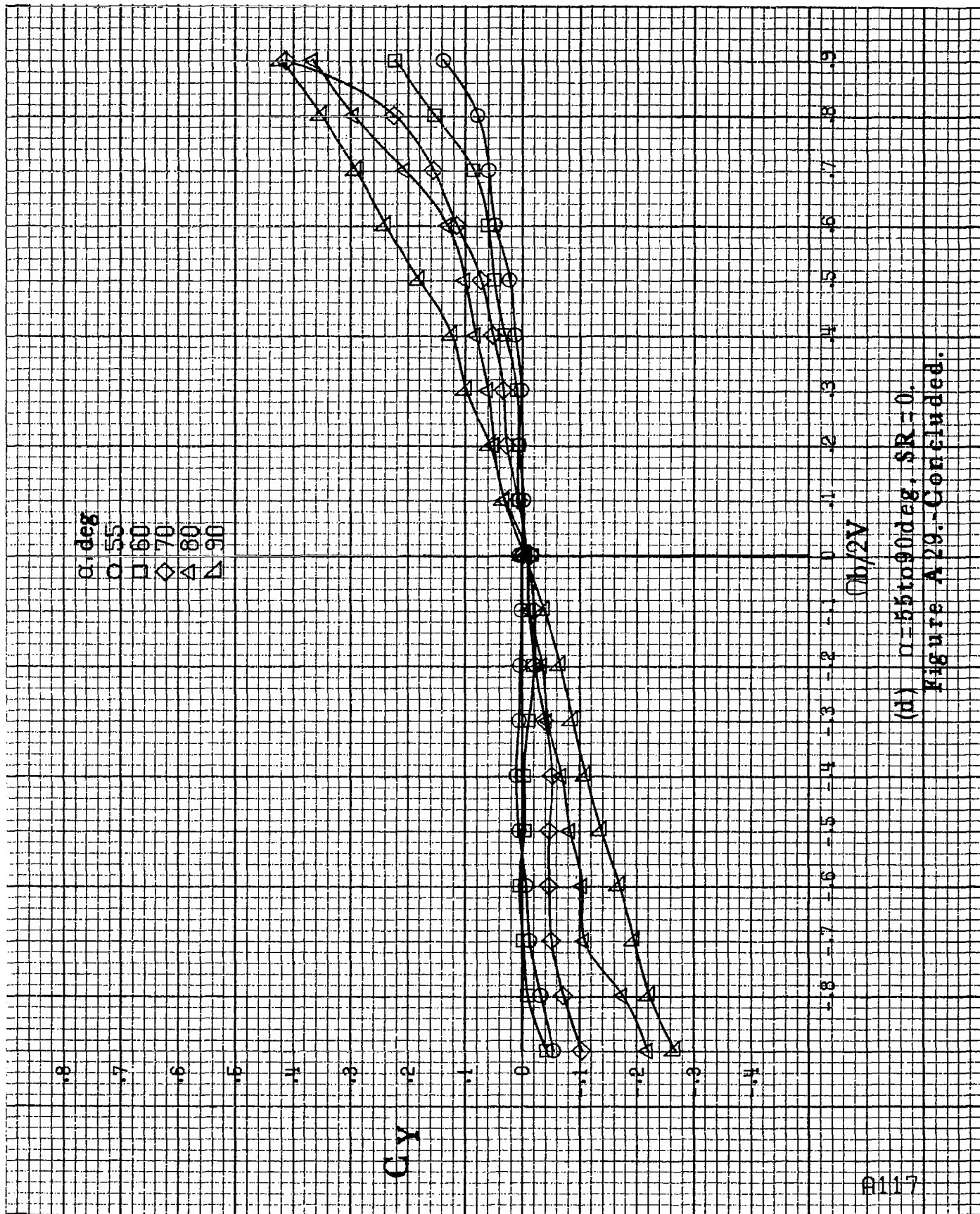
#1116

α, deg
 O 30
 □ 35
 ◇ 40
 △ 45
 ▲ 50

C_Y



(c) $\alpha=30$ to 50° , $SR=0$.
 Figure A29.-Continued.



(d) $\alpha = 55$ to 90 deg, $SR = 0$.
Figure A 29.-Concluded.

α , deg
 0.8
 1.0
 1.2
 1.4
 1.6

GA

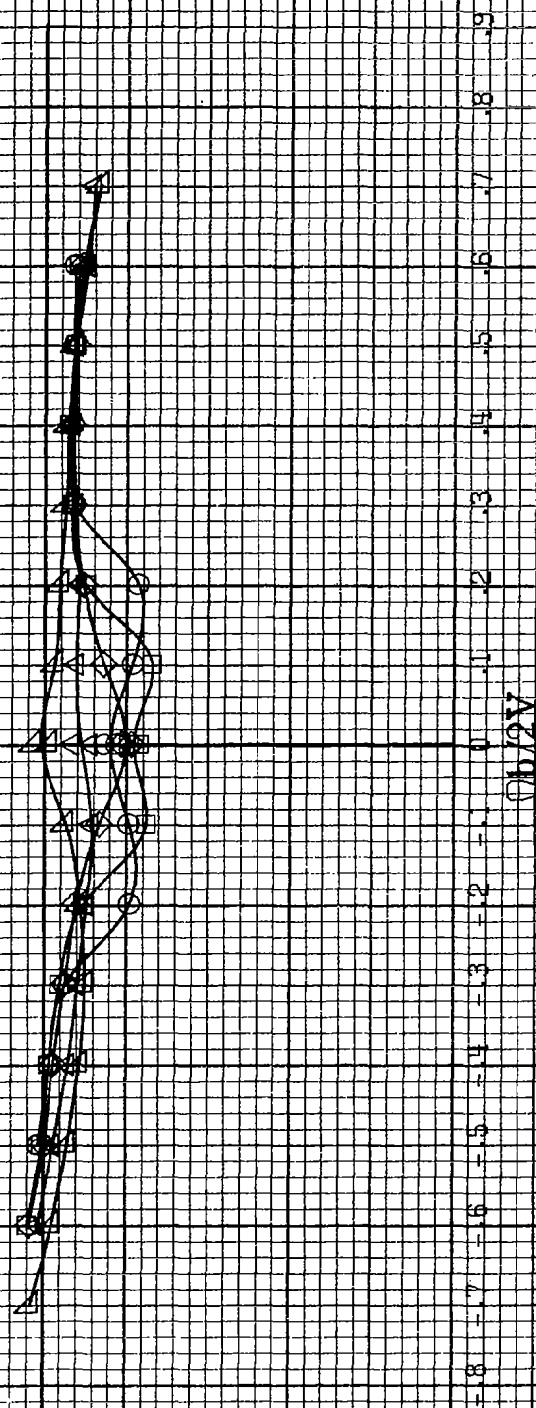
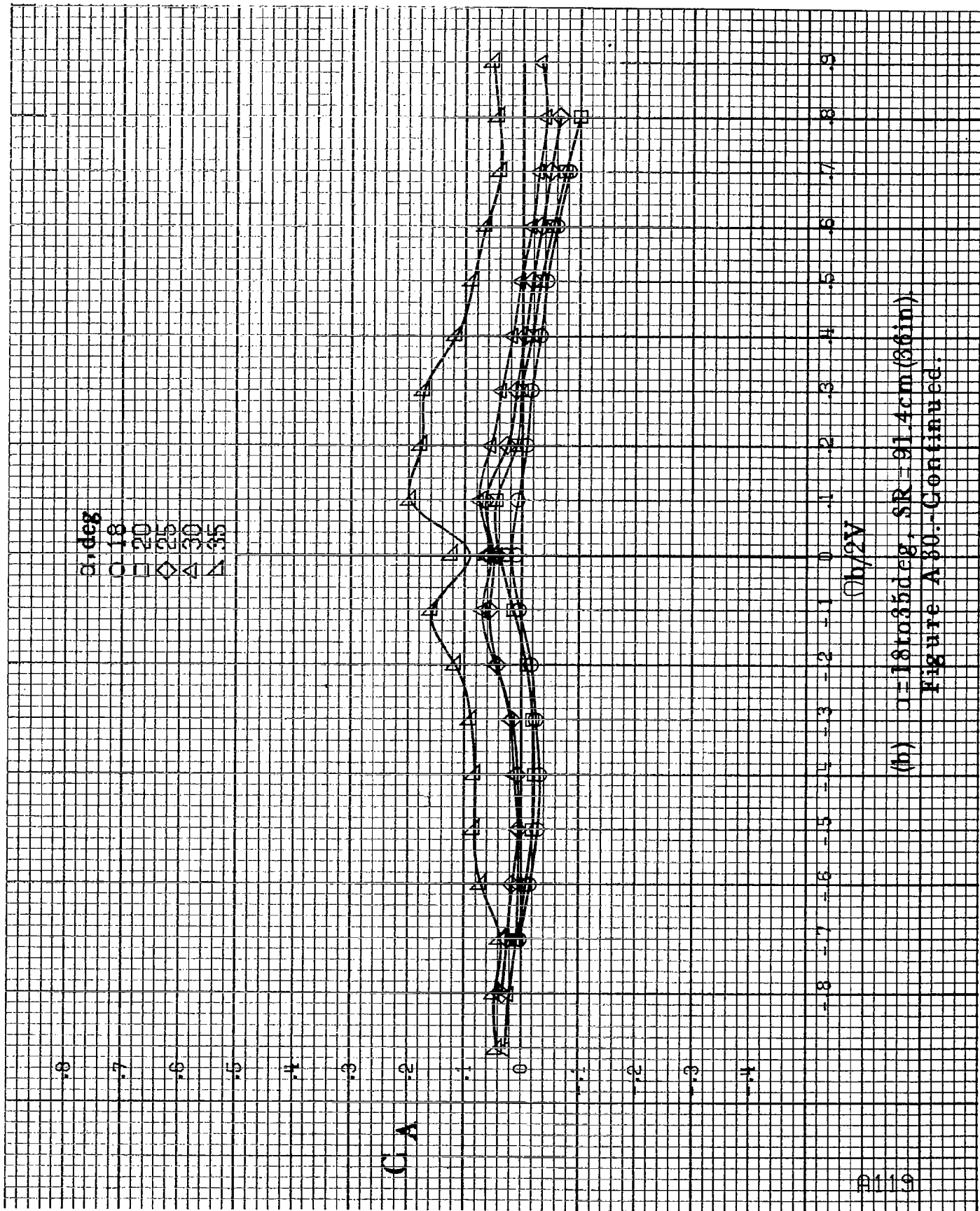


Figure A.30.-Effect of rotation rate and angle of attack on axial-force coefficient for short body, high wing, horizontal tail no. 1 configuration. $\delta a = 0^\circ$, $\delta s = 0^\circ$, $\delta r = 0^\circ$. $\beta = 0^\circ$. (a) $\alpha = 8$ to 16 deg, SR = 91.4 cm (36 in.).



(b) $\alpha = 18$ to 35 deg. $SR = 91.4 \text{ cm (86 in.)}$
 Figure A80.-Continued.

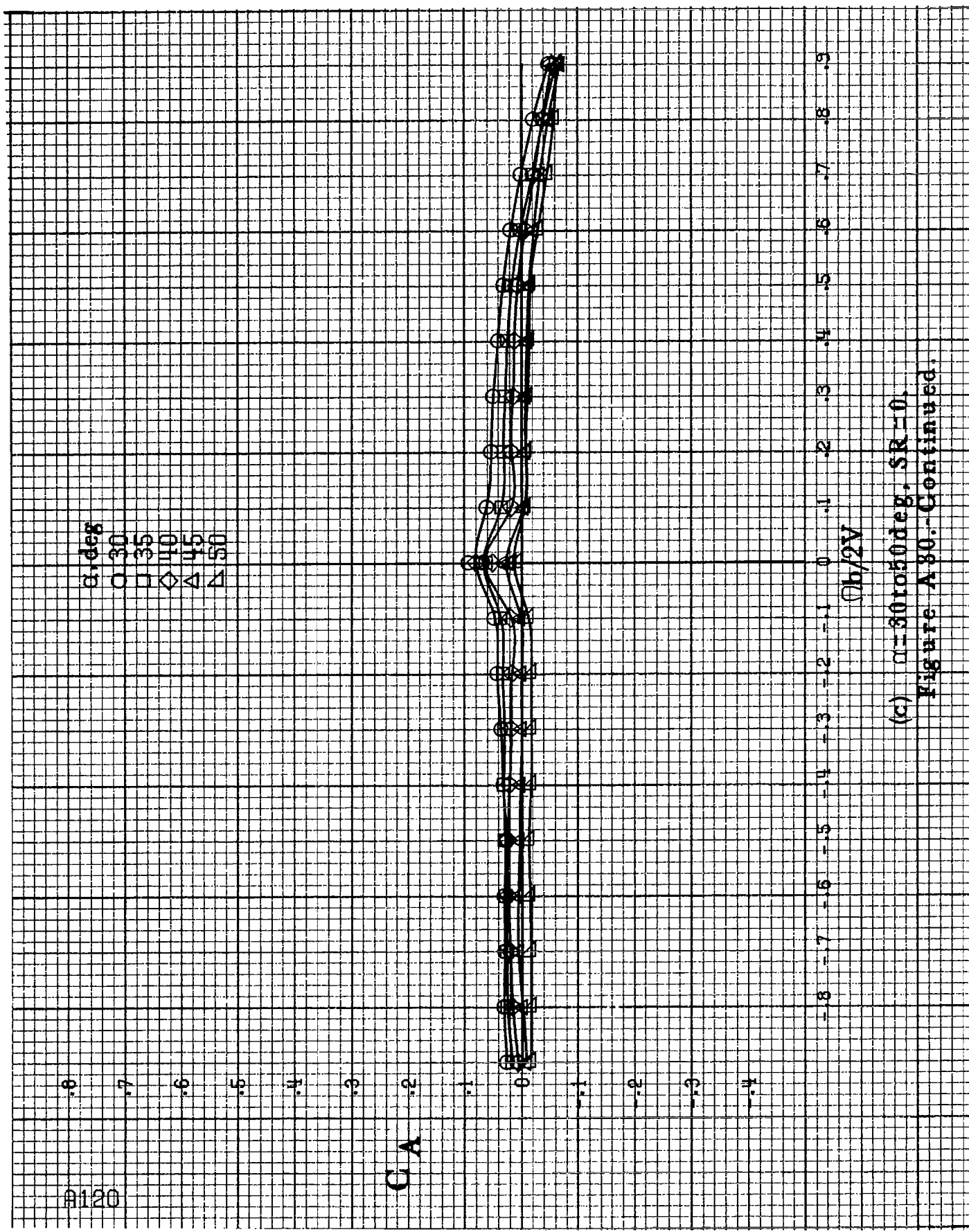
8120

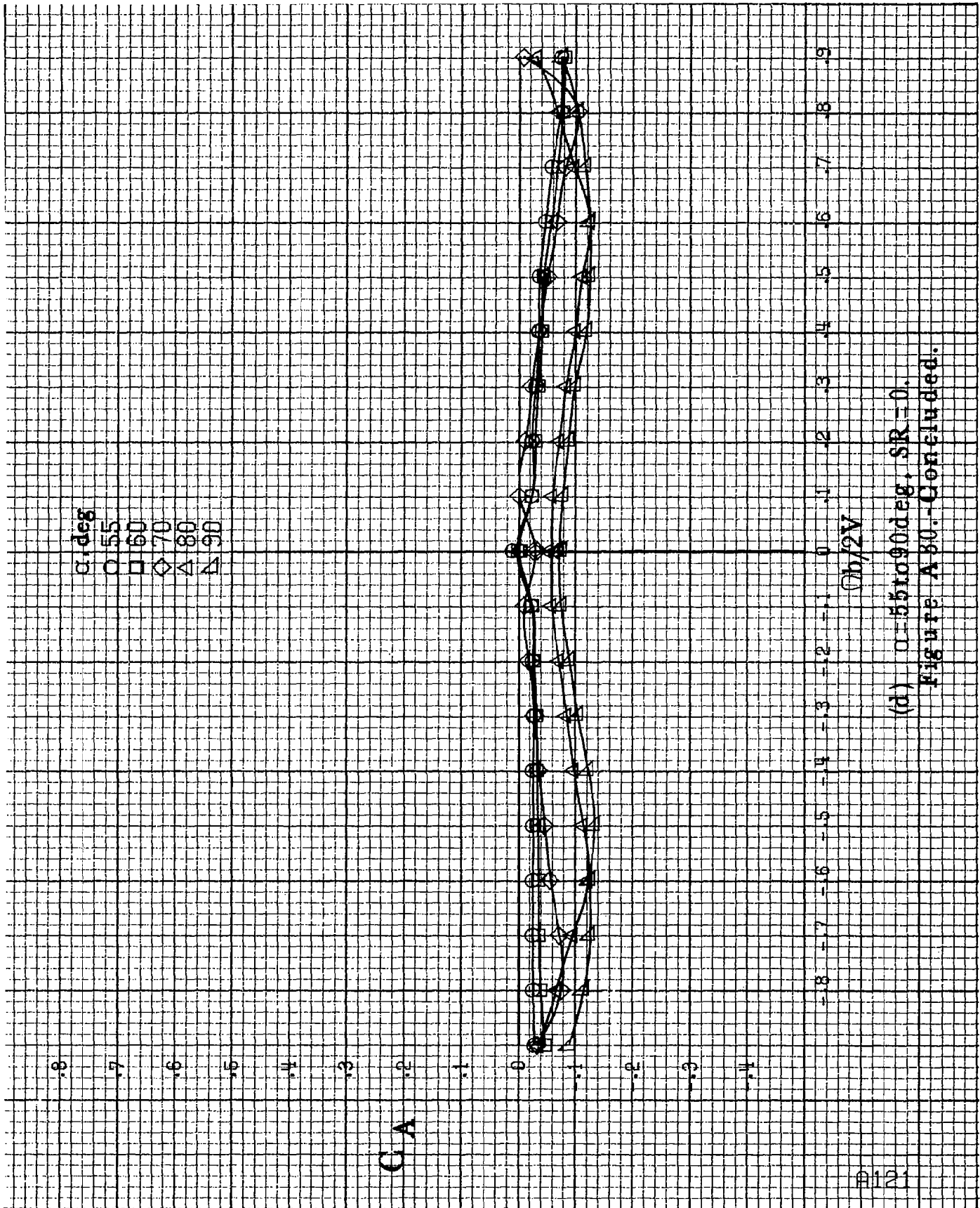
α, deg
 \square 30
 \square 35
 \diamond 40
 \triangle 45
 \triangle 50

CA

$\Omega b/2V$

(c) $\alpha=30$ to 50 deg. $SR=0$.
 Figure A 30.-Continued.





(d) $\alpha=55$ to 90° , $SR=0$.

Figure A 80.-Concluded.

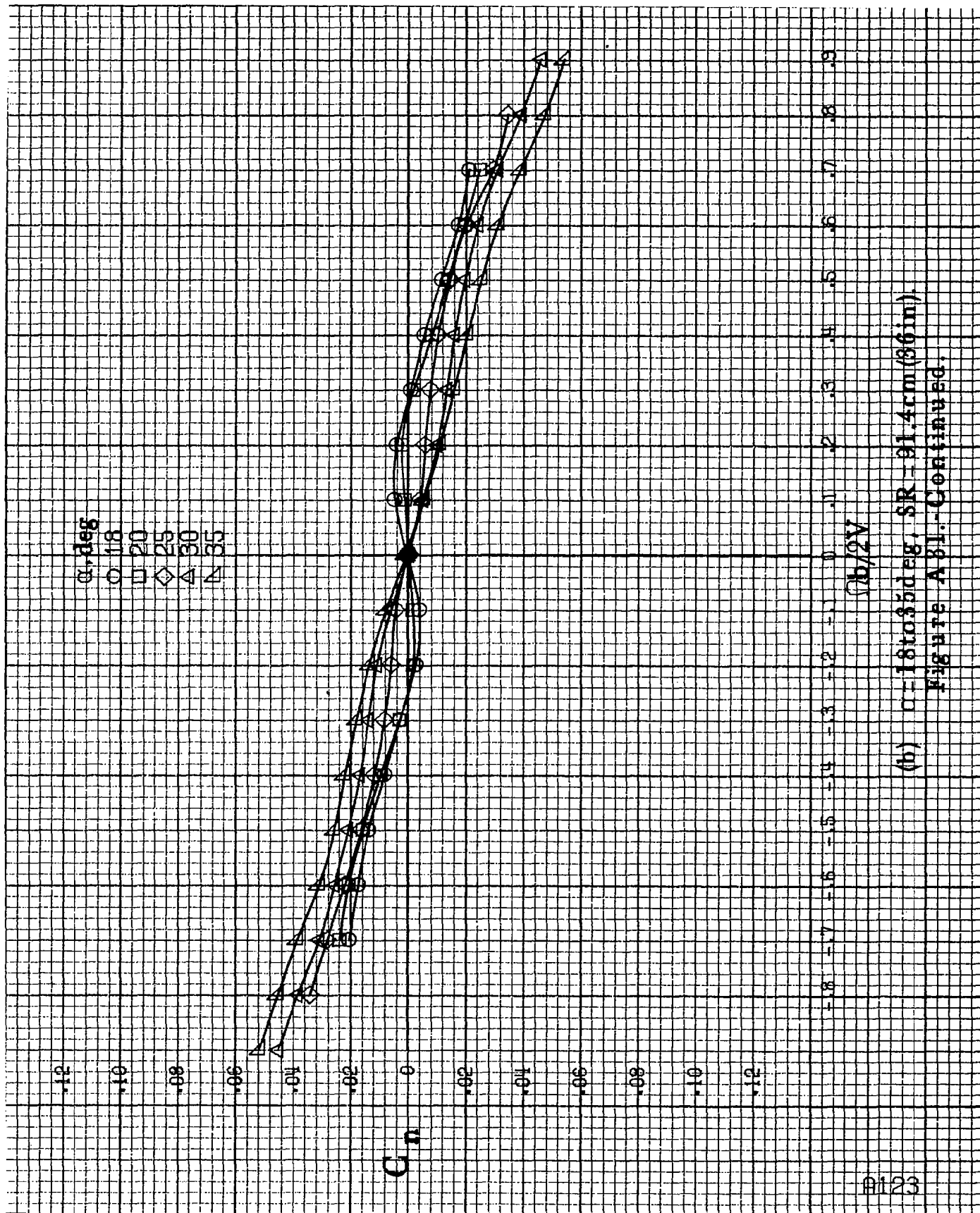
α, deg

\circ 8
 \square 10
 \diamond 12
 \triangle 14
 ∇ 16

 C_n $b/2V$ (a) $\beta = 8 \text{ to } 16 \text{ deg}$, $SR = 91.4 \text{ cm (36 in)}$.

Figure A31.-Effect of rotation rate and angle of attack on yawing-moment coefficient for short body, high wing, horizontal tail no. 8 configuration.

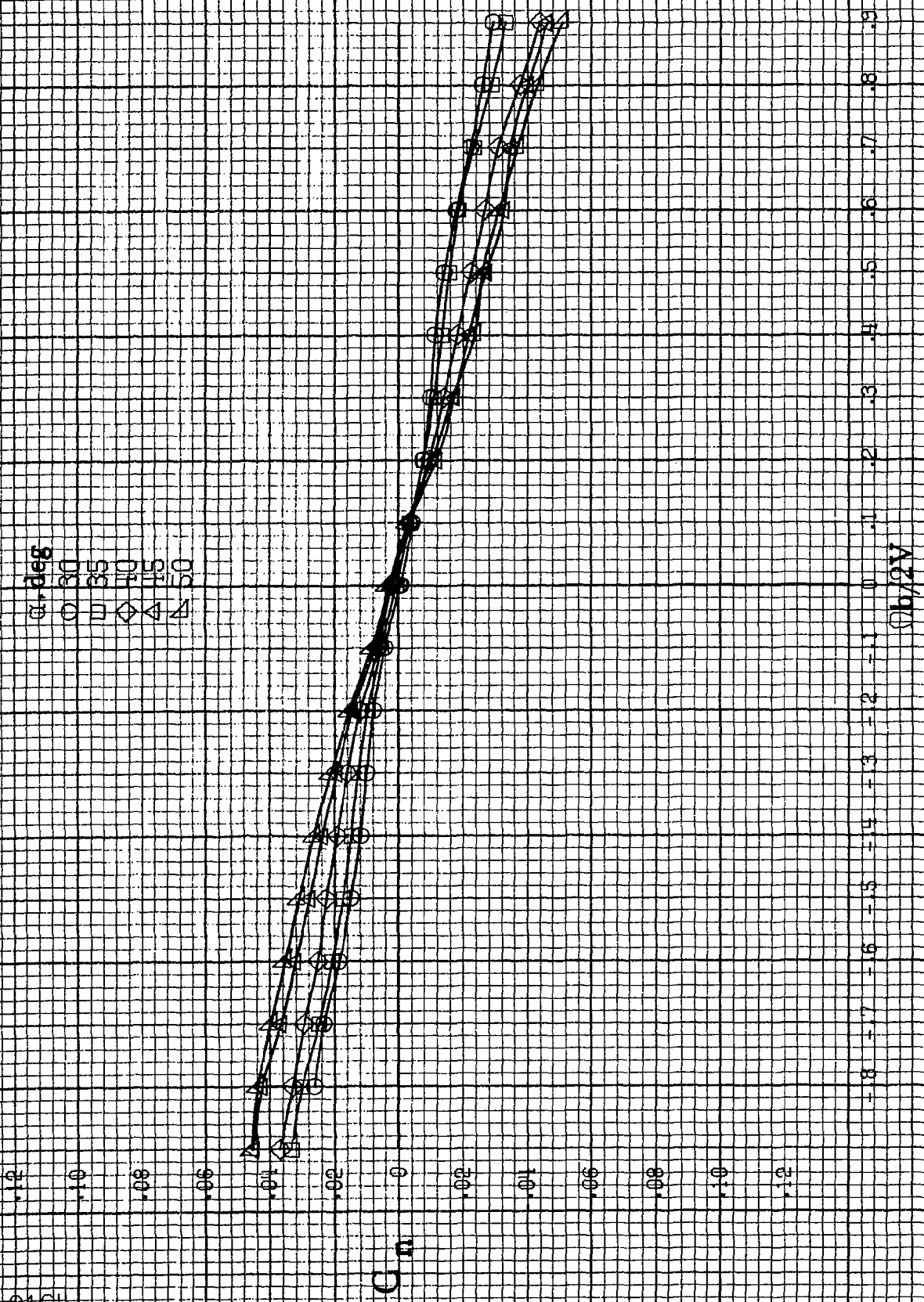
$\beta_a = 0^\circ$, $\beta_s = 0^\circ$, $\delta_T = 0^\circ$, $\delta = 10^\circ$.



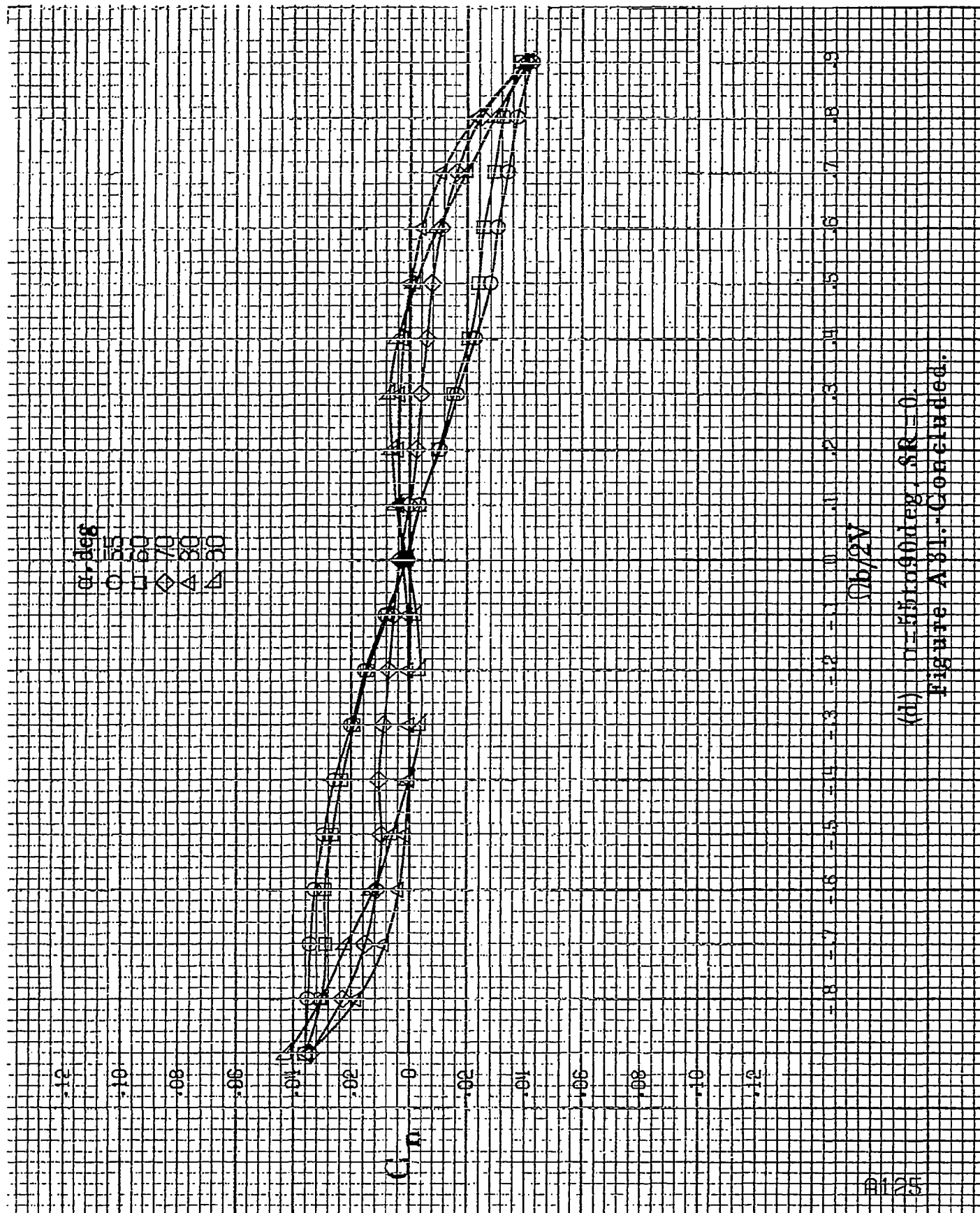
(b) $\alpha=18$ to 35° , $SR=31.4 \text{ cm} (36 \text{ in})$

Figure A81--Continued.

1124



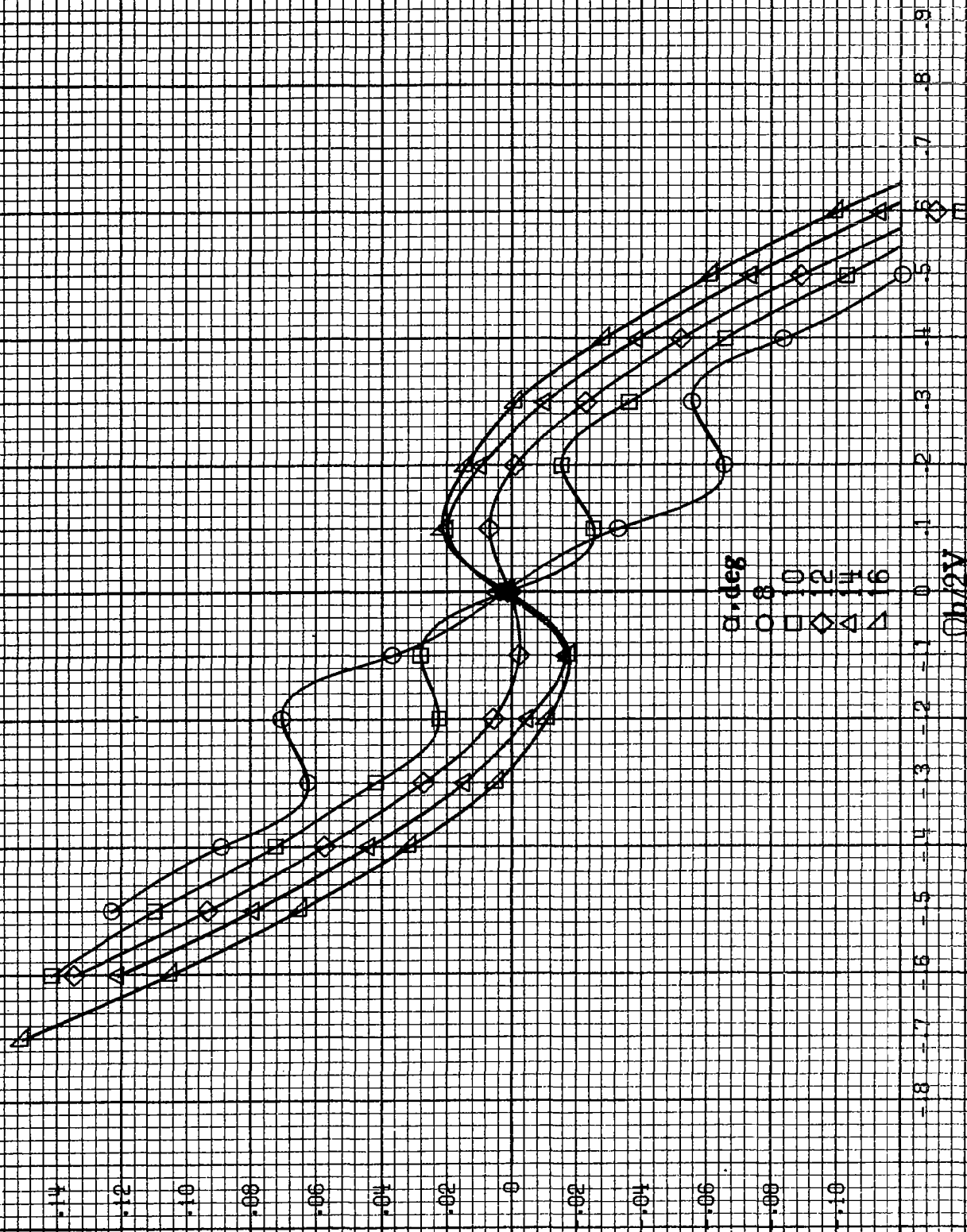
(c) $\alpha=30$ to 50 deg, $SR=0$.
Figure A31.-Continued.



(ii) $n = 55$ to 90 deg, $SR = 0$.

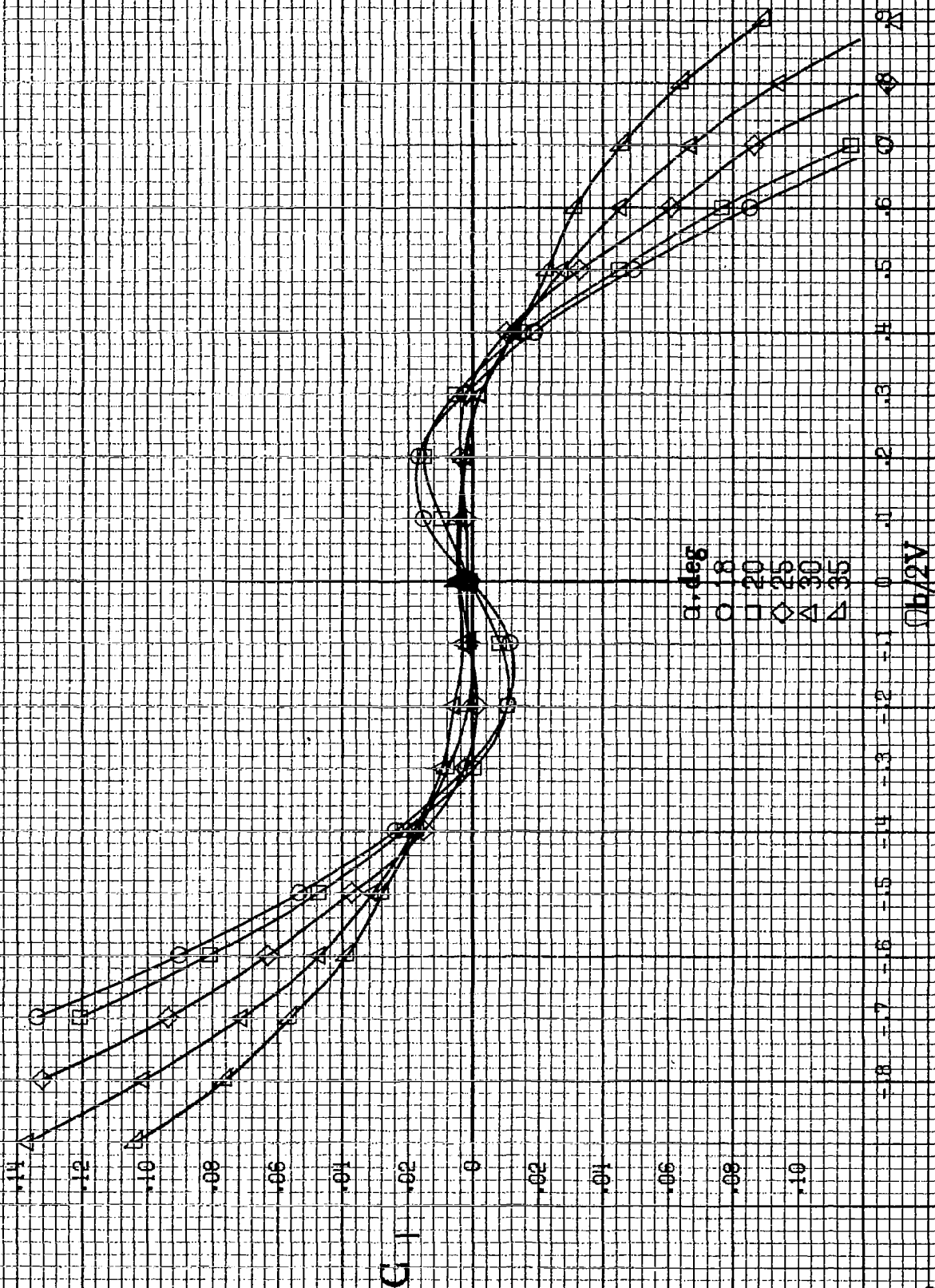
Figure A-81. - Concluded.

C_L

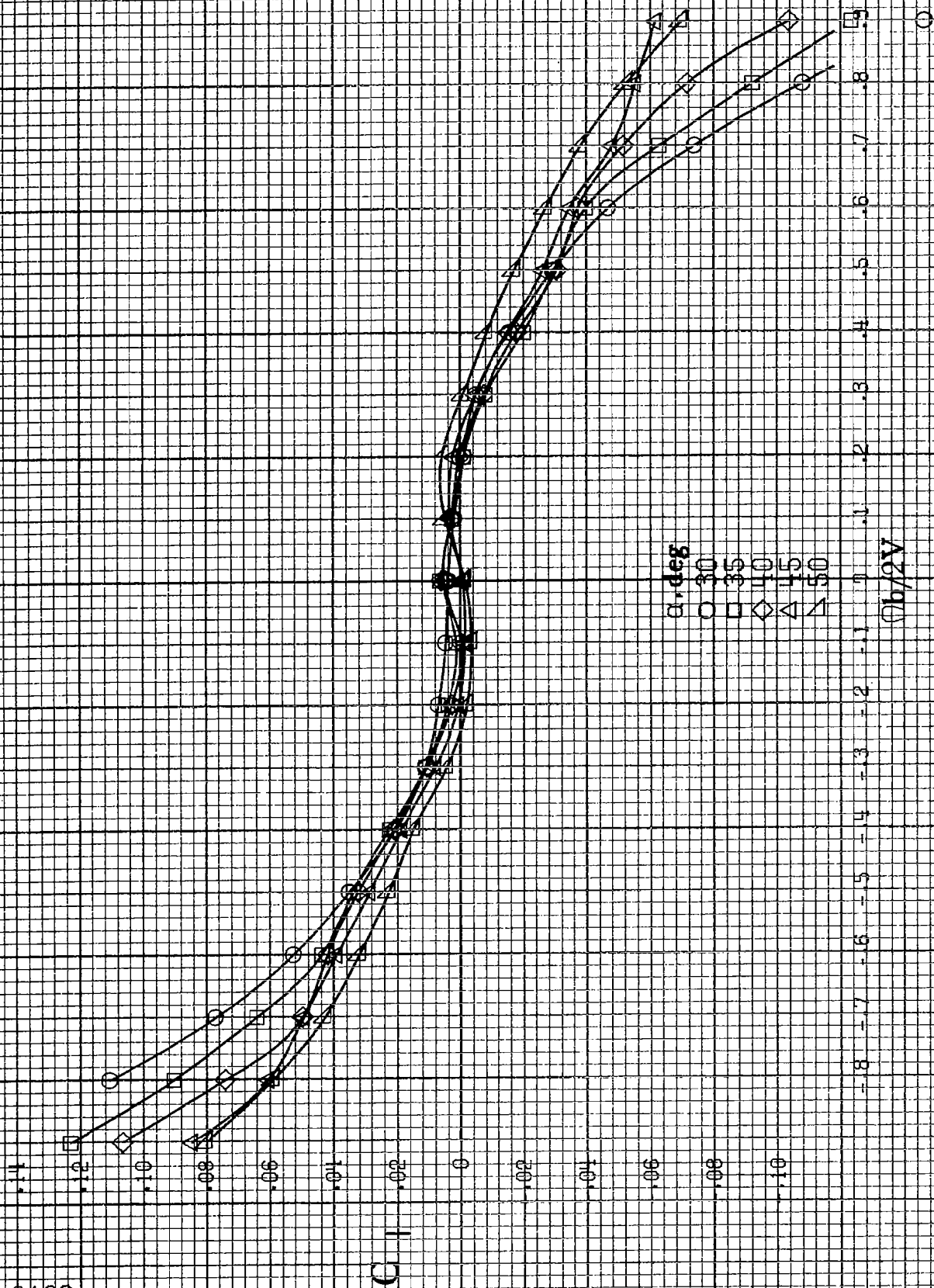


(a) $\alpha=8$ to 16° , $SR=91.4$ cm (36 in).

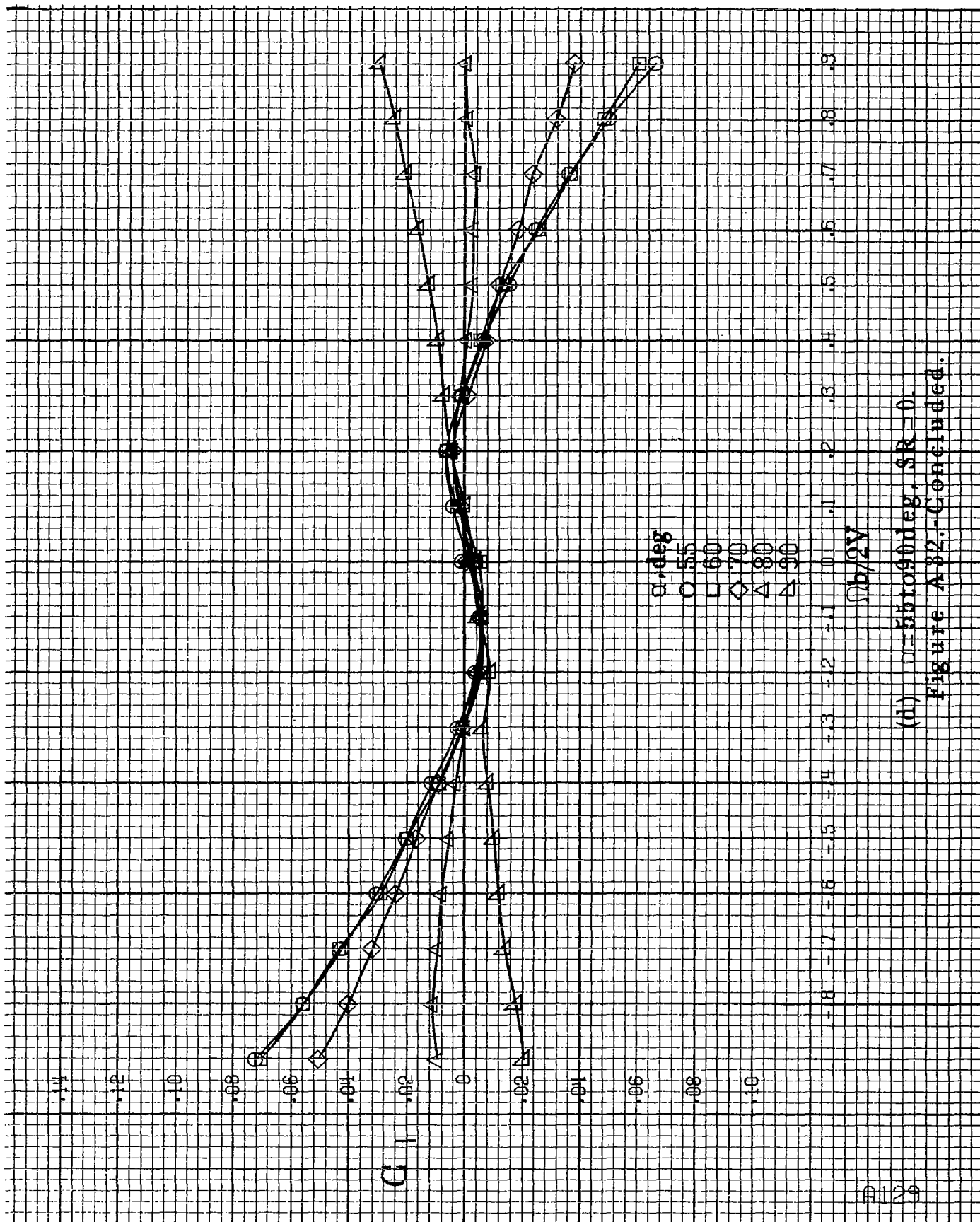
Figure A32.-Effect of notation rate and angle of attack on rolling-moment coefficient for short body, high wing, horizontal tail no. 3 configuration. $\delta_a = 0^\circ$, $\delta_s = 0^\circ$, $\delta_r = 10^\circ$, $\delta = 16^\circ$.



(b) $\alpha = 18$ to 35 deg, $SR = 91.4$ cm (36 in).
Figure A 32.-Continued.



(c) $\alpha = 30$ to 50° , $SR = 0$.
Figure A 32.-Continued.



(d) $\alpha=55$ to 90 deg, $SR=0$.
Figure A32.-Concluded.

A130

C_m

α, deg

8

10

12

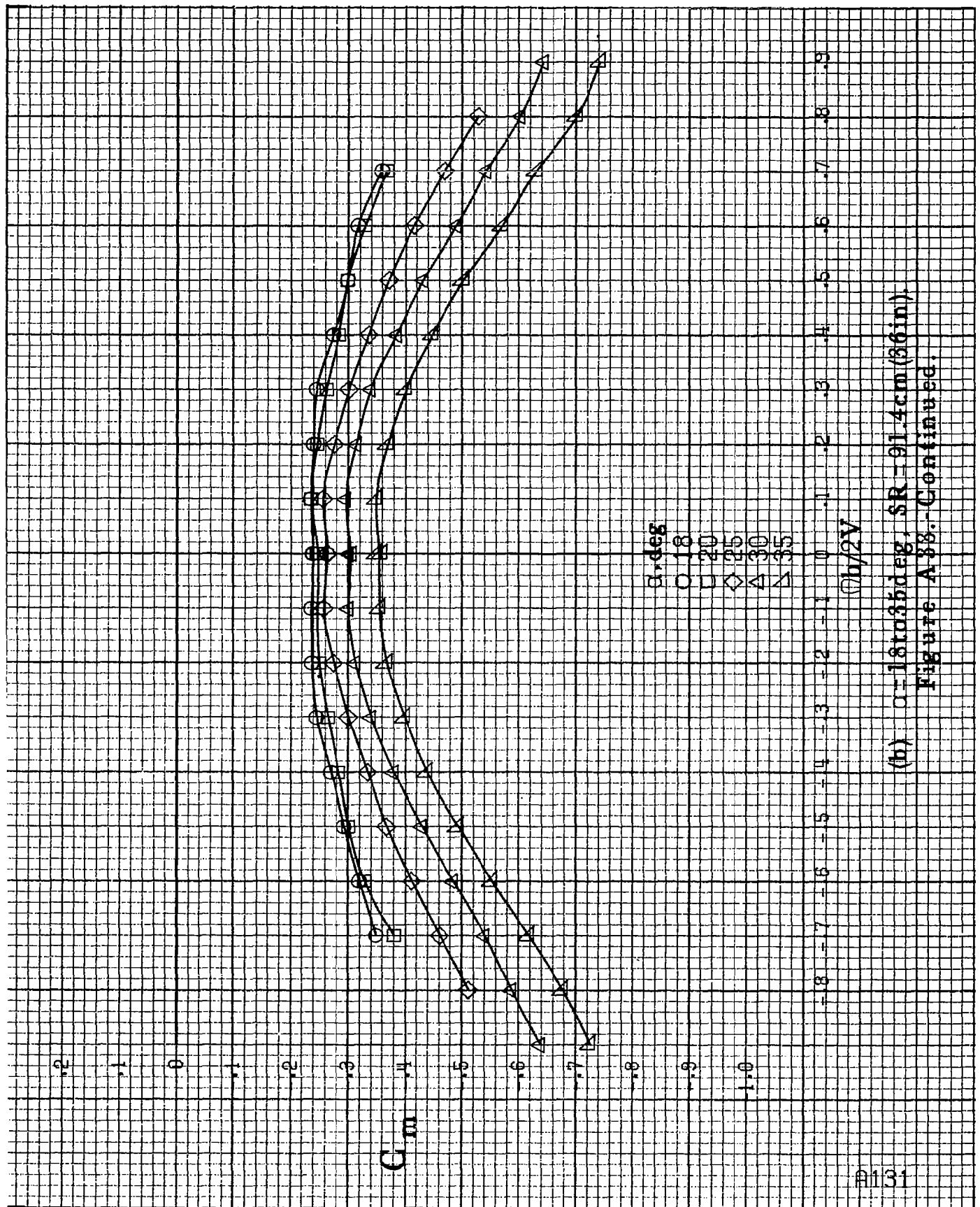
14

16

$\Omega b/2V$

(a) $\alpha = 8 \text{ to } 16 \text{ deg}$, $SR = 91.4 \text{ cm (36 in)}$.

Figure A.33 - Effect of rotation rate and angle of attack on pitching-moment coefficient for short body, high wing, horizontal tail no. 3 configuration. $\delta_e = 0^\circ$, $\delta_a = 0^\circ$, $\delta_r = 0^\circ$, $\beta = 0^\circ$.



(h) $\alpha = 18$ to 35 deg, $SR = 91.4$ cm (36 in).

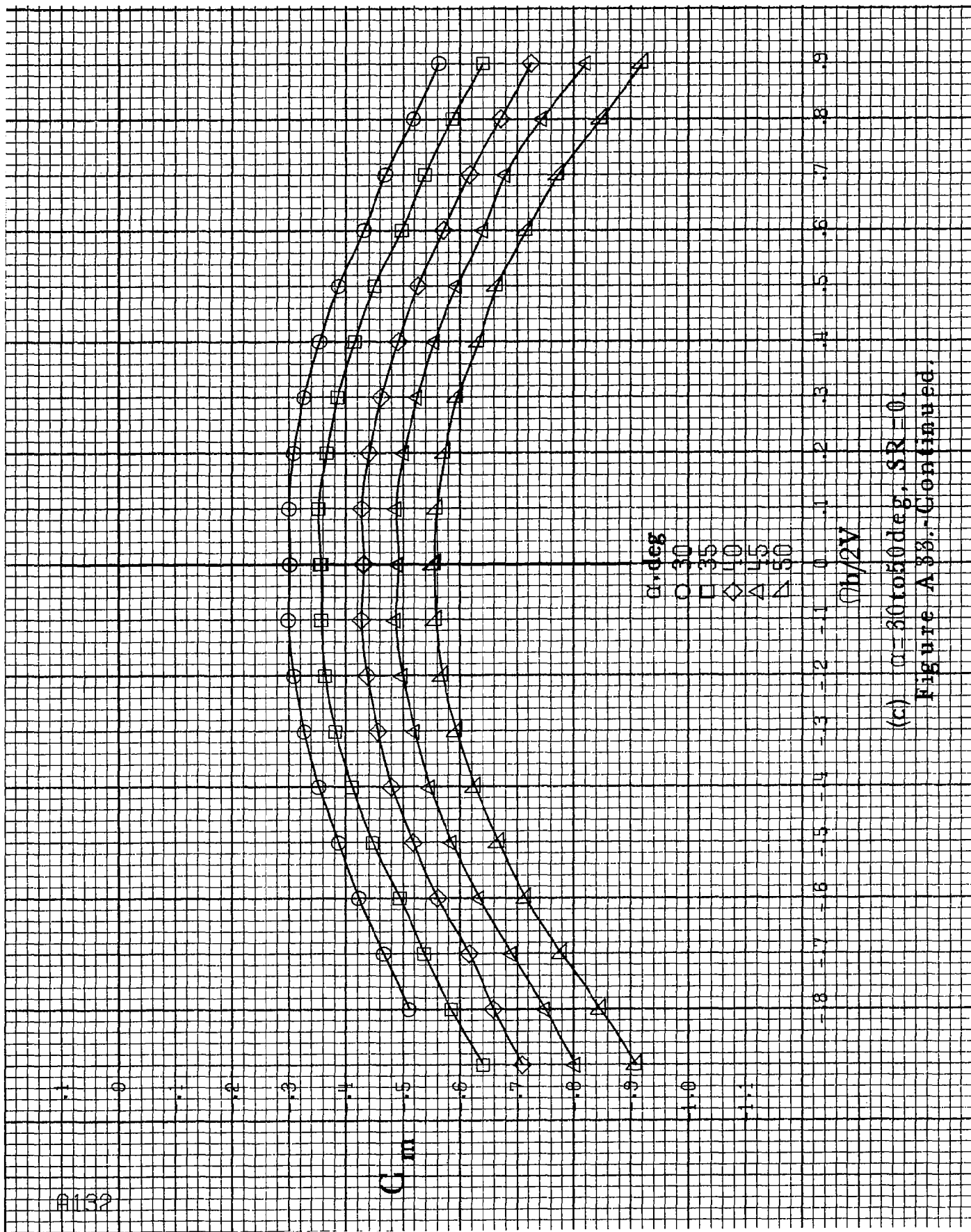
Figure A33. Continued.

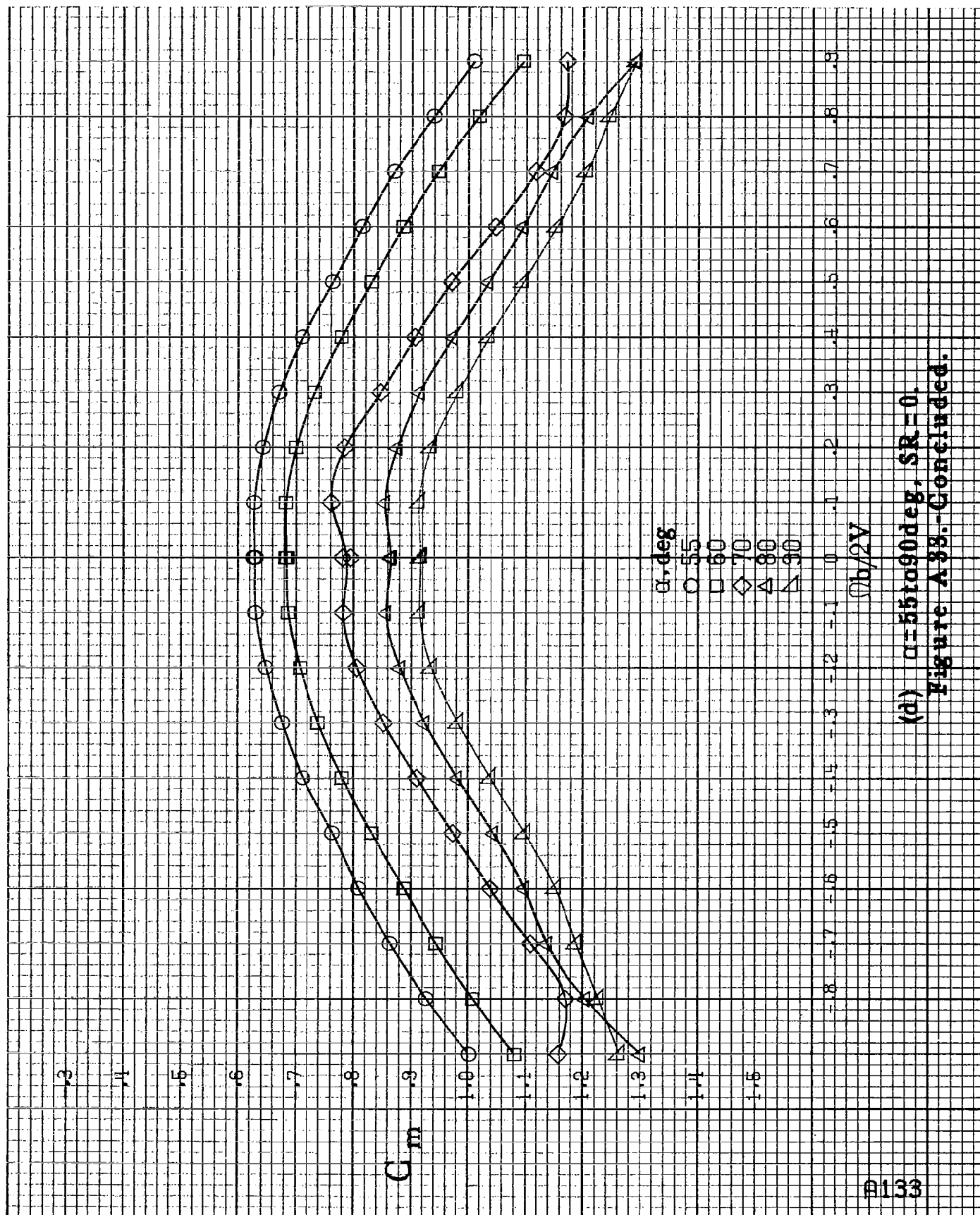
C_m

α, deg
 \circ 30
 \square 35
 \diamond 40
 \triangle 45
 ∇ 50

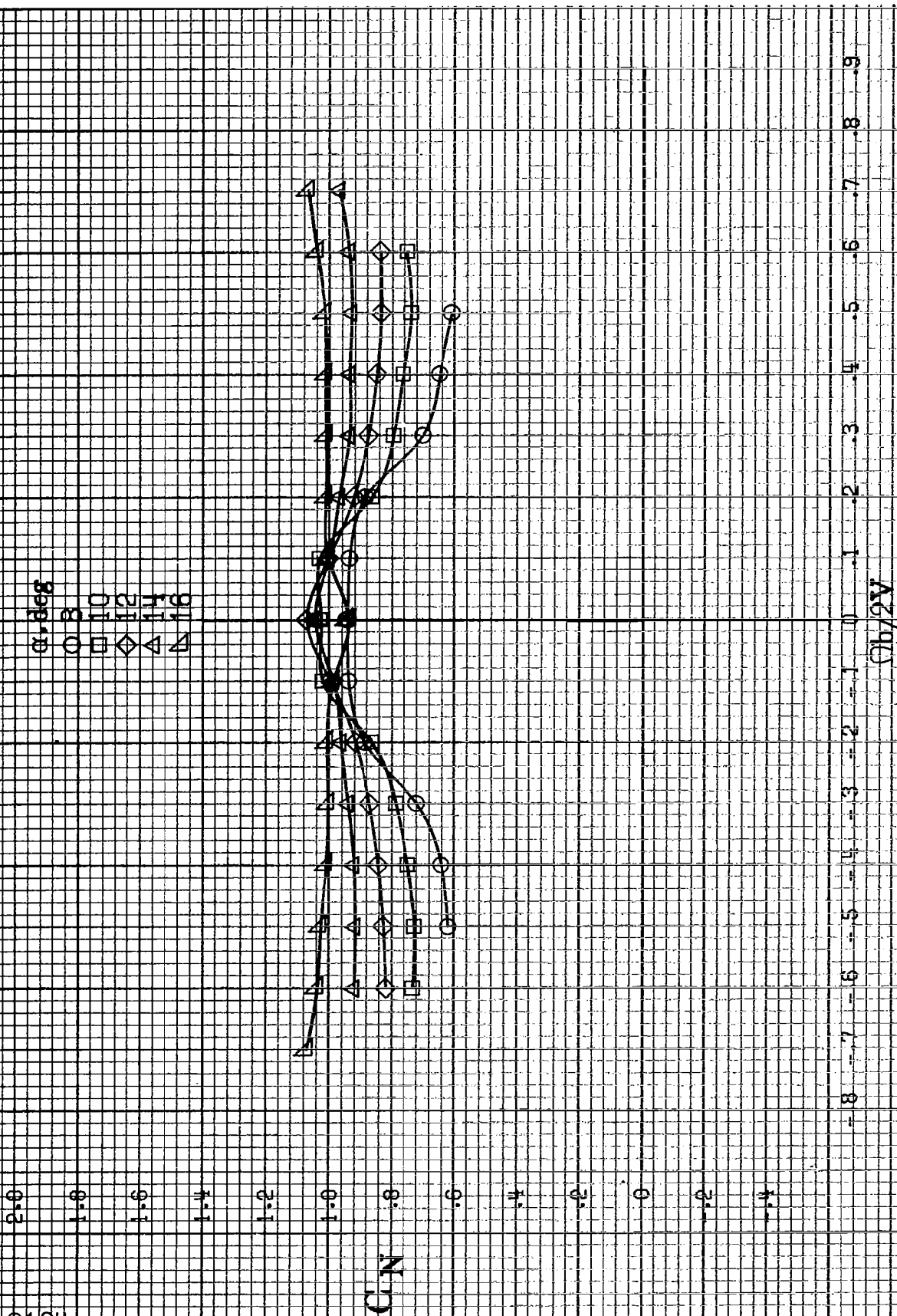
$\partial h/2V$

(c) $\alpha=30$ to 50 deg, $SR=0$.
 Figure A38.-Continued.



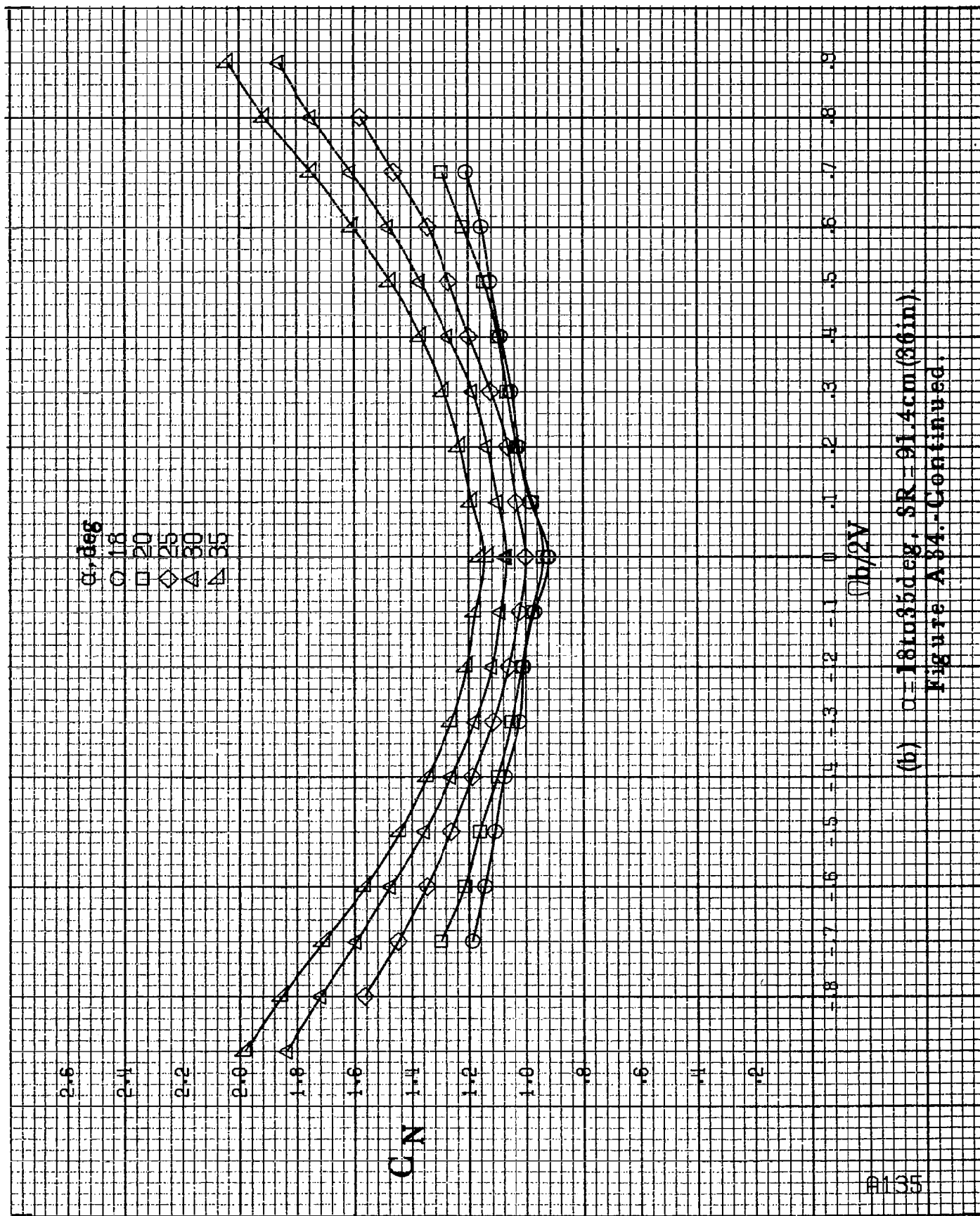


(a) $\alpha = 55$ to 90° , $SR = 0$.
Figure A33.-Concluded.



(a) $\alpha = 8$ to 16 deg, $SR = 91.4$ cm (36 in).

Figure A34.-Effect of rotation rate and angle of attack on normal-force coefficient for short body, high wing, horizontal tail no. 3 configuration. $\delta_a = 0^\circ$, $\delta_r = 0^\circ$, $\delta = 0^\circ$.



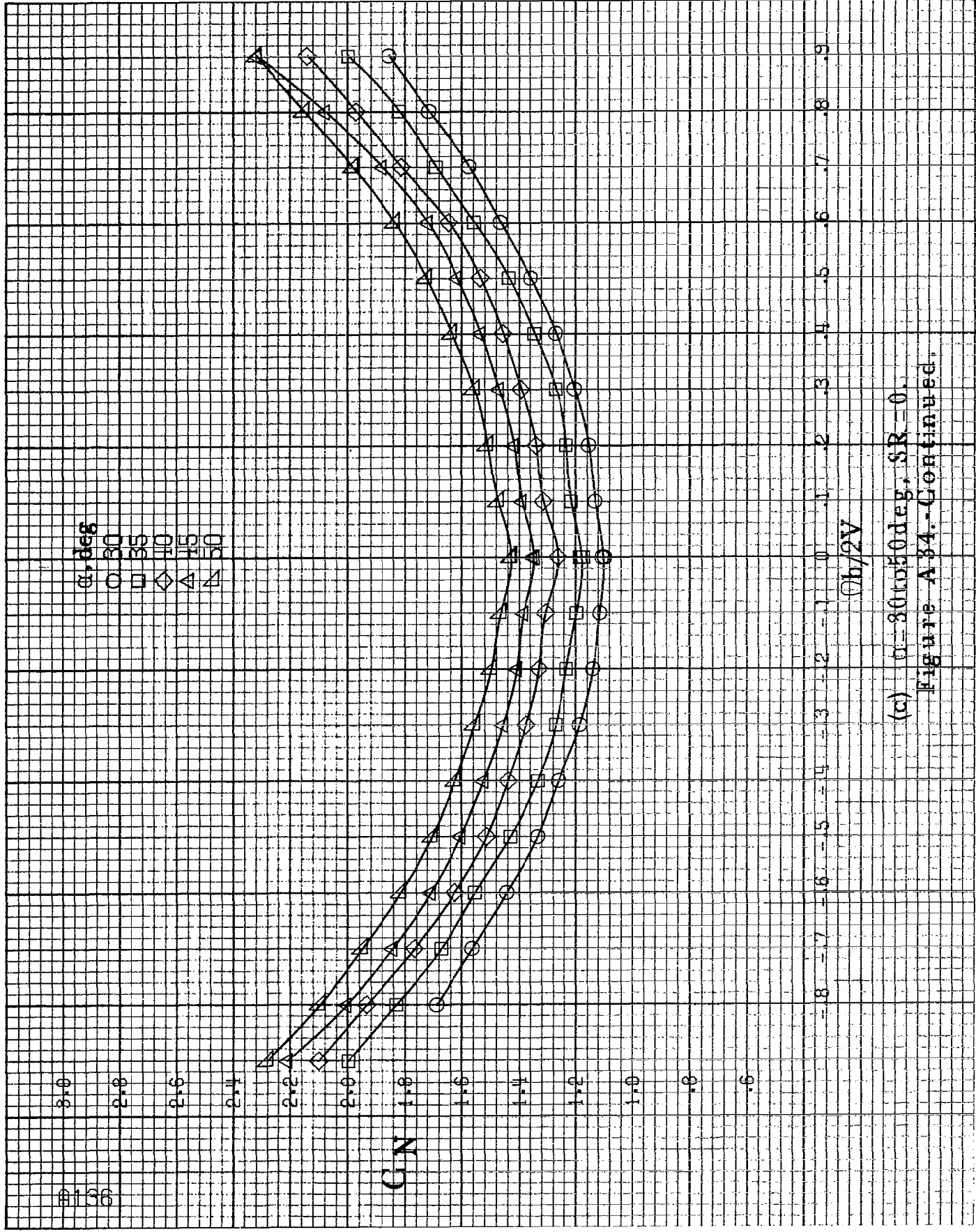
(b) $\alpha = 18$ to 35° deg, $SR = 91.4 \text{ cm (36 in.)}$.
Figure A34.-Continued.

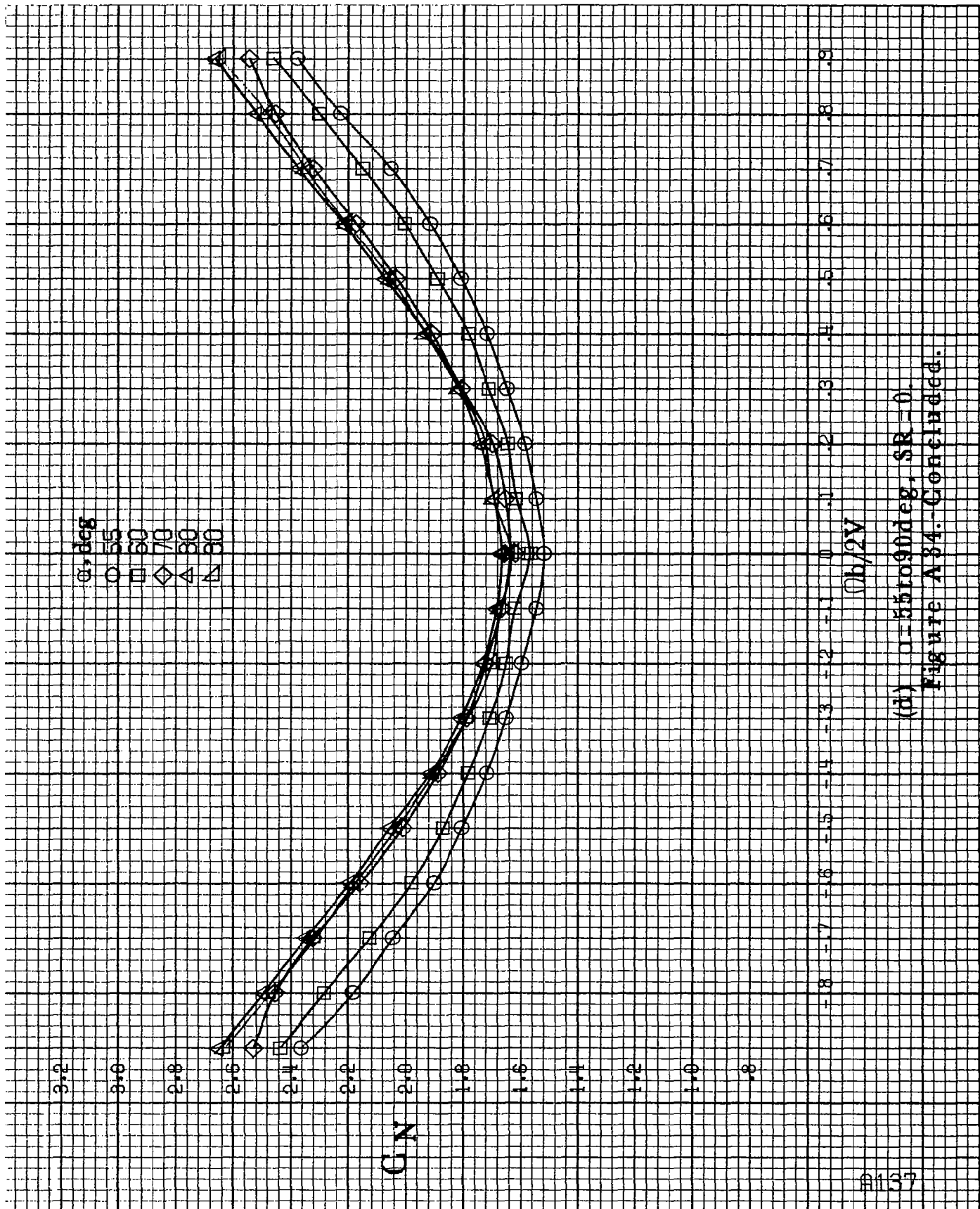
α , deg
 O 30
 □ 35
 ◇ 40
 △ 45
 ▽ 50

C/N

$\phi h/2V$

(c) $\alpha = 30$ to 50 deg, $SR = 0$.
 Figure A34.-Continued.





(d) $\alpha = 55$ to 90 deg, $SR = 0$.
Figure A34. Concluded.

#138

α, deg

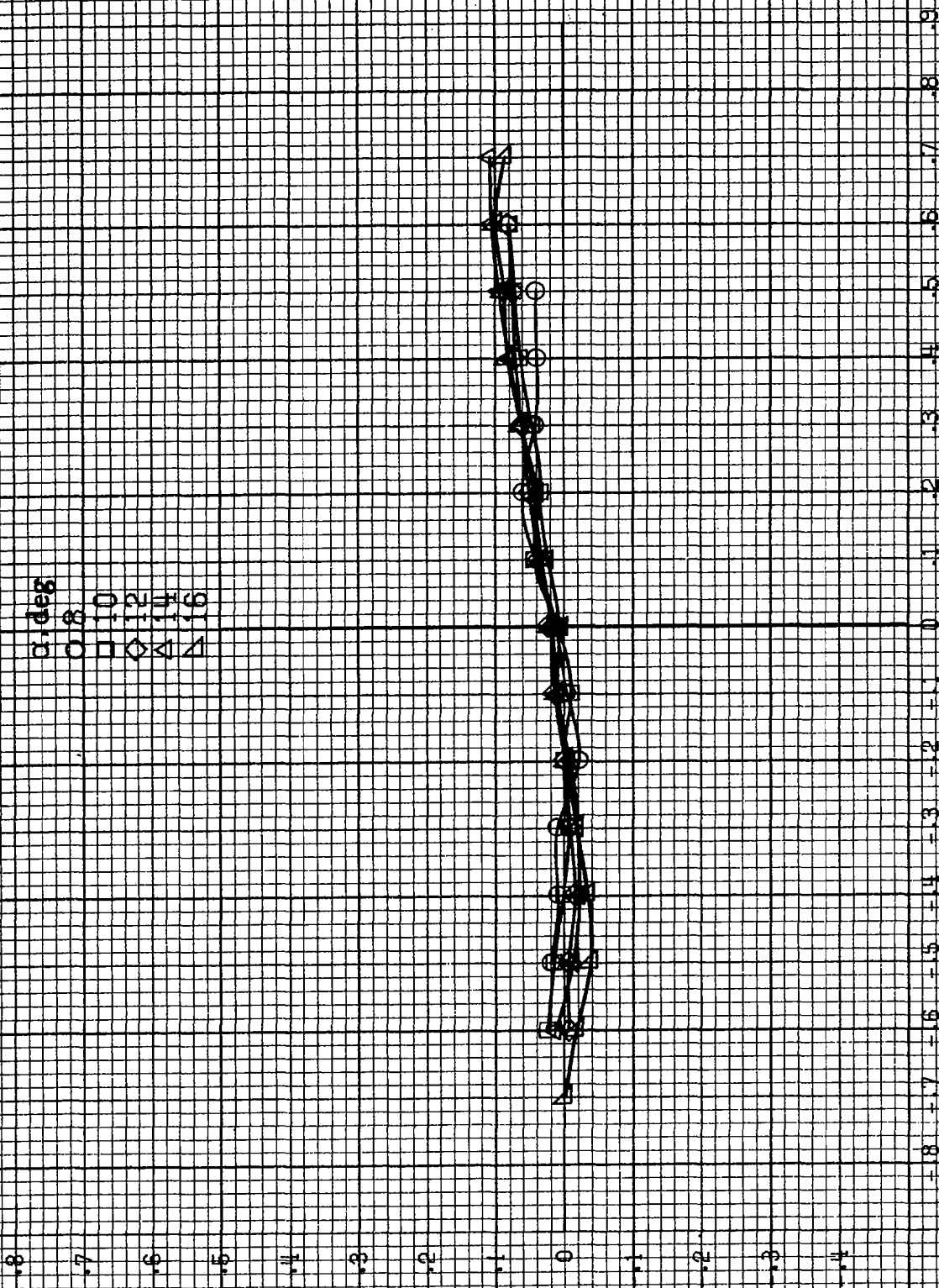
○ 8
□ 10
◇ 12
△ 14
▽ 16

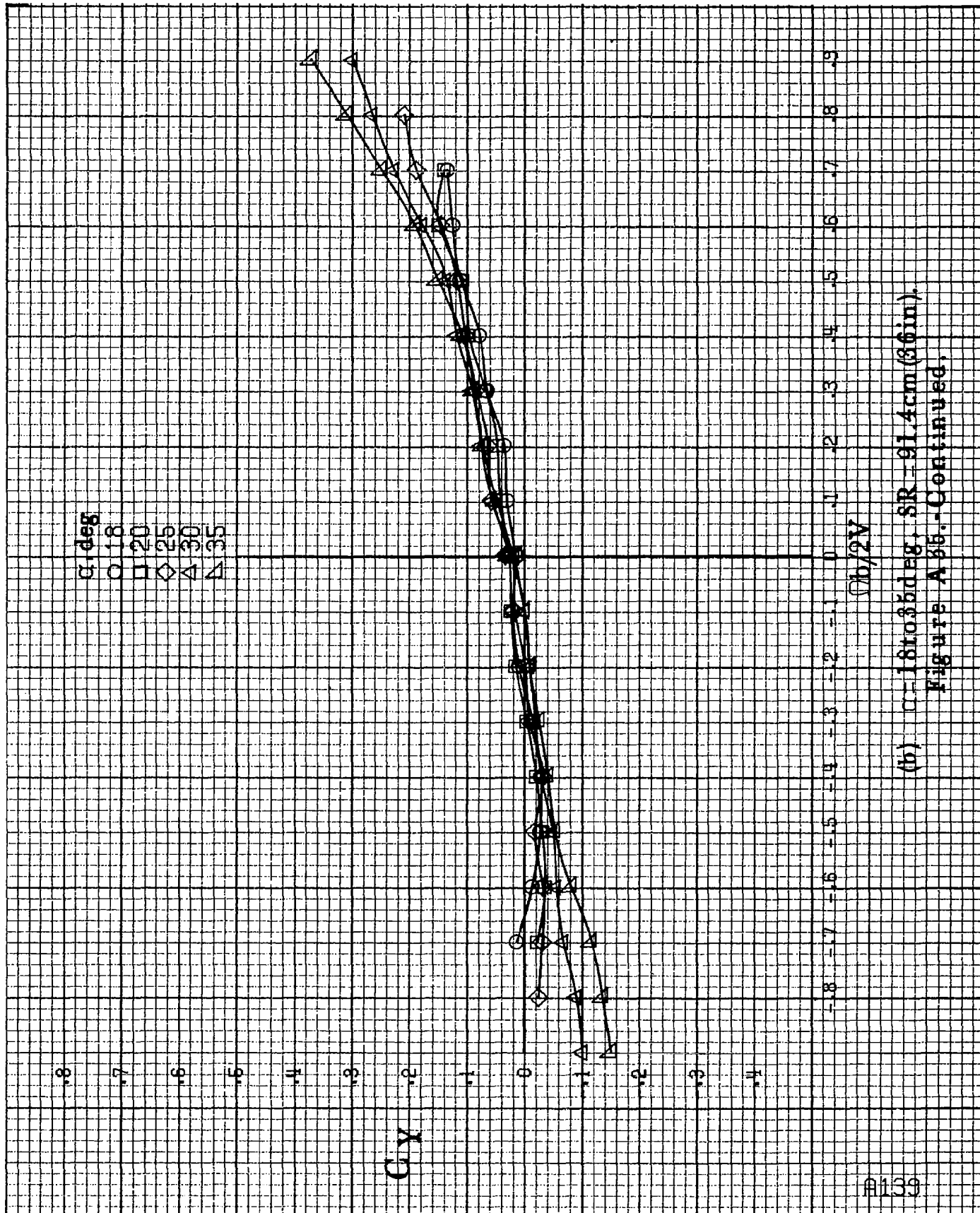
C_Y

$b/2V$

(a) $\alpha = 8 \text{ to } 16 \text{ deg}$, $SR = 911.4 \text{ cm (36 in)}$.

Figure A35 - Effect of rotation rate and angle of attack on side-force coefficient for short body, high wing, horizontal tail no. 3 configuration. $\delta_e = 0^\circ$, $\delta_a = 0^\circ$, $\delta_r = 0^\circ$, $\beta = 0^\circ$.





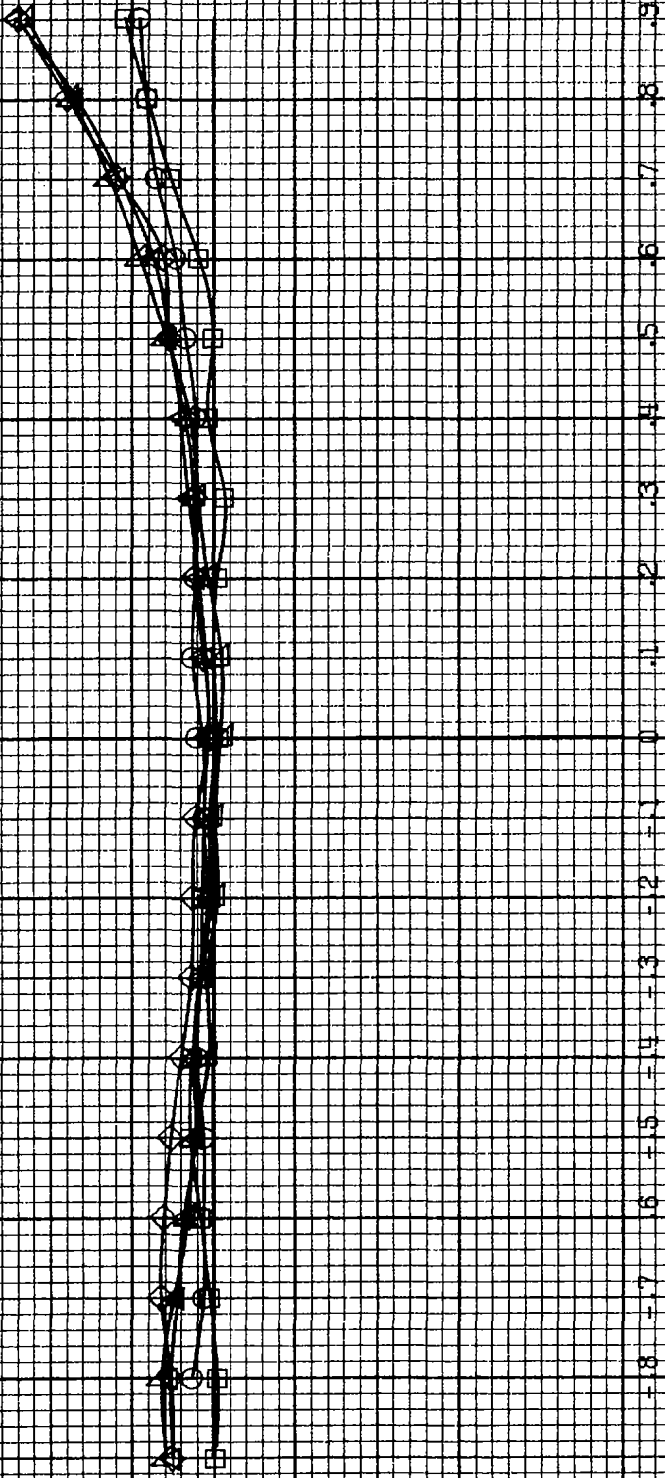
(b) $\alpha = 18$ to 35° , $SR = 91.4 \text{ cm (36 in.)}$.
Figure A 55.-Continued.

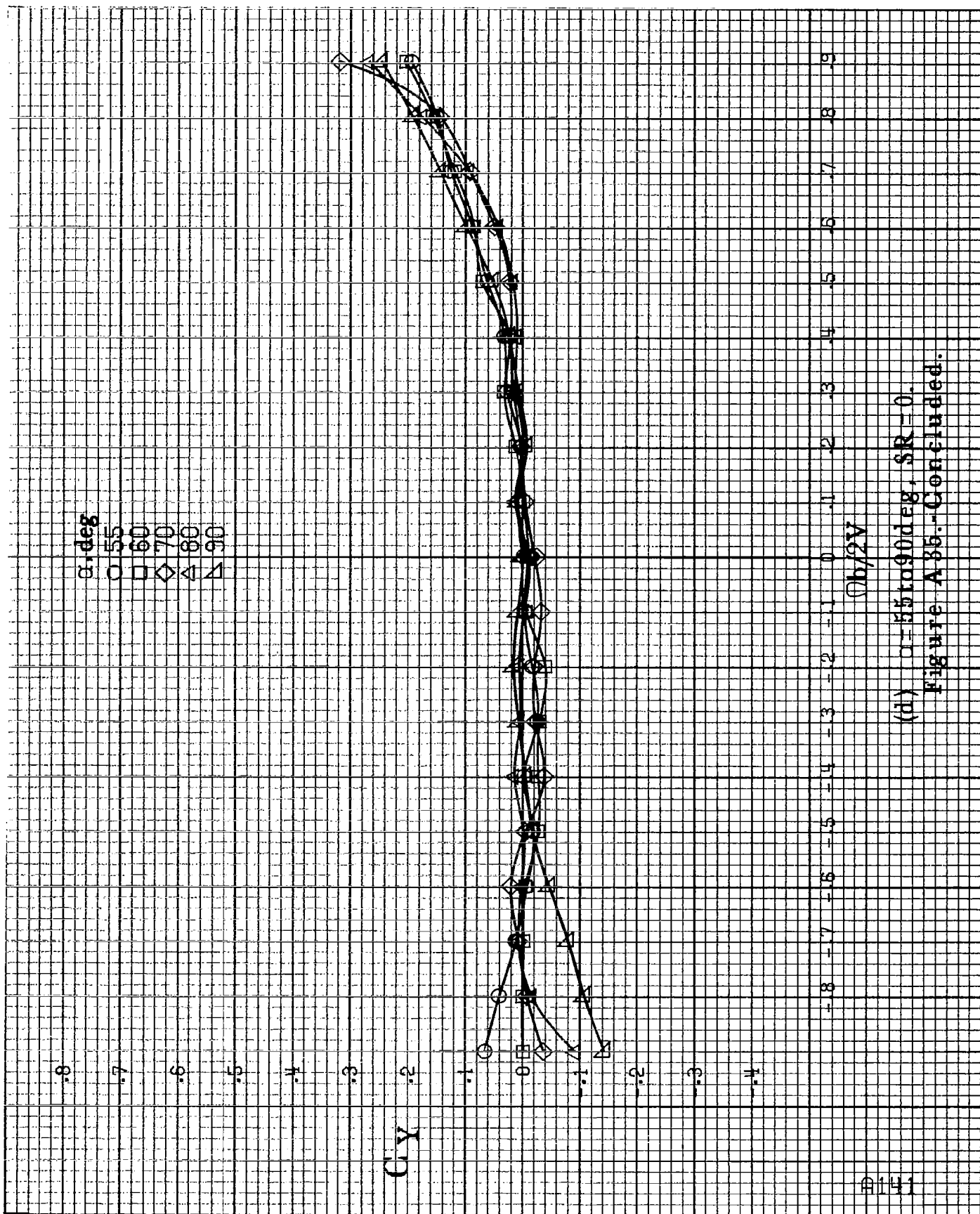
α, deg
 30
 35
 40
 45
 50

C_Y

$\phi b/2V$

(c) $\alpha=30$ to 50 deg, $SR=0$.
 Figure A35.-Continued.





(d) $\alpha=55$ to 90 deg, $SR=0$.

Figure A 85.-Concluded.

B142

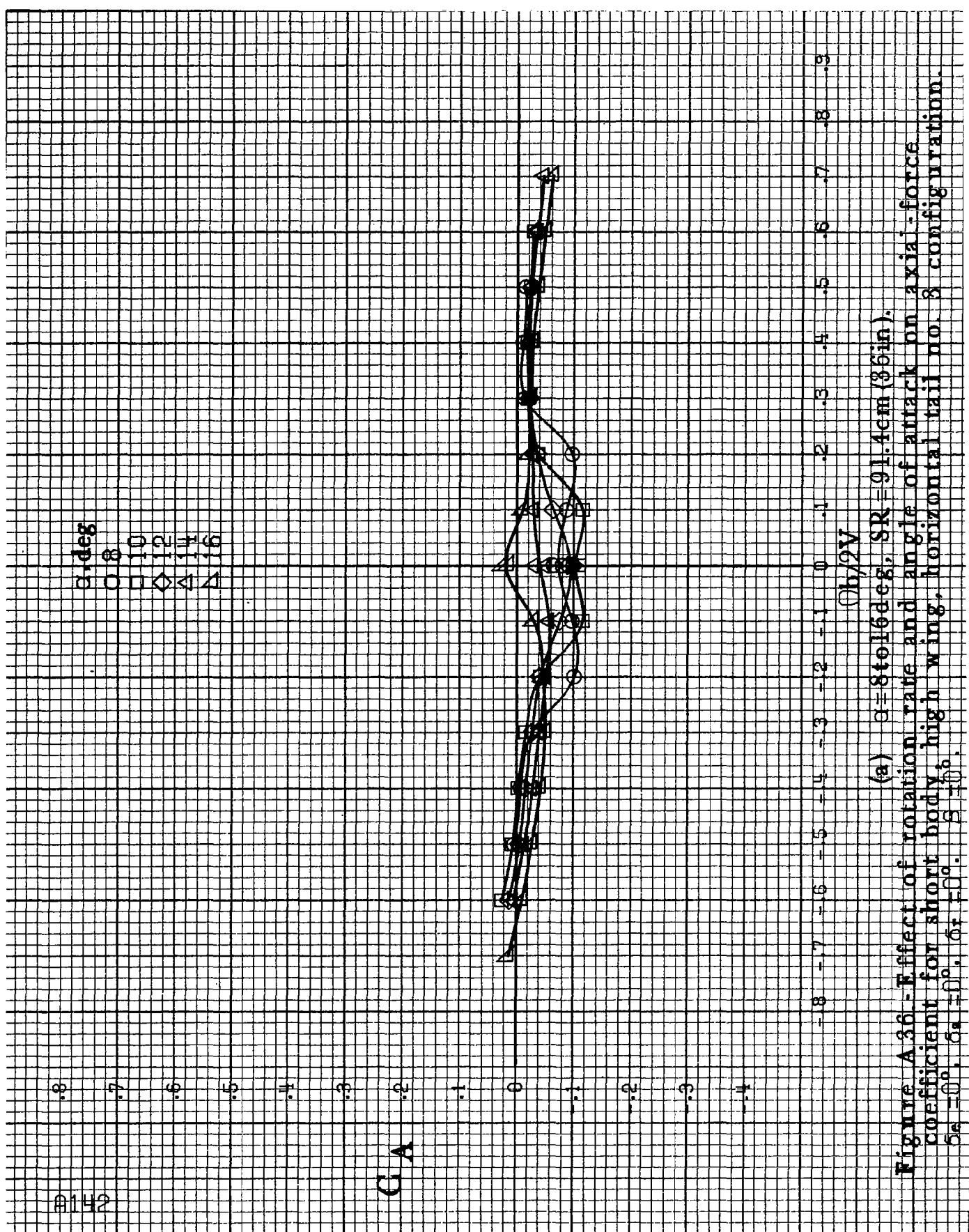
α, deg
 8
 10
 12
 14
 16

C_A

$C_{b/2V}$

(a) $\alpha = 8 \text{ to } 16 \text{ deg}$, $SR = 91.4 \text{ cm (36 in.)}$.

Figure A36.-Effect of rotation rate and angle of attack on axial-force coefficient for short body, high wing, horizontal tail no. 3 configuration. $\delta_a = 0^\circ$, $\delta_s = 0^\circ$, $\delta_r = 0^\circ$, $\beta = 0^\circ$.



CA

α, deg
 ○ 18
 □ 20
 ◇ 25
 △ 30
 ▽ 35

-.8
-.7
-.6
-.5
-.4
-.3
-.2
-.1
0
.1
.2
.3
.4
.5
.6
.7
.8
.9

$\phi b/2V$

(b) $\alpha = 18$ to 35 deg, $SR = 91.4$ cm (36 in).

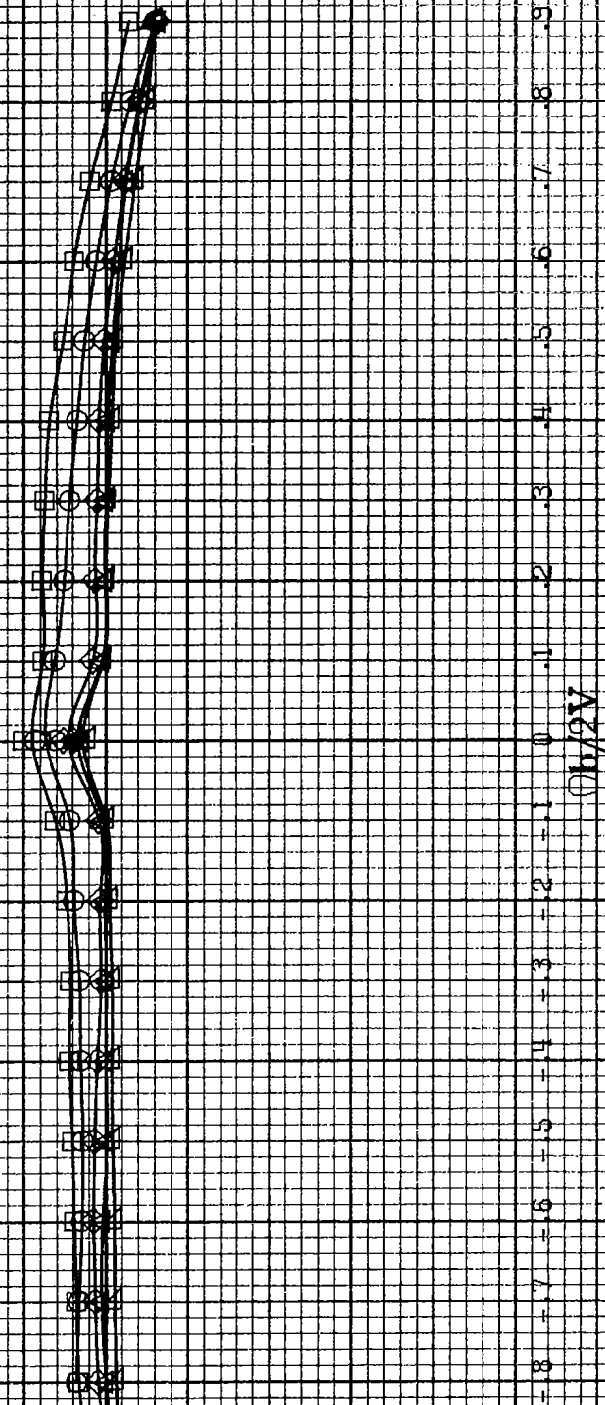
Figure A 36.-Continued.

A143

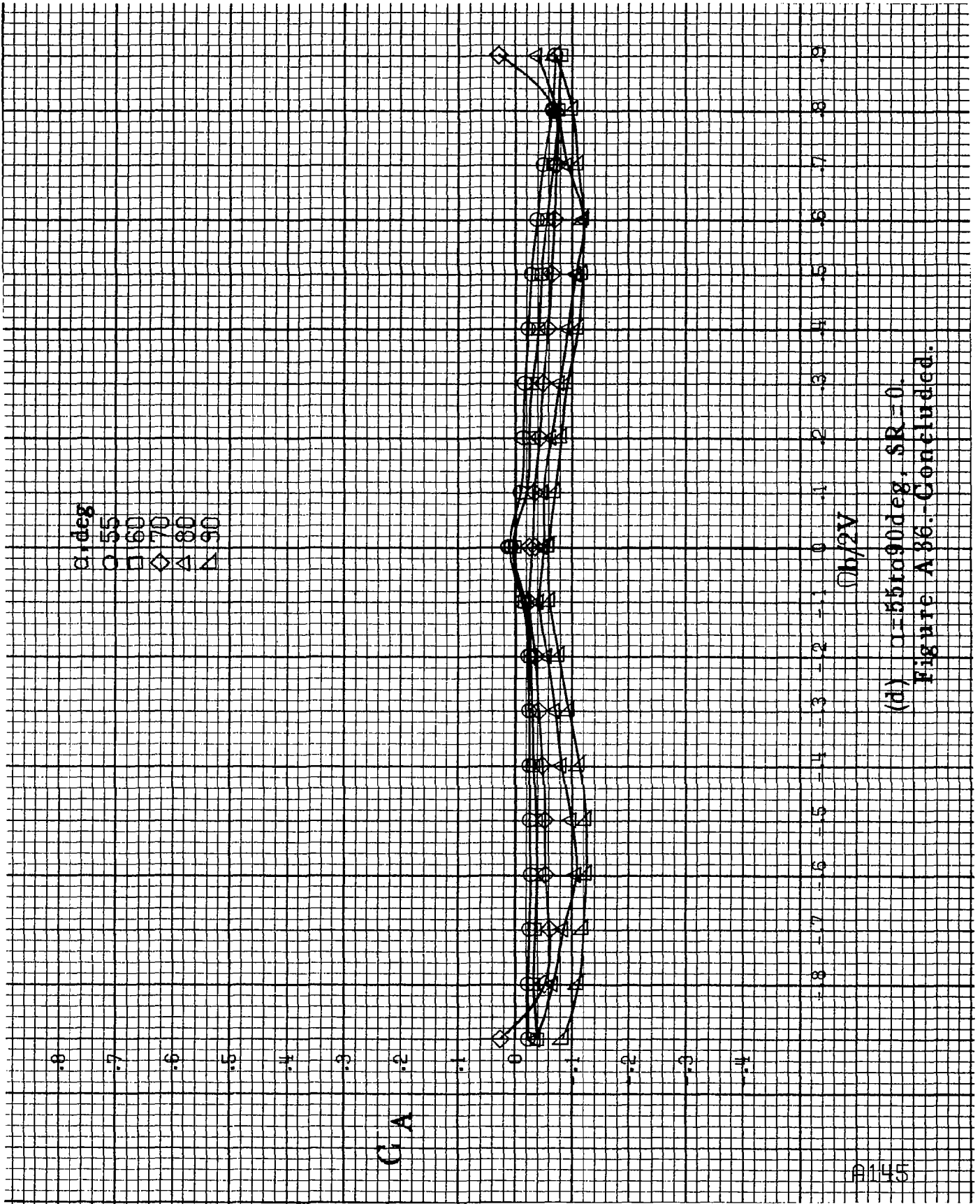
1144

α, deg
 \circ 30
 \square 35
 \diamond 40
 \triangle 45
 ∇ 50

CA



(a) $\alpha=30$ to 50° , $SR=0$.
 Figure A86.-Continued.



(d) $\alpha = 55$ to 90° deg, $SR = 0$.
Figure A 86. Concluded.

α, deg

○ 8

□ 10

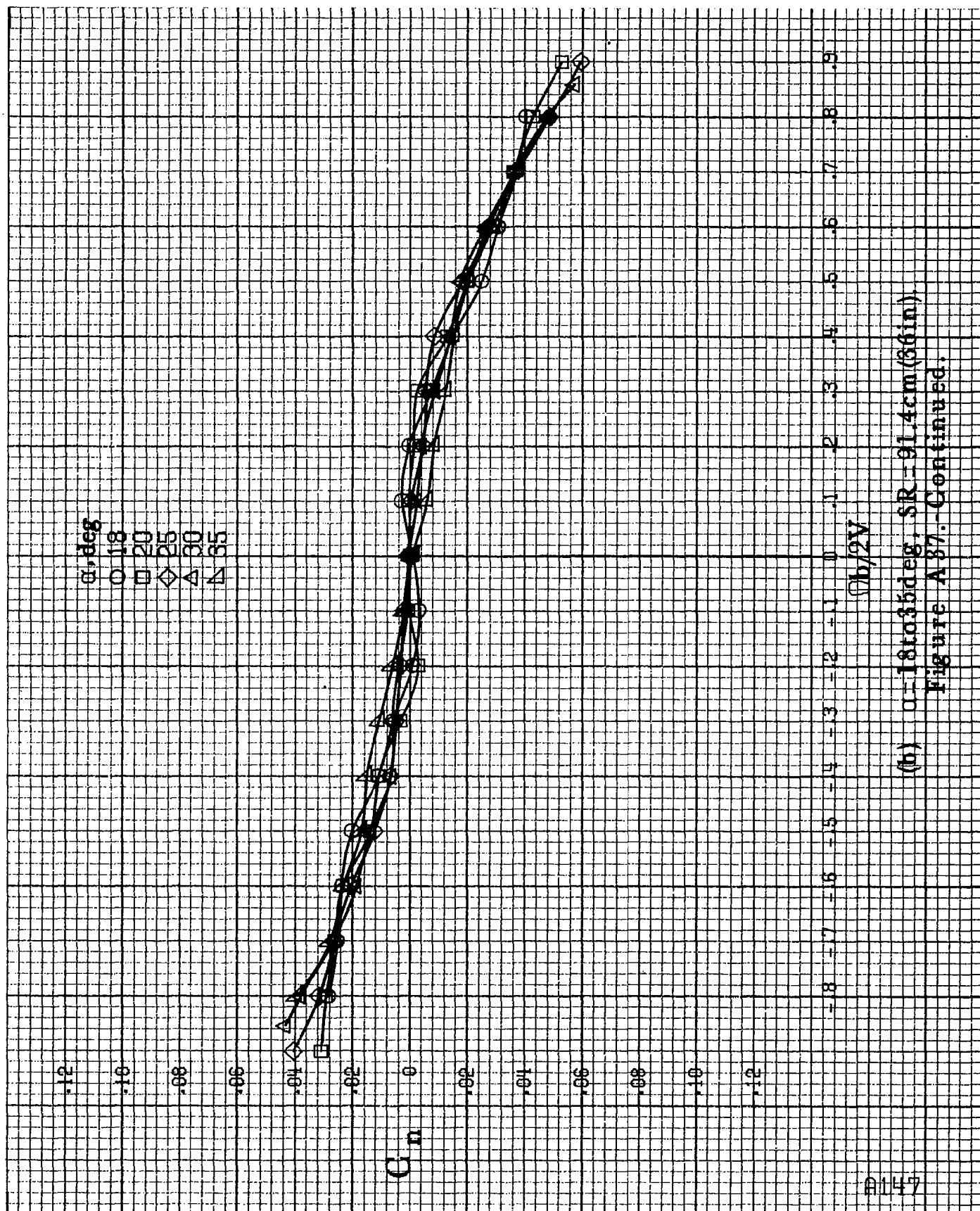
◇ 12

△ 14

▽ 16

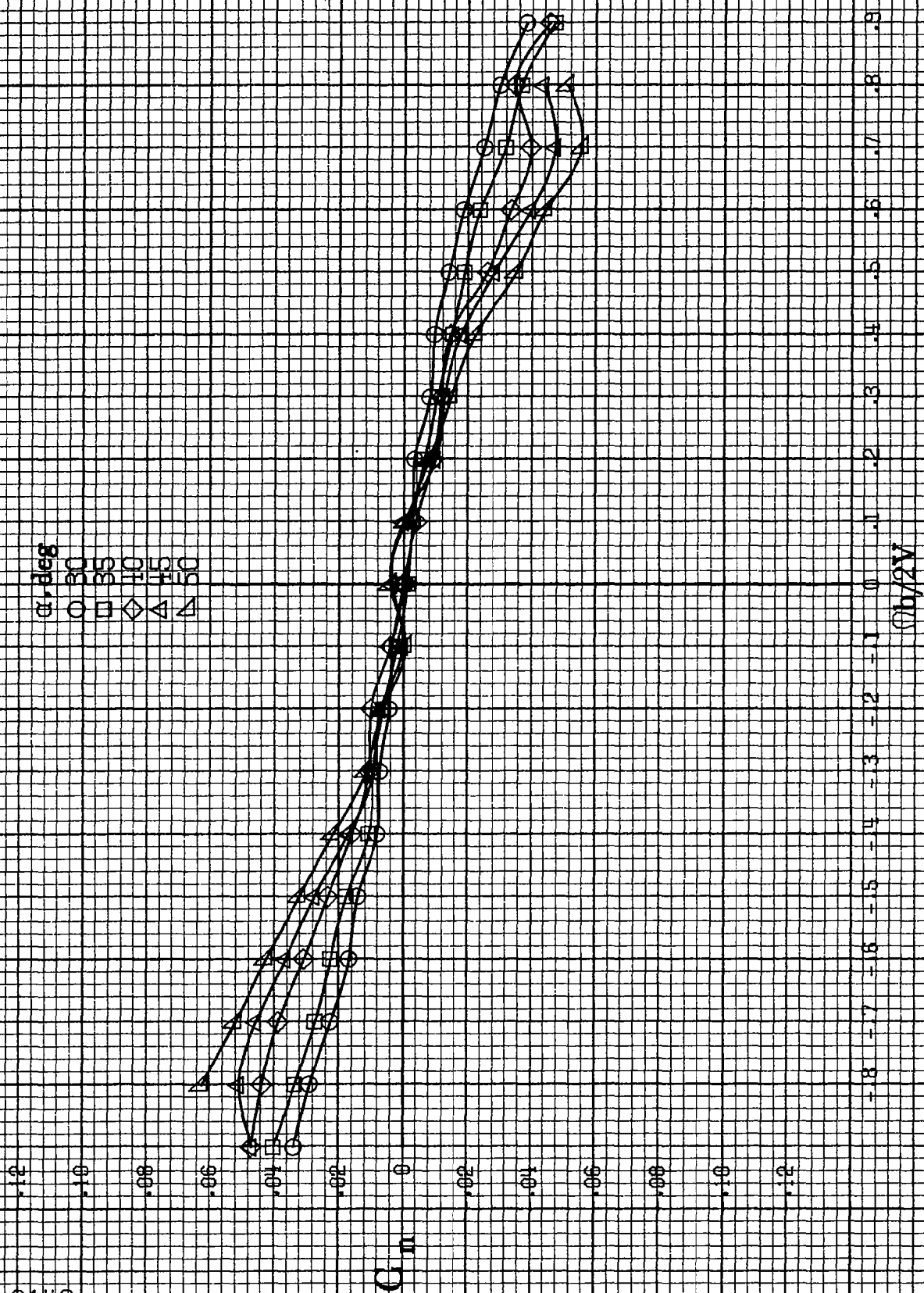
 C_m $b/2V$ (a) $\alpha = 8 \text{ to } 16 \text{ deg}$, $SR = 91.4 \text{ cm (36 in)}$.

Figure A37.-Effect of rotation rate and angle of attack on yawing-moment coefficient for long body, low wing, horizontal T-tail configuration.
 $\delta_e = 0^\circ$, $\delta_a = 0^\circ$, $\delta_r = 0^\circ$.

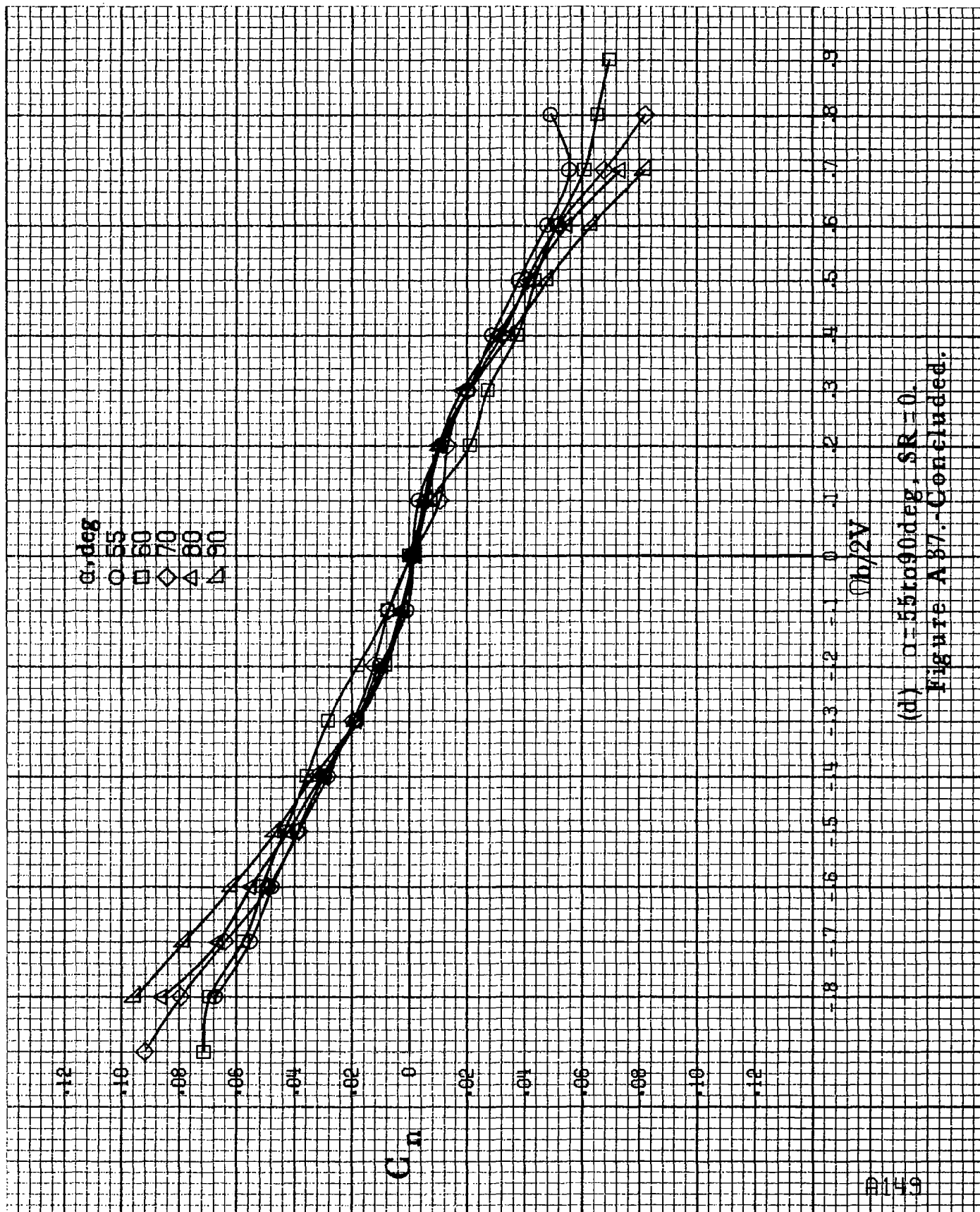


(b) $\alpha = 18$ to 35° , $SR = 91.4 \text{ cm (36 in.)}$

Figure A87.-Continued.

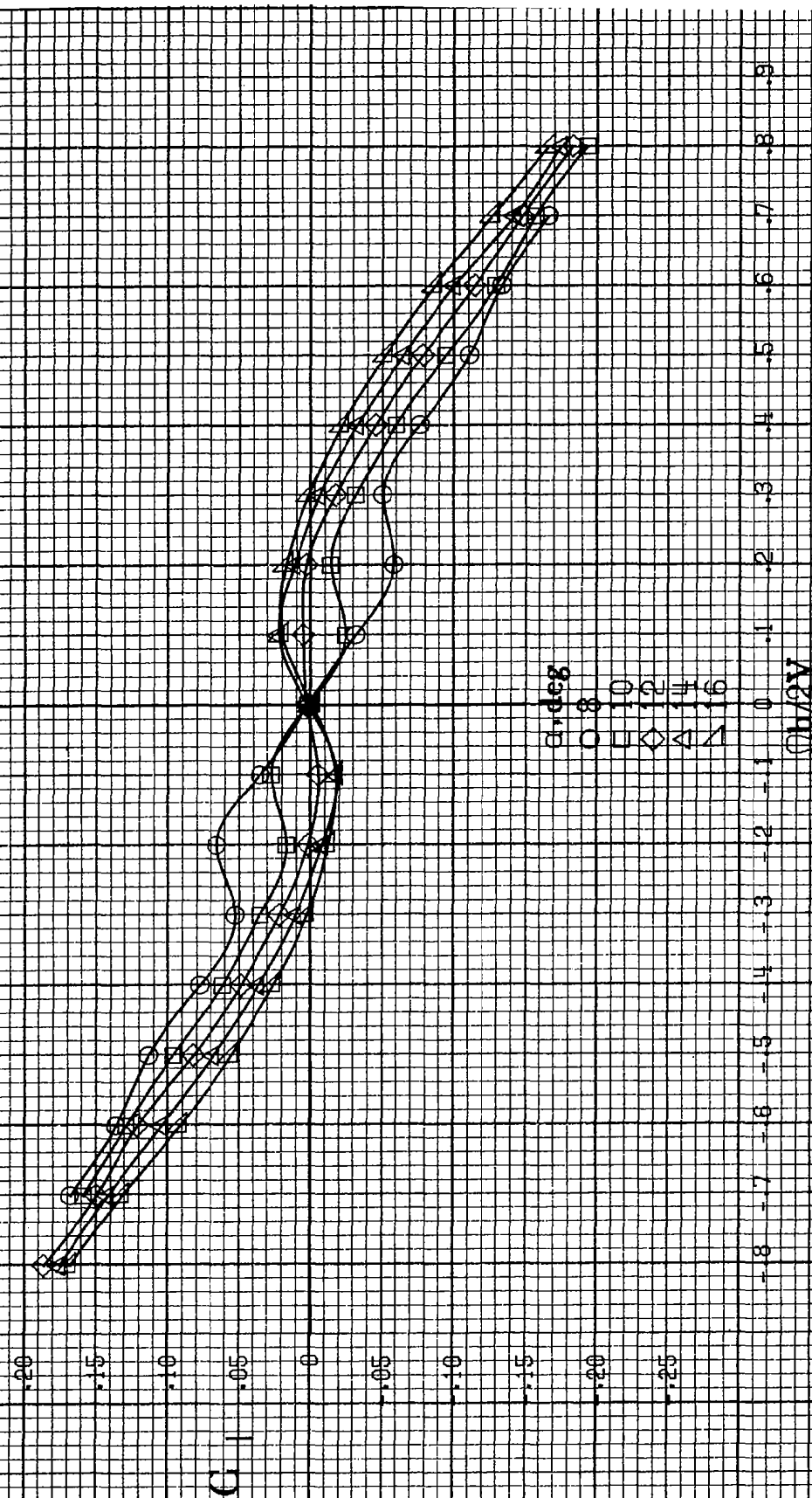


(c) $\omega = 30$ to 50 deg, $SR = 0$.
Figure A 37.-Continued.



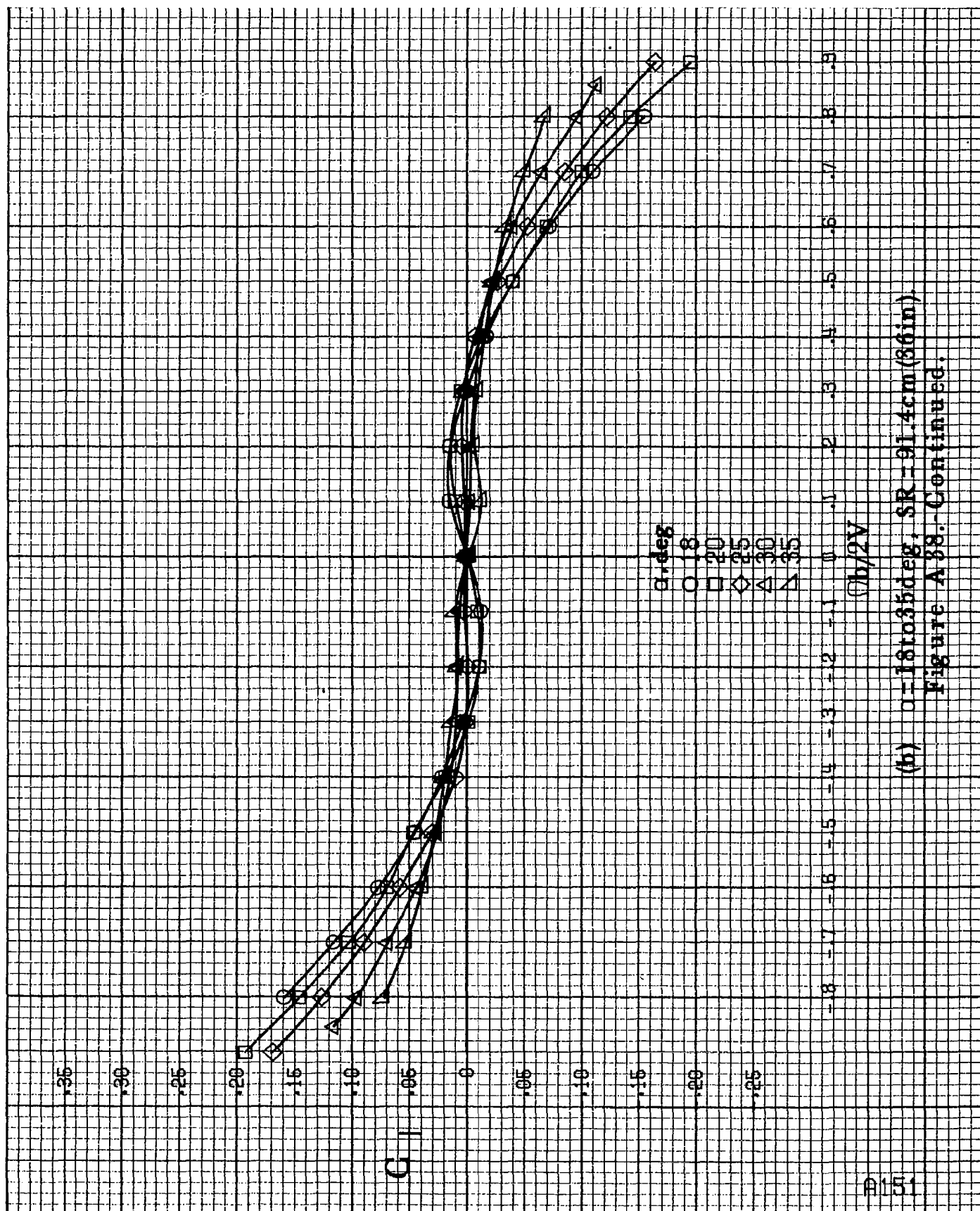
(d) $\alpha=55$ to 90° , $SR=0$.
Figure A87.-Concluded.

A150



(a) $\alpha = 8$ to 16° , $SR = 91.4 \text{ cm (36 in.)}$.

Figure A 38.-Effect of rotation rate and angle of attack on rolling-moment coefficient for long body, low wing, horizontal T-tail a configuration. $\delta_a = 0^\circ$, $\delta_s = 0^\circ$, $\delta_r = 0^\circ$.



(b) $\alpha=18$ to 35° , $SR=91.4\text{ cm (36 in.)}$.
Figure A38-Continued.

C

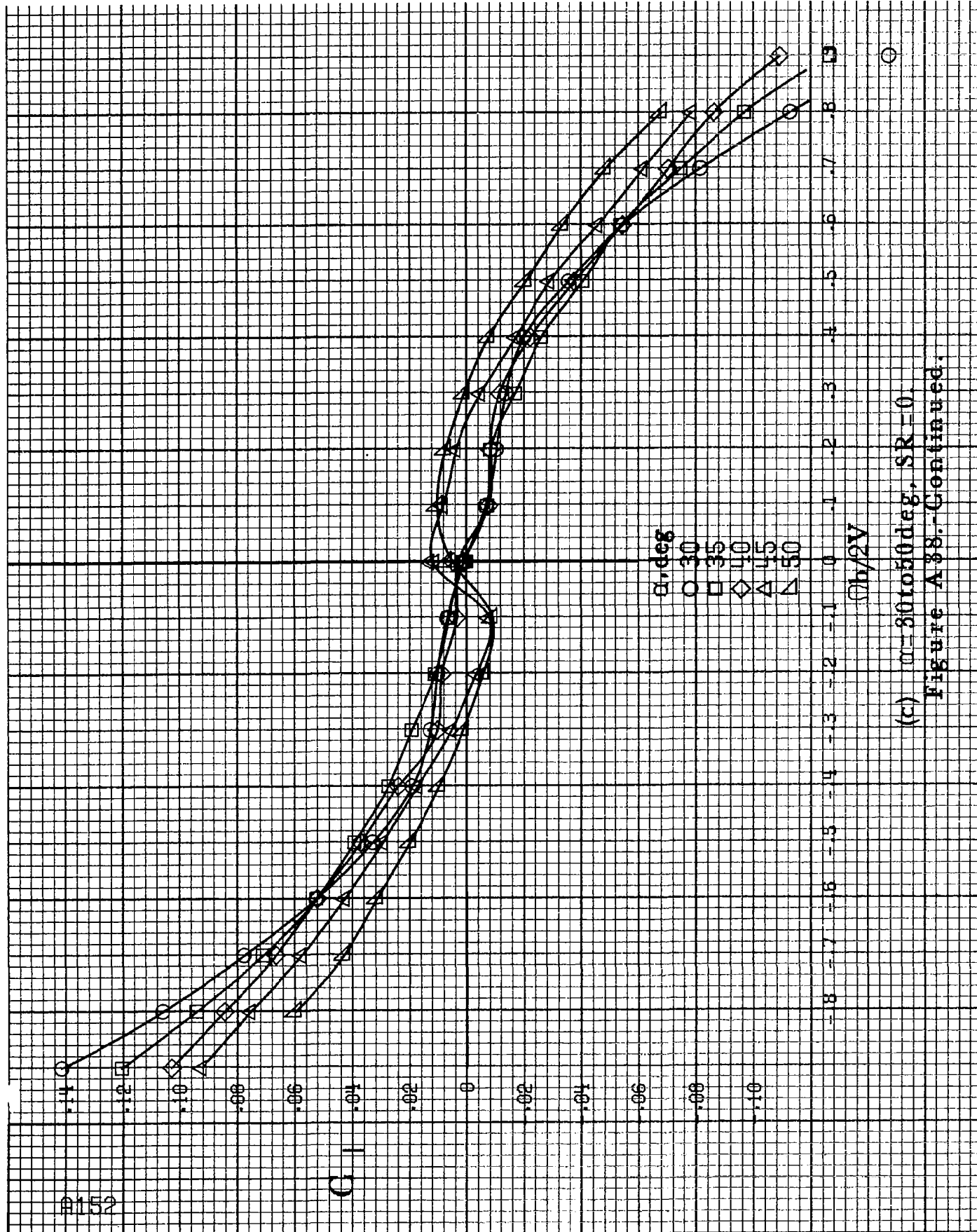
α, deg

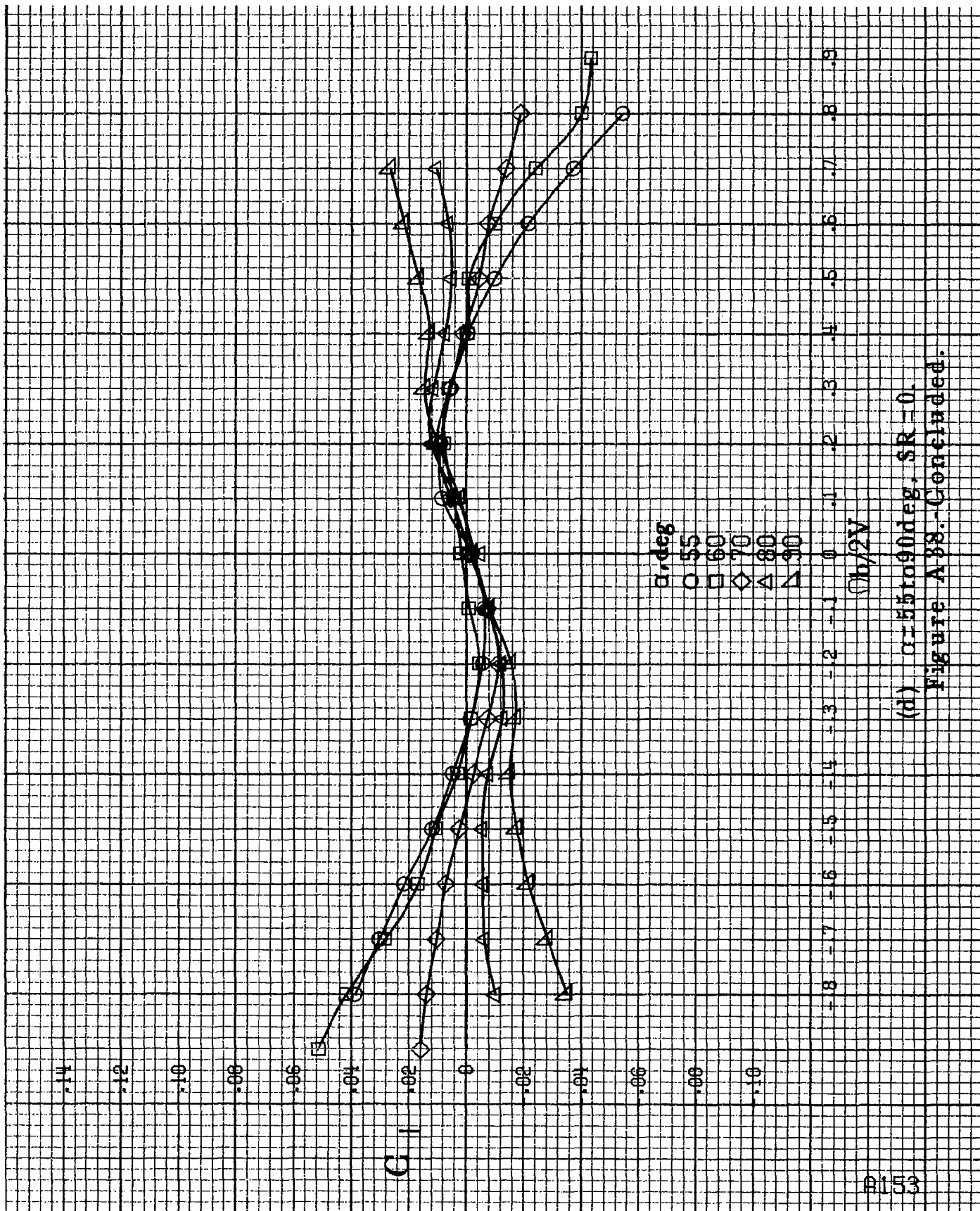
- \circ 30
- \square 35
- \diamond 40
- \triangle 45
- ∇ 50

$\phi_b/2V$

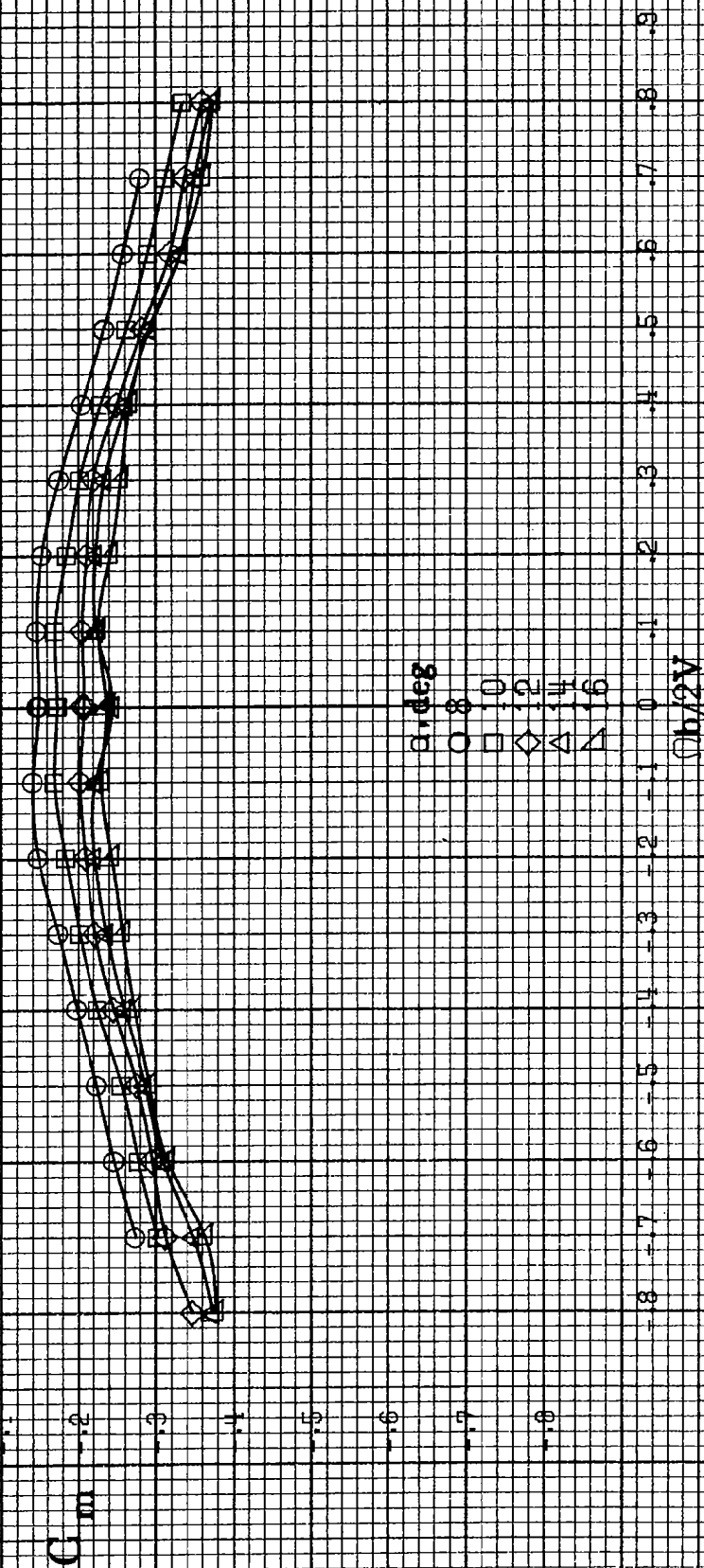
(c) $\alpha=30$ to 50 deg, $SR=0$.

Figure A38.-Continued.



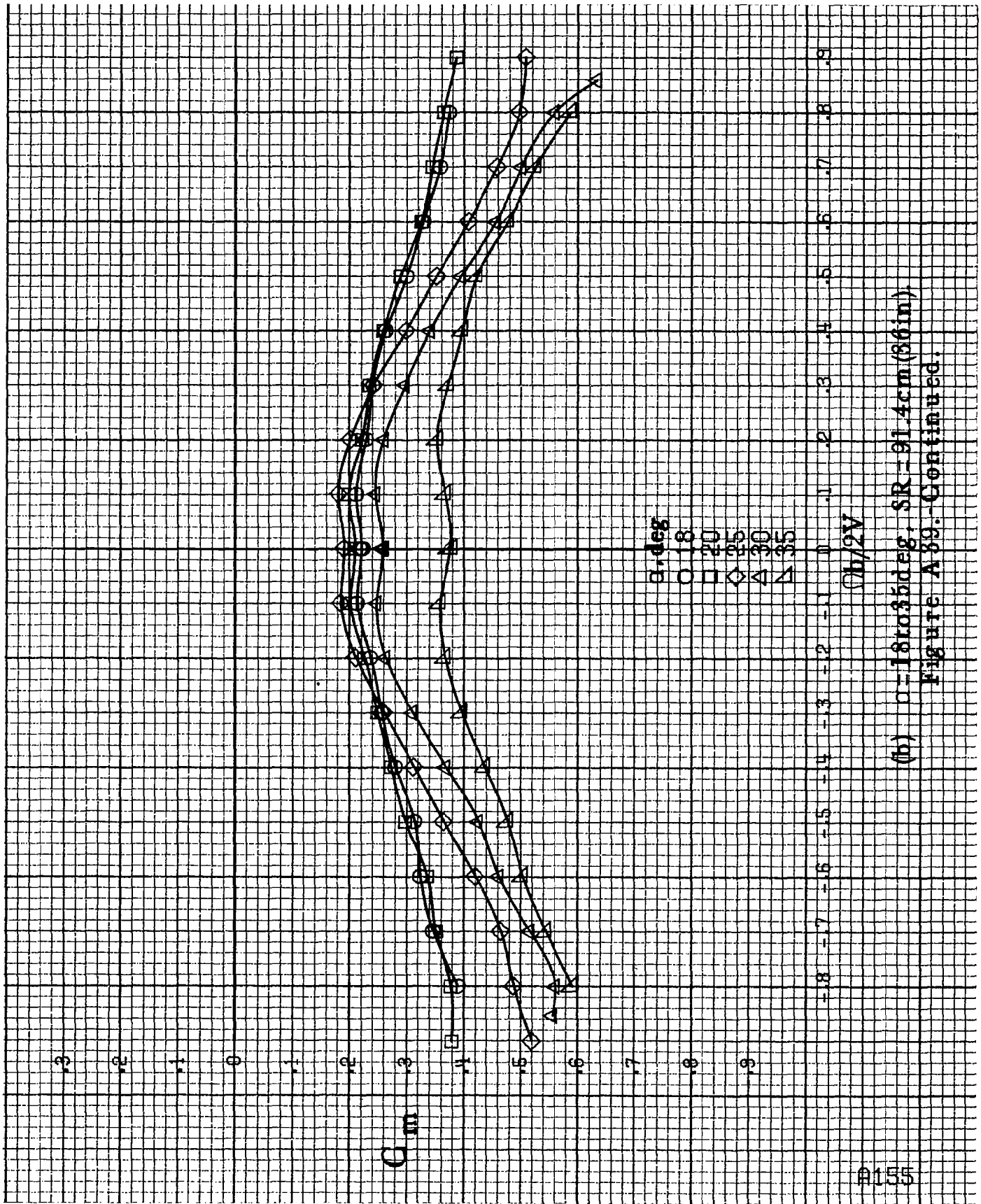


(d) $\alpha=55$ to 90° , $SR=0$.
Figure A38.-Concluded.



(a) $\alpha = 8$ to 16° , $SR = 91.4 \text{ cm (36 in.)}$.

Figure A39.- Effect of rotation rate and angle of attack on pitching-moment coefficient for long body, low wing, horizontal T-tail a configuration. $\delta_e = 0^\circ$, $\delta_a = 0^\circ$, $\delta_r = 0^\circ$.



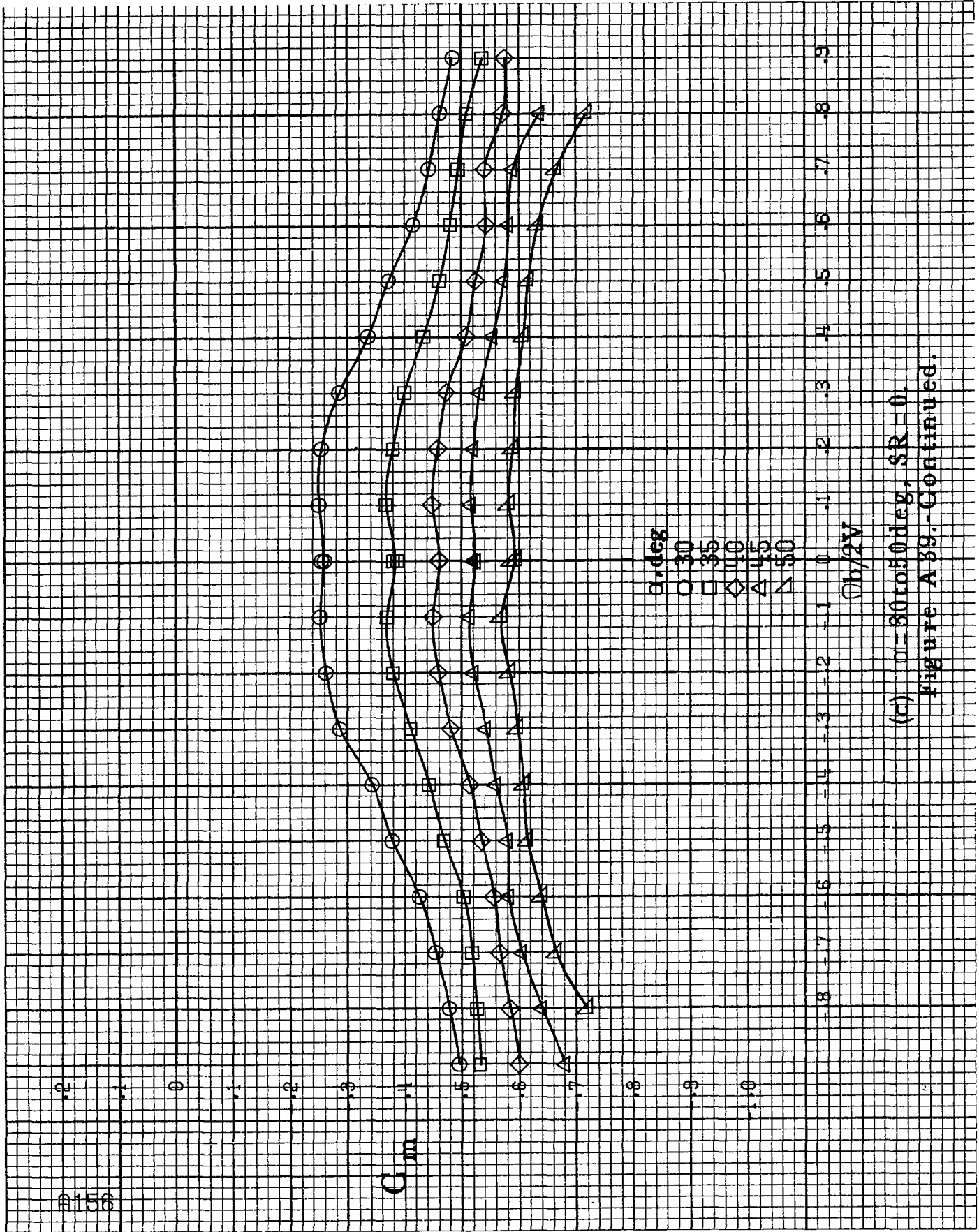
(b) $\alpha=18$ to 35° , $SR=91.4\text{cm}(36\text{in})$.
Figure A 39.-Continued.

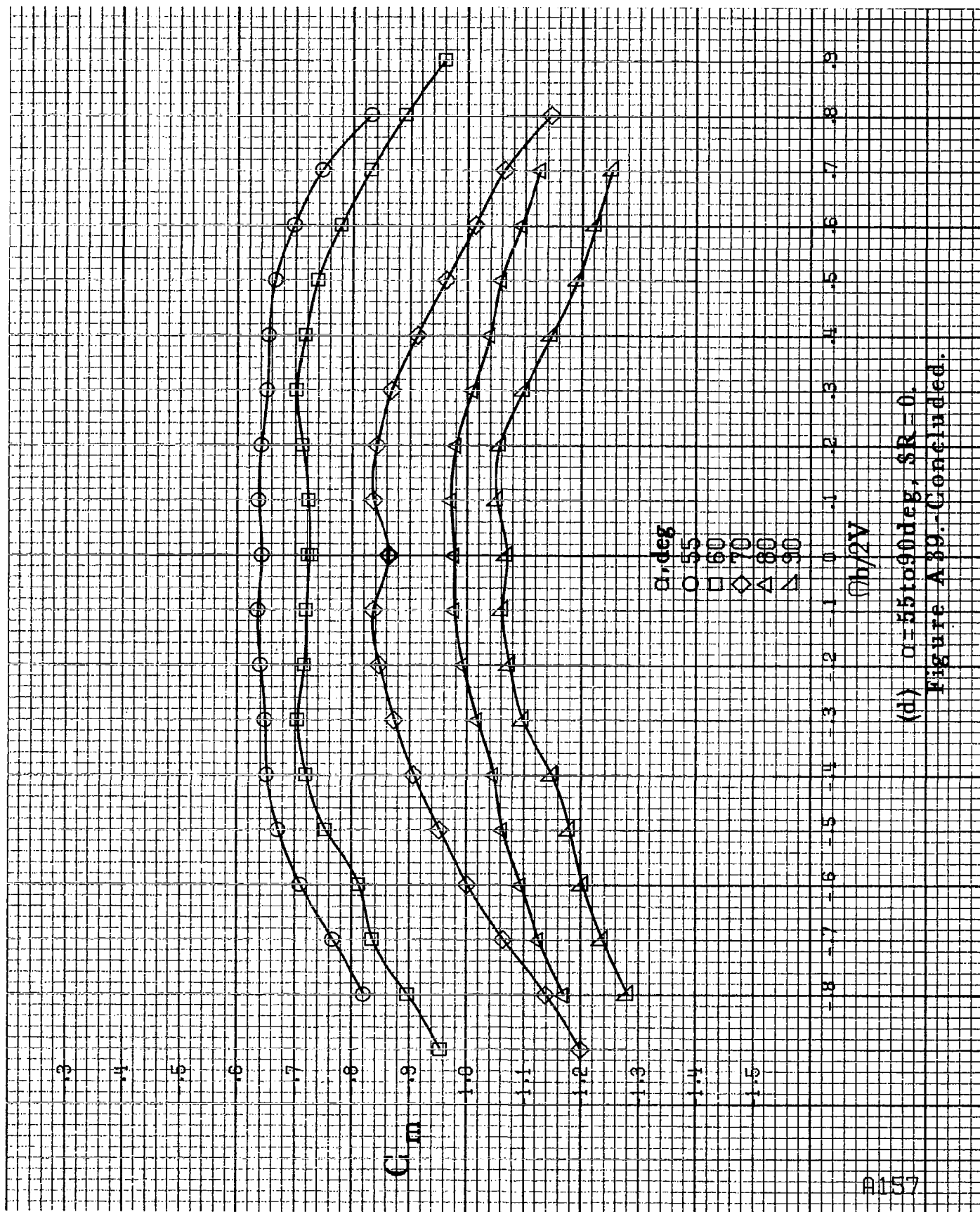
C_m

α, deg
 \circ 30
 \square 35
 \diamond 40
 \triangle 45
 ∇ 50

$\phi_b/2V$

(c) $\omega = 30 \text{ to } 50 \text{ deg}$, $SR = 0$.
 Figure A39.-Continued.





(d) $\alpha = 55$ to 90° , $SR = 0$.
Figure A39.-Concluded.

α, deg
 8
 10
 12
 14
 16

C_N

$\phi b/2V$

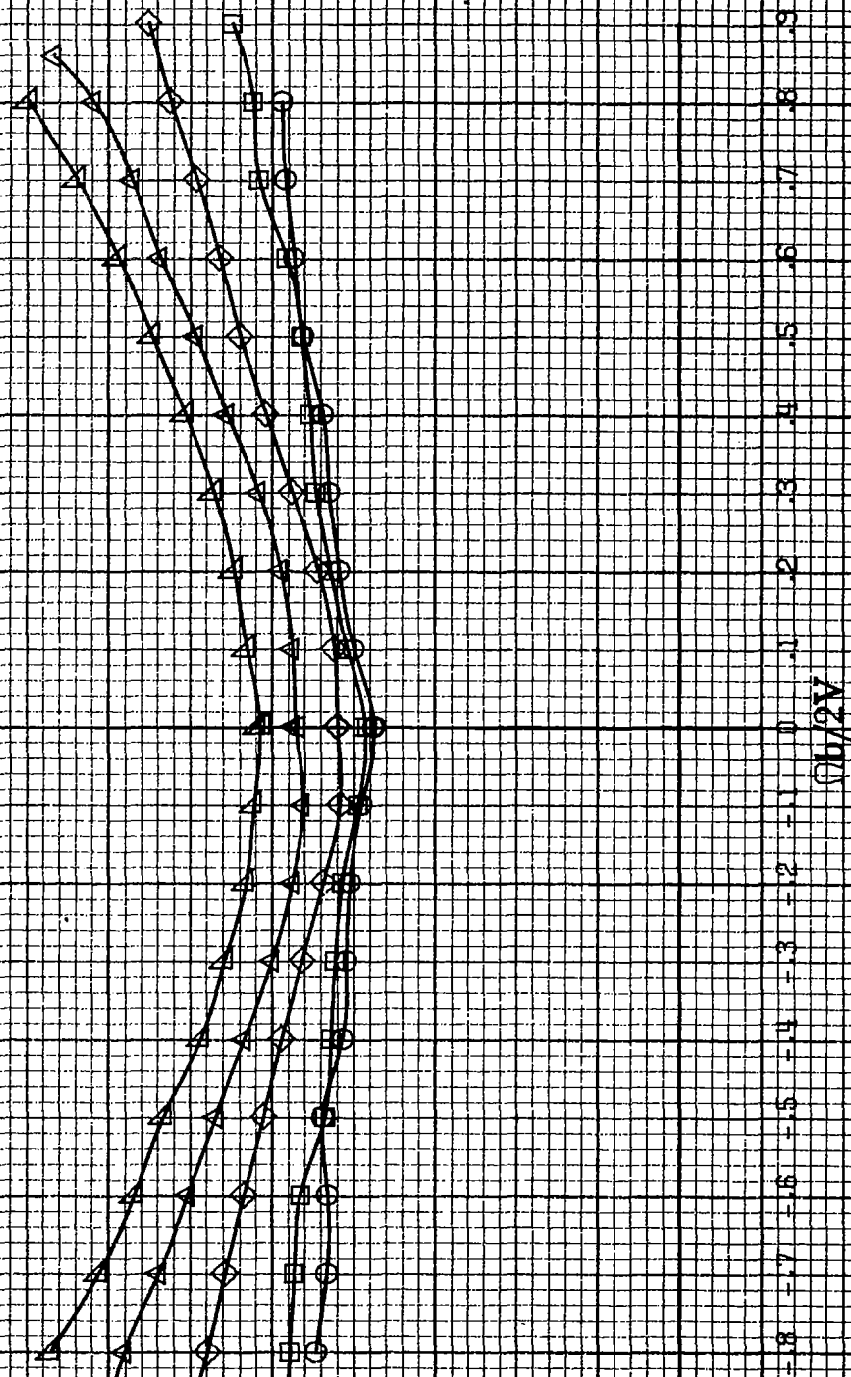
(a) $\alpha = 8 \text{ to } 16 \text{ deg}$, $SR = 91.4 \text{ cm (36 in.)}$.

Figure A 40.-Effect of rotation rate and angle of attack on normal-force coefficient for long body, low wing, horizontal T-tail a configuration. $\delta_e = 0^\circ$, $\delta_r = 0^\circ$, $\delta_a = 0^\circ$.

α , deg
 O 18
 □ 20
 ◇ 25
 ▲ 30
 ▽ 35

2.4
2.2
2.0
1.8
1.6
1.4
1.2
1.0
.8
.6
.4
.2
0

GN



(b/2V)

(b) $\alpha=18$ to 35 deg, SR = 91.4 cm (36 in)
 Figure A10.-Continued.

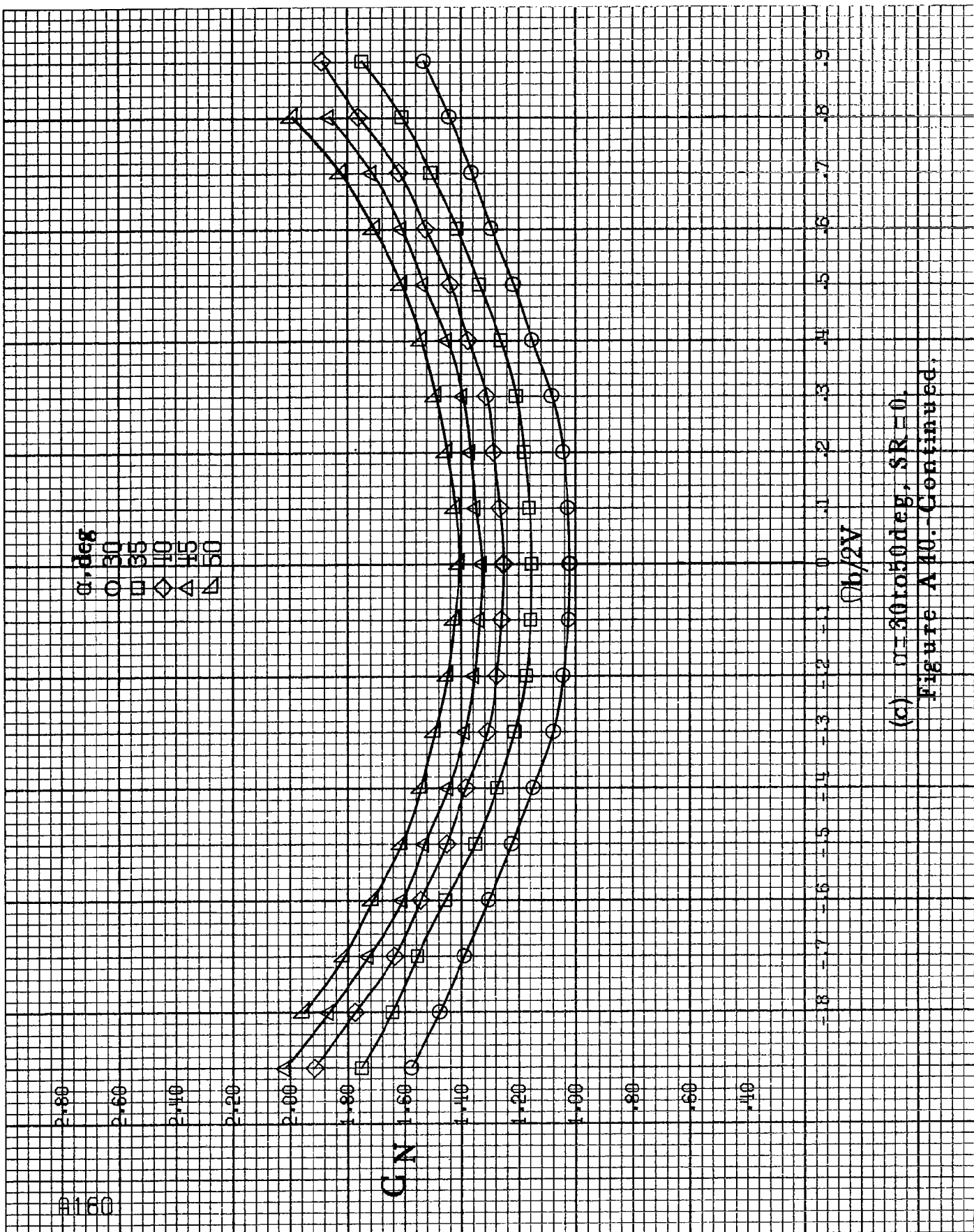
α, deg
 ○ 30
 □ 35
 ◇ 40
 △ 45
 ▽ 50

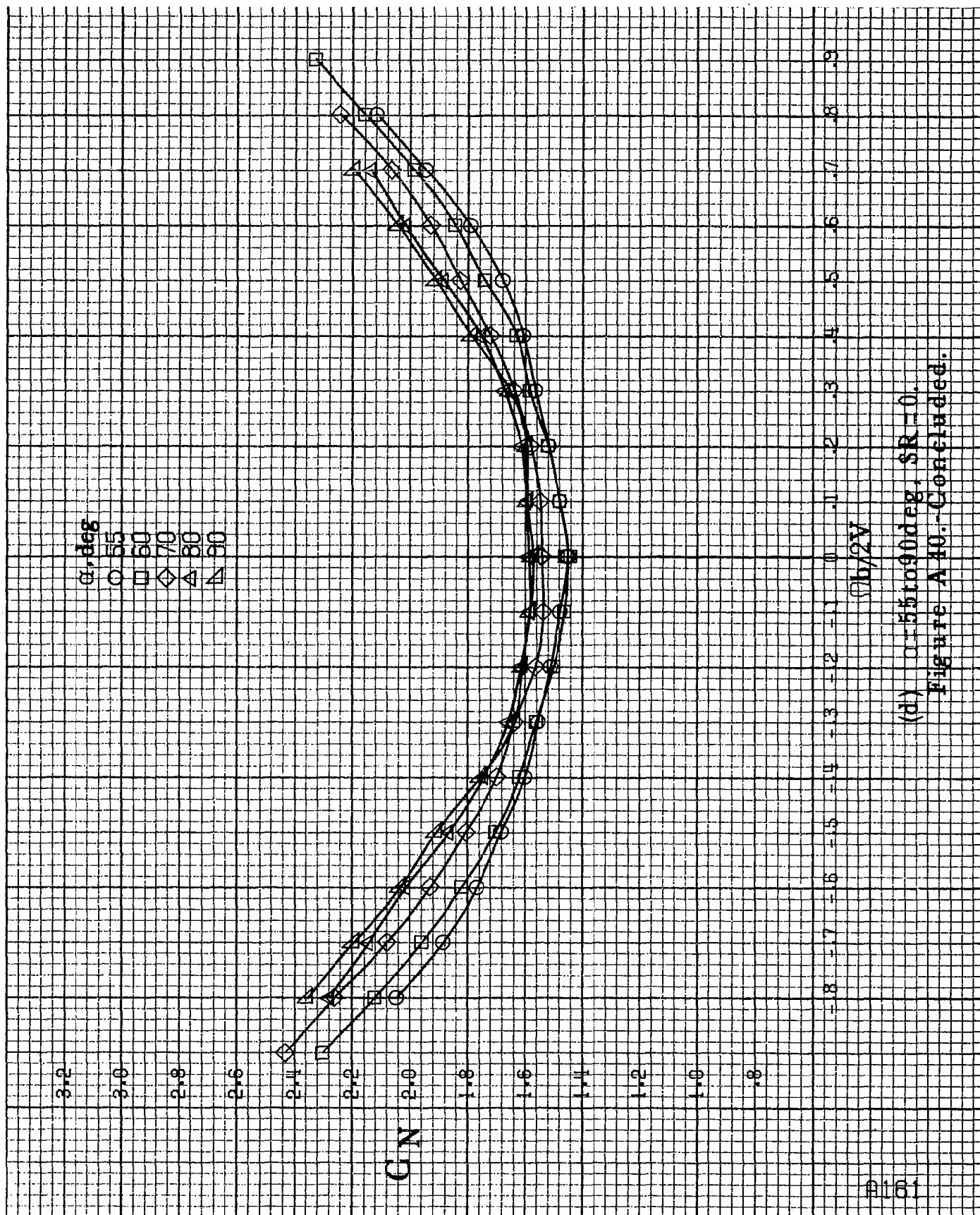
GN

$\phi b/2V$

(a) $\alpha = 30 \text{ to } 50 \text{ deg}$, $SR = 0$.

Figure A40.-Continued.





(d) $\alpha = 55$ to 90° , $SR = 0$.
Figure A 40.-Concluded.

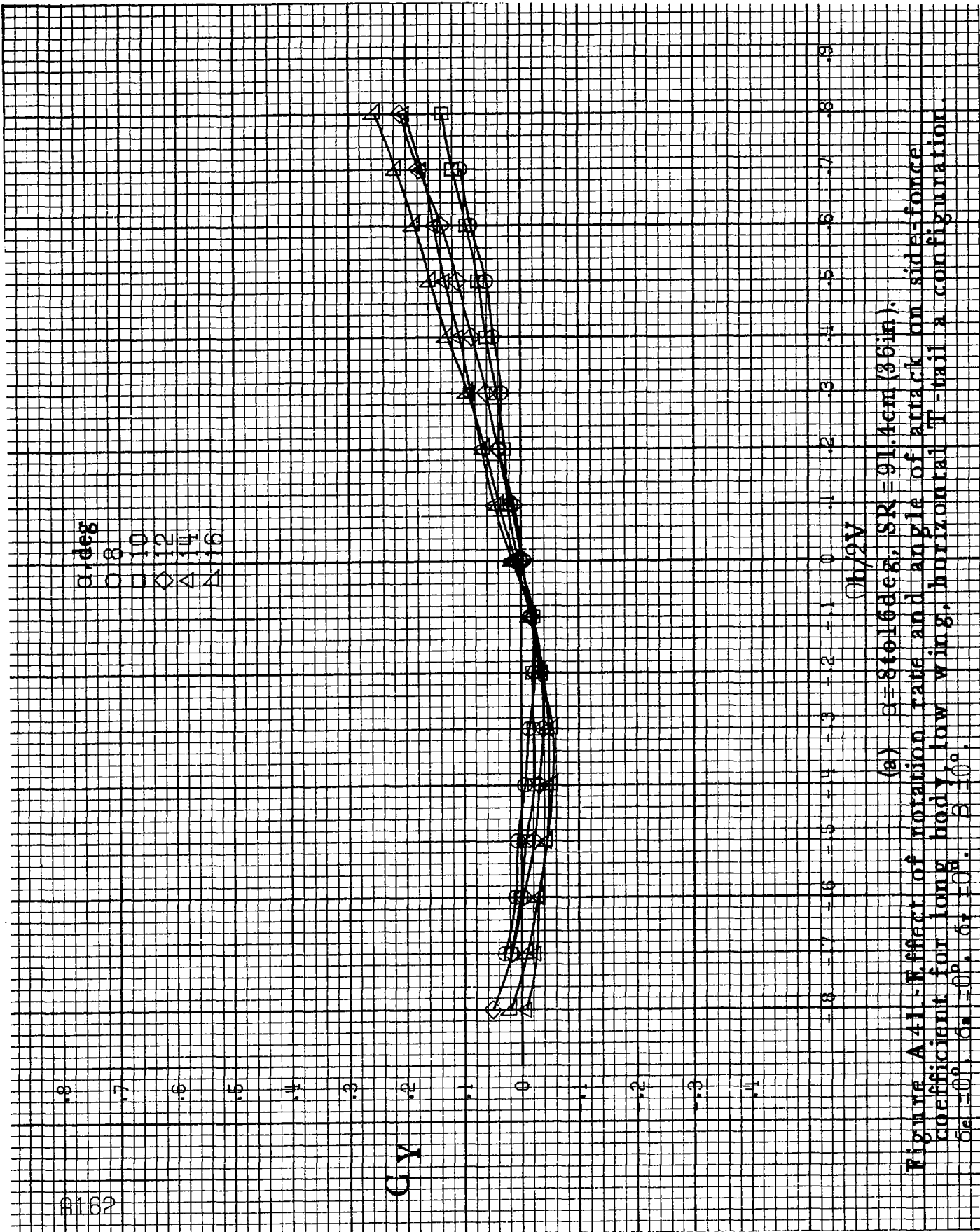
α, deg
 8
 10
 12
 14
 16

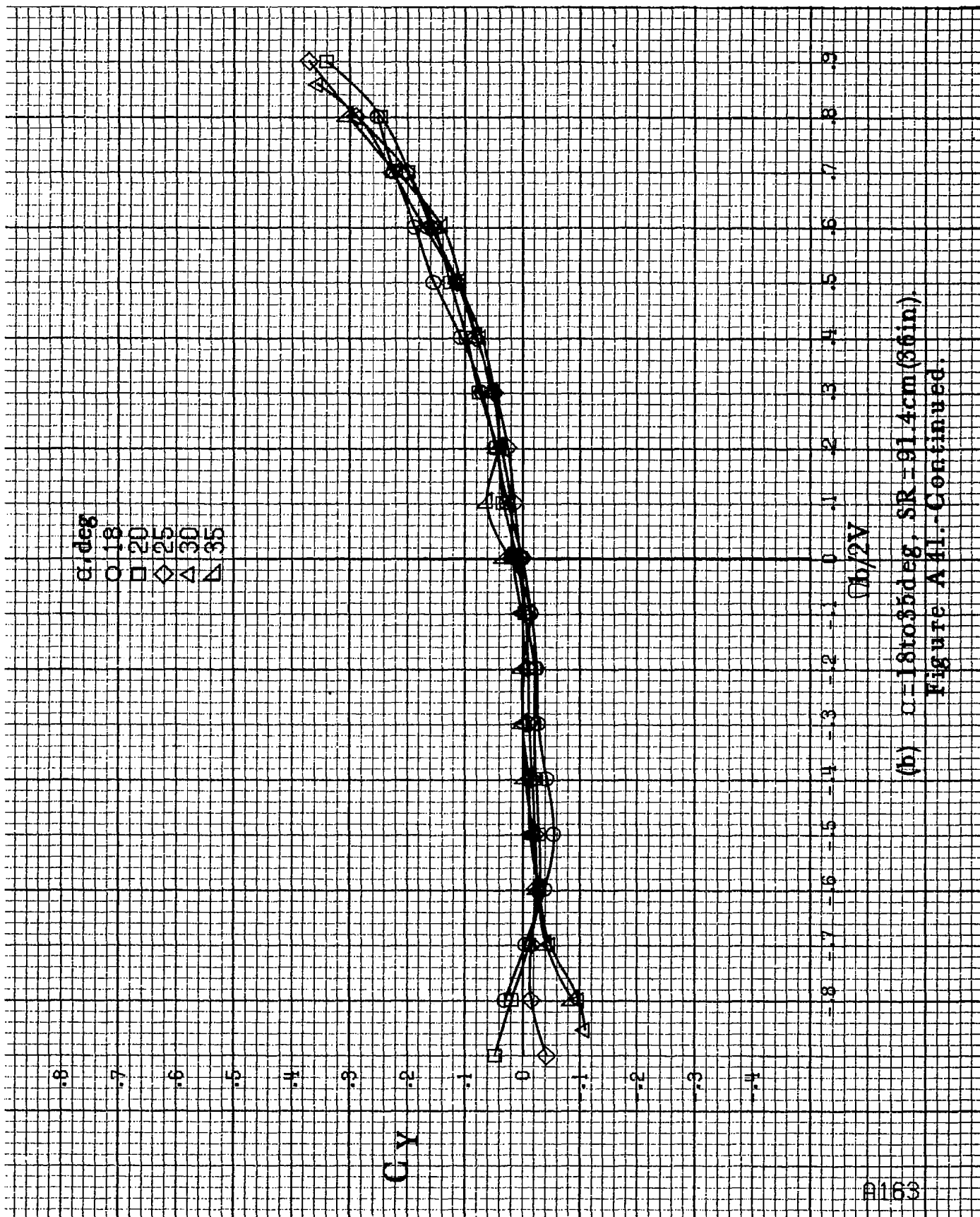
C_Y

$\phi b/2V$

(a) $\alpha = 8 \text{ to } 16 \text{ deg}$, $SR = 91.4 \text{ cm (36 in)}$.

Figure A41.-Effect of rotation rate and angle of attack on side-force coefficient for long body, low wing, horizontal T-tail a configuration $\delta a = 0^\circ$, $\delta s = 0^\circ$, $\delta r = 0^\circ$.





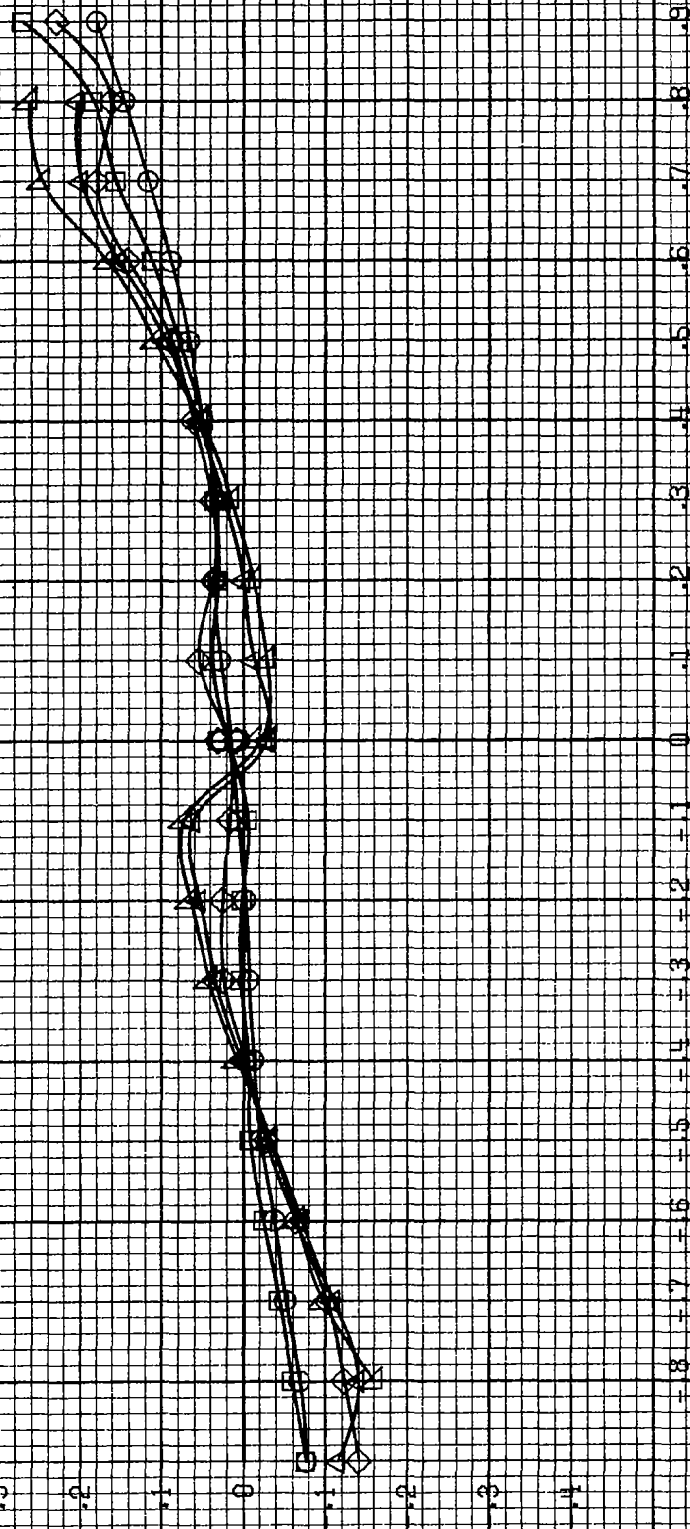
(b) $\alpha=18$ to 35° , $SR=91.4\text{cm}(36\text{in})$.
Figure A41-Continued.

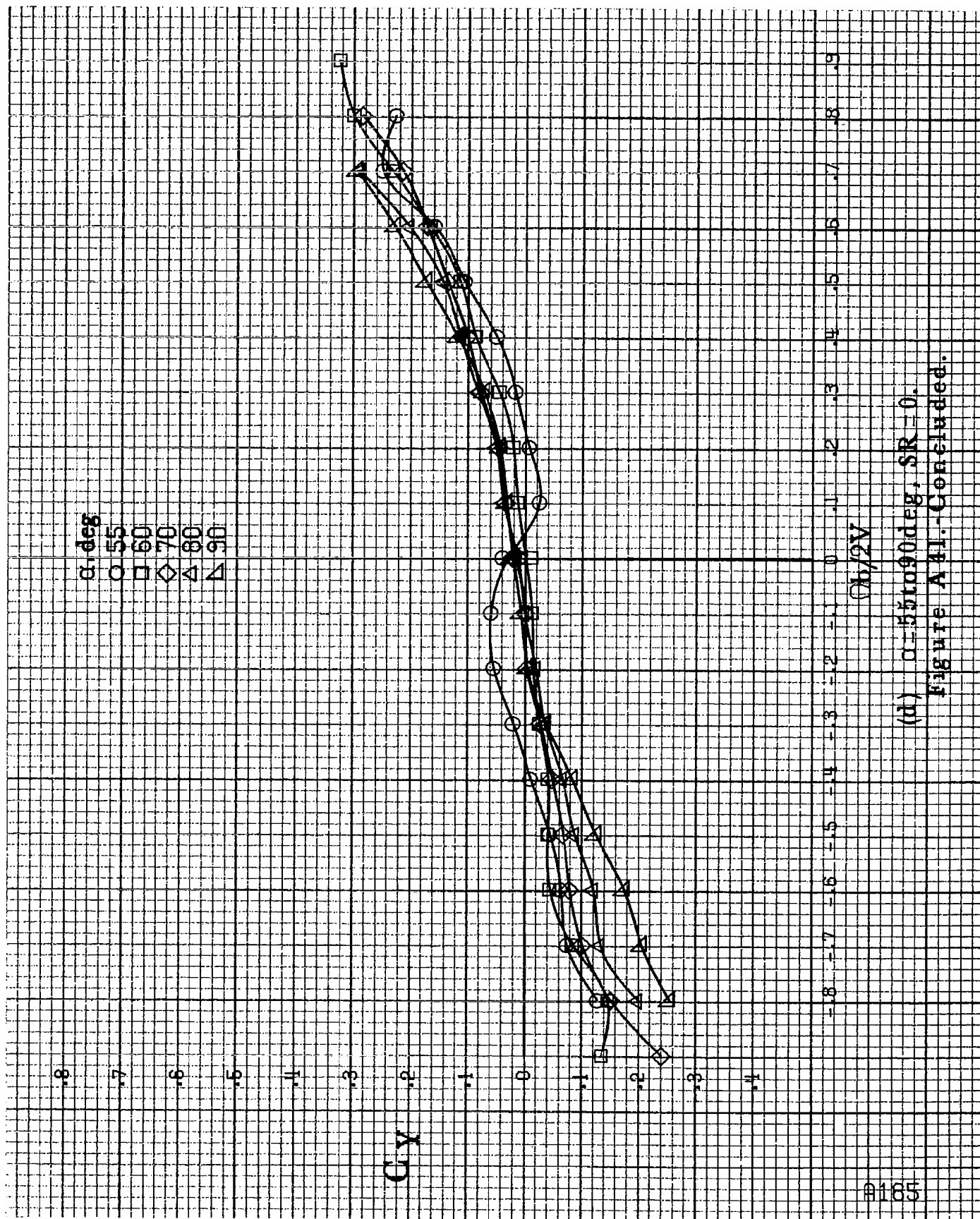
α, deg
 \circ 30
 \square 35
 \diamond 40
 \triangle 45
 ∇ 50

G_Y

$\phi_b/2V$

(c) $\alpha=30$ to 50 deg, $SR=0$.
 Figure A41.-Continued.



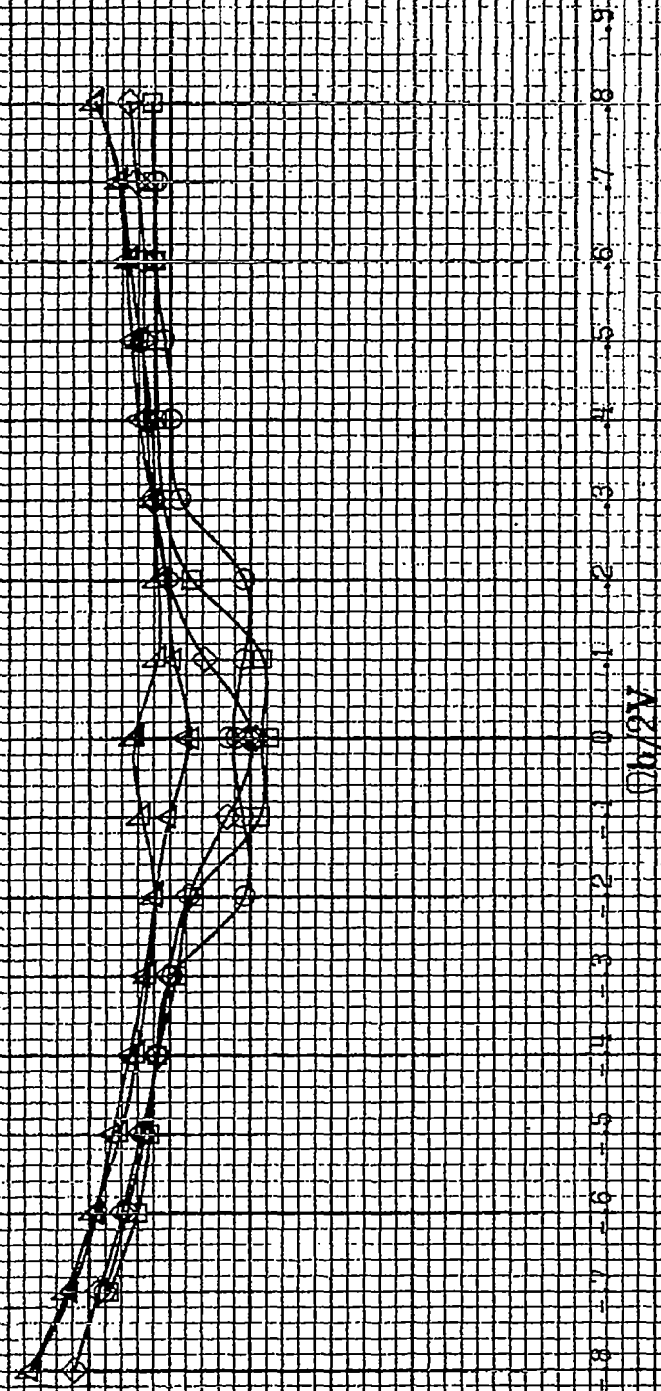


(d) $\alpha = 55$ to 90° , $SR = 0$.
Figure A41. Concluded.

#166

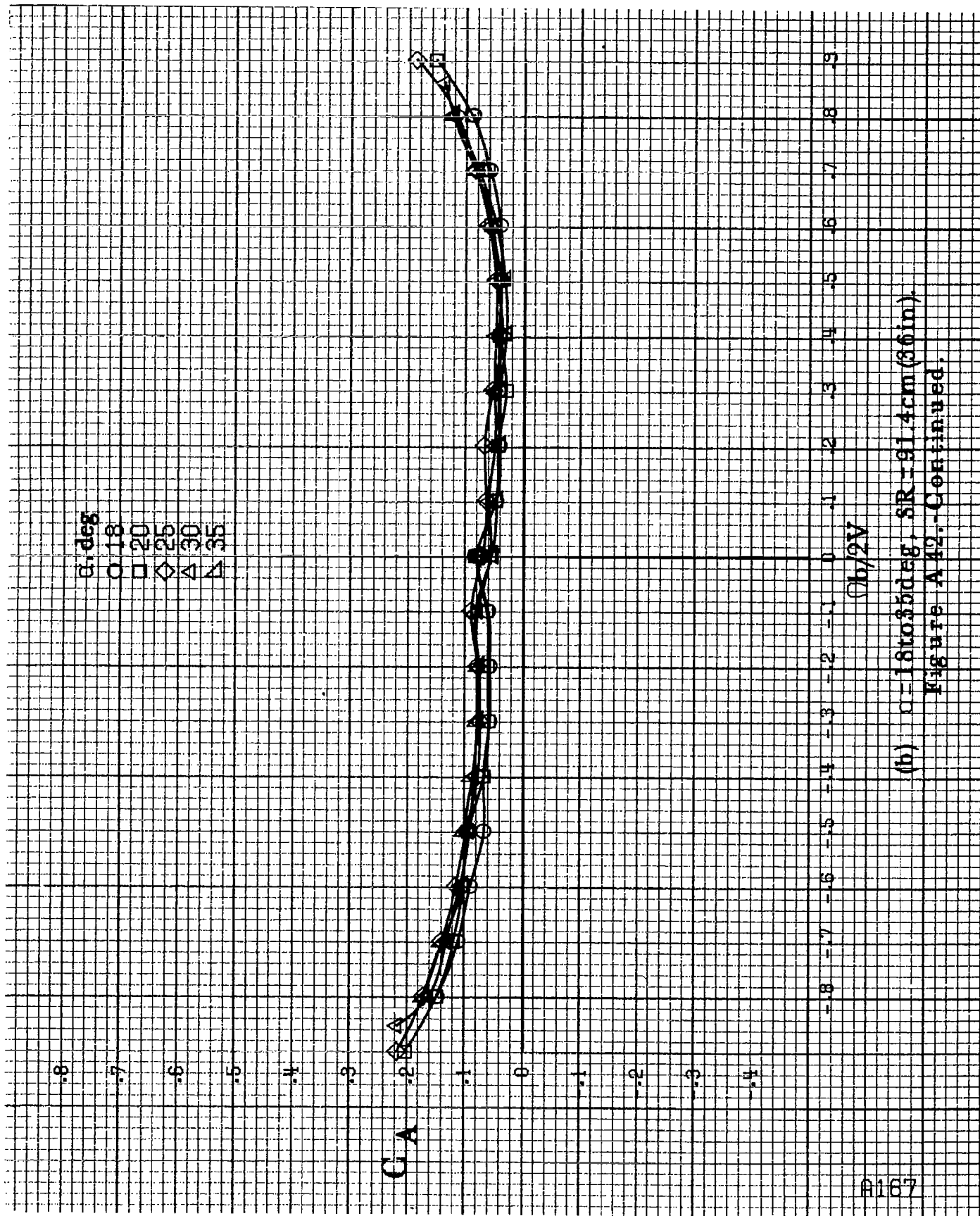
α , deg
 0 8 10 12 14 16

C_L



(a) $\alpha = 8$ to 16 deg, $SR = 91.4$ cm (36 in).

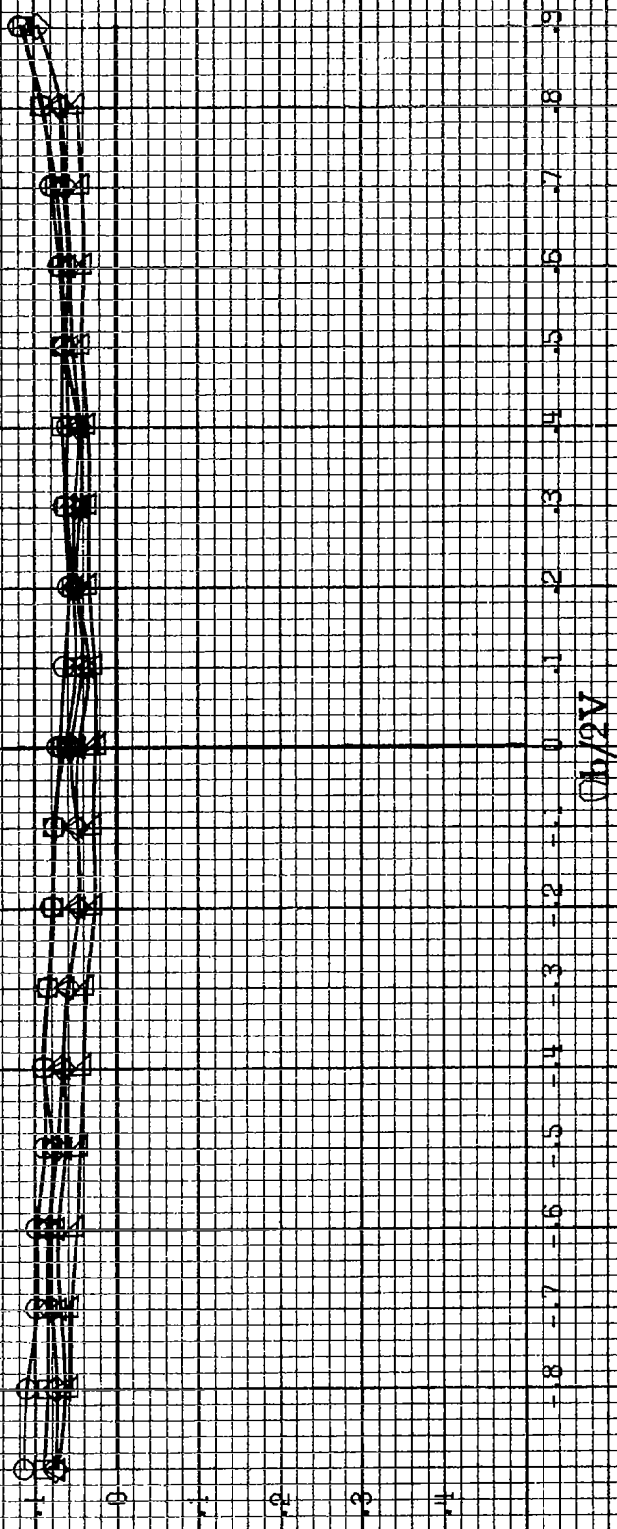
Figure A49. Effect of rotation rate and angle of attack on axial-force coefficient for long body, low wing, horizontal T-tail configuration. $\delta_a = 0^\circ$, $\delta_r = 0^\circ$, $\delta_s = 0^\circ$.



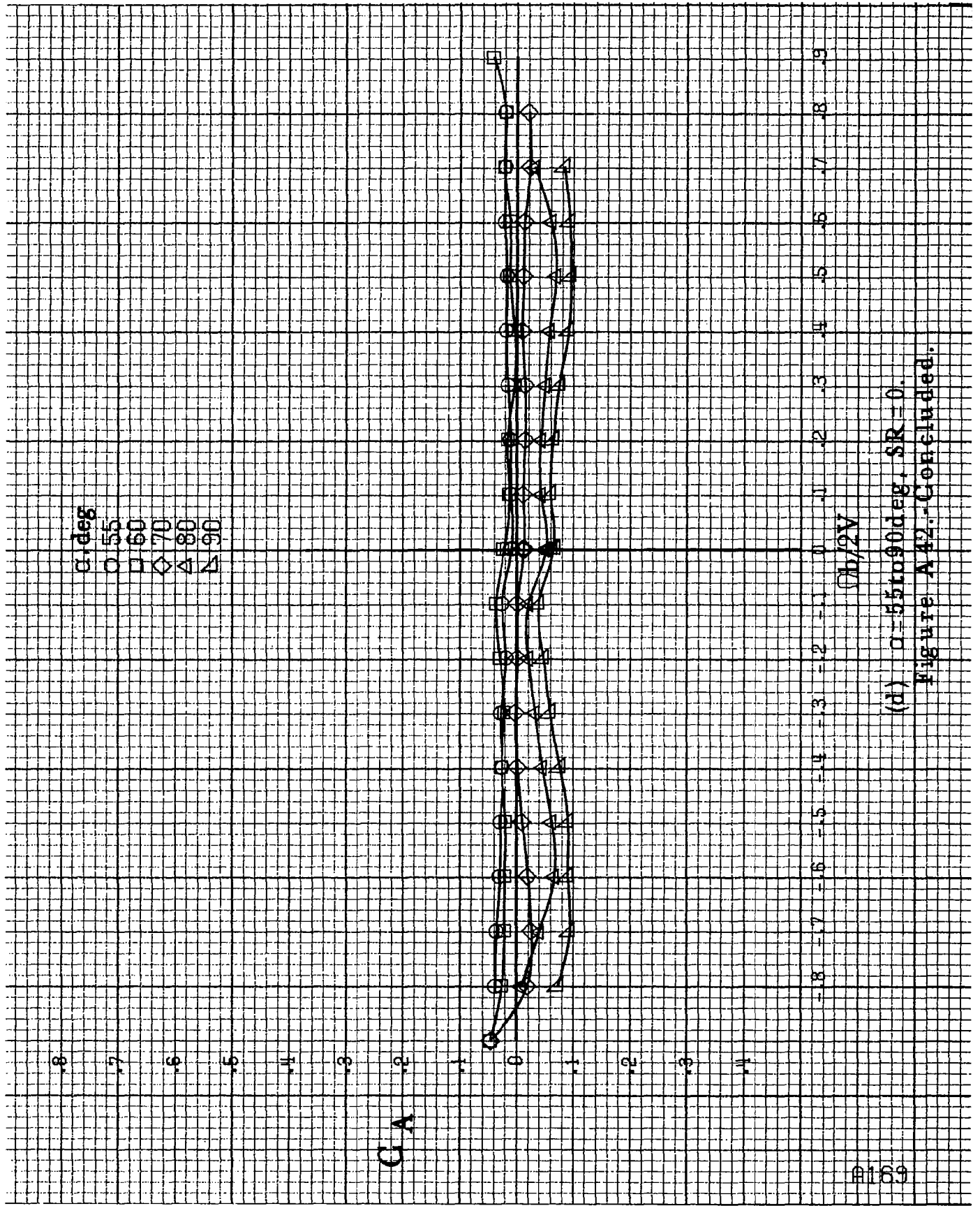
(b) $\alpha = 18$ to 35° , $SR = 91.4 \text{ cm (36 in.)}$.
Figure A 42.-Continued.

α, deg
 \circ 30
 \square 35
 \diamond 40
 \triangle 45
 ∇ 50

G_A

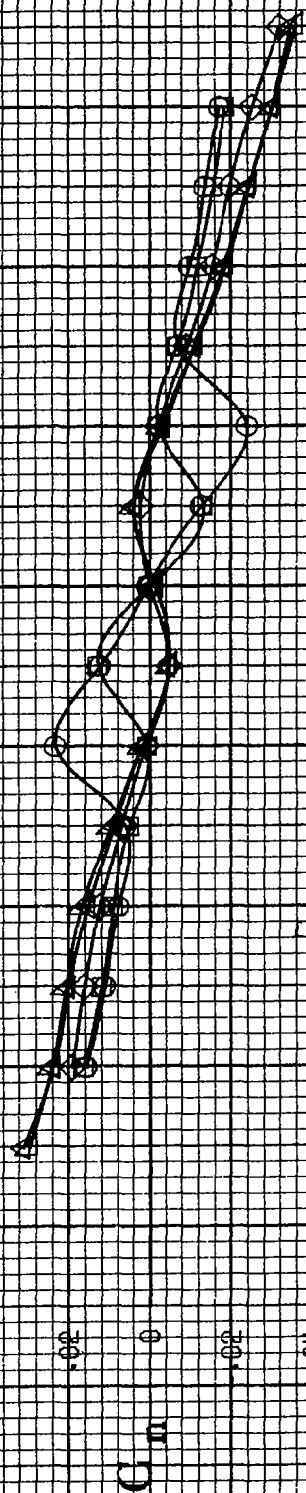


(c) $\alpha=30$ to 50° , $SR=0$.
 Figure A42.-Continued.



A170

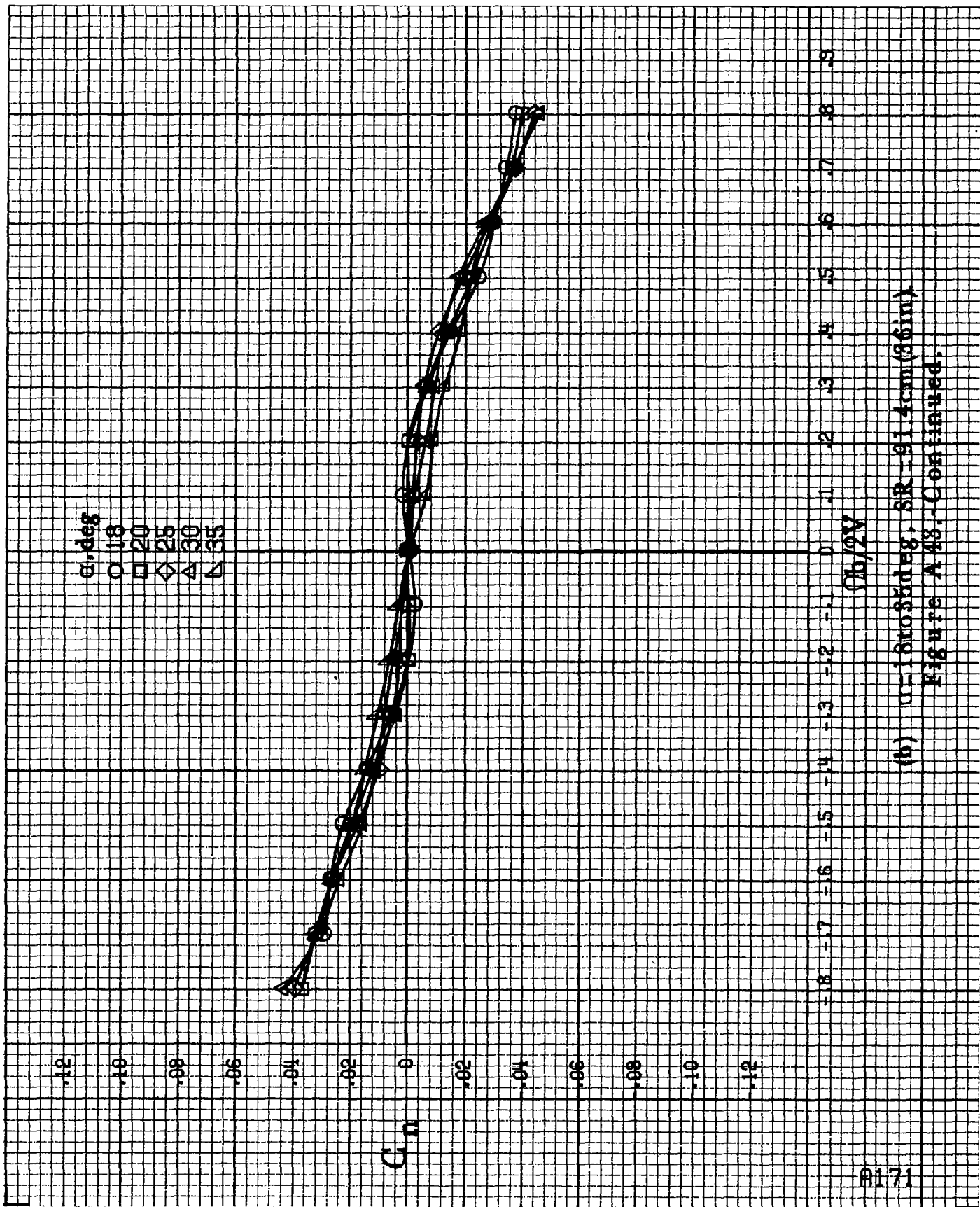
α , deg
 0 8
 10
 12
 14
 16



$Qb/2V$

(a) $\alpha=8$ to 16° , $SR=91.4$ cm (36 in).

Figure A43.-Effect of notation rate and angle of attack on yawing-moment coefficient for long body, low wing, horizontal T-tail b configuration. $\delta_a=0^\circ$, $\delta_r=0^\circ$, $\delta_z=0^\circ$.



(b) $\alpha = 18$ to 35° , $SR = 91.4 \text{ cm (36 in.)}$
Figure A43. - Continued.

α, deg

○ 30

□ 35

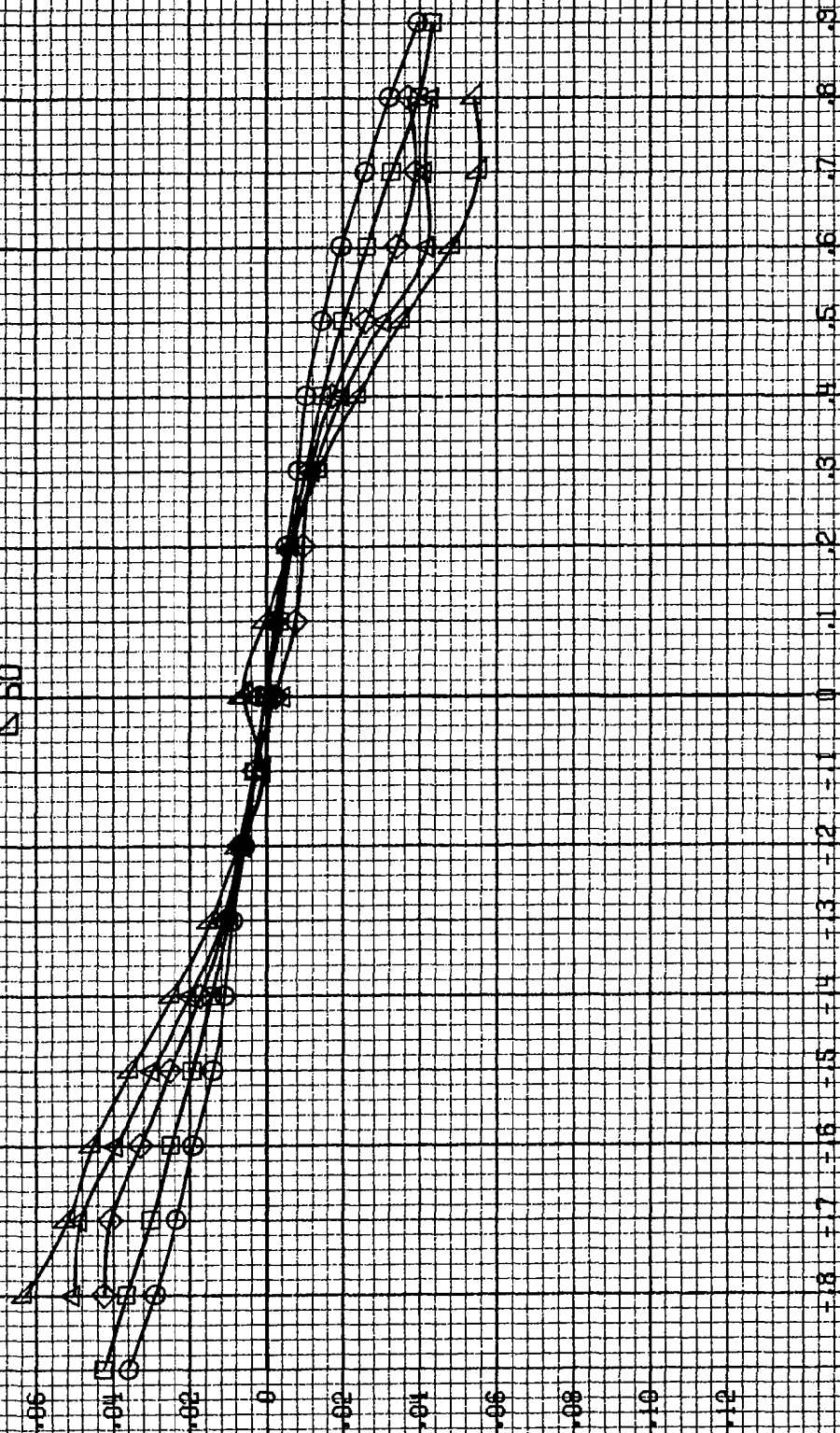
◇ 40

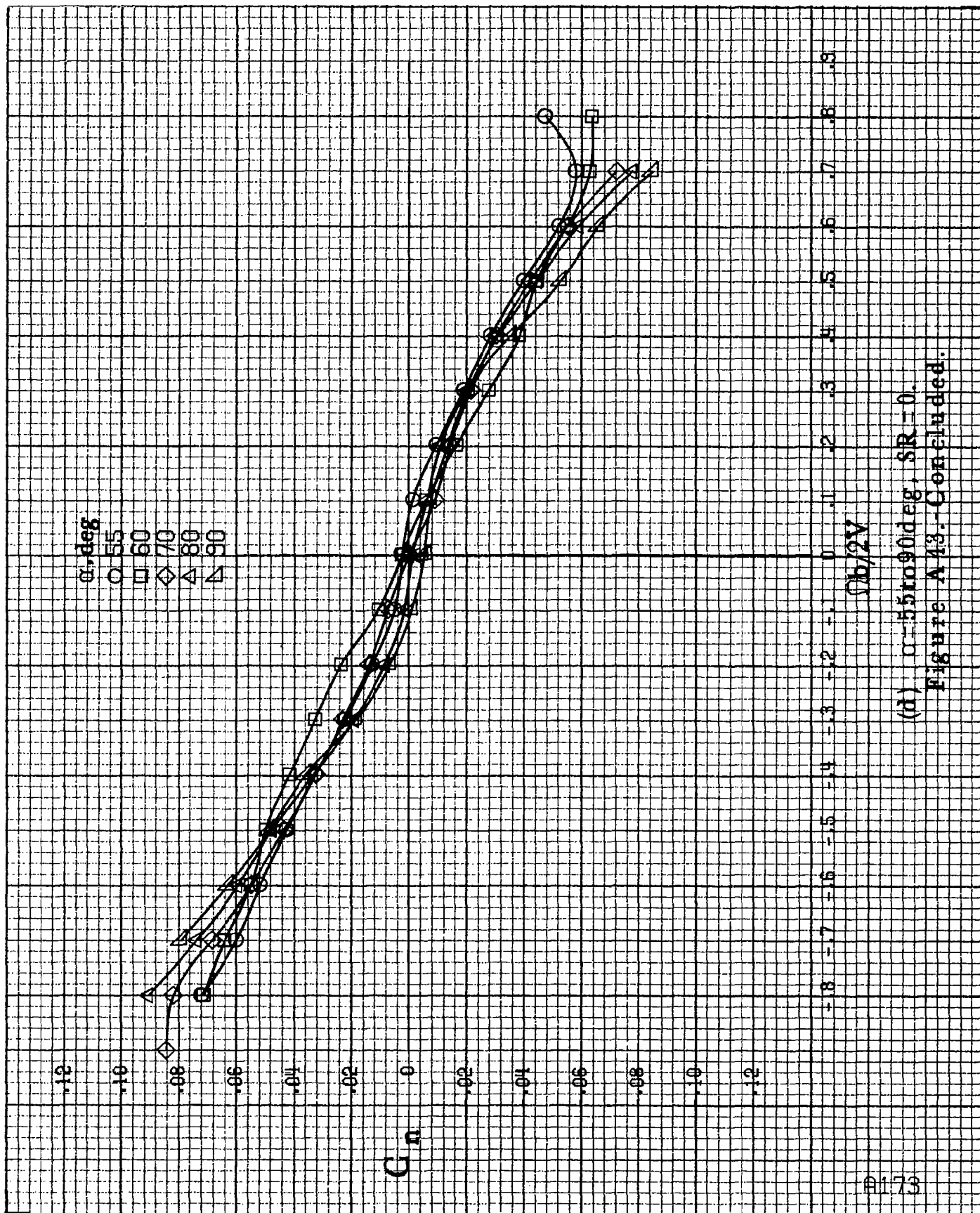
△ 45

▽ 50

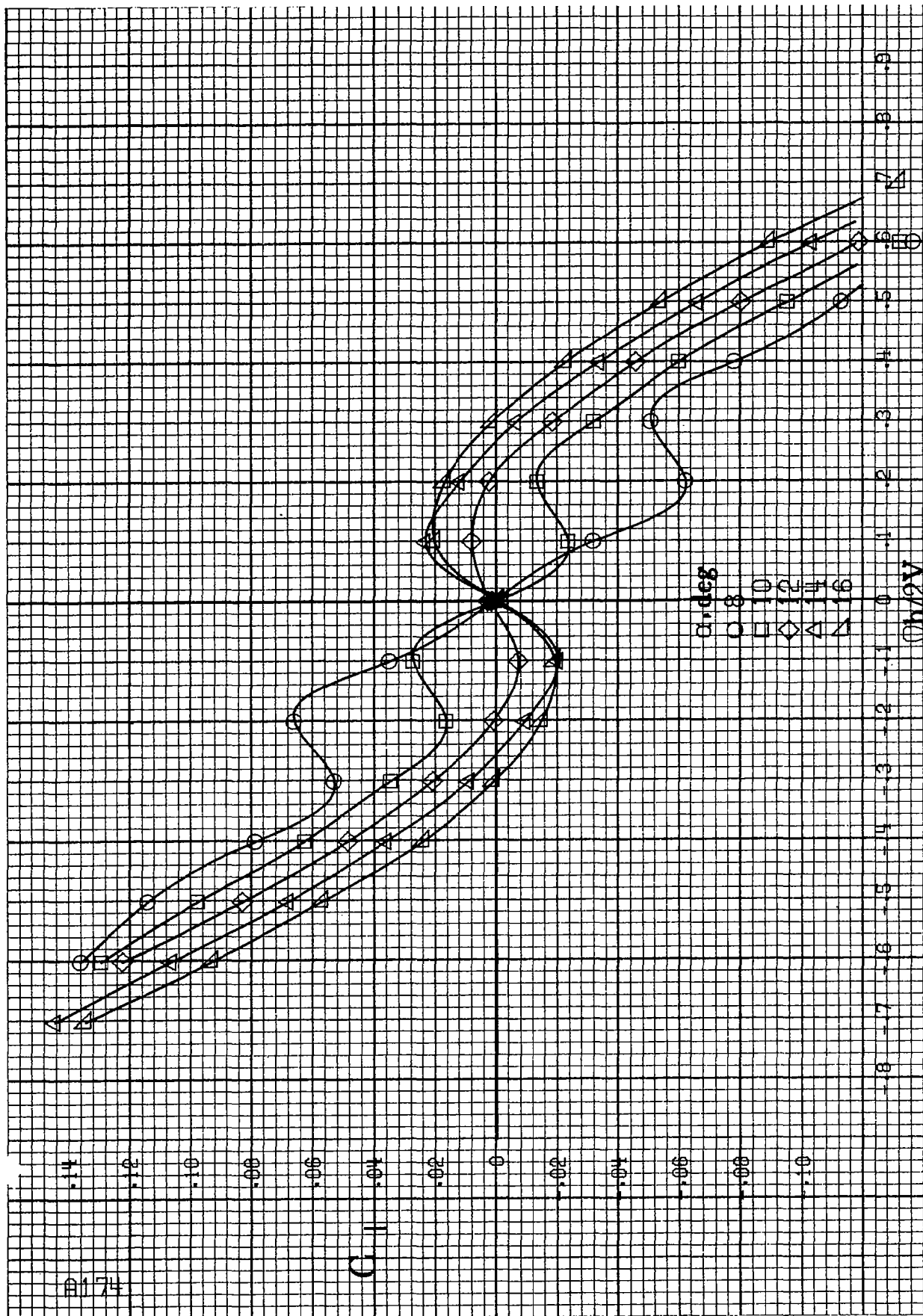
 G_n $Ob/2V$

(c) $\alpha = 30 \text{ to } 50 \text{ deg}$, $SR = 0$,
Figure A13.-Continued.



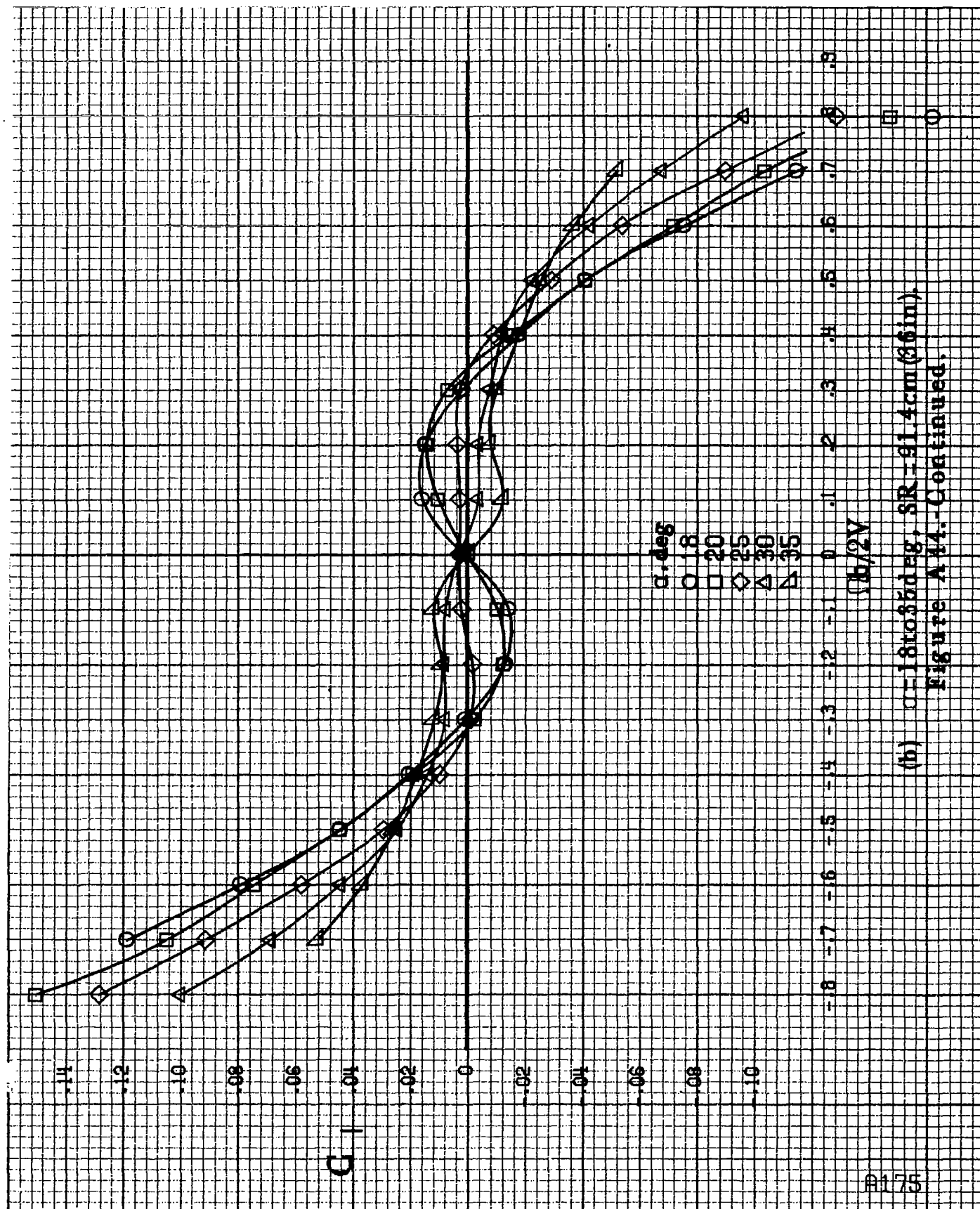


(d) $\alpha=55$ to 90 deg, $SR=0$.
Figure A43.--Concluded.

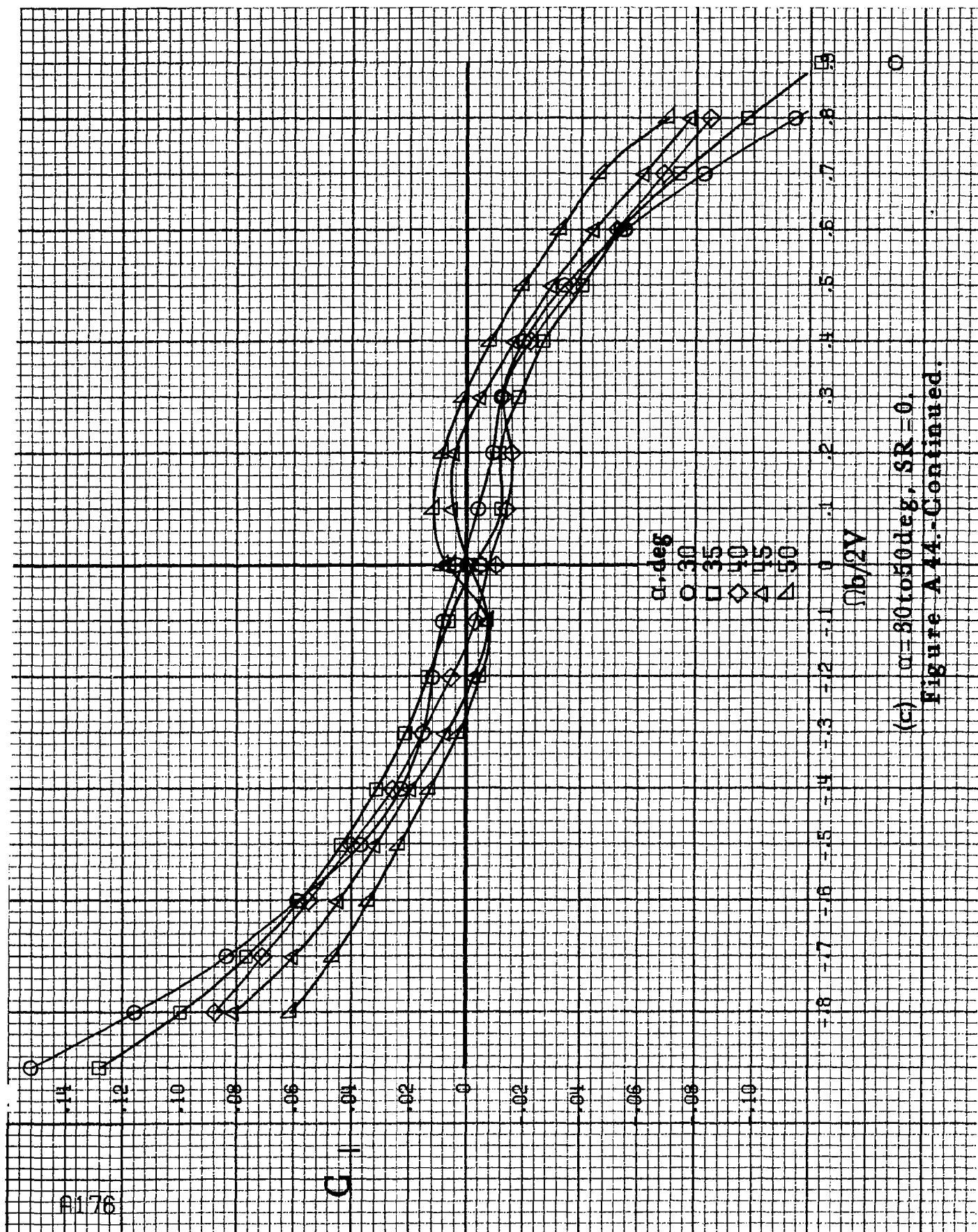


(a) $\alpha = 8$ to 16° , $SR = 91.4$ cm (36 in).

Figure A44 - Effect of rotation rate and angle of attack on rolling-moment coefficient for long body, low wing, horizontal T-tail b configuration. $\delta_e = 0^\circ$, $\delta_a = 0^\circ$, $\delta_r = 0^\circ$, $\beta = 0^\circ$.

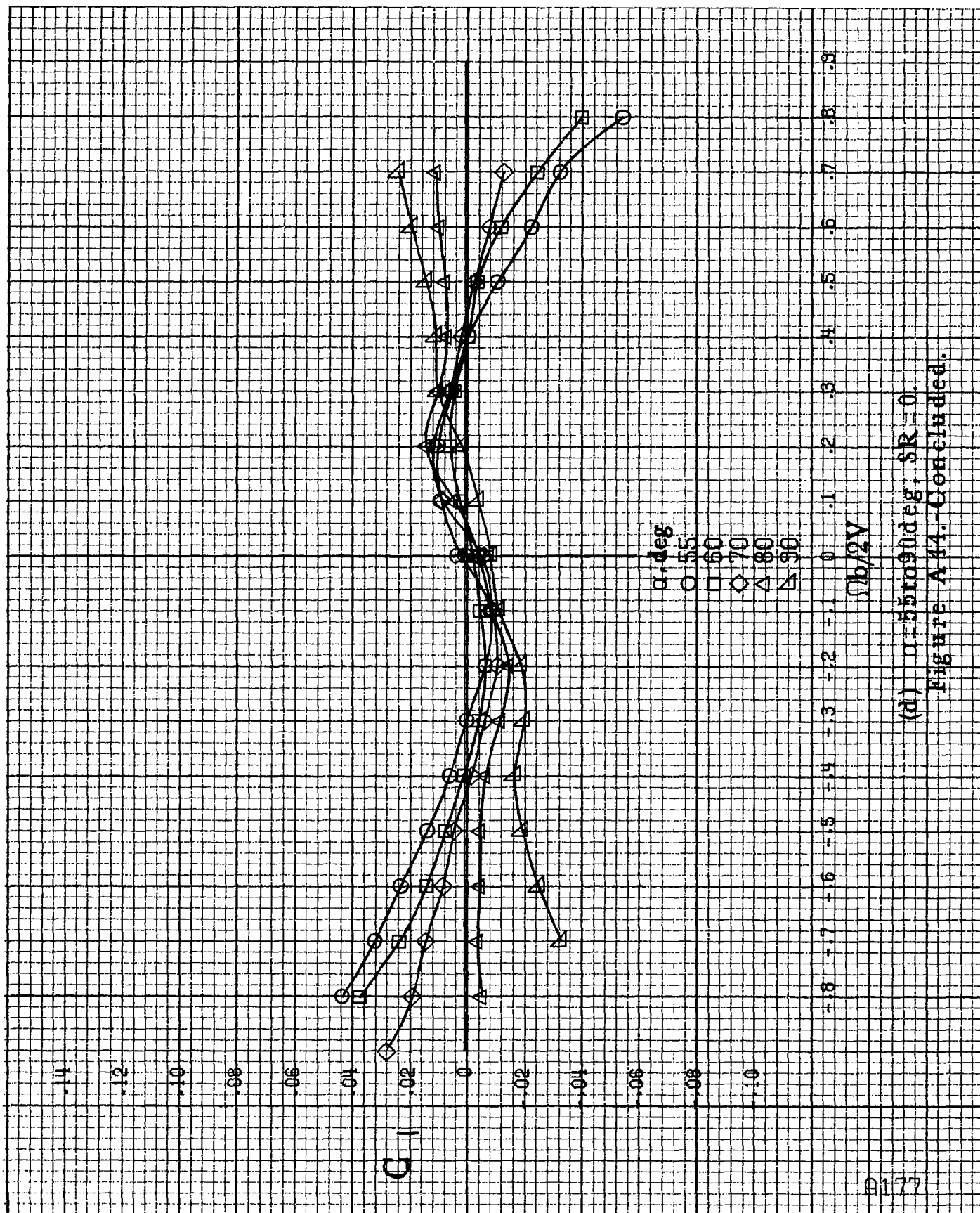


(b) $\alpha = 18$ to 35° , $SR = 91.4 \text{ cm (36 in.)}$
Figure A44.-Continued.



(c) $\alpha=30$ to 50 deg, $SR=0$.

Figure A44.-Continued.



(d) $\alpha = 55$ to 90° , $SR = 0$.
Figure A44. - Concluded.

C_m

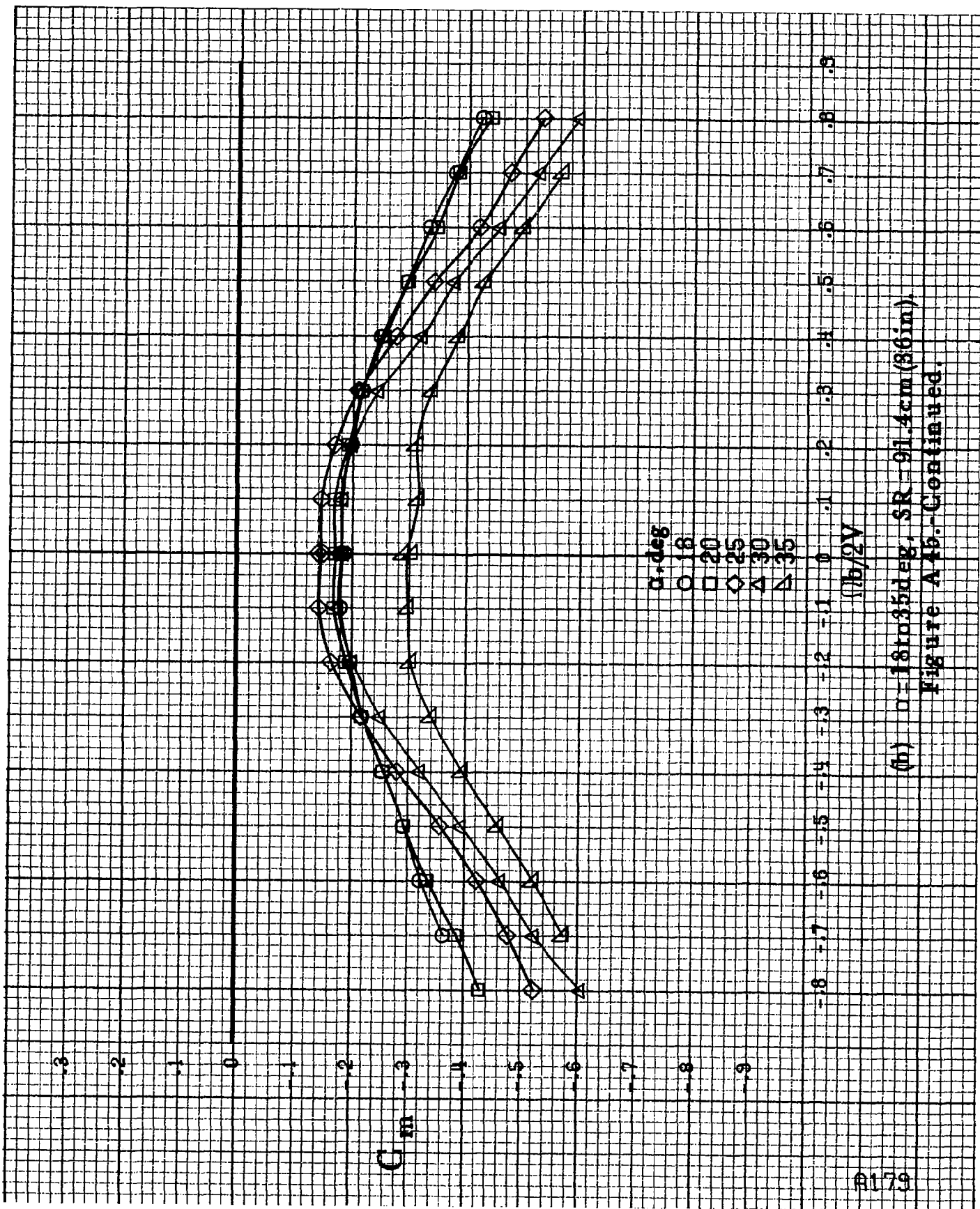
α, deg

○ 8
□ 10
◇ 12
△ 14
▽ 16

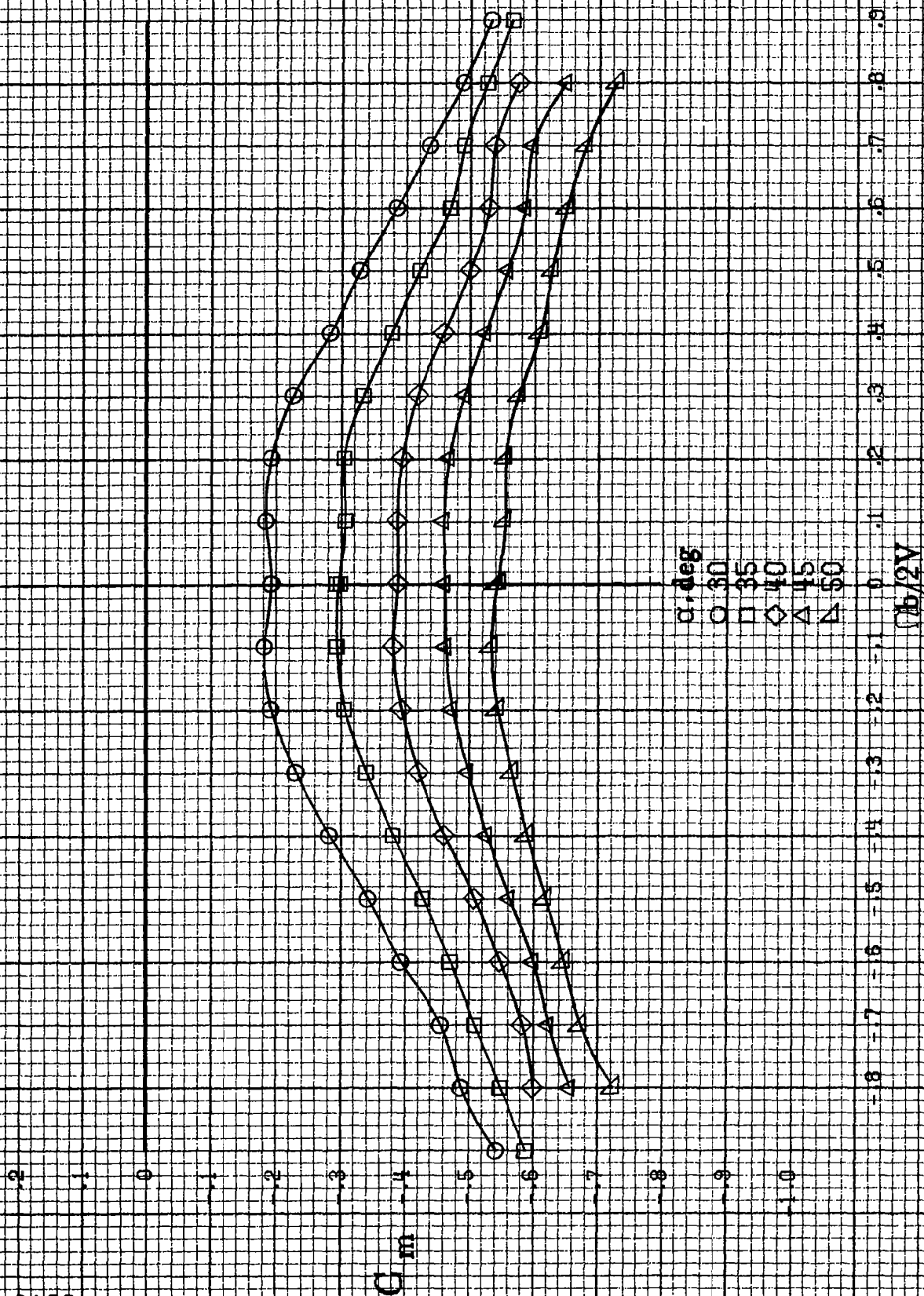
$C_{b/2V}$

(a) $\alpha = 8 \text{ to } 16 \text{ deg}$, $SR = 91.4 \text{ cm (36 in)}$.

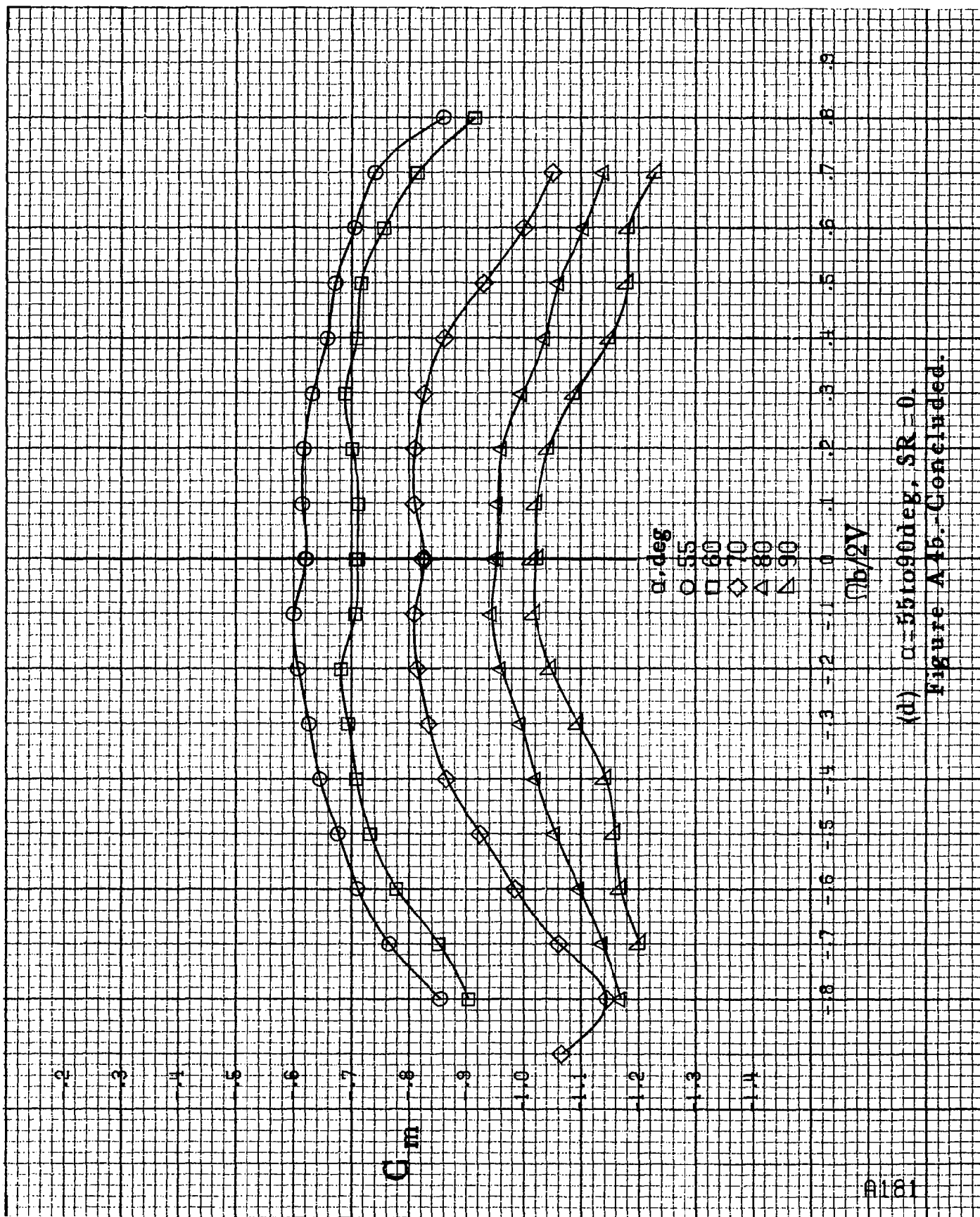
Figure A45b.-Effect of rotation rate and angle of attack on pitching-moment coefficient for long body, low wing, horizontal T-tail b configuration
 $\delta_e = 0^\circ$, $\delta_a = 0^\circ$, $\delta_r = 0^\circ$, $\beta = 0^\circ$.



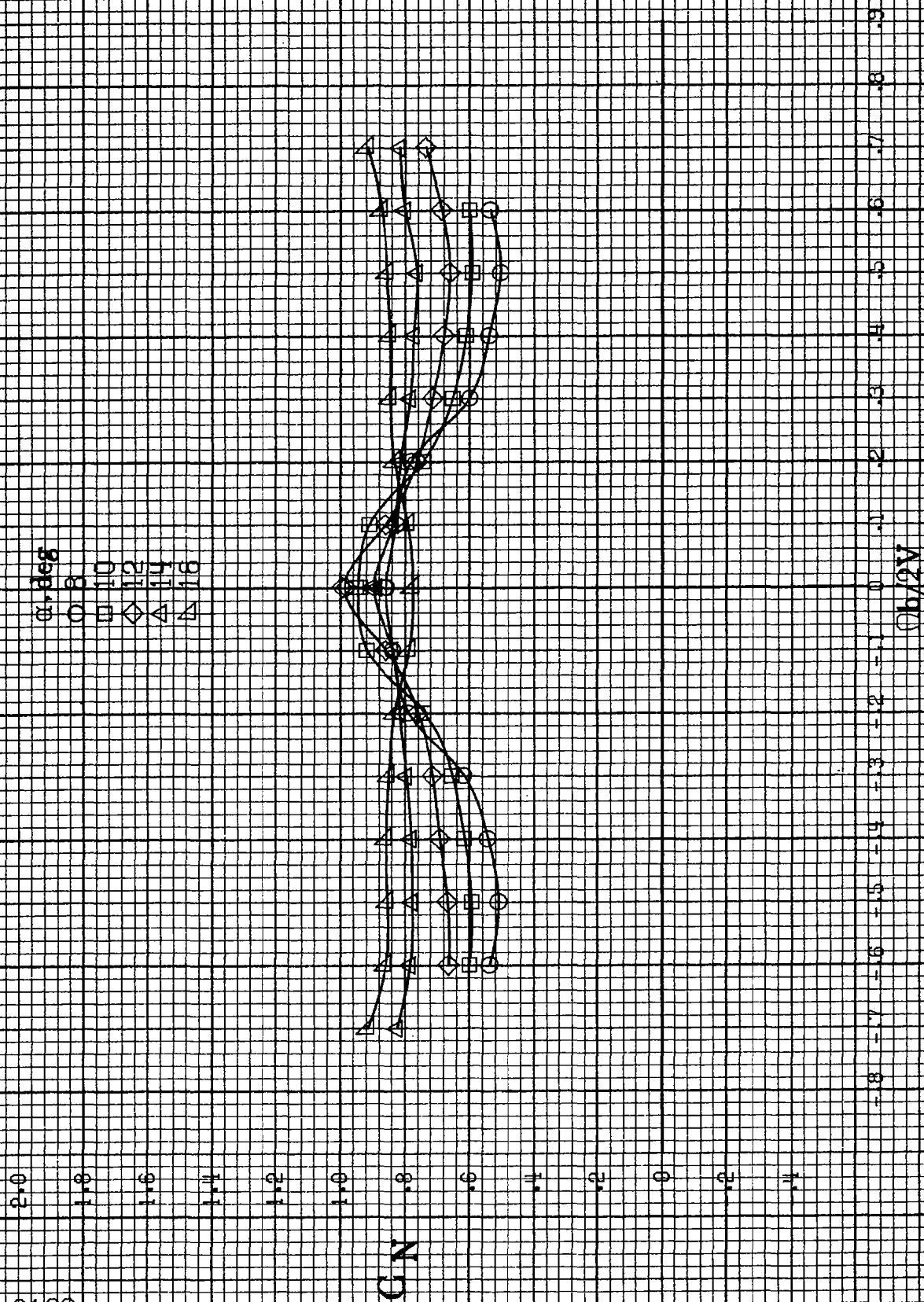
(b) $\alpha=18$ to 35° deg, SR=91.4cm (36in).
Figure A45.-Continued.



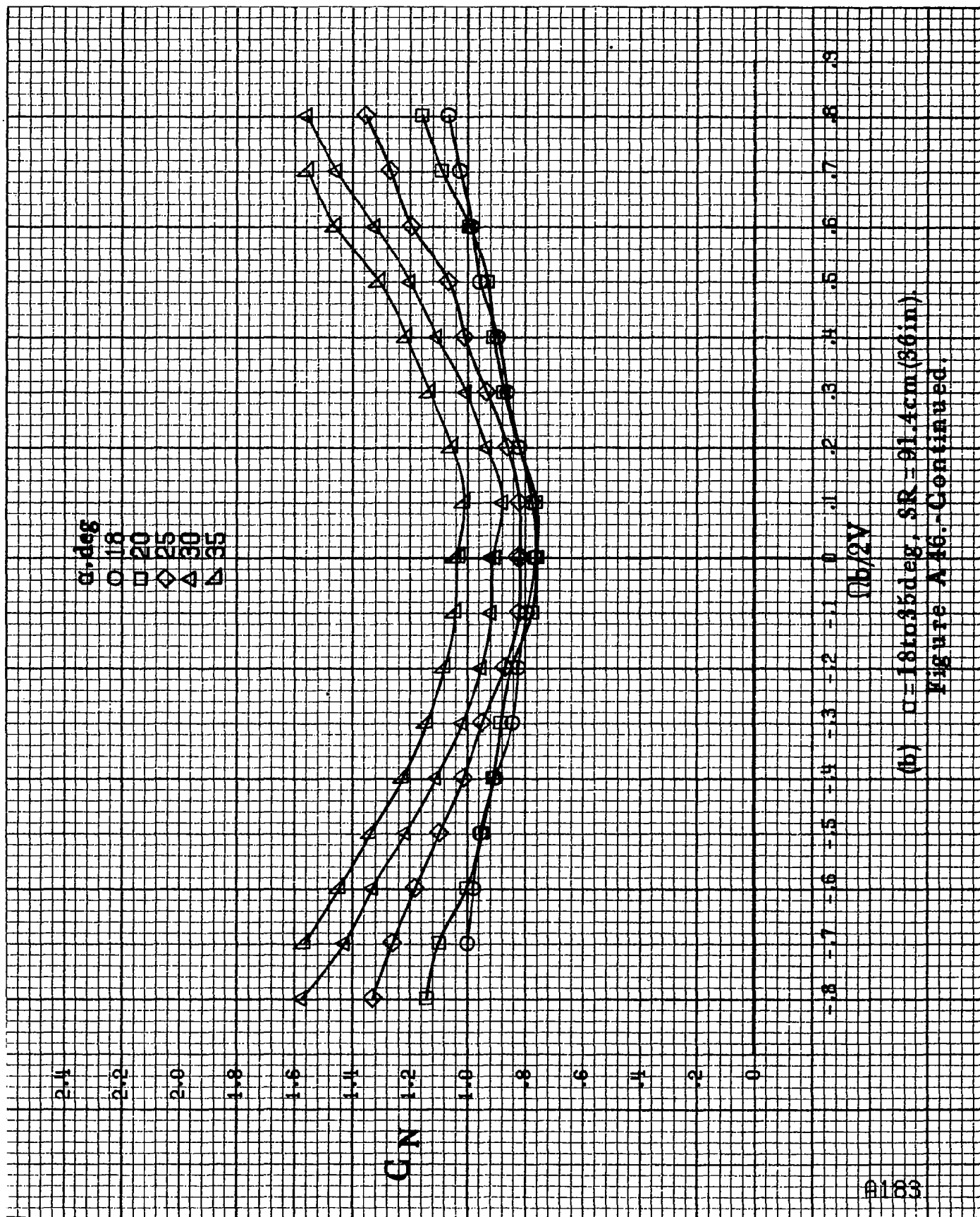
(c) $\alpha = 30$ to 50 deg, $SR = 0$.
Figure A45.-Continued.



(d) $\alpha = 55$ to 90° , $SR = 0$.
Figure A1b.-Concluded.



(a) $\alpha = 8$ to 16° , $SR = 91.4 \text{ cm (36 in.)}$.
 Figure A46 - Effect of rotation rate and angle of attack on normal force coefficient for long body, low wing, horizontal T-tail b configuration.
 $\delta_a = 0^\circ$, $\delta_s = 0^\circ$, $\delta_r = 0^\circ$, $S = 10^\circ$.



(b) $\alpha = 18$ to 35° , $SR = 91.4 \text{ cm (36 in.)}$
Figure A 16.-Continued.

A184

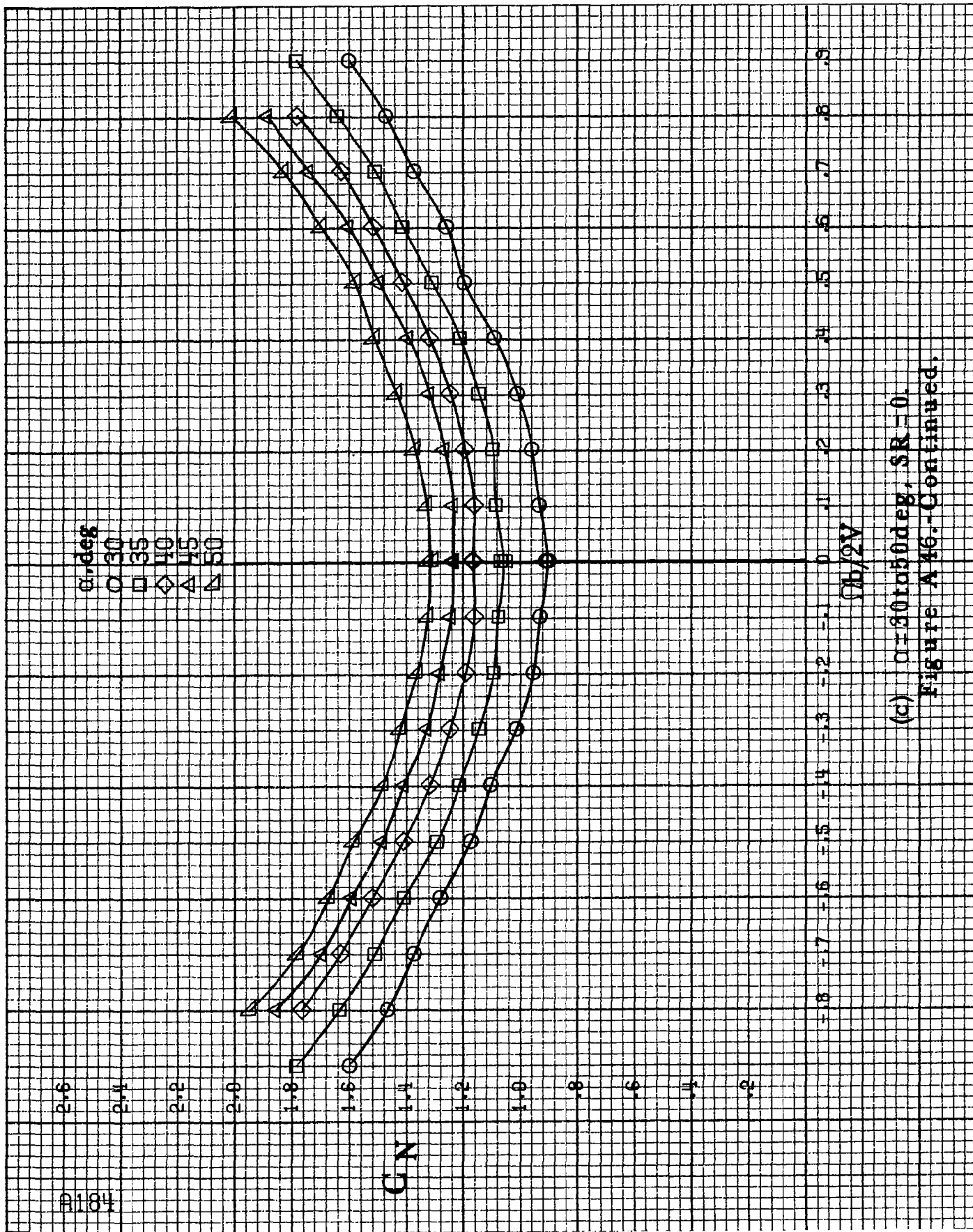
α, deg
 ○ 30
 □ 35
 ◇ 40
 △ 45
 ▽ 50

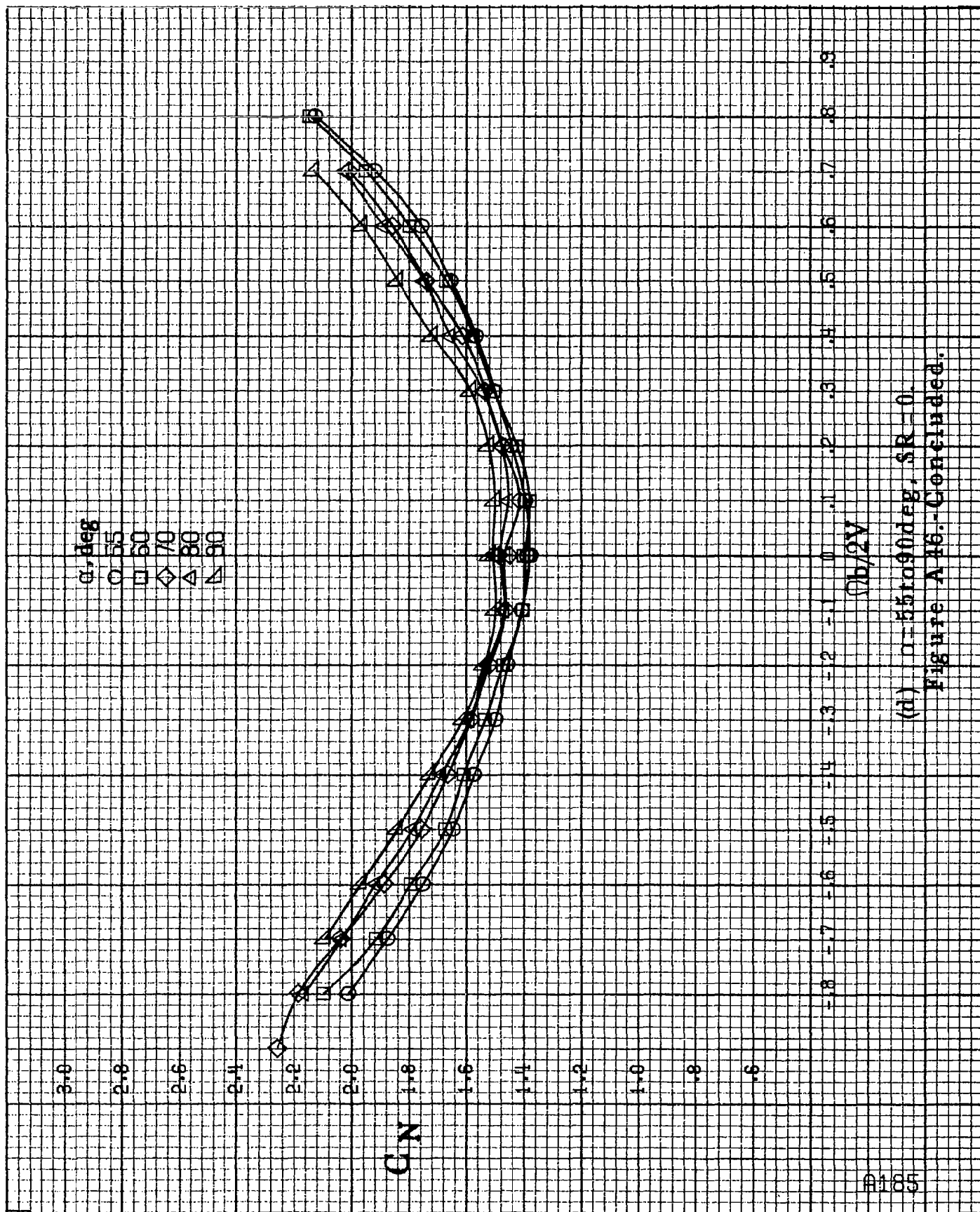
G_N

$\Omega_b/2V$

(c) $\alpha=30$ to 50 deg, $SR=0$.

Figure A46.-Continued.





(d) $\alpha = 55$ to 90° , $SR = 0$.
Figure A16.-Concluded.

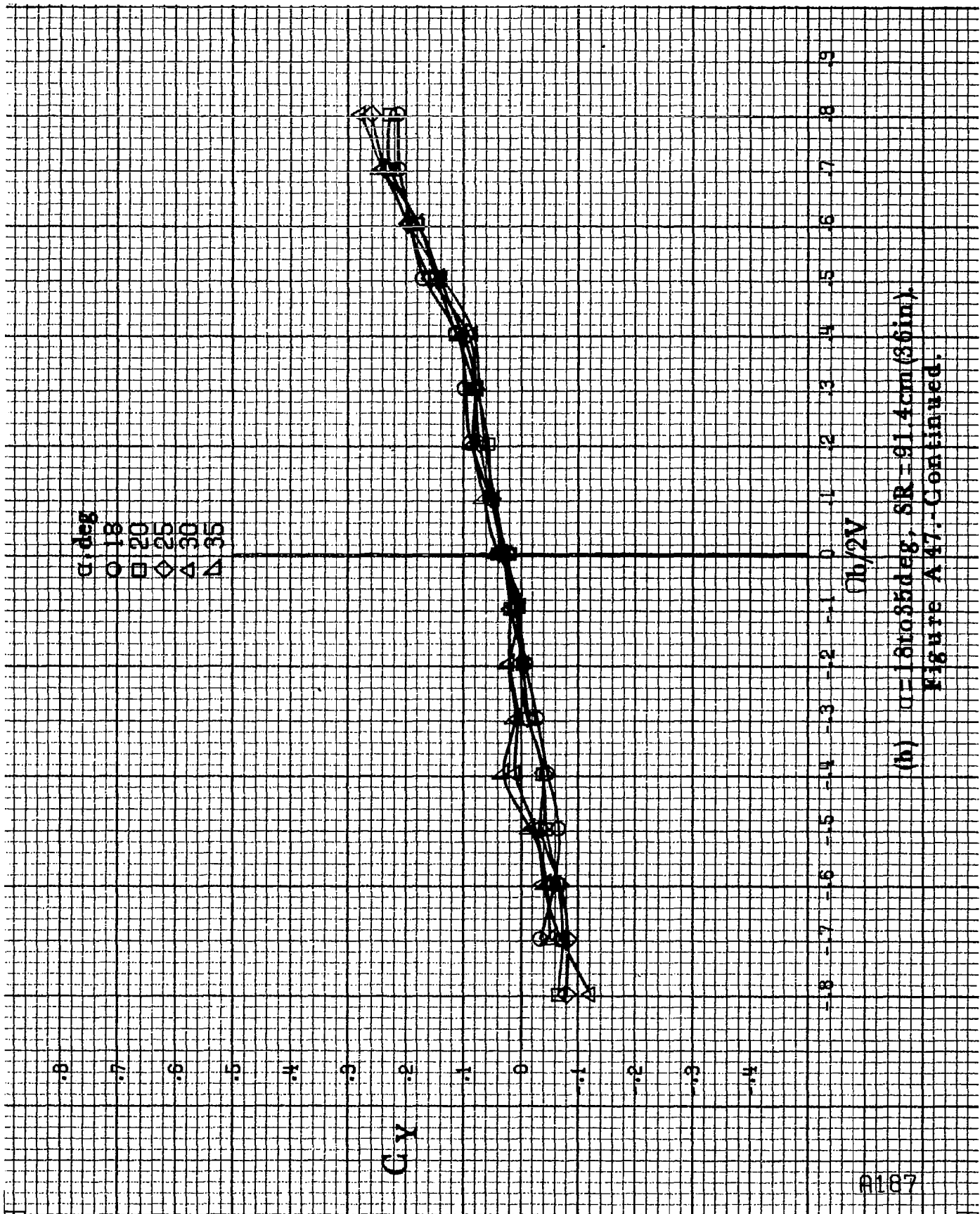
α, deg
 O 8
 □ 10
 ◇ 12
 △ 14
 ▽ 16

C_Y

$0.5/2V$

(a) $\alpha = 8 \text{ to } 16 \text{ deg}$, $SR = 91.4 \text{ cm (35 in)}$.

Figure A 47. - Effect of rotation rate and angle of attack on side-force coefficient for long body, low wing, horizontal T-tail b configuration
 $\delta_e = 0^\circ$, $\delta_a = 0^\circ$, $\delta_r = 0^\circ$, $\beta = 10^\circ$.



(b) $\alpha=18$ to 35° , $SR=91.4\text{ cm (36 in.)}$.
Figure A 47.-Continued.

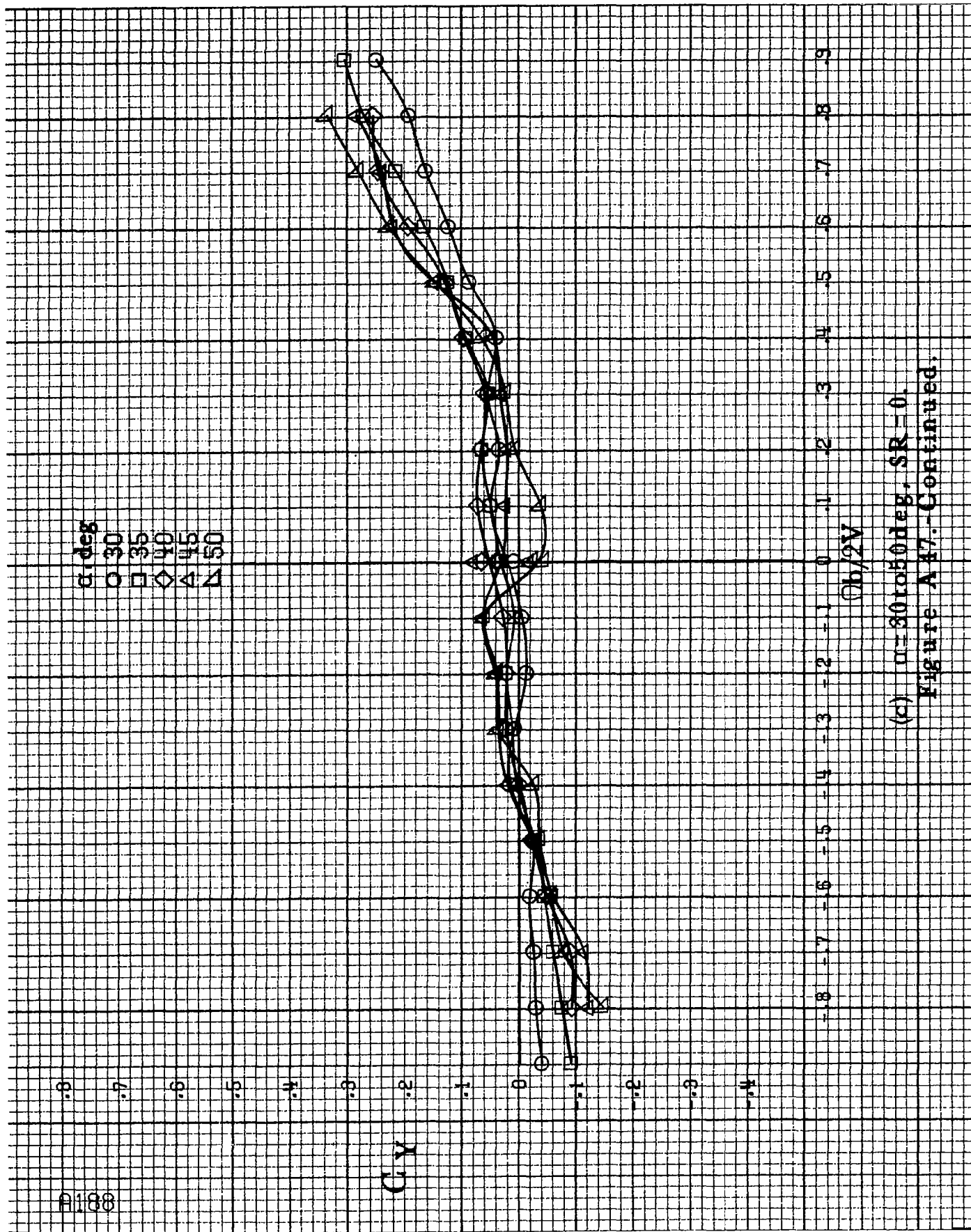
1188

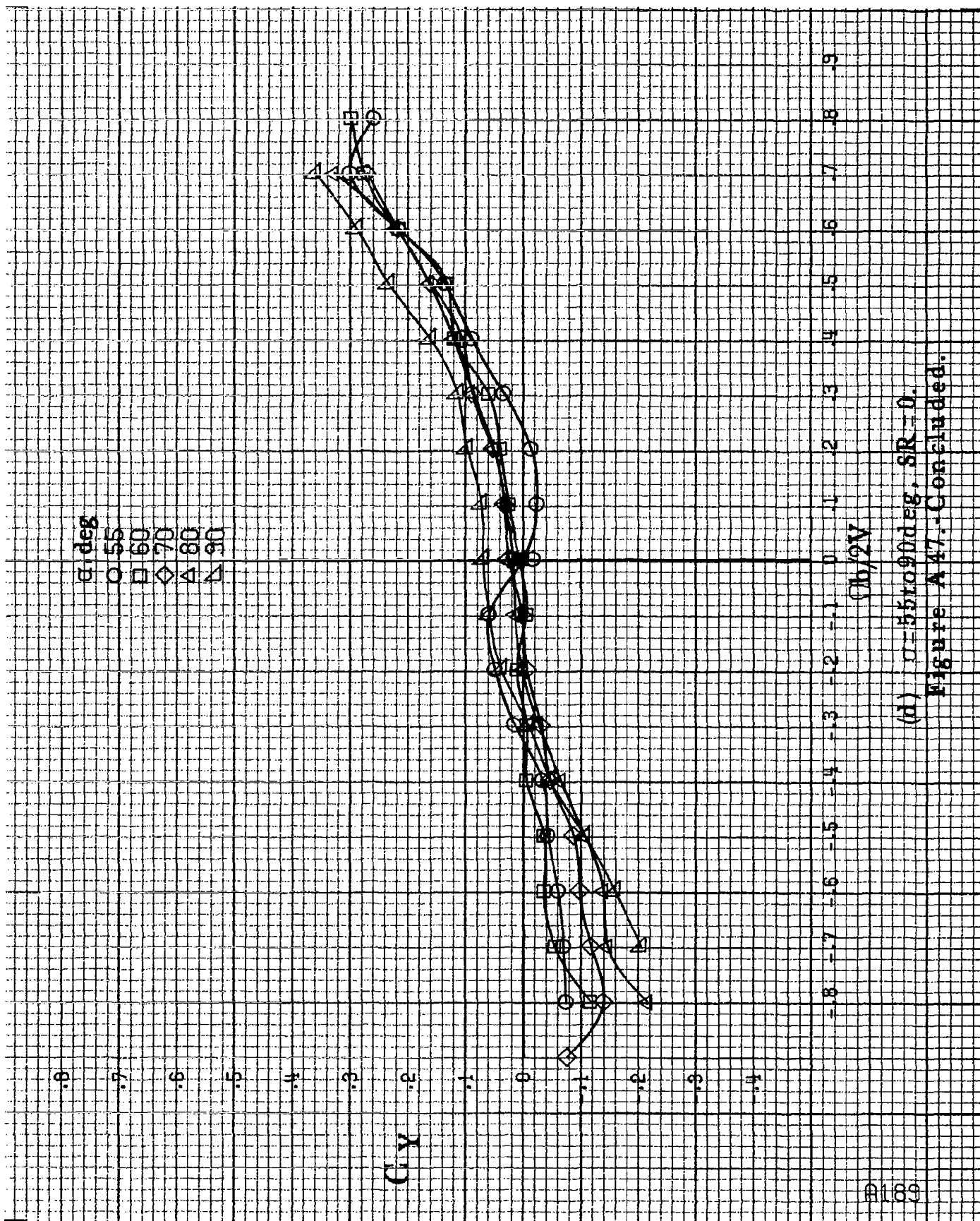
α deg
 ○ 30
 □ 35
 ◇ 40
 △ 45
 ▲ 50

CY

$\phi_b/2V$

(c) $\alpha=30$ to 50 deg, $SR=0$.
 Figure A17.-Continued.



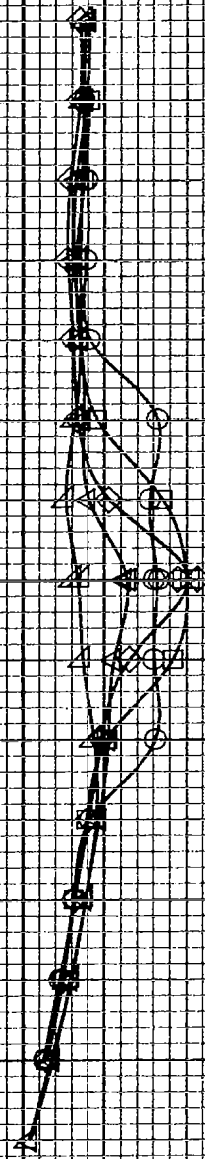


(d) $\sigma=55$ to 90° deg, $SR=0$.

Figure A47.-Concluded.

α, deg
 $\circ 8$
 $\square 10$
 $\diamond 12$
 $\triangle 14$
 $\nabla 16$

C_A



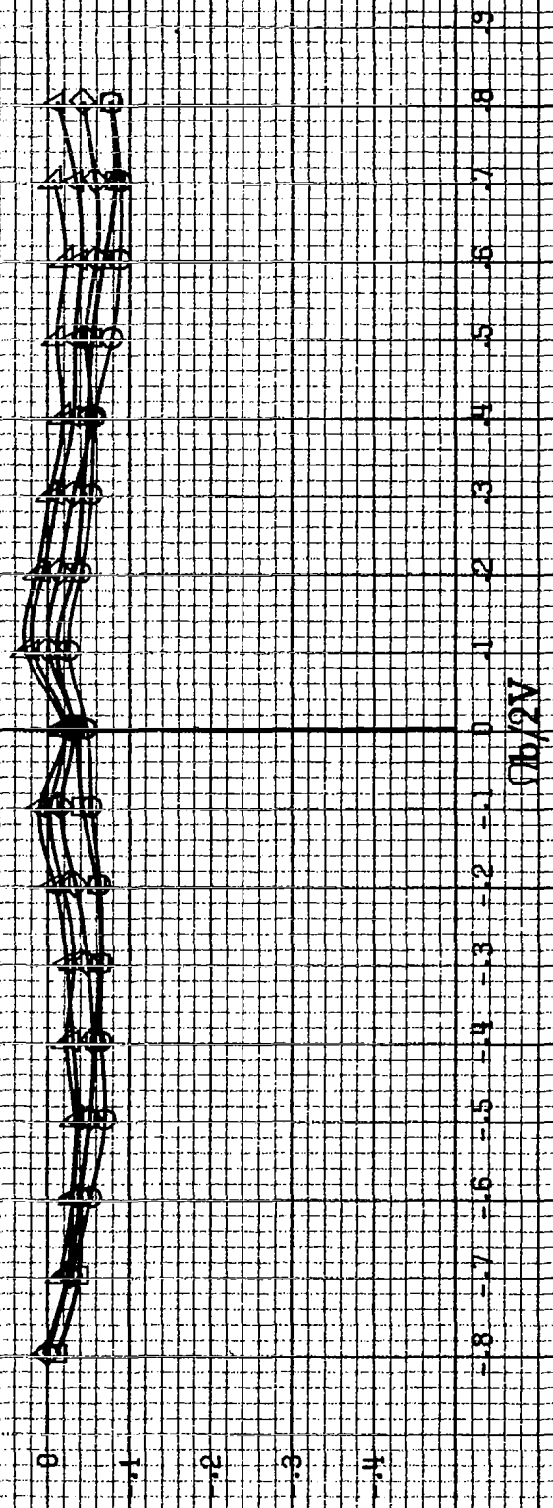
$b/2V$

(a) $\alpha = 8$ to 16 deg, $SR = 91.4$ cm (36 in).

Figure A.43.-Effect of rotation rate and angle of attack on axial force coefficient for long body, low wing, horizontal T-tail configuration. $\delta_e = 0^\circ$, $\delta_w = 0^\circ$, $\delta_r = 0^\circ$, $\delta = 0^\circ$.

C_A

α , deg
 ○ 18
 □ 20
 ◇ 25
 △ 30
 ▲ 35



(b) $\alpha = 18$ to 35° , $SR = 91.4 \text{ cm (36 in.)}$.
 Figure A 48.-Continued.

α , deg

○ 30

□ 35

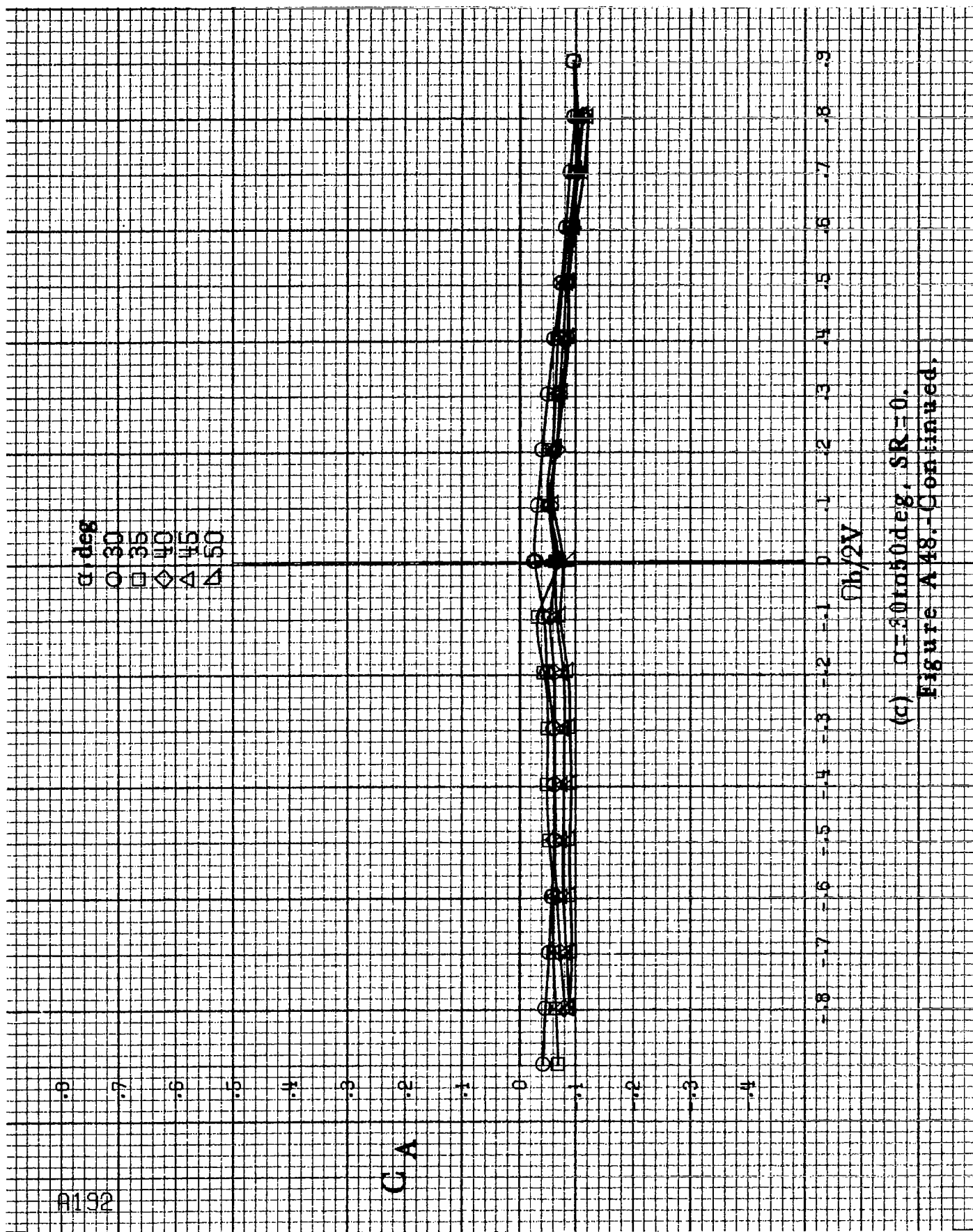
◇ 40

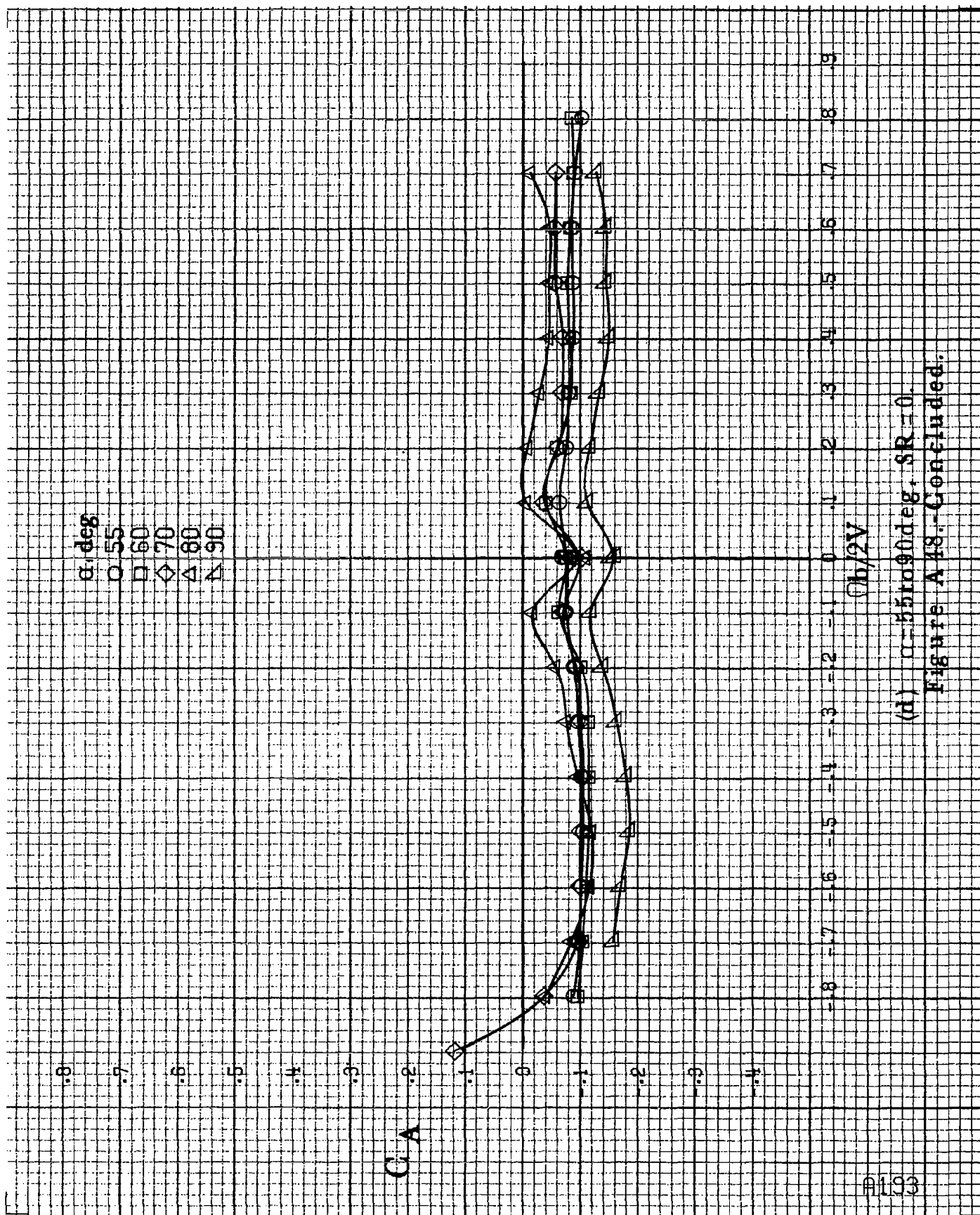
△ 45

▲ 50

 C_A $Ch/2V$ (a) $\alpha = 30$ to 50 deg, $SR = 0$.

Figure A48.-Continued.





(d) $\alpha=55$ to 90 deg. $SR=0$.
Figure A48--Continued.

A134

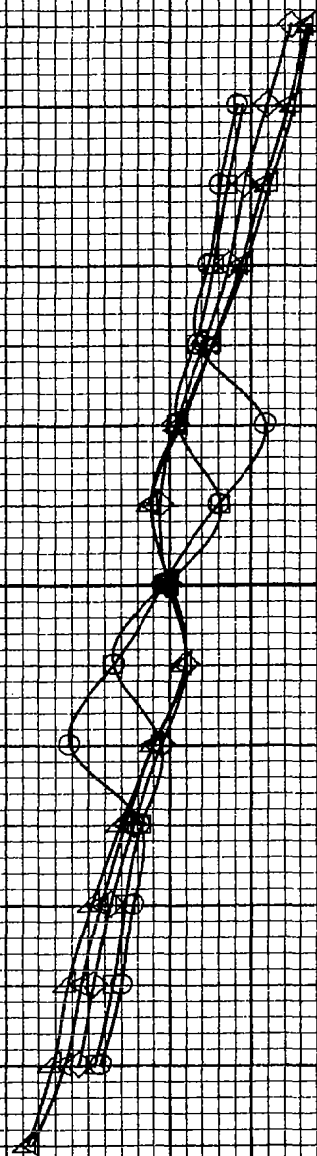
α , deg
 O 8
 □ 10
 ◇ 12
 △ 14
 ▴ 16

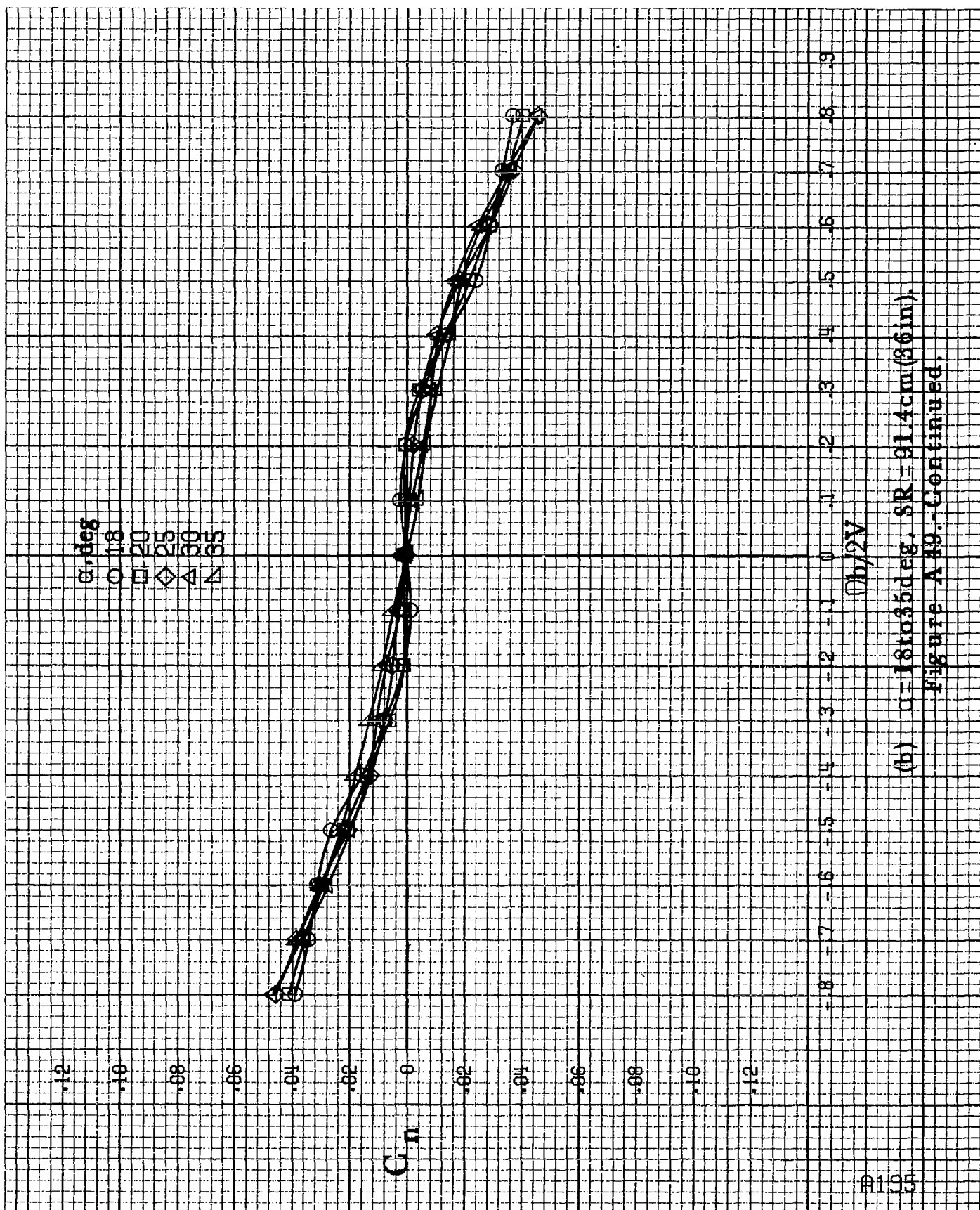
C_n

$b/2V$

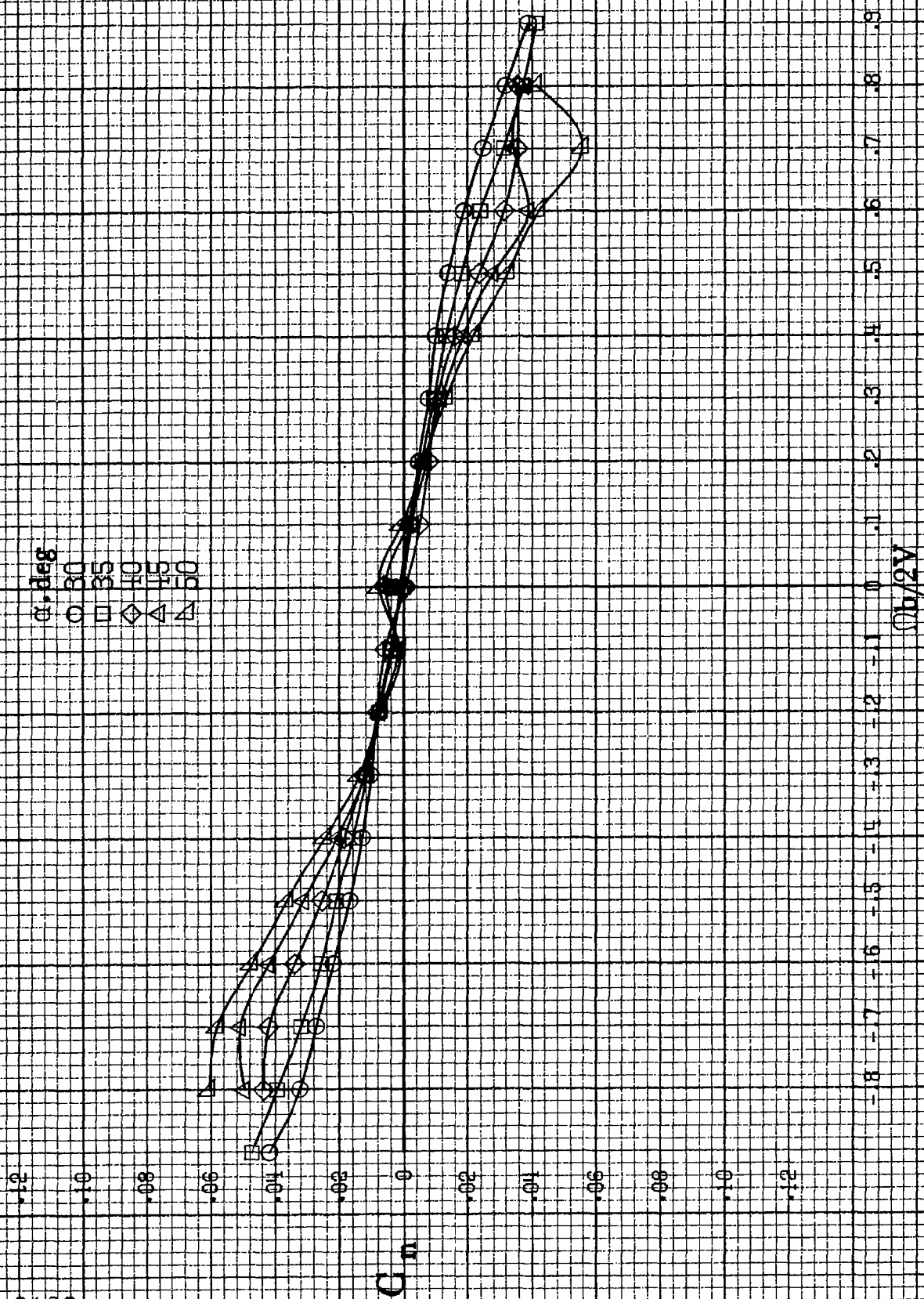
(a) $\alpha = 8$ to 16 deg, $SR = 91.4$ cm (36 in).

Figure A42.-Effect of rotation rate and angle of attack on yawing-moment coefficient for long body, low wing, horizontal T-tail configuration.
 $\delta_a = 0^\circ$, $\delta_r = 0^\circ$, $\delta_s = 0^\circ$.

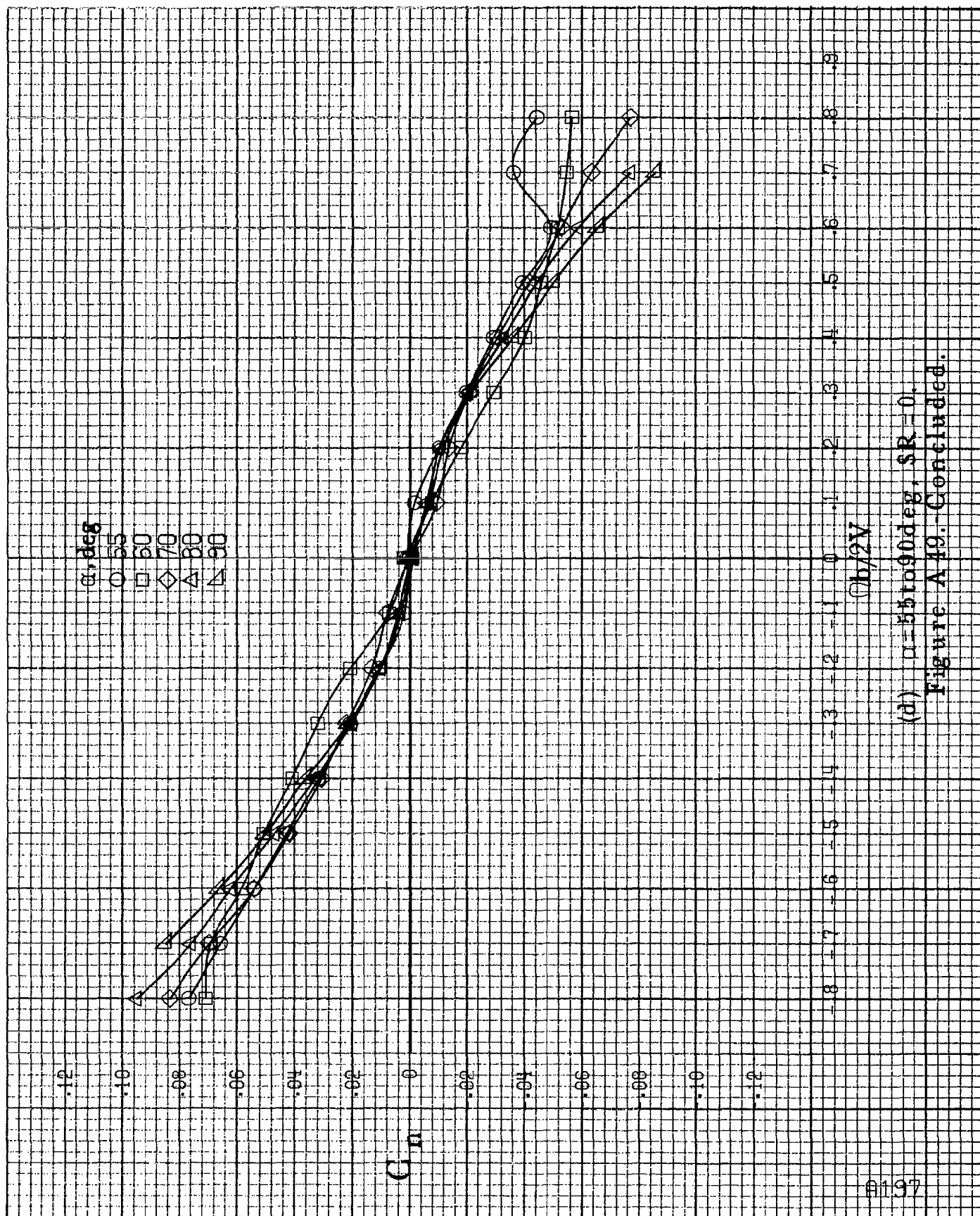




(b) $\alpha=18$ to 35° deg, $SR=91.4$ cm (36 in).
Figure A 49.-Continued.

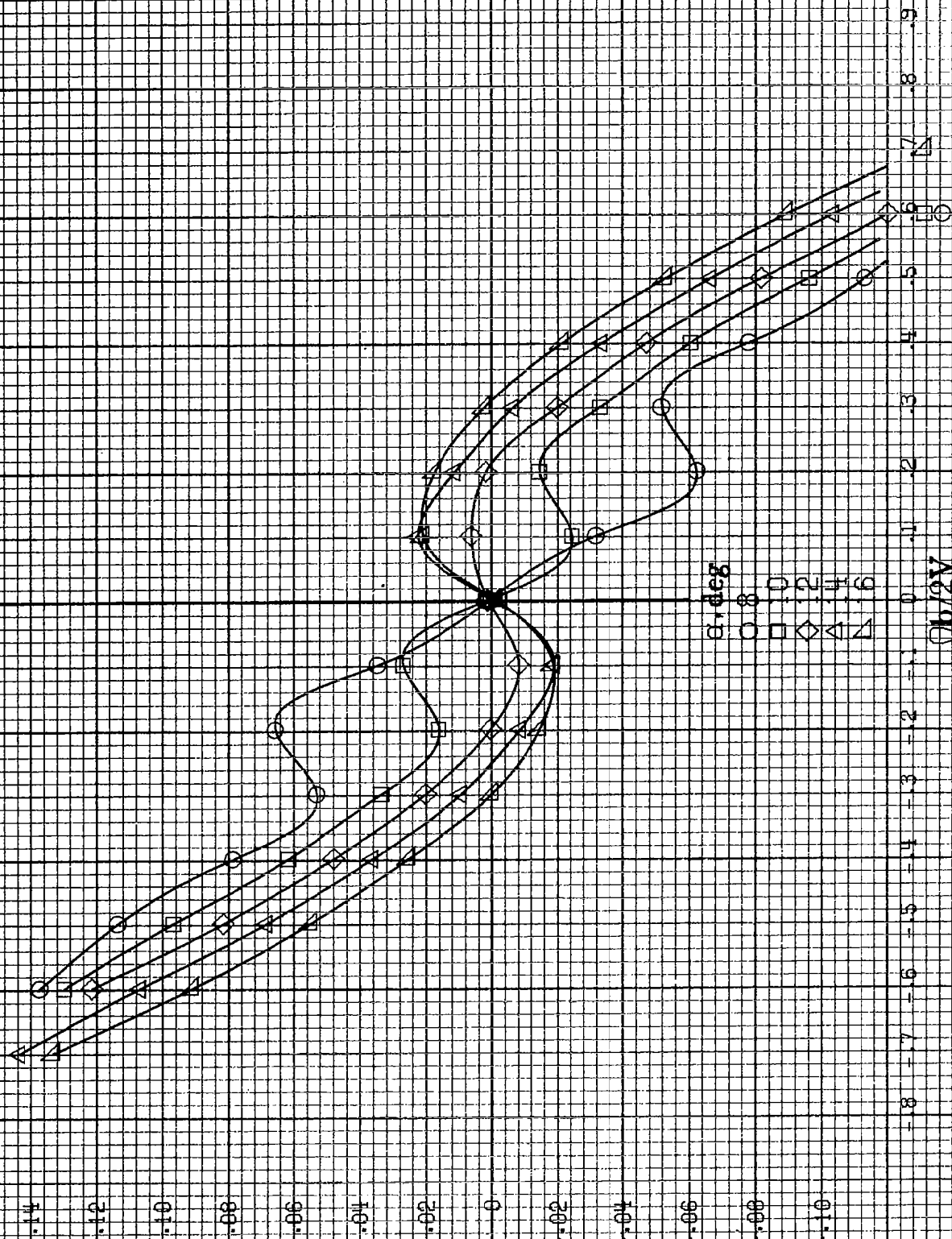


(c) $\alpha=30$ to 50 deg, $SR=0$.
Figure A49.-Continued.



(d) $\alpha=55$ to 90 deg, $SR=0$.
Figure A19. - Concluded.

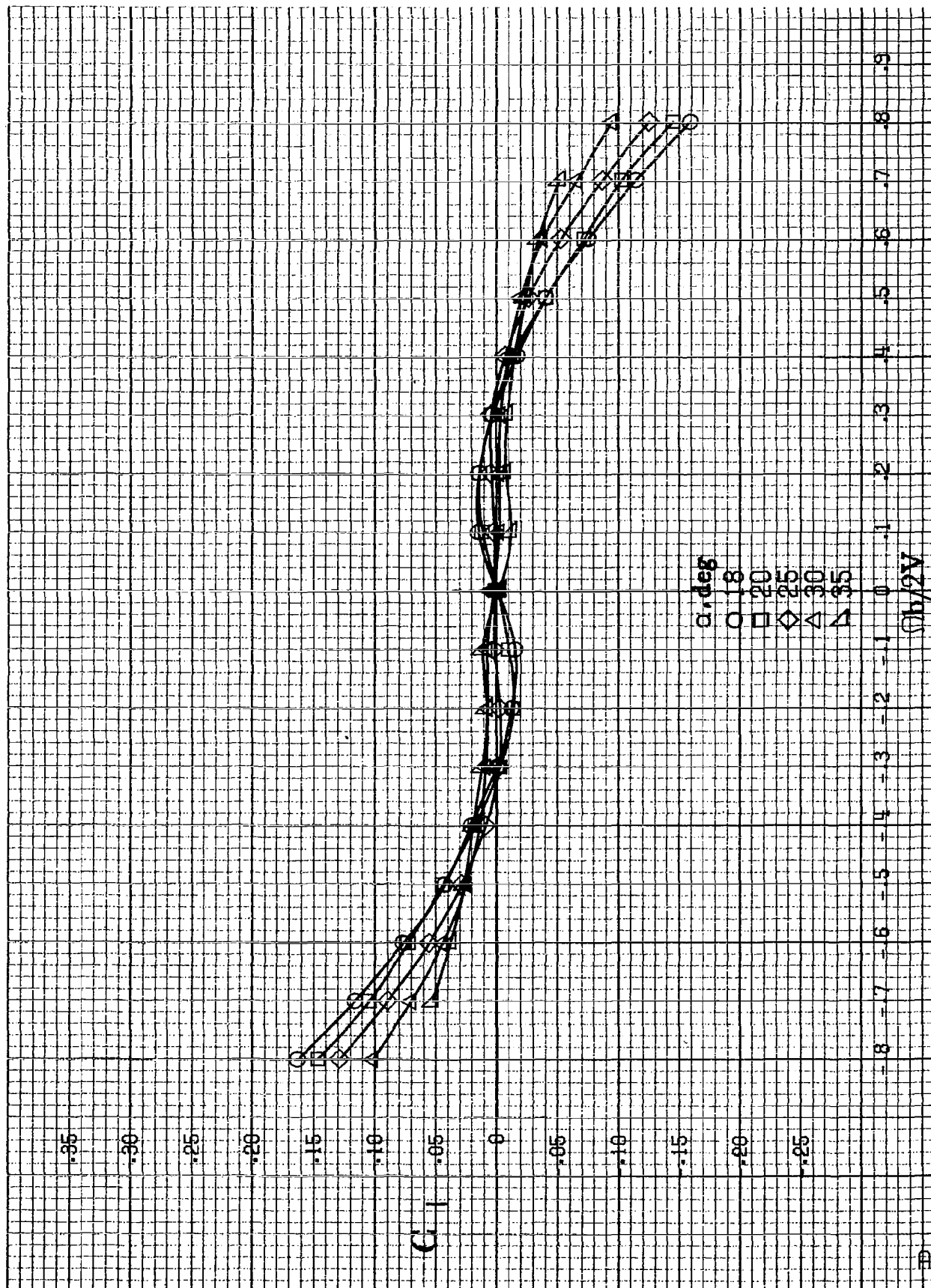
C_l



(a) $C = 8$ to 16° , $SR = 91.4$ cm (36 in).

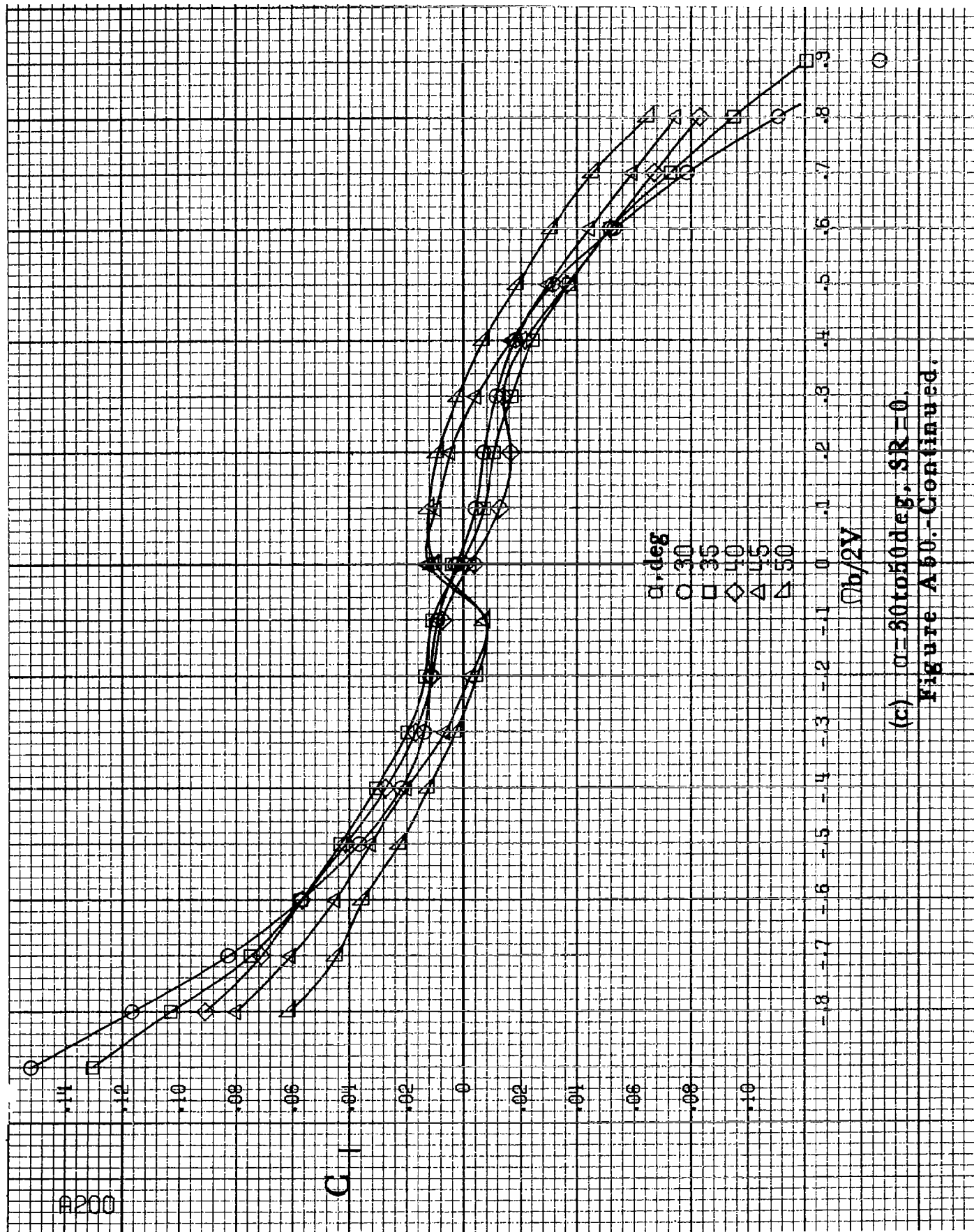
Figure A.50. - Effect of rotation rate and angle of attack on rolling-moment coefficient for long body, low wing, horizontal T-tail configuration.

$\delta_e = 0^\circ$, $\delta_r = 0^\circ$, $\delta_a = 0^\circ$.



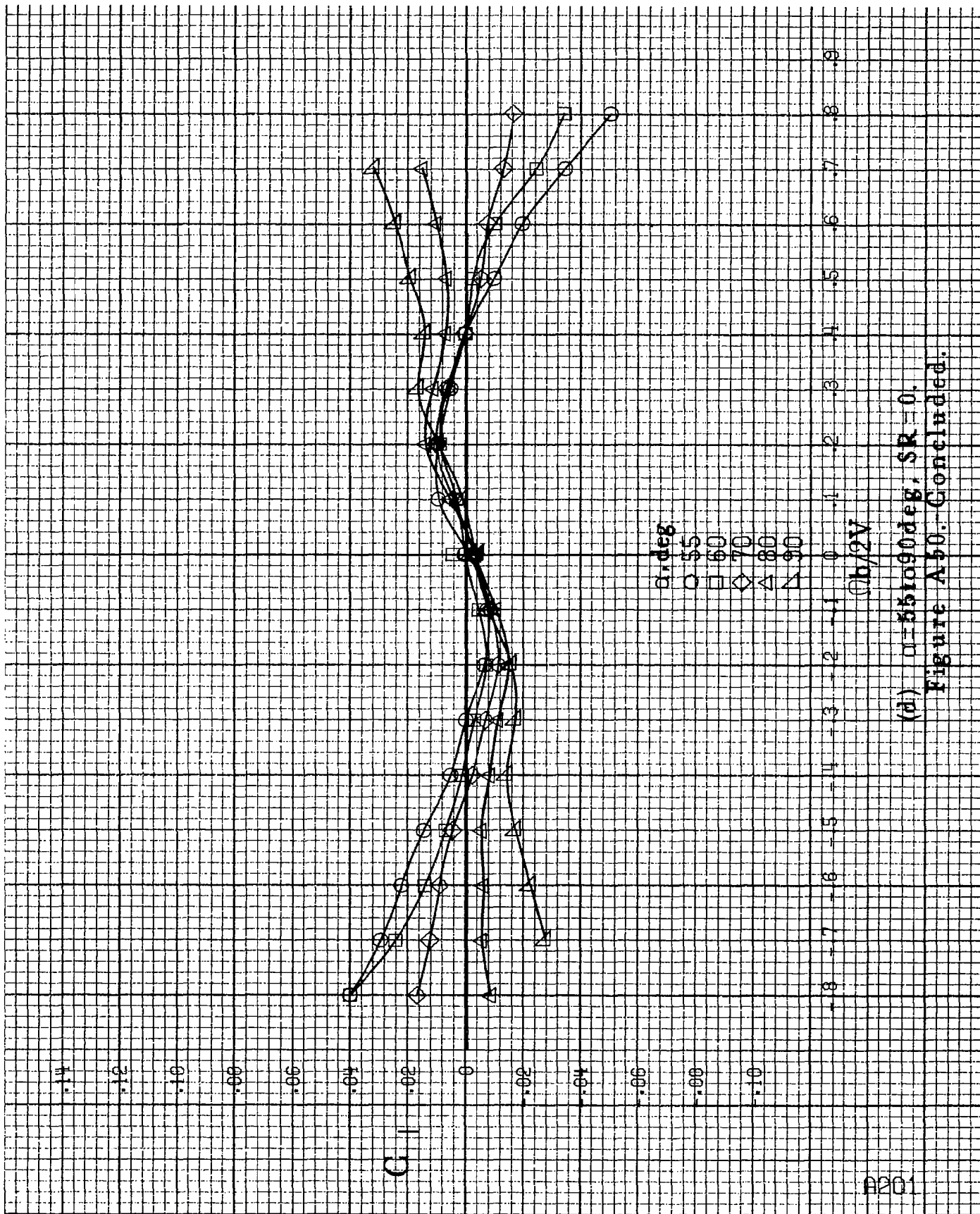
(b) $\alpha = 18$ to 35° , SR-91.4cm (36in).

Figure A50.-Continued.

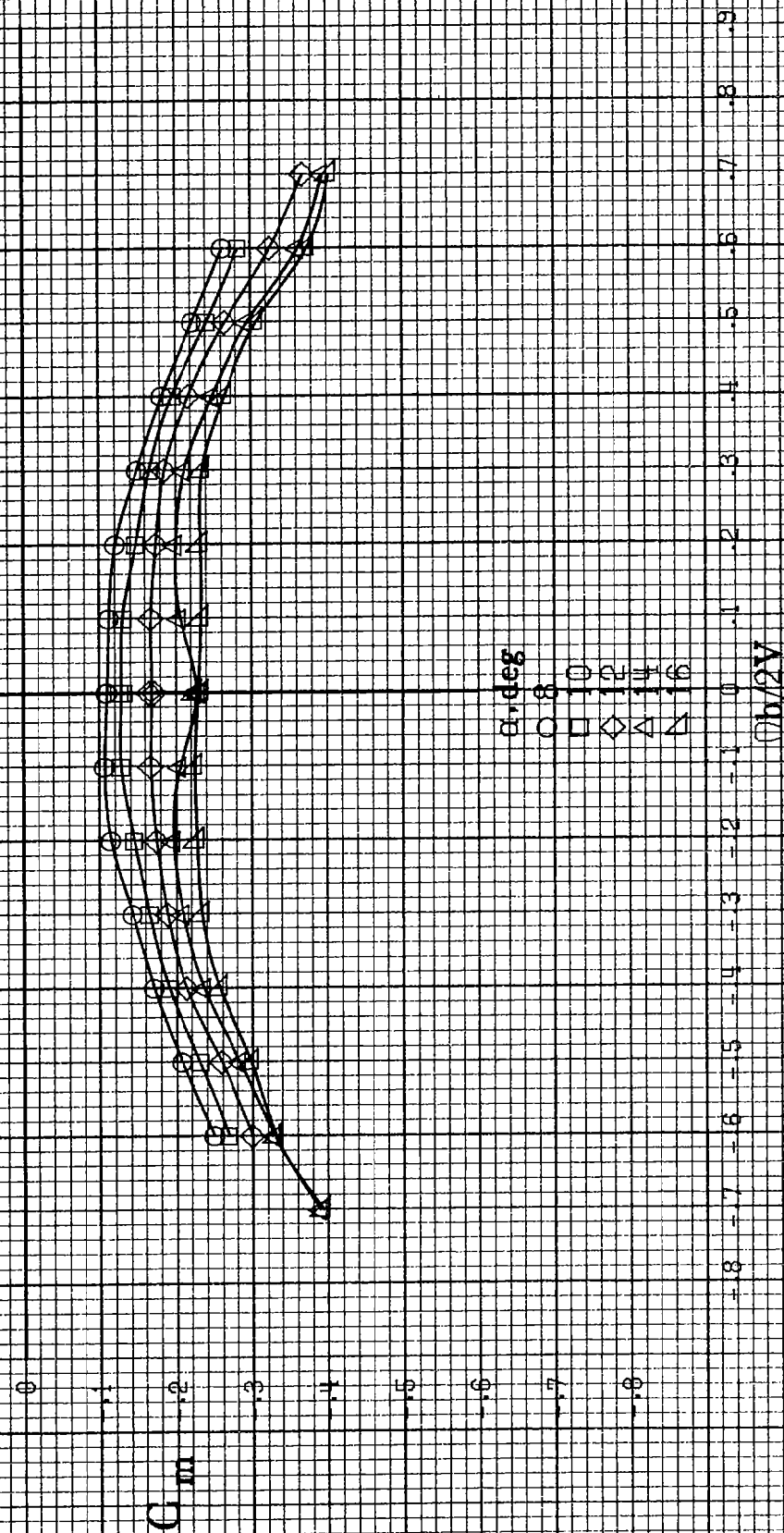


(c) $\alpha=30$ to 50 deg, $SR=0$.

Figure A60.-Continued.

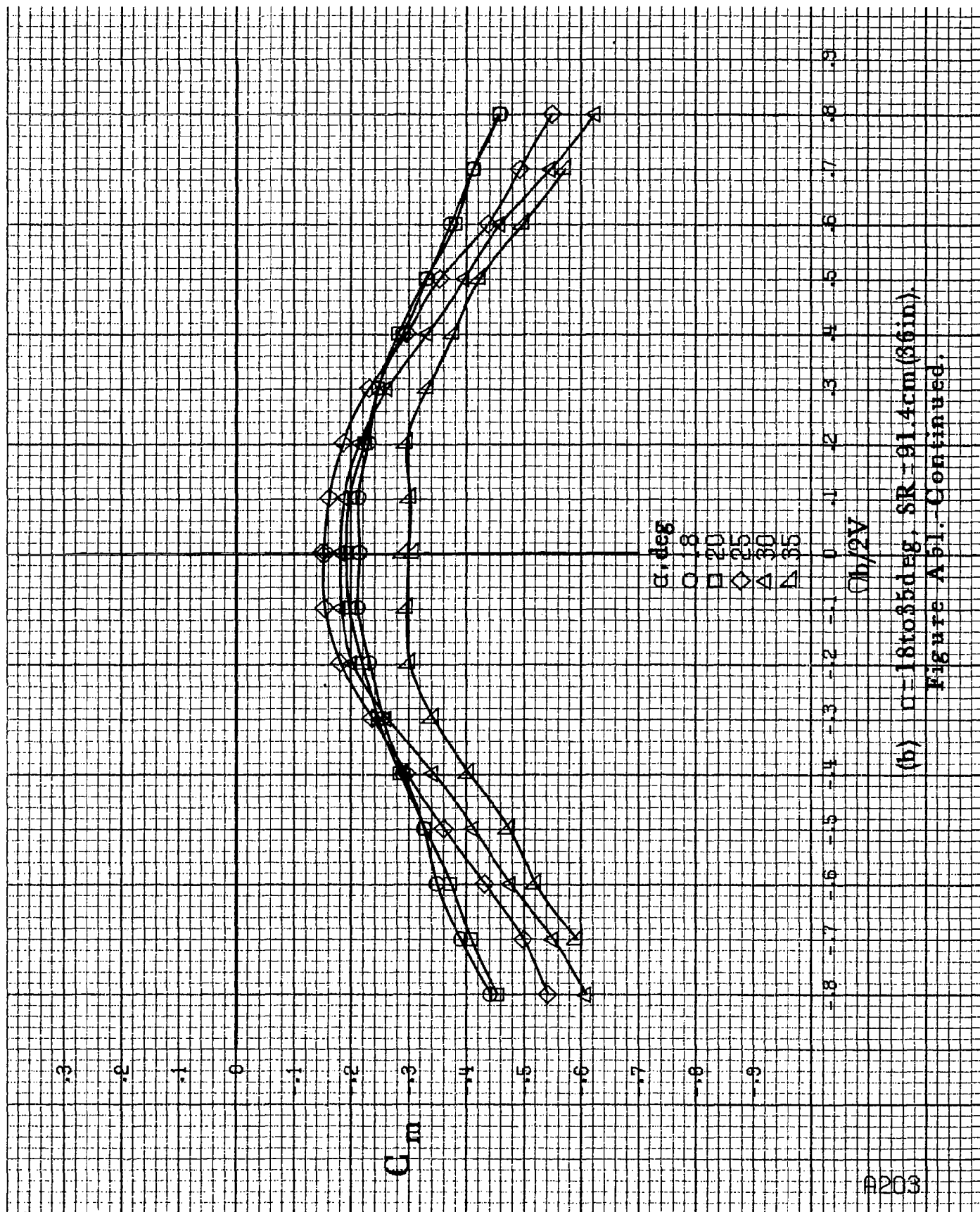


(d) $\alpha = 55$ to 90° , $SR = 0$.
Figure A50. Concluded.



(a) $\alpha = 8$ to 16° , $SR = 91.4$ cm (36 in.).

Figure A51.-Effect of rotation rate and angle of attack on pitching-moment coefficient for long body, low wing, horizontal T-tail configuration. $\delta\alpha = 0^\circ$, $\delta\alpha = 0^\circ$, $\delta\alpha = 10^\circ$, $\delta\alpha = 10^\circ$.



8204

C_m

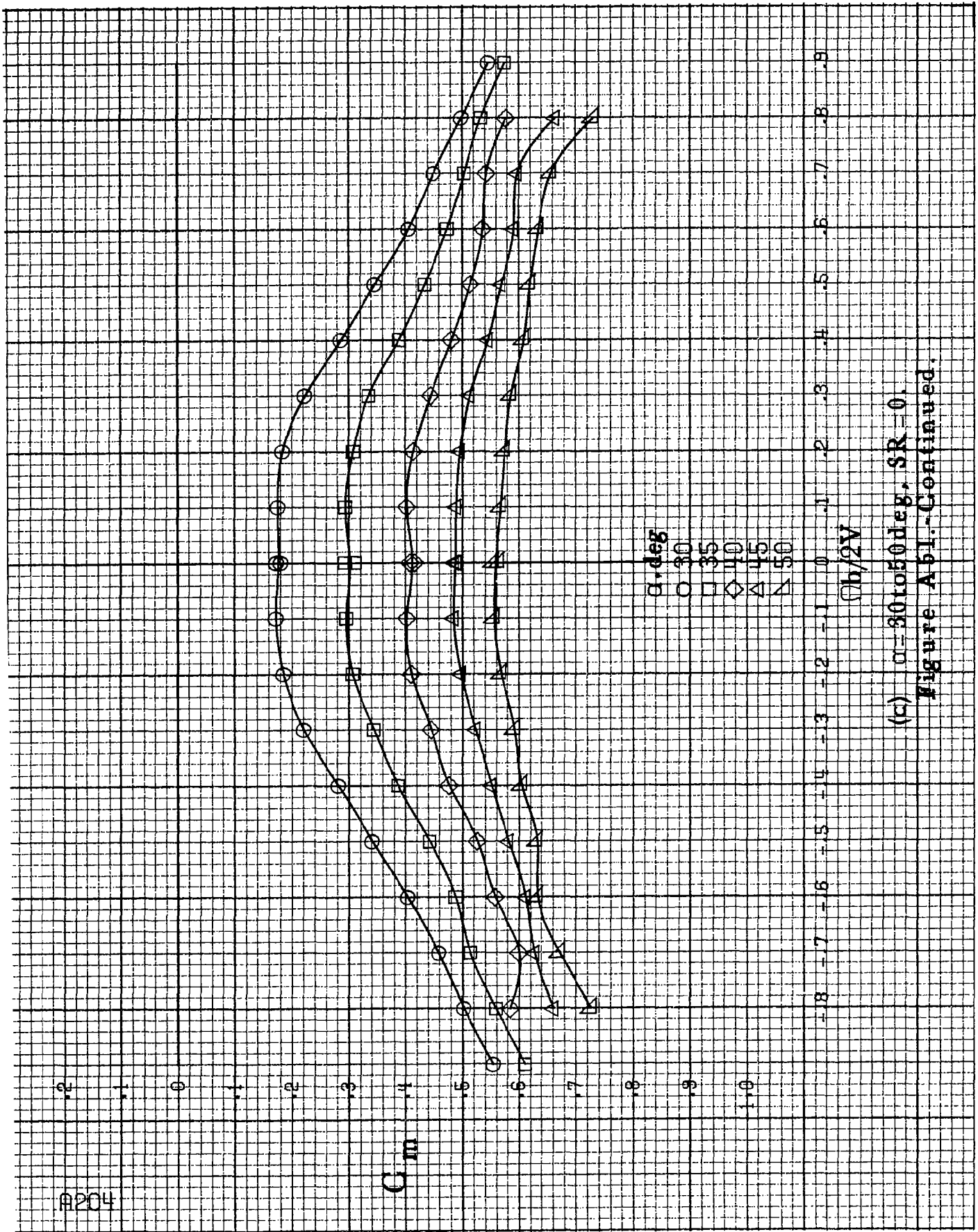
α, deg

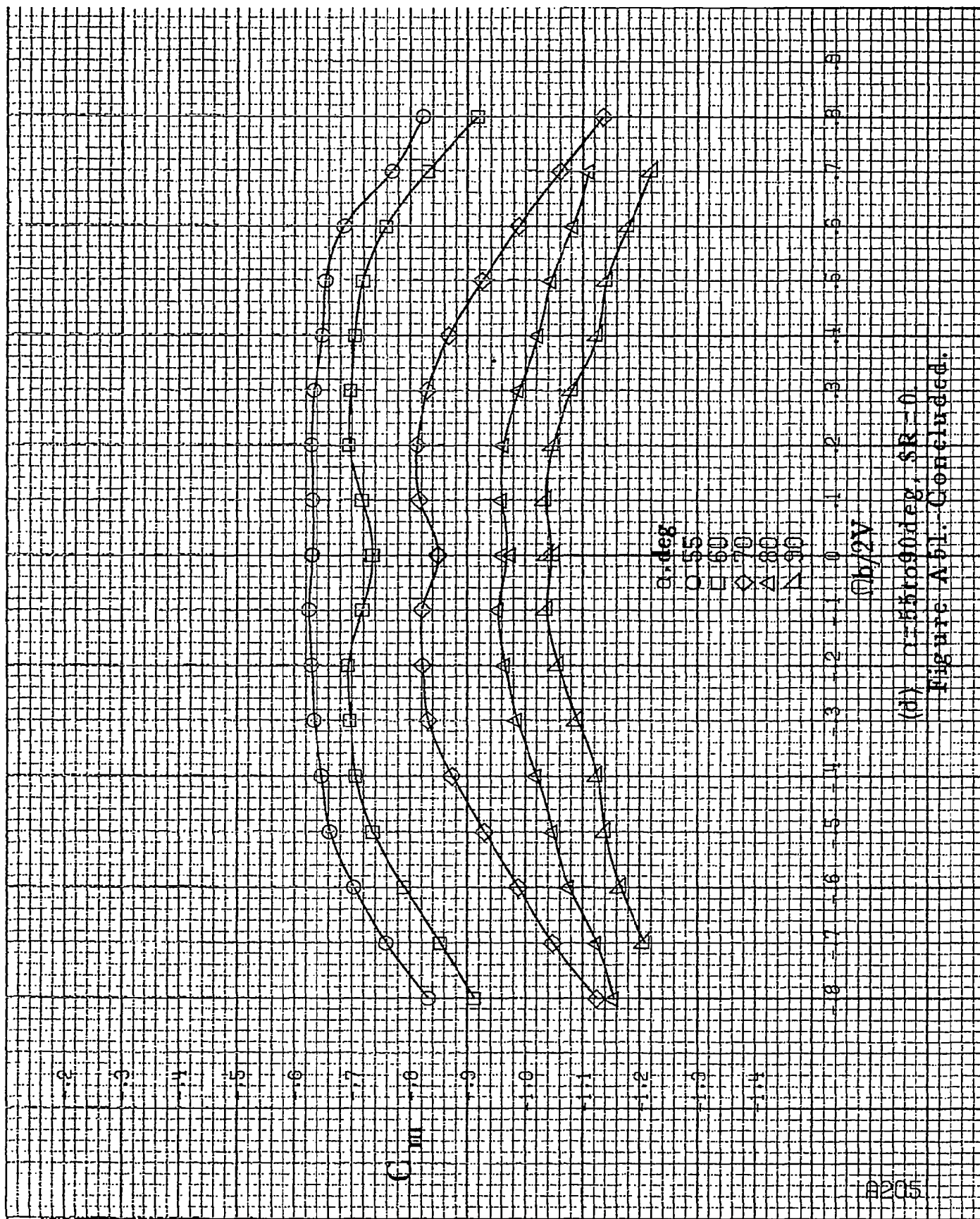
- 30
- 35
- ◇ 40
- △ 45
- ▽ 50

$b/2V$

(c) $\alpha=30$ to 50 deg, $SR=0$.

Figure A61.-Continued.

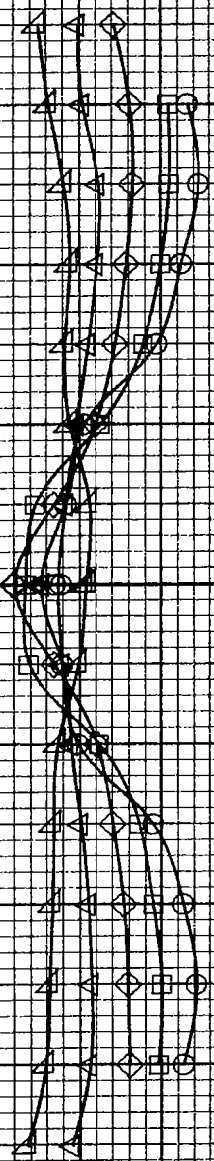




(a) $\alpha=55$ to 90° , $SR=0$
Figure A51. Concluded.

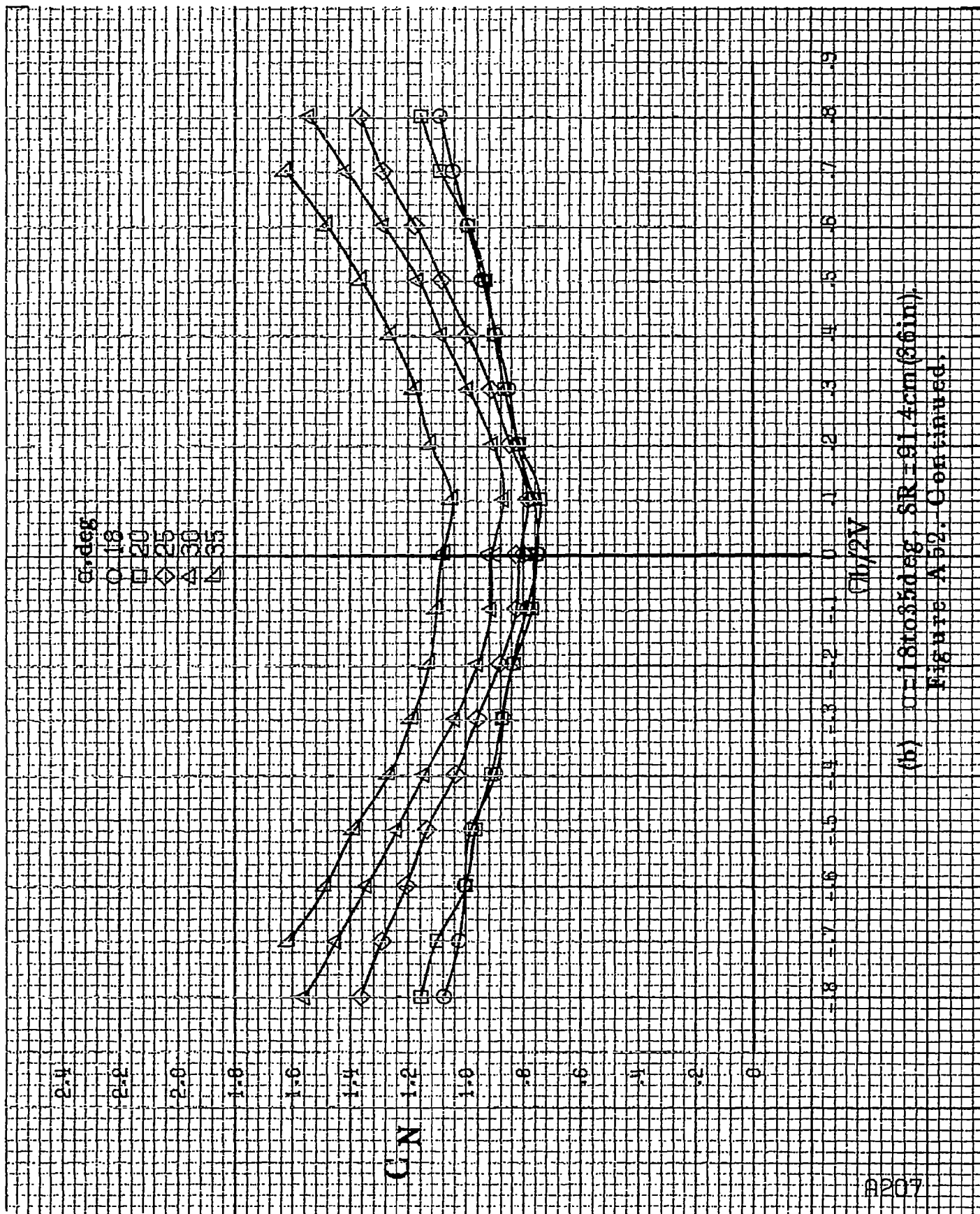
α, deg

3
10
12
14
16



(a) $\alpha = 8 \text{ to } 16^\circ$, $SR = 0.14 \text{ cm (36 in.)}$.

Figure A52.-Effect of notation rate and angle of attack on normal-force coefficient for long body, low wing, horizontal T-tail configuration. $\delta_e = 0^\circ$, $\delta_a = 0^\circ$, $\delta_r = 0^\circ$, $\beta = 0^\circ$.



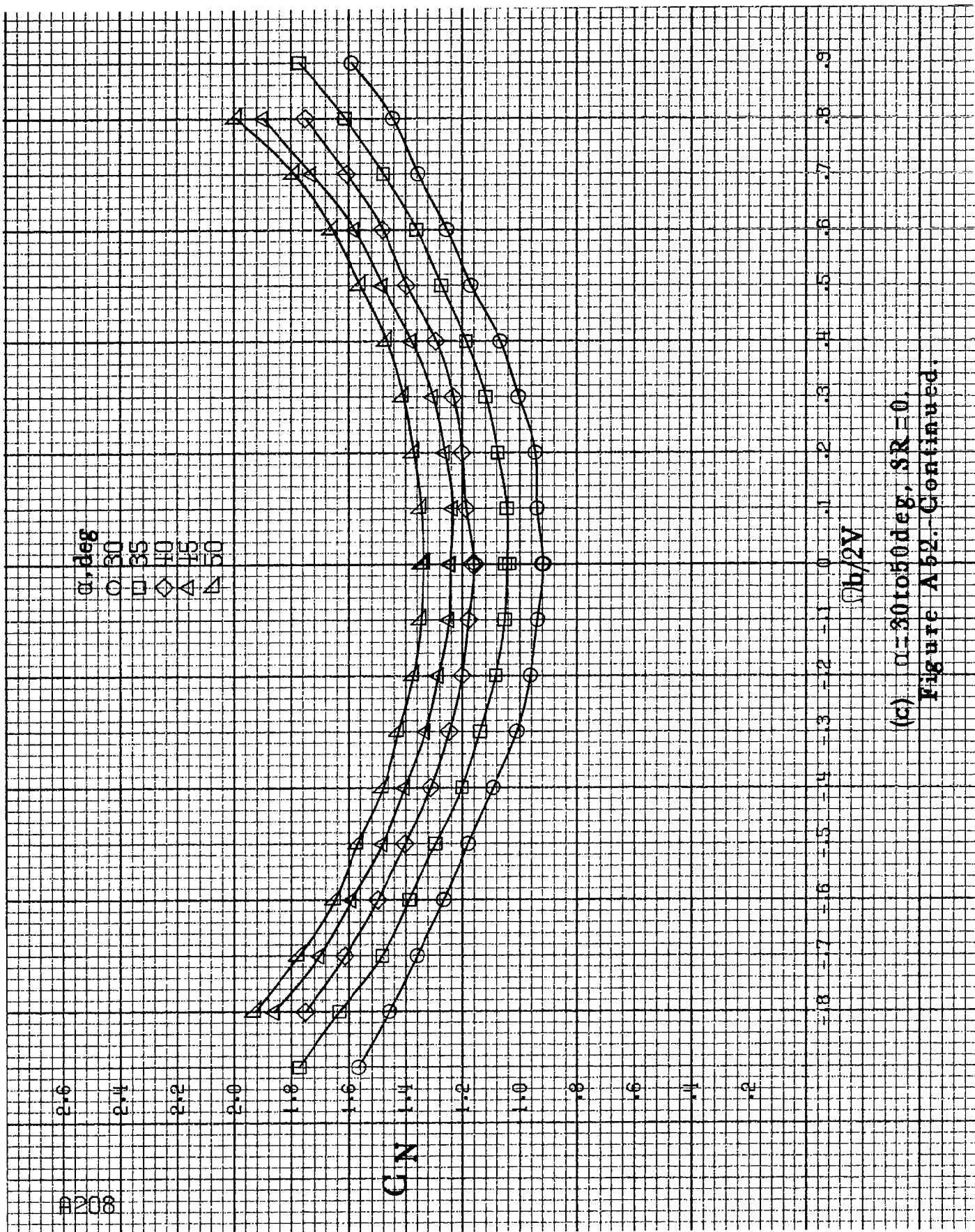
(b) $\alpha=18$ to 35° , $SR=91.4\text{cm}(36\text{in})$.
Figure A52. Continued.

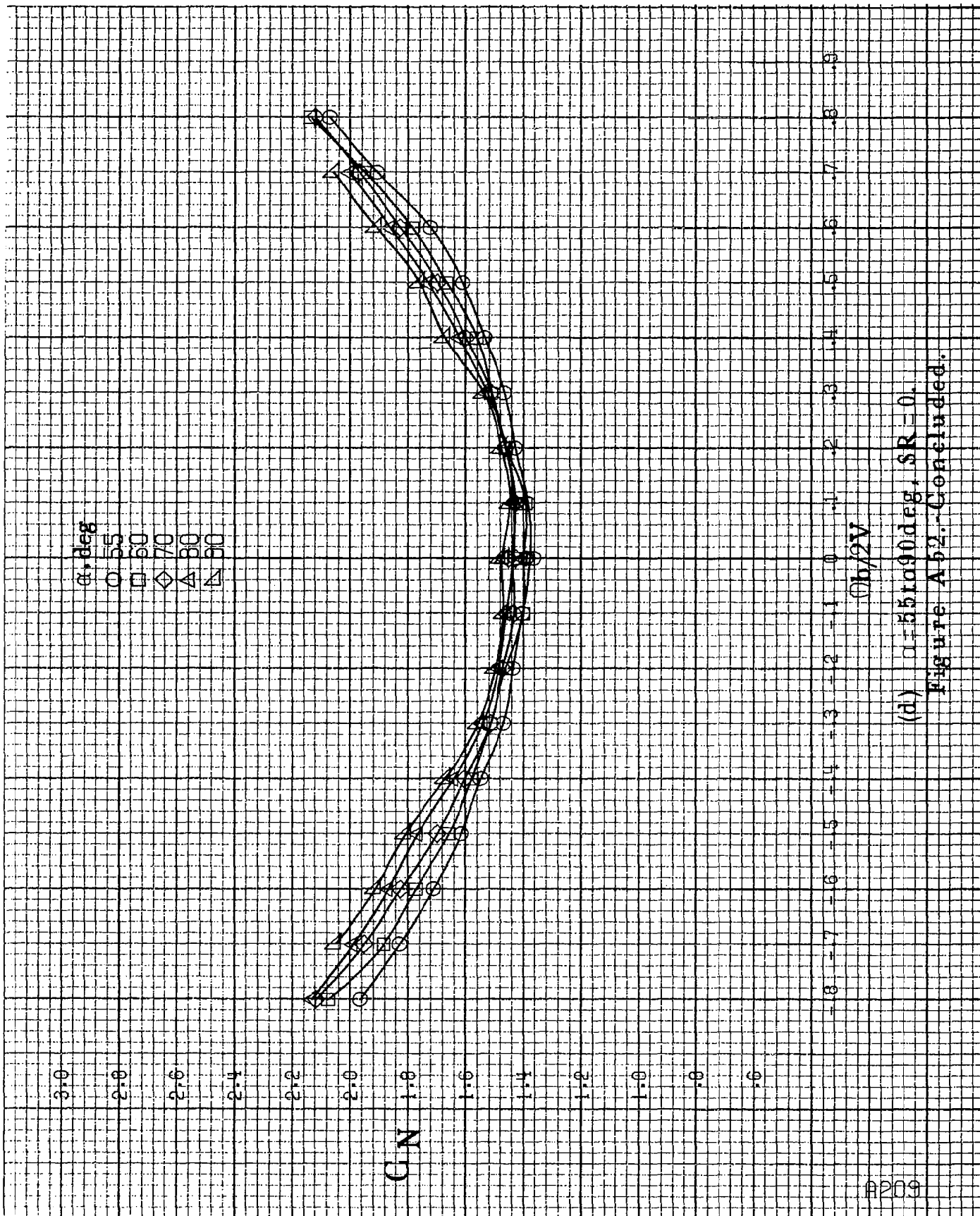
α, deg
 ○ 30
 □ 35
 ◇ 40
 △ 45
 ▽ 50

C/N

$b/2V$

(c) $\alpha=30$ to 50 deg, $SR=0$,
 Figure A52.-Continued.





(d) $\alpha = 55$ to 90° , $SR = 0$.
Figure A52.-Concluded.

210

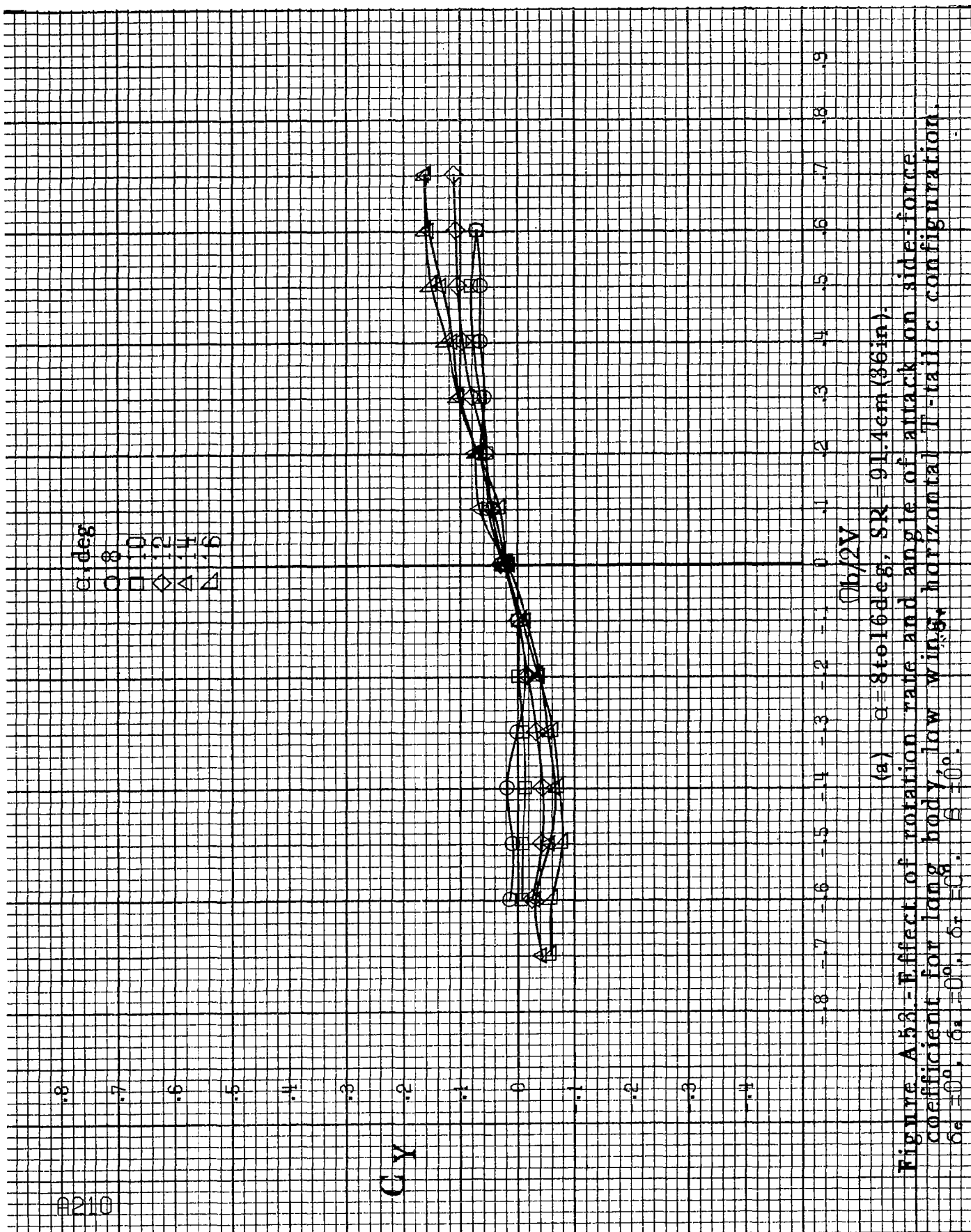
α, deg
 8
 10
 12
 14
 16

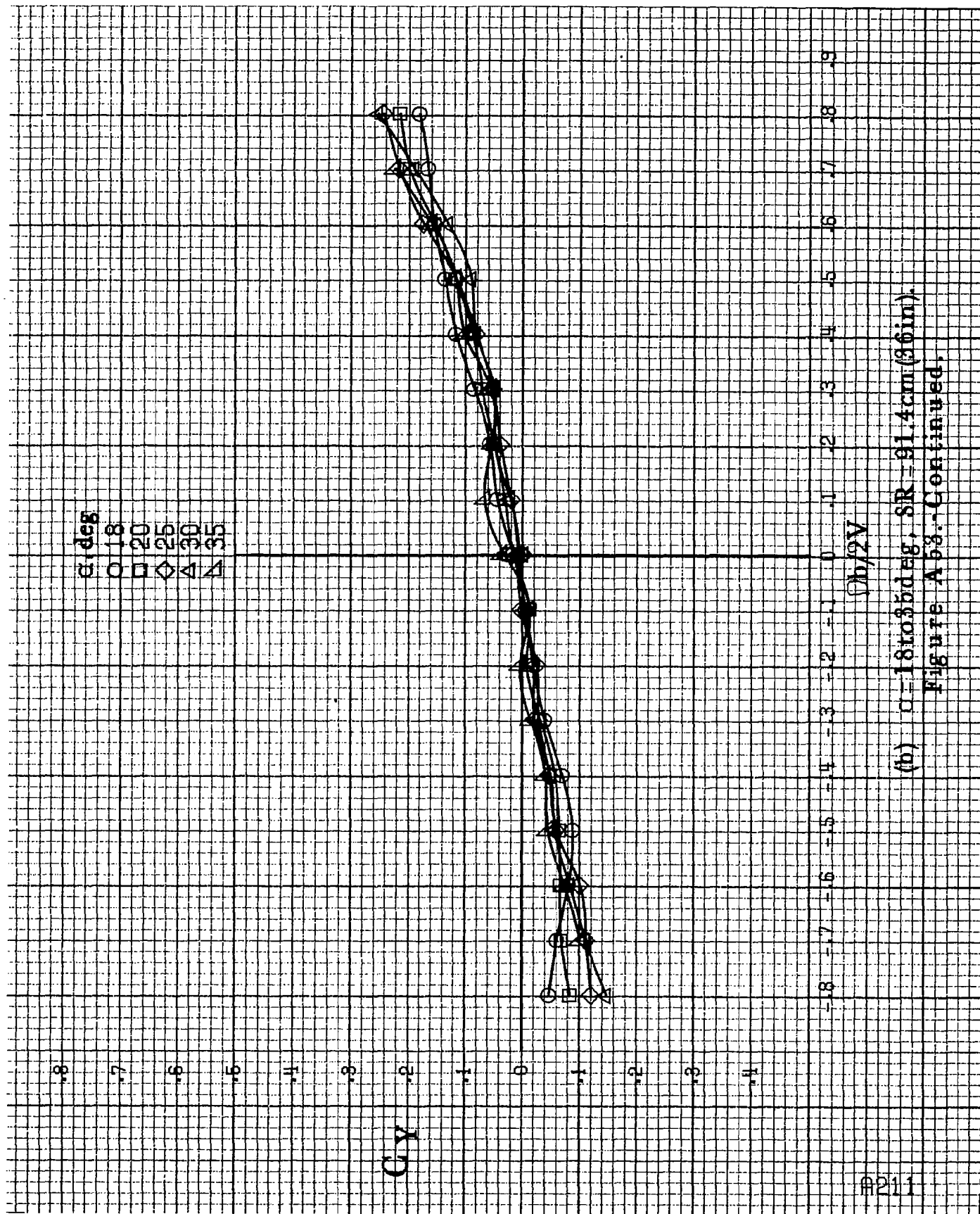
C_y

$Q_b/2V$

(a) $\alpha = 8 \text{ to } 16 \text{ deg}$, $SR = 91.4 \text{ cm (36 in)}$.

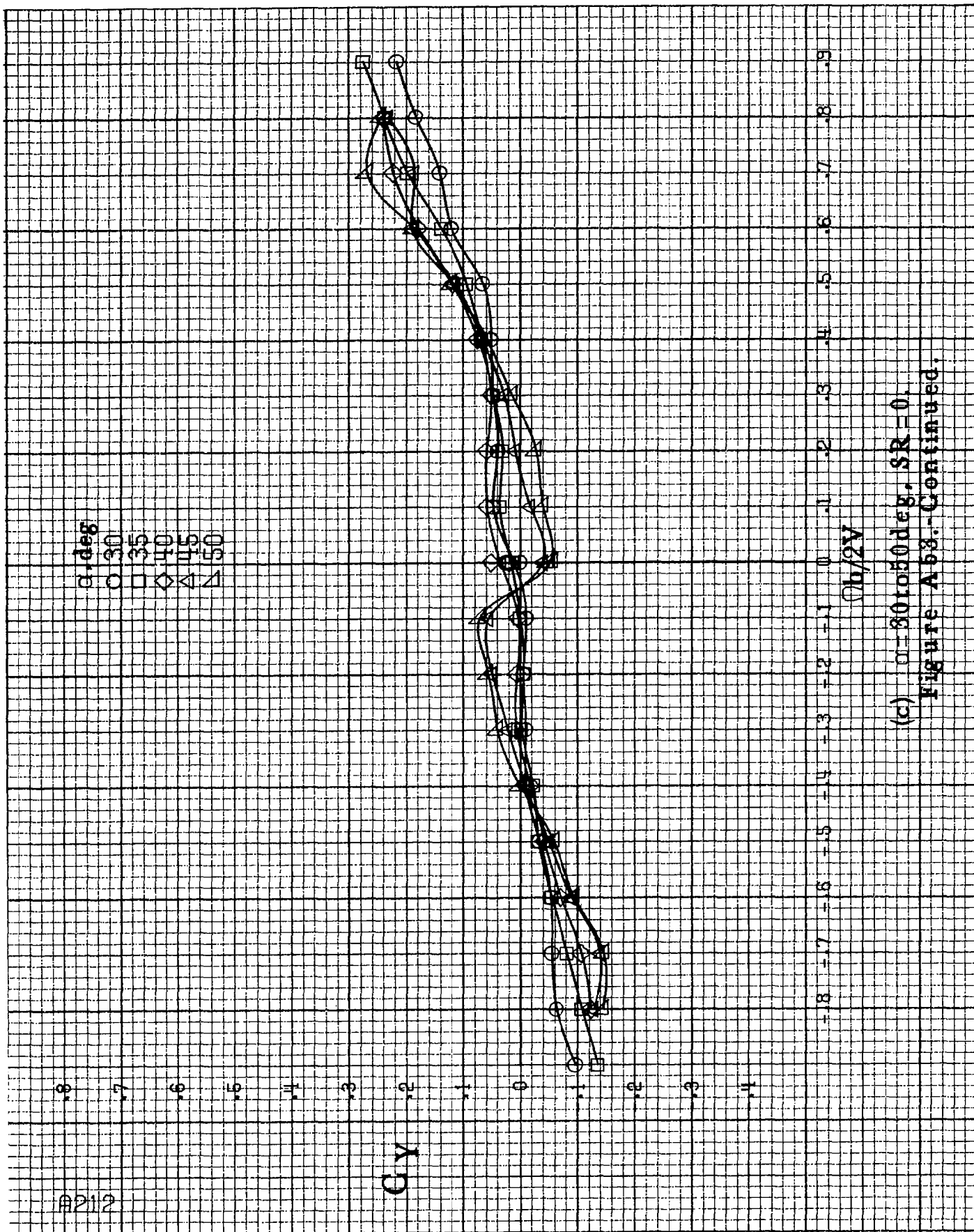
Figure A53 - Effect of rotation rate and angle of attack on side-force coefficient for long body, low wing, horizontal T-tail c configuration. $\delta_a = 0^\circ$, $\delta_r = 0^\circ$, $\delta_s = 0^\circ$.

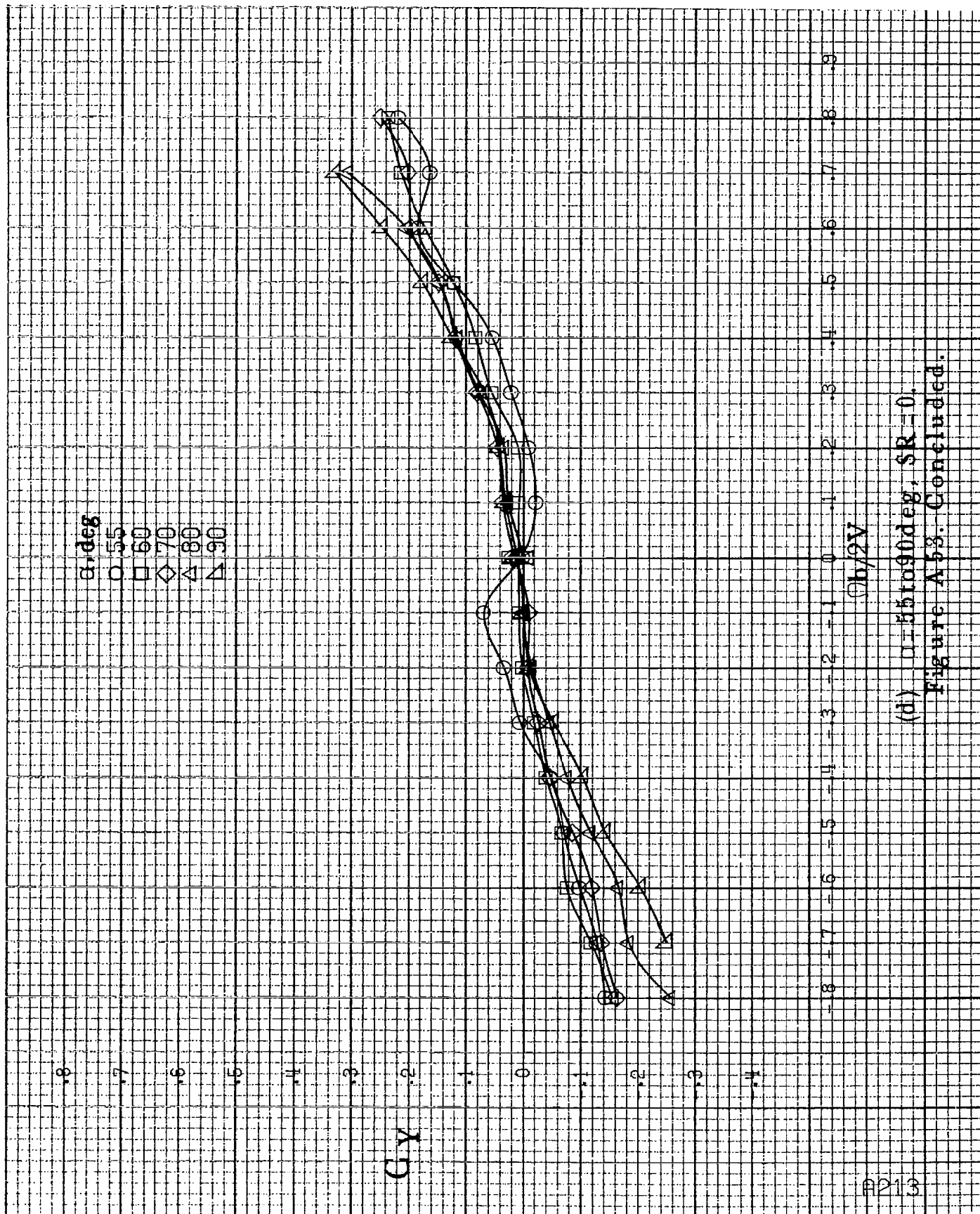




(b) $\alpha=18$ to 35° , $SR=91.4\text{cm}(36\text{in})$.

Figure A53.-Continued.





82114

α , deg
 0 8 10 12 14 16
 ○ □ ◇ △ ▽

C.A

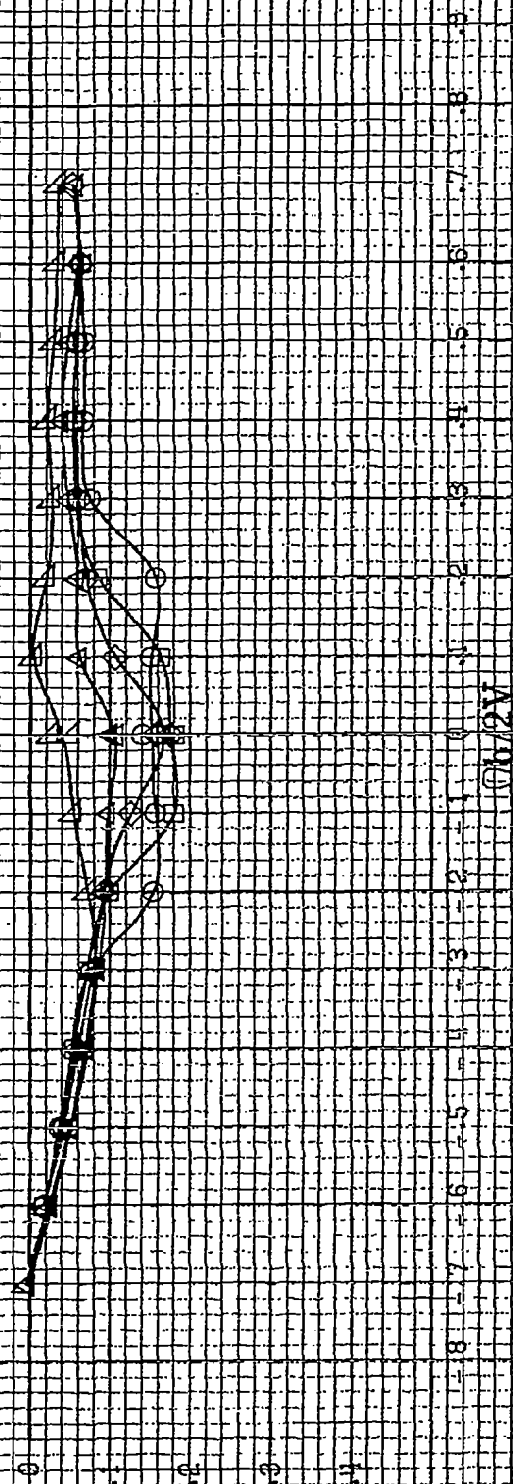
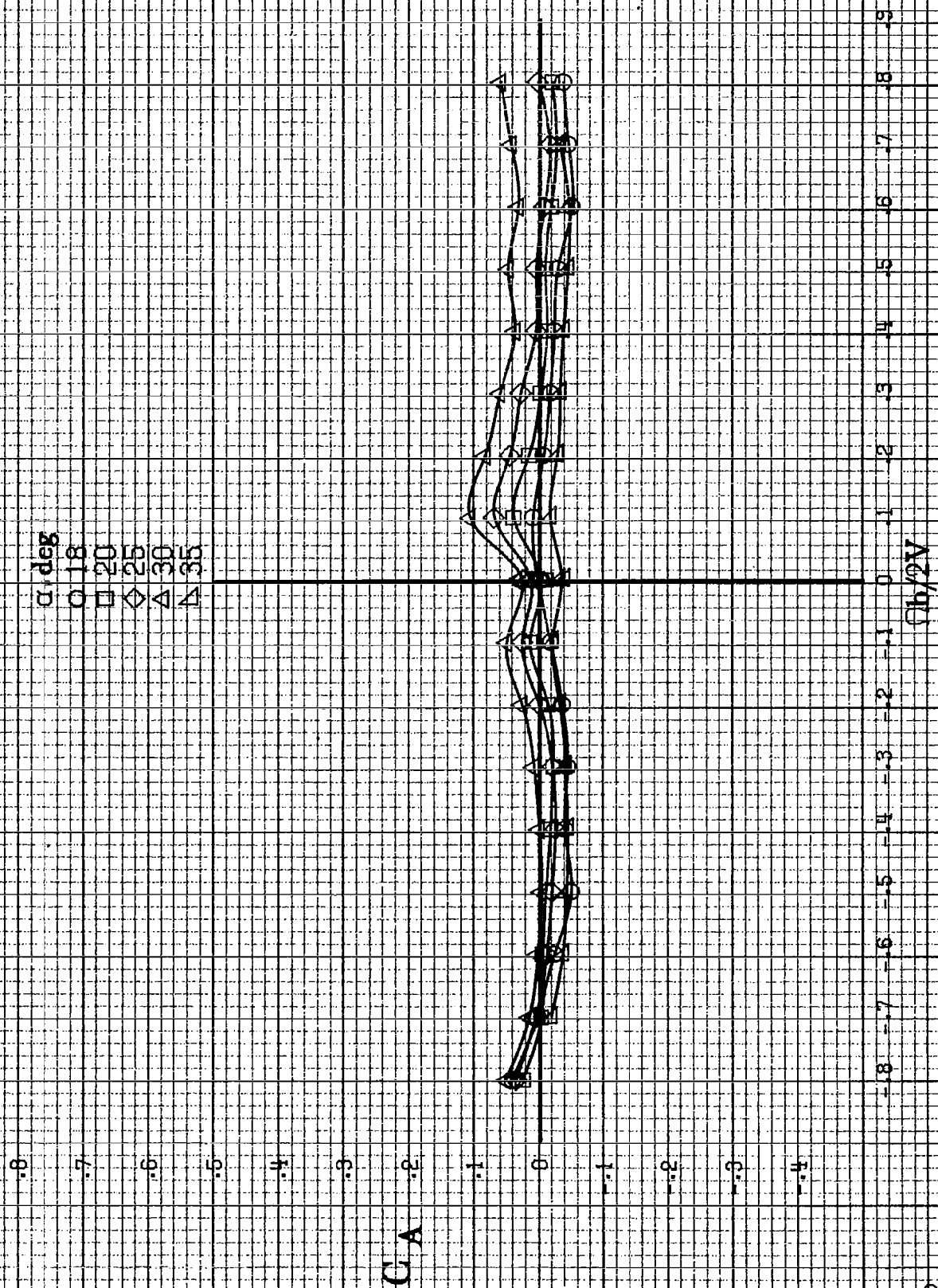


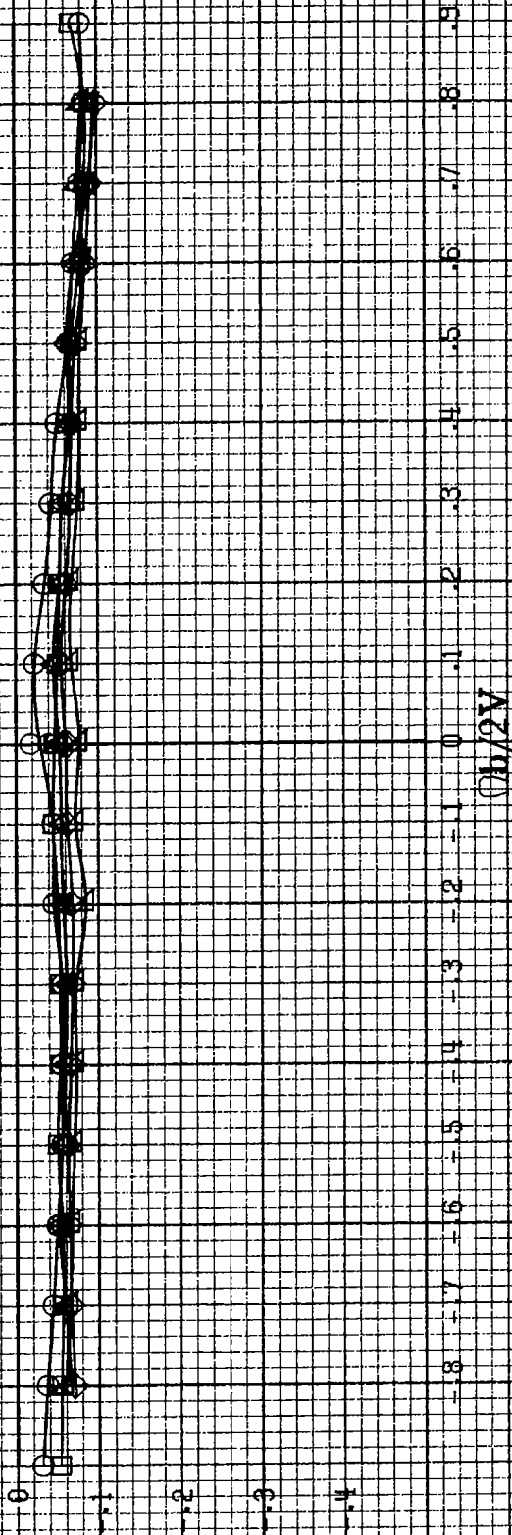
Figure A154 - Effect of rotation rate and angle of attack on lift coefficient for long body, low wing, horizontal T-tail configuration.
 $\alpha = 0^\circ, 8^\circ, 10^\circ, 12^\circ, 14^\circ, 16^\circ$
 (a) $B = 8$ to 16 deg, $SR = 91.4$ cm (36 in).



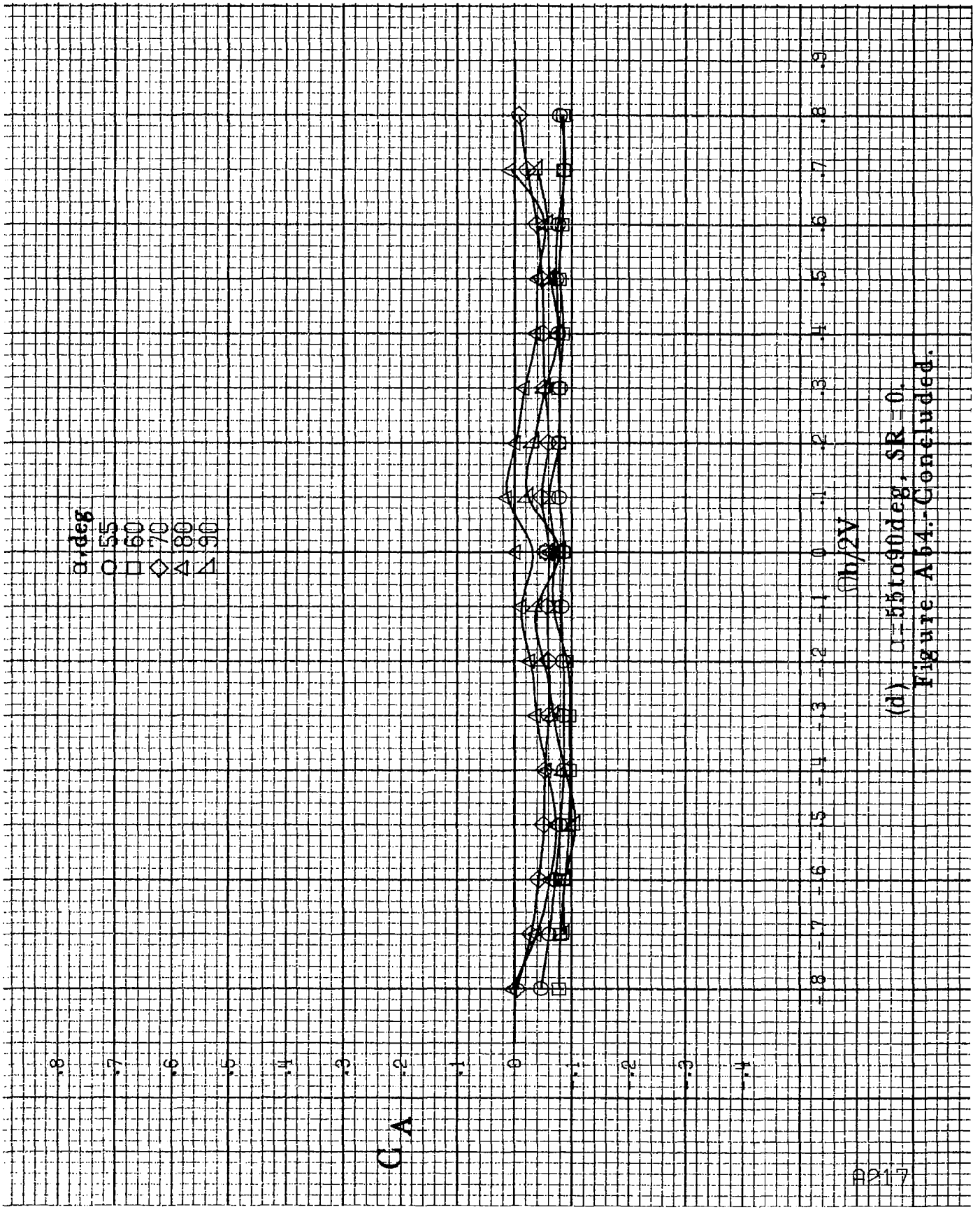
(b) $\alpha = 18$ to 35° , $SR = 91.4 \text{ cm (36 in.)}$.
Figure A 54. Continued.

α, deg
 \circ 30
 \square 35
 \diamond 40
 \triangle 45
 ∇ 50

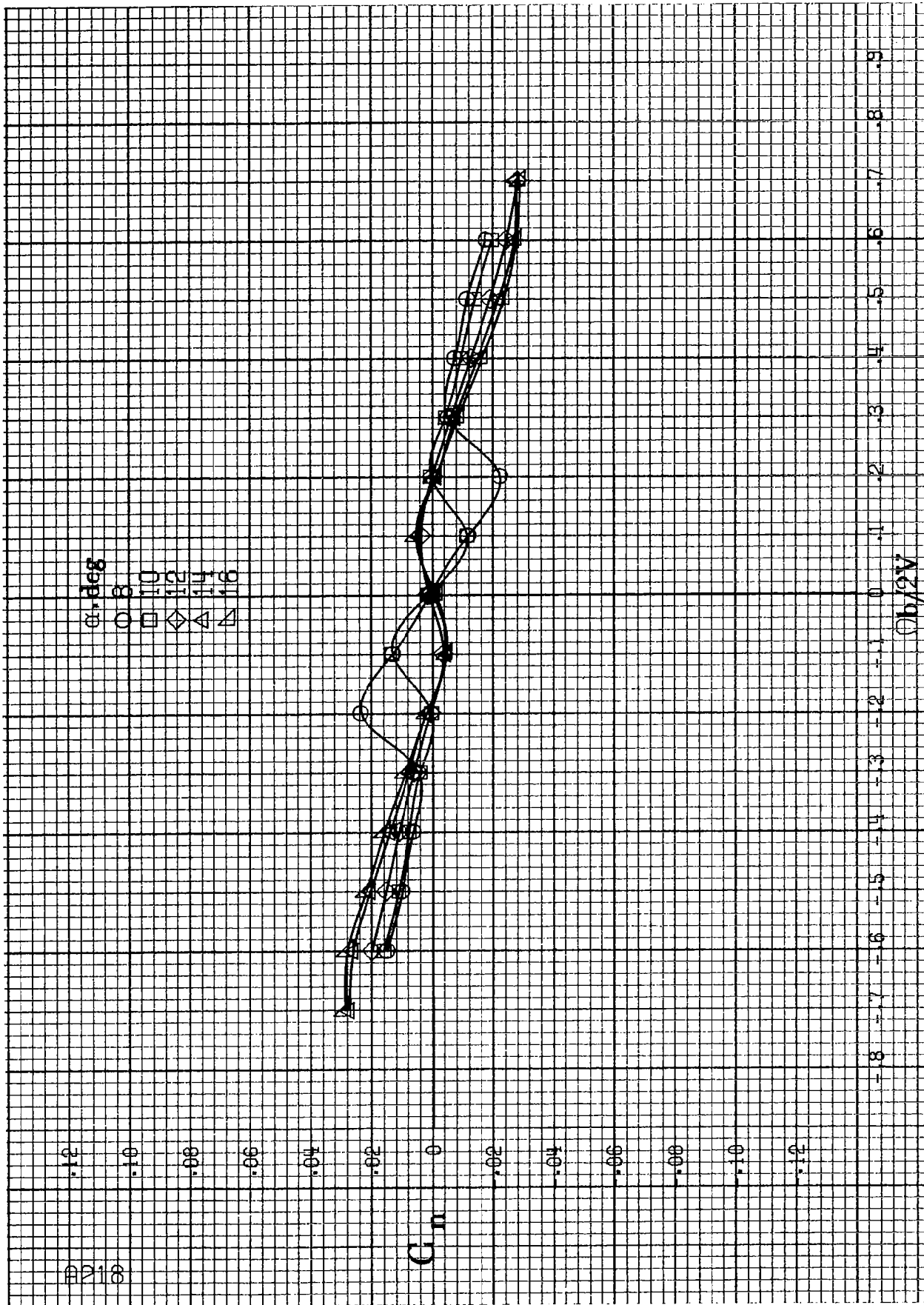
G_A



(c) $\alpha=30$ to 50 deg, $SR=0$.
 Figure A64.-Continued.

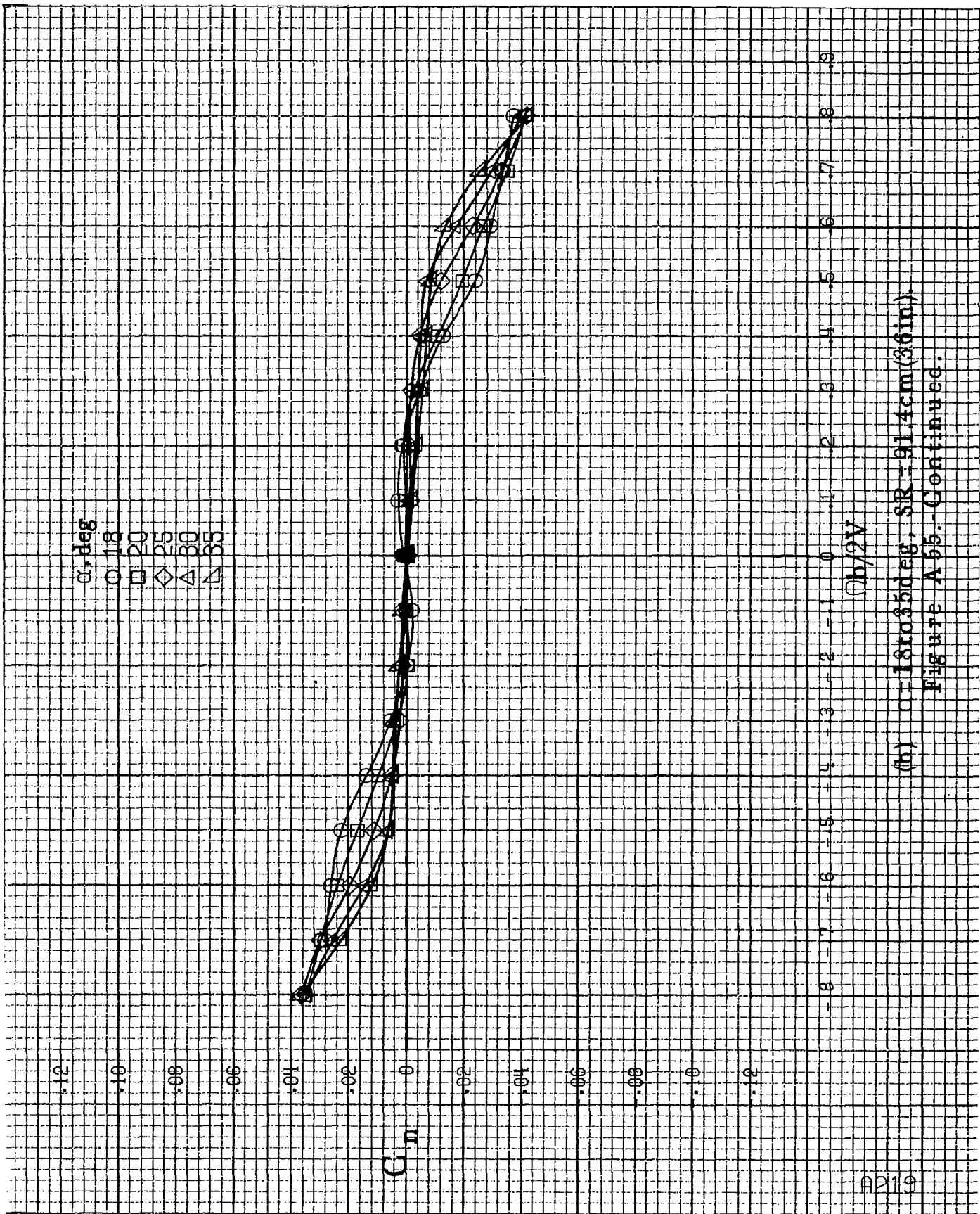


(d) $\alpha = 55^\circ$ to 90° , $SR = 0$.
Figure A 64.-Concluded.



(a) $\alpha=8$ to 16° , $SR=91.4\text{cm}$ (36in).

Figure A55 - Effect of rotation rate and angle of attack on yawing-moment coefficient for long body, low wing, horizontal tail no. 1 configuration. $\delta_E=0^\circ$, $\delta_A=0^\circ$, $\delta_T=0^\circ$.

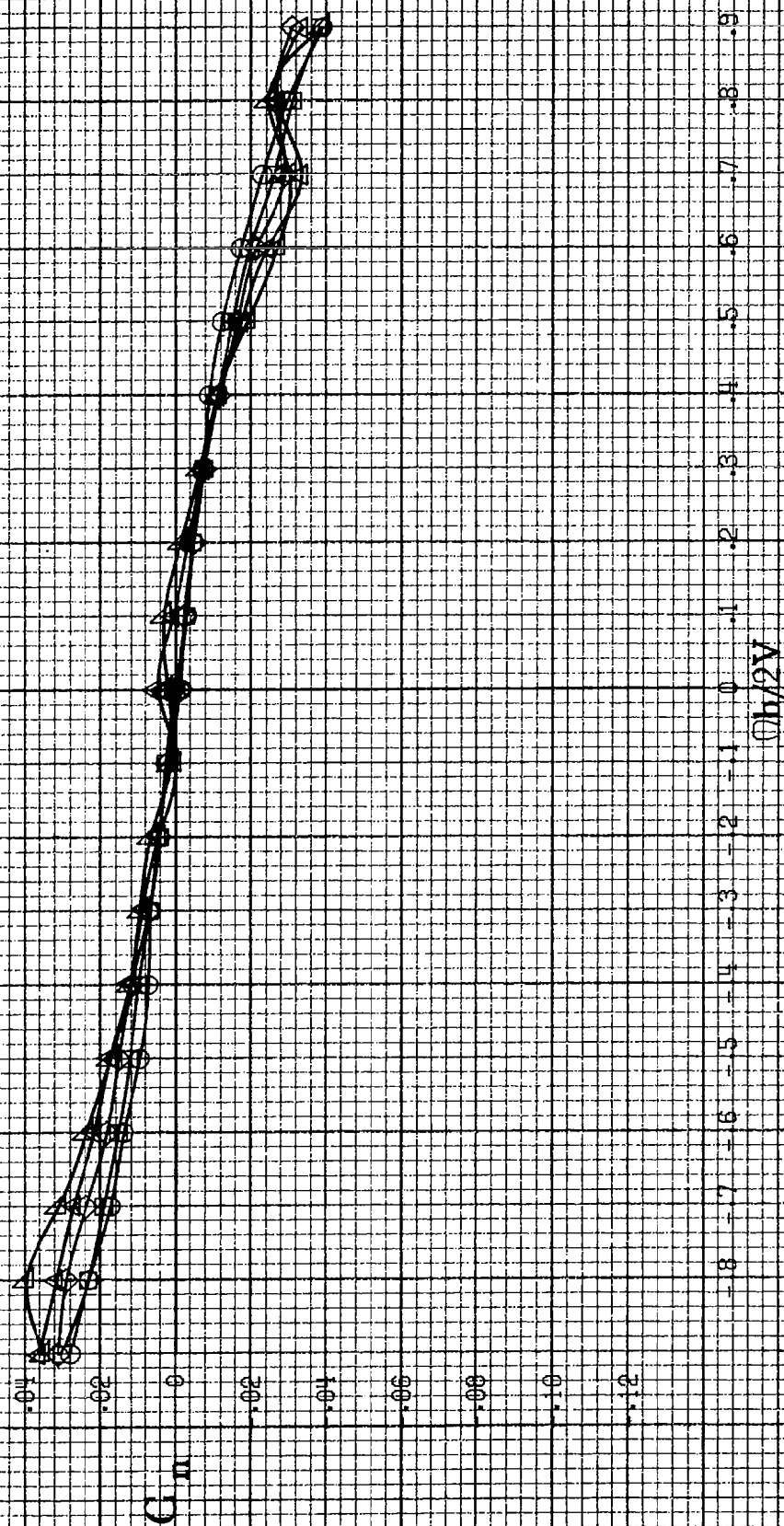


(b) $\alpha=18$ to 35° , SR=91.4cm (36in).

Figure A55.-Continued.

A220

α, deg
 ○ 30
 □ 35
 ◇ 40
 ▲ 45
 △ 50



(a) $\alpha=30$ to 50° , $SR=0$.
 Figure A55.-Continued.

α , deg
 ○ 55
 □ 60
 ◇ 70
 △ 80
 ▴ 90

C_n

$\phi h/2V$

(d) $\alpha = 55$ to 90 deg, $SR = 0$.

Figure A66.-Concluded.

A221

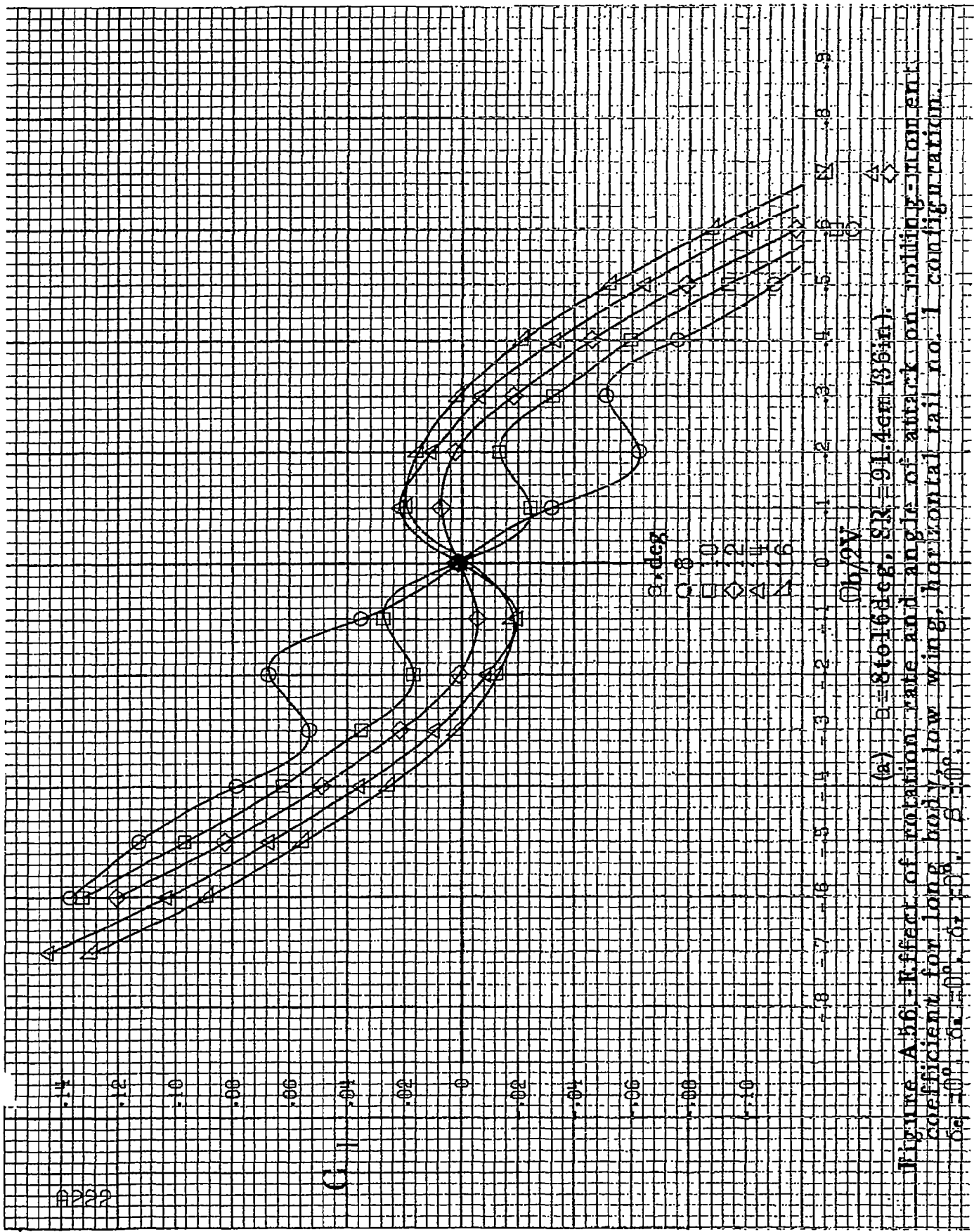
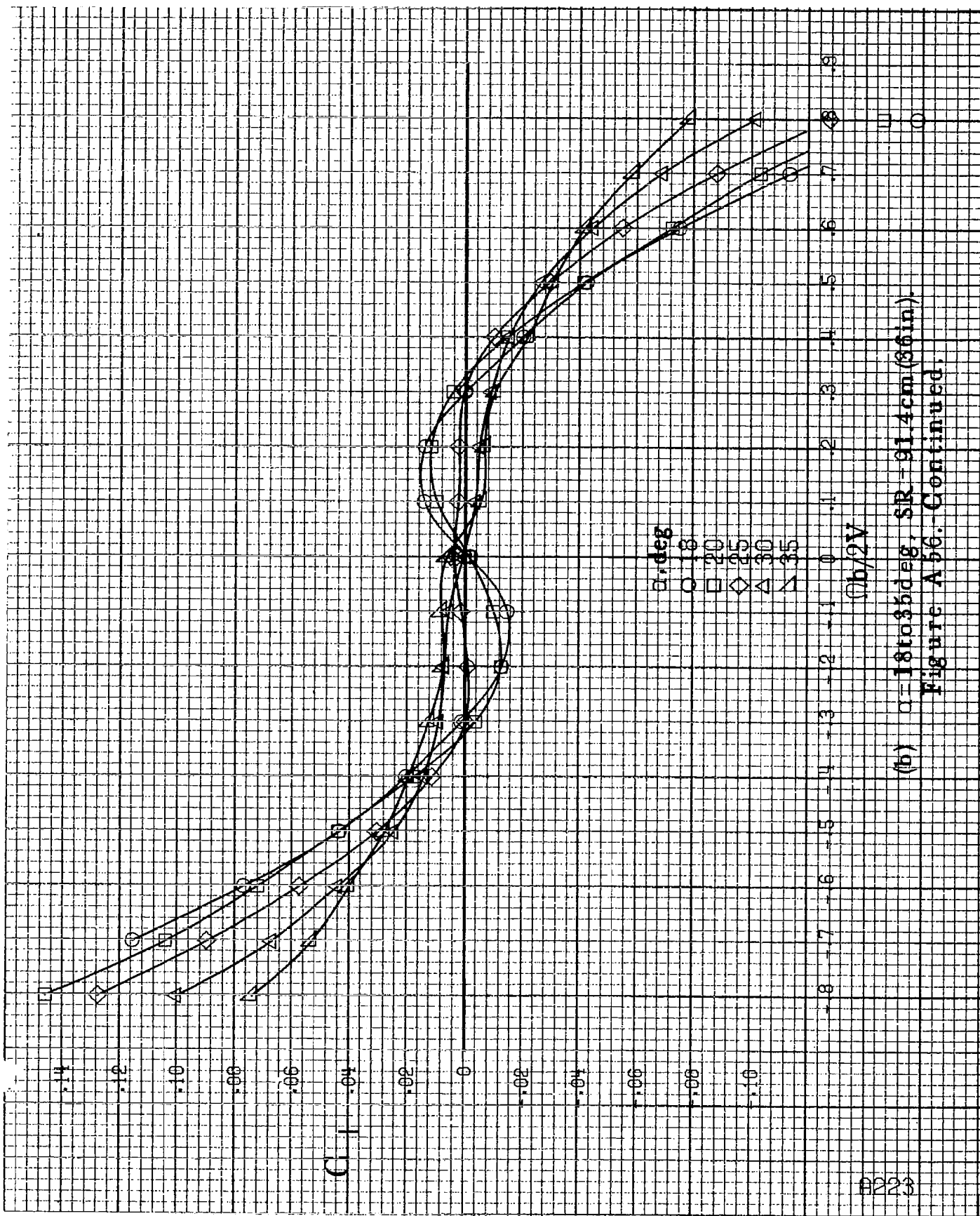
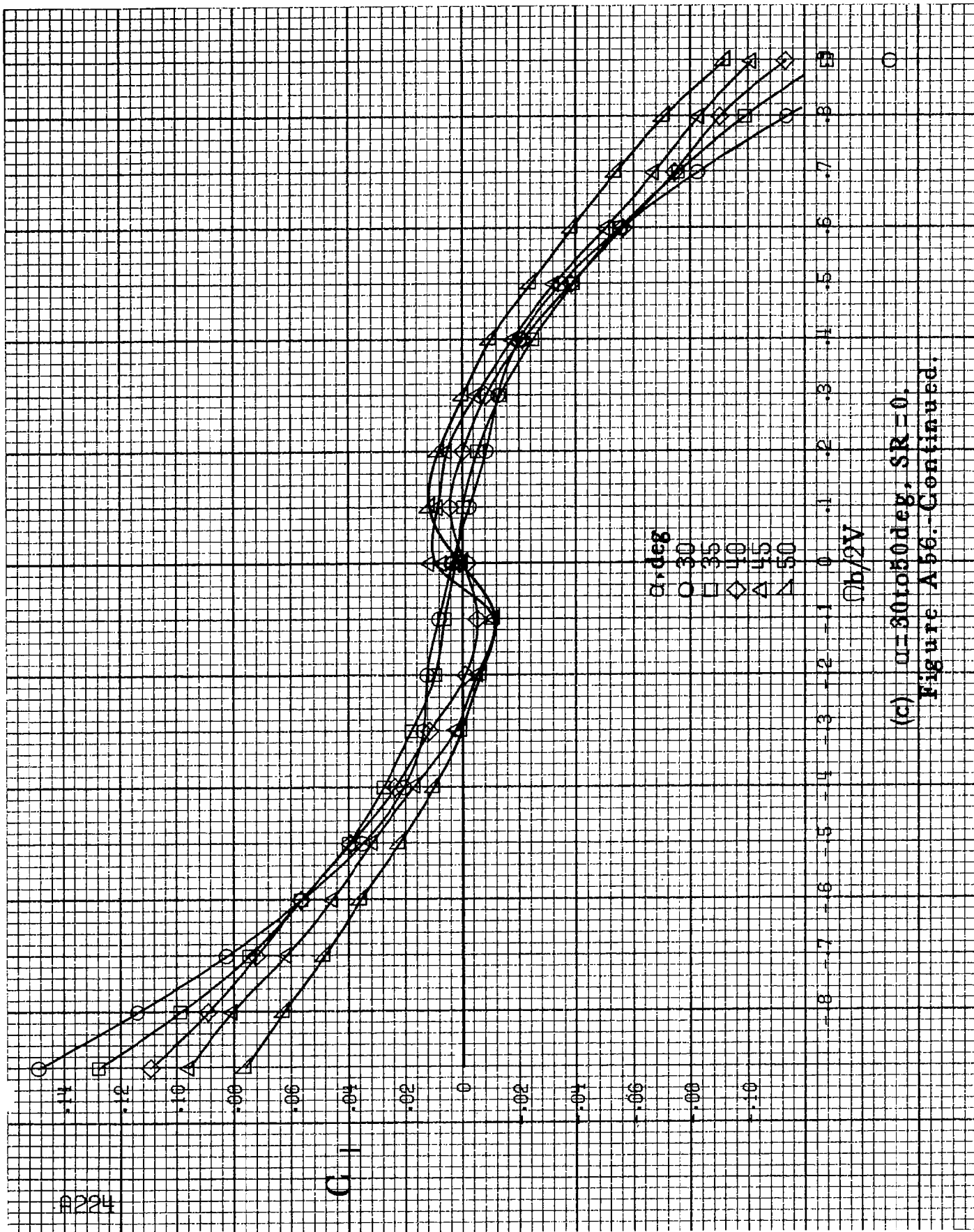


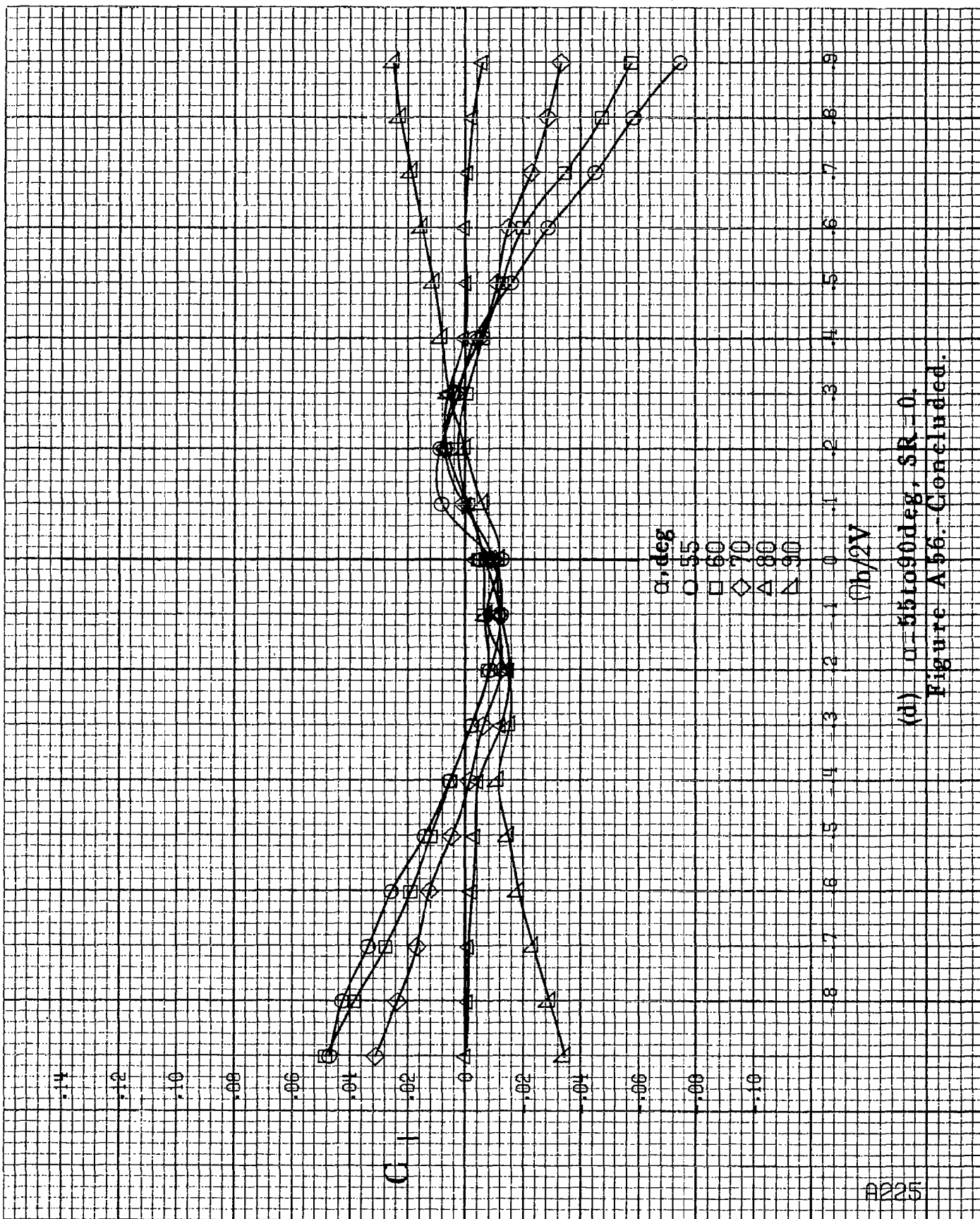
Figure A.561 - Effect of rotation rate and angle of attack on rolling-moment coefficient for long body, low wing, horizontal tail no. 1 configuration. $\delta_a = 0^\circ$, $\delta_e = 0^\circ$, $\delta_r = 0^\circ$.



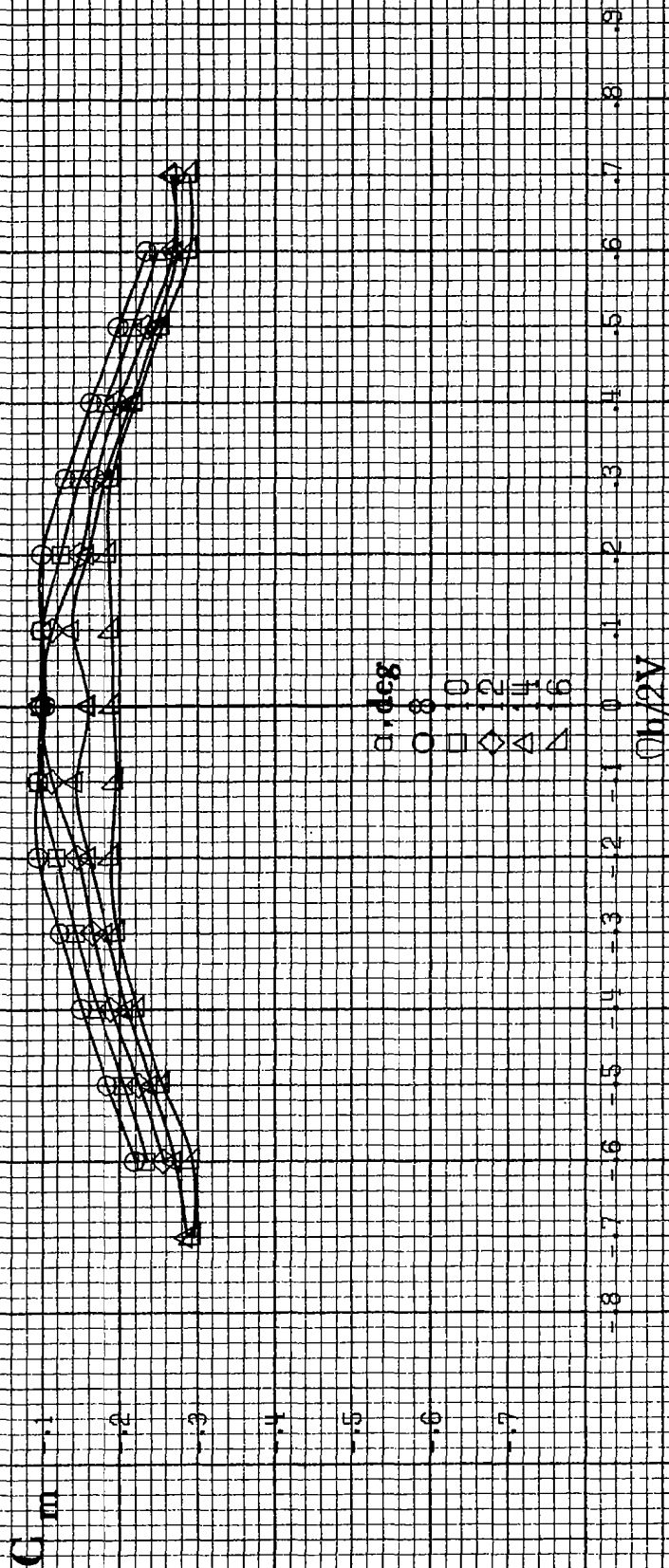
(b) $\alpha=18$ to 35 deg, SR = 91.4 cm (36 in).
Figure A56. Continued.



(c) $\alpha=30$ to 50 deg, $SR=0$.
Figure A56.-Continued.

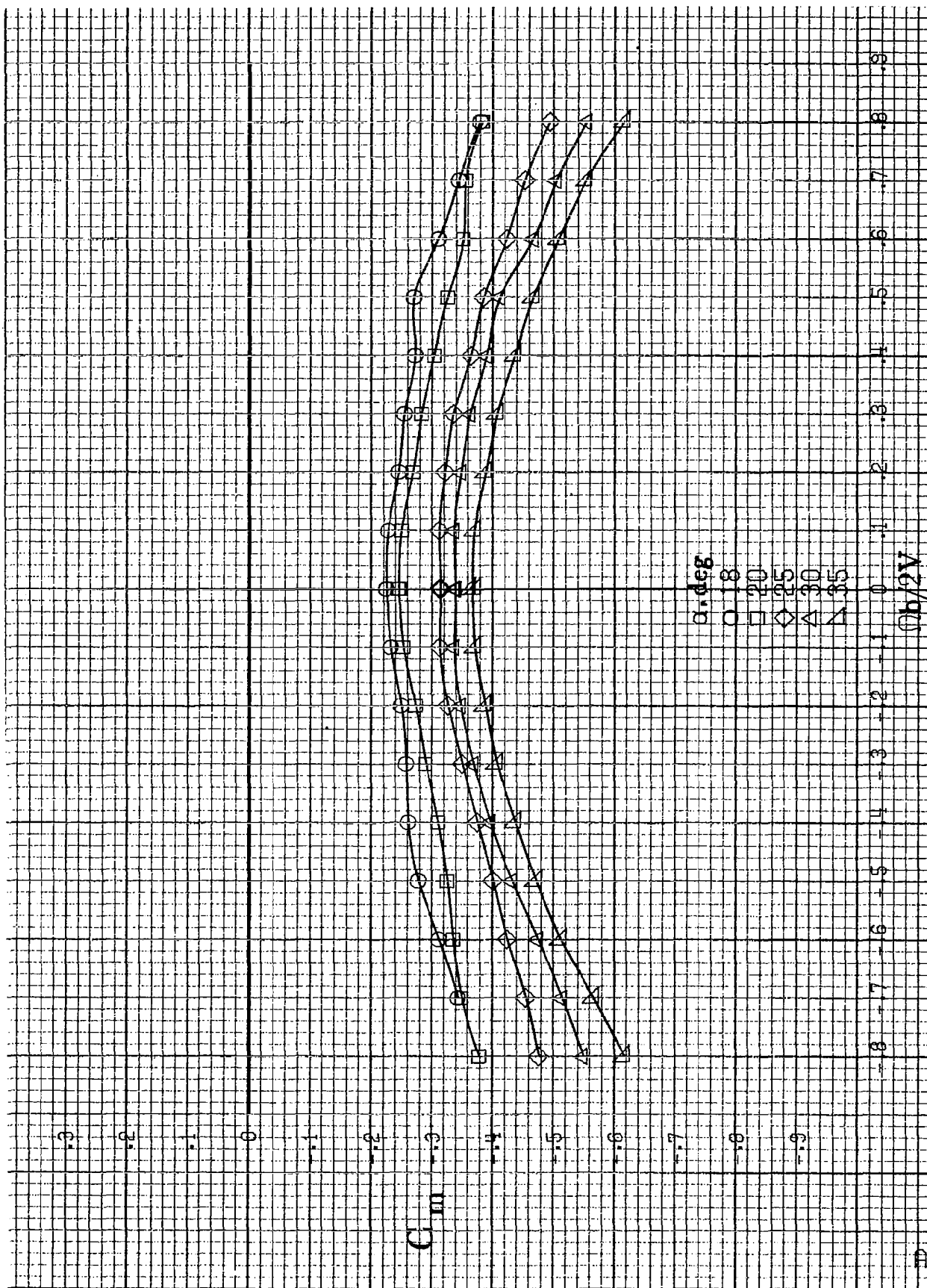


(d) $\alpha=55$ to 90 deg, $SR=0$.
Figure A56. Concluded.



(a) $\alpha=8$ to 16° , $SR=91.4$ cm (36 in).

Figure A57 - Effect of rotation rate and angle of attack on pitching-moment coefficient for long body, low wing, horizontal tail no. 1 configuration. $\delta a=0^\circ$, $\delta r=0^\circ$, $\delta \tau=0^\circ$.



(b) $\alpha = 18$ to 35 deg. $SR = 91.4$ cm (36 in).
Figure A 57.-Continued.

U_m

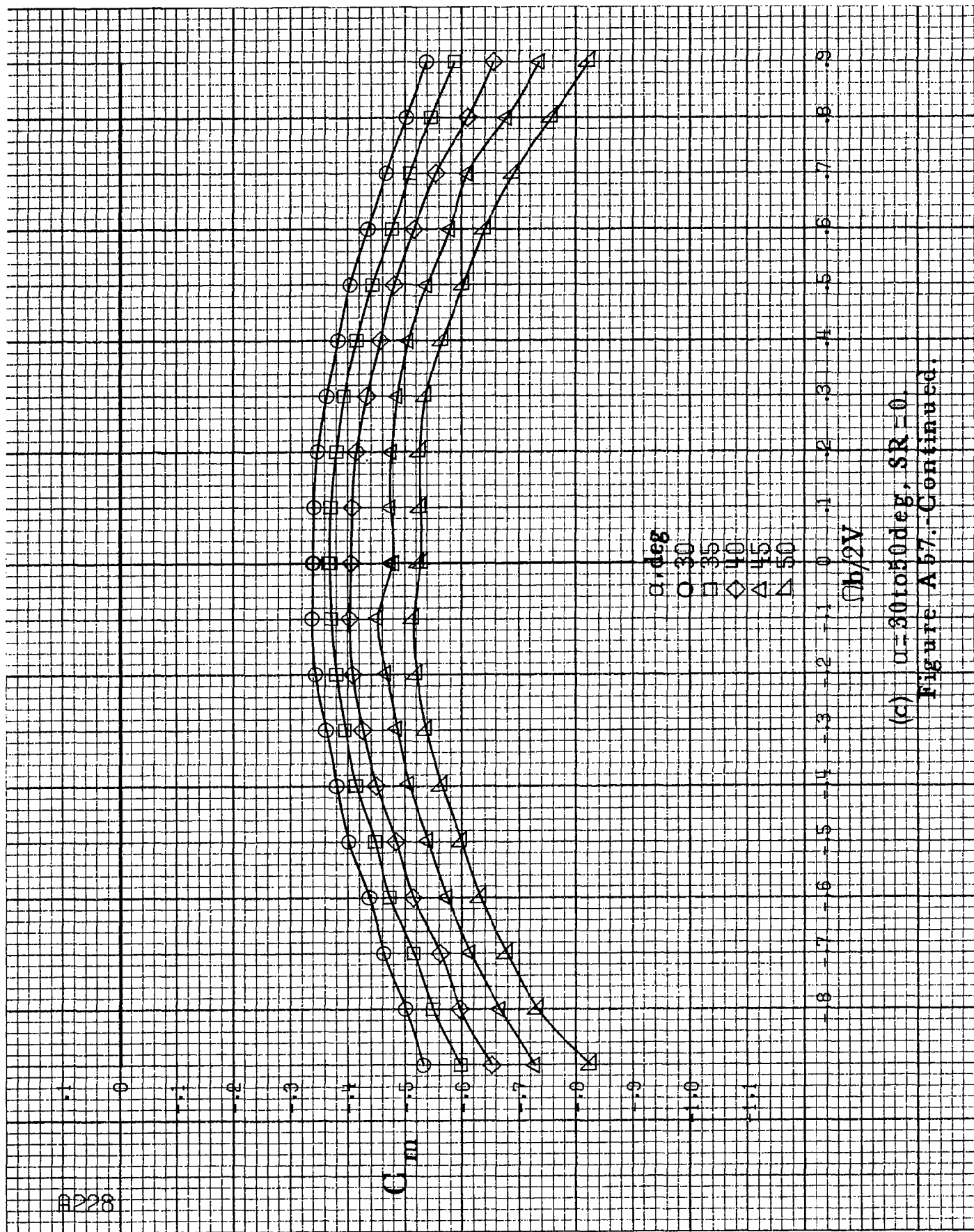
α, deg

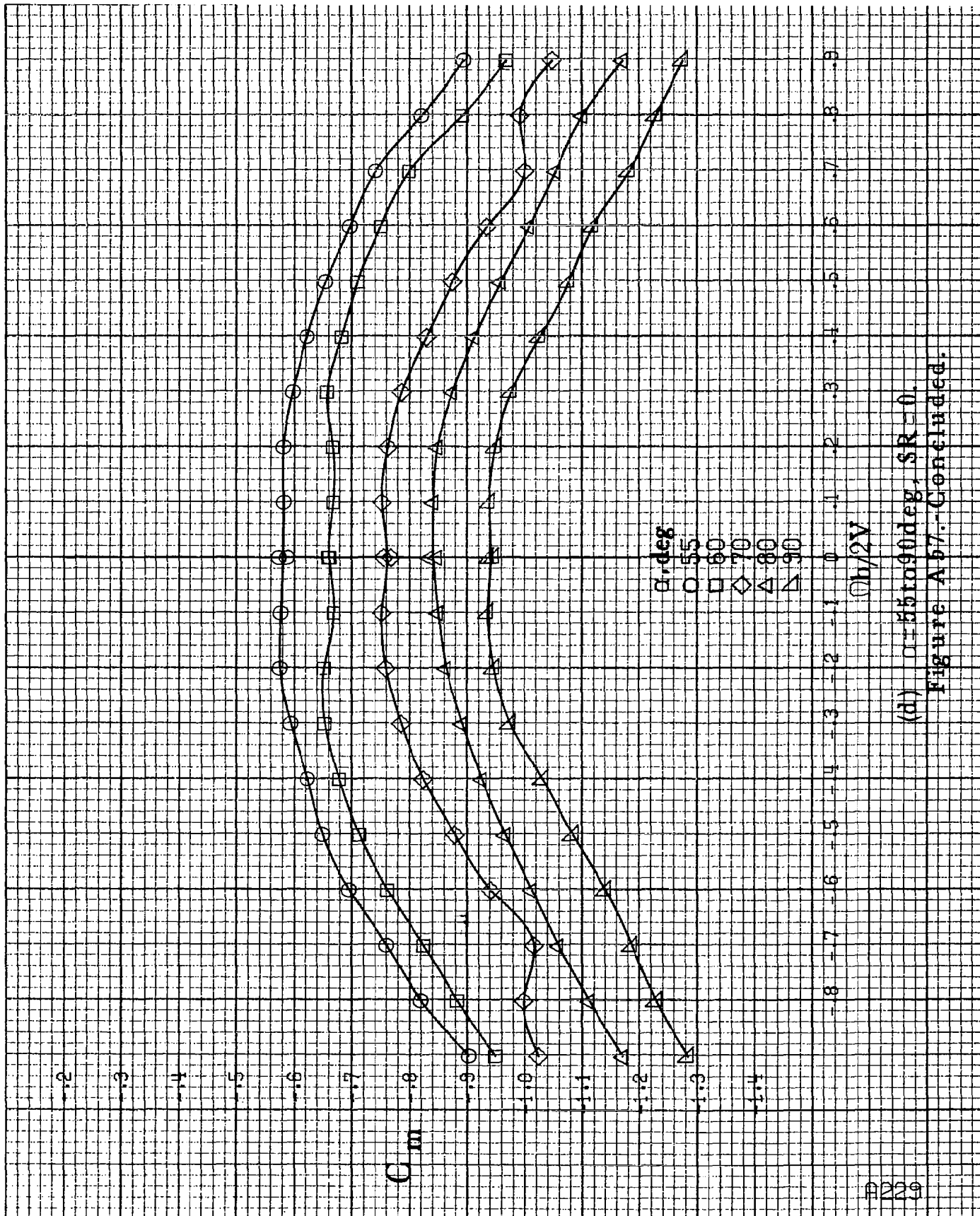
- 30
- 35
- ◇ 40
- △ 45
- ▽ 50

$\Omega b/2V$

(c) $\alpha = 30$ to 50 deg, $SR = 0$.

Figure A 57.-Continued.





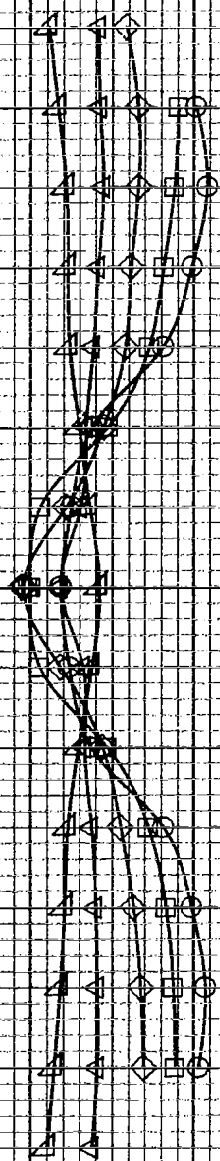
(d) $\alpha = 55$ to 90° , $SR = 0$.
 Figure A 67--Concluded.

A230

α, deg

○ 8
□ 10
◇ 12
△ 14
▽ 16

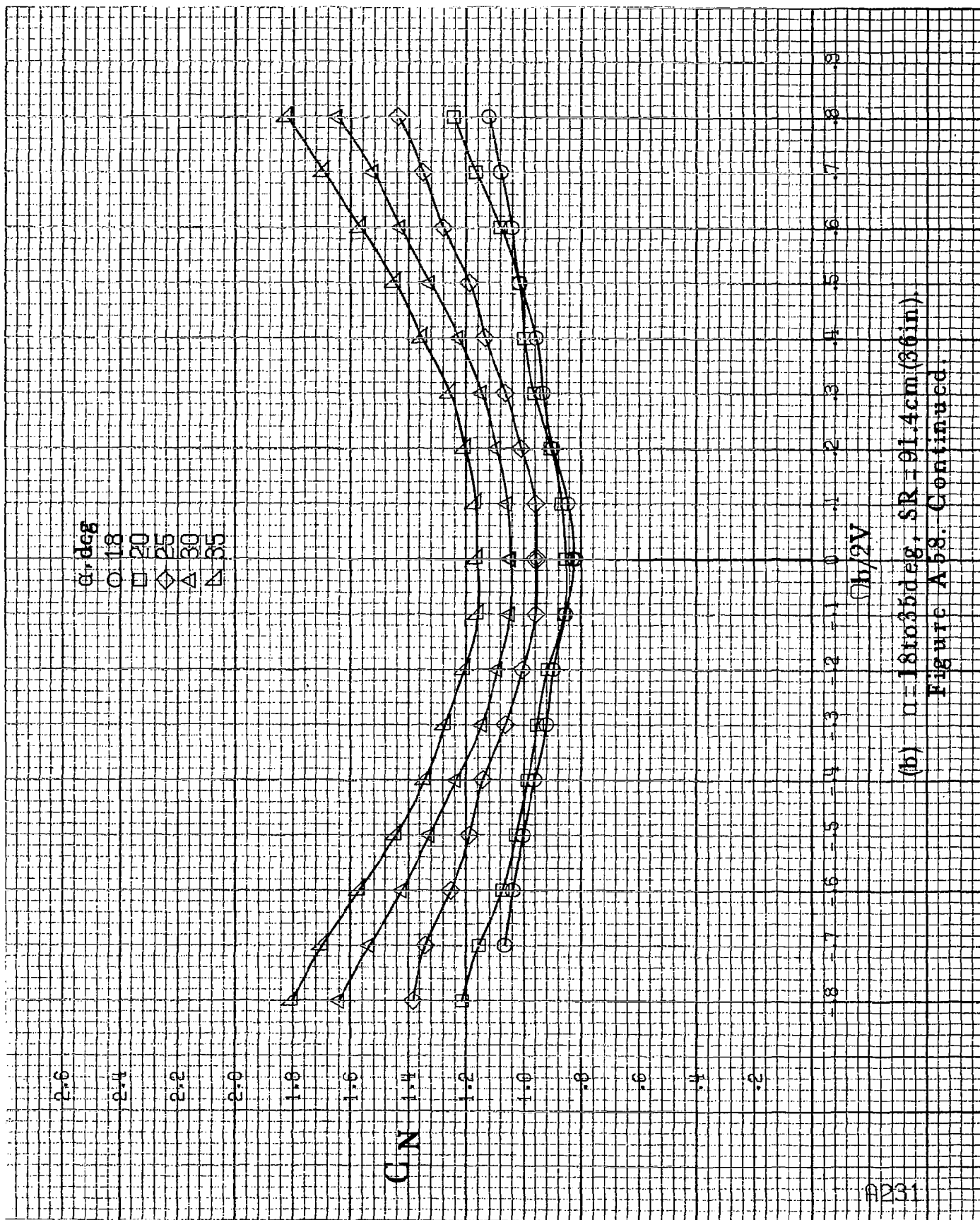
C_N



$Cb/2V$

(a) $\alpha = 8$ to 16° , $SR = 91.4 \text{ cm (36 in.)}$.

Figure A58.-Effect of rotation rate and angle of attack on normal-force coefficient for long body, low wing, horizontal tail no. 1 configuration.
 $\delta_a = 0^\circ$, $\delta_w = 0^\circ$, $\delta_t = 0^\circ$.



(b) $\alpha = 18$ to 35° deg. $SR = 91.4 \text{ cm (36 in.)}$.
Figure A58. Continued.

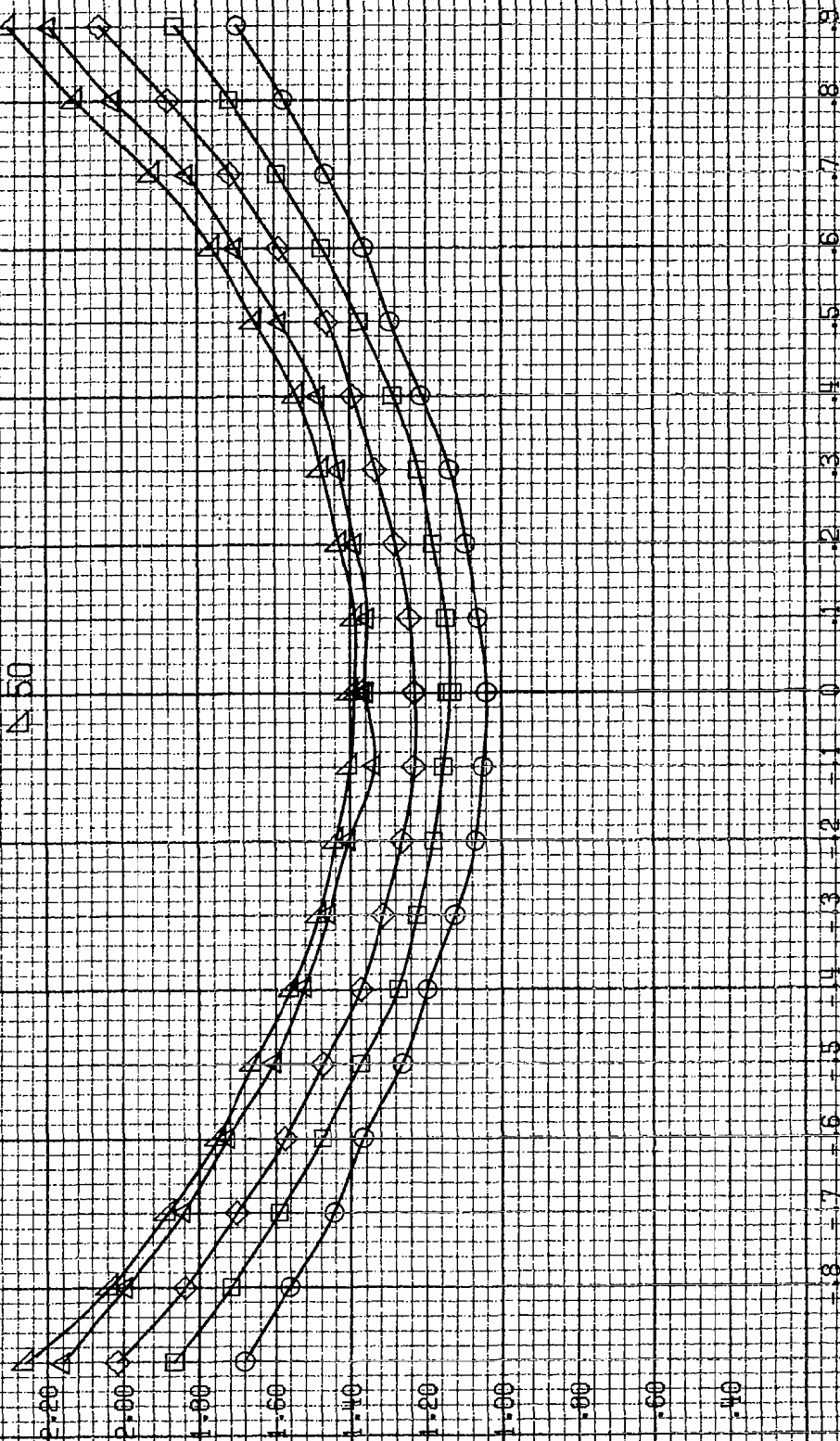
α , deg

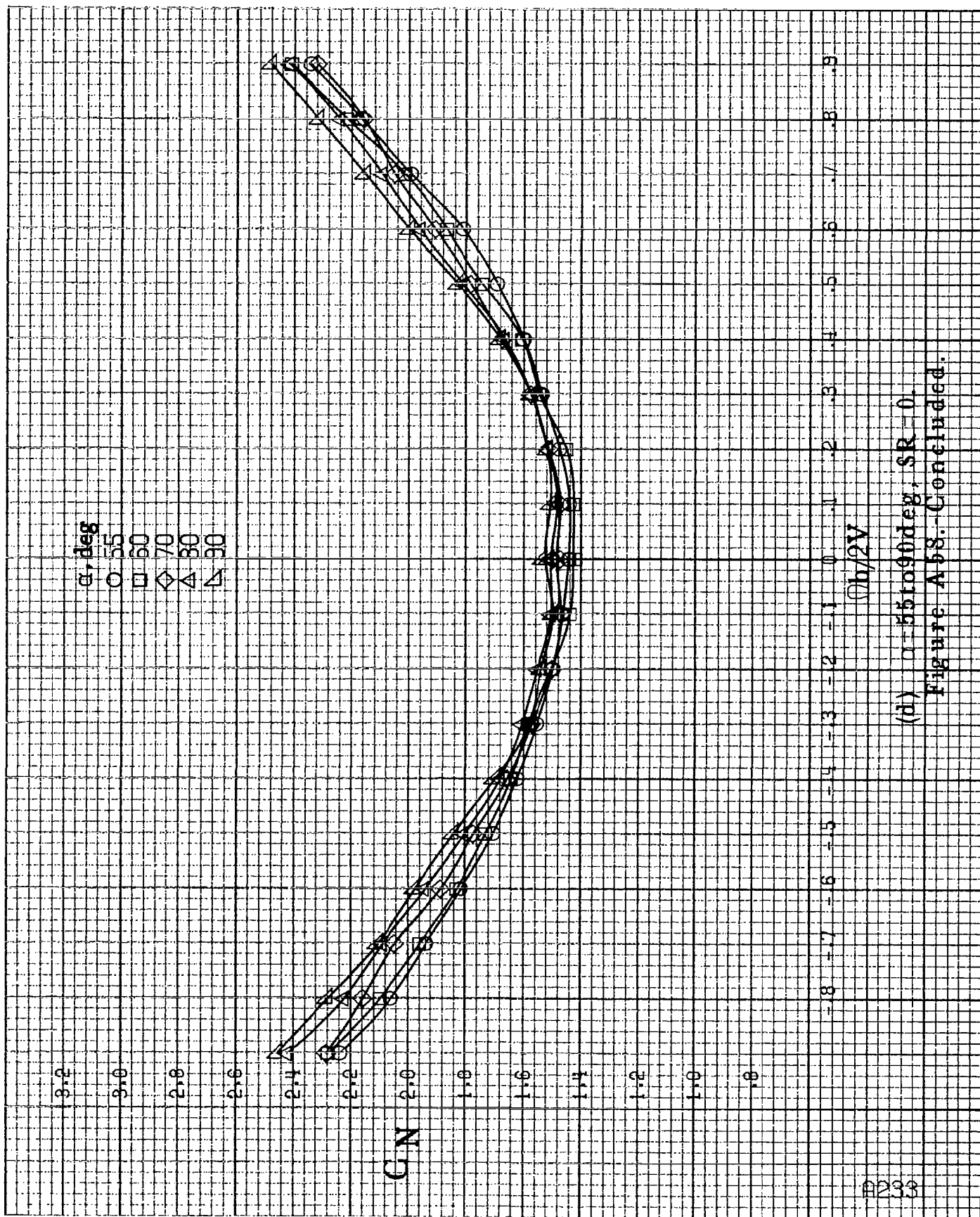
○ 30
□ 35
◇ 40
△ 45
▽ 50

C/N

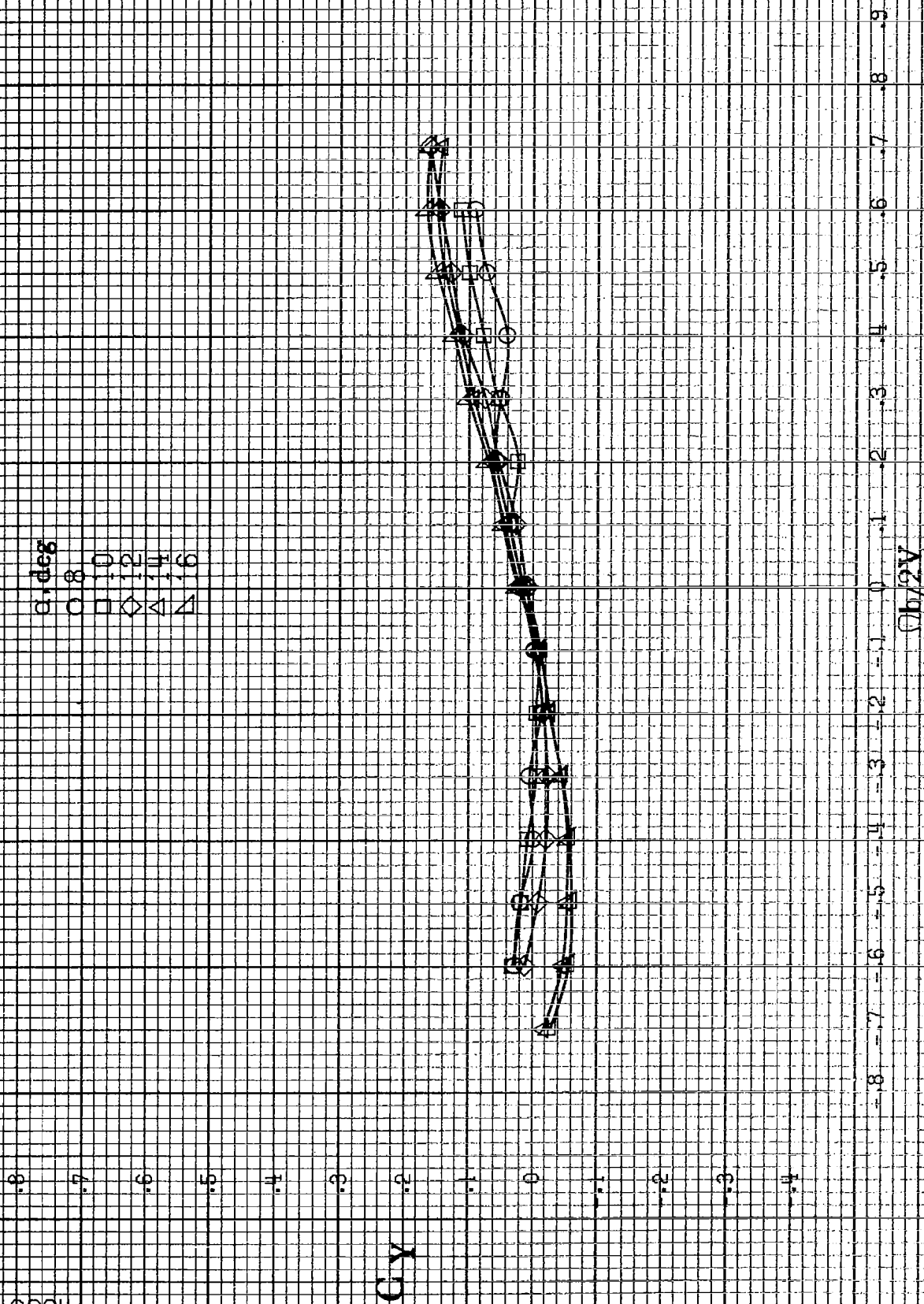
$Ch/2V$

(c) $\alpha = 30$ to 50 deg, $SR = 0$.
Figure A58. Continued.



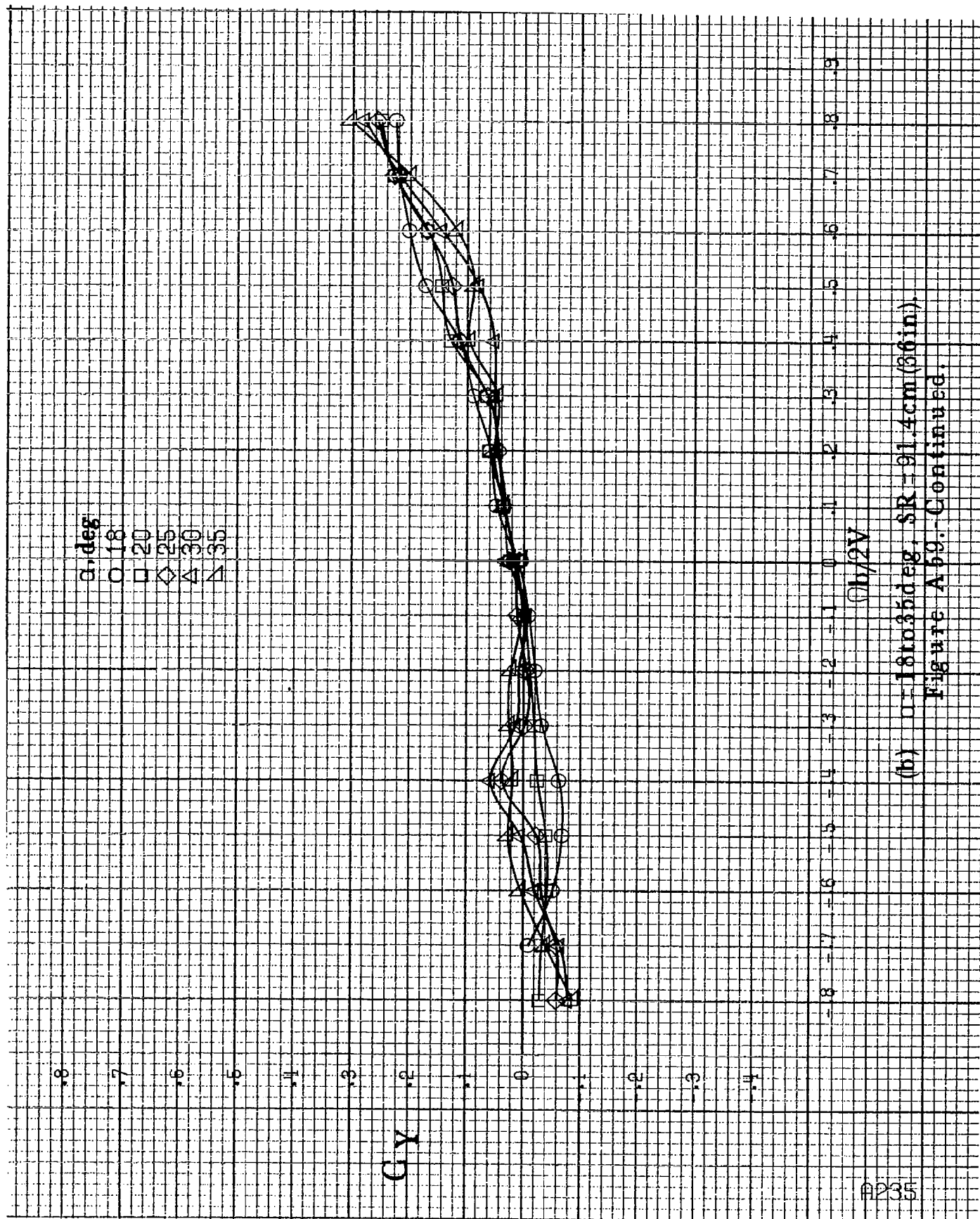


(d) $\alpha = 55$ to 90° , $SR = 0$.
Figure A6S.-Concluded.



(a) $\alpha = 8$ to 16° , $SR = 91.4 \text{ cm (36 in.)}$.

Figure A60.-Effect of rotation rate and angle of attack on side-force coefficient for long body, low wing, horizontal tail no. 1 configuration. $\delta_a = 0^\circ$, $\delta_r = 0^\circ$, $\delta = 0^\circ$.



(b) $\alpha = 18$ to 35° , SR = 91.4 cm (36 in).
 Figure A59. Continued.

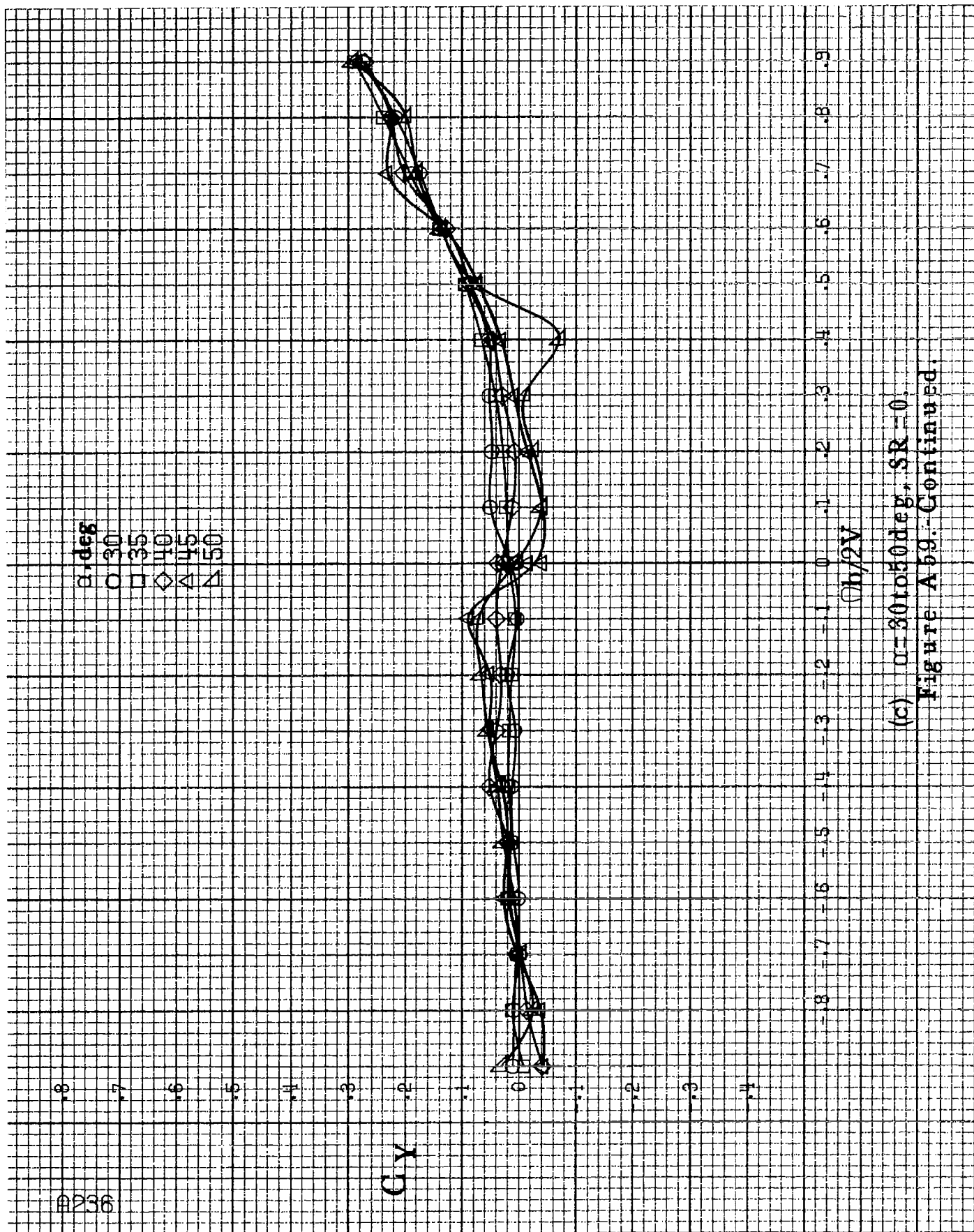
α, deg
 \circ 30
 \square 35
 \diamond 40
 \triangle 45
 ∇ 50

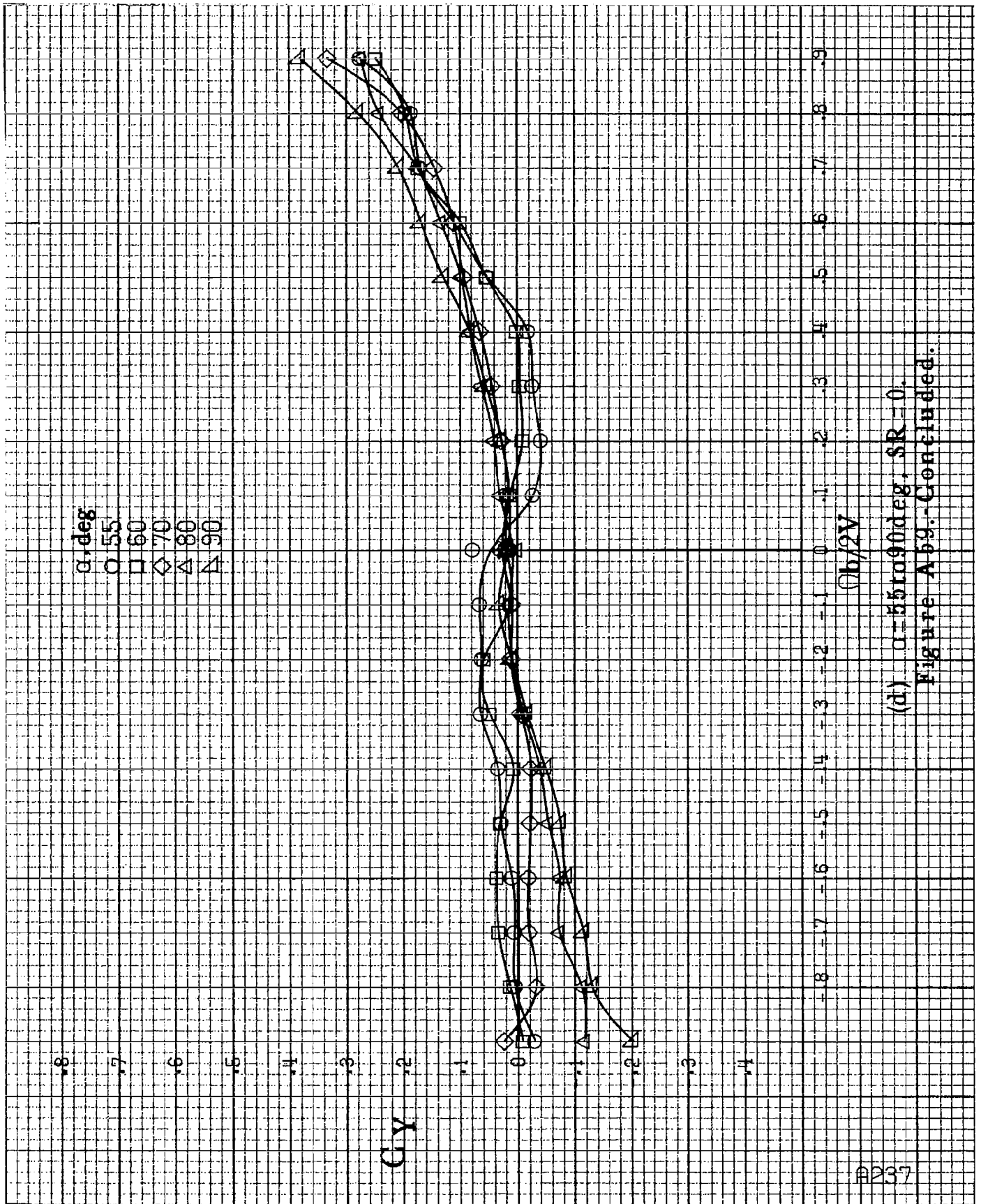
C_Y

$h/2V$

(c) $\alpha=30$ to 50 deg, $SR=0$.

Figure A59.-Continued.



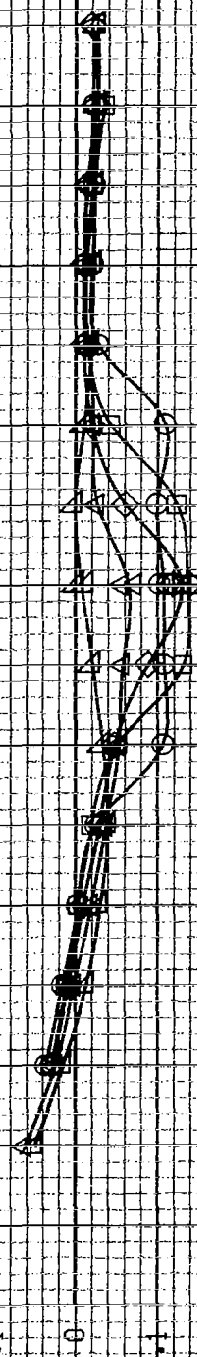


(d) $\alpha=55$ to 90 deg, $SR=0$.
Figure A69.-Concluded.

7238

α, deg
 O 8
 □ 10
 ◇ 12
 △ 14
 ▽ 16

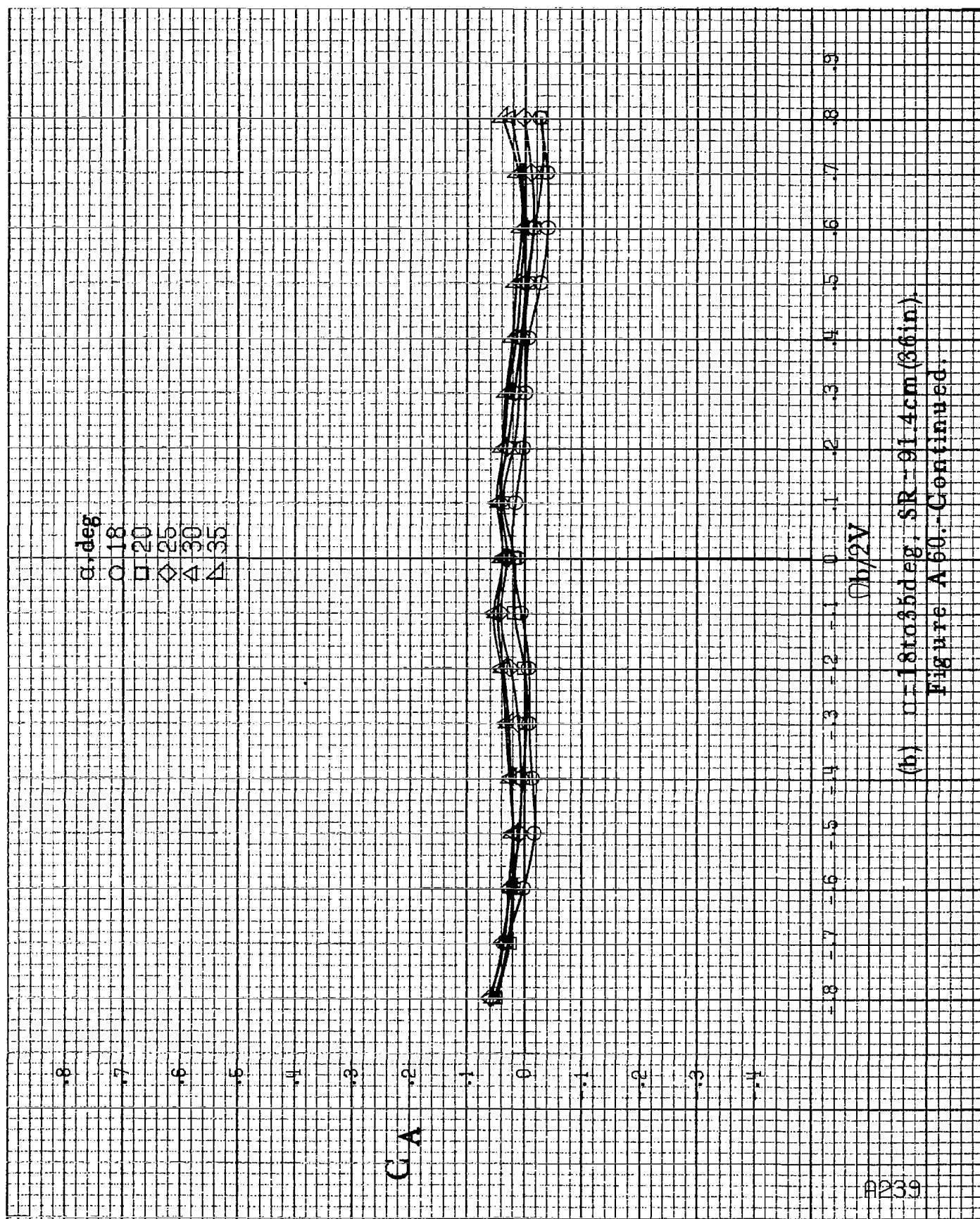
C_A



$C_b/2V$

$\alpha = 8 \text{ to } 16 \text{ deg}, SR = 01.4 \text{ cm (36 in.)}$

Figure A60.-Effect of rotation rate and angle of attack on axial force coefficient for long body, low wing, horizontal tail no. 1 configuration. $\delta_a = 0^\circ$, $\delta_r = 0^\circ$, $\delta = 0^\circ$.



(h) $\alpha=18$ to 35° , SR-91.4cm (36in).

Figure A60.-Continued.

A240

θ, deg
 \circ 30
 \square 35
 \diamond 40
 \triangle 45
 ∇ 50

C_A

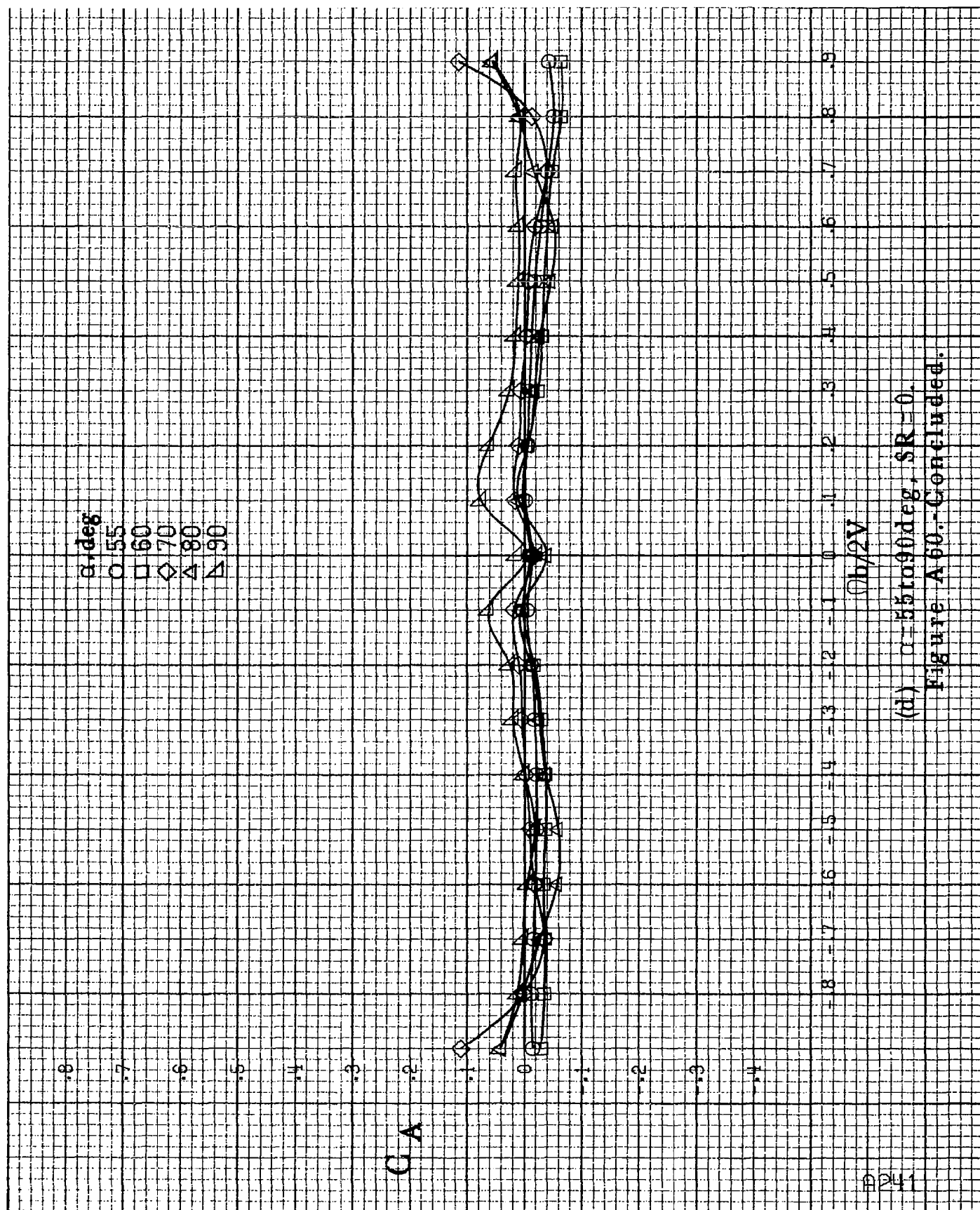
$\phi h/2V$

(a) $\theta = 30$ to 50 deg, $SR = 0$.

Figure A60.-Continued.

.8
.7
.6
.5
.4
.3
.2
.1
0
-.1
-.2
-.3
-.4

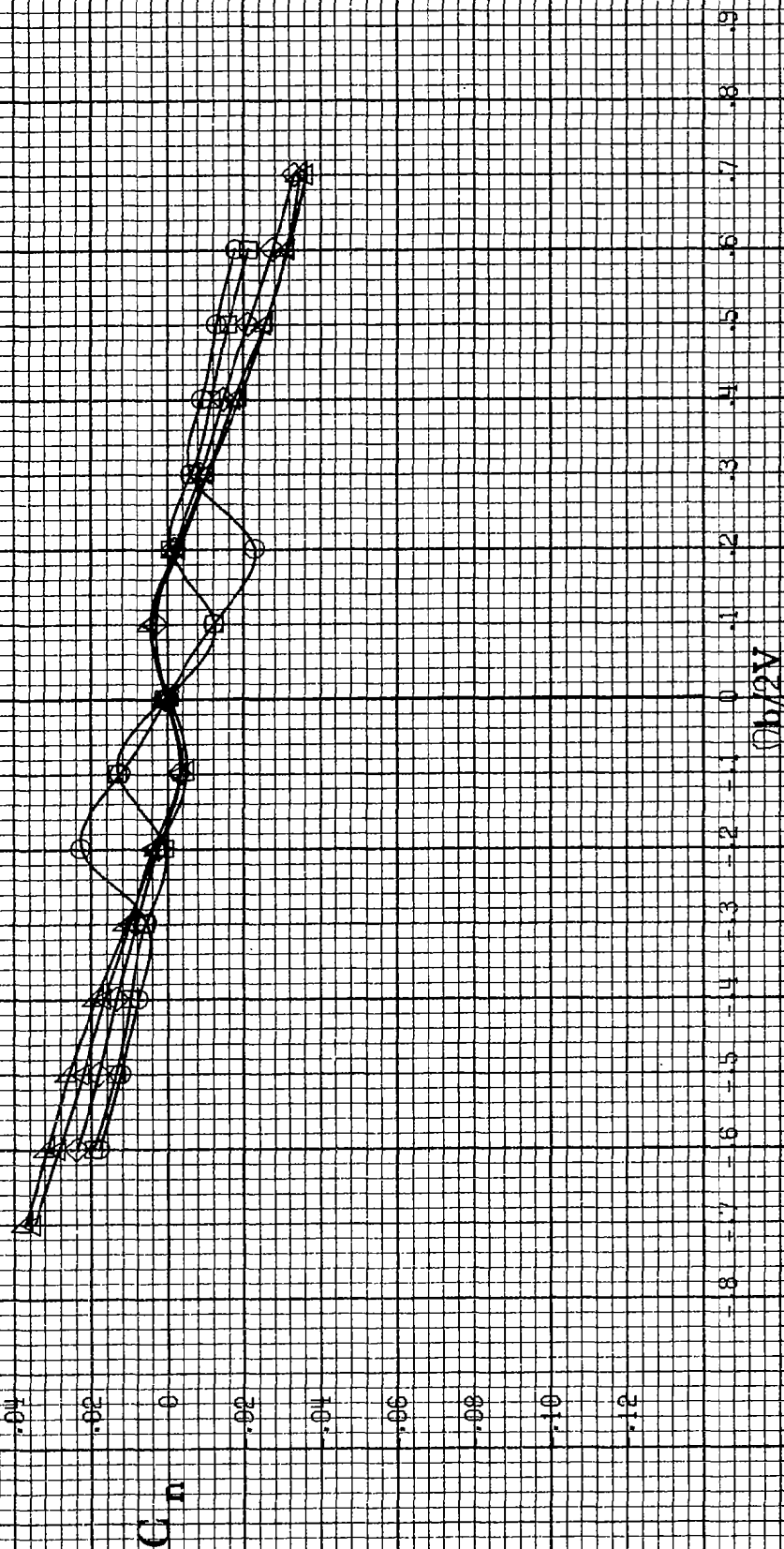
-.8 -.7 -.6 -.5 -.4 -.3 -.2 -.1 0 .1 .2 .3 .4 .5 .6 .7 .8 .9



(d) $\alpha=55$ to 90 deg, $SR=0$.
Figure A 60.- Concluded.

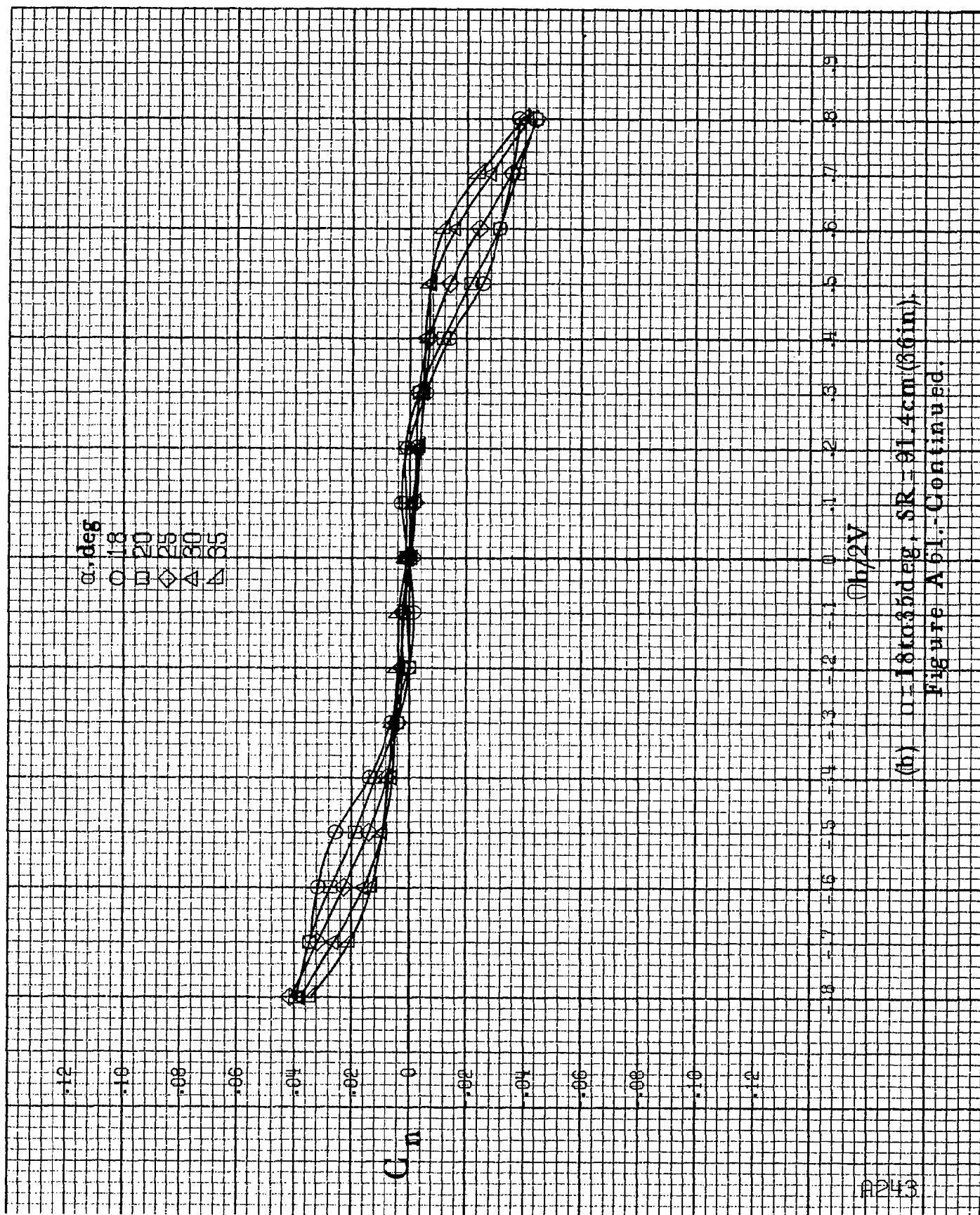
A242

α, deg
 O 8
 □ 10
 ◇ 12
 ▲ 14
 ▽ 16



(a) $\alpha=8$ to 16° , $SR=91.4\text{cm}$ (36in).

Figure A61.-Effect of notation rate and angle of attack on yawing-moment coefficient for long body, low wing, horizontal tail no. 2 configuration. $\delta_a=0^\circ$, $\delta_w=0^\circ$, $\delta_r=0^\circ$.



(b) $\alpha=18$ to 35° , $SR=31.4\text{cm}(86\text{in})$.

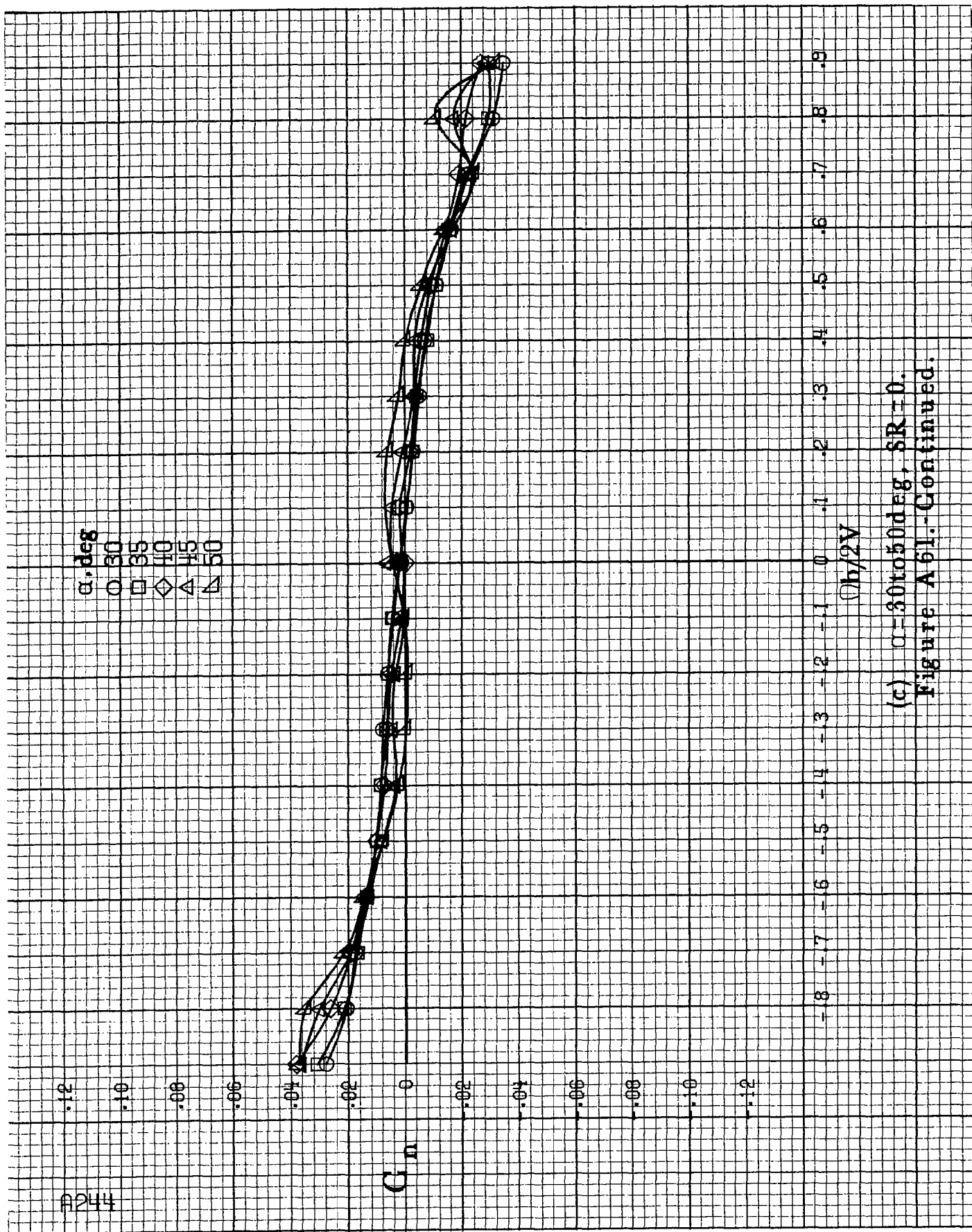
Figure A61.-Continued.

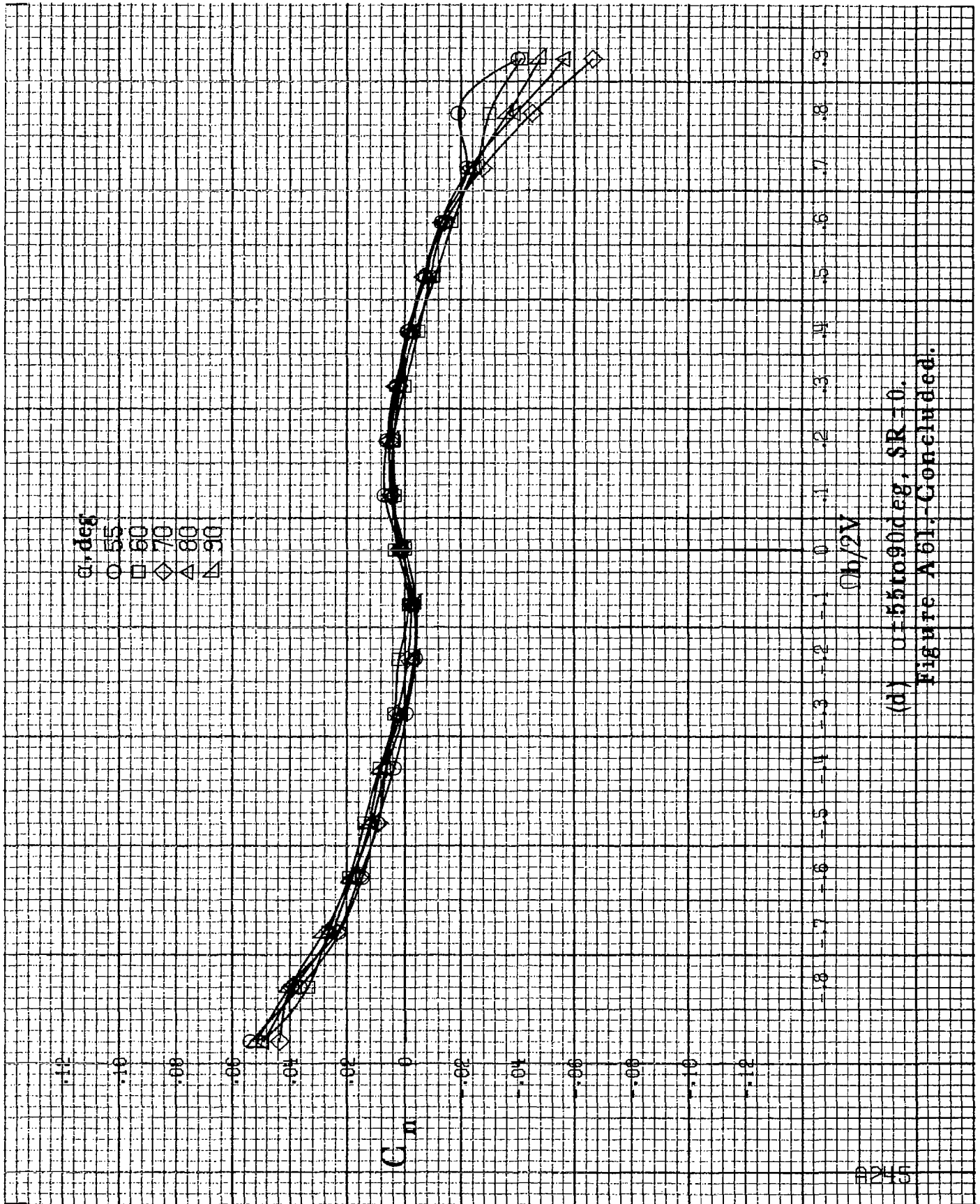
α , deg
 ○ 30
 □ 35
 ◇ 40
 △ 45
 ▽ 50

C_n

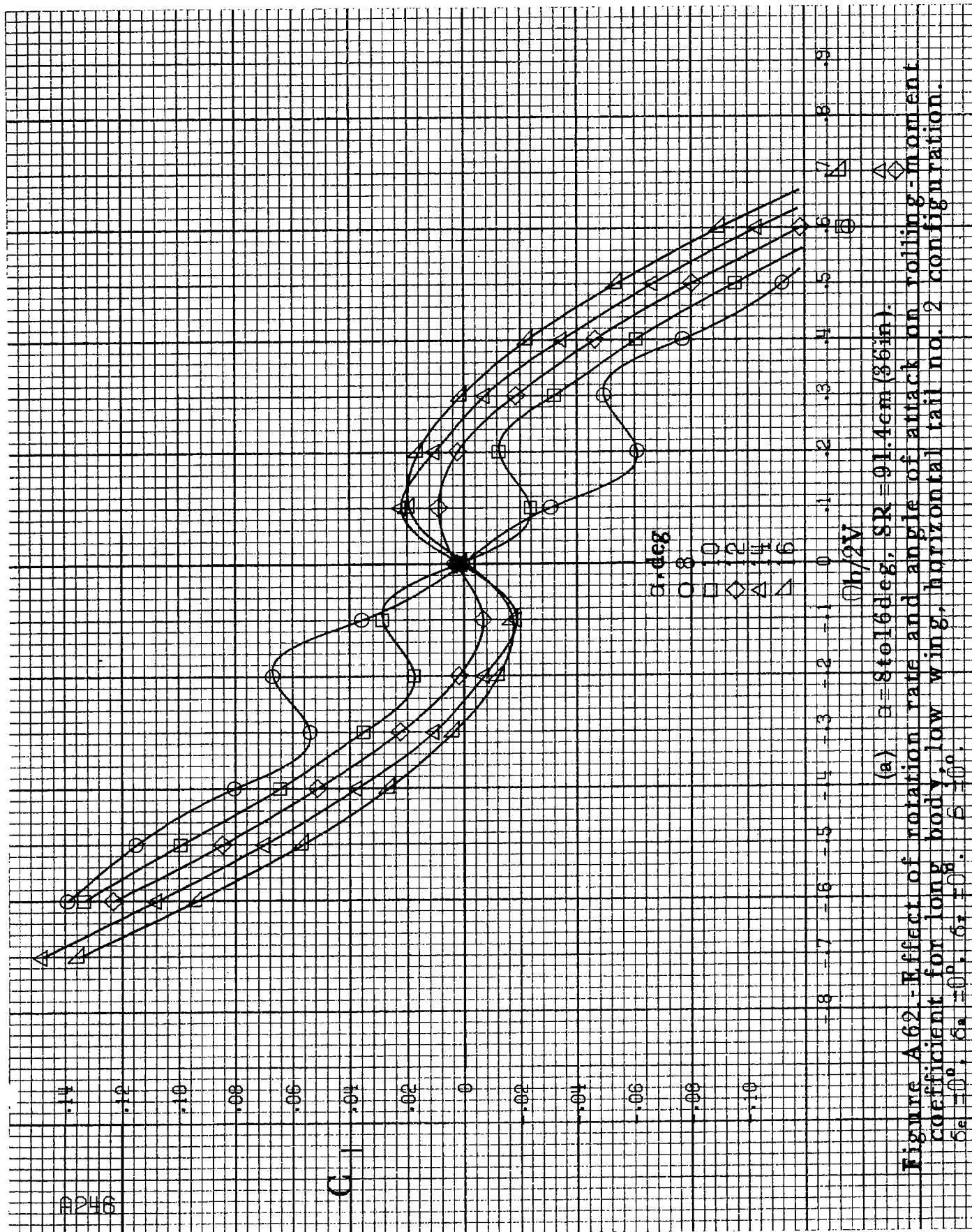
$\phi h/2V$

(c) $\alpha=30$ to 50 deg, $\delta R=0$.
 Figure A61.-Continued.



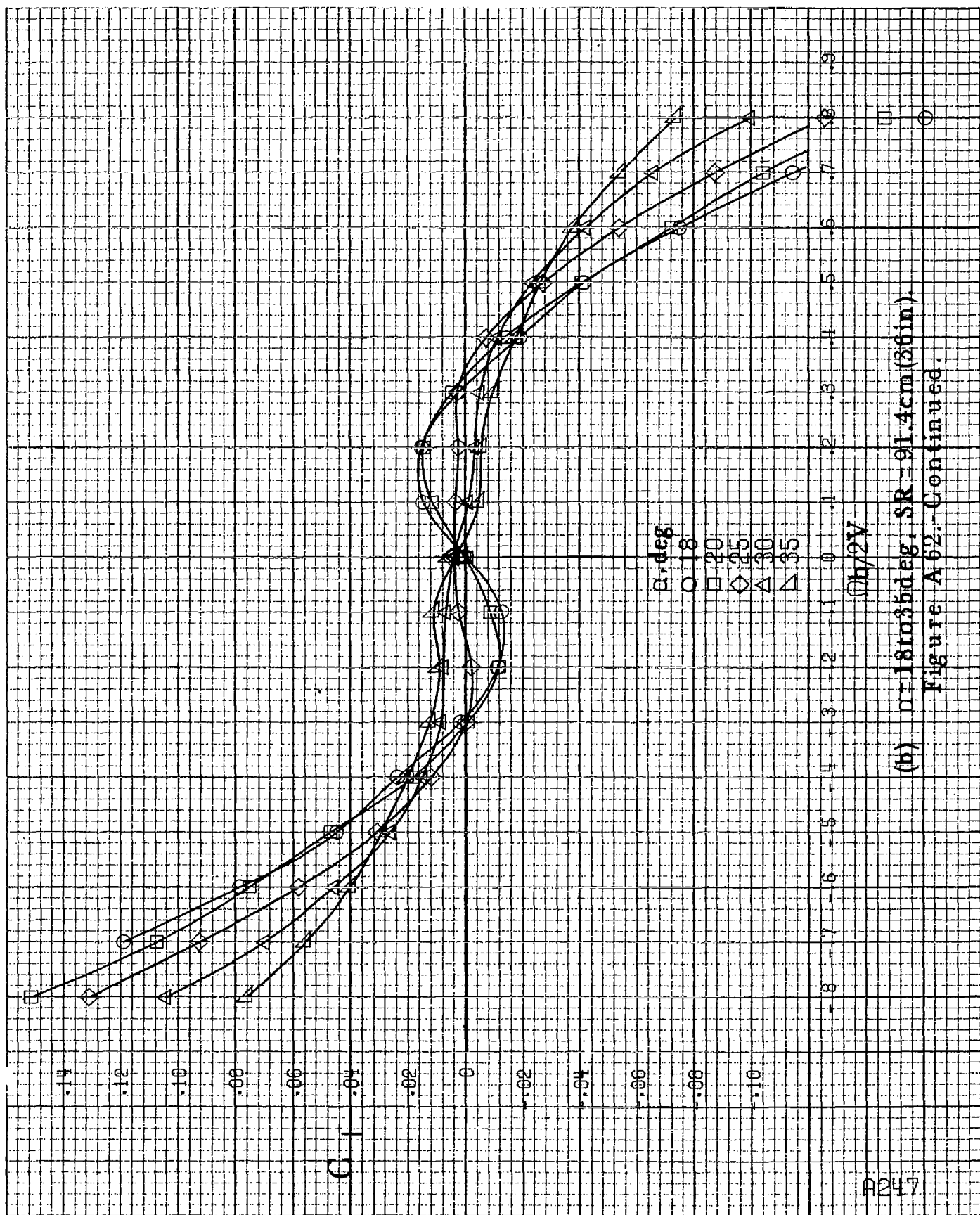


(d) $\alpha = 55$ to 90 deg, $SR = 0$.
Figure A61.-Concluded.

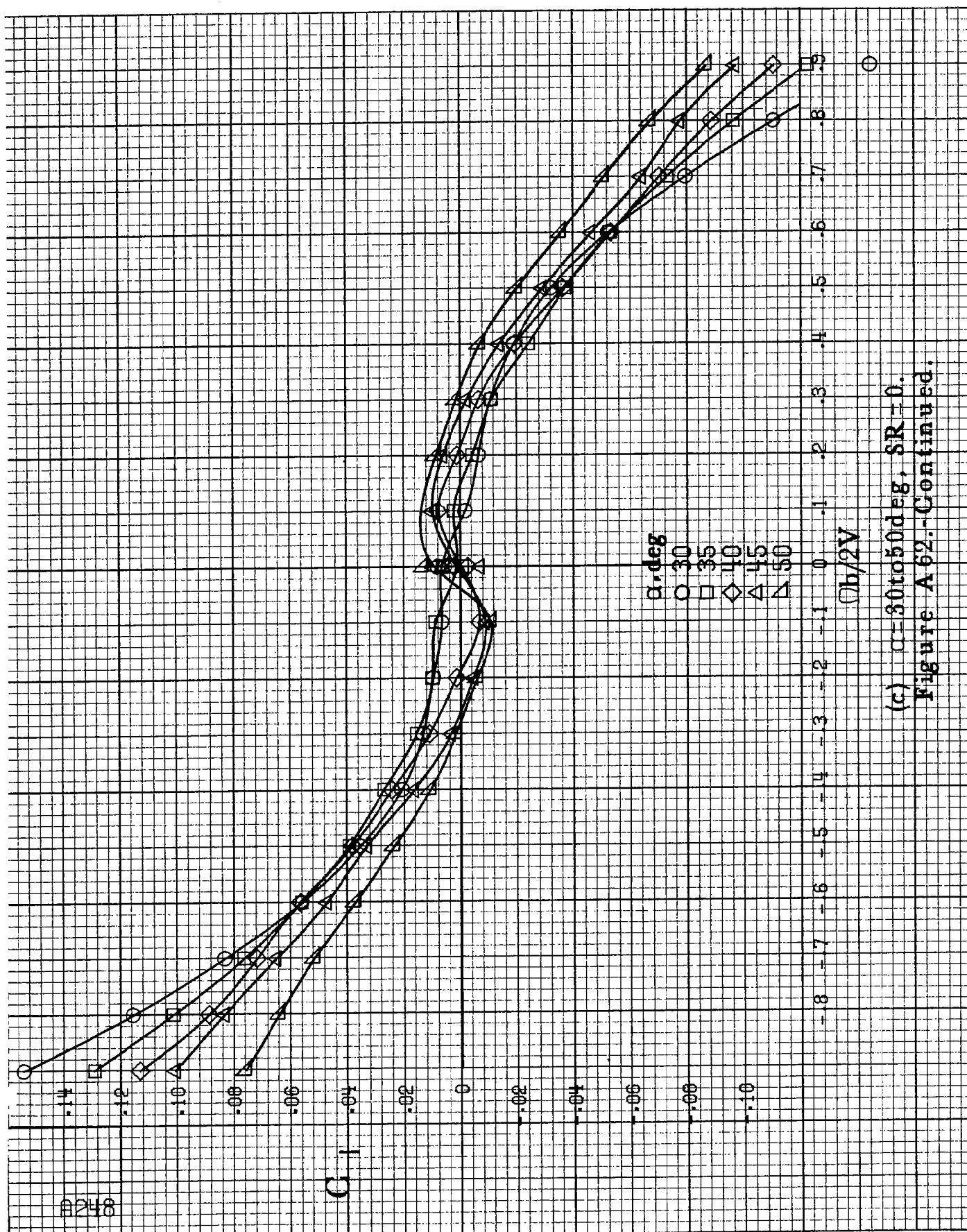


(a) $\alpha = 8$ to 16 deg, $SR = 91.4$ cm (36 in).

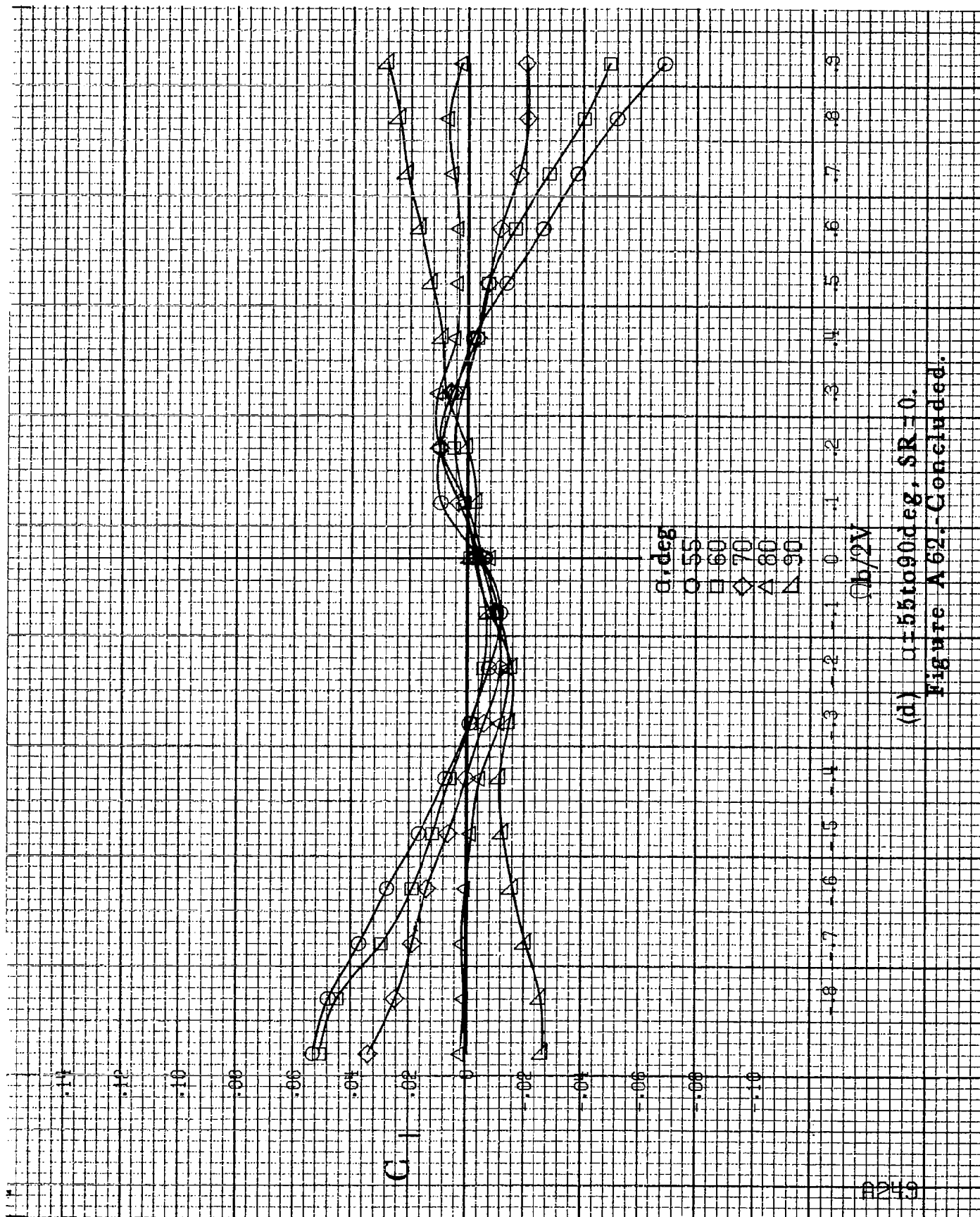
Figure A 62 - Effect of rotation rate and angle of attack on rolling-moment coefficient for long body, low wing, horizontal tail no. 2 configuration.
 $\delta_a = 0^\circ$, $\delta_s = 0^\circ$, $\delta_r = 0^\circ$, $\delta = 10^\circ$.



(b) $\alpha=18$ to 35° , $SR=91.4\text{cm}$ (36in).
Figure A62.-Continued.



(c) $\alpha=30$ to 50 deg, $SR=0$.
Figure A 62.-Continued.



(d) $\alpha=55$ to 90° , $SR=0$.
Figure A 62.-Concluded.

C_m

α, deg

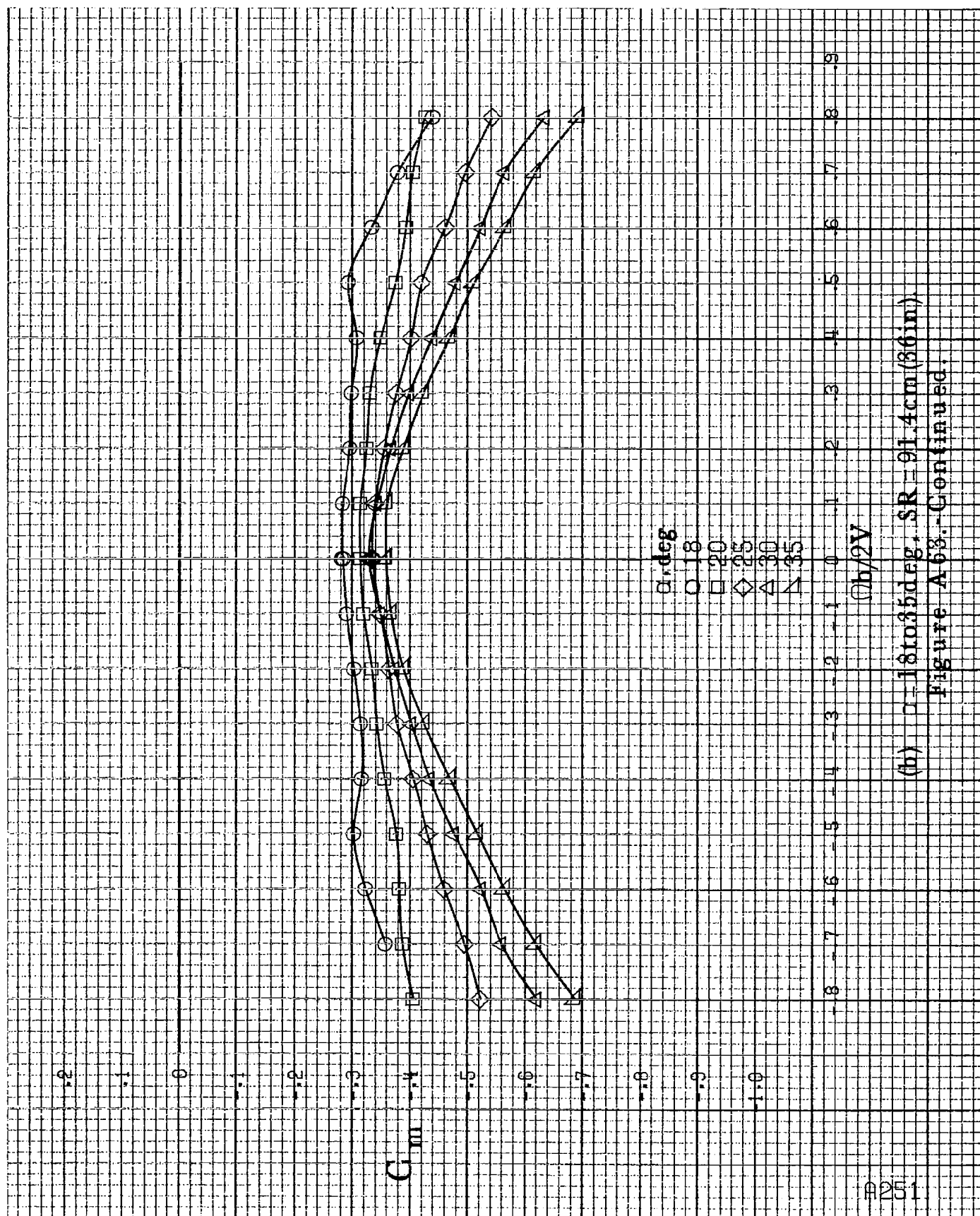
○ 8
□ 10
◇ 12
△ 14
▽ 16

$\Omega b/2V$

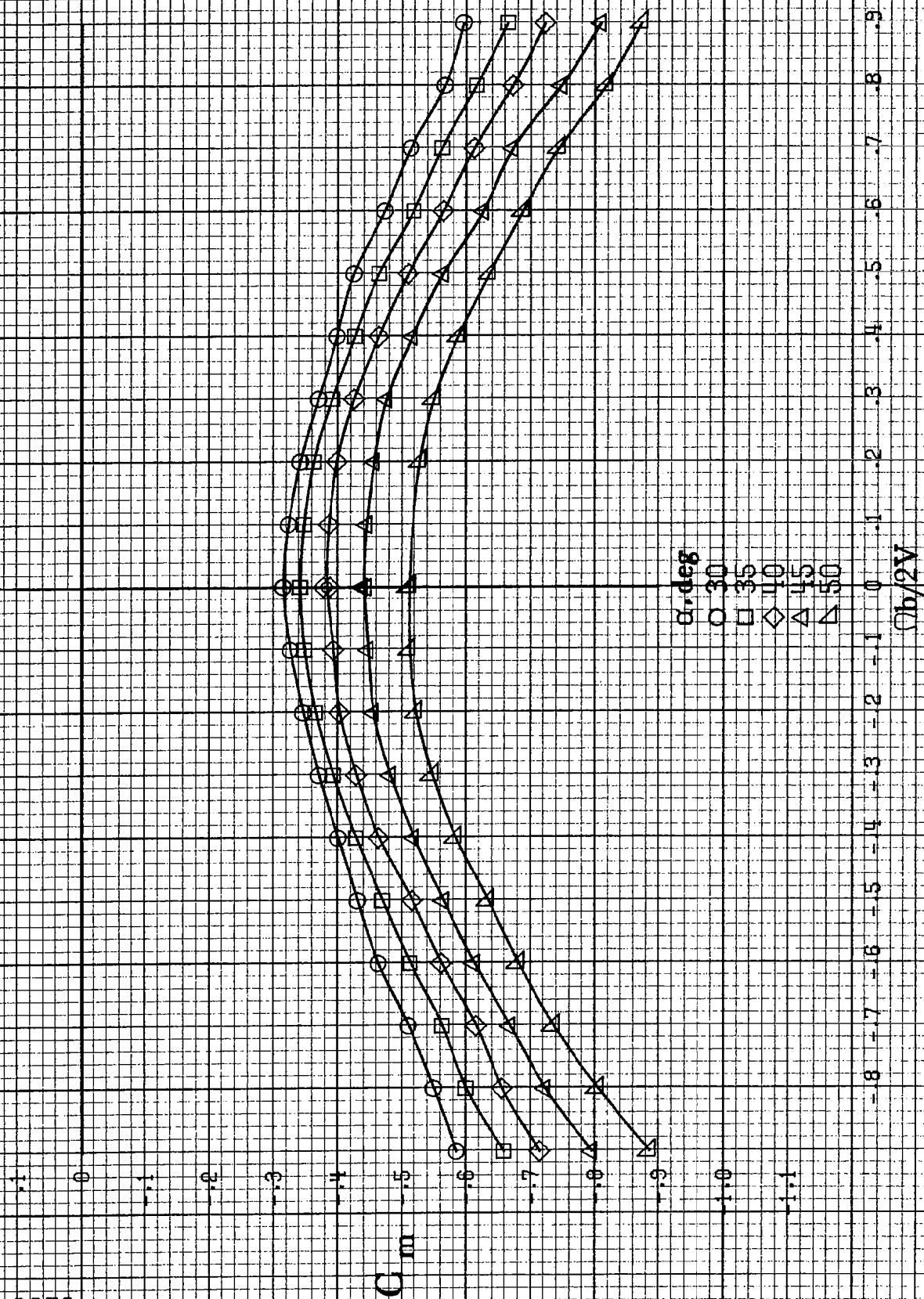
(a) $\alpha = 8$ to 16 deg, $SR = 91.4 \text{ cm (35 in.)}$.

Figure A63 - Effect of rotation rate and angle of attack on pitching-moment coefficient for long body, low wing, horizontal tail no. 2 configuration.

$\delta_a = 0^\circ$, $\delta_s = 0^\circ$, $\delta_r = 0^\circ$, $\beta = 0^\circ$.



(b) $\alpha = 18$ to 35° , $SR = 91.4 \text{ cm (36 in.)}$
 Figure A63.-Continued.



(c) $\alpha = 30$ to 50° , $SR = 0$.
Figure A 68.-Continued.

-2

-3

-4

-5

-6

-7

-8

-9

-10

-11

-12

-13

-14

-15

-16

-17

-18

-19

C_m

α, deg

○ 55

□ 60

◇ 70

△ 80

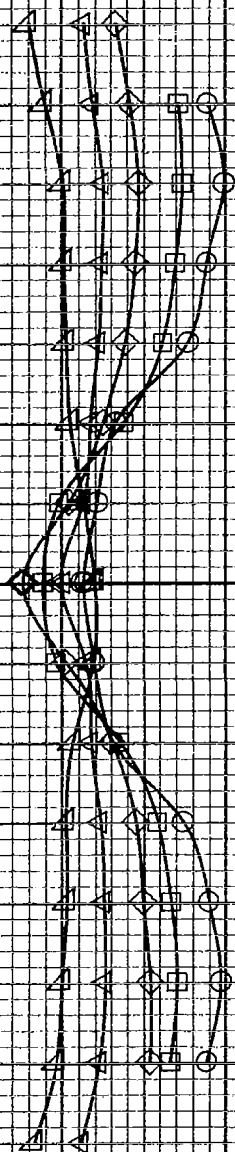
▽ 90

$\Omega b/2V$

(d) $\alpha=55$ to 90 deg, $SR=0$.
Figure A63.-Concluded.

α, deg
 $\circ 8$
 $\square 10$
 $\diamond 12$
 $\triangle 14$
 $\nabla 16$

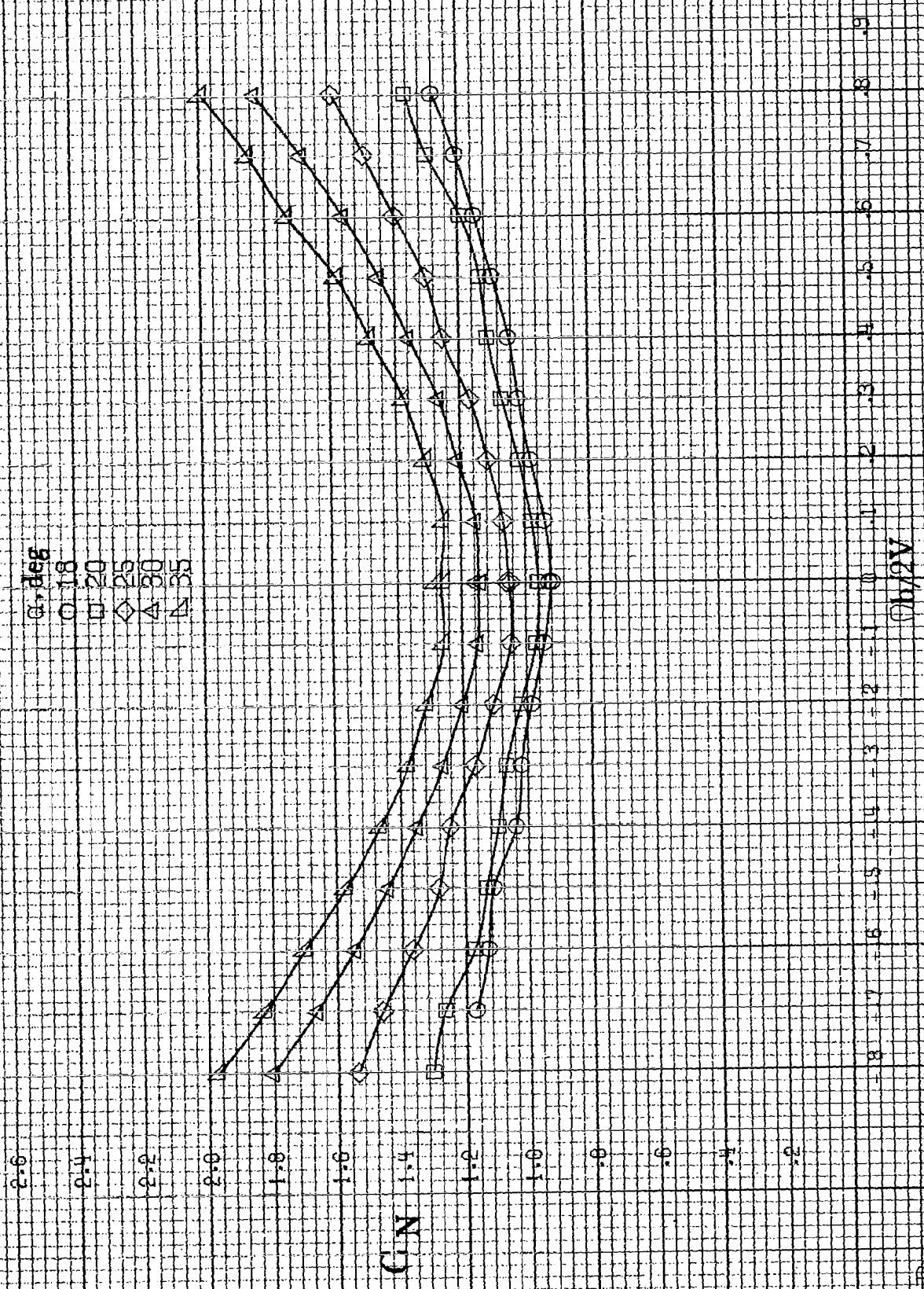
C_N



$\alpha/2V$

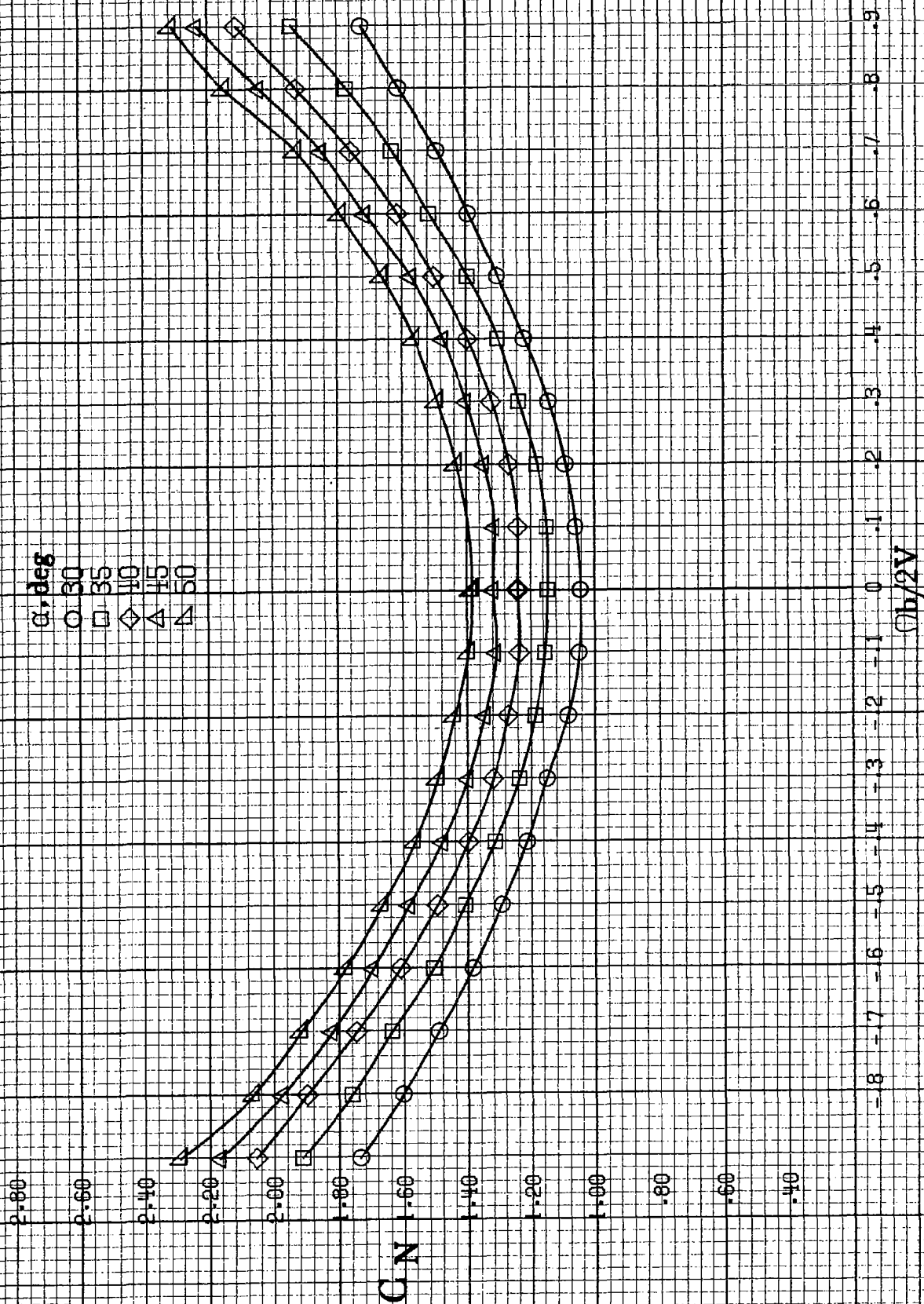
(a) $\alpha = 8$ to 16° , $SR = 91.4 \text{ cm (36 in)}$.

Figure A64.-Effect of rotation rate and angle of attack on normal-force coefficient for long body, low wing, horizontal tail no. 2 configuration. $\delta_e = 0^\circ$, $\delta_a = 0^\circ$, $\delta_r = 0^\circ$, $\beta = 0^\circ$.

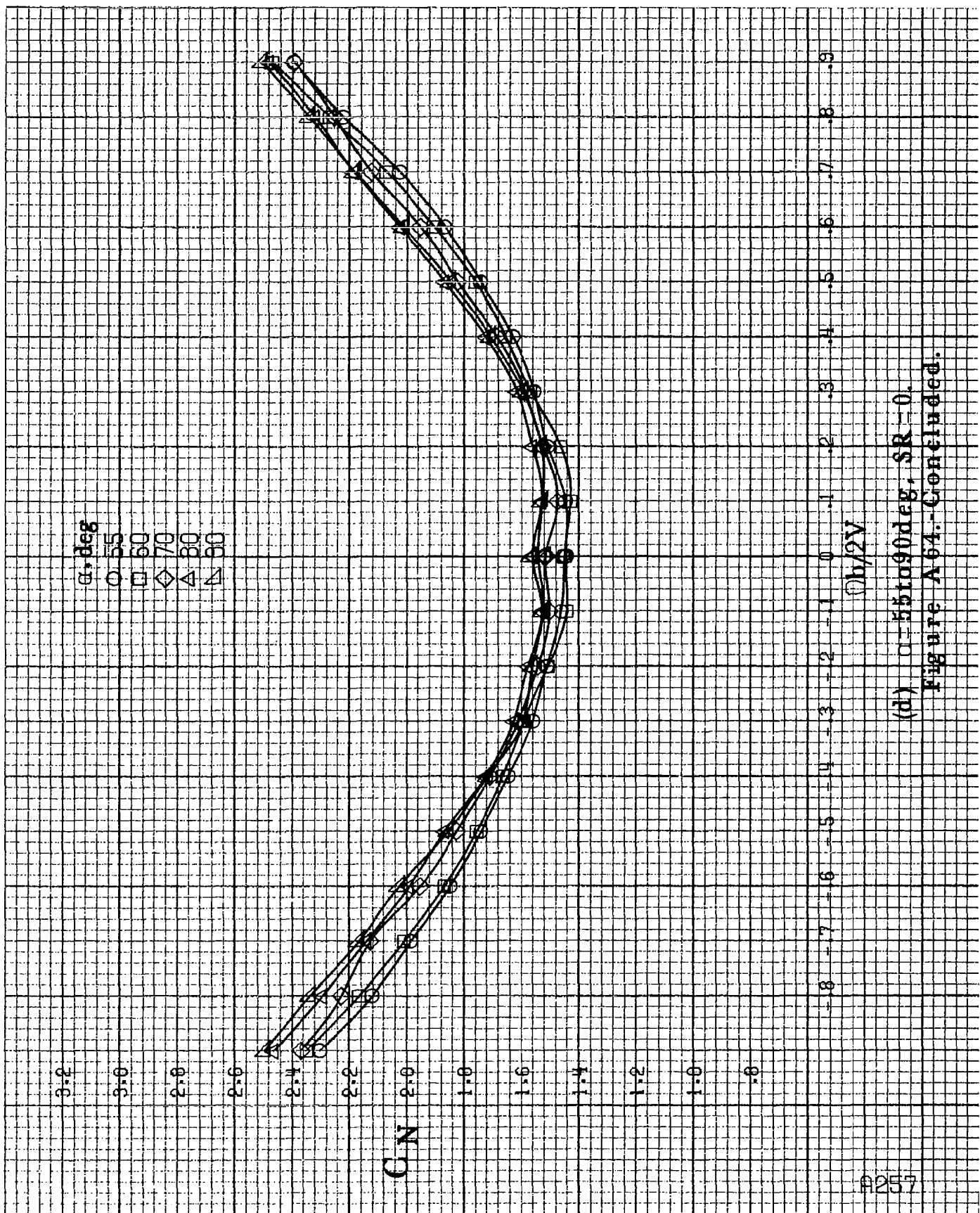


(b) $\alpha = 18$ to 35 deg. SR = 91.4 cm (86 in).
Figure A 54 - Continued.

A256



(a) $\alpha = 30$ to 50° , $SR = 0$.
Figure A 64.-Continued.



(d) $\alpha = 55$ to 90° , $SR = 0$.
Figure A64.-Concluded.

α, deg

○ 8
□ 10
◇ 12
△ 14
▽ 16

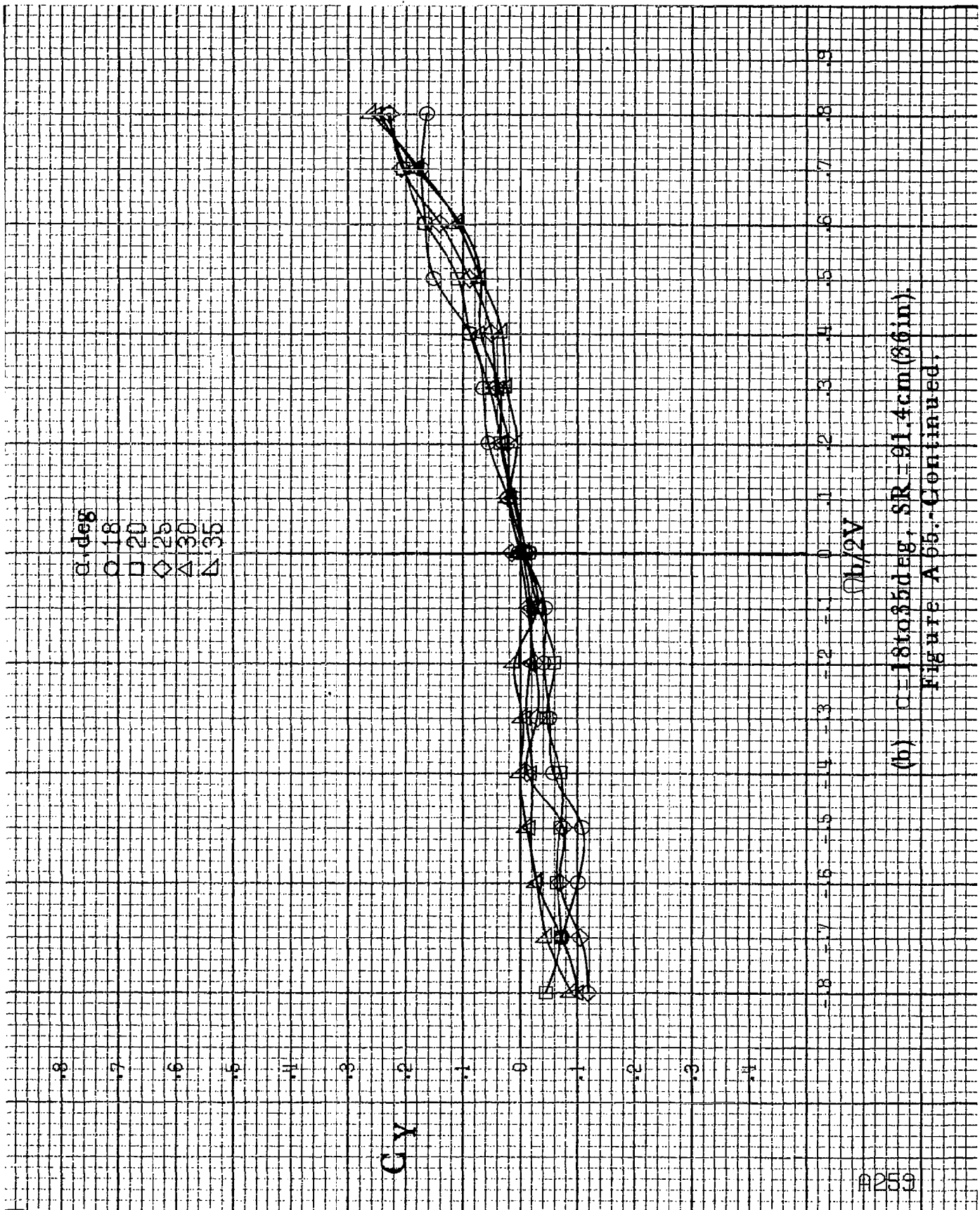
C_Y

$Ob/2V$

(a) $\alpha = 8 \text{ to } 16 \text{ deg}$, $SR = 91.4 \text{ cm (36 in)}$.

Figure A65 - Effect of rotation rate and angle of attack on side-force coefficient for long body, low wing, horizontal tail no. 2 configuration. $\delta_a = 0^\circ$, $\delta_r = 0^\circ$, $\beta = 0^\circ$.

-.8
-.7
-.6
-.5
-.4
-.3
-.2
-.1
0
0.1
0.2
0.3
0.4
0.5
0.6
0.7
0.8
0.9



(b) $\alpha = 18$ to 35 deg, $SR = 21.4 \text{ cm (86 in.)}$
Figure A 65.-Continued.

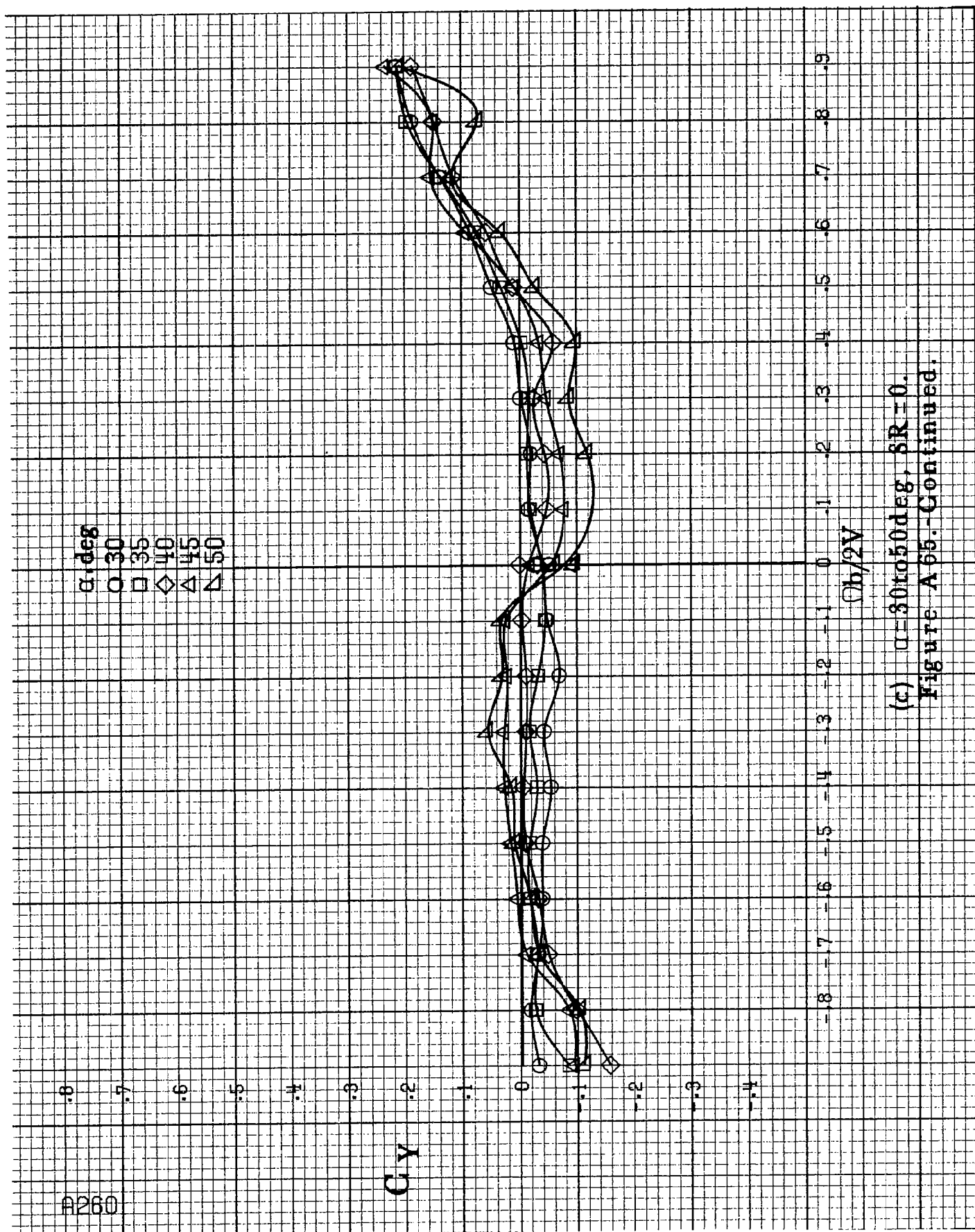
A260

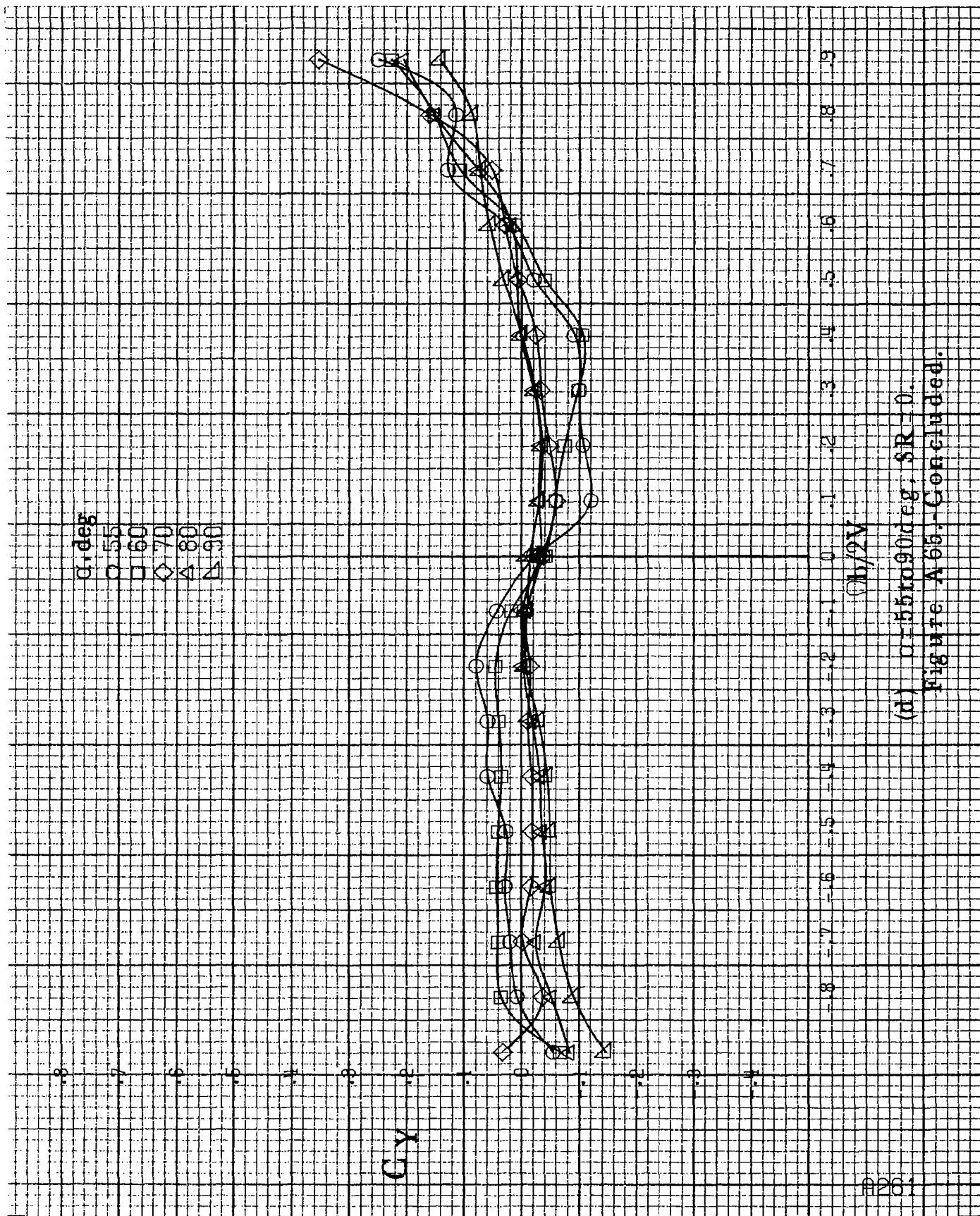
α, deg
 O 30
 □ 35
 ◇ 40
 △ 45
 ▲ 50

C_Y

$C_b/2V$

(c) $\alpha=30$ to 50 deg, $\delta R=0$.
 Figure A 65.-Continued.

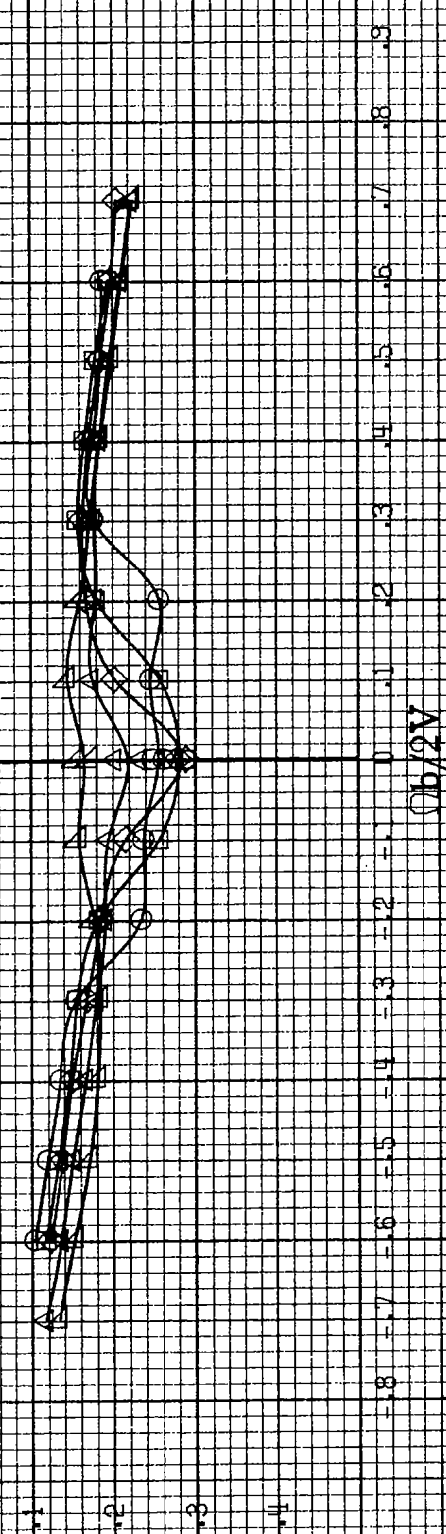




(d) $\alpha=55$ to 90° , $\$R=0$.
Figure A65.-Concluded.

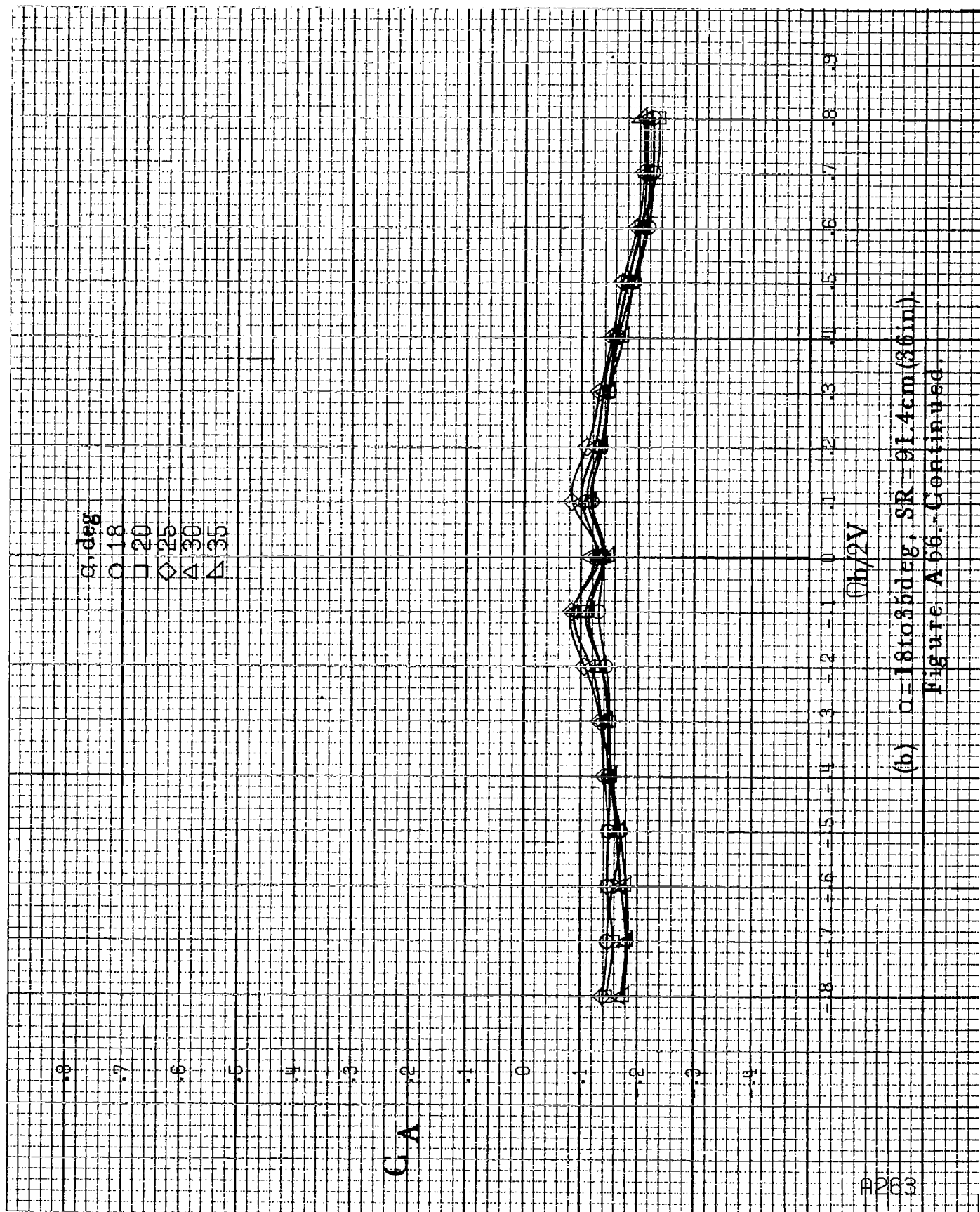
α, deg
 8
 10
 12
 14
 16

C_A



(a) $\alpha=8$ to 16° , $SR=91.4\text{cm}(36\text{in})$.

Figure A66.-Effect of rotation rate and angle of attack on axial-force coefficient for long body, low wing, horizontal tail no. 2 configuration. $\delta\alpha=0^\circ$, $\delta\alpha=0^\circ$, $\delta\tau=0^\circ$.



(b) $\alpha = 18$ to 35° , $SR = 91.4\text{cm} (36\text{in})$,
Figure A 56. Continued.

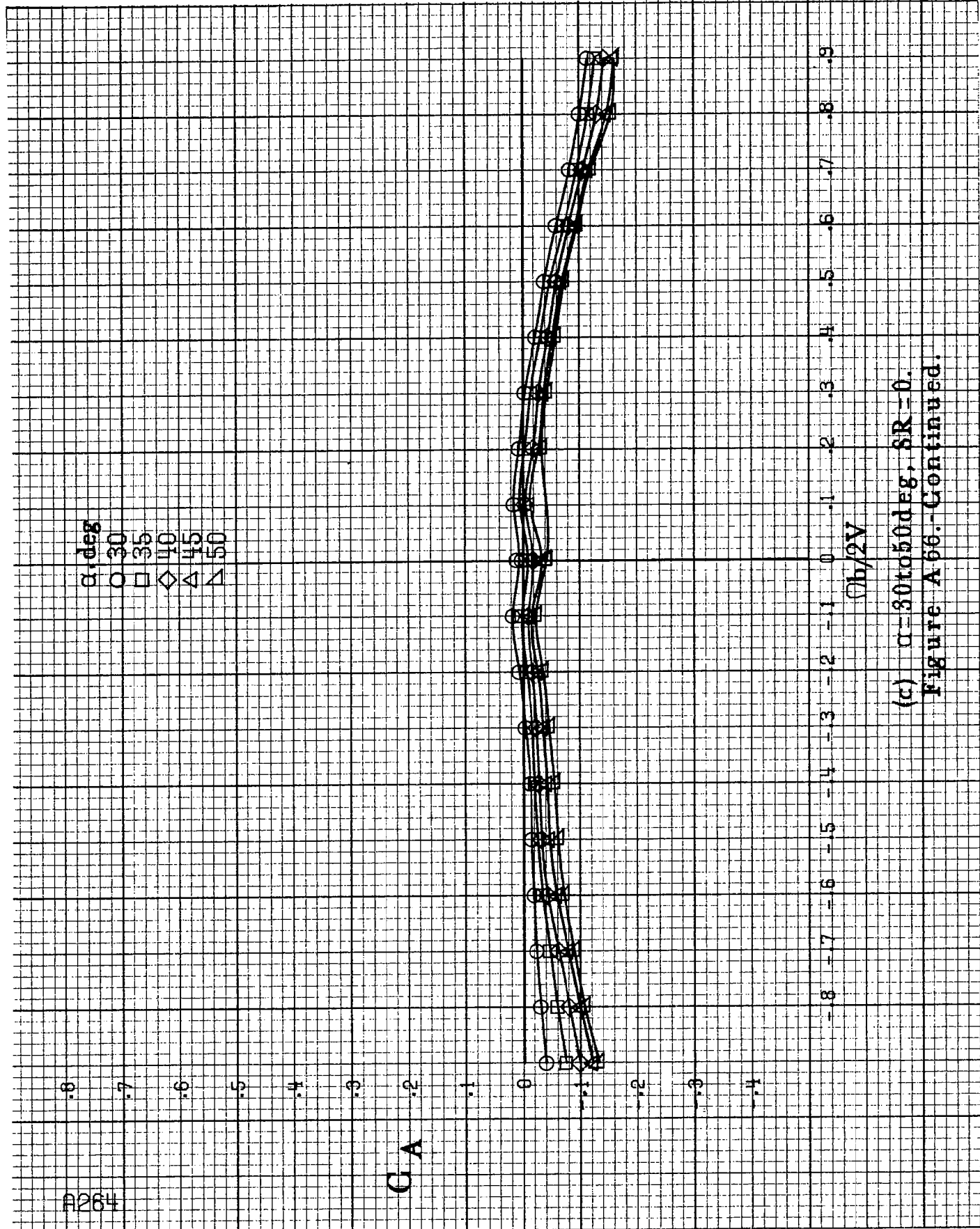
A264

α, deg
 O 30
 □ 35
 ◇ 40
 △ 45
 ▲ 50

G_A

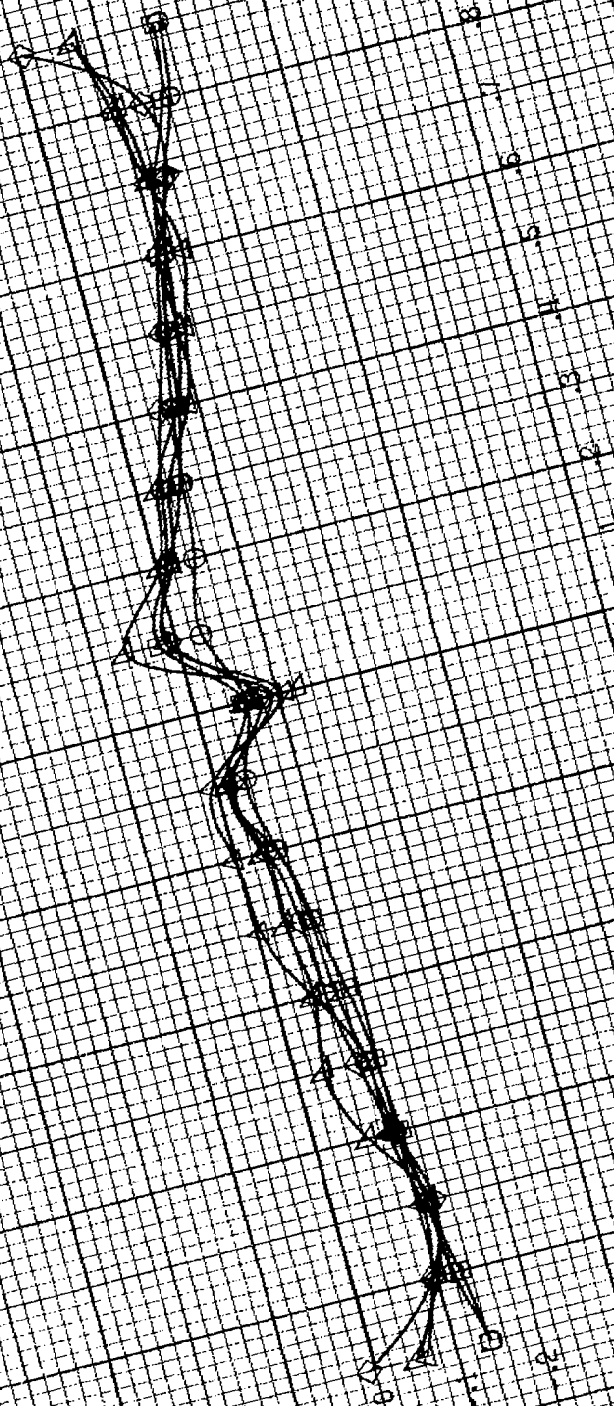
$\phi_b/2V$

(c) $\alpha=30$ to 50 deg, $\delta R=0$.
 Figure A 66.-Continued.

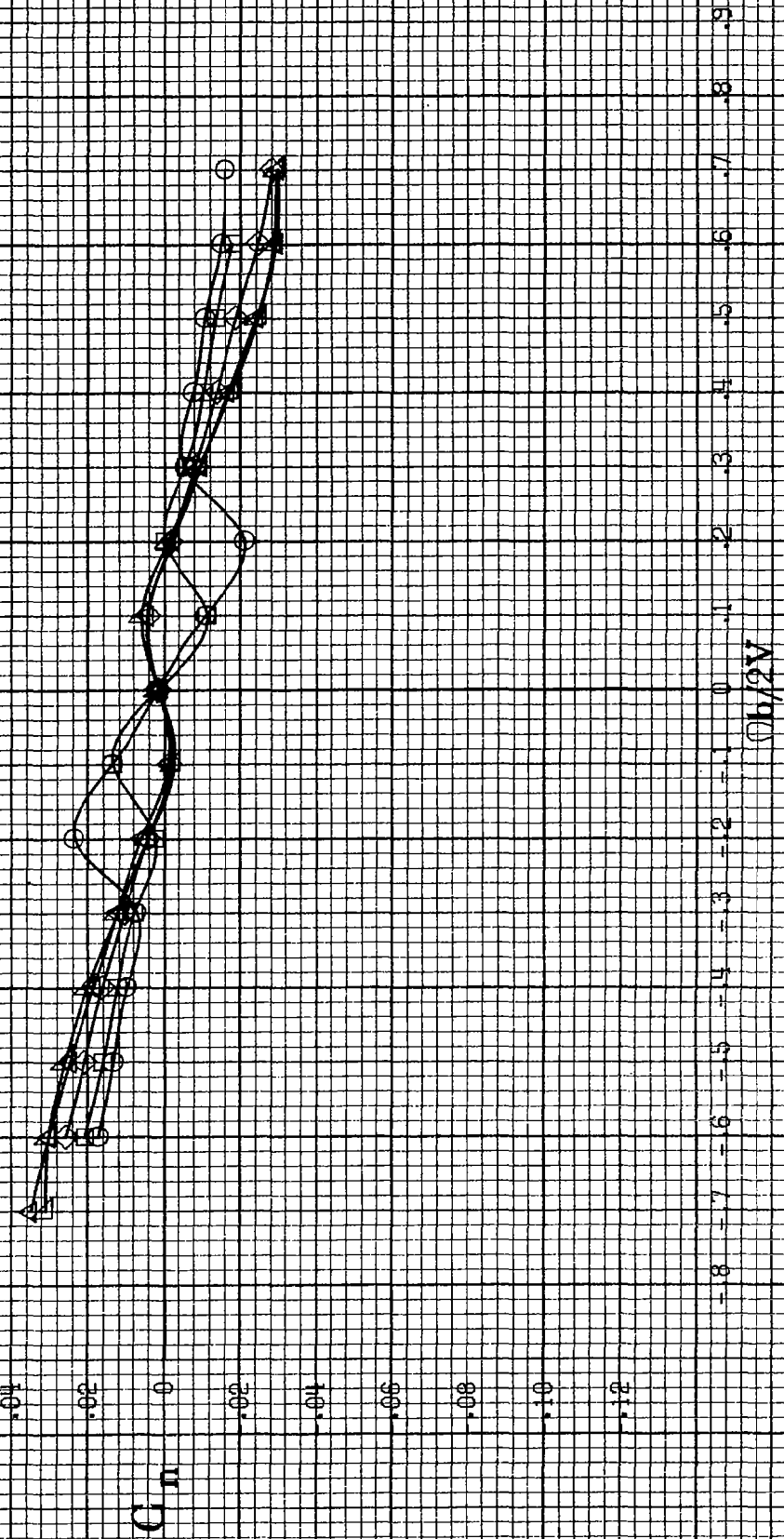


3.48
 5.5
 6.6
 7.7
 8.8
 9.9

CA

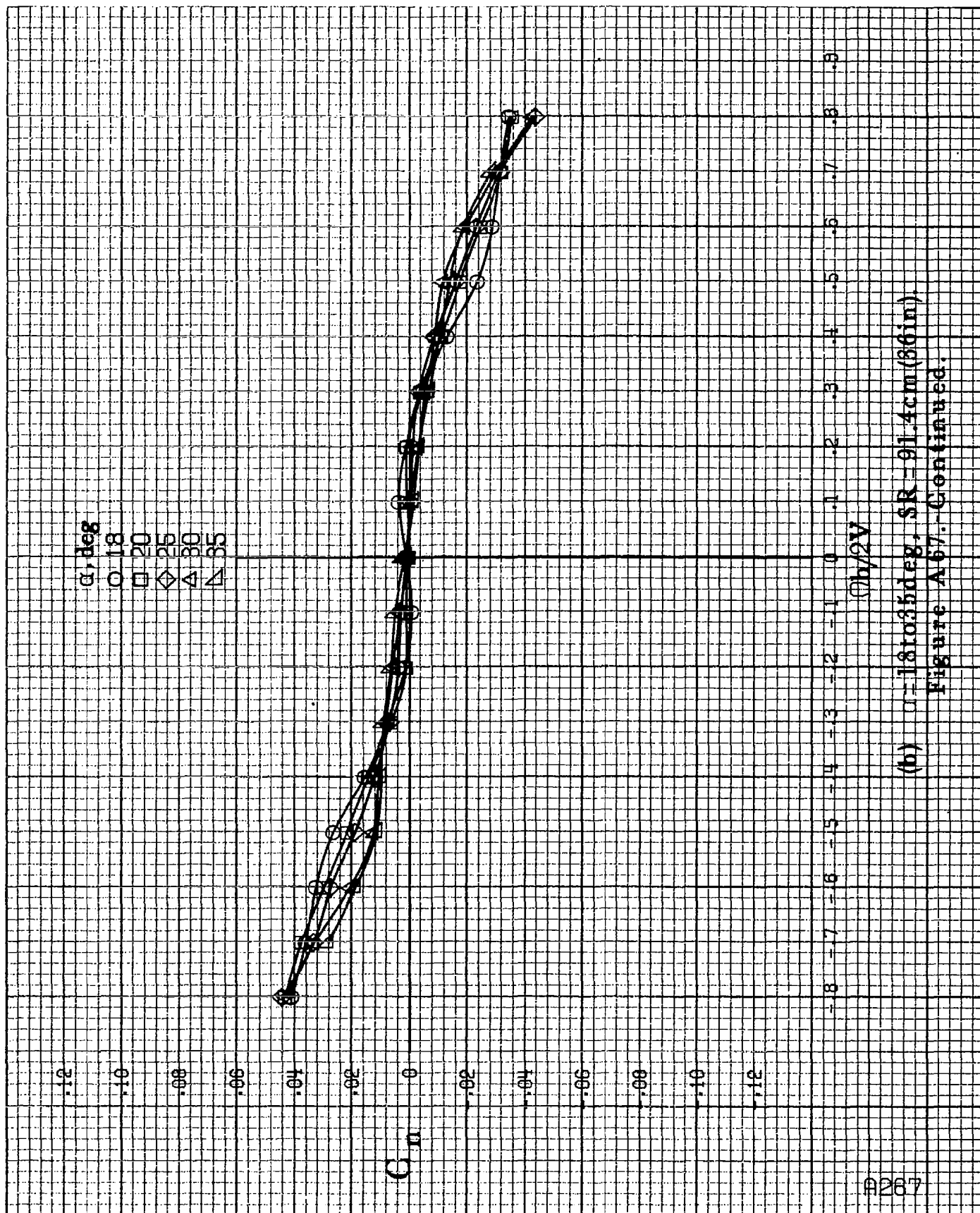


α, deg
 ○ 8
 □ 10
 ◇ 12
 △ 14
 ▴ 16



(a) $\alpha=8$ to 16° , $SR=91.4\text{cm}(36\text{in})$.

Figure A.67. - Effect of rotation rate and angle of attack on yawing-moment coefficient for long body, low wing, horizontal tail no. 3 configuration. $\delta_e=0^\circ$, $\delta_s=0^\circ$, $\delta_r=0^\circ$.

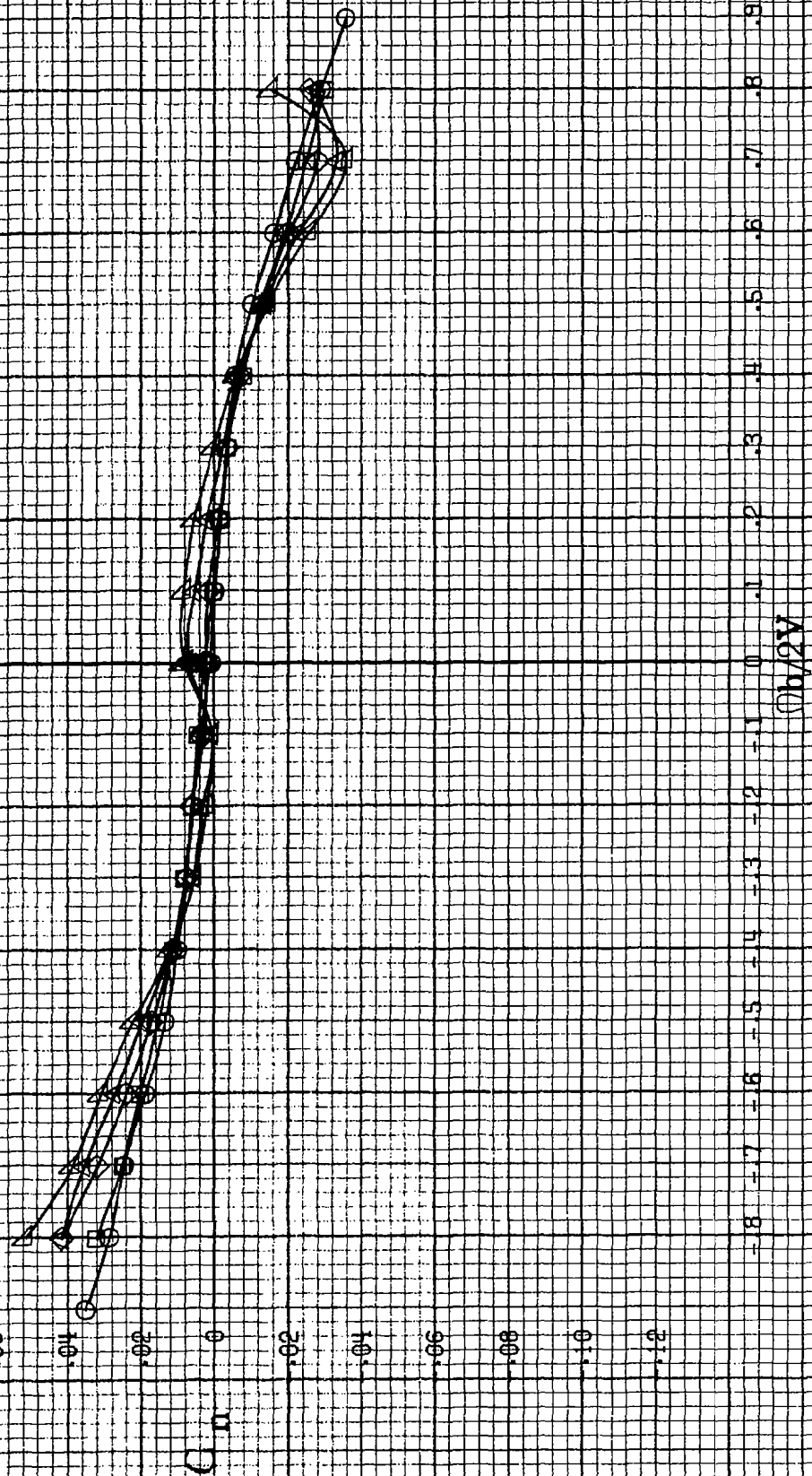


(b) $\alpha=18$ to 35° , $SR=91.4\text{cm}(86\text{in})$.

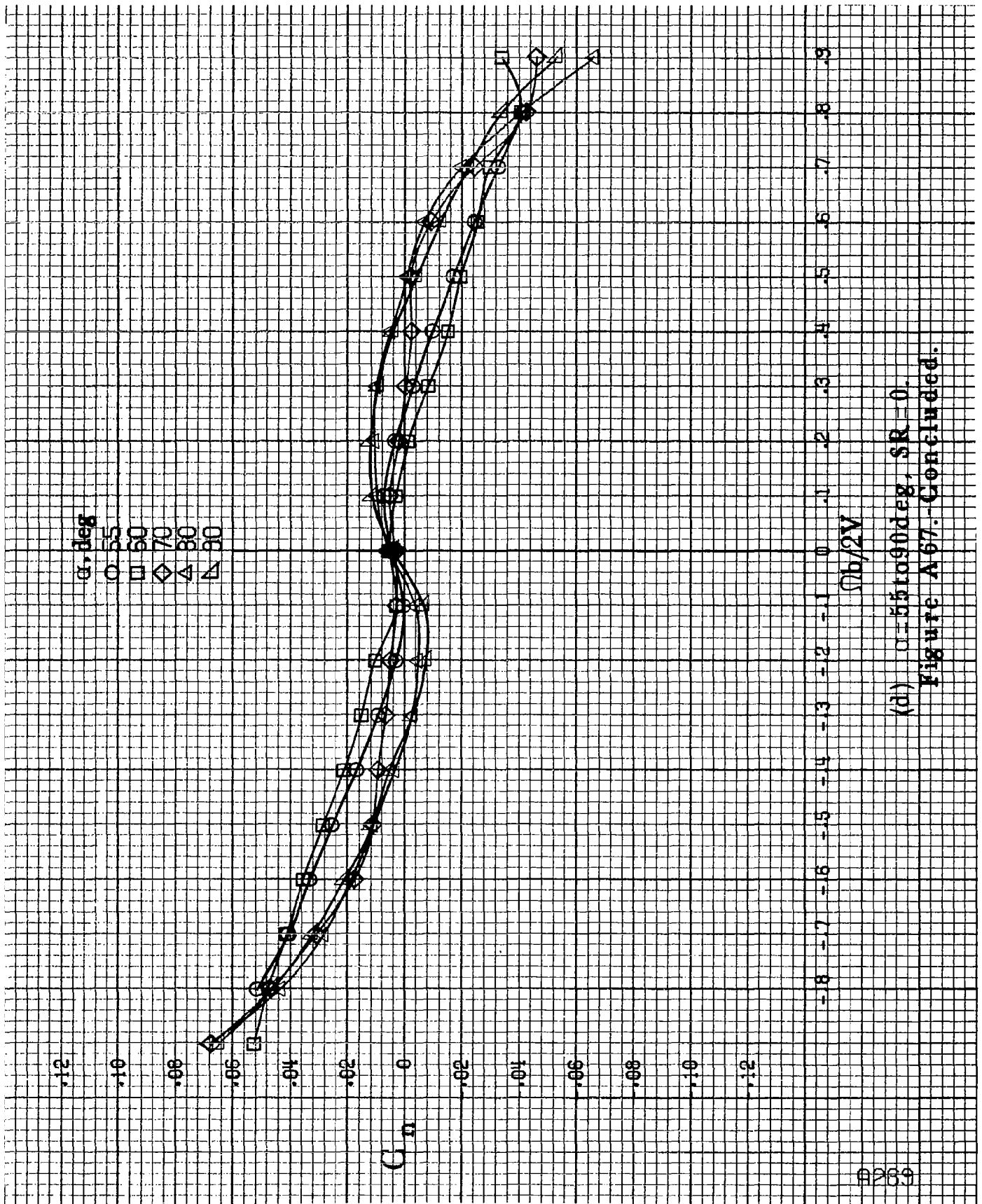
Figure A67.-Continued.

B268

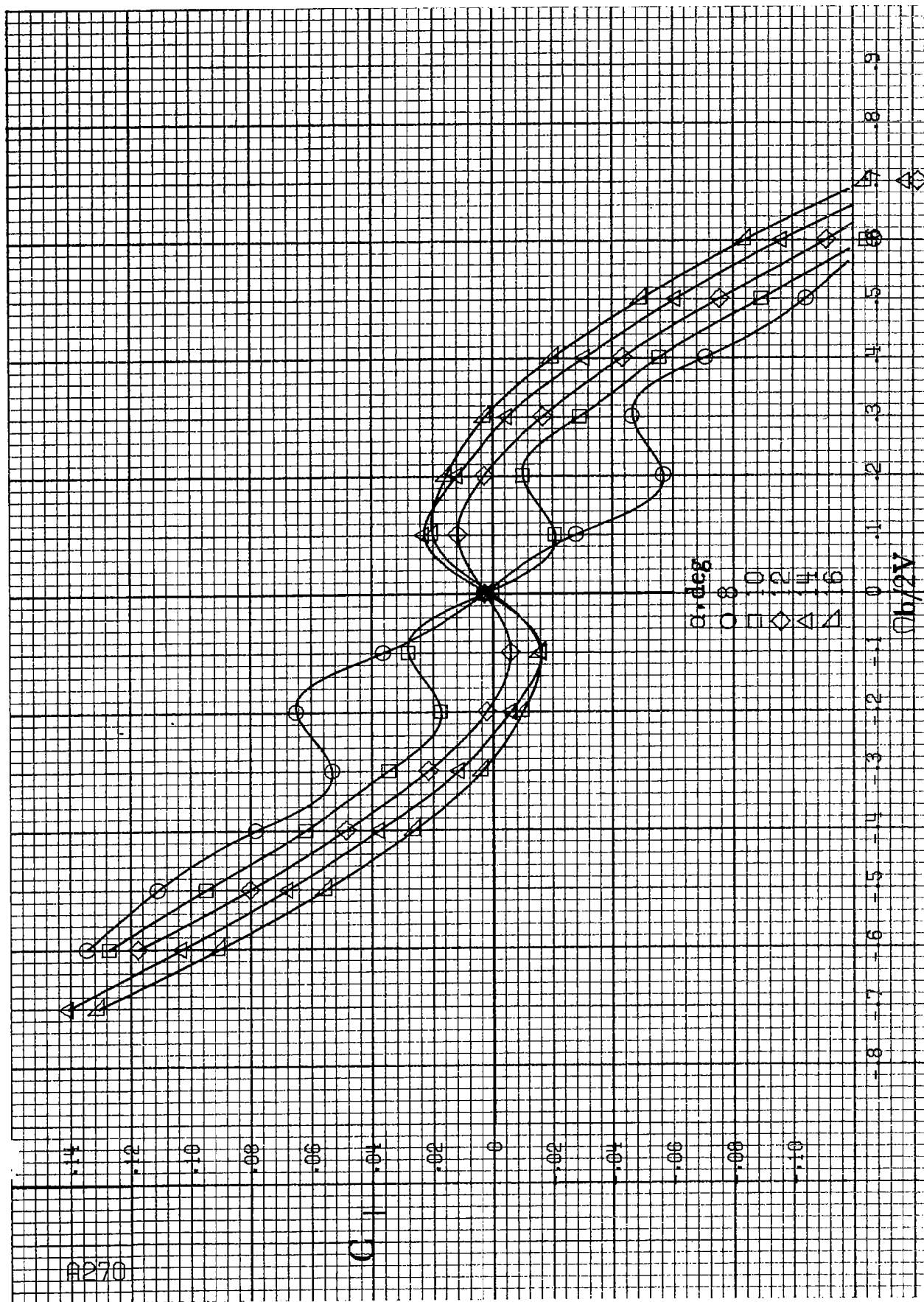
α, deg
 ○ 30
 □ 35
 ◇ 40
 △ 45
 ▴ 50



(c) $\alpha=30$ to 50 deg, $SR=0$,
 Figure A67.-Continued.

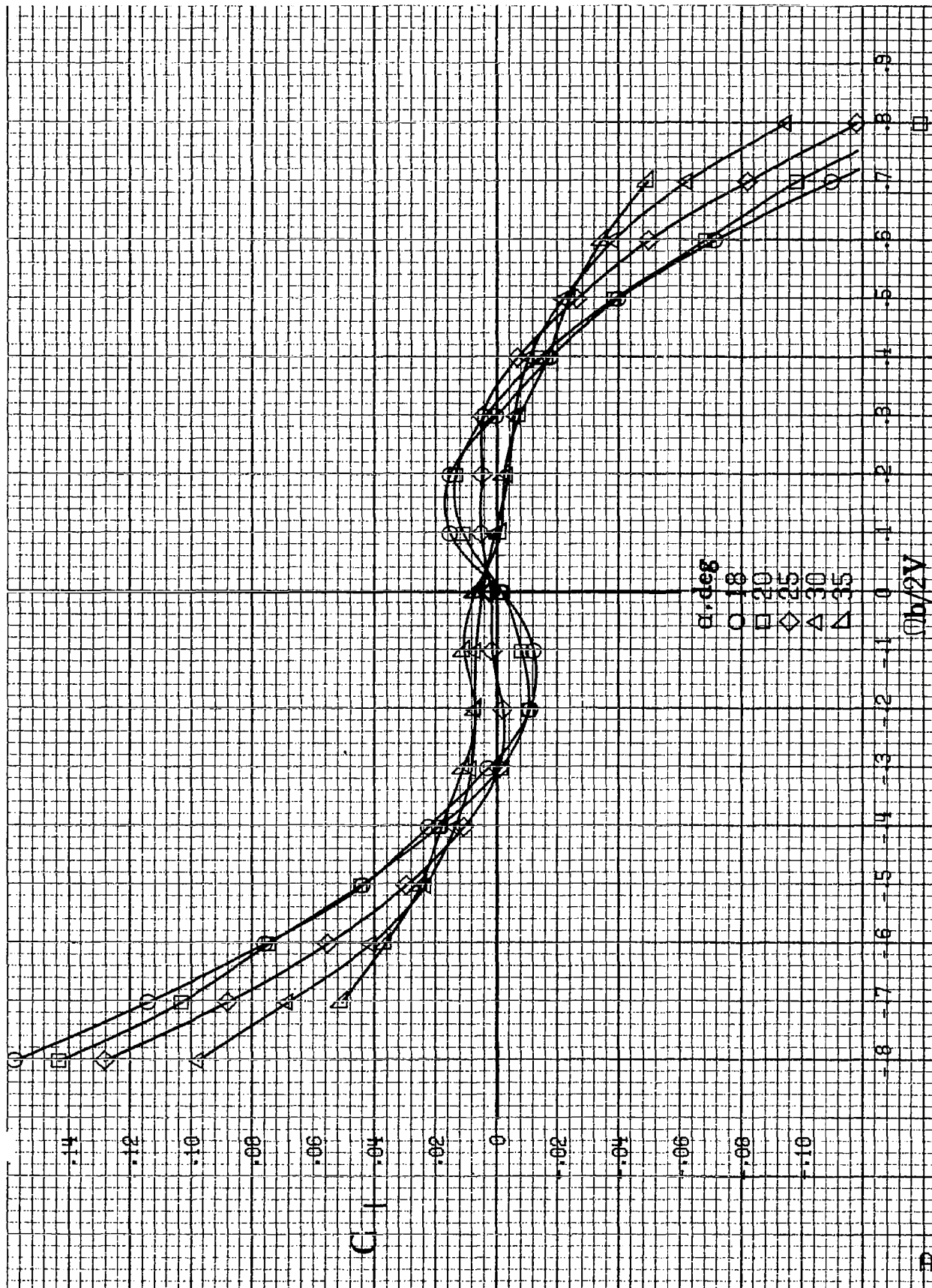


(d) $\alpha=55$ to 90° , $SR=0$.
Figure A67--Concluded.

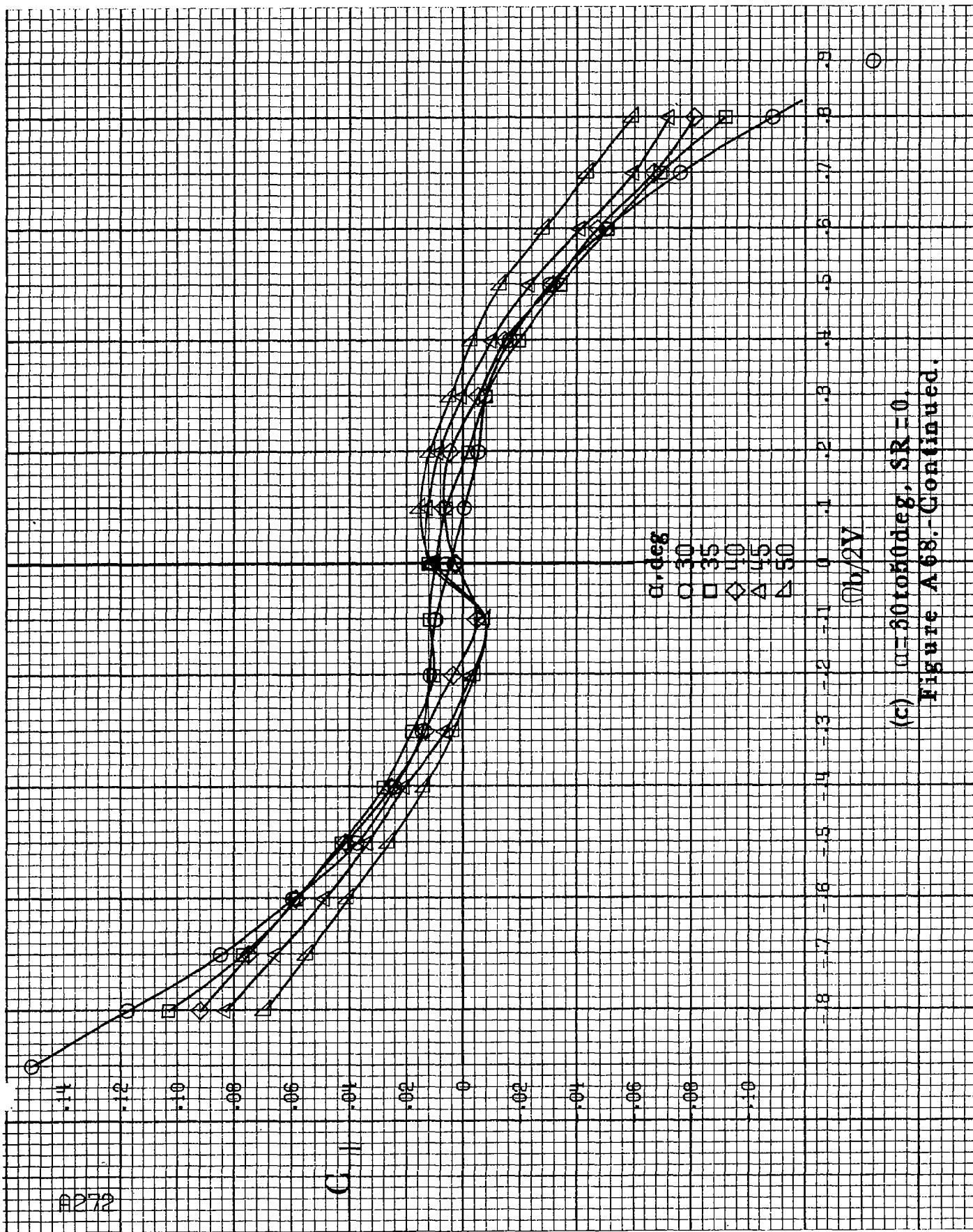


(a) $c=8$ to 16 deg, $SR=91.4$ cm (36 in).

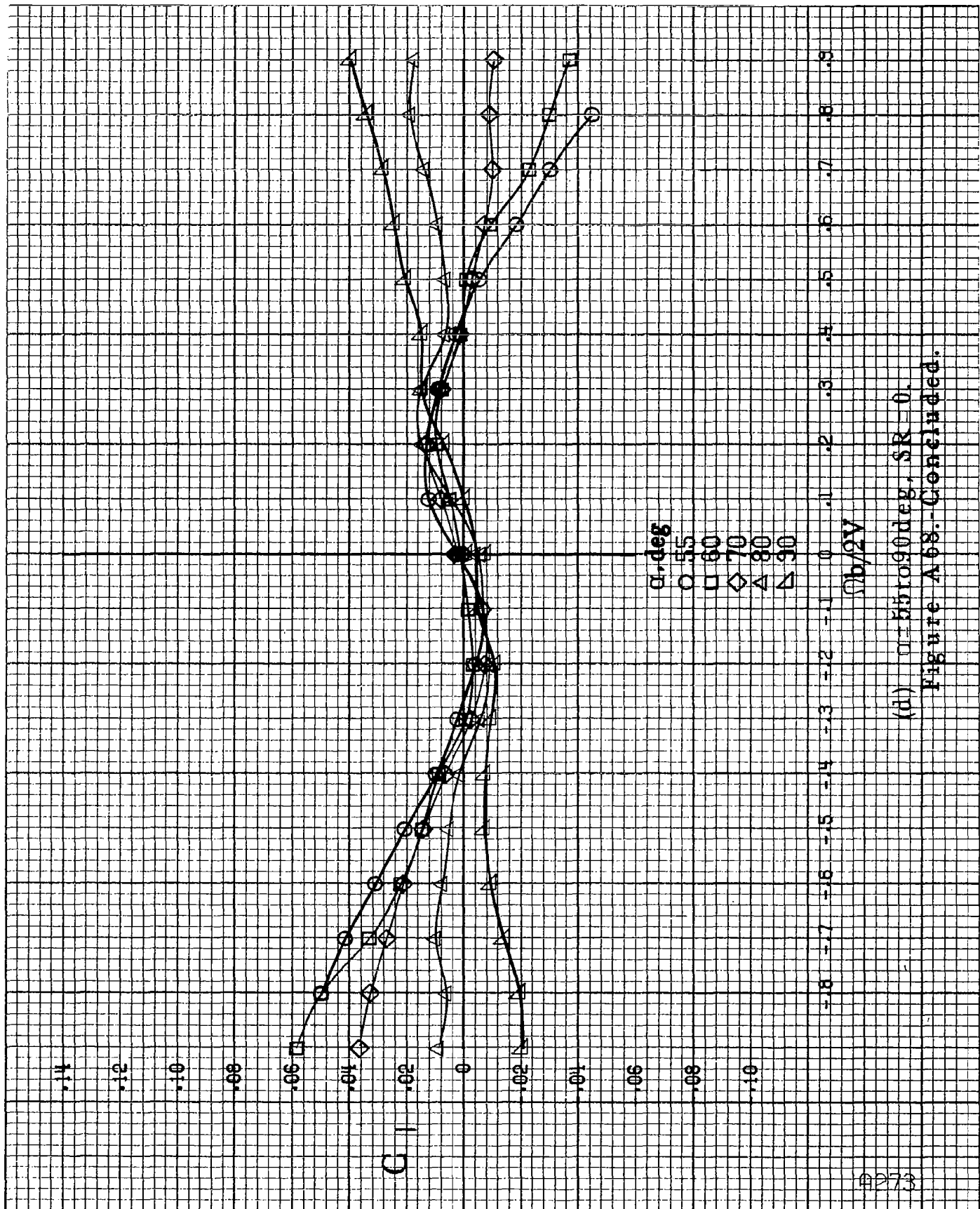
Figure A.68 - Effect of rotation rate and angle of attack on rolling-moment coefficient for long body, low wing, horizontal tail no. 3 configuration. $\delta a=0^\circ$, $\delta s=0^\circ$, $\delta r=0^\circ$, $\delta \alpha=10^\circ$.



(b) $\alpha=18$ to 35° , $SR=91.4\text{cm}$ (36in).
Figure A68.-Continued.



(c) $\omega = 30 \text{ to } 0 \text{ deg}$, $SR = 0$,
Figure A68.-Continued.



(d) $\alpha=55$ to 90° , $SR=0$.
Figure A68.-Concluded.

#274

C_m

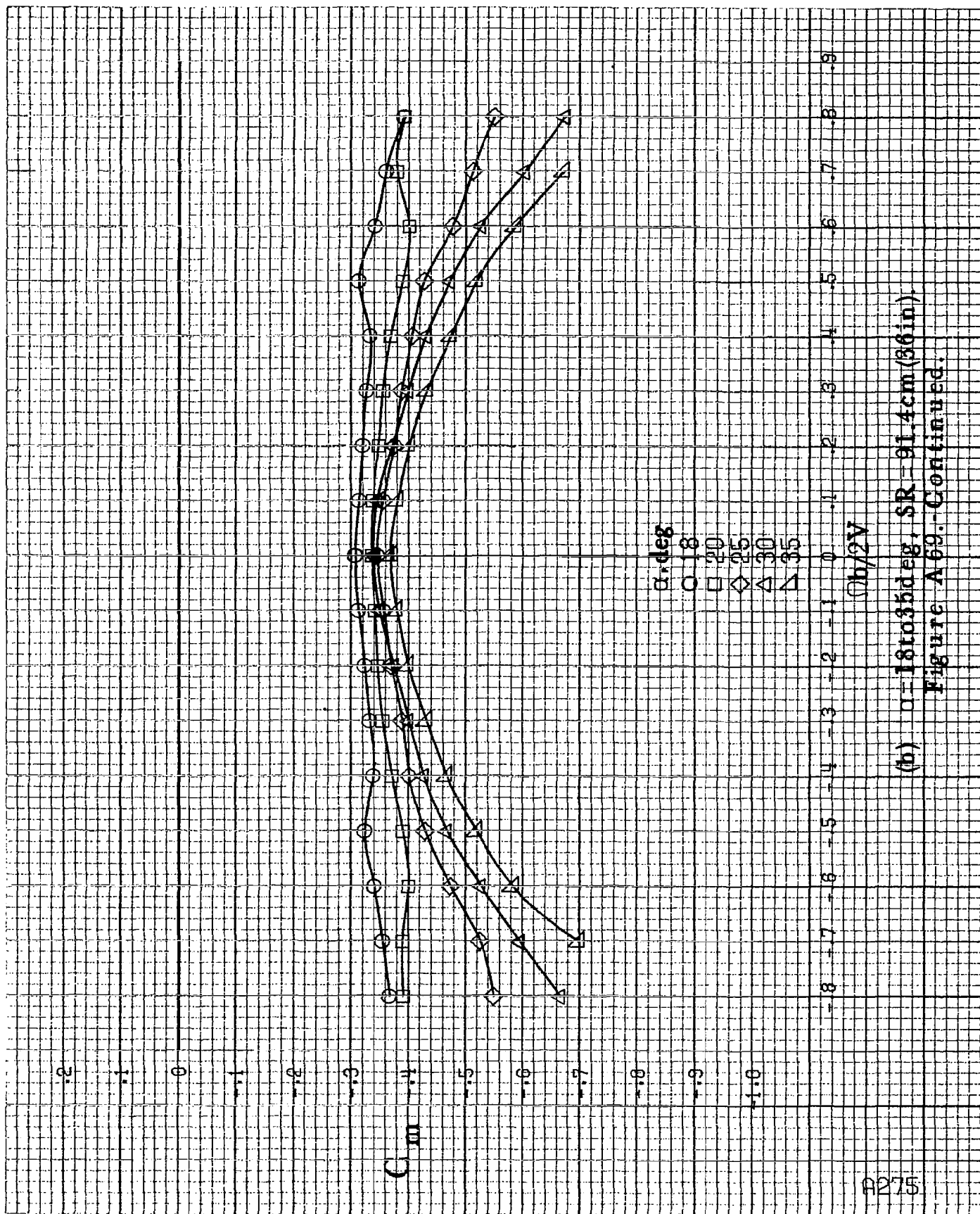
α, deg

○ 8
□ 10
◇ 12
△ 14
▽ 16

$b/2V$

(a) $\alpha = 8$ to 16 deg, $SR = 91.4 \text{ cm (36 in)}$.

Figure A69.-Effect of rotation rate and angle of attack on pitching-moment coefficient for long body, low wing, horizontal tail no. 3 configuration.
 $\delta_e = 0^\circ$, $\delta_a = 0^\circ$, $\delta_r = 0^\circ$, $\beta = 0^\circ$.



(b) $\alpha = 18$ to 35° , SR = 91.4 cm (36 in).

Figure A69.-Continued.

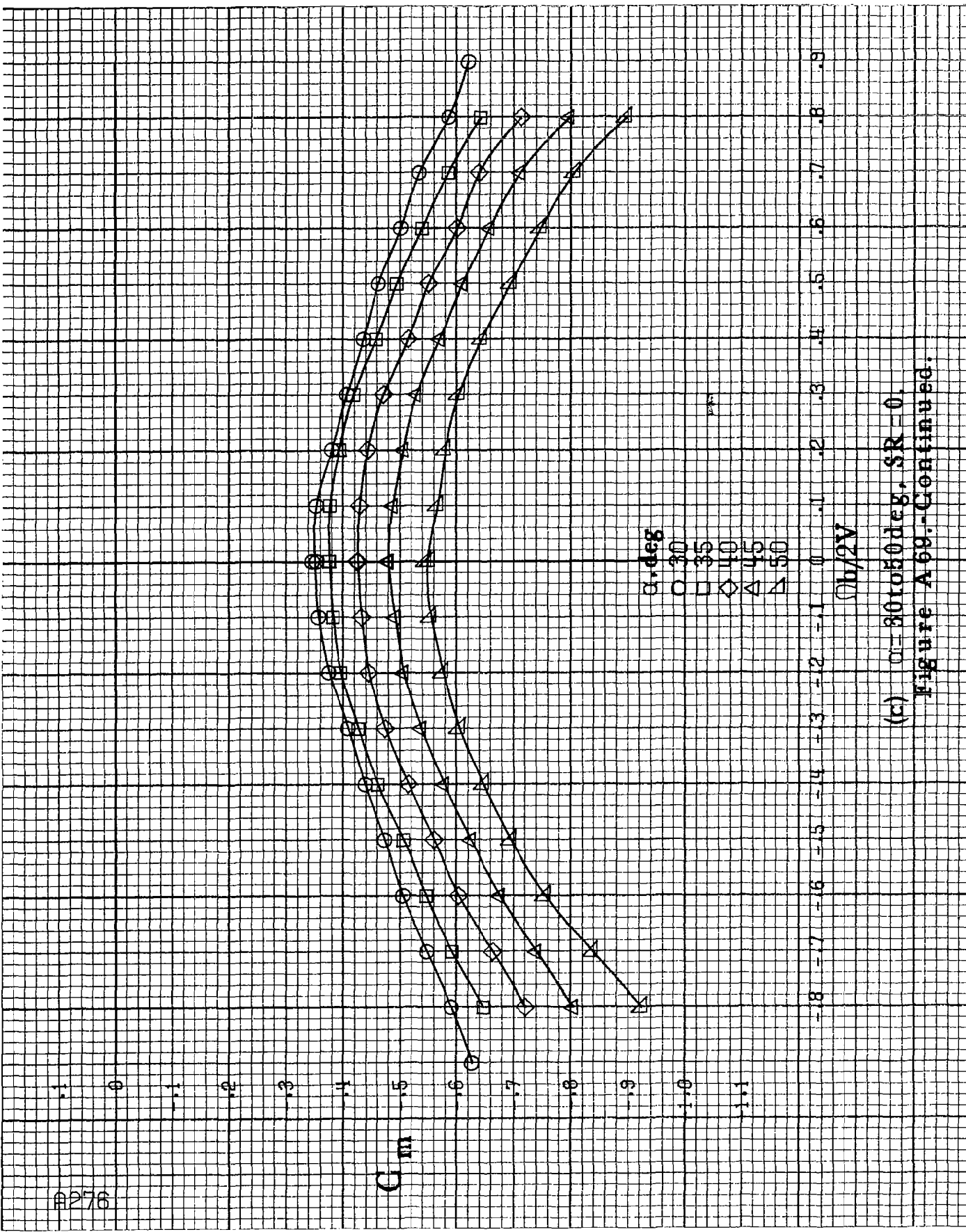
G_m

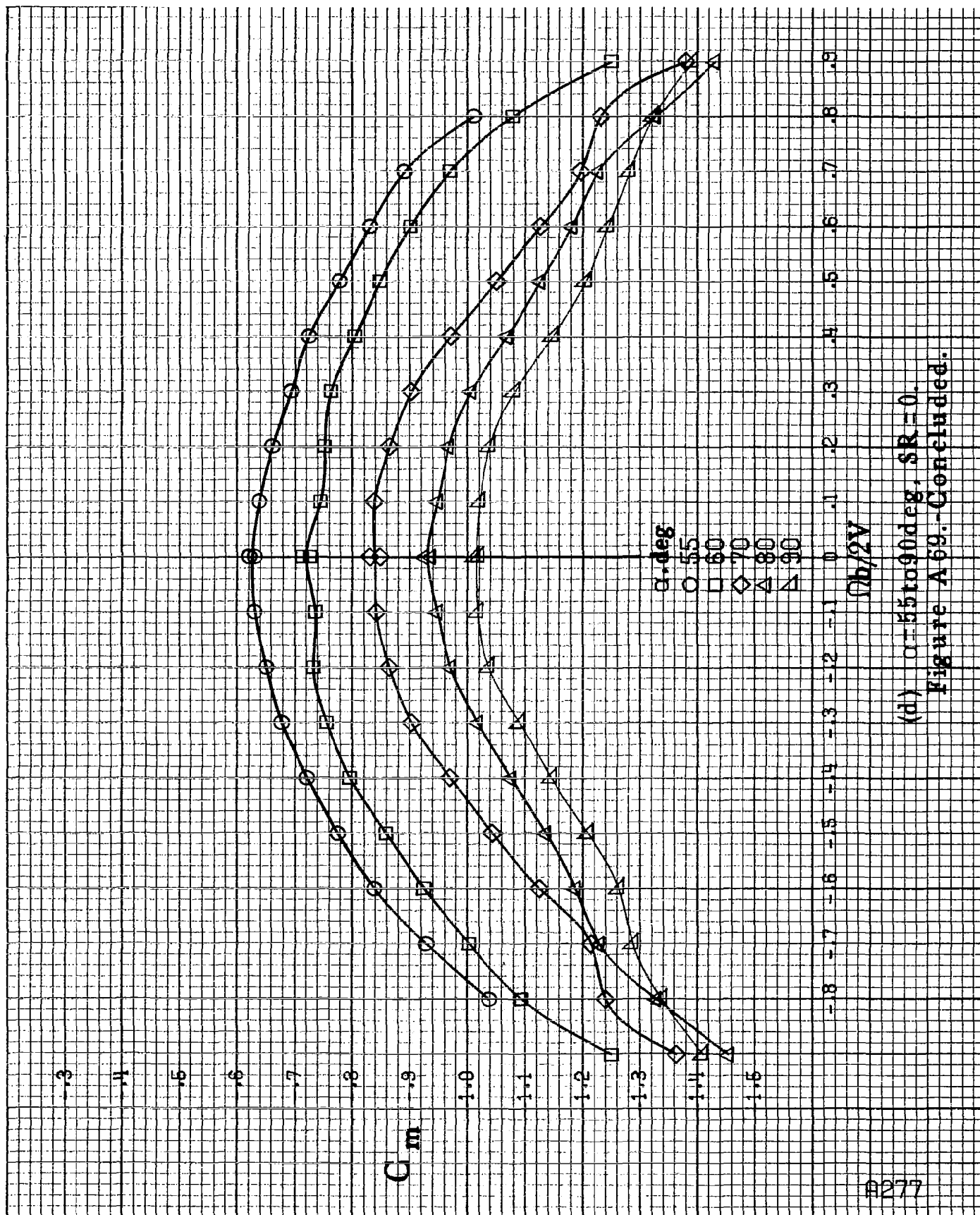
α, deg

- 30
- 35
- ◇ 40
- △ 45
- ▽ 50

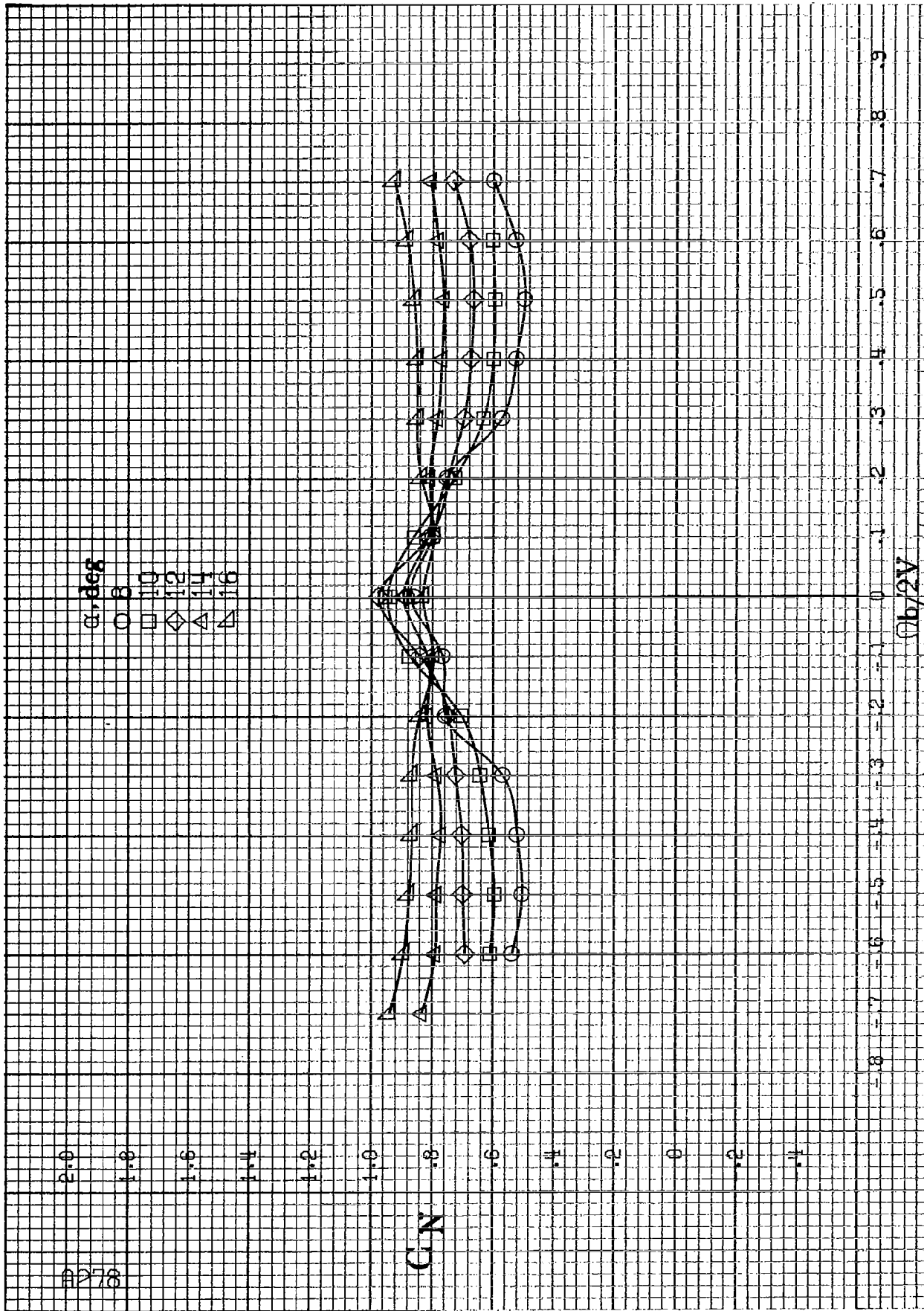
$V_b/2V$

(c) $\alpha = 30$ to 50 deg, $SR = 0$.
Figure A 69.-Continued.



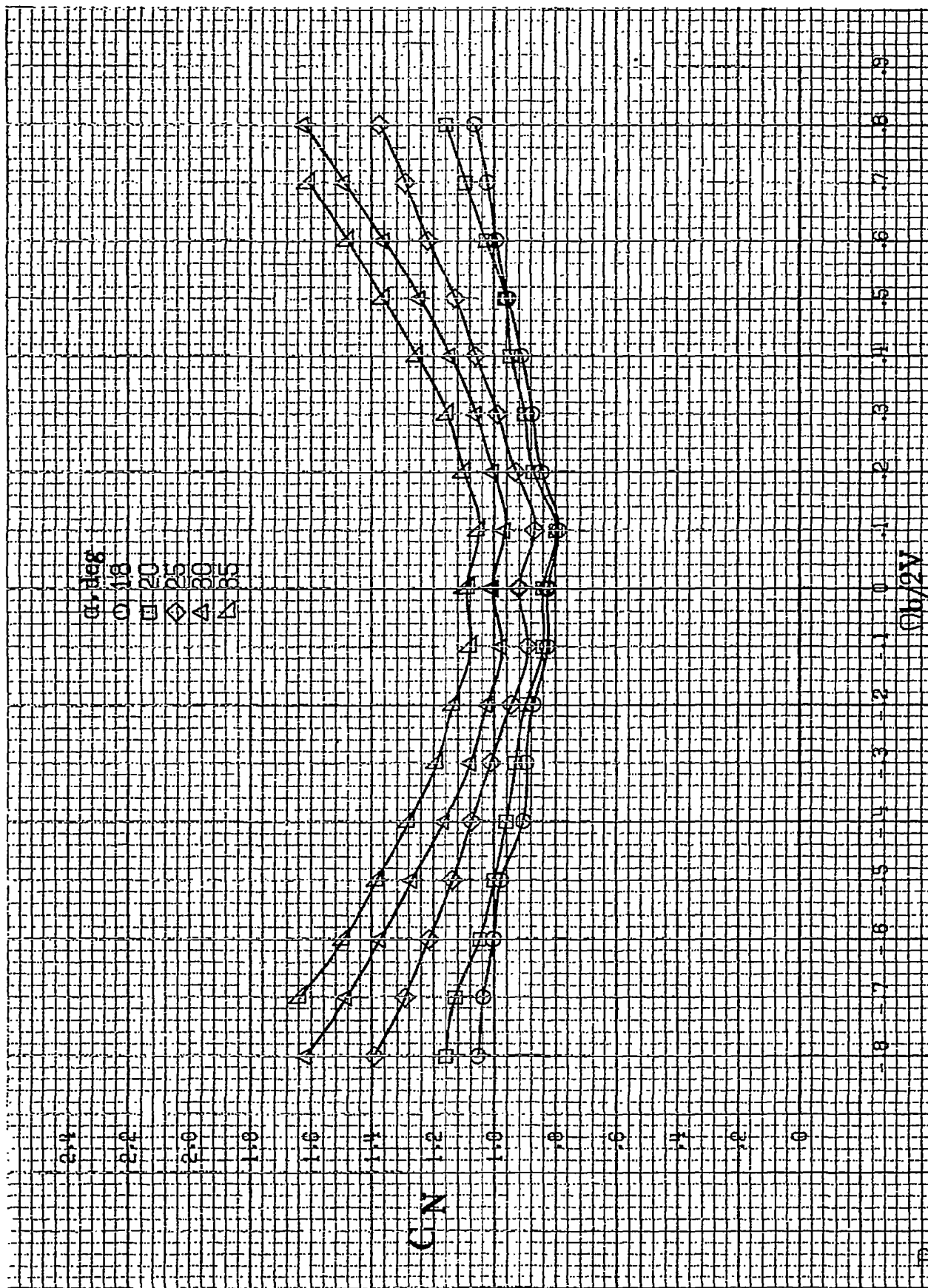


(d) $\alpha=55$ to 90° , $SR=0$.
Figure A 69. -- Concluded.



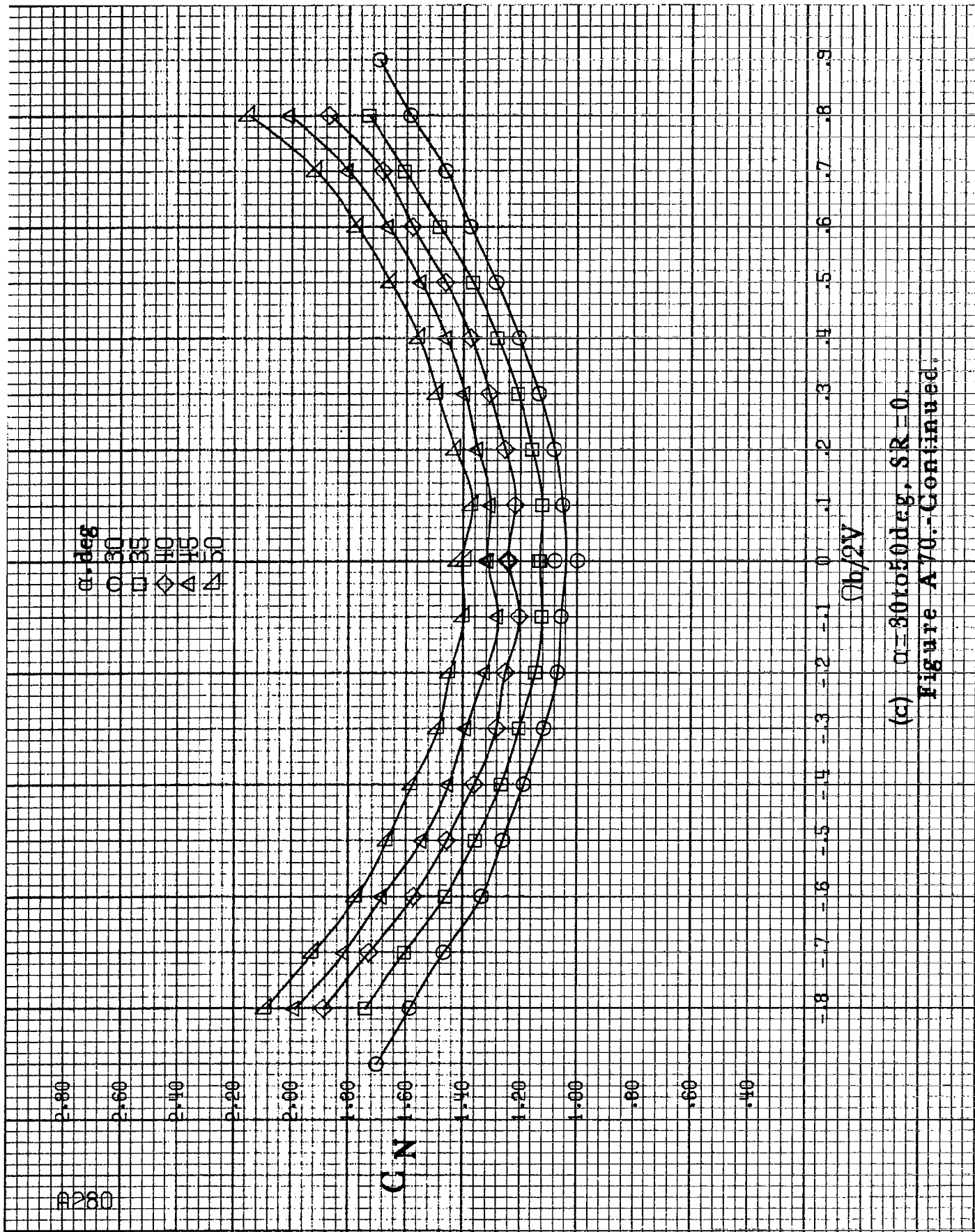
(a) $\alpha = 8$ to 16 deg, $SR = 91.4$ cm (36 in).

Figure A70.-Effect of rotation rate and angle of attack on normal-force coefficient for long body, low wing, horizontal tail no. 3 configuration. $\delta\alpha = 0^\circ$, $\delta\alpha = 0^\circ$, $\delta\alpha = 0^\circ$.

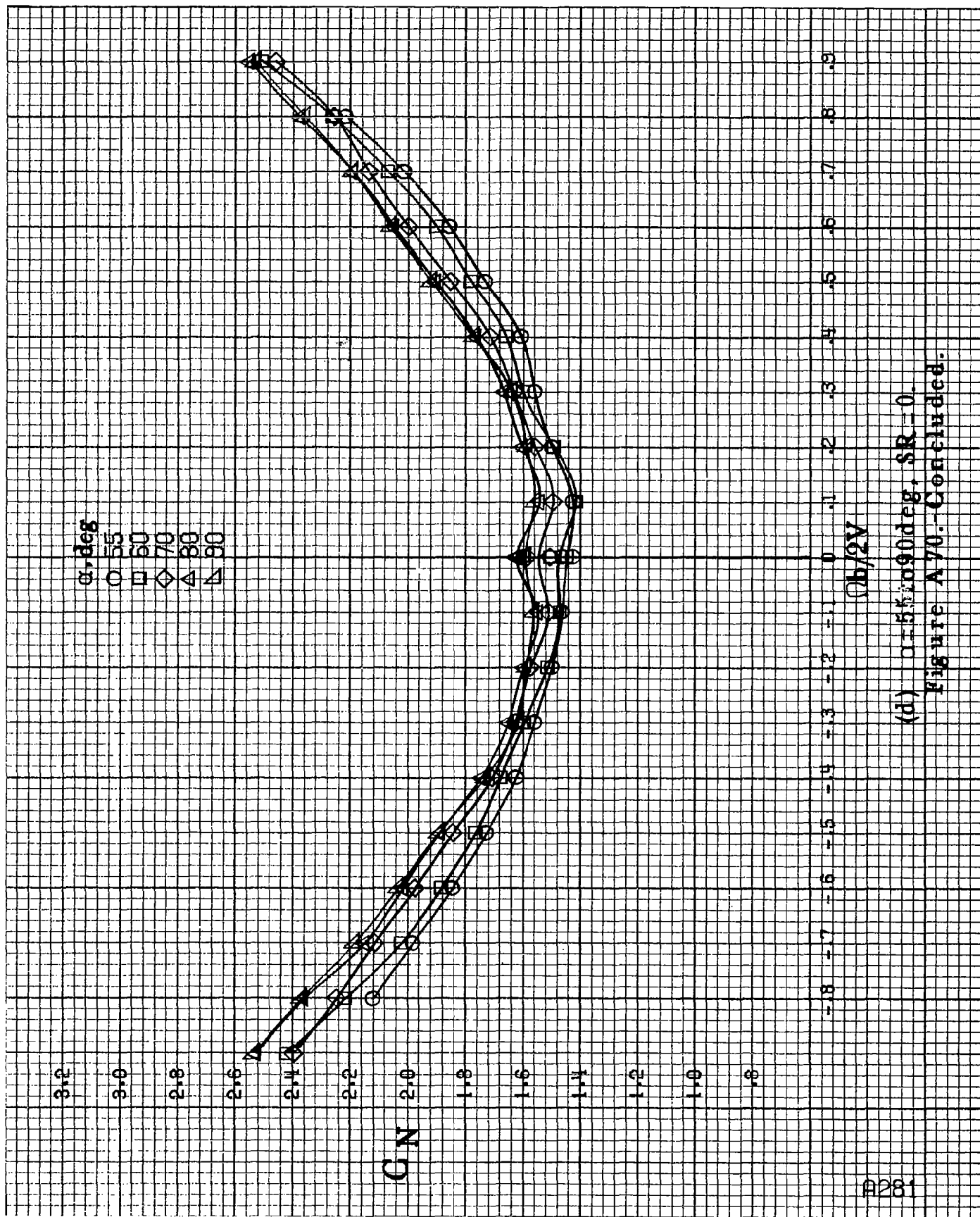


(b) $\alpha=18$ to 35 deg, SR = 91.4 cm (36 in.)

Figure A 70. Continued.



(c) $\alpha=30$ to 50 deg, $SR=0$.
Figure A70.-Continued.



(d) $\alpha = 55^\circ$ to 90° , $SR = 0$.
Figure A70.-Concluded.

α, deg

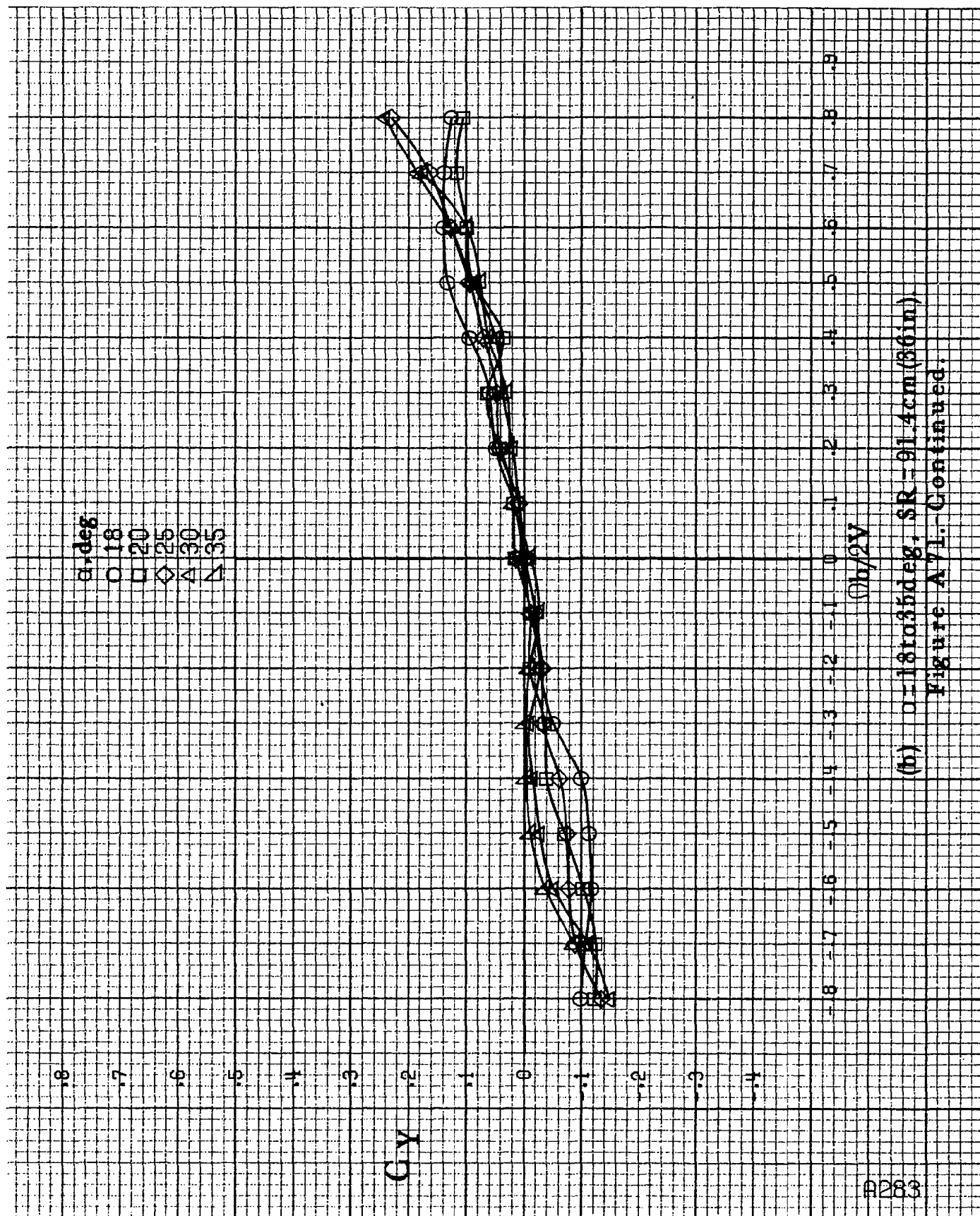
8
10
12
14
16

C_y

$b/2V$

(a) $\alpha = 8 \text{ to } 16 \text{ deg}$, $SR = 91.4 \text{ cm (36 in)}$.

Figure A.71.-Effect of rotation rate and angle of attack on side-force coefficient for long body, low wing, horizontal tail no. 3 configuration. $\delta_e = 0^\circ$, $\delta_s = 0^\circ$, $\delta_r = 0^\circ$.



A283

(b) $\alpha=18$ to 35 deg, $SR=91.4$ cm (36 in).

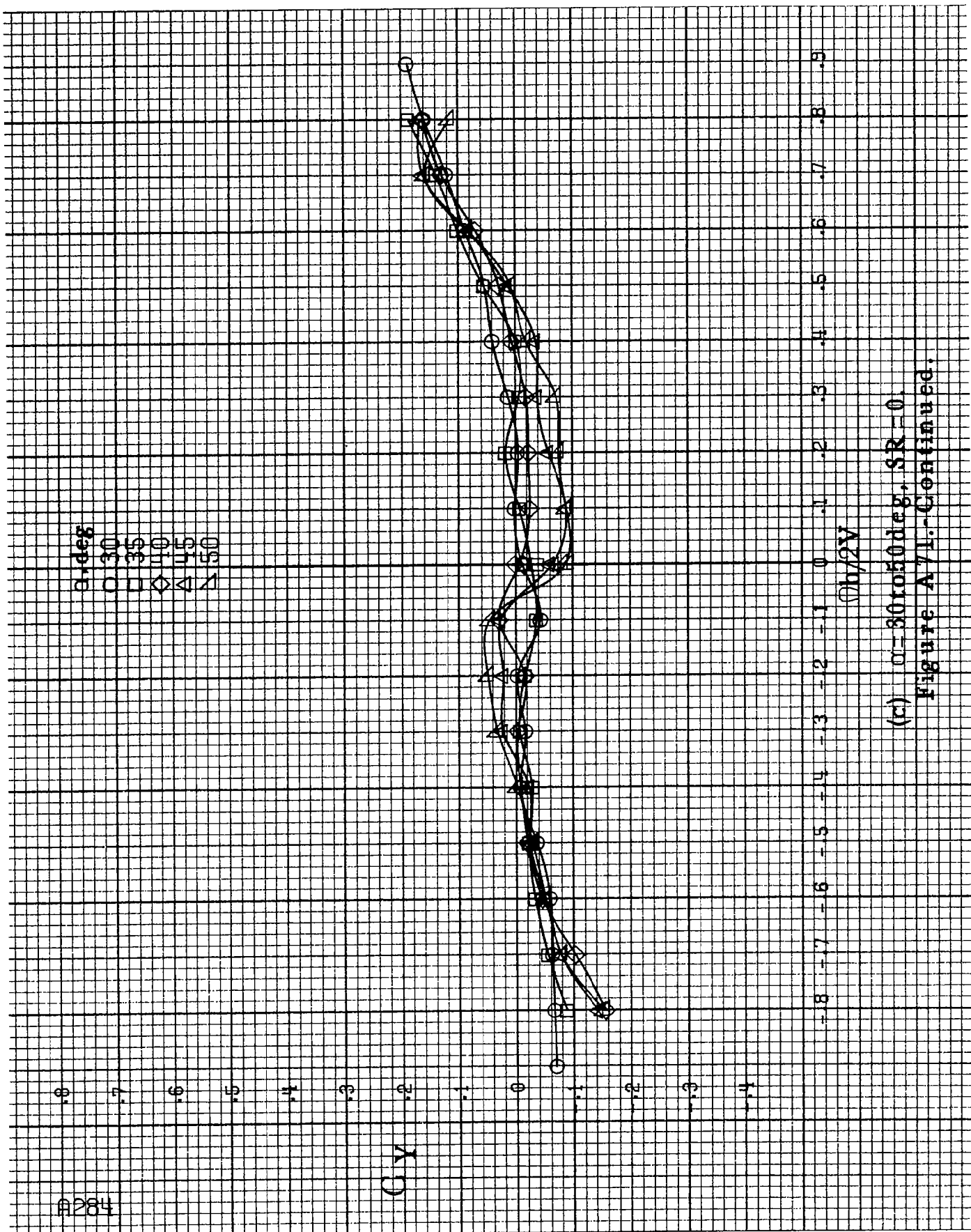
Figure A71. Continued.

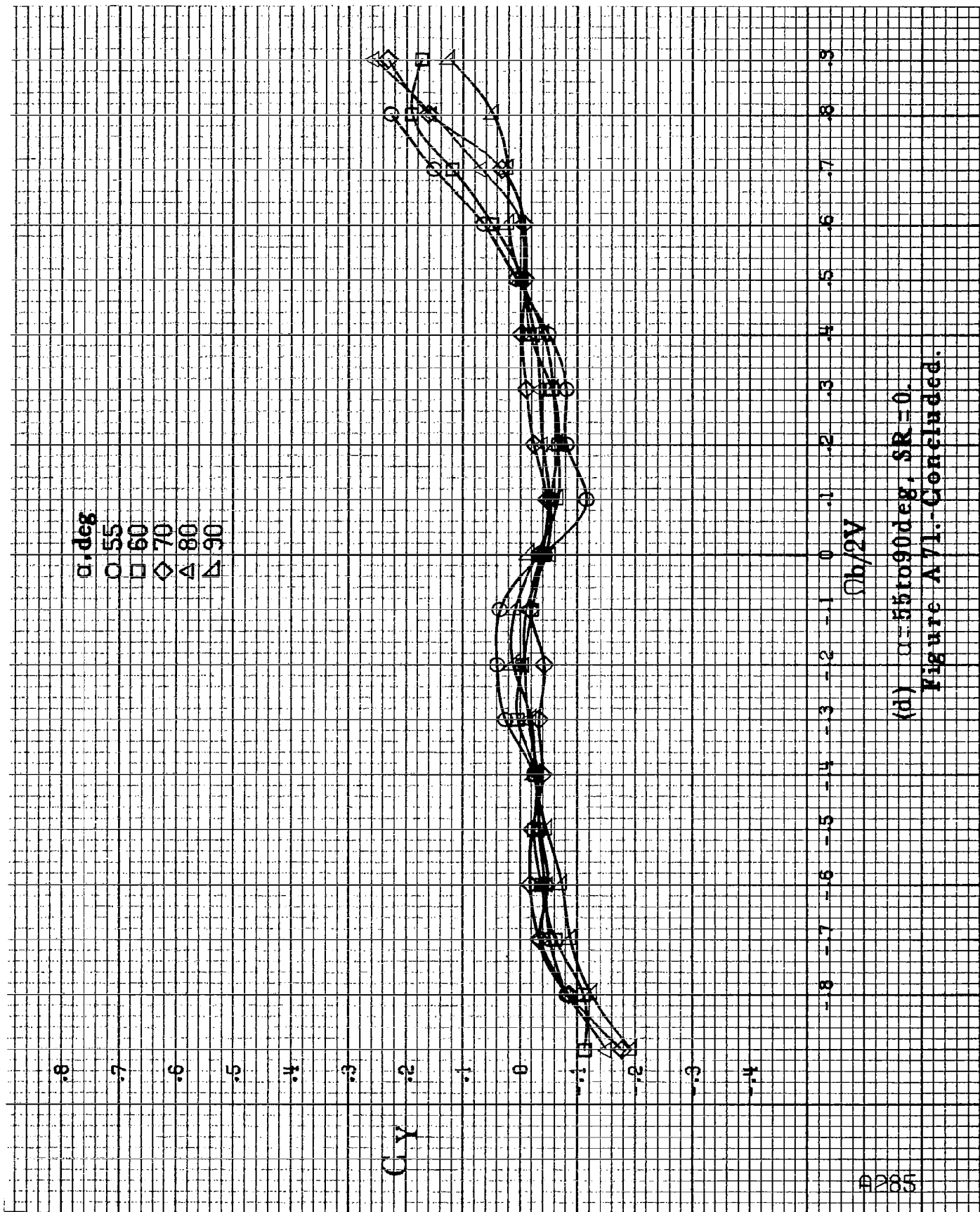
α, deg
 \circ 30
 \square 35
 \diamond 40
 \triangle 45
 ∇ 50

C_V

$\phi h/2V$

(c) $\alpha = 30$ to 50 deg, $SR = 0$.
 Figure A7/L.-Continued.

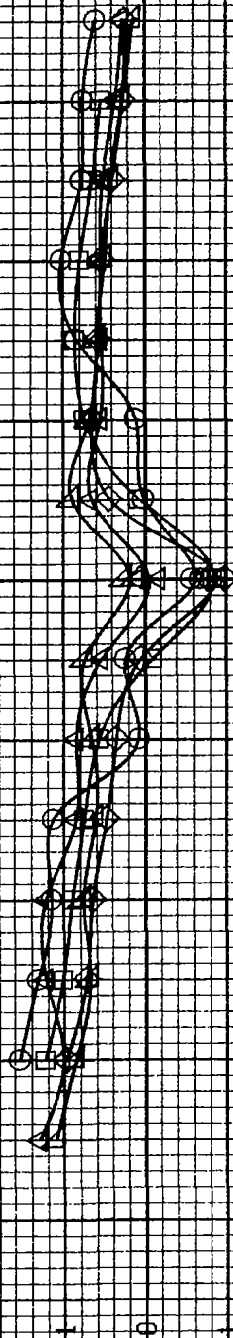




(d) $\alpha=55$ to 90 deg, $SR=0$.
Figure A71. Concluded.

α, deg
 0 8
 1 10
 2 12
 3 14
 4 16

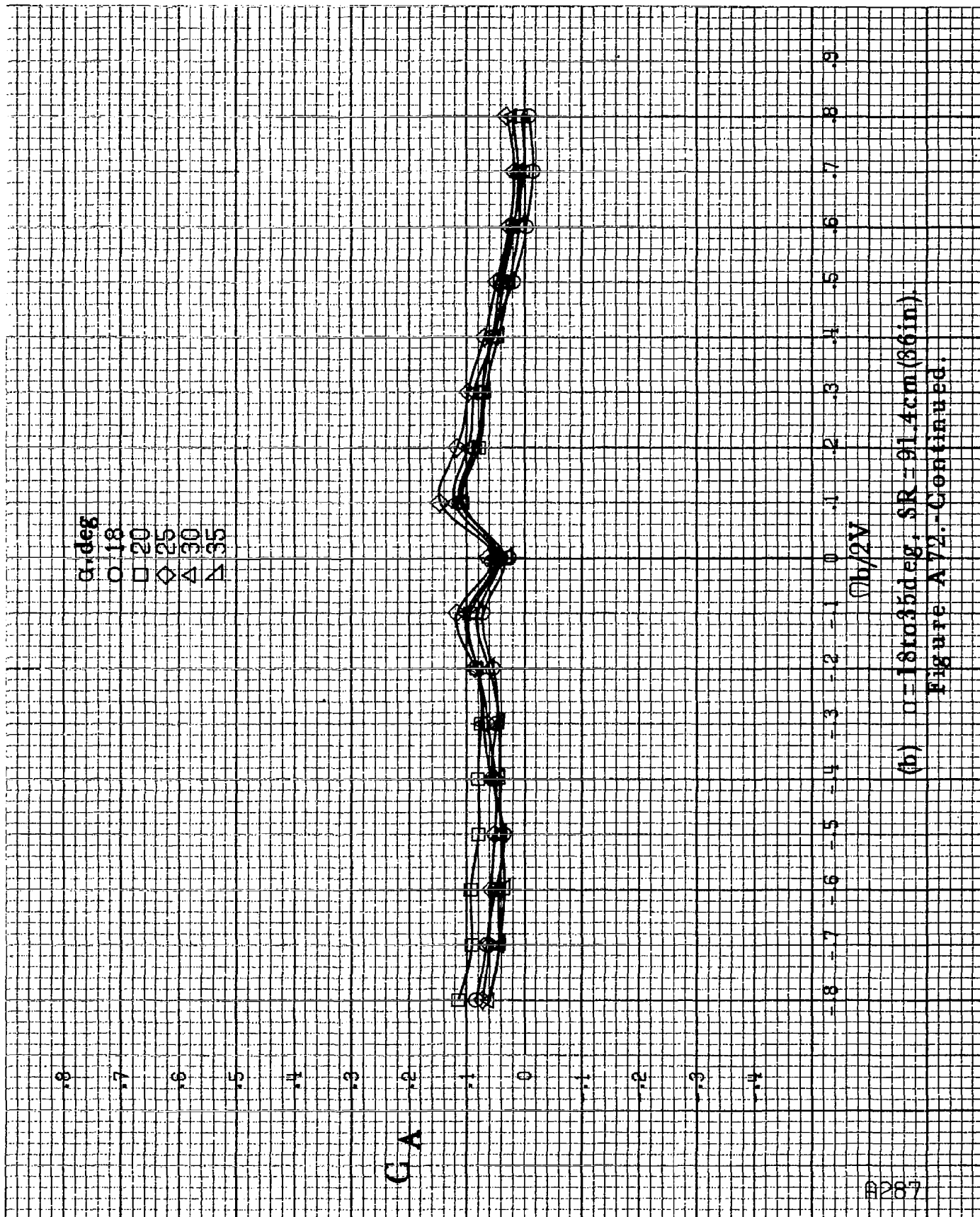
C_A



$C_A/2V$

(a) $\alpha = 8 \text{ to } 16 \text{ deg}$, $SR = 91.4 \text{ cm (36 in)}$.

Figure A72.-Effect of rotation rate and angle of attack on axial-force coefficient for long body, low wing, horizontal tail no. 3 configuration. $\delta_a = 0^\circ$, $\delta_w = 0^\circ$, $\delta_r = 0^\circ$.



(b) $\alpha = 18$ to 35° ; SR = 91.4 cm (36 in).
Figure A72.-Continued.

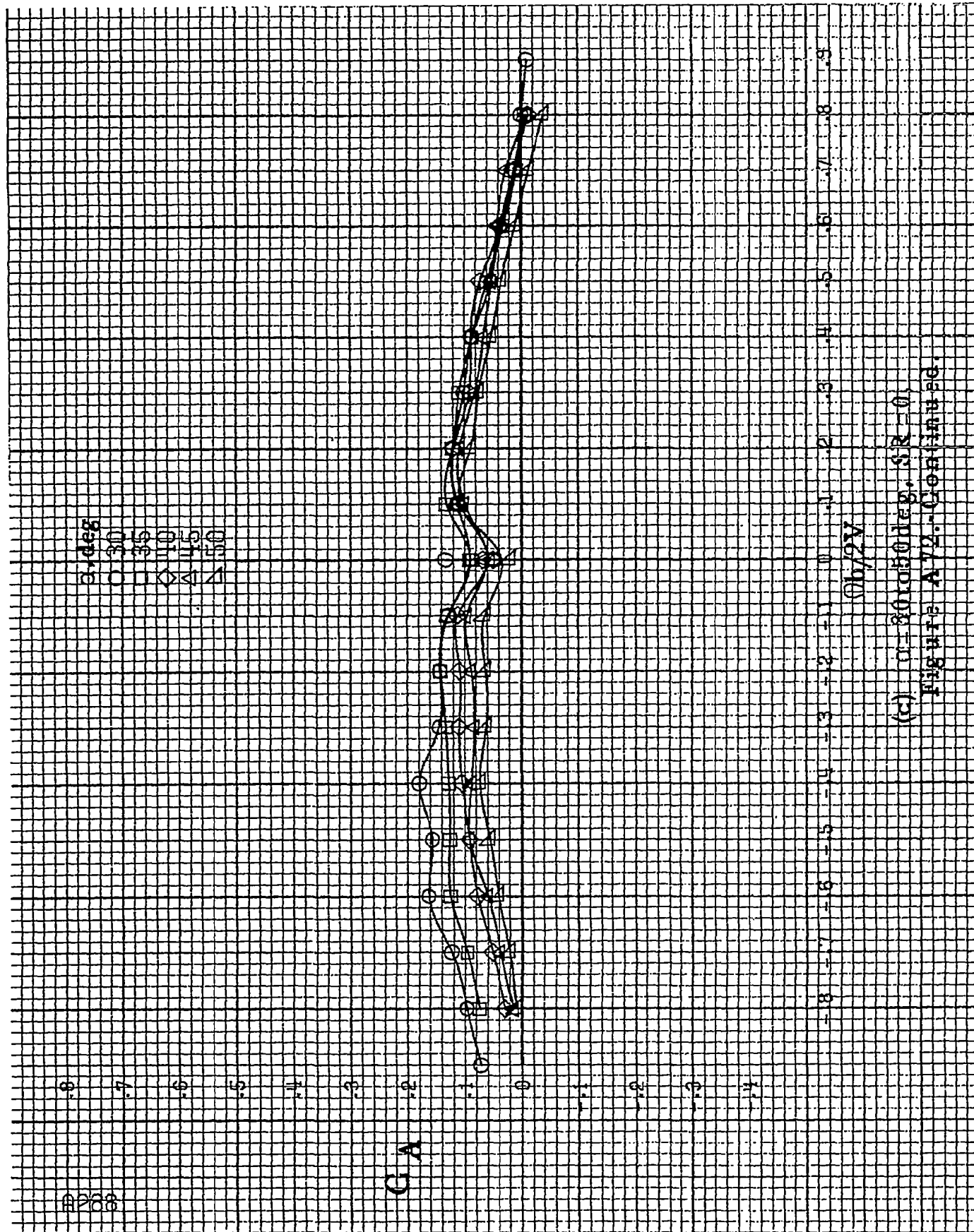
8203

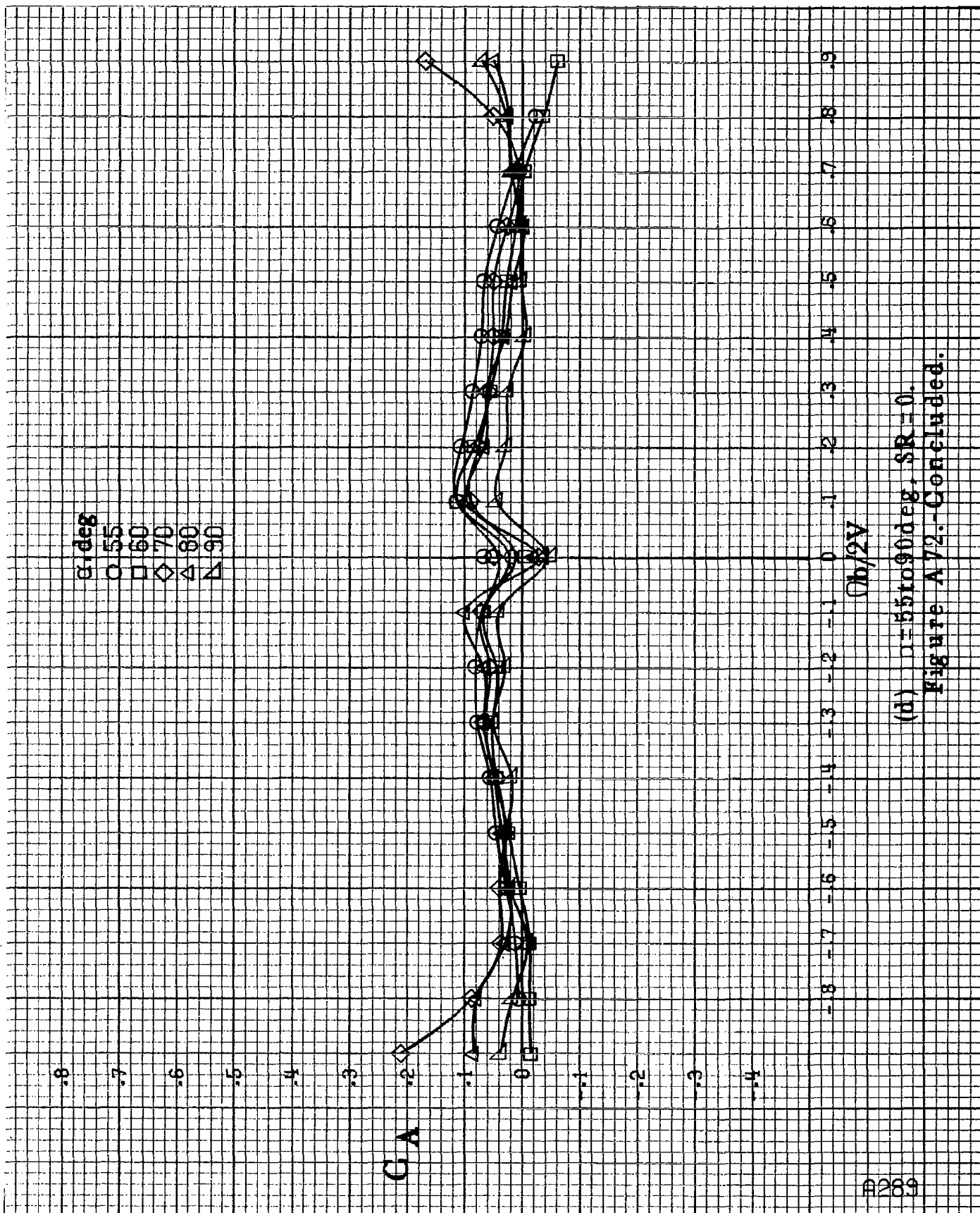
CA

3 deg
 O 30
 □ 35
 △ 40
 ▲ 45
 ▴ 50

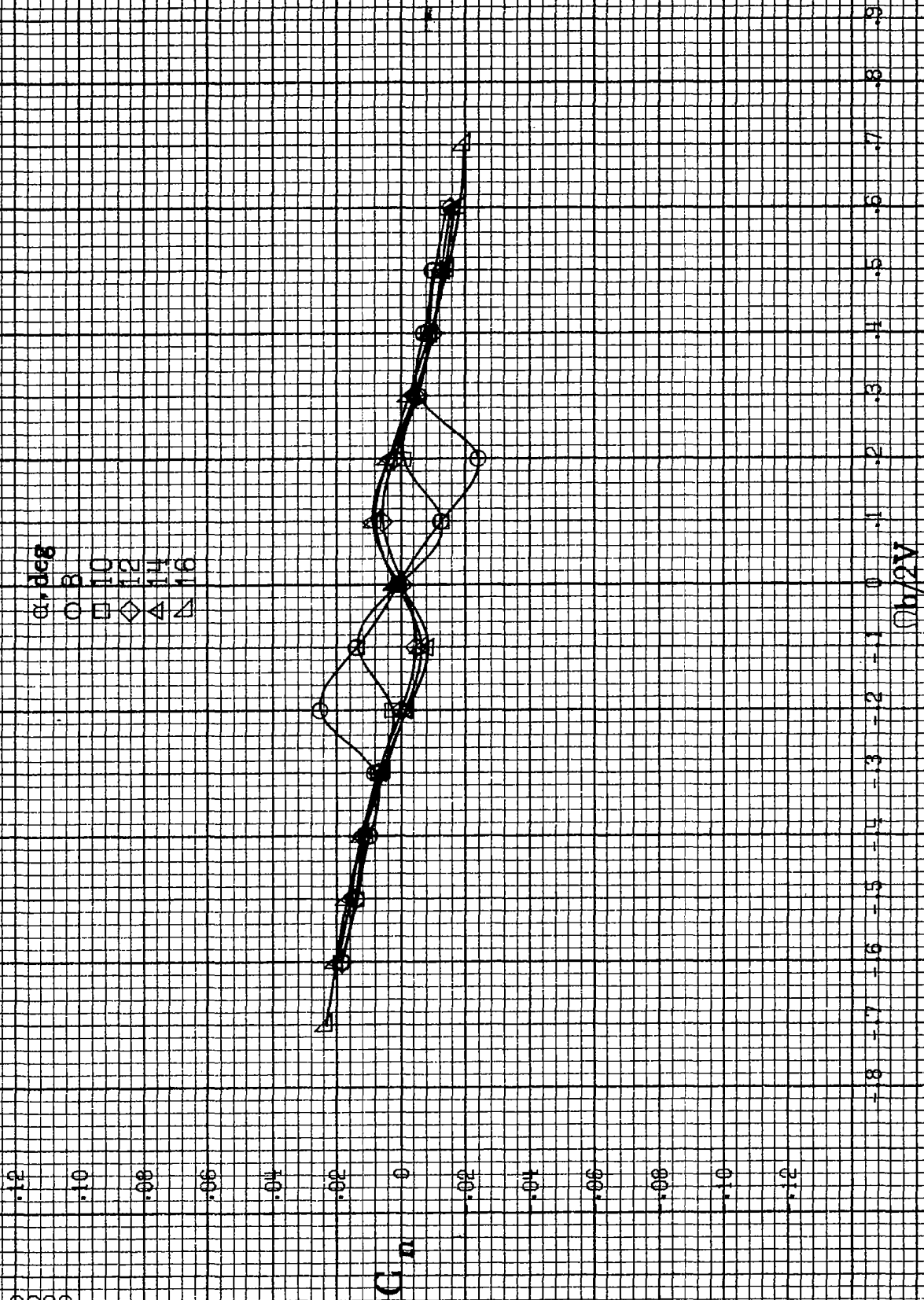
0b/2V

(c) $\alpha = 30$ to 50 deg, $\beta R = 0$,
 Figure A 12. Continued



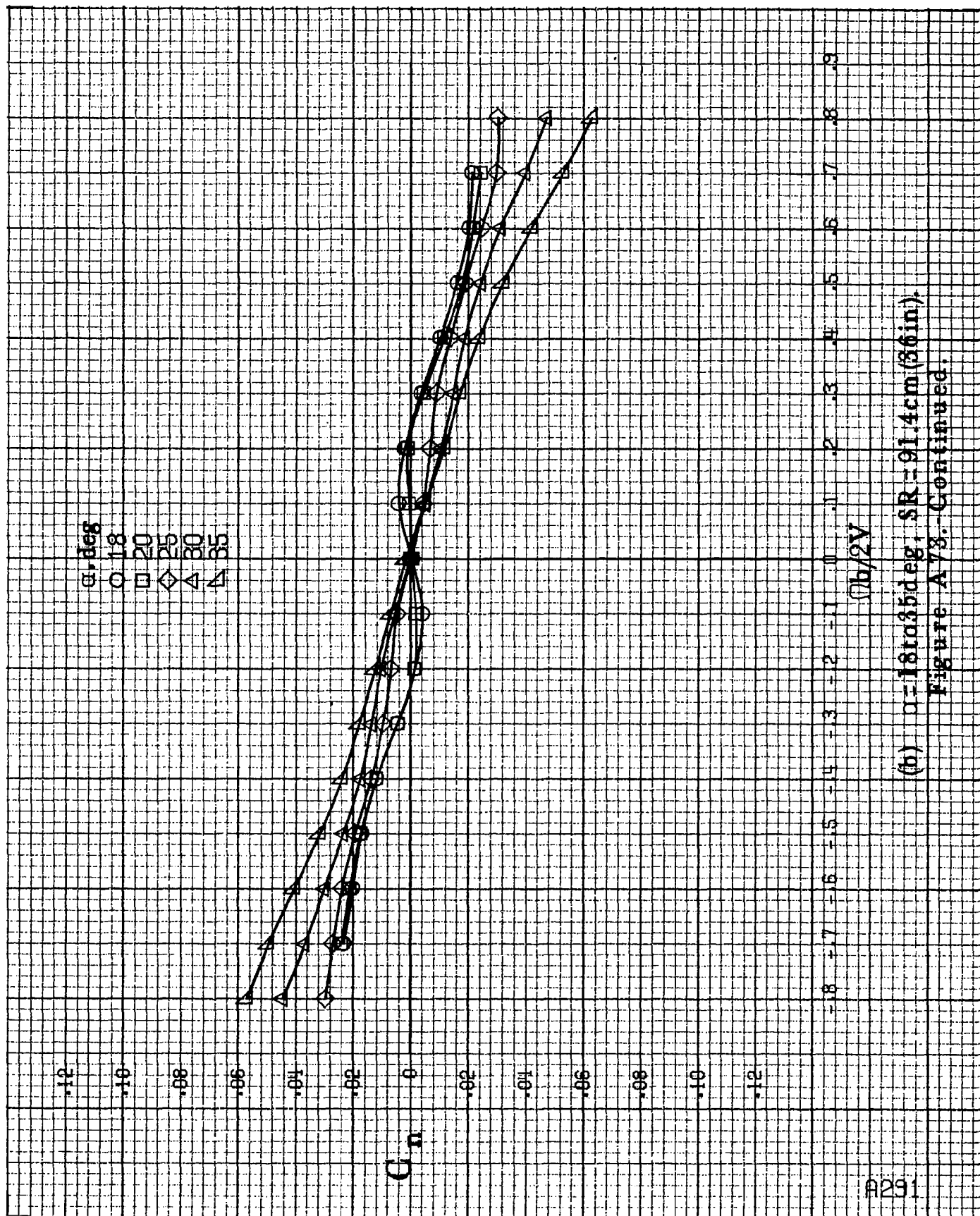


(d) $\rho = 55$ to 90 deg, $SR = 0$.
Figure A72.-Concluded.



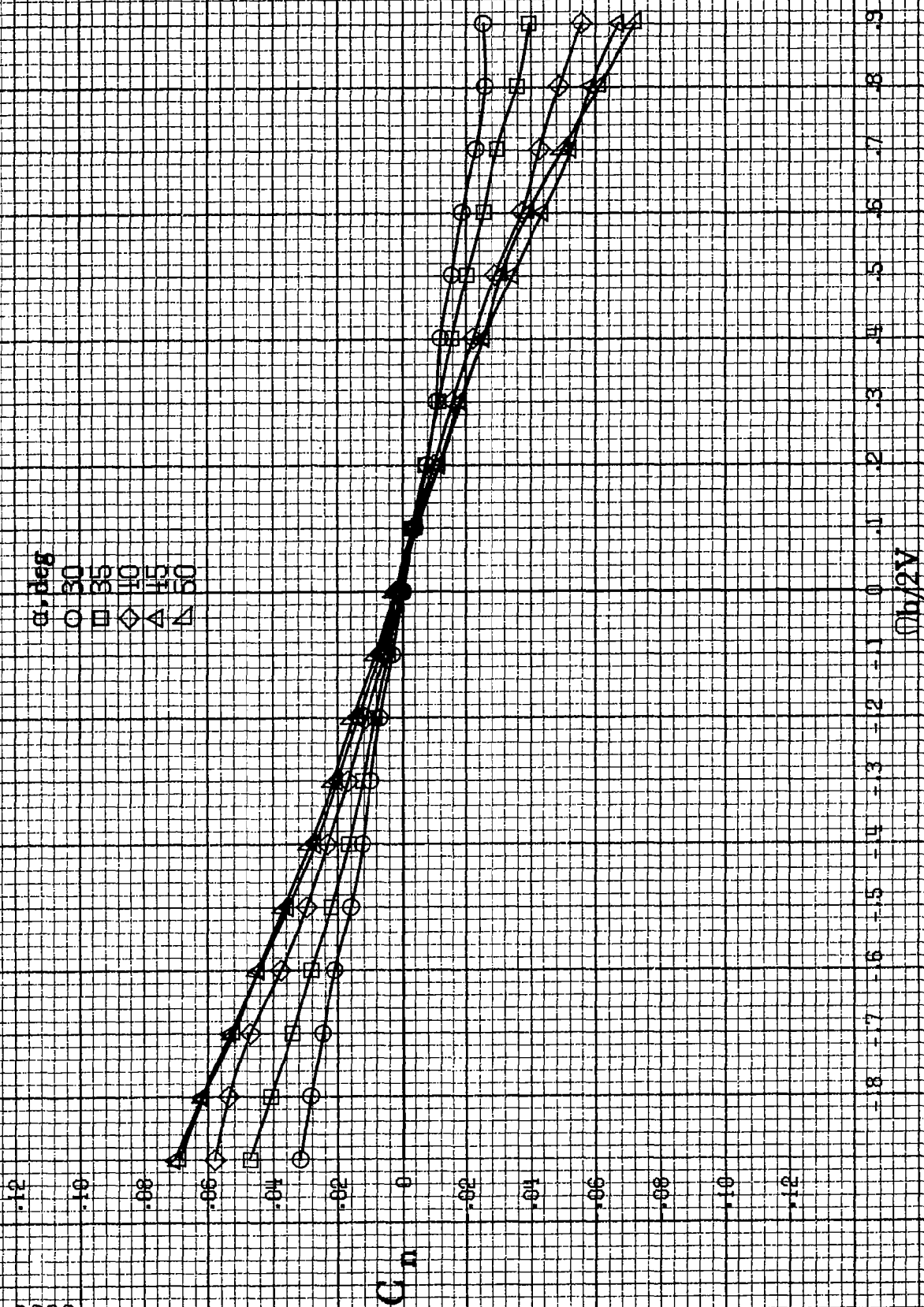
(a) $\alpha = 8$ to 16° , $SR = 91.4$ cm (35 in.).

Figure A73.-Effect of rotation rate and angle of attack on yawing-moment coefficient for long body, high wing, horizontal T-tail A configuration. $\delta a \pm 0^\circ$, $\delta \alpha \pm 0^\circ$, $\delta r \pm 0^\circ$.

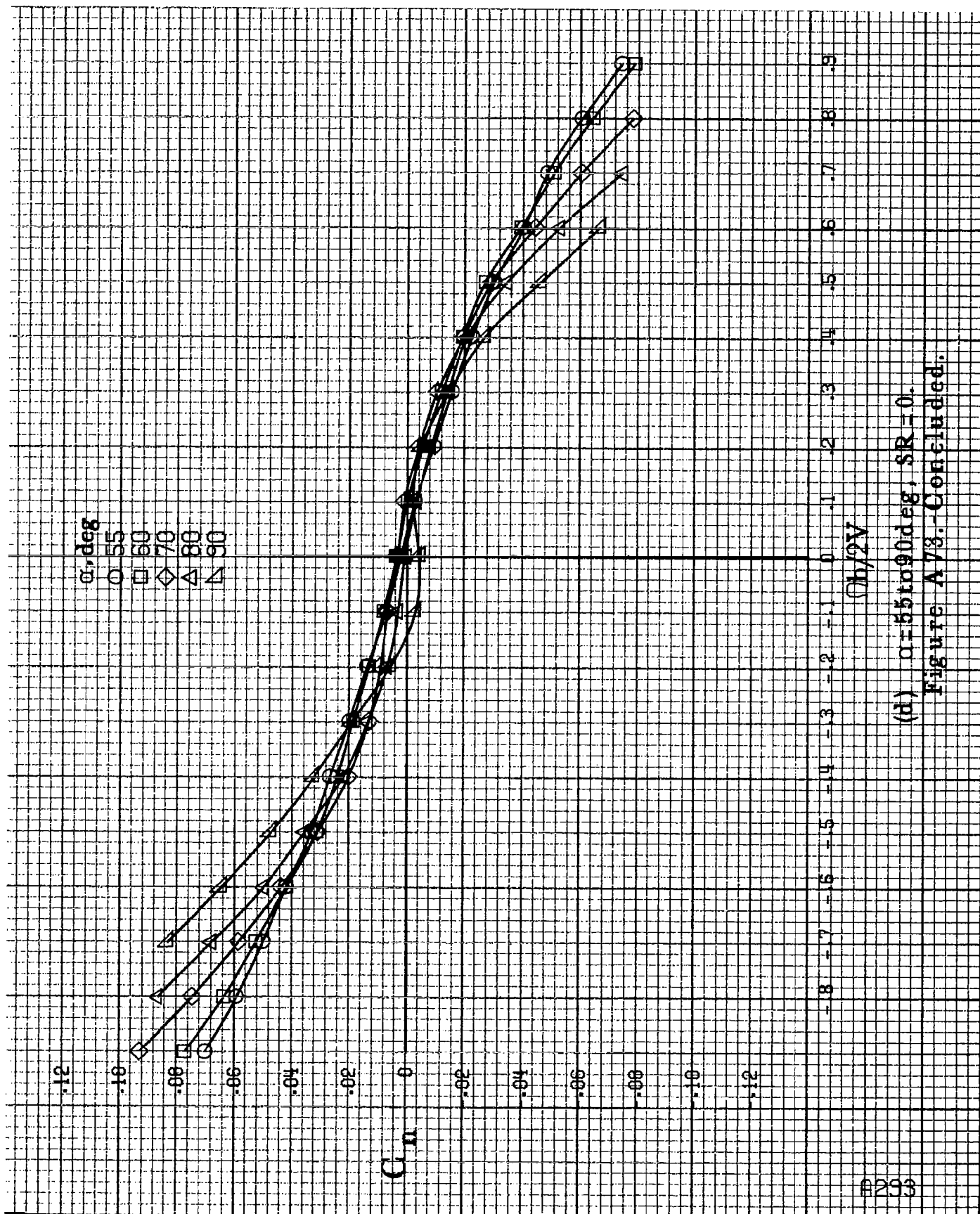


(b) $\alpha = 18$ to 35° , $SR = 91.4 \text{ cm (36 in.)}$.

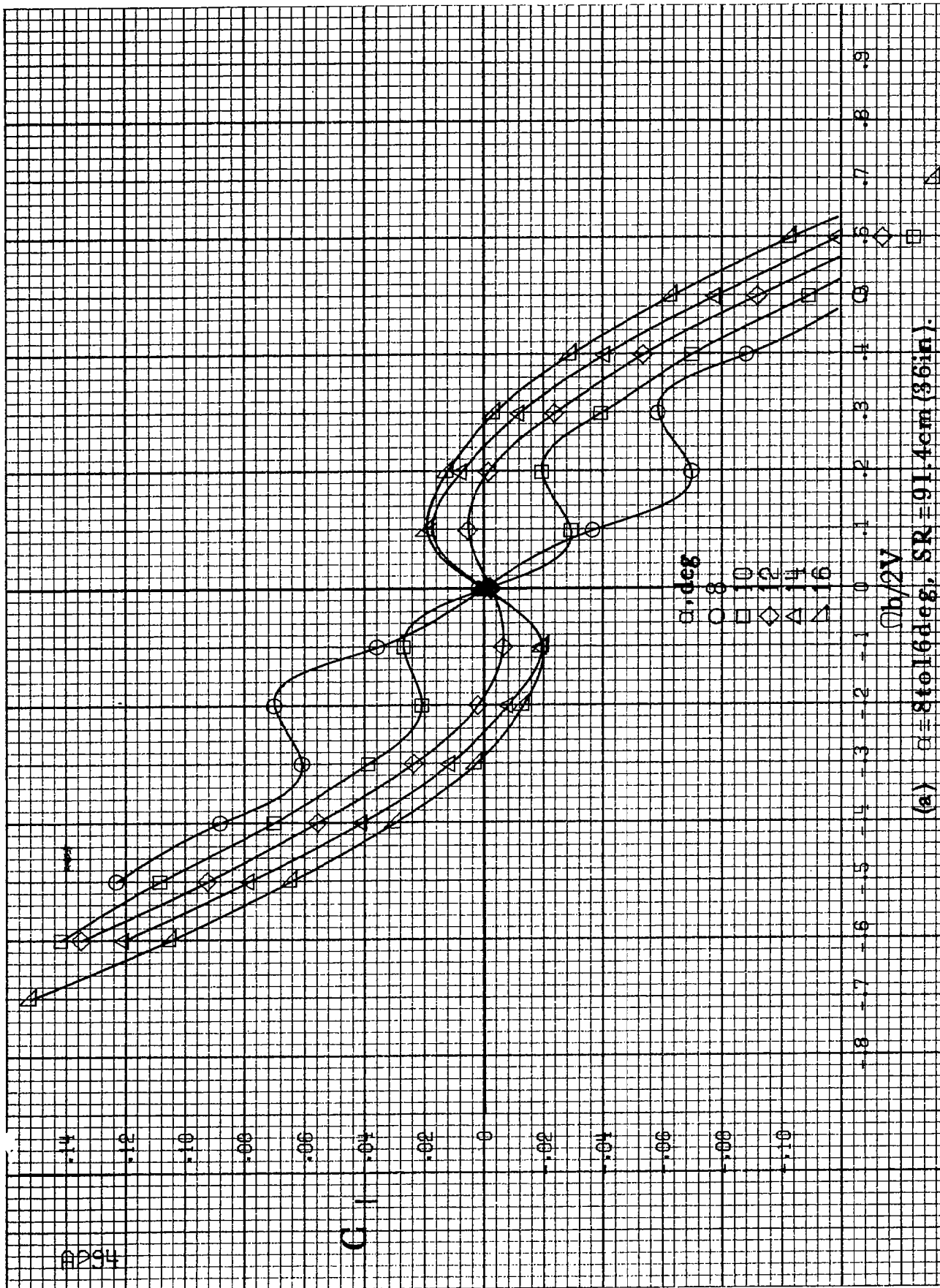
Figure A73. Continued.



(c) $\alpha=30$ to 50° , $SR=0$.
Figure A73. Continued.

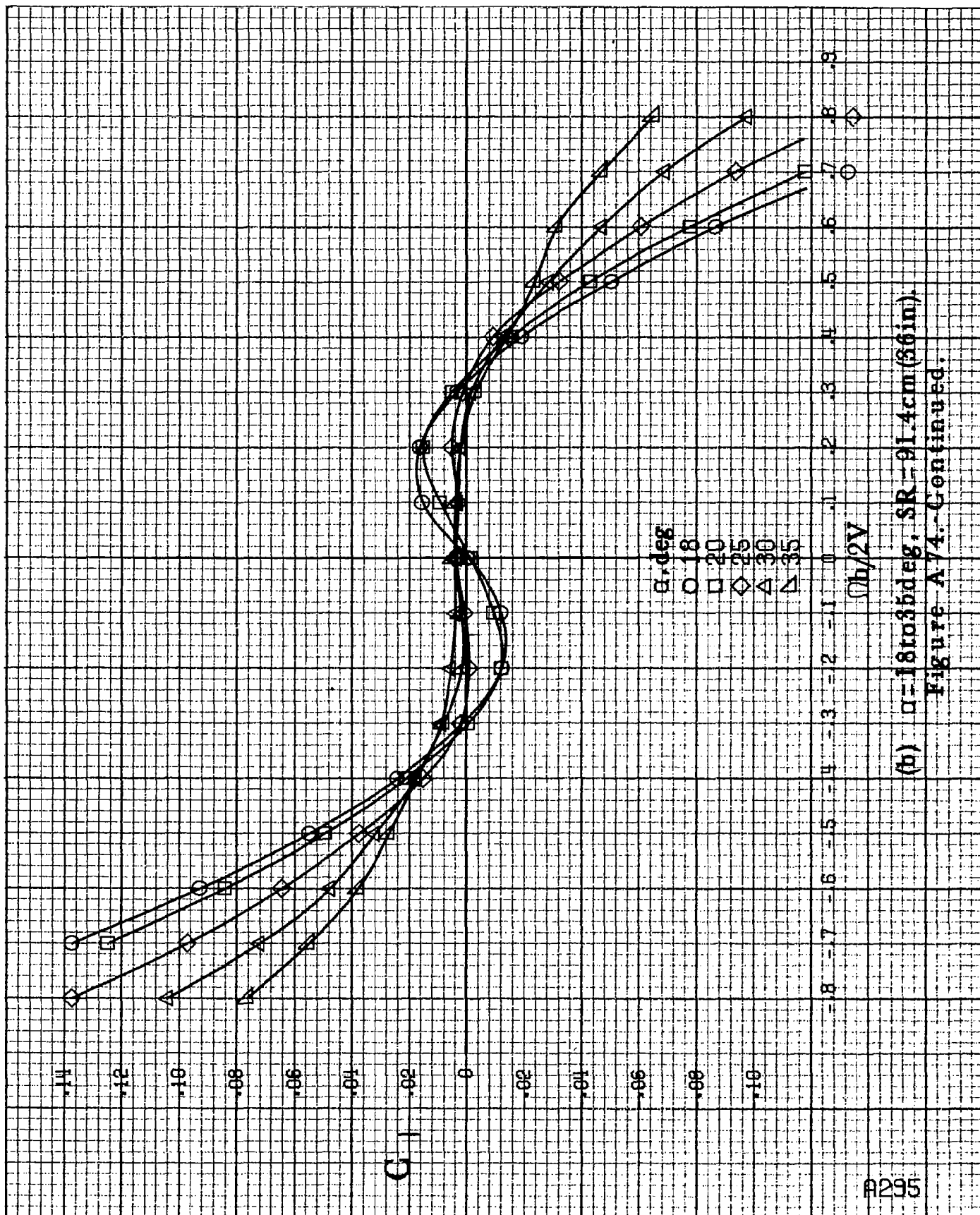


(d) $\alpha = 55$ to 90 deg, $SR = 0$.
Figure A73.-Concluded.



(a) $\alpha=8$ to 16 deg, $SR=91.4$ cm (36 in).

Figure A74.-Effect of rotation rate and angle of attack on rolling-moment coefficient for long body, high wing, horizontal T-tail A configuration. $\delta_e=0^\circ$, $\delta_w=0^\circ$, $\delta_r=0^\circ$.



(b) $\alpha=18$ to 35° , SR=91.4cm (36in).

Figure A74-Continued.

C_1

α, deg

○ 30

□ 35

◇ 40

△ 45

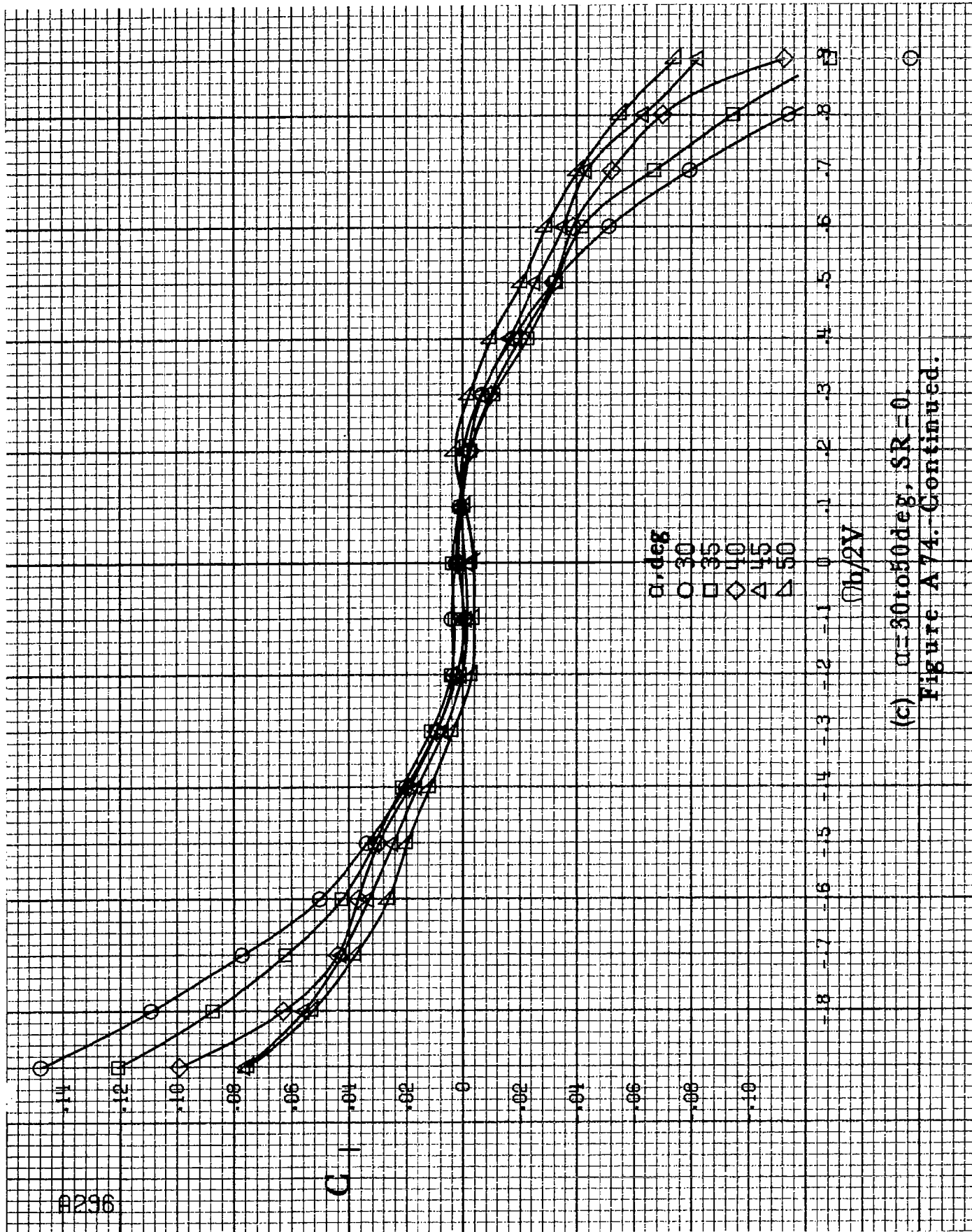
▽ 50

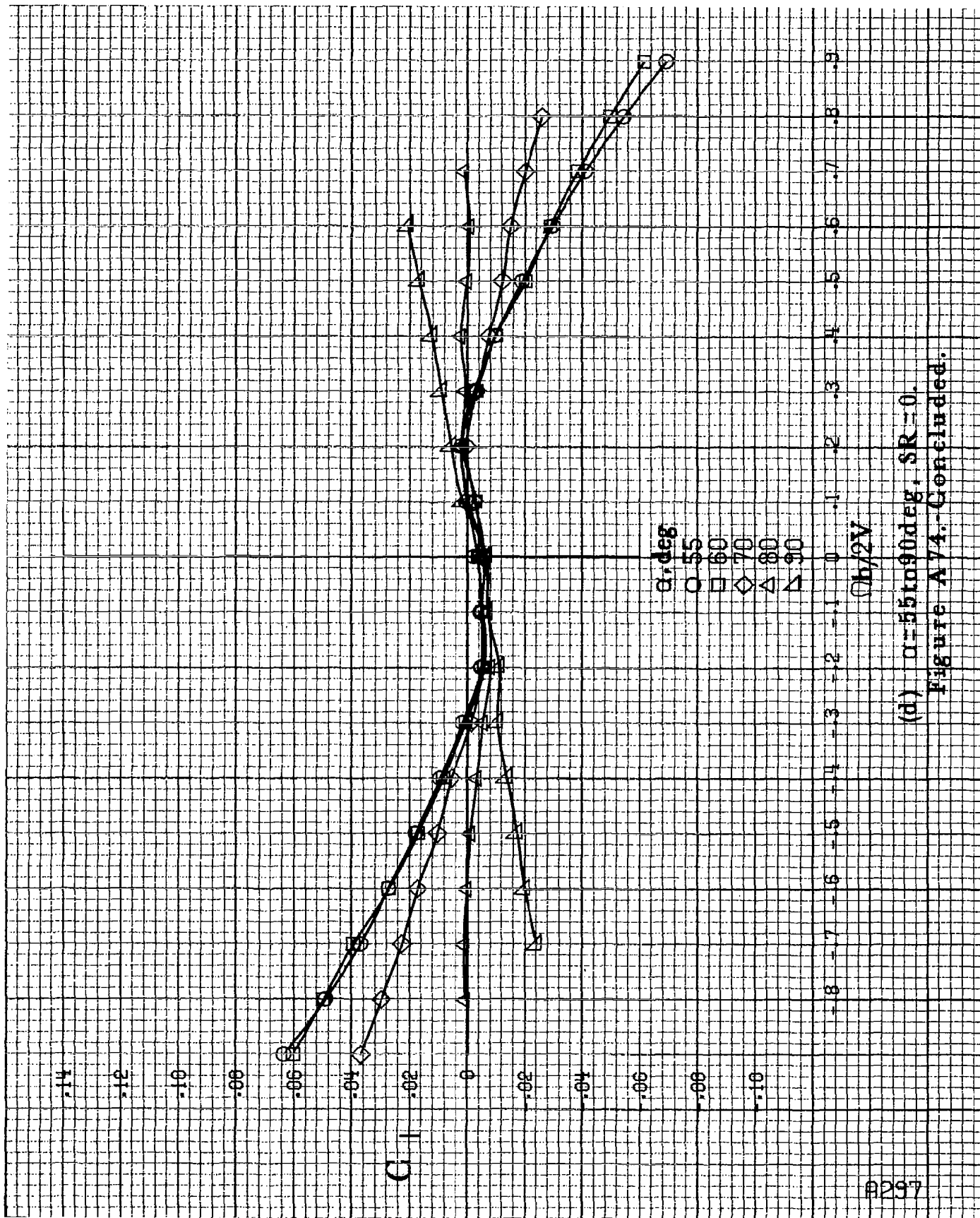
$\eta_b/2V$

(c) $\alpha=30$ to 50 deg, $SR=0$.

Figure A 74.-Continued.

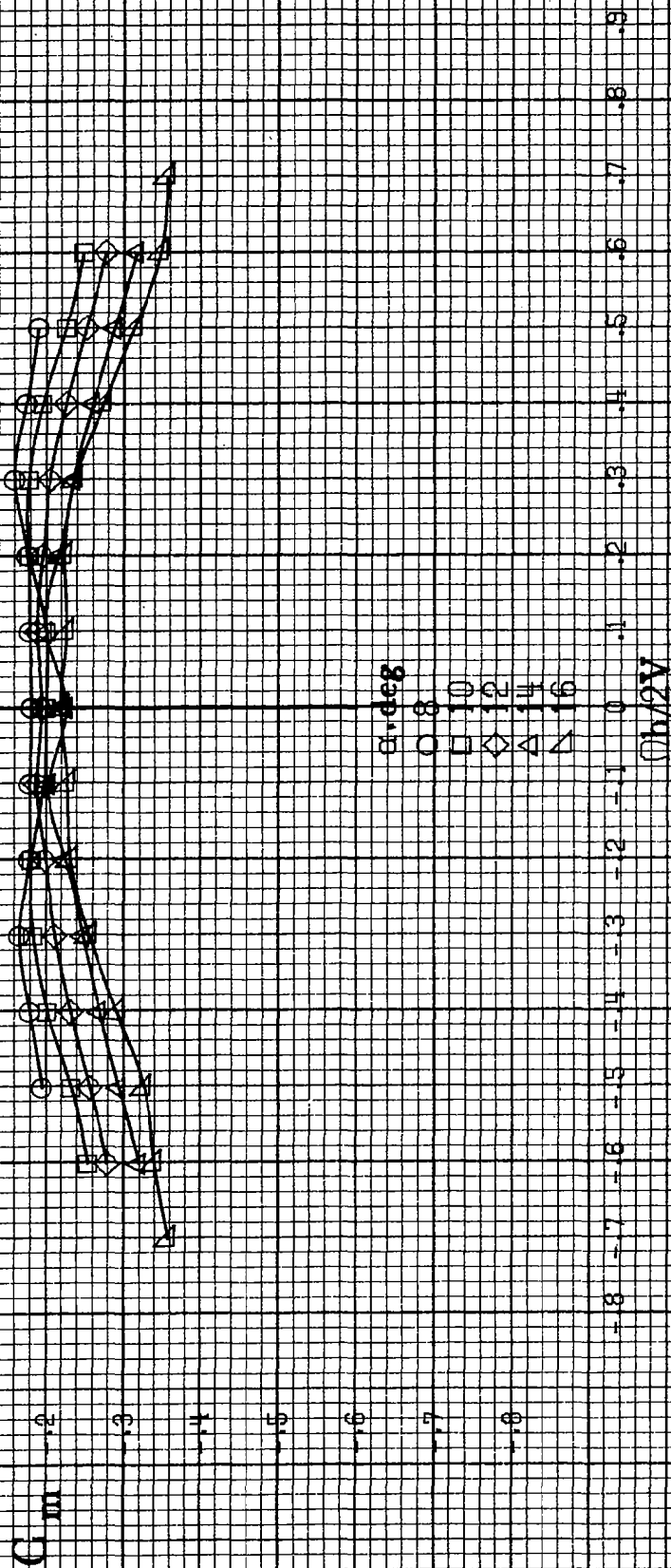
○





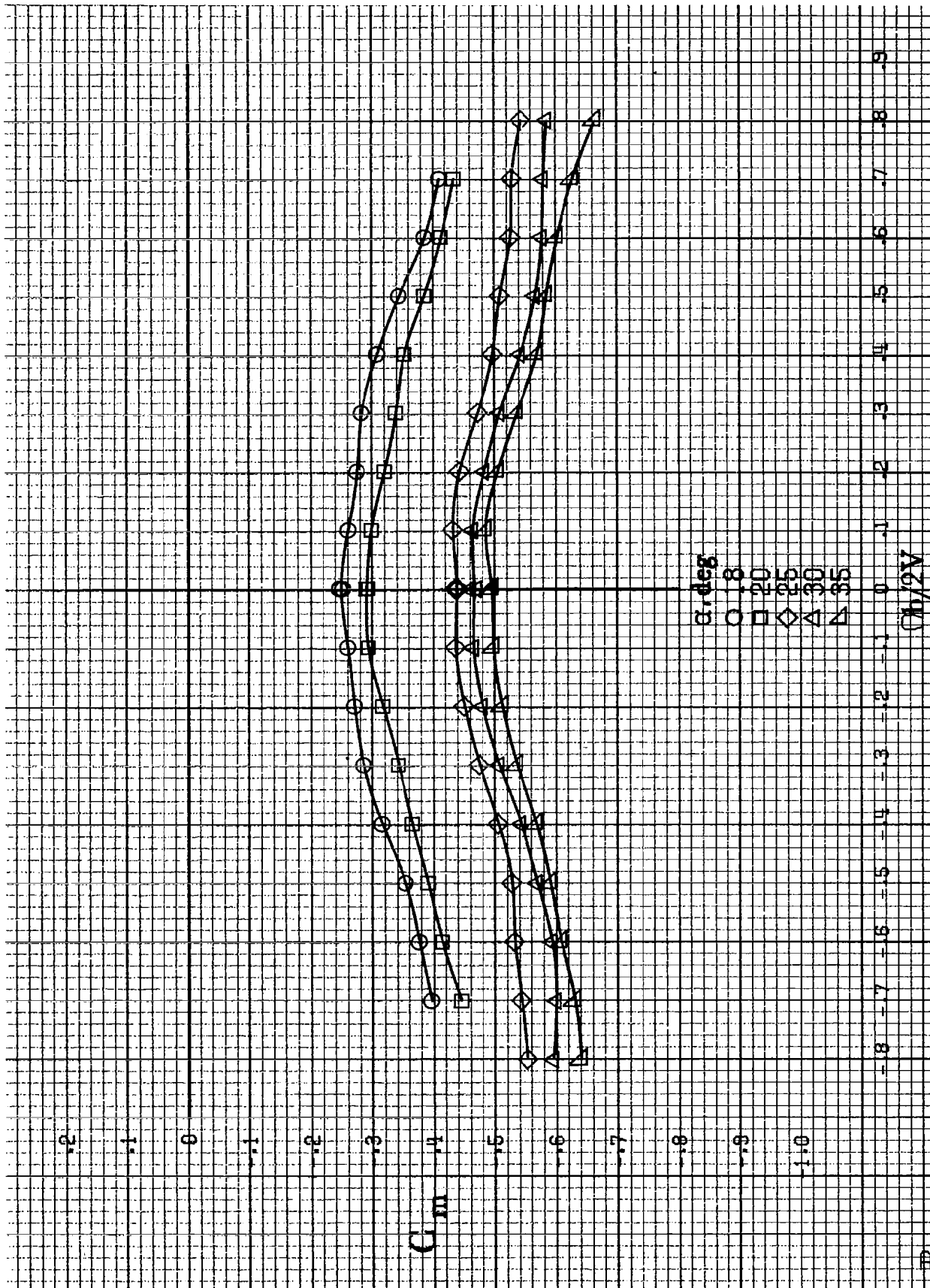
A297

(d) $\alpha=55$ to 90° , $SR=0$.
Figure A74. Concluded.



(a) $\alpha = 8 \text{ to } 16 \text{ deg/sec}$, $SR = 91.4 \text{ cm (36 in.)}$.

Figure A75b - Effect of rotation rate and angle of attack on pitching-moment coefficient for long body, high wing, horizontal T-tail A configuration. $\delta a = 0^\circ$, $\delta a = 0^\circ$, $\delta r = 0^\circ$, $\beta = 0^\circ$.



(b) $n = 18$ to 35° , $SR = 91.4 \text{ cm (36 in.)}$.
Figure A75.-Continued.

A300

C_m

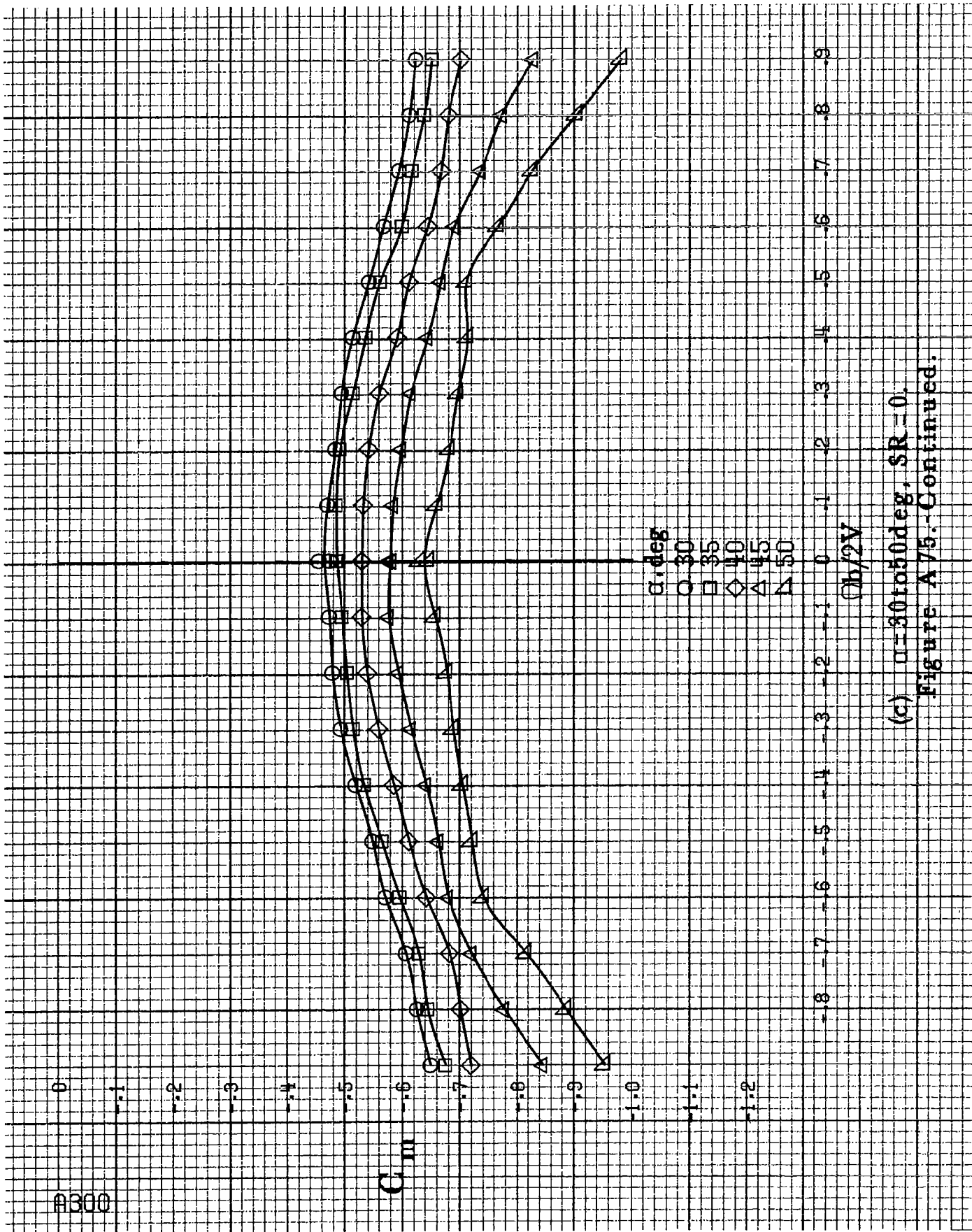
α, deg

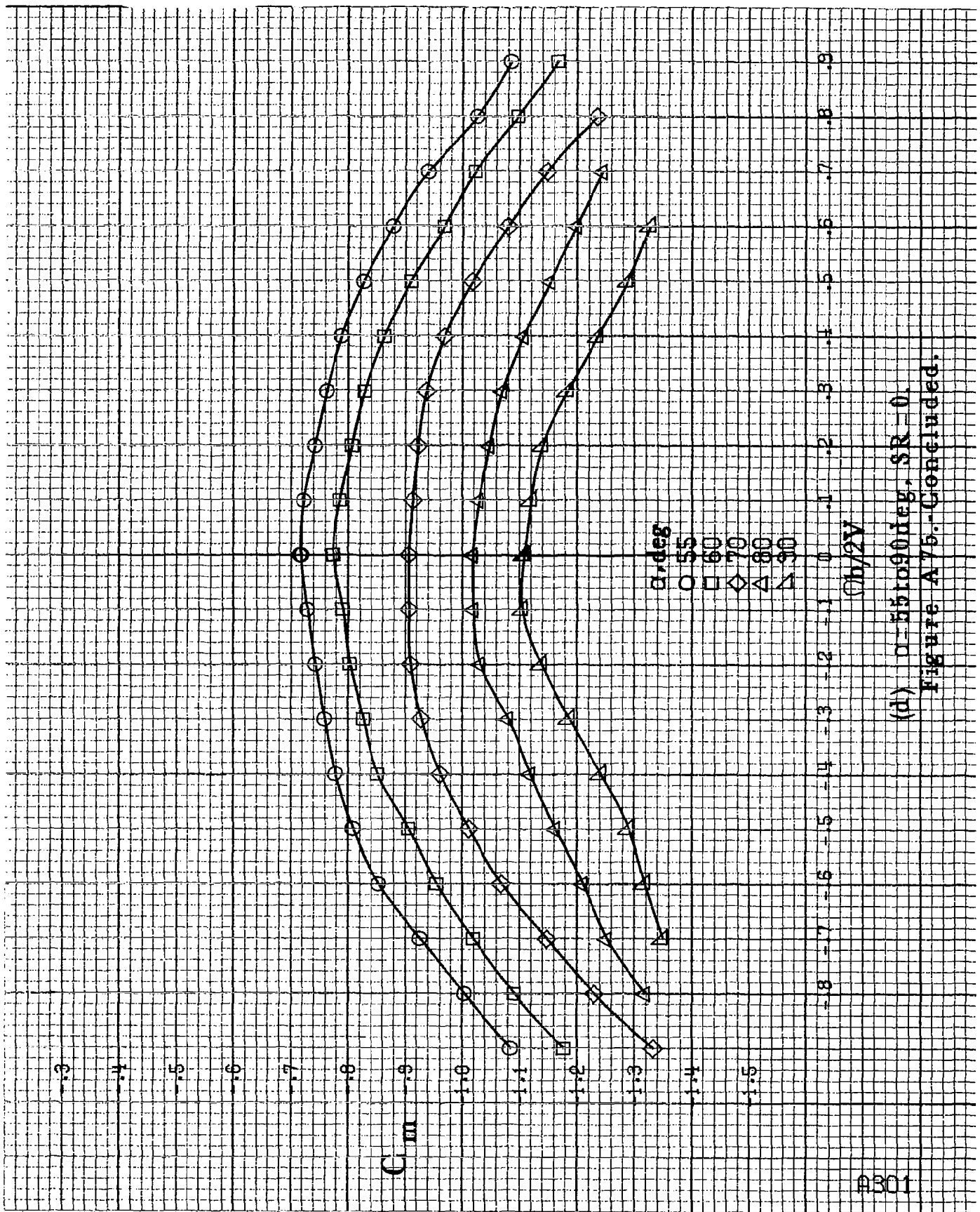
- 30
- 35
- ◇ 40
- △ 45
- ▽ 50

$C_b/2V$

(c) $\alpha=30$ to 50 deg, $SR=0$.

Figure A75.-Continued.





(d) $\alpha = 55$ to 90° , $SR = 0$.
Figure A 75.-Concluded.

#302

α , deg

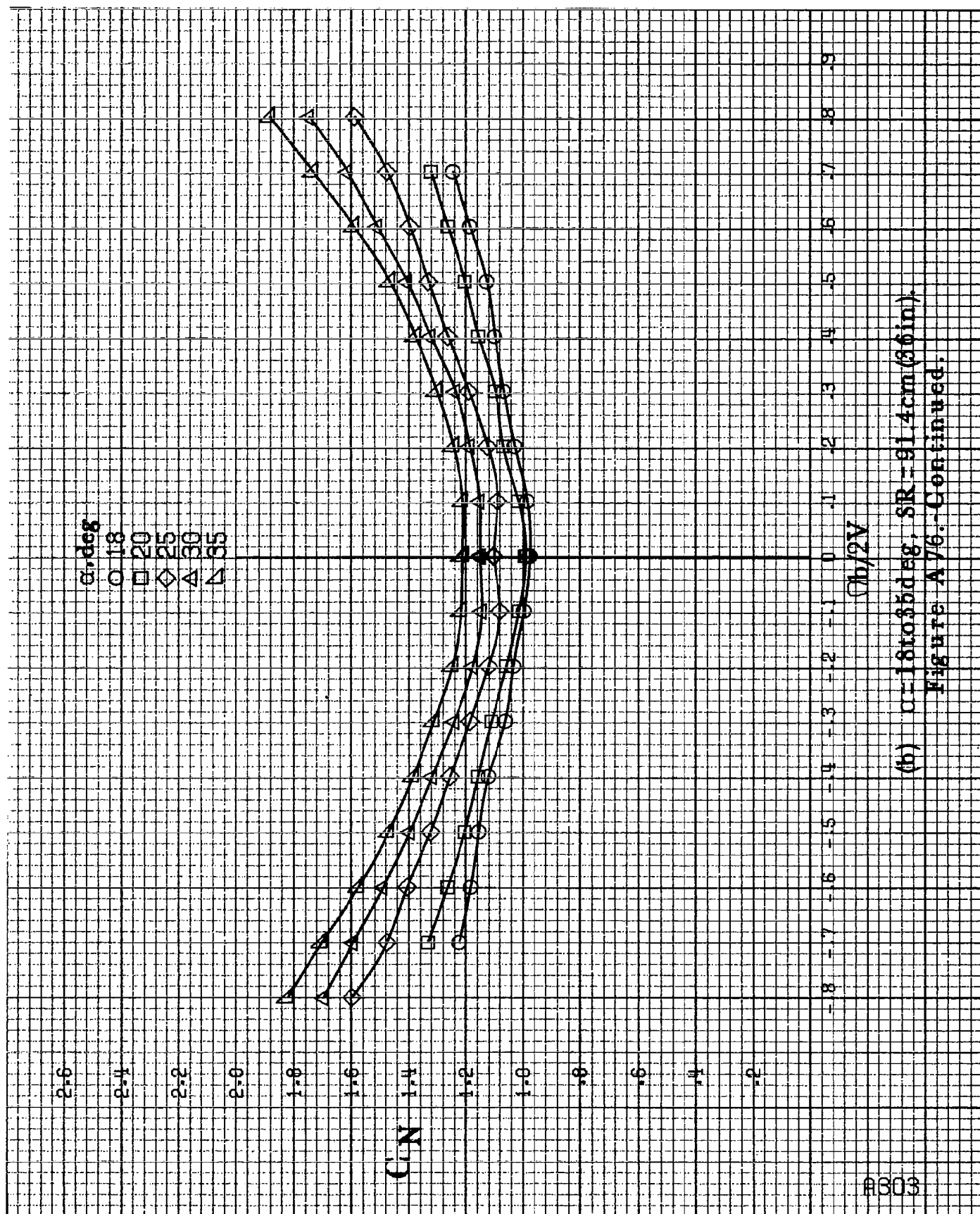
○ 8
□ 10
◇ 12
△ 14
▽ 16

CN

$Ob/2V$

(a) $\alpha = 8$ to 16 deg, $SR = 91.4$ cm (36 in).

Figure A.76 - Effect of rotation rate and angle of attack on normal-force coefficient for long body, high wing, horizontal T-tail A configuration.
 $\delta\alpha = 0^\circ$; $\delta\alpha = 0^\circ$; $\delta\alpha = 0^\circ$; $\delta\alpha = 0^\circ$.



(b) $\alpha = 18$ to 35° ; $SR = 91.4 \text{ cm (36 in.)}$.
Figure A76.-Continued.

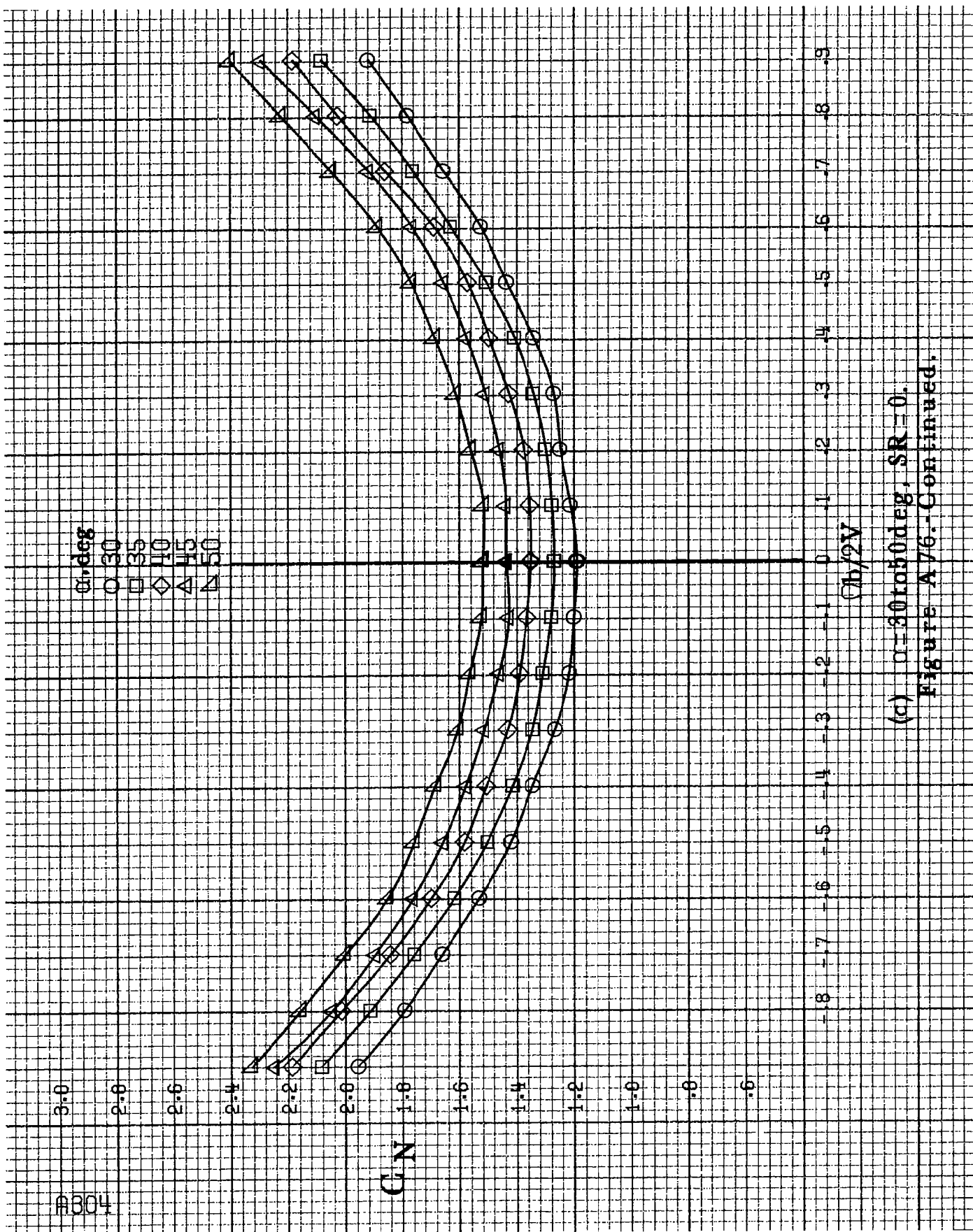
A304

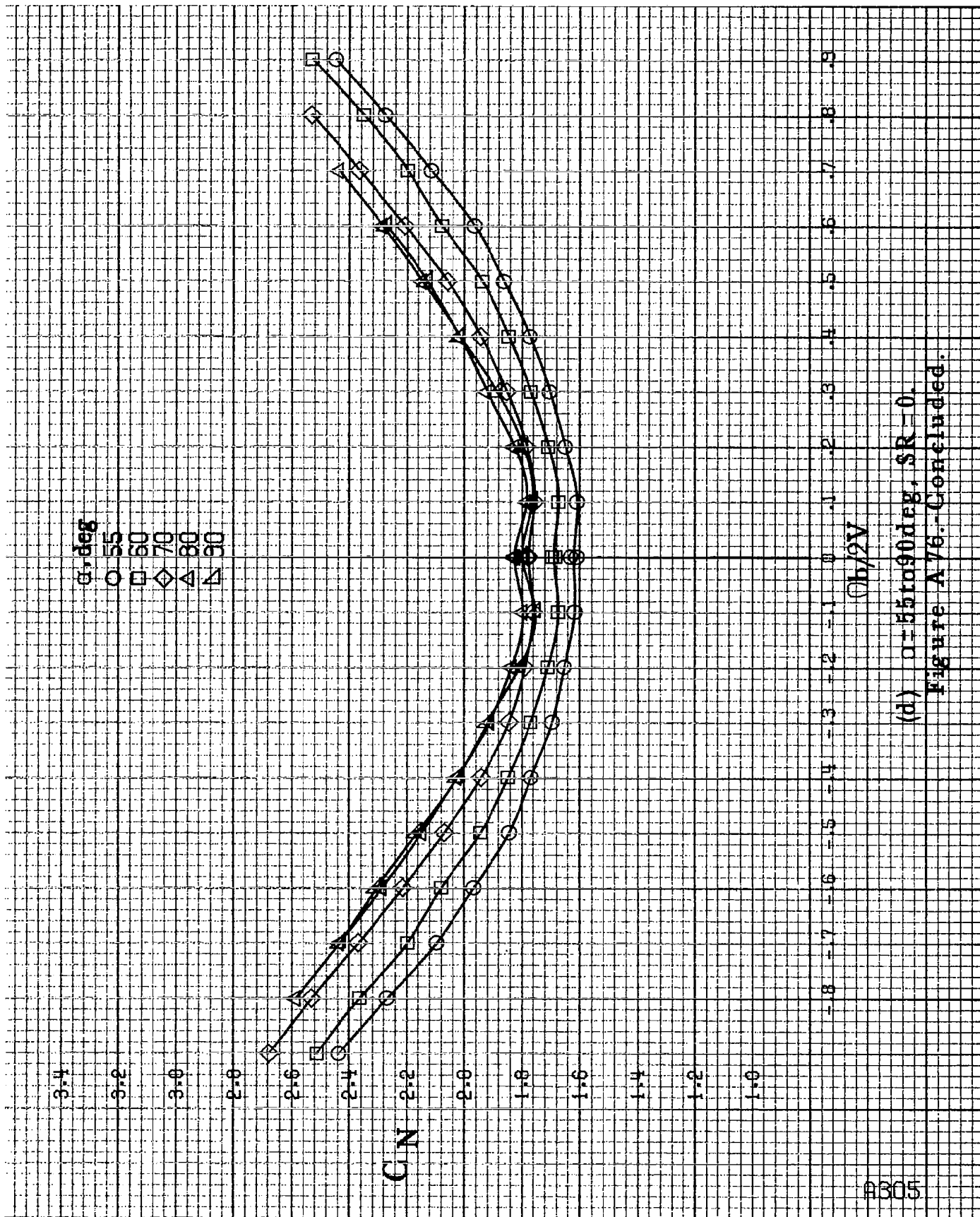
α, deg
 ○ 30
 □ 35
 ◇ 40
 △ 45
 ▽ 50

G_N

$Q_b/2V$

(c) $\alpha=30$ to 50 deg, $SR=0$.
 Figure A76.-Continued.





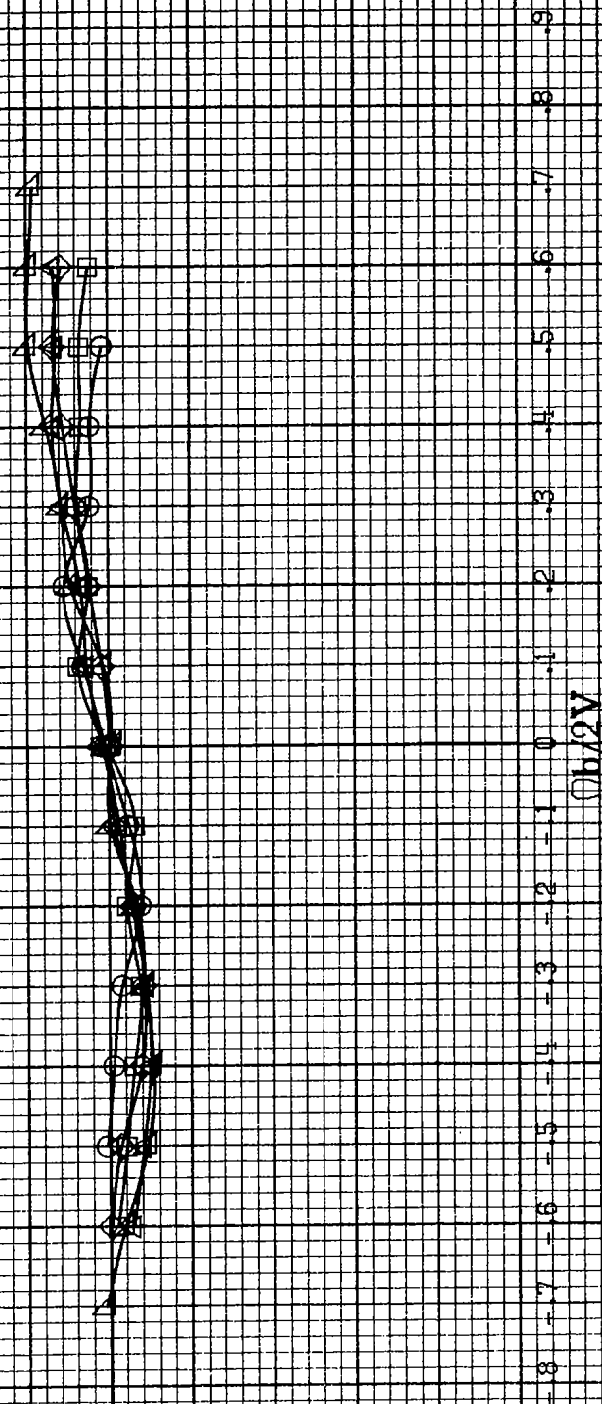
(d) $\alpha=55$ to 90° deg, $SR=0$.
Figure A76.-Concluded.

#306

α , deg

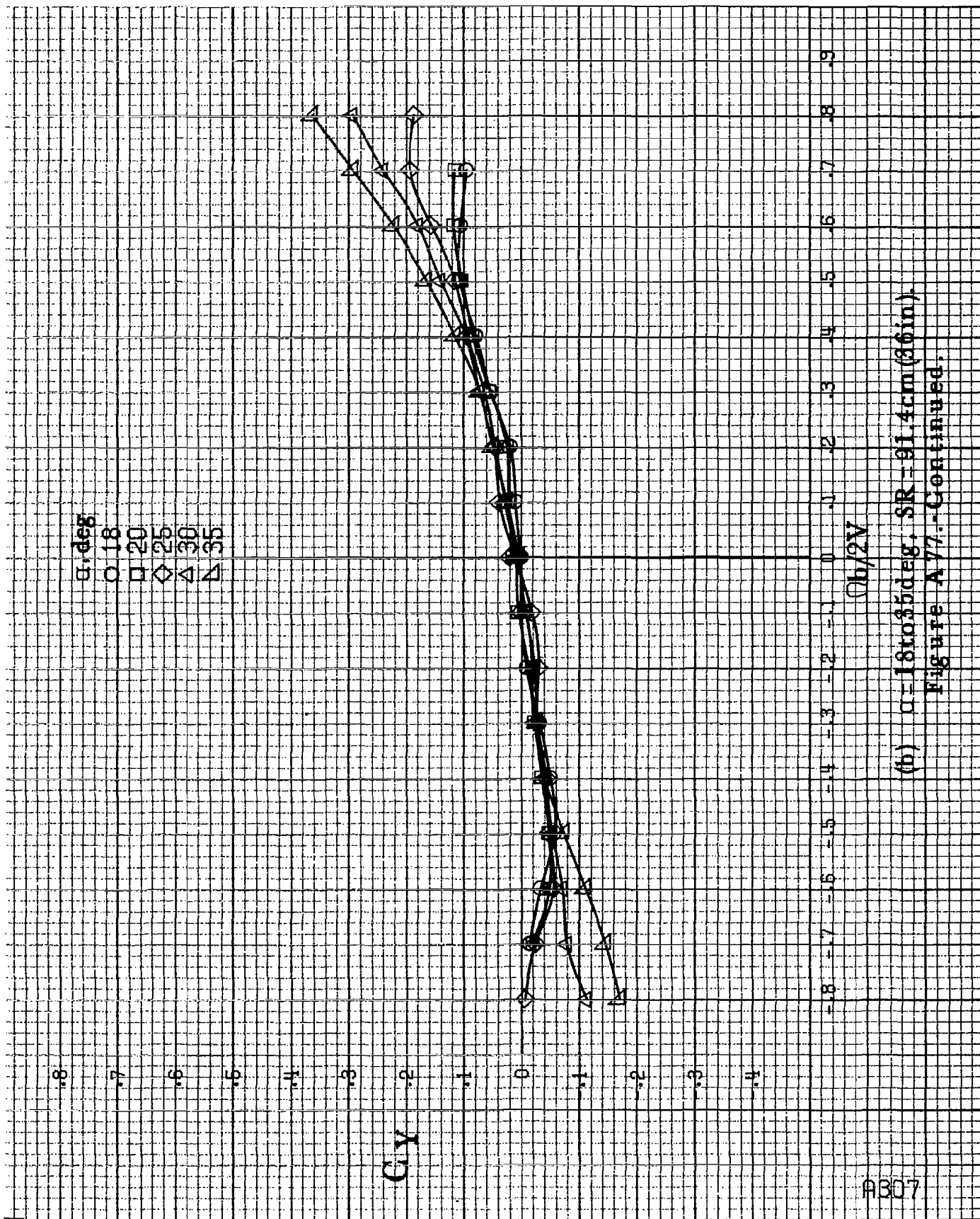
○ 8
□ 10
◇ 12
△ 14
▽ 16

C_y



(a) $\alpha = 8$ to 16 deg, $SR = 91.4$ cm (36 in).

Figure A77.-Effect of rotation rate and angle of attack on side-force coefficient for long body, high wing, horizontal T-tail A configuration. $\delta a = 0^\circ$, $\delta r = 0^\circ$, $\delta \tau = 0^\circ$.



(b) $\alpha=18$ to 35° , $SR=91.4\text{cm}(36\text{in})$.

Figure A 77.-Continued.

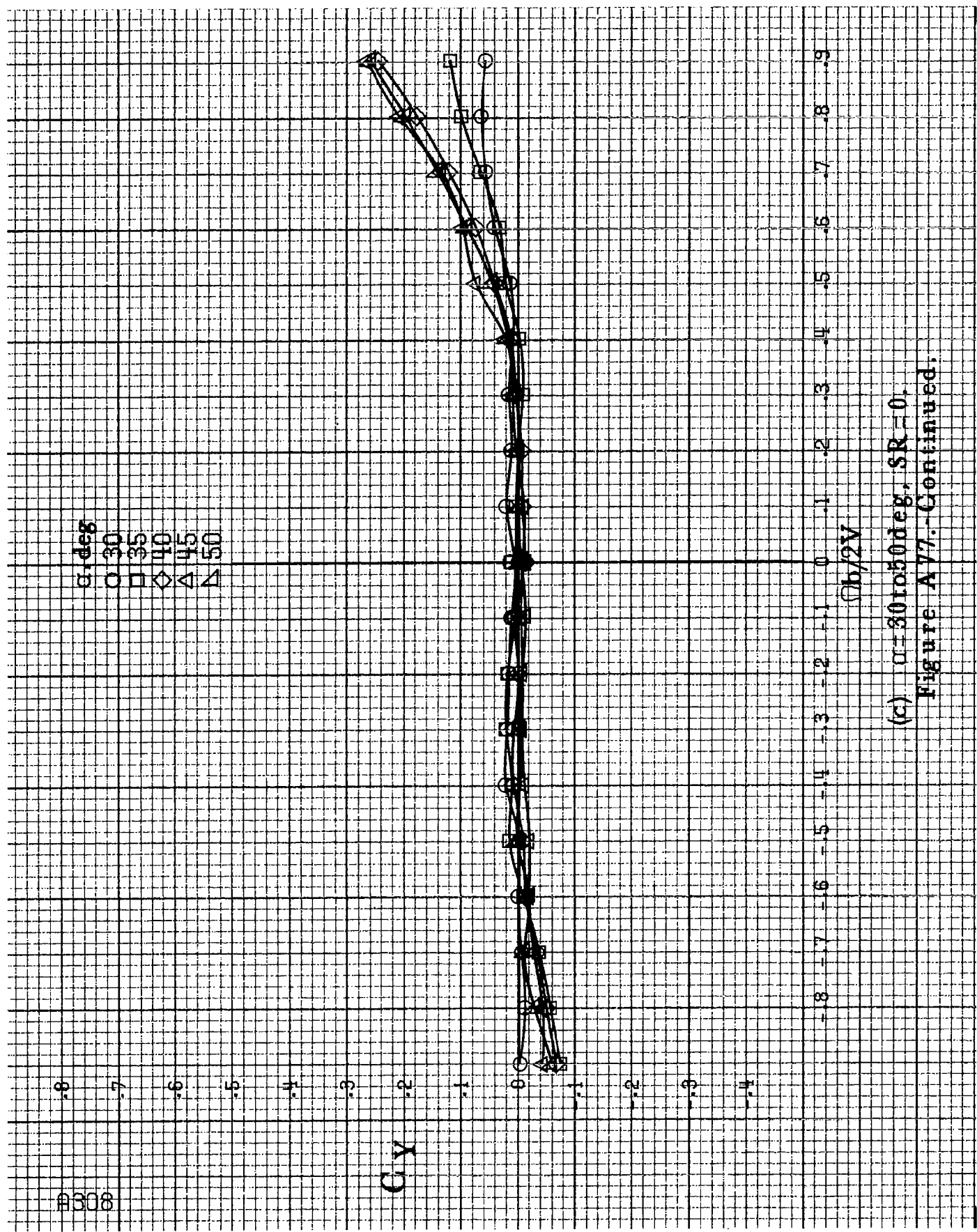
H308

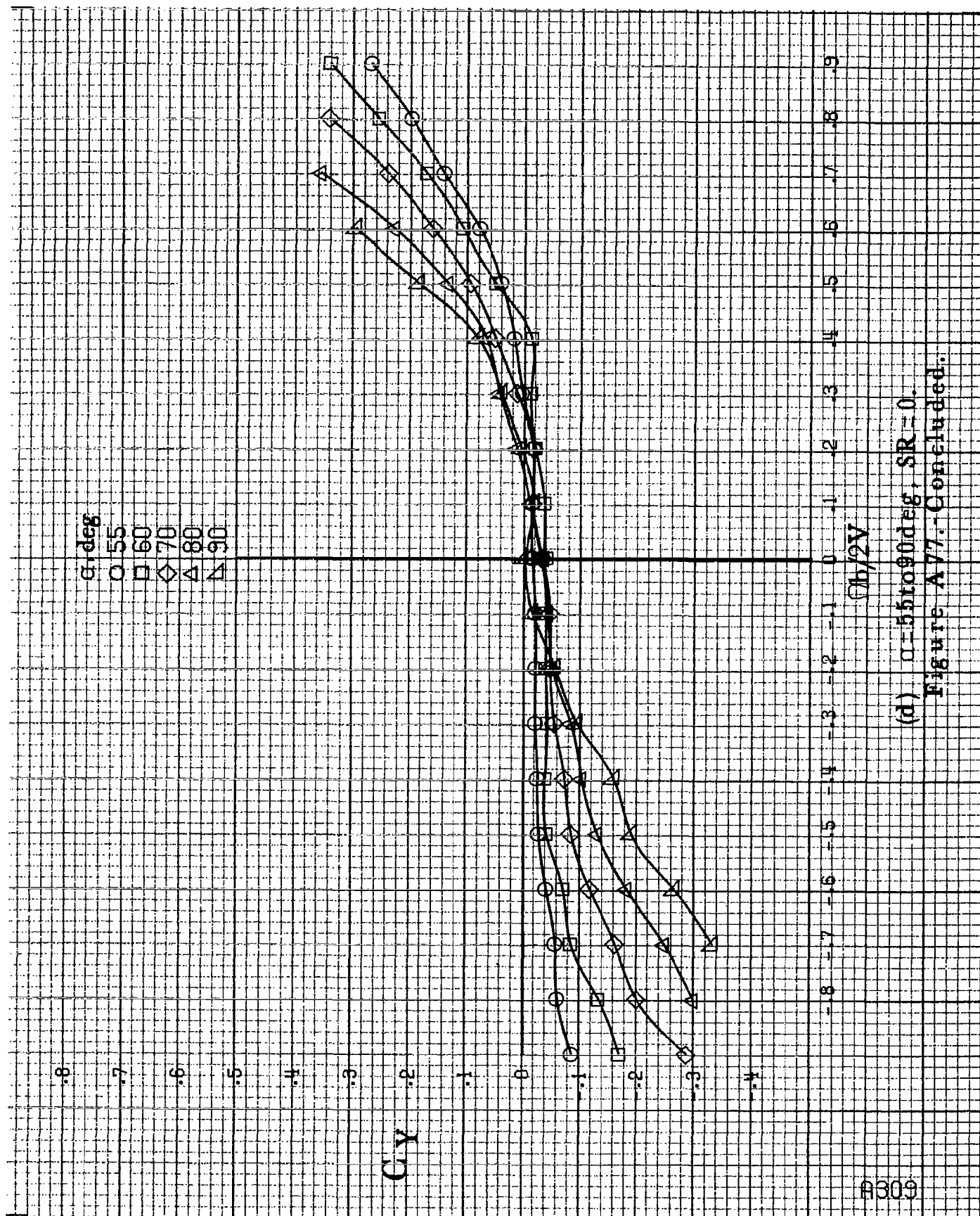
α, deg
 O 30
 □ 35
 ◇ 40
 △ 45
 ▲ 50

C_y

$b/2V$

(c) $\alpha=30$ to 50 deg, $SR=0$.
 Figure A77.-Continued.





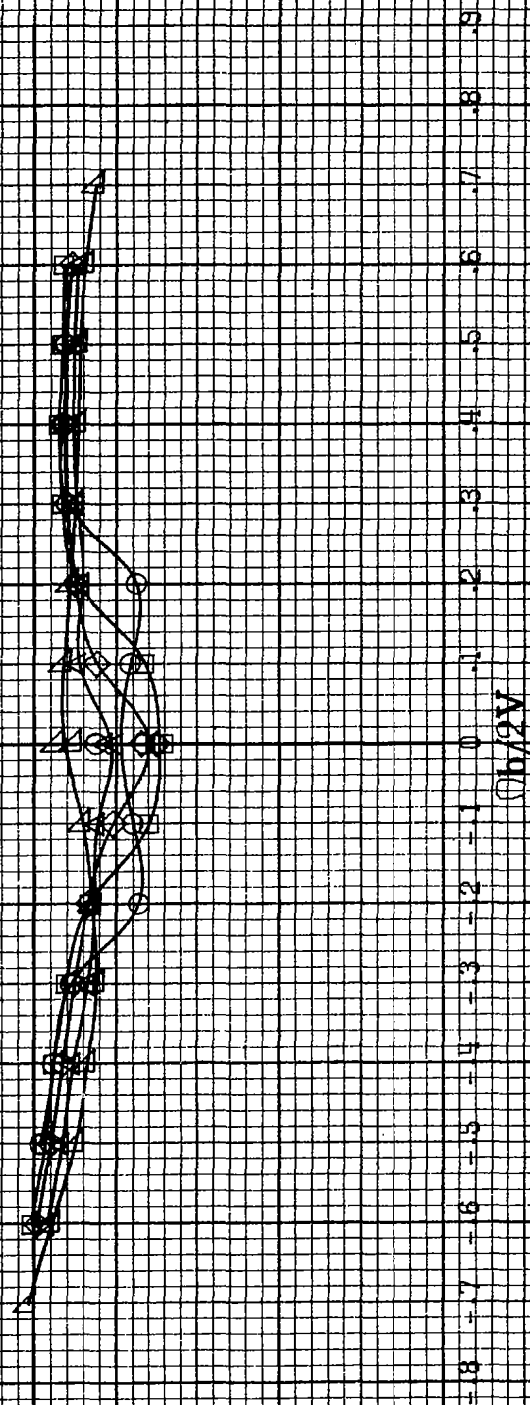
A309

(d) $\alpha=55$ to 90° , $SR=0$.
Figure A77.-Concluded.

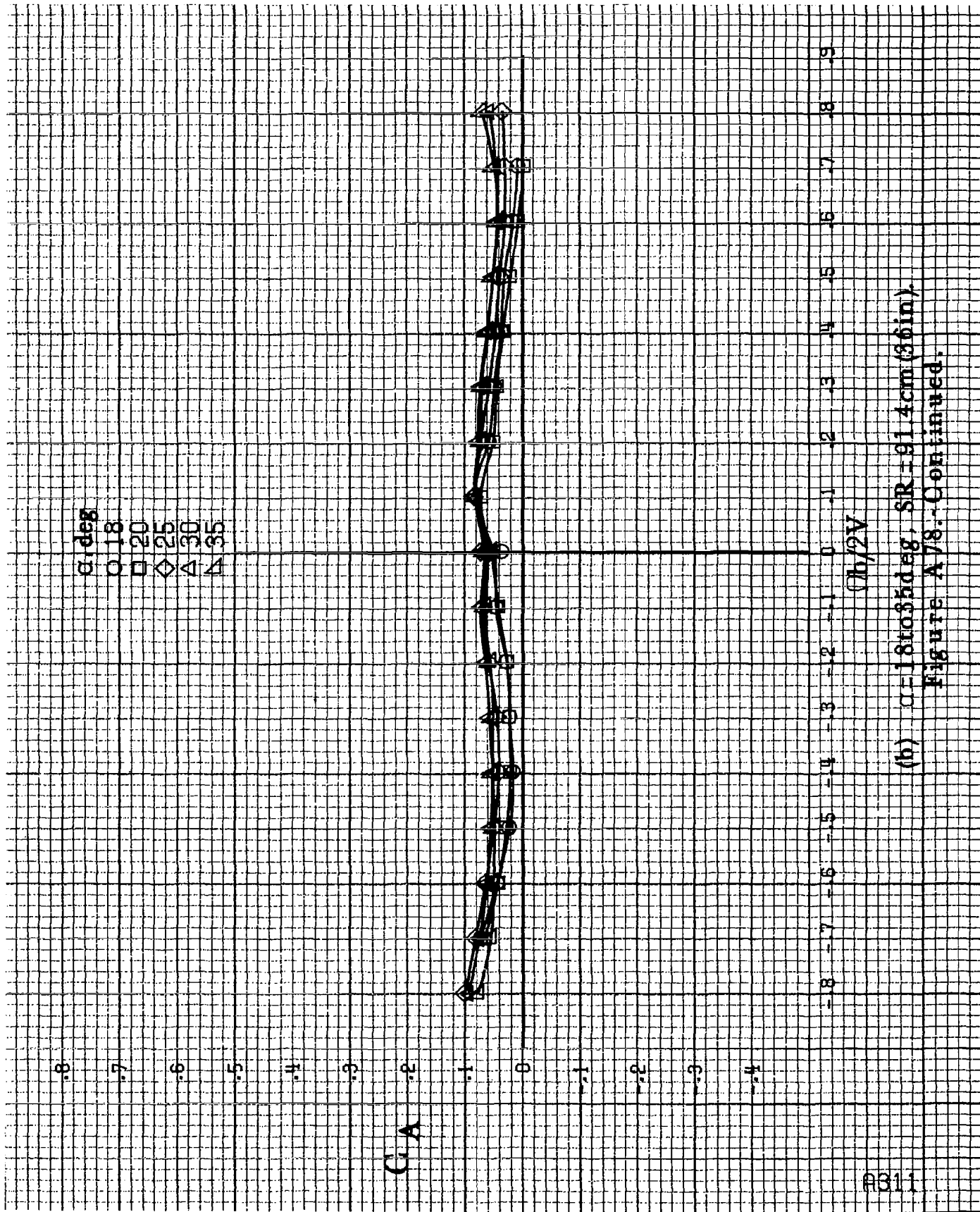
8310

α, deg
 8
 10
 12
 14
 16

CA



(a) $\alpha=8$ to 16 deg, $SR=91.4$ cm (36 in).
 Figure A78.-Effect of rotation rate and angle of attack on axial-force coefficient for long body, high wing, horizontal T-tail A configuration.
 $\delta_a=0^\circ$, $\delta_s=0^\circ$, $\delta_r=0^\circ$, $\beta=10^\circ$.



(b) $\alpha = 18$ to 35° , $SR = 91.4 \text{ cm (36 in.)}$
 Figure A78.-Continued.

A312

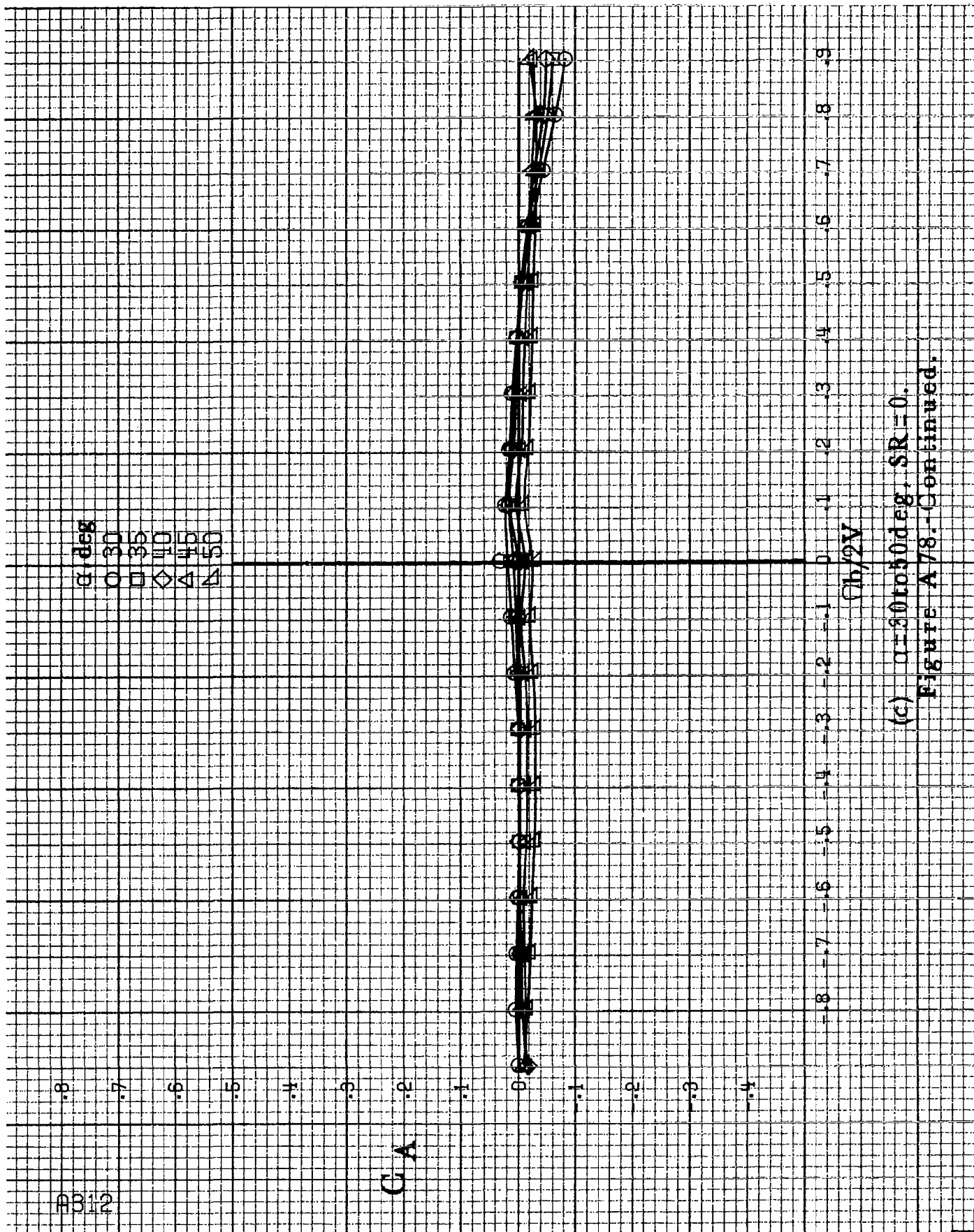
α , deg
 O 30
 □ 35
 ◇ 40
 △ 45
 ▽ 50

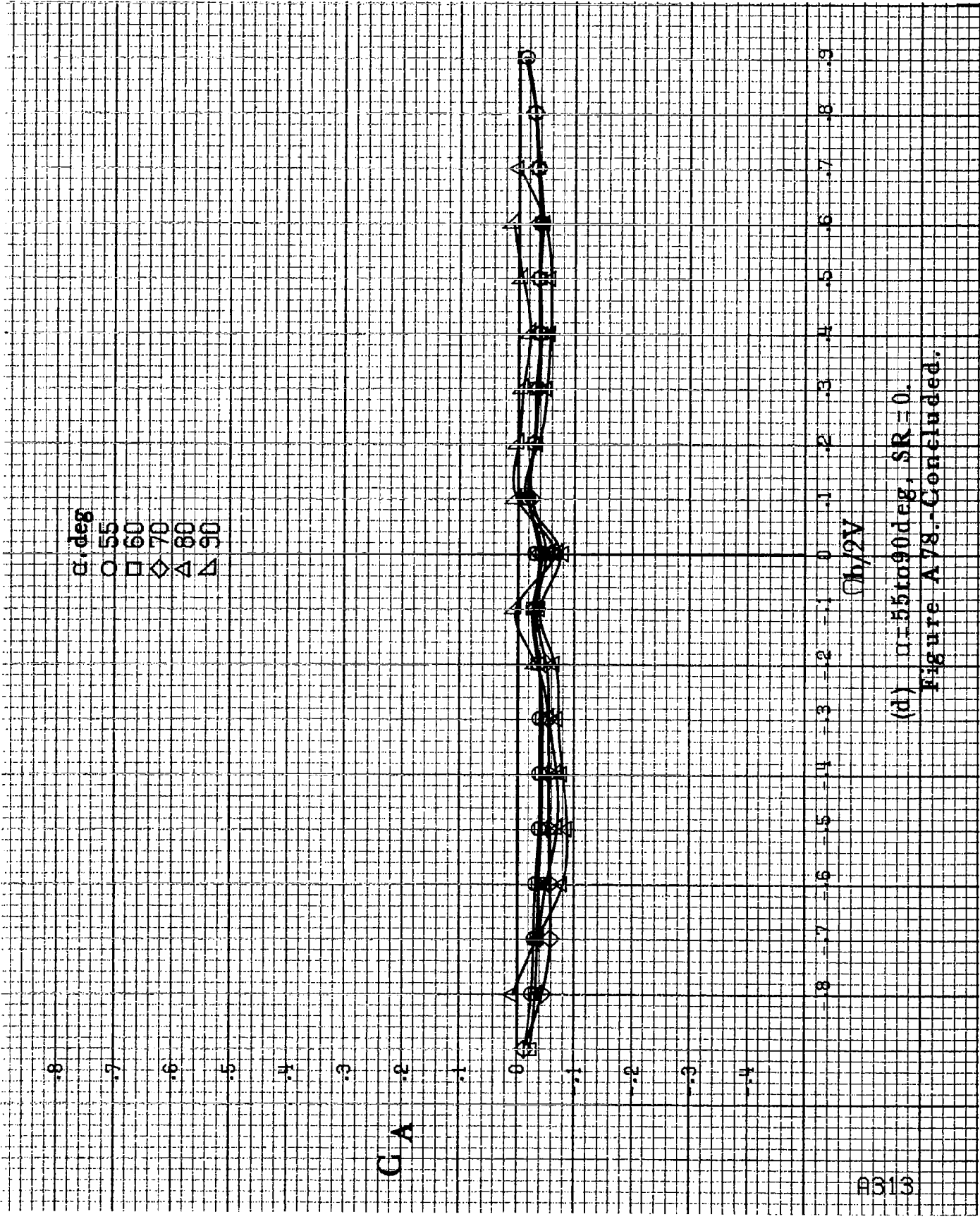
C_A

$C_b/2V$

(c) $\alpha=30$ to 50 deg, $SR=0$.

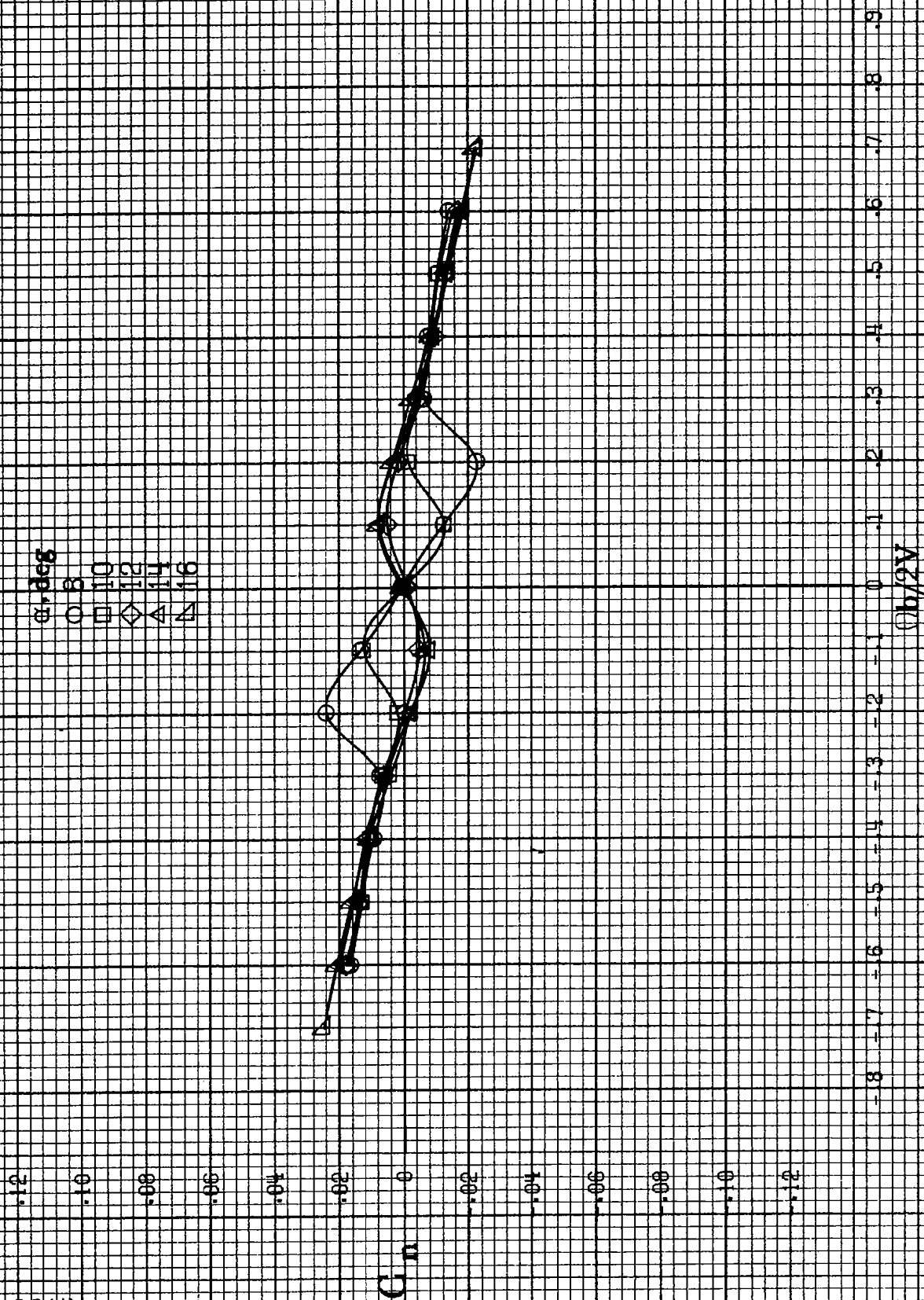
Figure A78.-Continued.





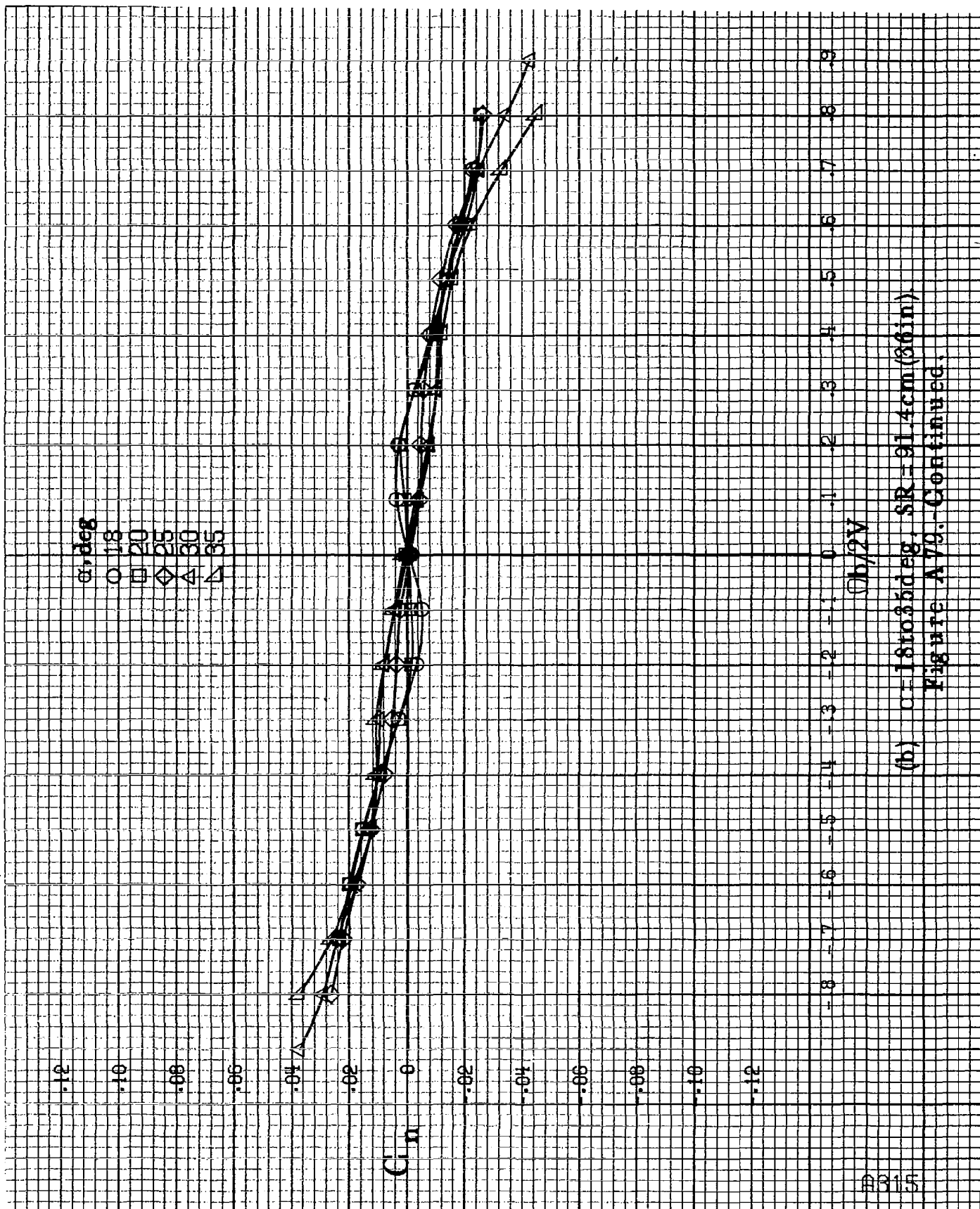
(d) $\alpha=55$ to 90 deg, $SR=0$.
 Figure A78.-Concluded.

4314



(a) $\alpha = 8$ to 16° , $SR = 91.4$ cm (36 in).

Figure A79.-Effect of rotation rate and angle of attack on yawing-moment coefficient for long body, high wing, horizontal tail no. 1 configuration. $\delta_a = 10^\circ$, $\delta_s = 10^\circ$, $\delta_r = 10^\circ$.



(b) $\alpha = 18$ to 36° , $SR = 31.4 \text{ cm (36 in)}$

Figure A79.-Continued.

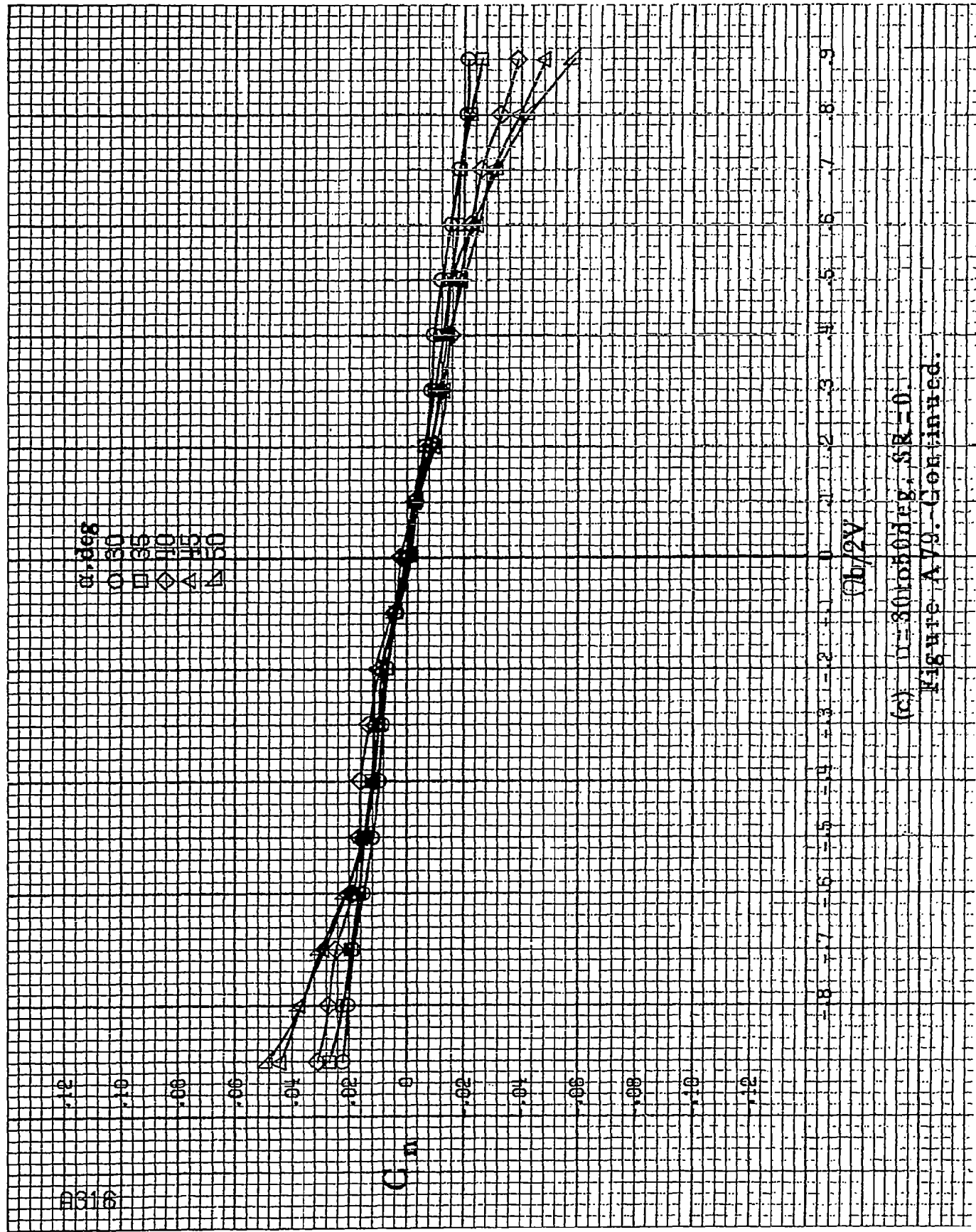
8316

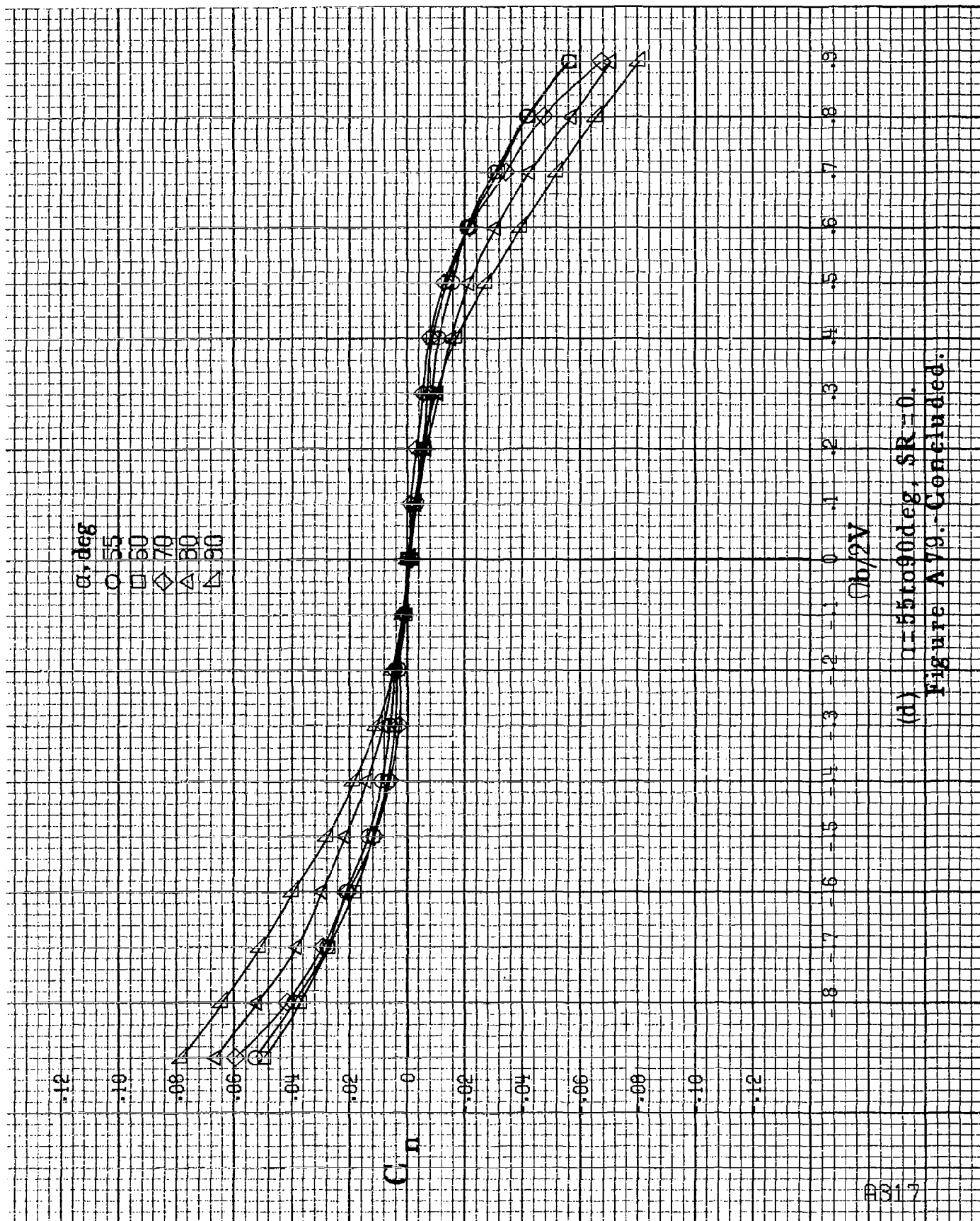
α , deg
 O 30
 □ 35
 ◇ 40
 △ 45
 ▽ 50

C_m

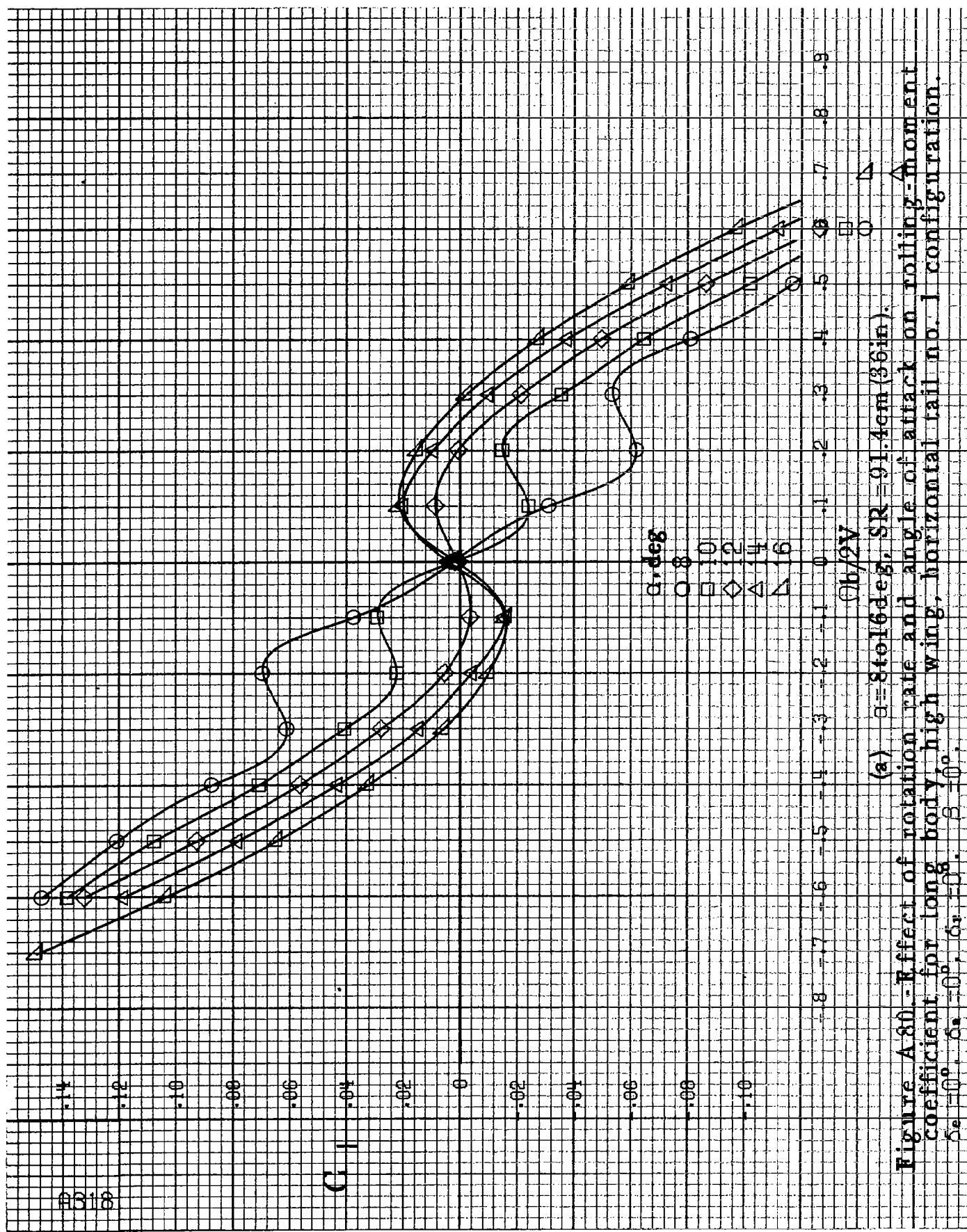
$Ob/2V$

(c) $\alpha = 30$ to 50 deg, $SR = 0$
 Figure A 79. Continued.



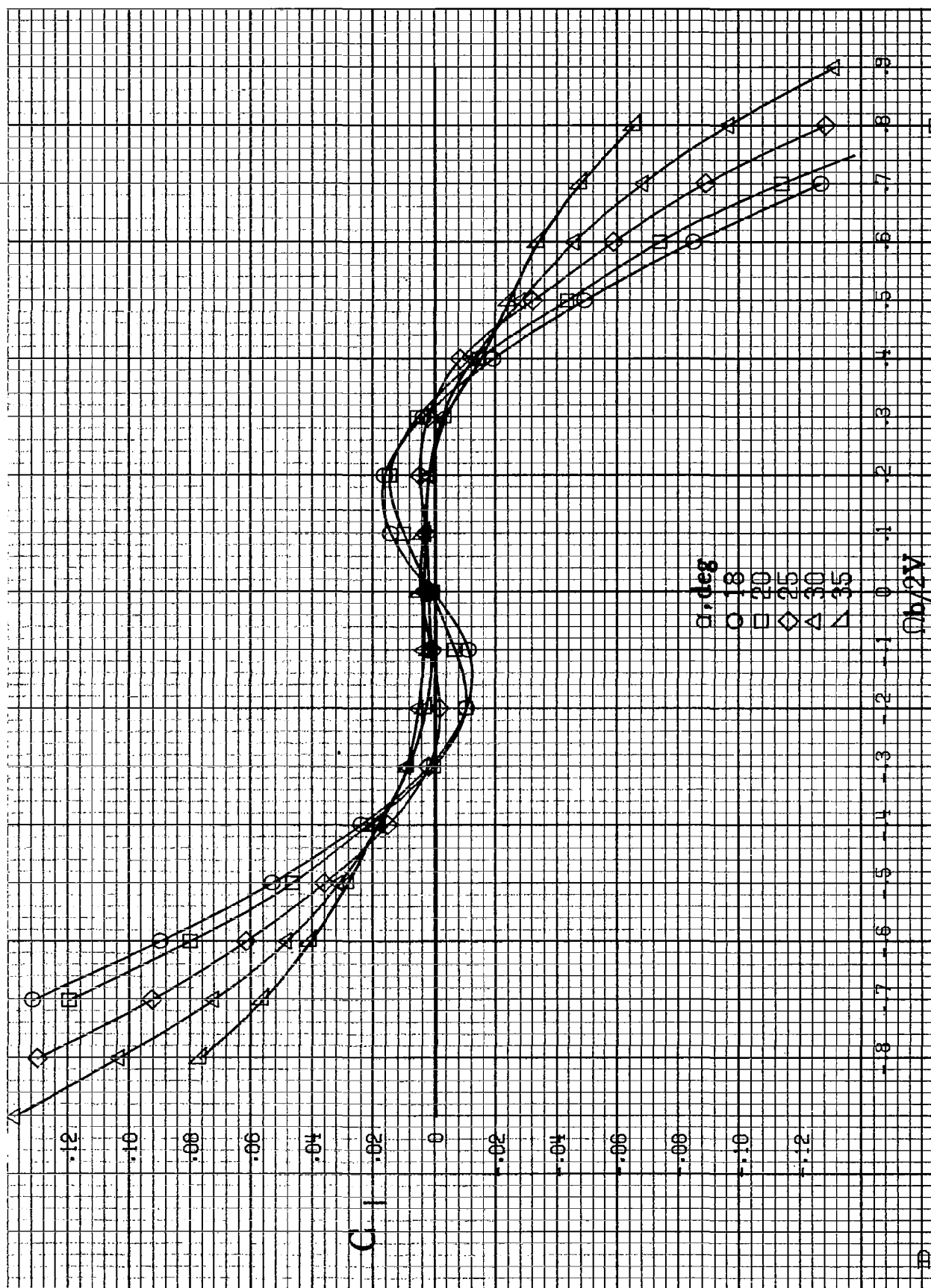


(d) $\alpha=55$ to 90° , $SR=0$.
Figure A79.-Concluded.

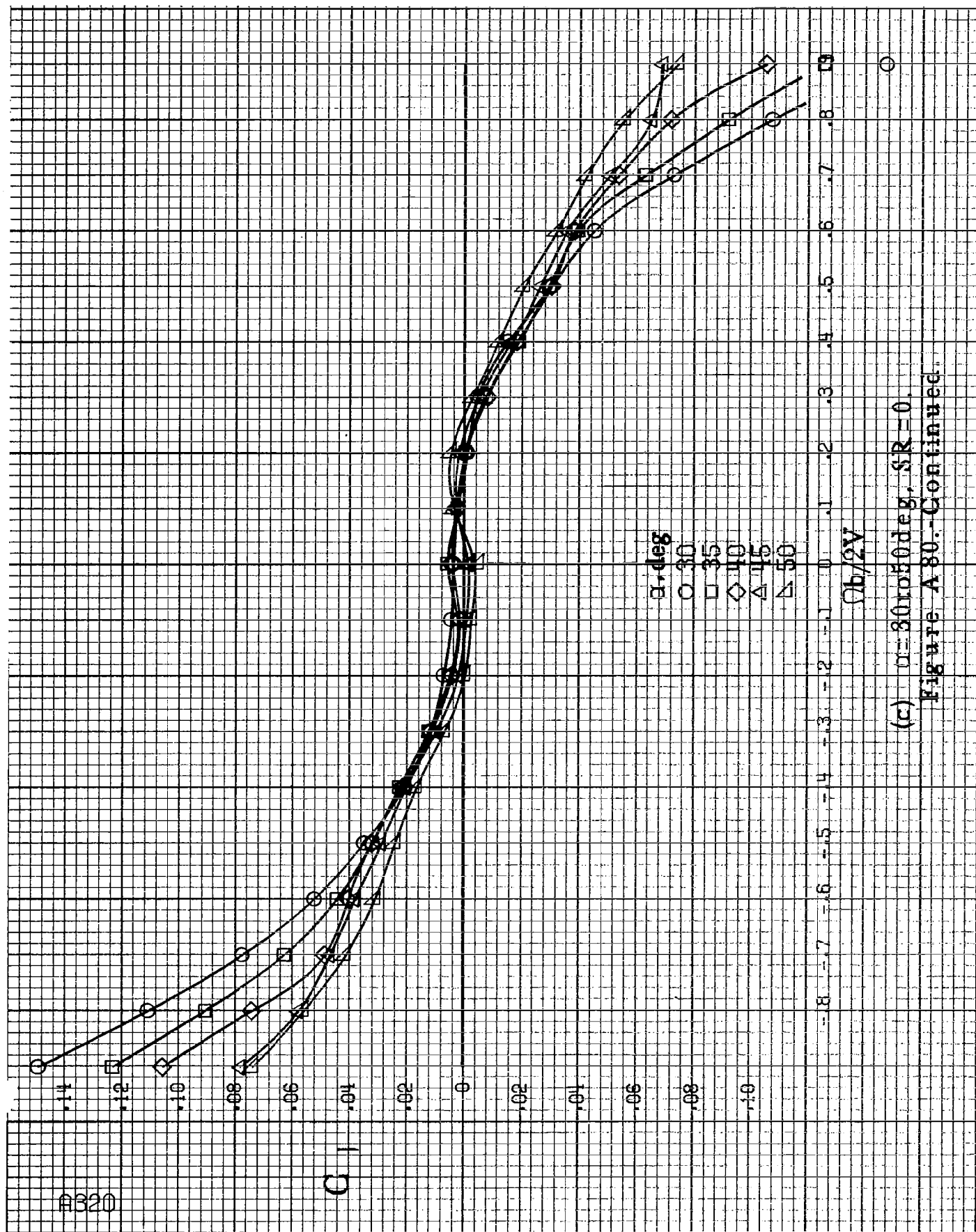


(a) $\alpha=8$ to 16° , $SR=91.4$ cm (36 in).

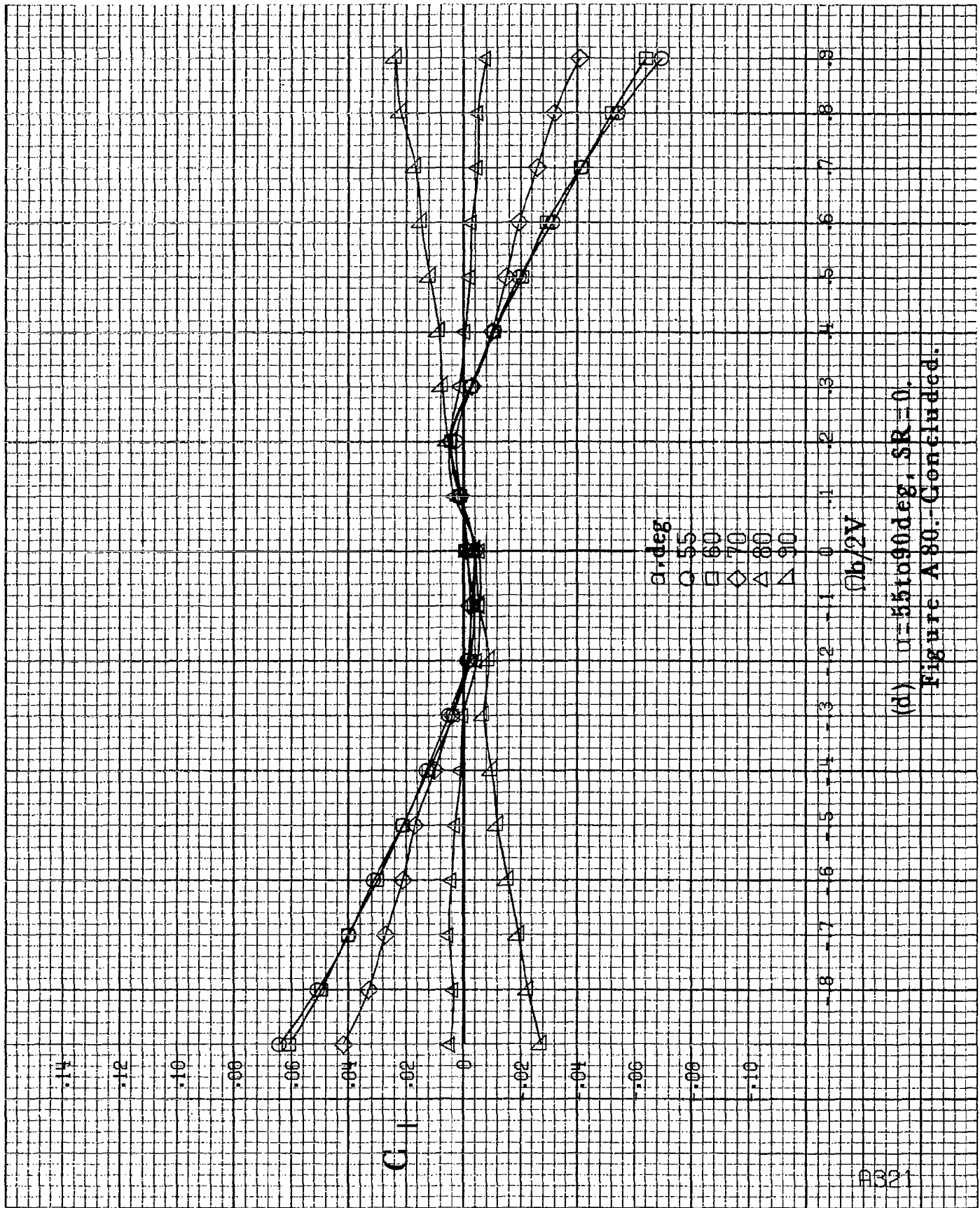
Figure A80.-Effect of rotation rate and angle of attack on rolling-moment coefficient for long body, high wing, horizontal tail no. 1 configuration. $\delta_e=0^\circ$, $\delta_a=0^\circ$, $\delta_v=0^\circ$, $\beta=0^\circ$.



(b) $\alpha = 18$ to 35° , $SR = 91.4 \text{ cm (36 in)}$
Figure A80.-Continued.



(c) $\alpha=30$ to 50° , $SR=0$.
Figure A80.--Continued.



(d) $\alpha=55$ to 90° , $SR=0$.
 Figure A 80.-Concluded.

C_m

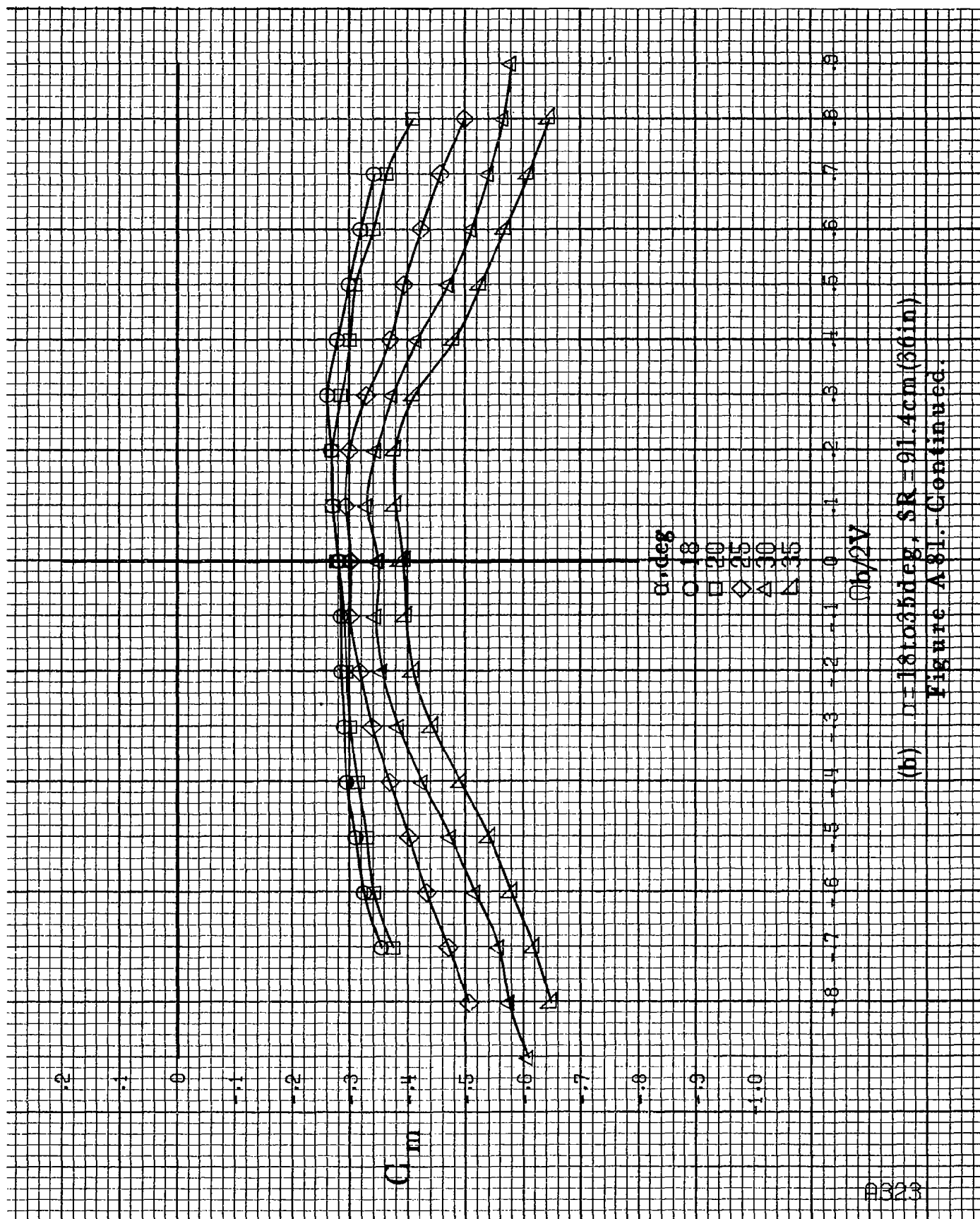
α, deg

○ 8
□ 10
◇ 12
△ 14
▽ 16

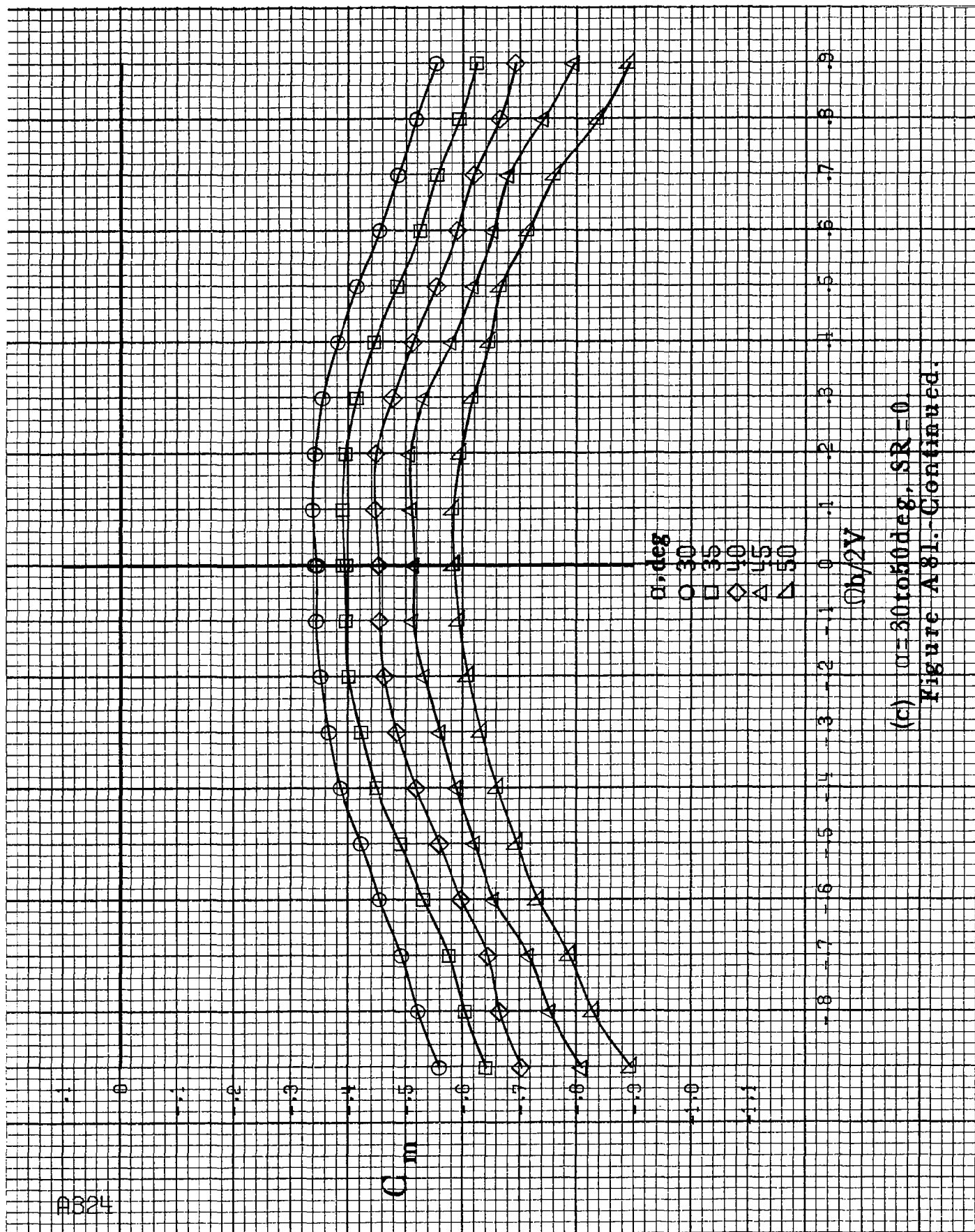
$h/2V$

(a) $\alpha = 8$ to 16 deg, $SR = 91.4 \text{ cm (36 in.)}$.

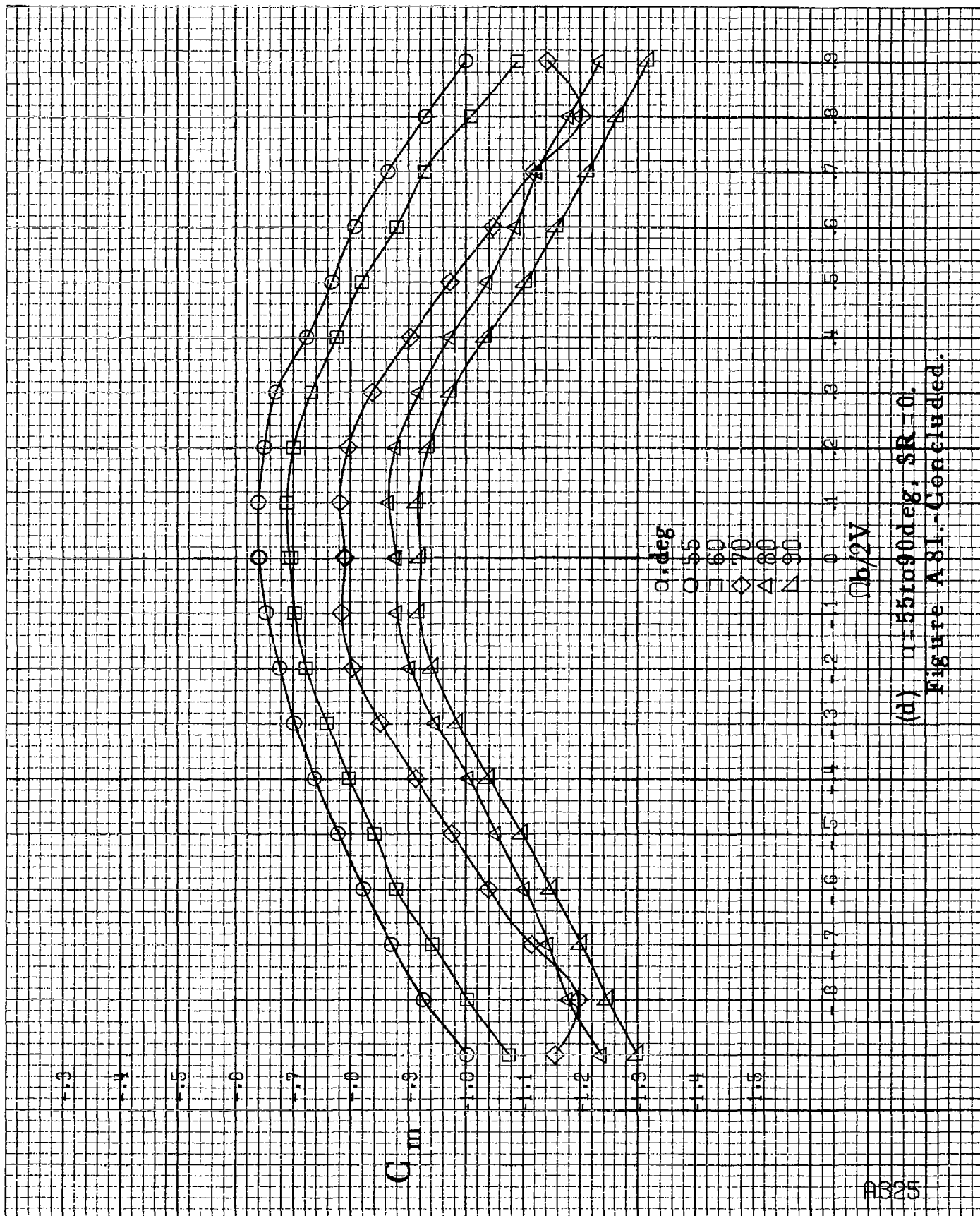
Figure A.81. Effect of rotation rate and angle of attack on pitching-moment coefficient for long body, high wing, horizontal tail no. 1 configuration. $\delta_a = 0^\circ$, $\delta_e = 0^\circ$, $\delta_r = 0^\circ$, $\beta = 0^\circ$.



(b) $D=1.8$ to 3 kg, $SR=21.4$ cm (8.6 in).
Figure A81. Continued.

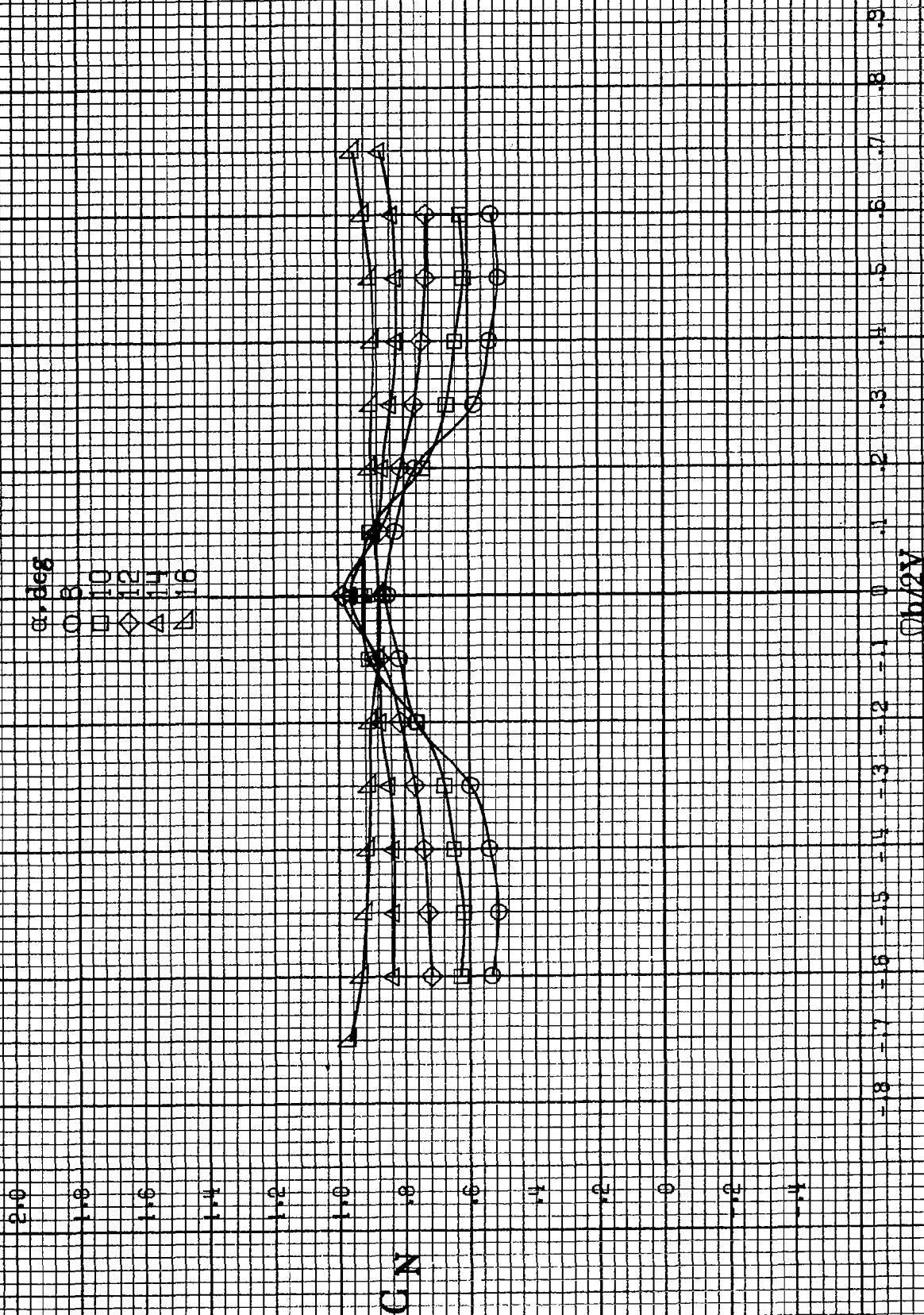


(c) $\alpha=30$ to 50° , $SR=0$
Figure A31. Continued.



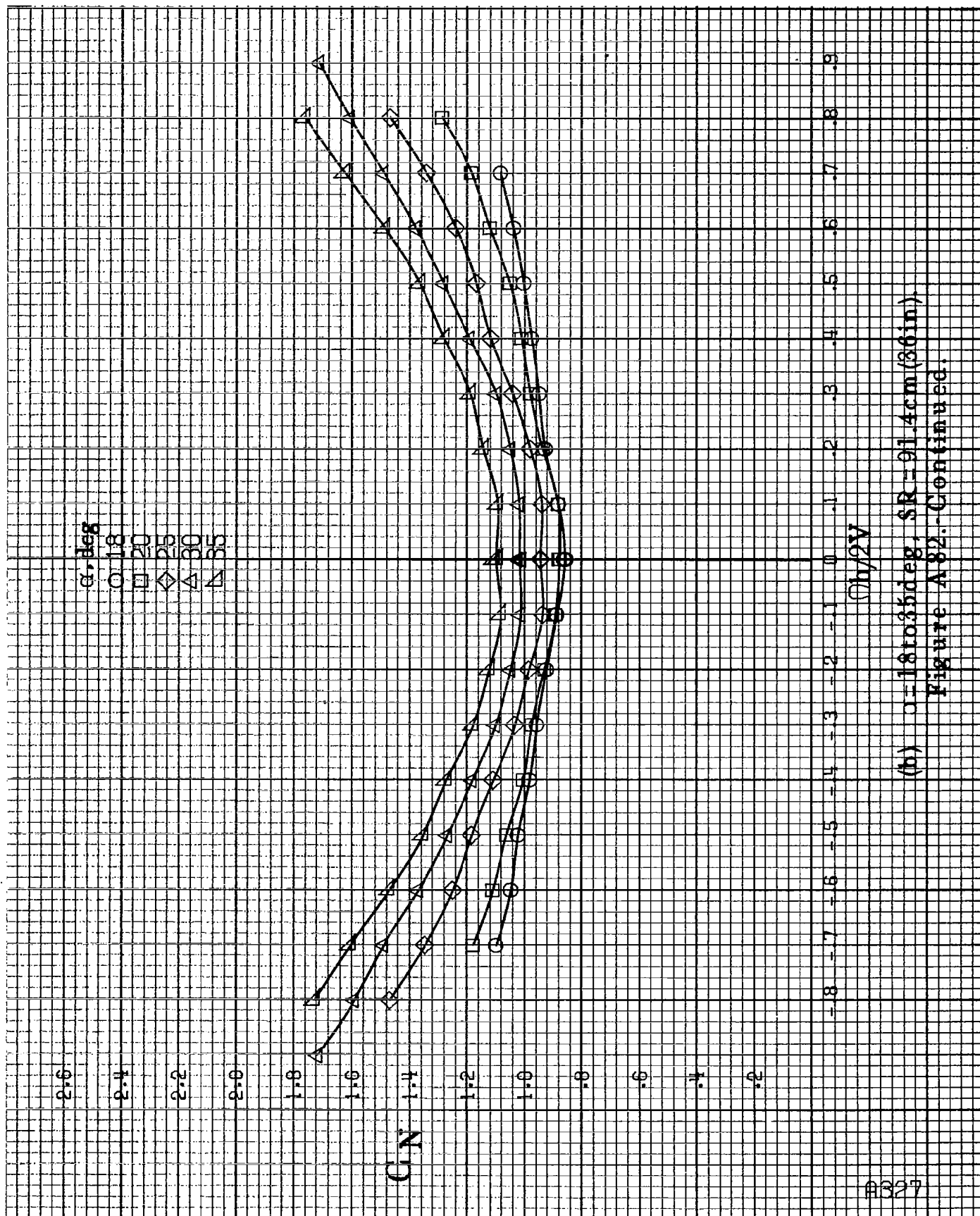
(d) $\alpha=55$ to 90° , $SR=0$.
Figure A.81.-Concluded.

#326



(a) $\alpha = 8$ to 16 deg, $SR = 91.4 \text{ cm (36 in.)}$.

Figure A89 - Effect of rotation rate and angle of attack on normal-force coefficient for long body, high wing, horizontal tail no. 1 configuration. $\delta_a = 0^\circ$, $\delta_r = 0^\circ$, $\beta = 0^\circ$.



(b) $\alpha = 18$ to 35° , $SR = 91.4 \text{ cm (36 in)}$
Figure A82.-Continued.

A328

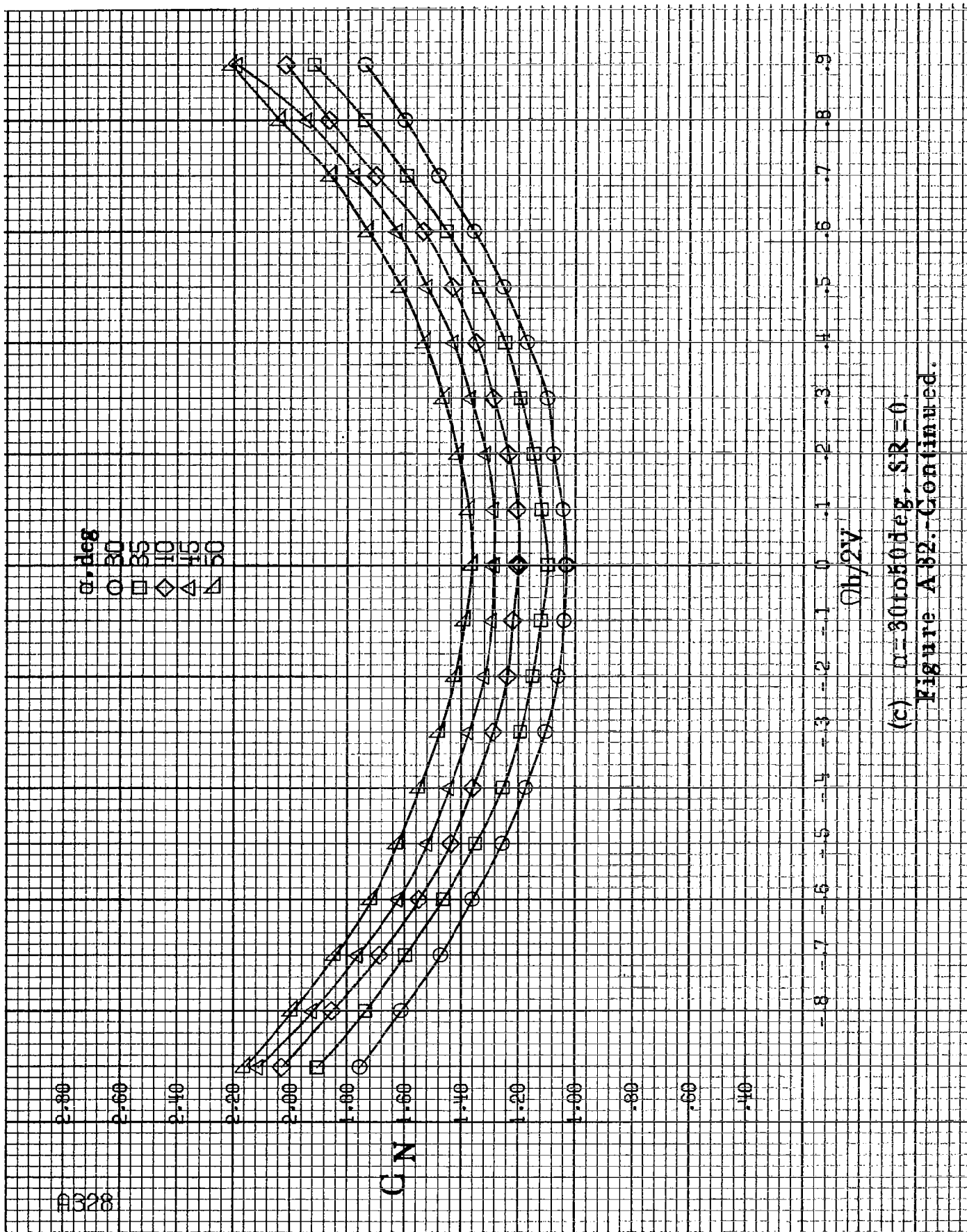
α , deg
 O 30
 □ 35
 ◇ 40
 △ 45
 ▽ 50

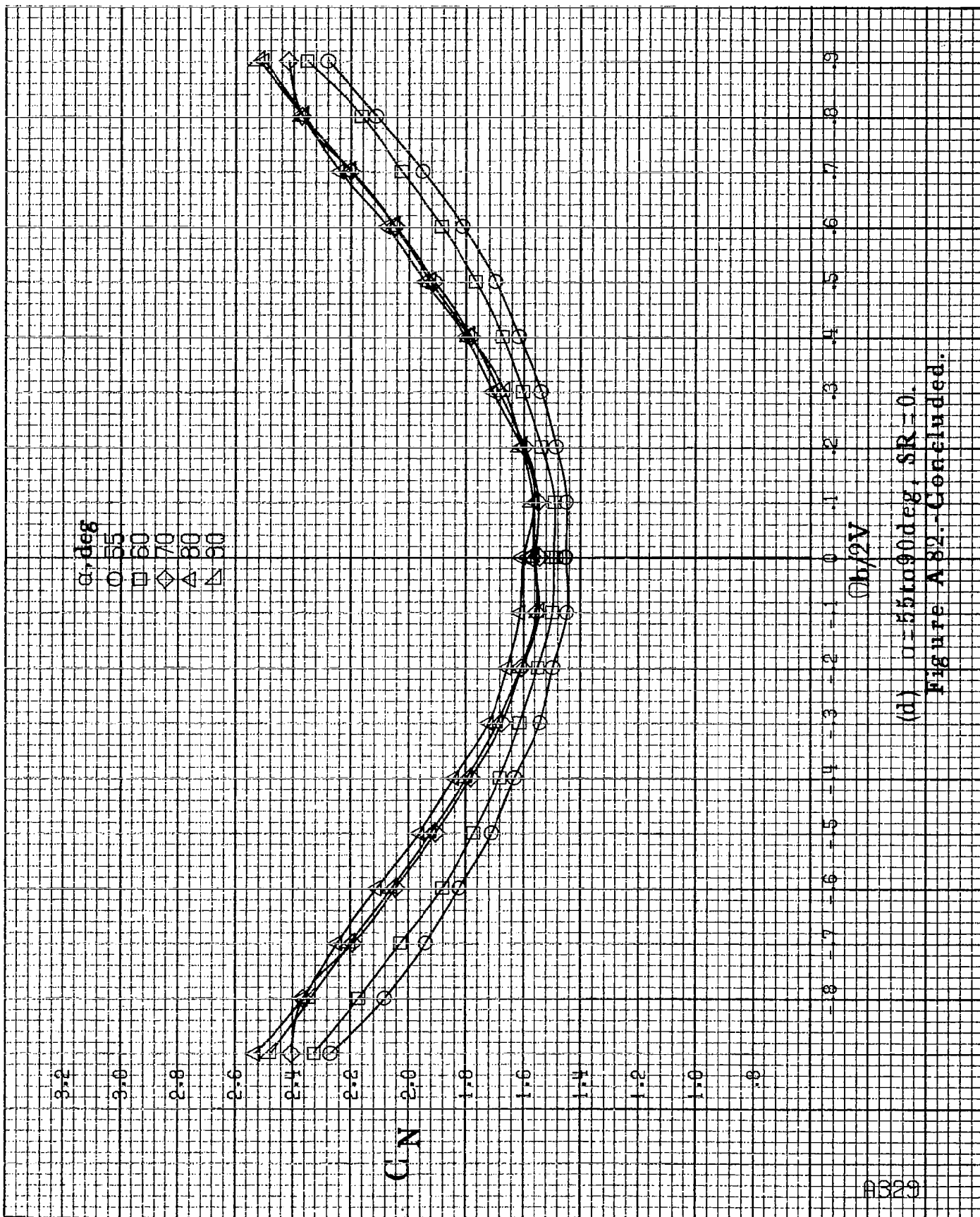
CN

$Qh/2V$

(c) $\alpha=30$ to 50 deg, $SR=0$

Figure A82.-Continued.





(d) $\alpha=55$ to 90° deg, $SR=0$.
Figure A82.-Concluded.

A330

α , deg

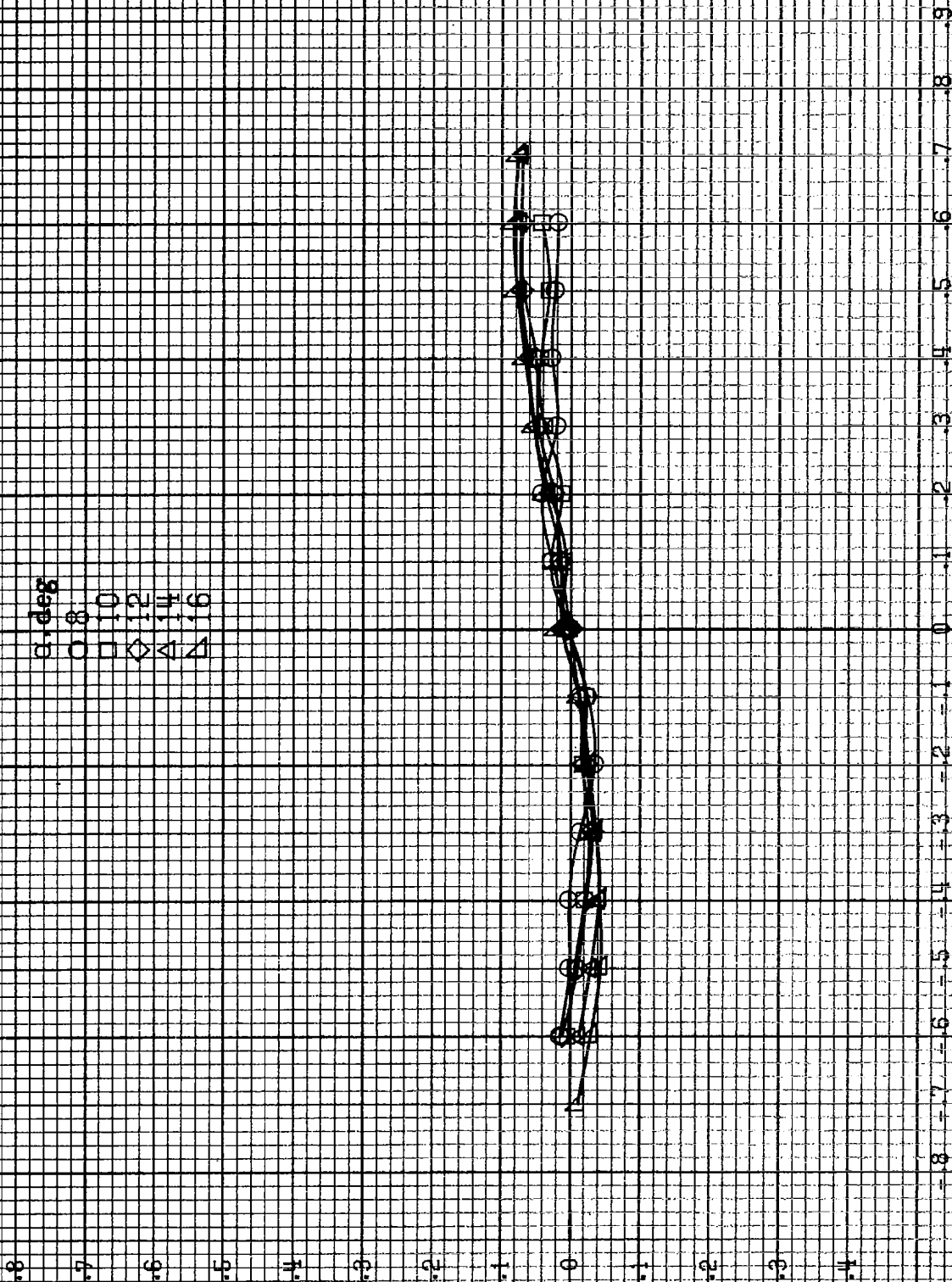
○ 8
□ 10
◇ 12
△ 14
▽ 16

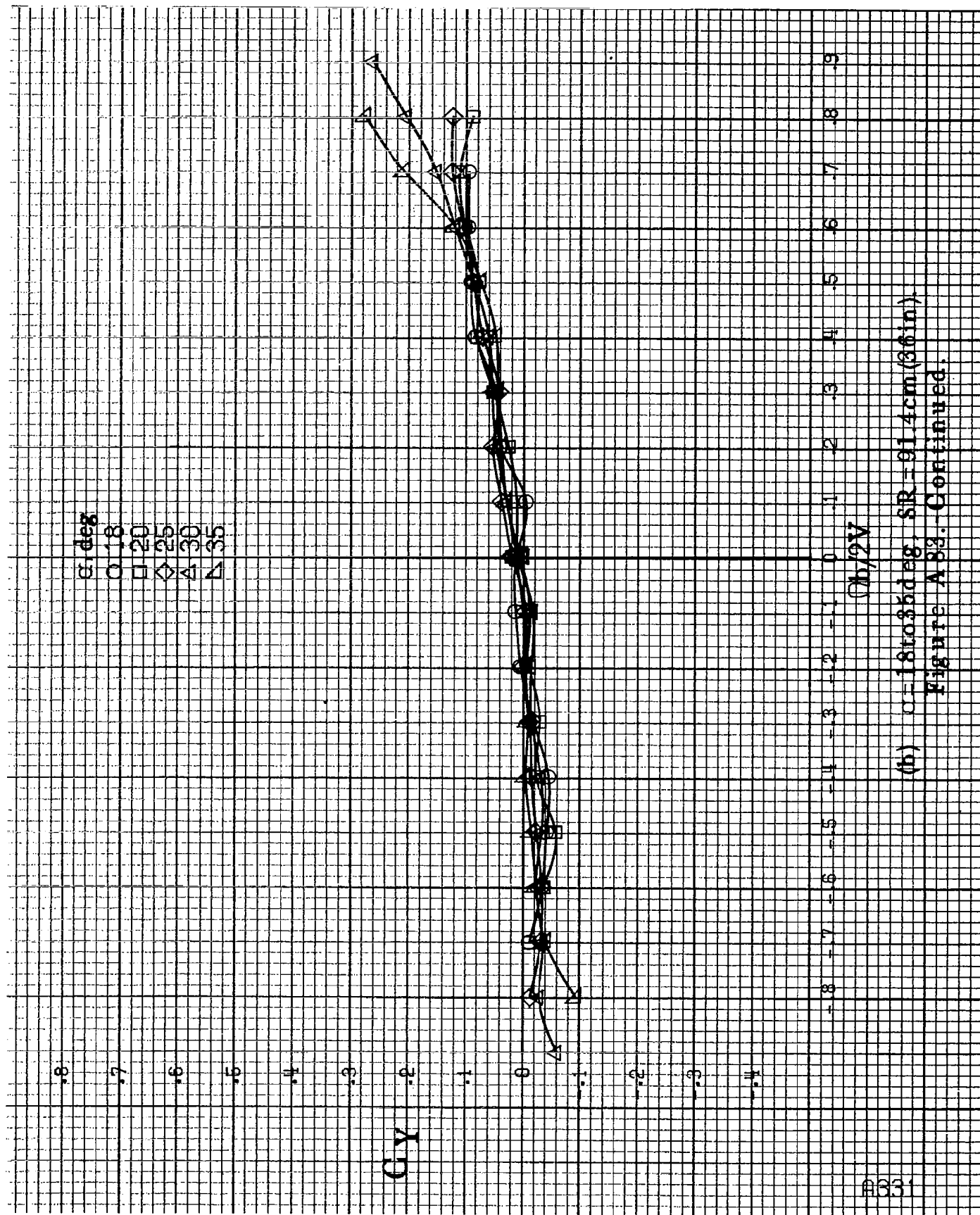
C_{ly}

$(h/2V)$

(a) $\alpha = 8$ to 16 deg, $SR = 91.4$ cm (36 in).

Figure A83 - Effect of rotation rate and angle of attack on side-force coefficient for long body, high wing, horizontal tail no. 1 configuration. $\delta e = 0^\circ$, $\delta a = 0^\circ$, $\delta r = 0^\circ$, $\beta = 0^\circ$.





(b) $\alpha=18$ to 35° , $SR=91.4\text{cm}(36\text{in})$
 Figure A 83.-Continued.

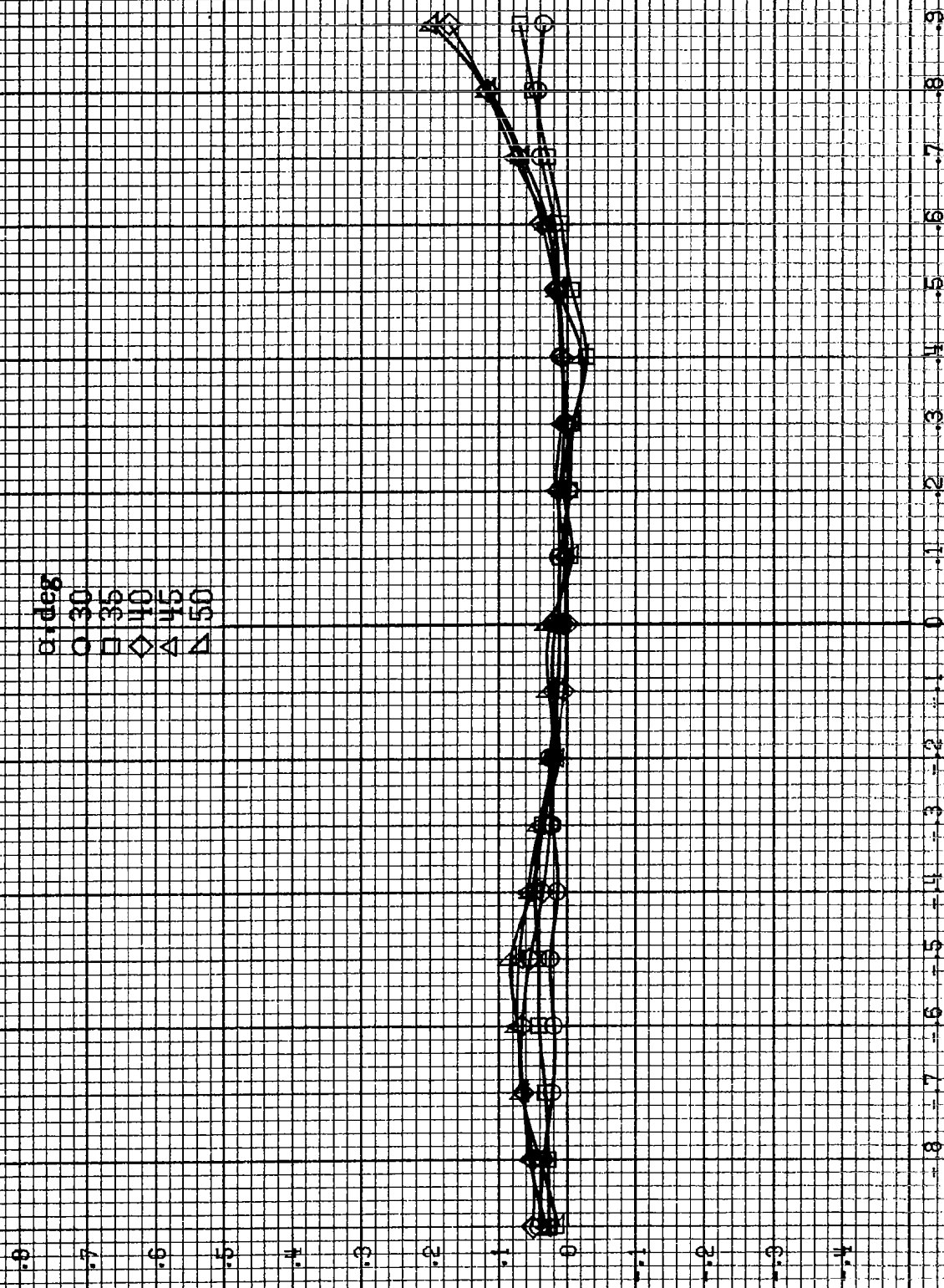
8332

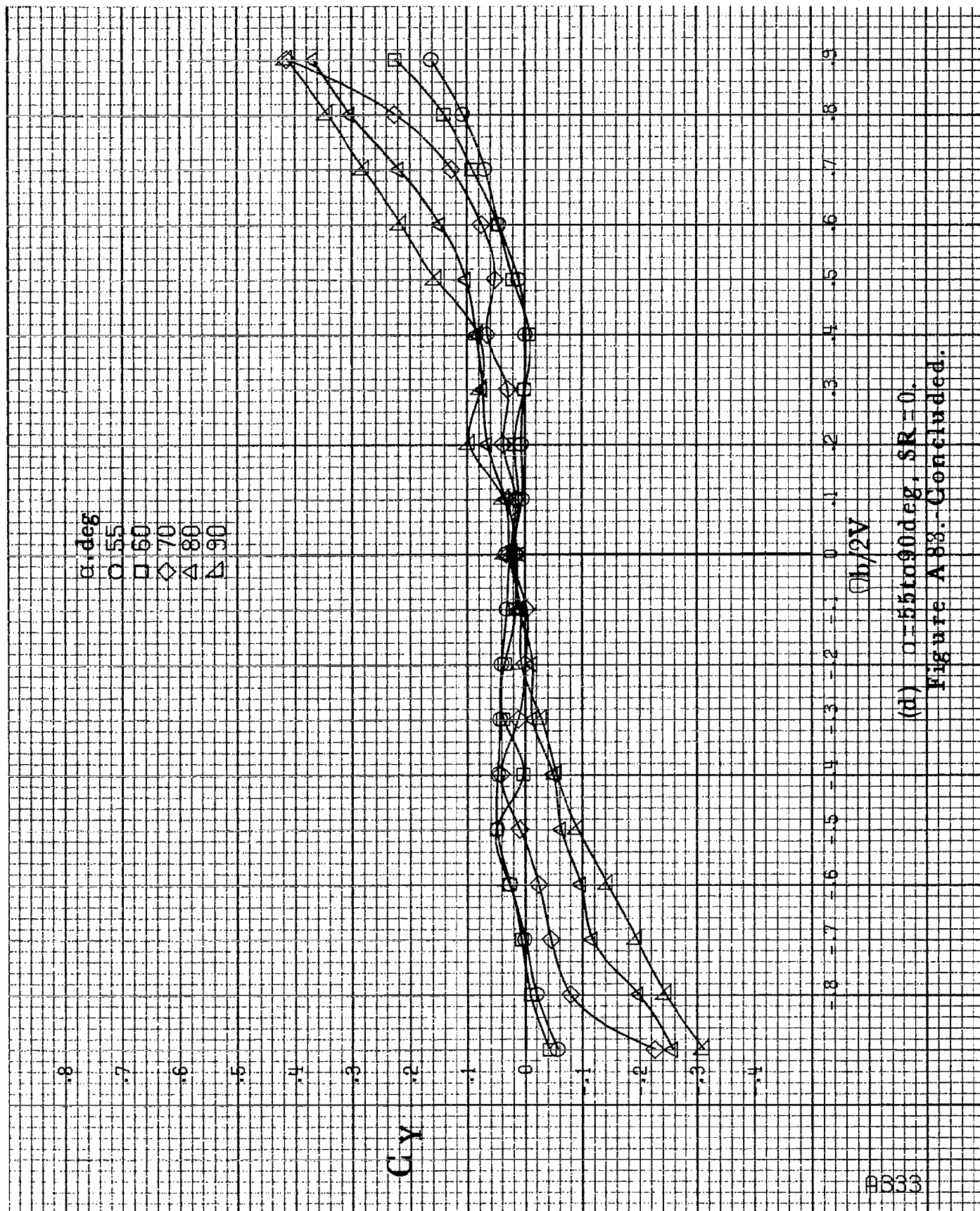
α, deg
 O 30
 □ 35
 ◇ 40
 △ 45
 ▲ 50

Cy

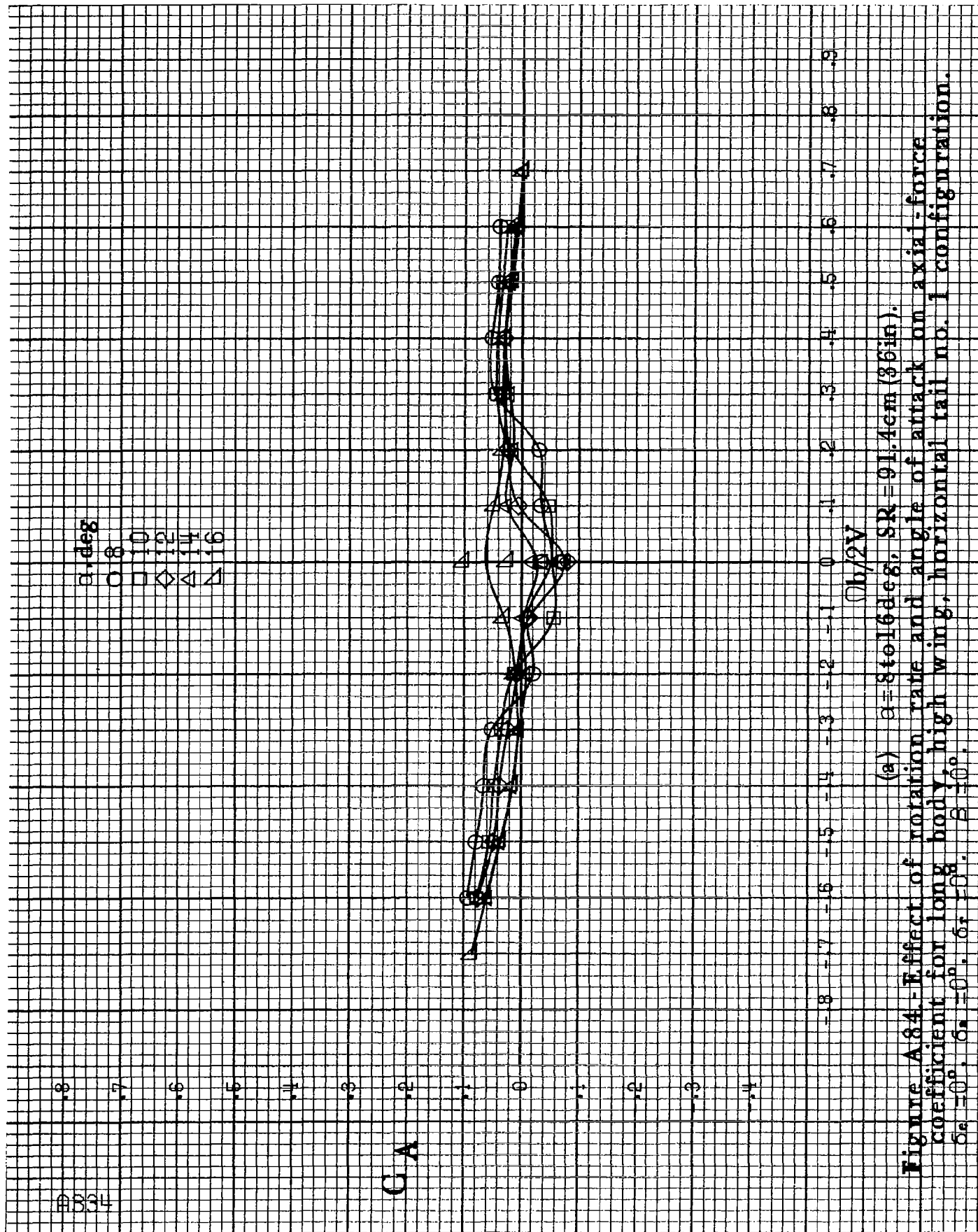
$\square b/2V$

(c) $\alpha=30$ to 50 deg, $SR=0$.
 Figure A 83.-Continued.





(d) $\alpha=55$ to 90° , $SR=0$.
Figure A 88. Concluded.



C₁A

α, deg
 ○ 18
 □ 20
 ◇ 25
 △ 30
 ▴ 35



αh/2V

(b) α = 18 to 35 deg, SR = 91.4 cm (36 in)
 Figure A84.-Continued.

8336

α, deg
 \circ 30
 \square 35
 \diamond 40
 \triangle 45
 ∇ 50

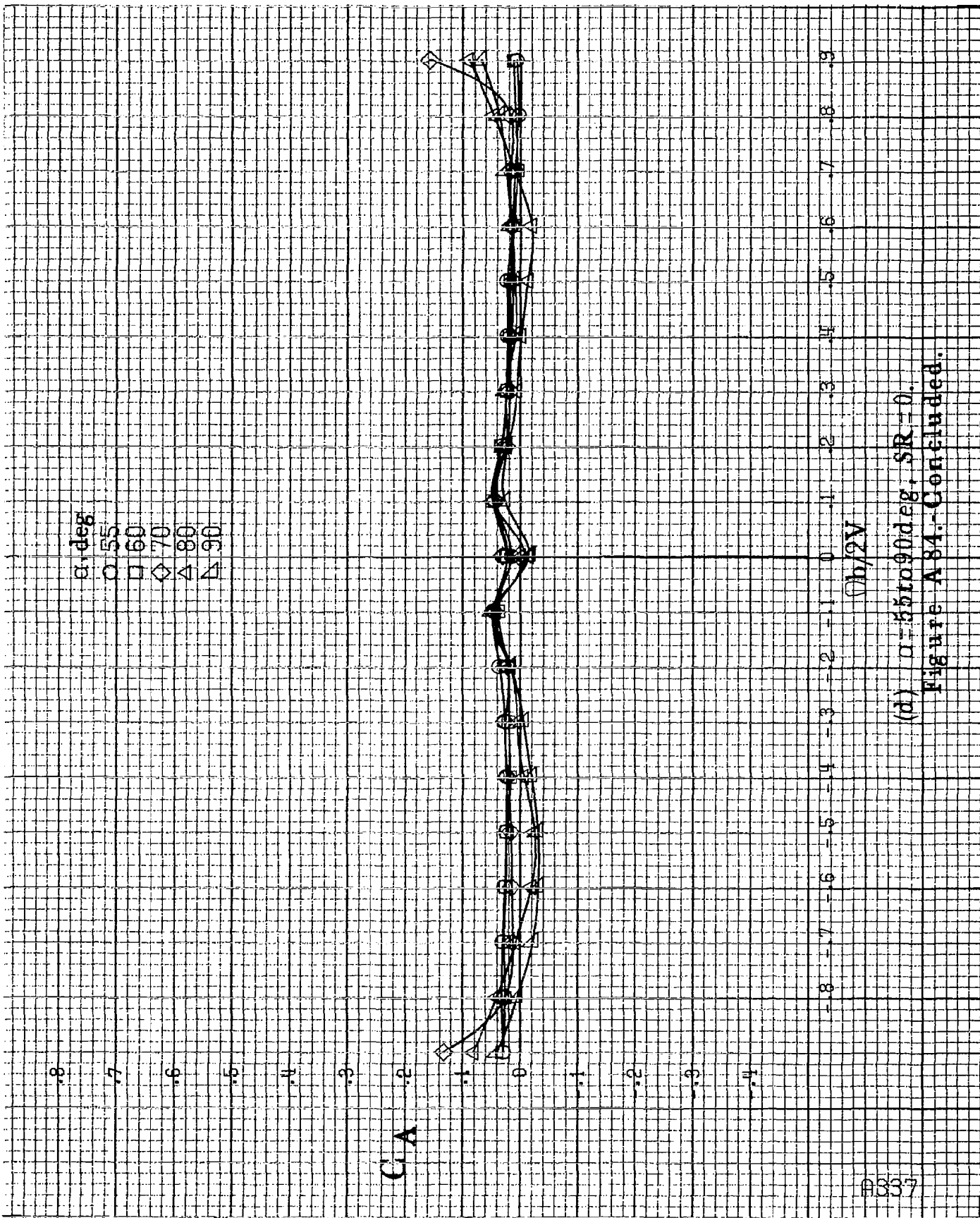
C_A



$Ob/2V$

(c) $\alpha = 30$ to 50 deg, $SR = 0$.

Figure A34.-Continued.



(d) $\alpha=55$ to 90 deg, $SR=0$.
 Figure A84.-Concluded.

α , deg

○ 8
 □ 10
 ◇ 12
 △ 14
 ▽ 16

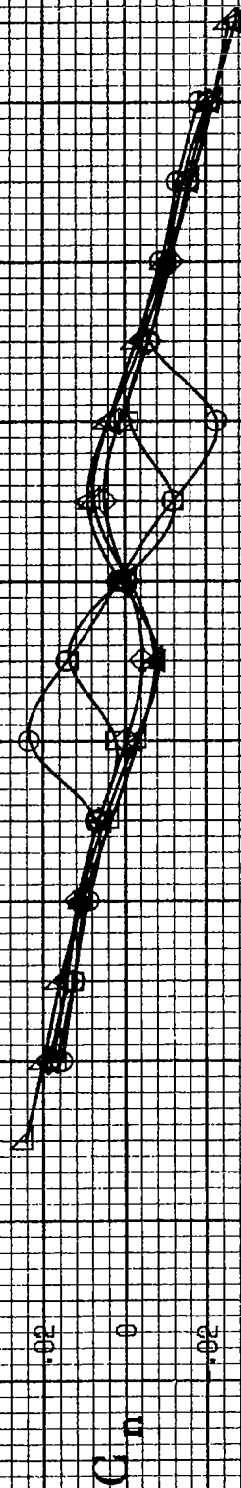
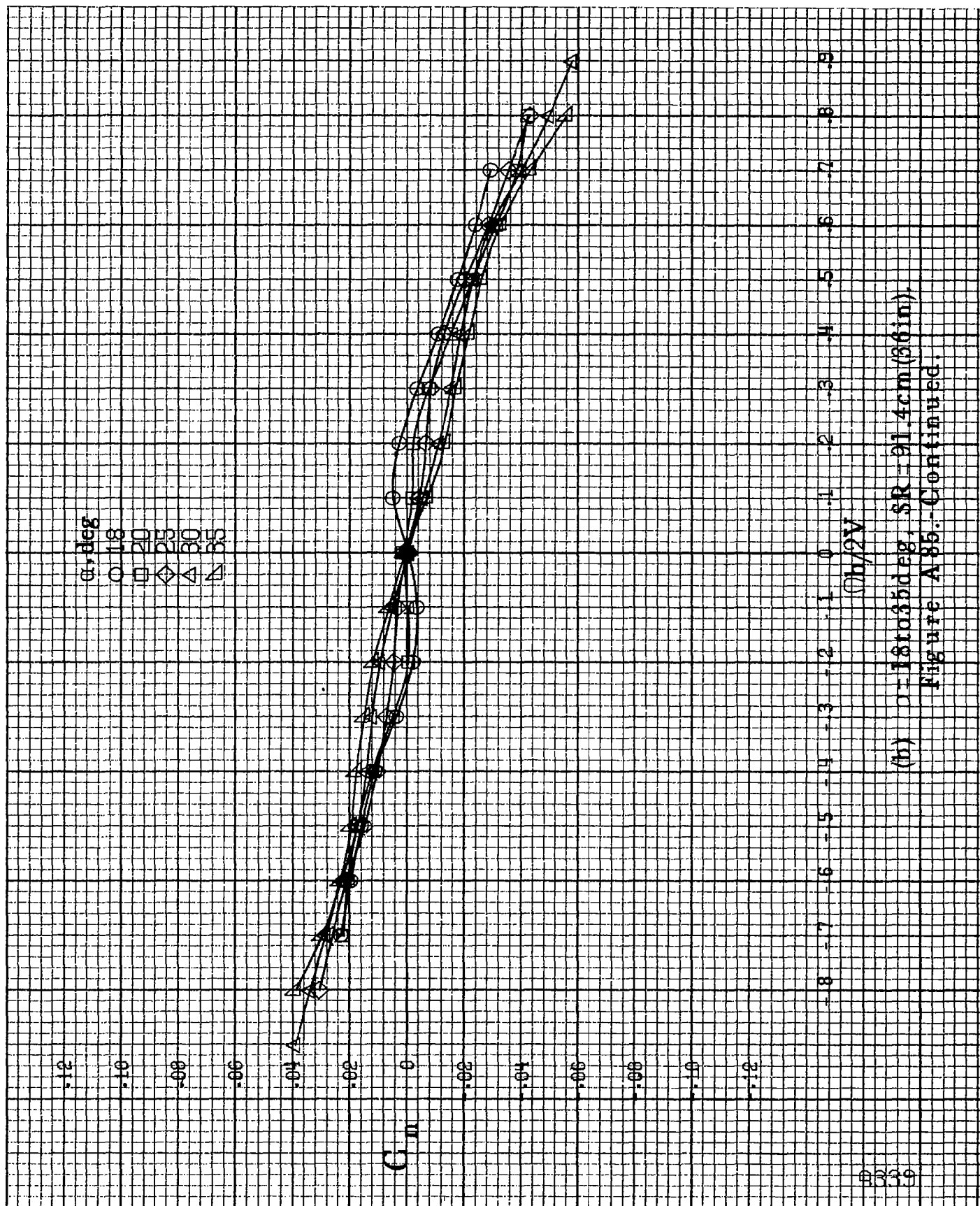
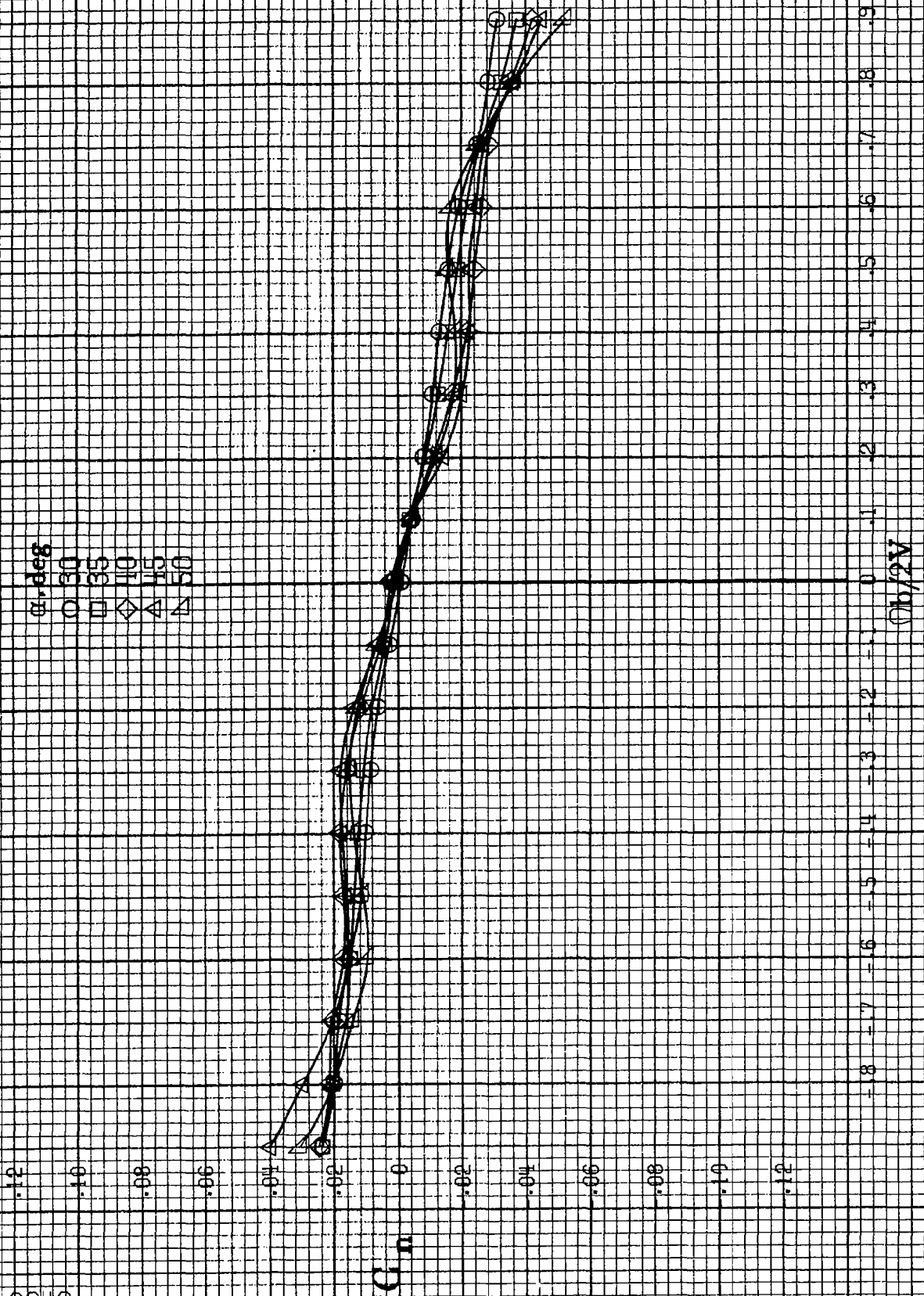
 $Qb/2V$ (a) $\alpha = 8$ to 16 deg, $SR = 91.4$ cm (35 in).

Figure A85 - Effect of rotation rate and angle of attack on yawing-moment coefficient for long body, high wing, horizontal tail no. 2 configuration. $\delta a = 0^\circ$, $\delta r = 0^\circ$, $\delta \tau = 0^\circ$.



(b) $\alpha = 18$ to 35° , $SR = 91.4 \text{ cm (36 in.)}$.
Figure A85.-Continued.



(c) $\alpha = 30$ to 50° , $SR = 0$.

Figure A 85.-Continued.

α , deg
 ○ 55
 □ 60
 ◇ 70
 △ 80
 ▽ 90

.12

.10

.08

.06

.04

.02

0

.02

.04

.06

.08

.10

.12

C_n

$Ch/2V$

-18

-17

-16

-15

-14

-13

-12

-11

-10

-9

-8

-7

-6

-5

-4

-3

-2

-1

0

1

2

3

4

5

6

7

8

9

(d) $\alpha = 55$ to 90 deg, $SR = 0$.

Figure A.85.-Concluded.

8341

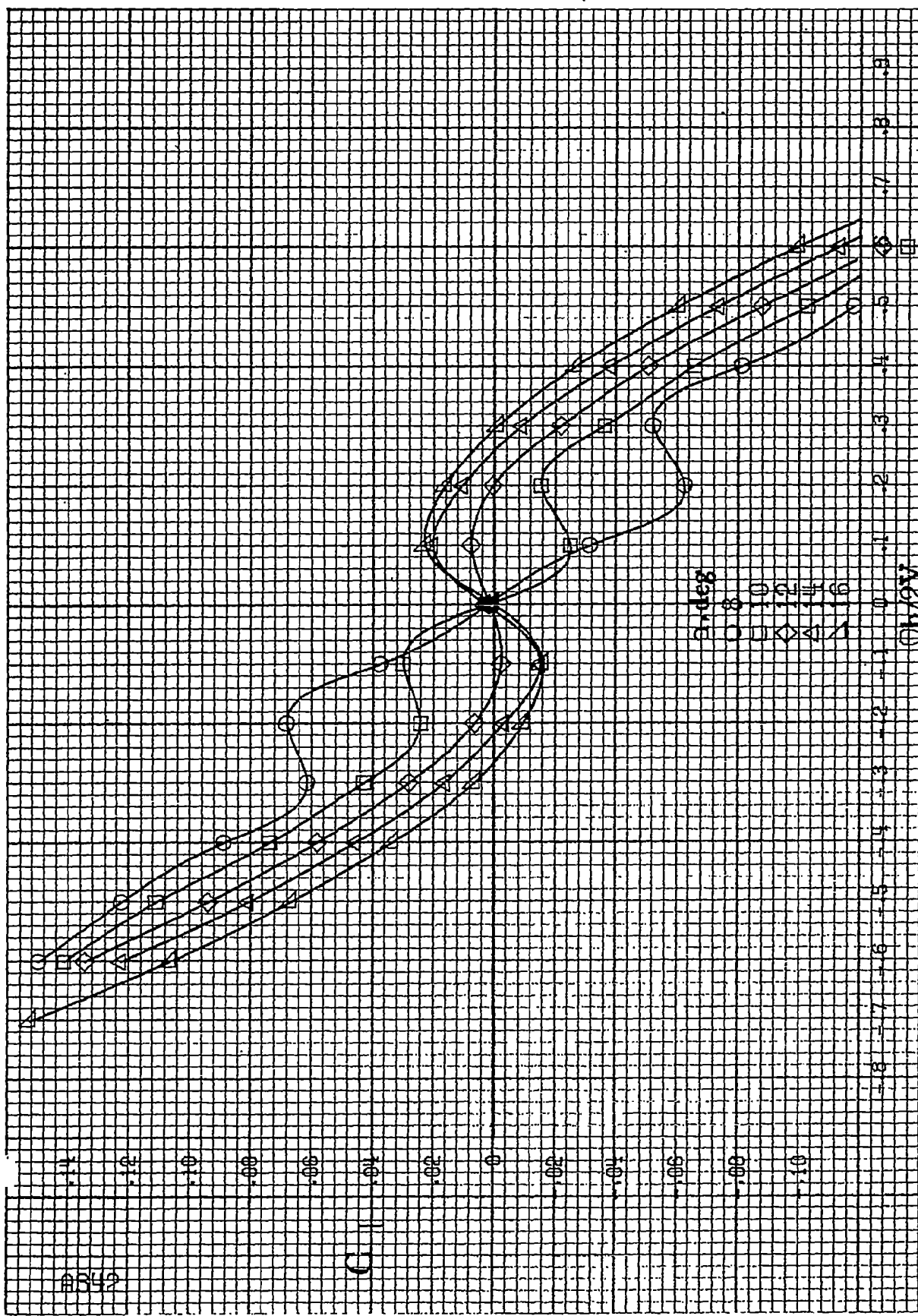
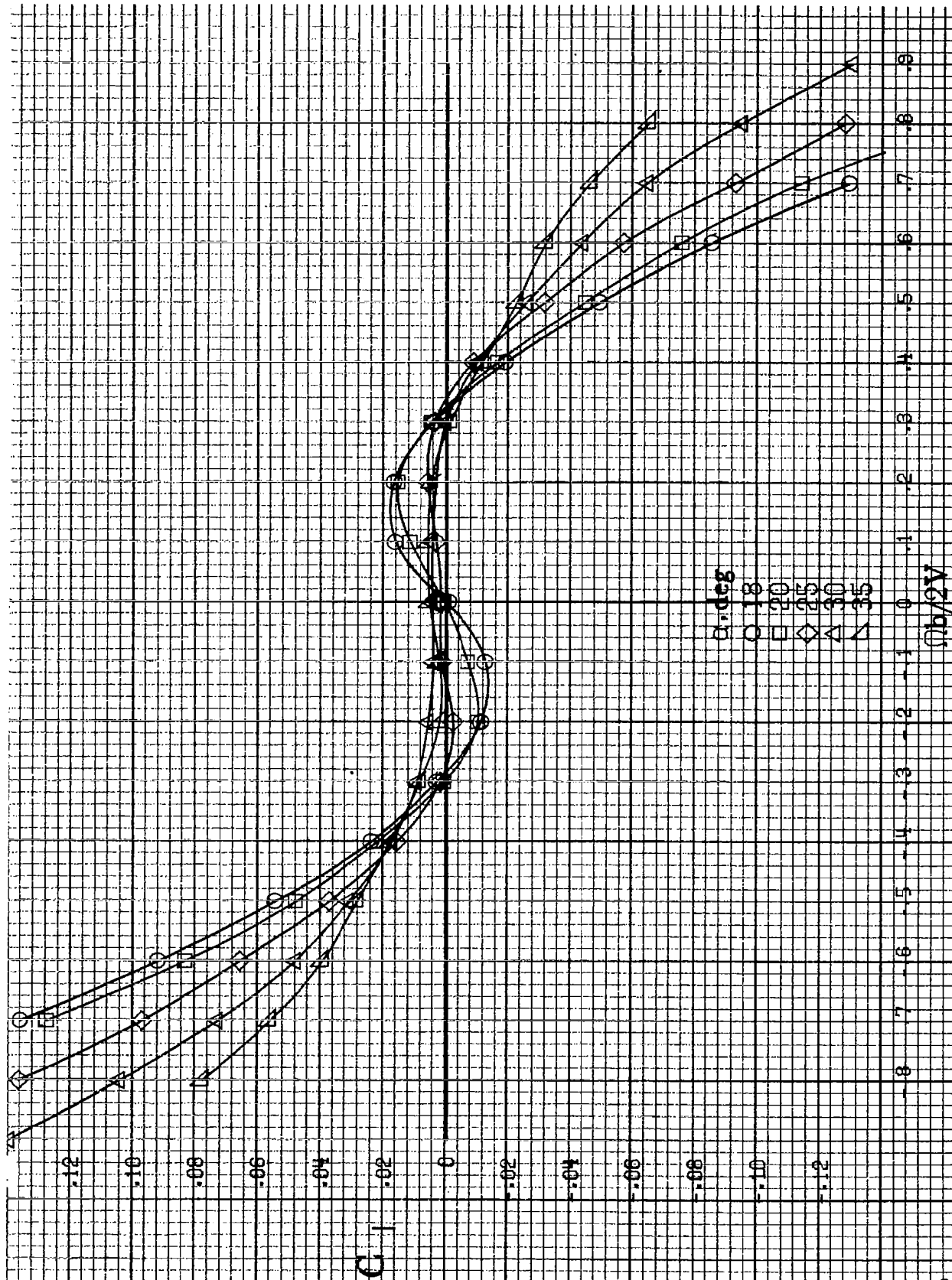
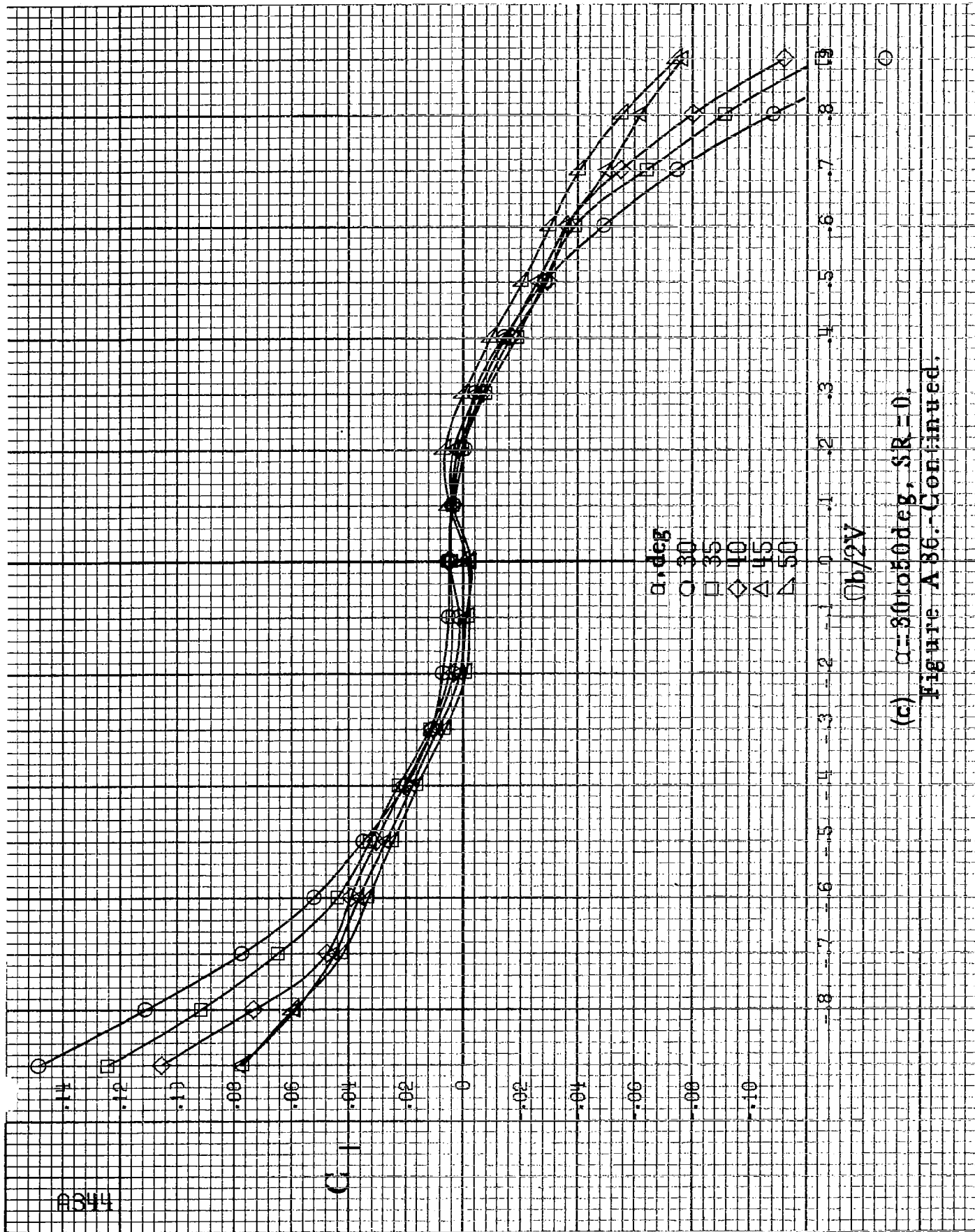


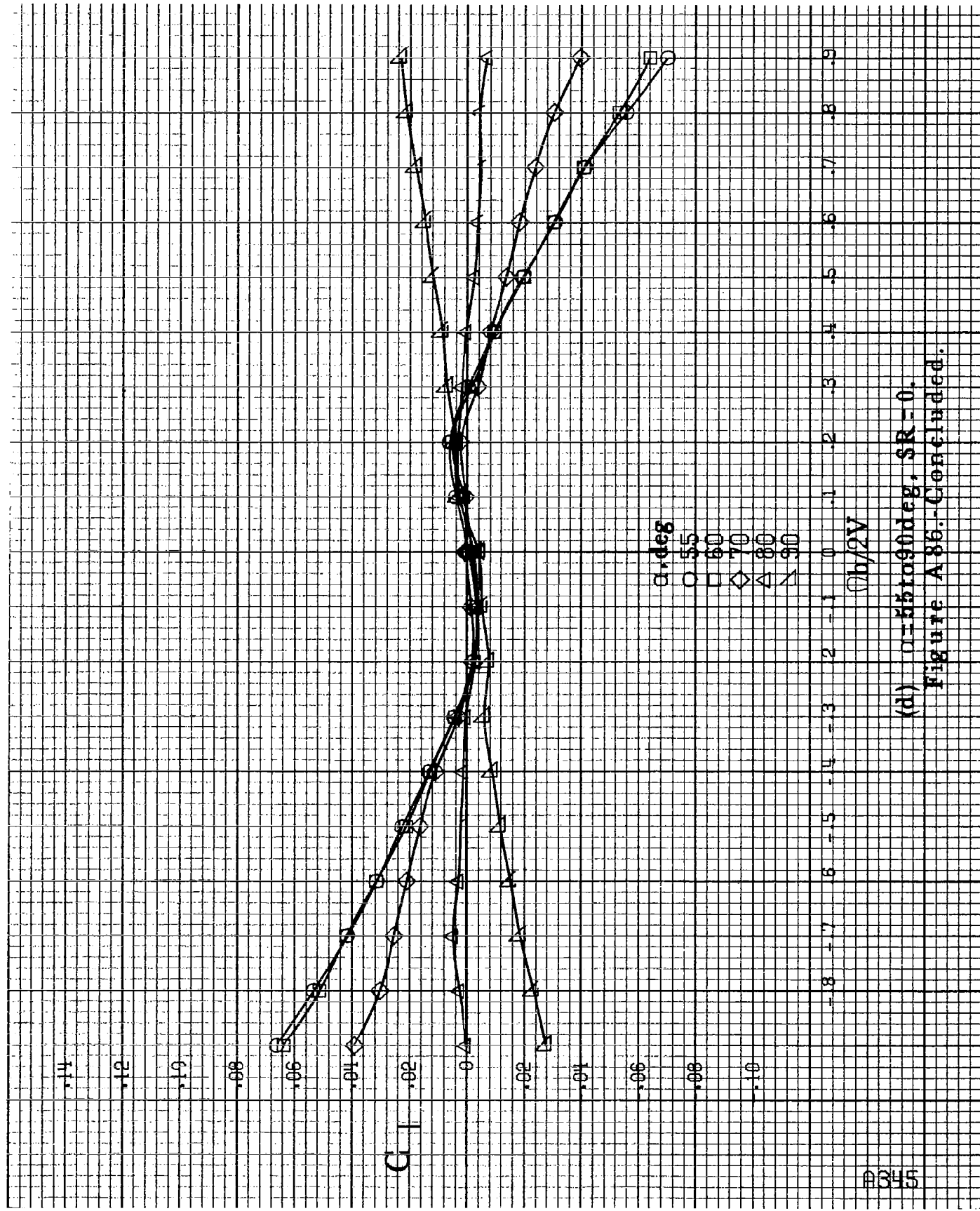
Figure A86. Effect of rotation rate and angle of attack on rolling-moment coefficient for long body, high wing, horizontal tail no. 2 configuration. $\delta_a = -10^\circ$, $\delta_e = -10^\circ$, $\delta_r = -10^\circ$, $\delta = -10^\circ$.



(b) $\theta = 18$ to 35° , SR = 91.4 cm (36 in).

Figure A85. Continued.





(d) $\alpha=55$ to 90° , $SR=0$.
Figure A 86.-Concluded.

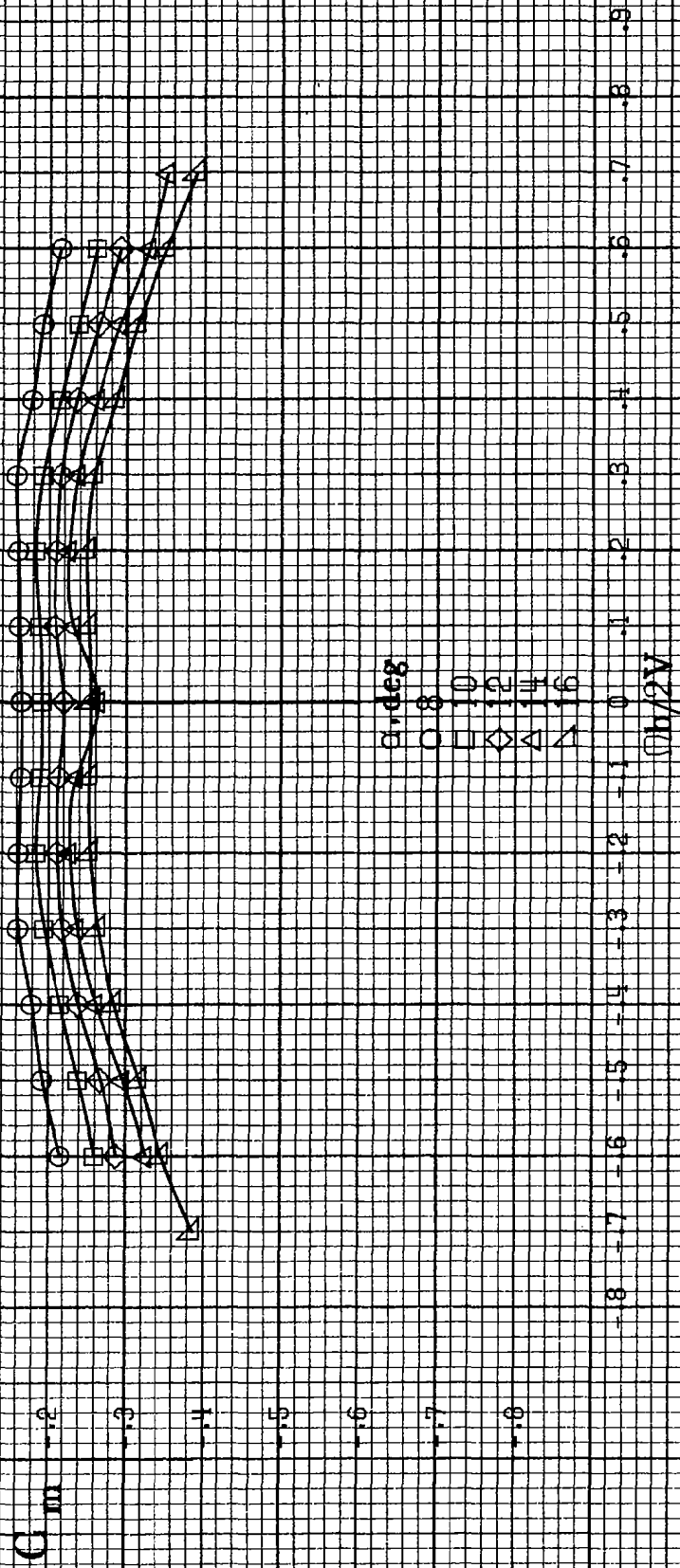
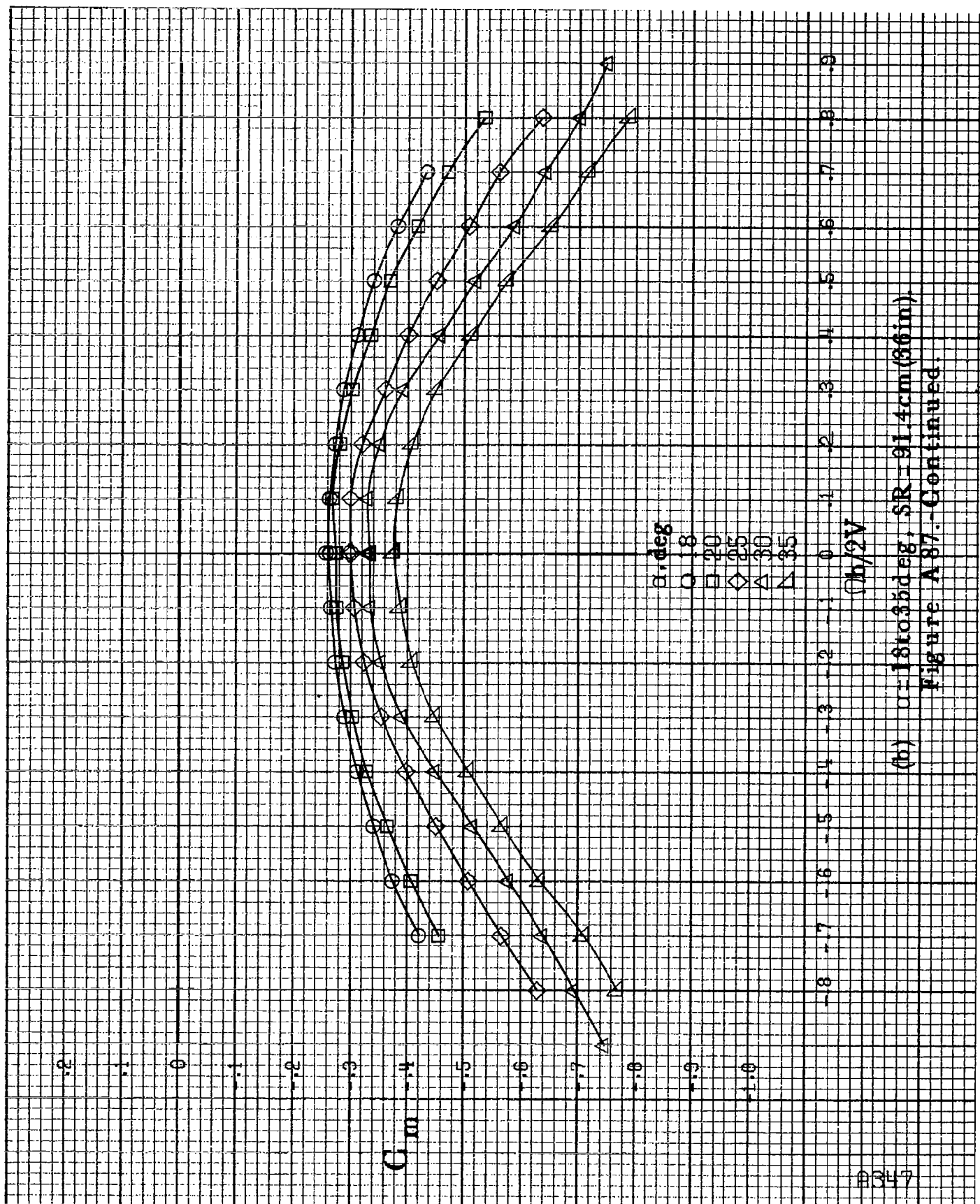


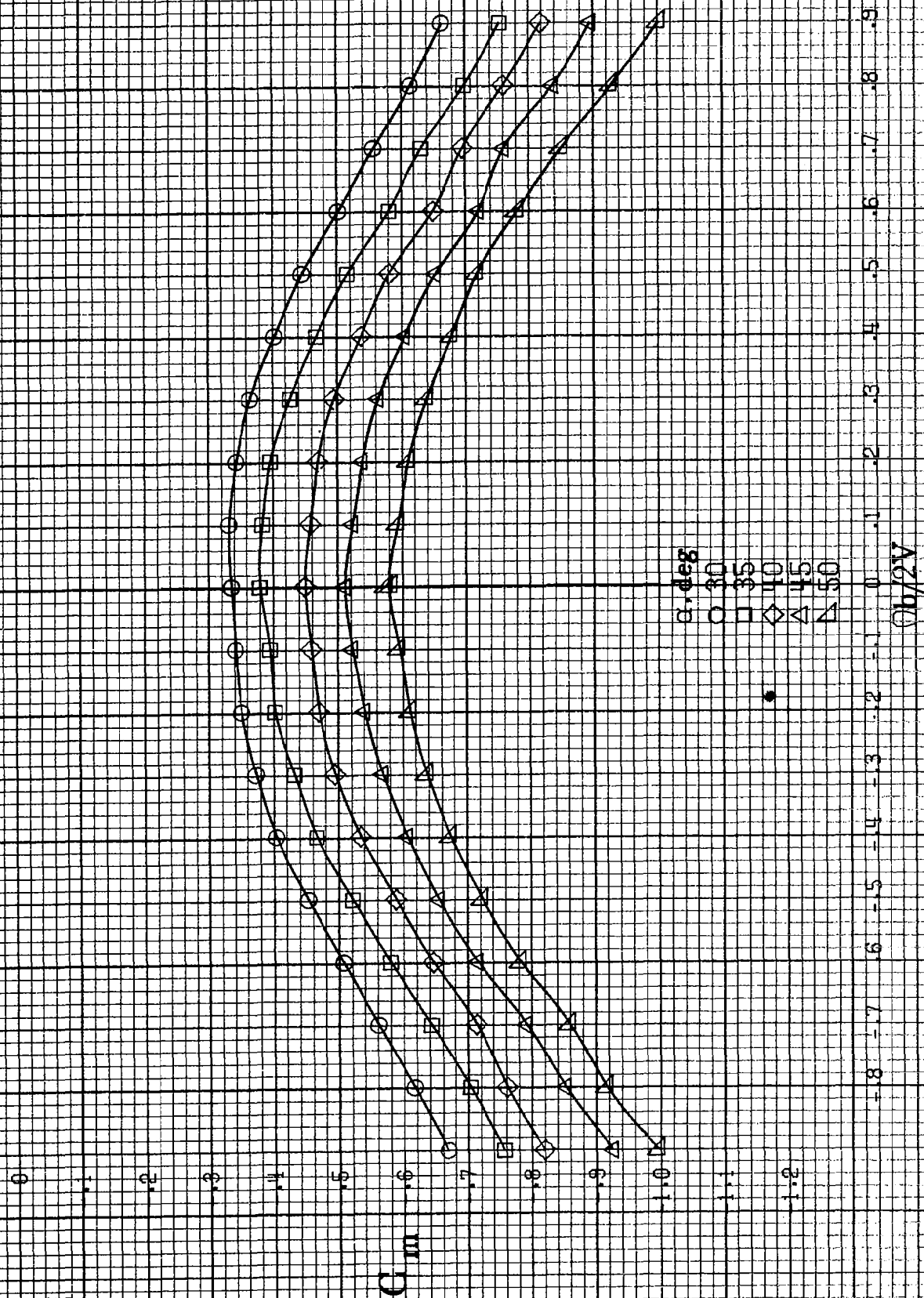
Figure A.87 - Effect of rotation rate and angle of attack on pitching-moment coefficient for long body, high wing, horizontal tail no. 2 configuration. $\delta_e = 0^\circ$, $\delta_a = 0^\circ$, $\delta_r = 0^\circ$. $\beta = 0^\circ$.



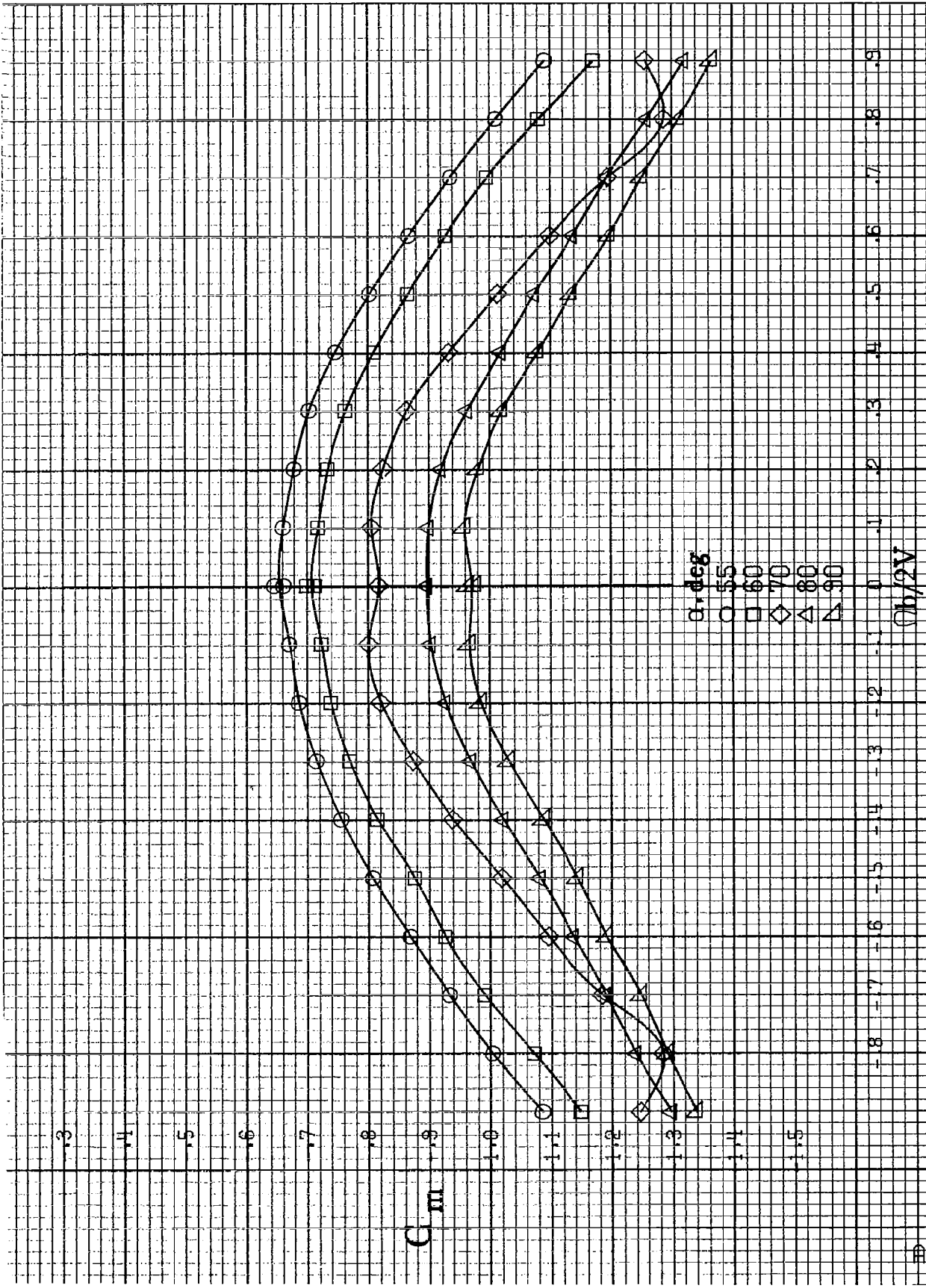
(b) $\alpha = 18$ to 35 deg, SR = 91.4 cm (36 in).

Figure A 87 - Continued.

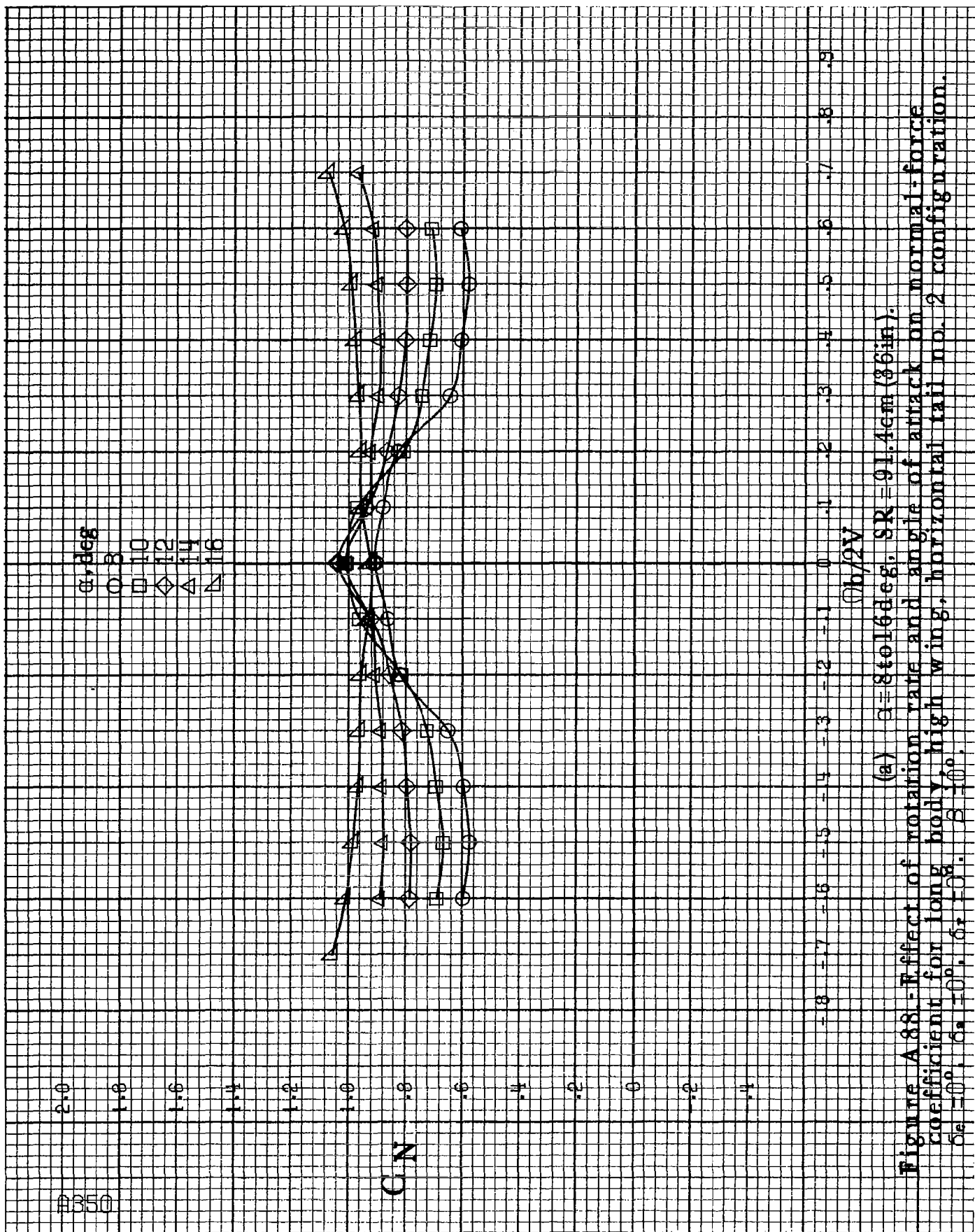
#346

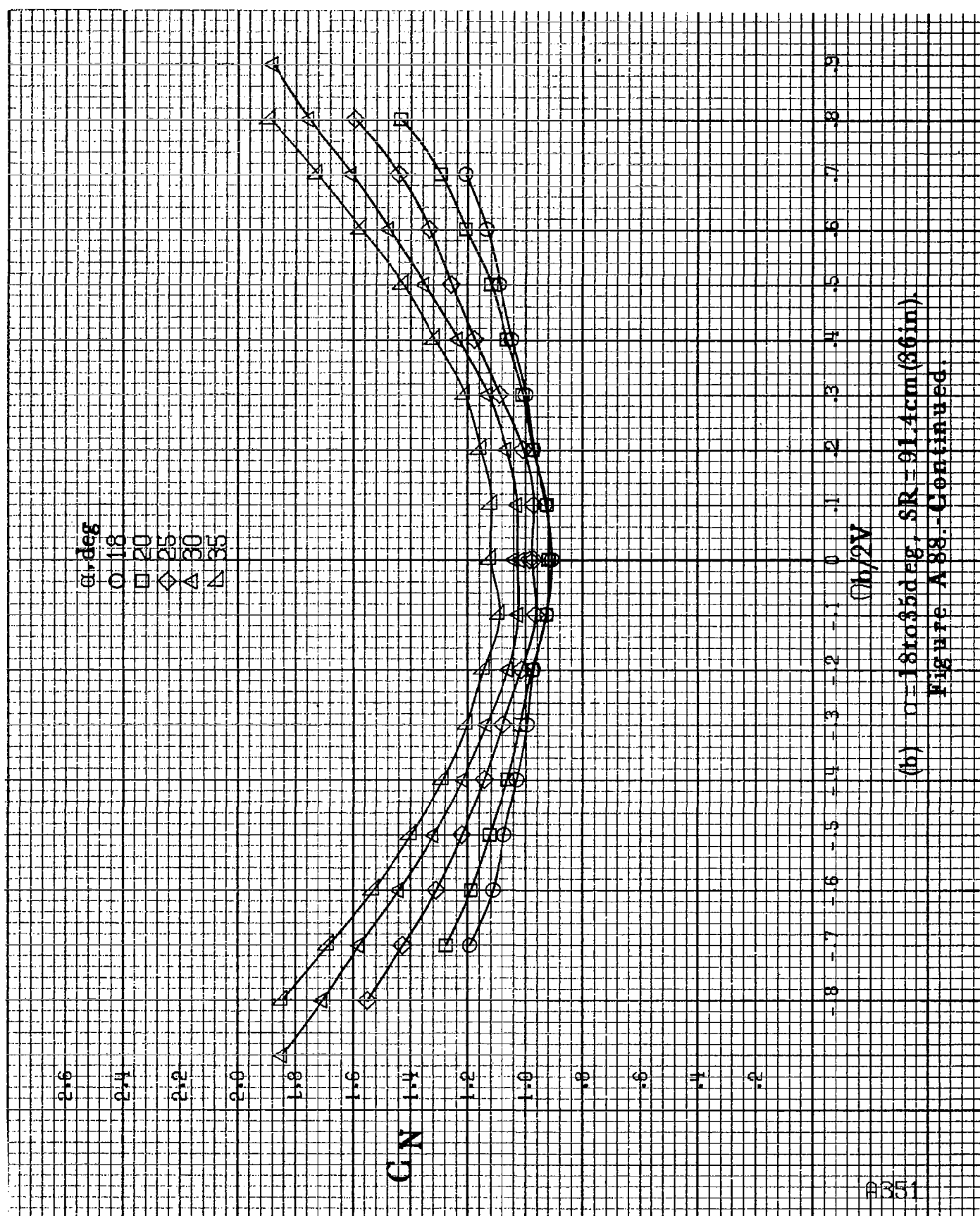


(c) $\alpha = 30$ to 50° , $SR = 0$.
Figure A87.-Continued.



(d) $\alpha = 55$ to 90° , $SR = 0$.
Figure A 87.-Concluded.





(b) $\alpha=18$ to 35 deg, $SR=91.4\text{cm}(36\text{in})$.

Figure A 88.-Continued.

#352

α , deg

○ 30

□ 35

◇ 40

△ 45

▽ 50

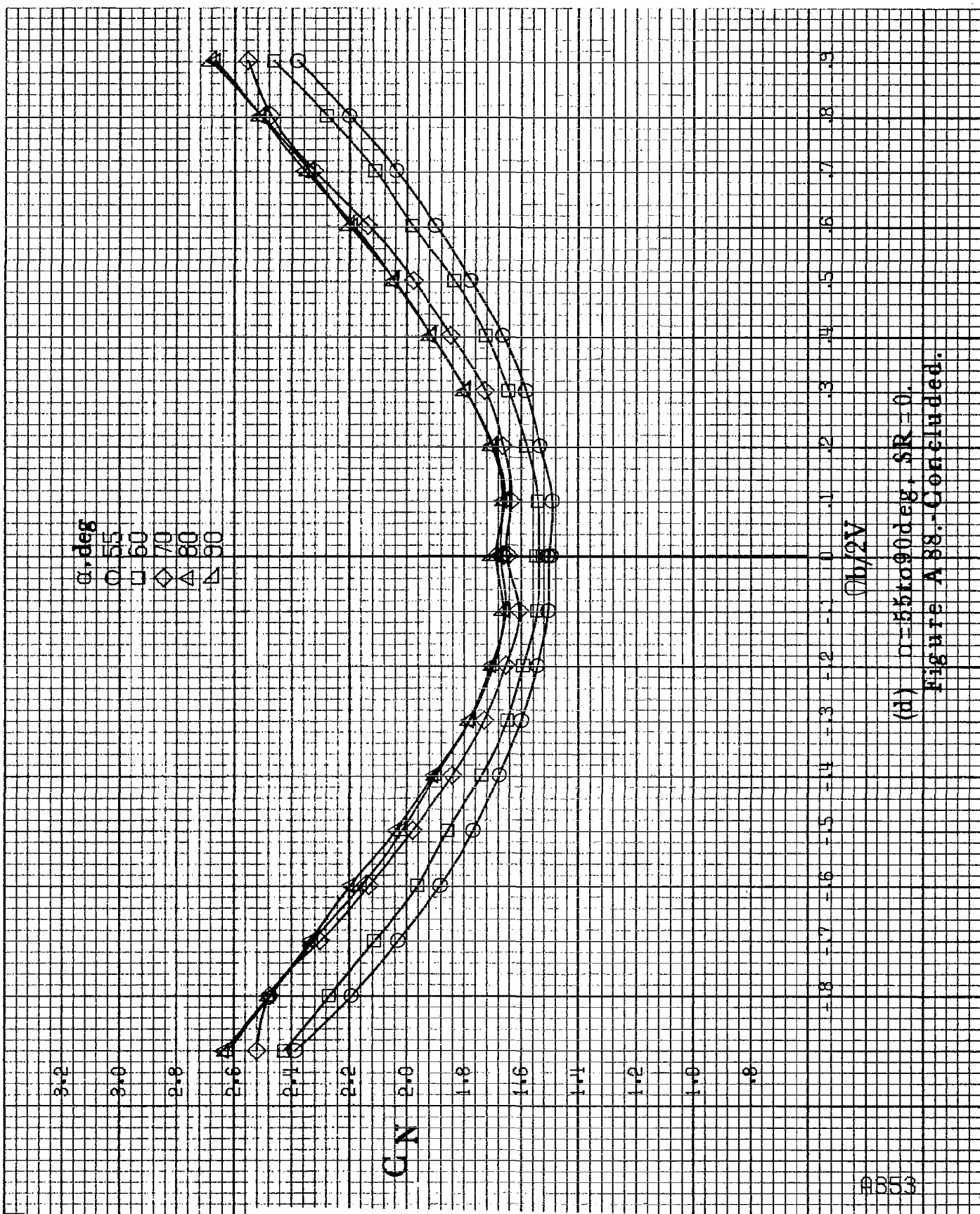
CN

$\Omega b/2V$

(c) $\Omega = 30$ to 50 deg, $SR = 0$.

Figure A 88.-Continued.



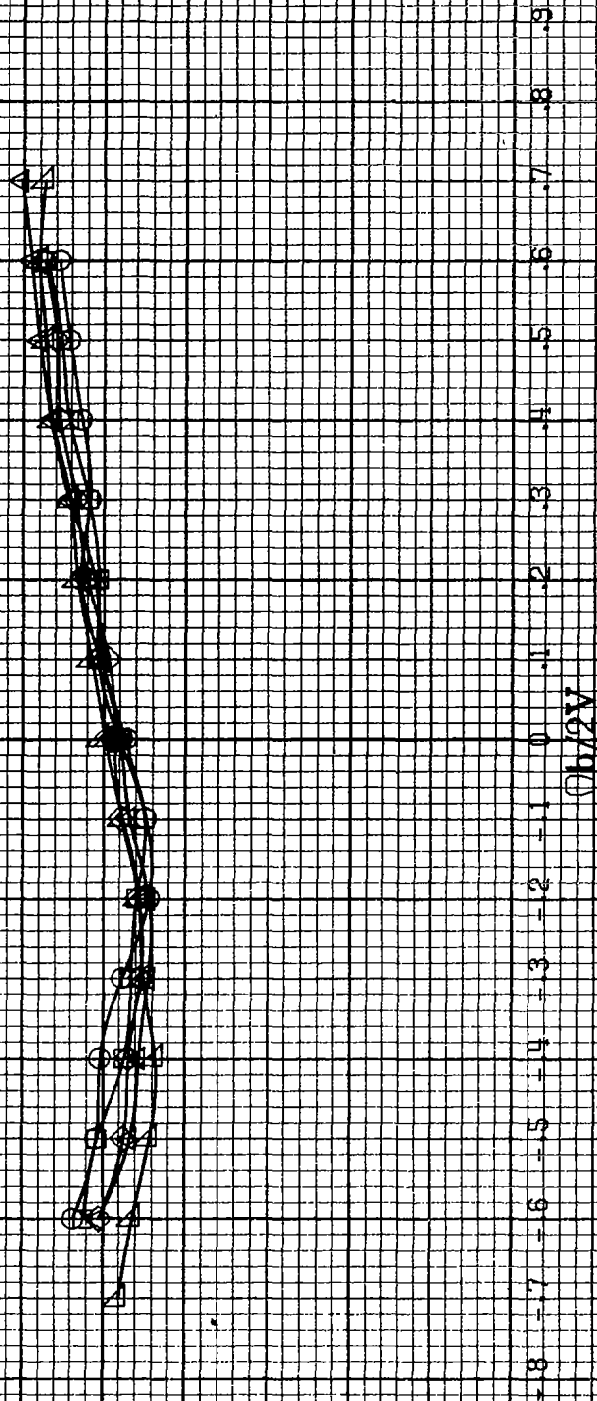


(d) $\alpha=55$ to 90° , $SR=0$.
Figure A 88.-Concluded.

A354

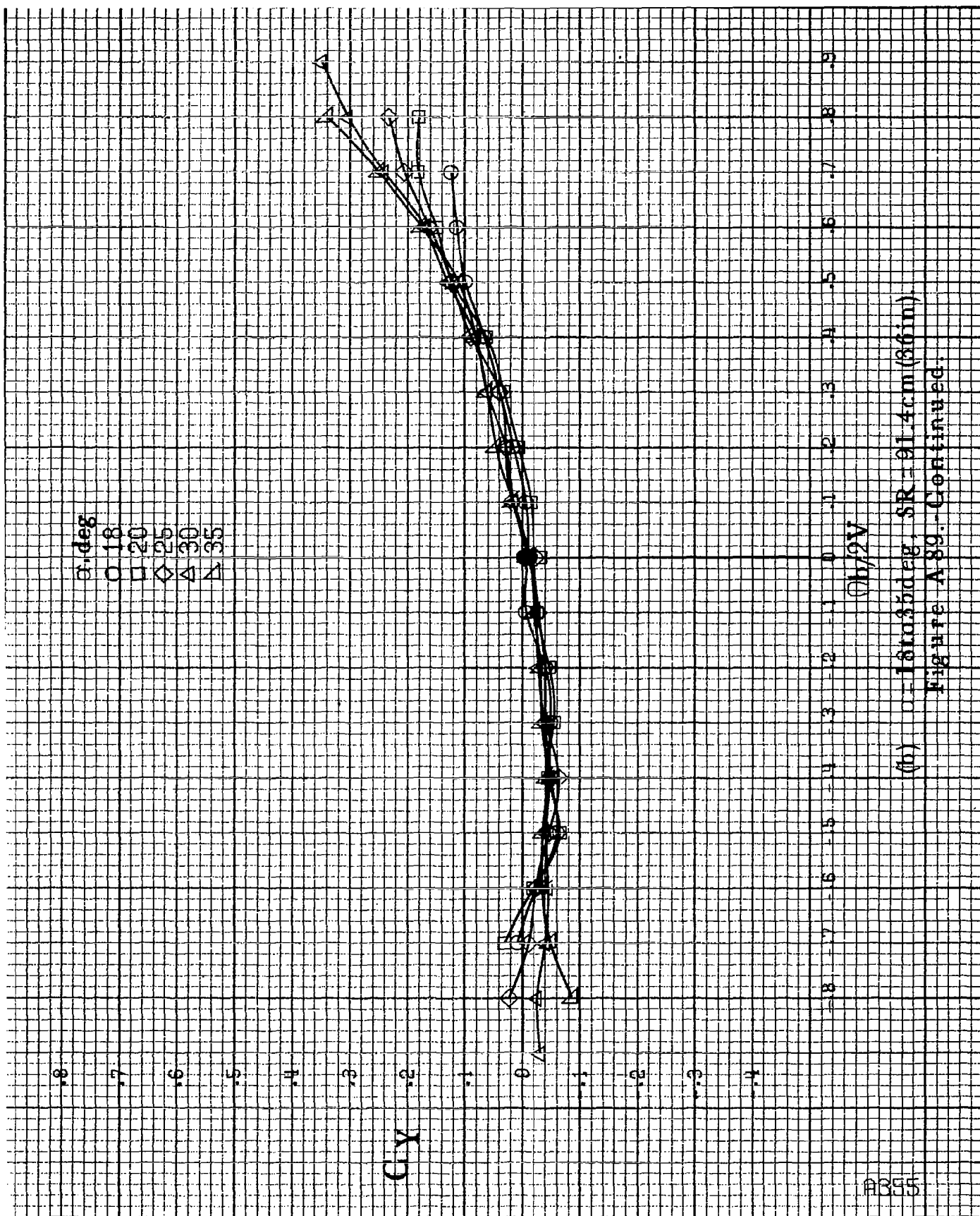
α -deg
 0 8
 1 10
 2 12
 4 14
 7 16

C_y



(a) $\alpha=8$ to 16 deg, $SR=91.4$ cm (36 in).

Figure A89.-Effect of rotation rate and angle of attack on side-force coefficient for long body, high wing, horizontal rail no. 2 configuration. $\delta_a=0^\circ$, $\delta_a=10^\circ$, $\delta_a=20^\circ$.



(b) $\alpha = 18$ to 35° , $SR = 91.4 \text{ cm (36 in.)}$.

Figure A89.-Continued.

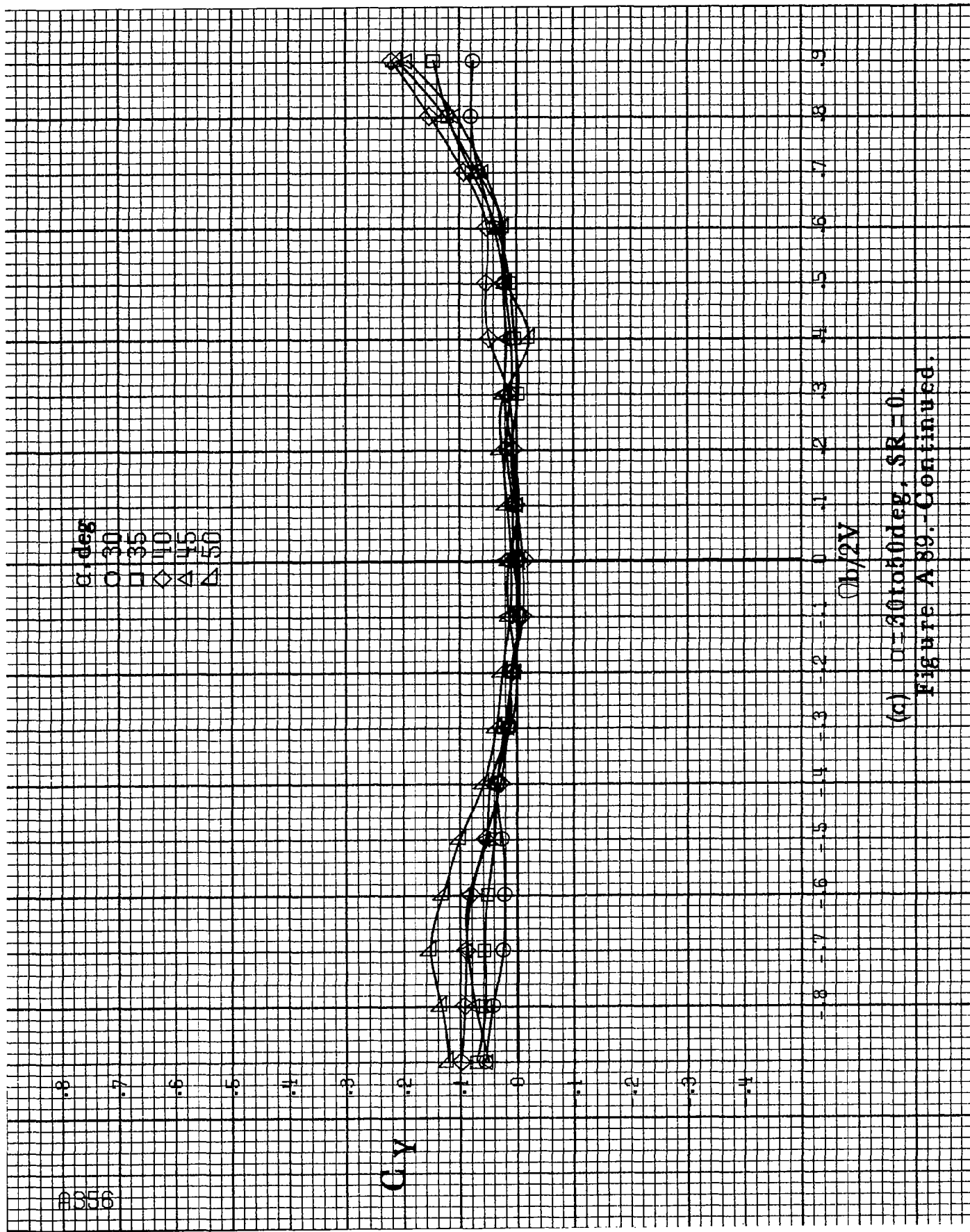
#356

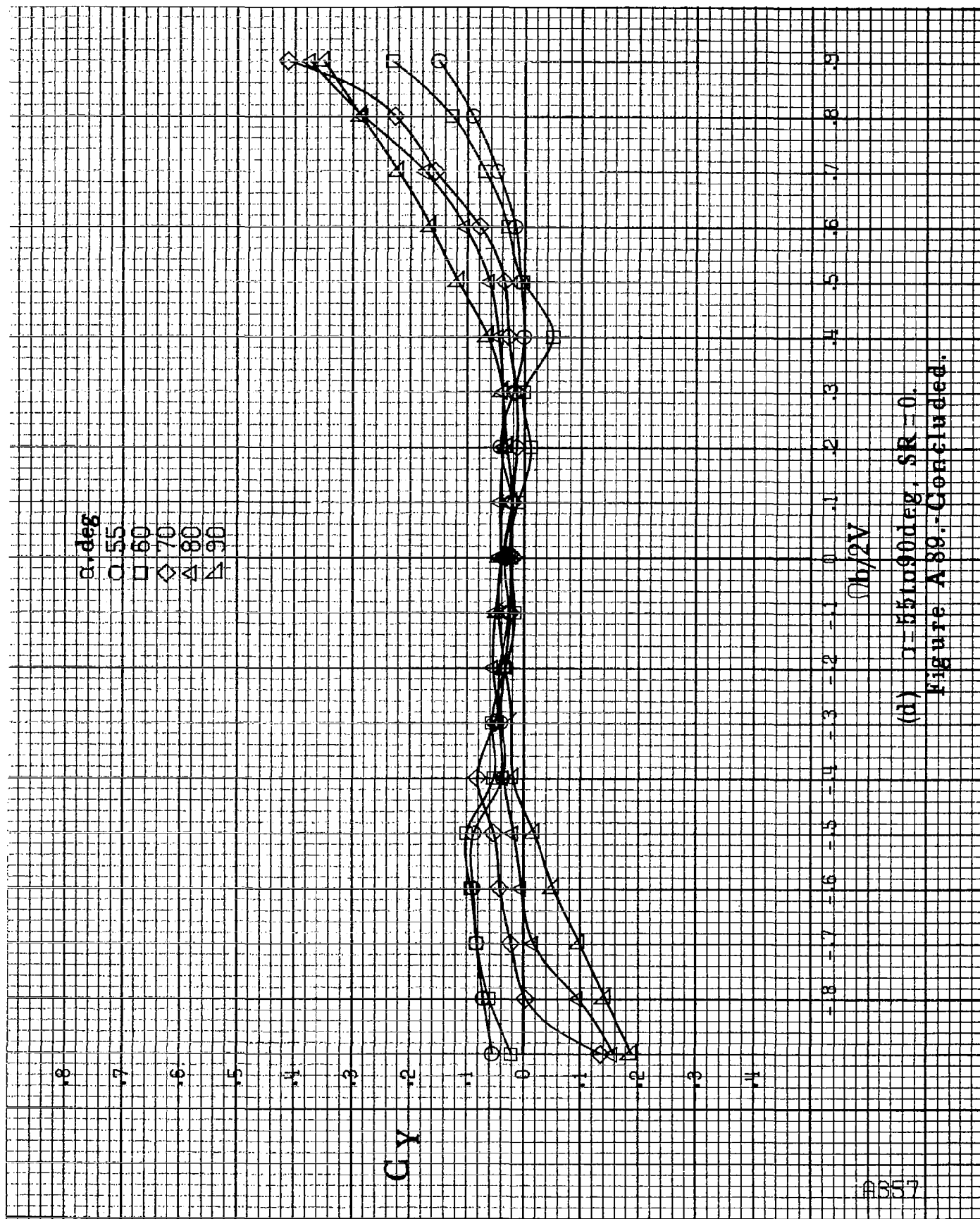
α, deg
 O 30
 □ 35
 ◇ 40
 △ 45
 ▽ 50

C_Y

$b/2V$

(a) $\alpha = 30 \text{ to } 50 \text{ deg}$, $SR = 0$.
 Figure A89. - Continued.



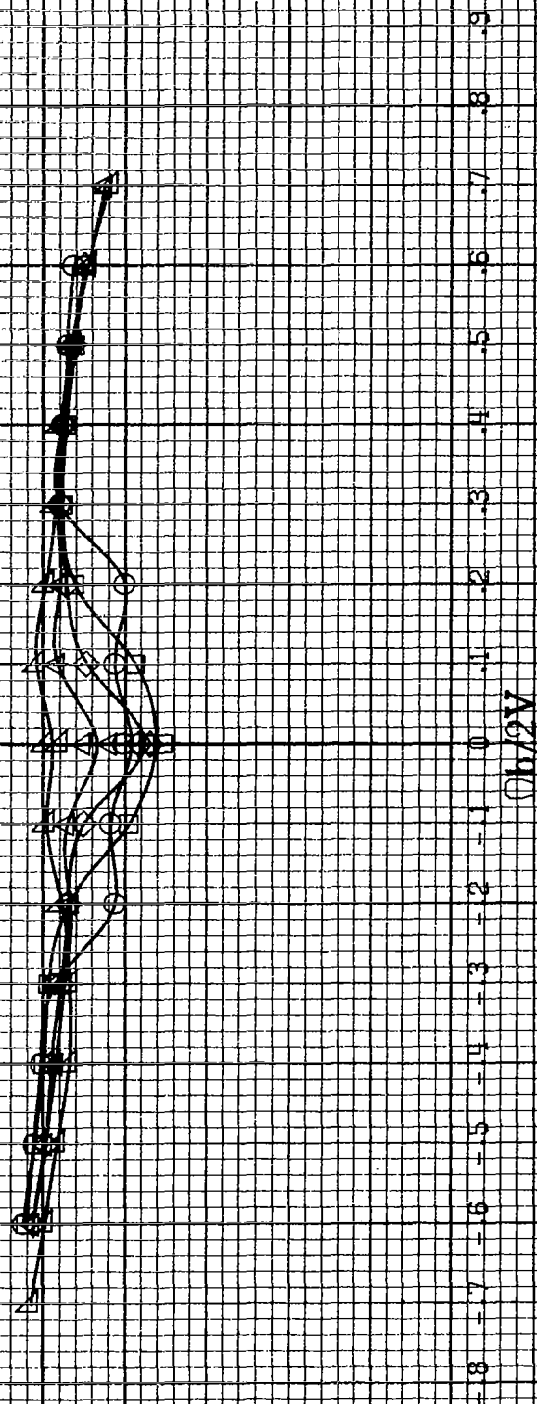


(d) $\alpha = 55$ to 90° , $SR = 0$.
Figure A89. - Concluded.

A358

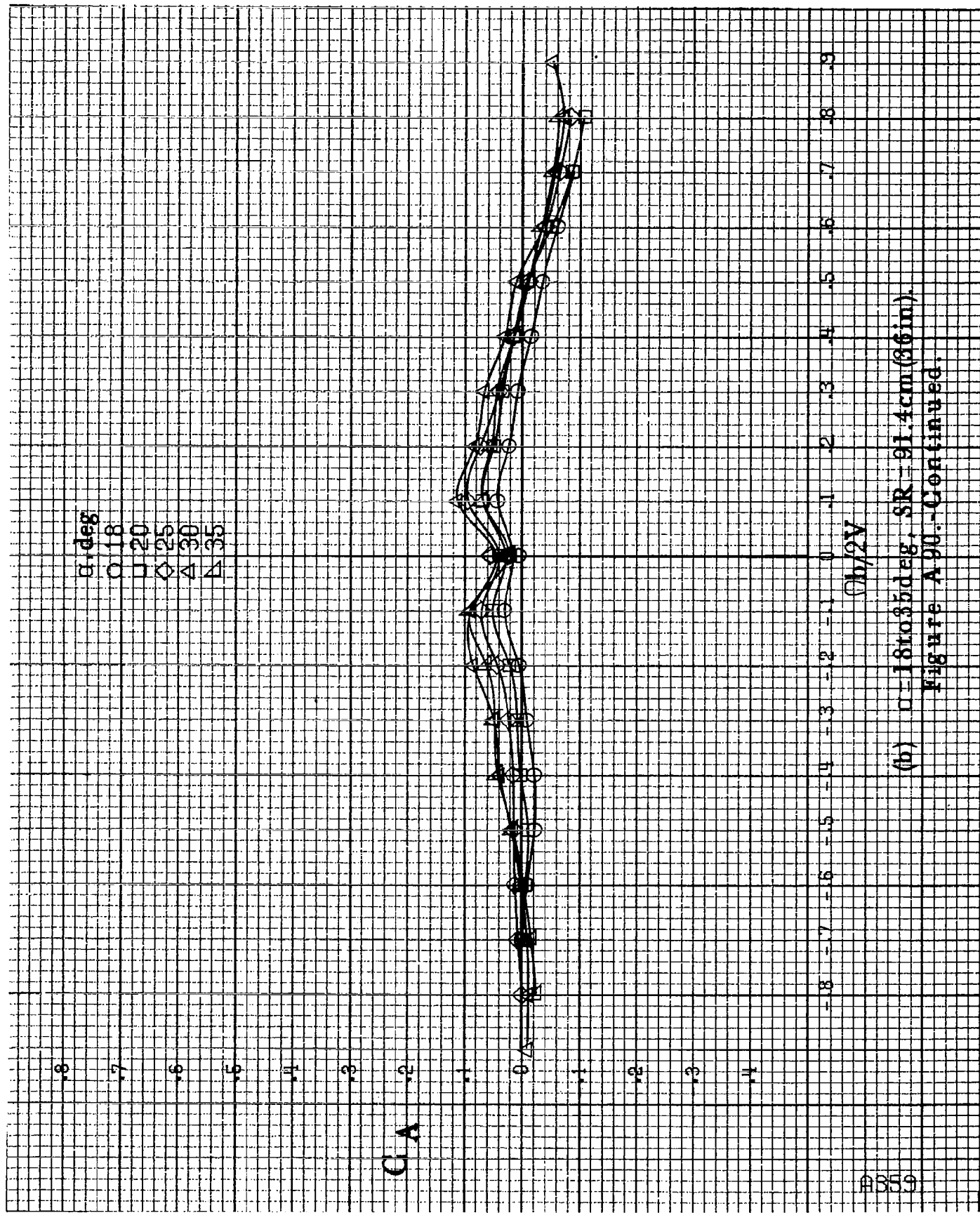
α, deg
 O 8
 □ 10
 ◇ 12
 △ 14
 ▽ 16

C_LA



(a) $\alpha = 8$ to 16° , $SR = 91.4 \text{ cm (36 in)}$.

Figure A.90.-Effect of notation rate and angle of attack on axial-force coefficient for long body, high wing, horizontal tail no. 2 configuration. $\delta_a = 0^\circ$, $\delta_w = 0^\circ$, $\delta_r = 0^\circ$.



(b) $\alpha = 18$ to 35° , $SR = 91.4 \text{ cm (36 in.)}$.
Figure A 90.-Continued.

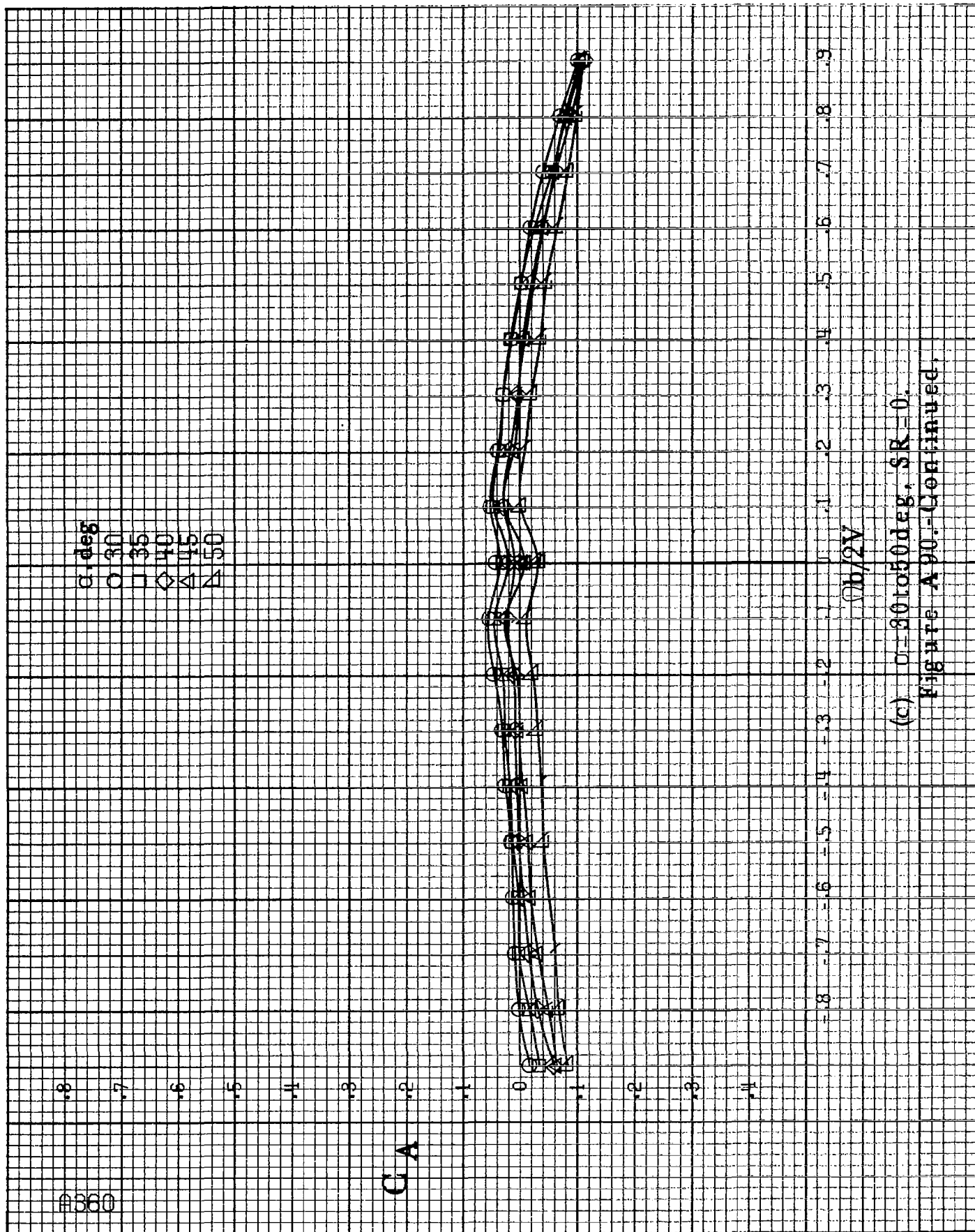
#360

α, deg
 O 30
 □ 35
 ◇ 40
 △ 45
 ▲ 50

CA

$V_b/2V$

(c) $\theta = 30$ to 50 deg, $SR = 0$.
 Figure A90.-Continued.



α, deg
 ○ 55
 □ 60
 ◇ 70
 △ 80
 ▽ 90

CA



0.1 0.2 0.3 0.4 0.5 0.6 0.7 0.8 0.9

$\phi b/2V$

(d) $\alpha = 55 \text{ to } 90 \text{ deg}, SR = 0$.
 Figure A 90.-Concluded.

α , deg

○ 8
 □ 10
 ◇ 12
 △ 14
 ▽ 16

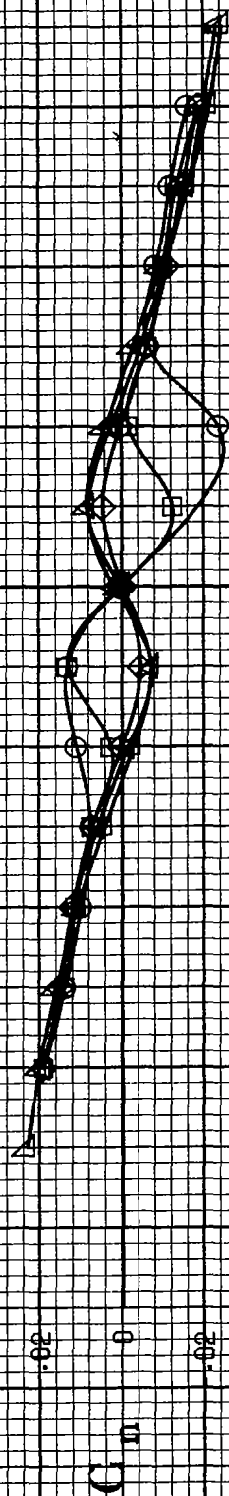
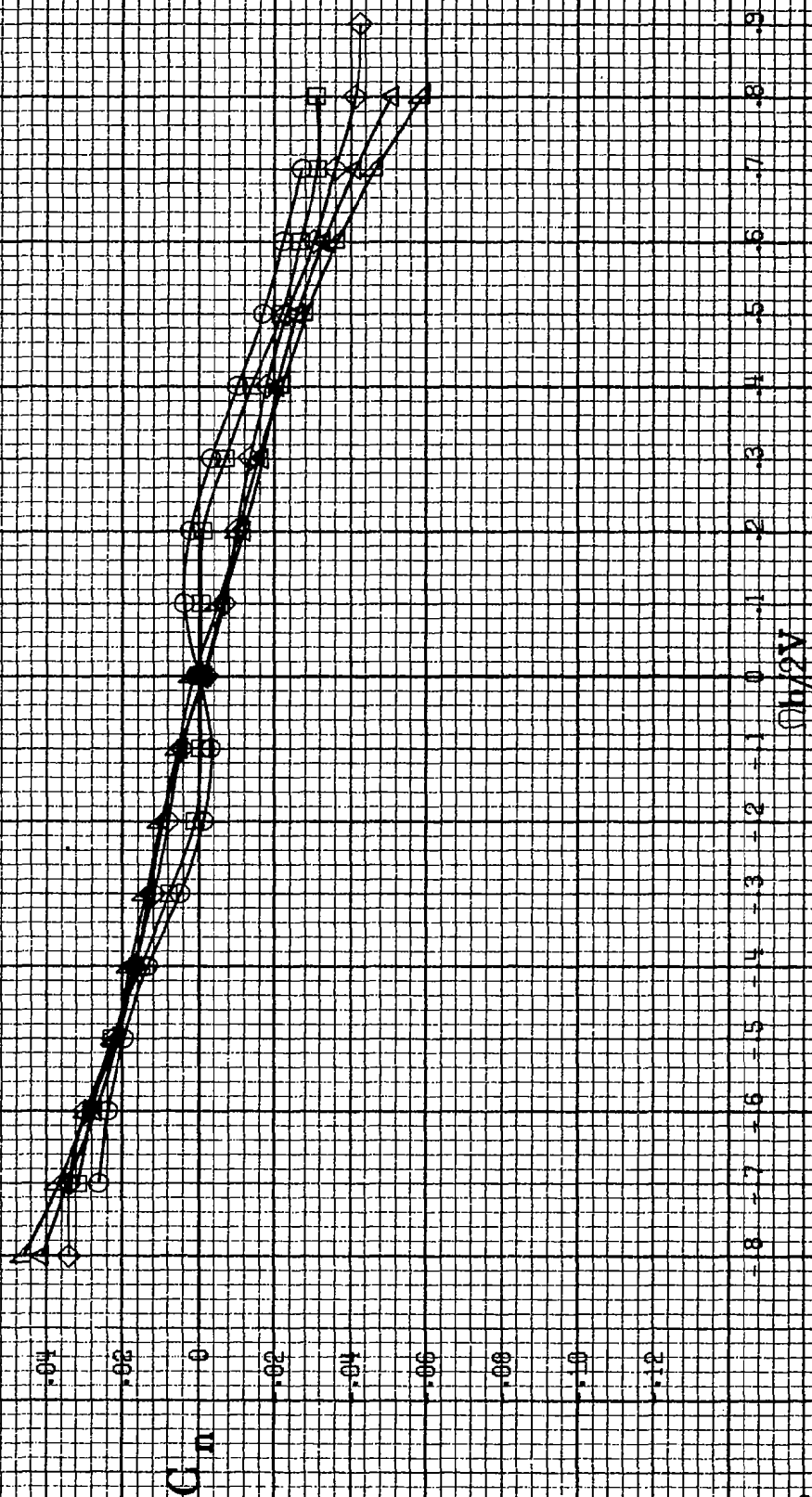
 $Qh/2V$ (a) $\alpha = 8$ to 16 deg, $SR = 91.4$ cm (36 in).

Figure A91.-Effect of notation rate and angle of attack on yawing-moment coefficient for long tail, high wing, horizontal tail location no. 3. $\delta\alpha = 0^\circ$, $\delta\tau = 0^\circ$, $\beta = 0^\circ$.

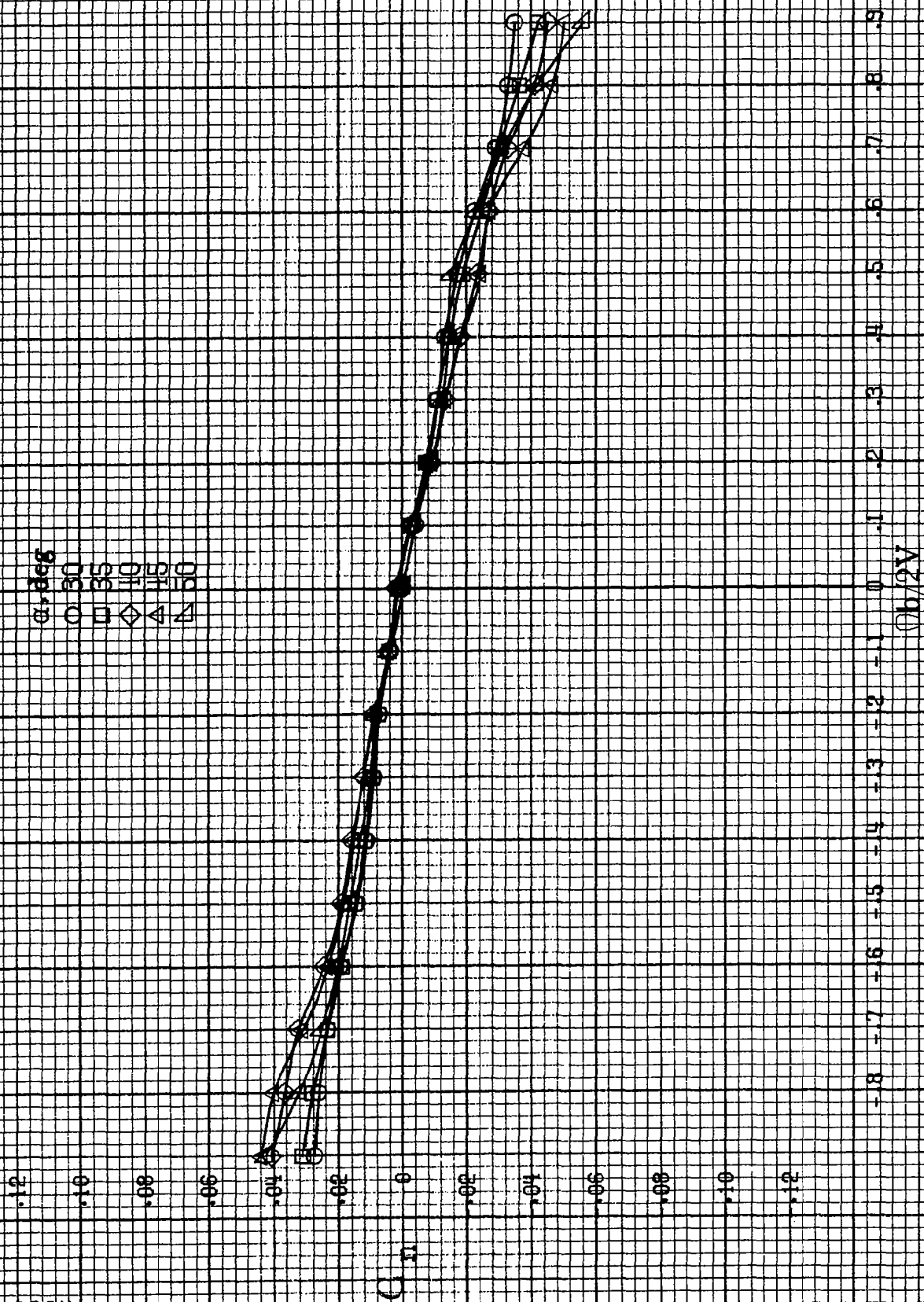
α , deg
 ○ 18
 □ 20
 ◇ 25
 △ 30
 ▽ 35



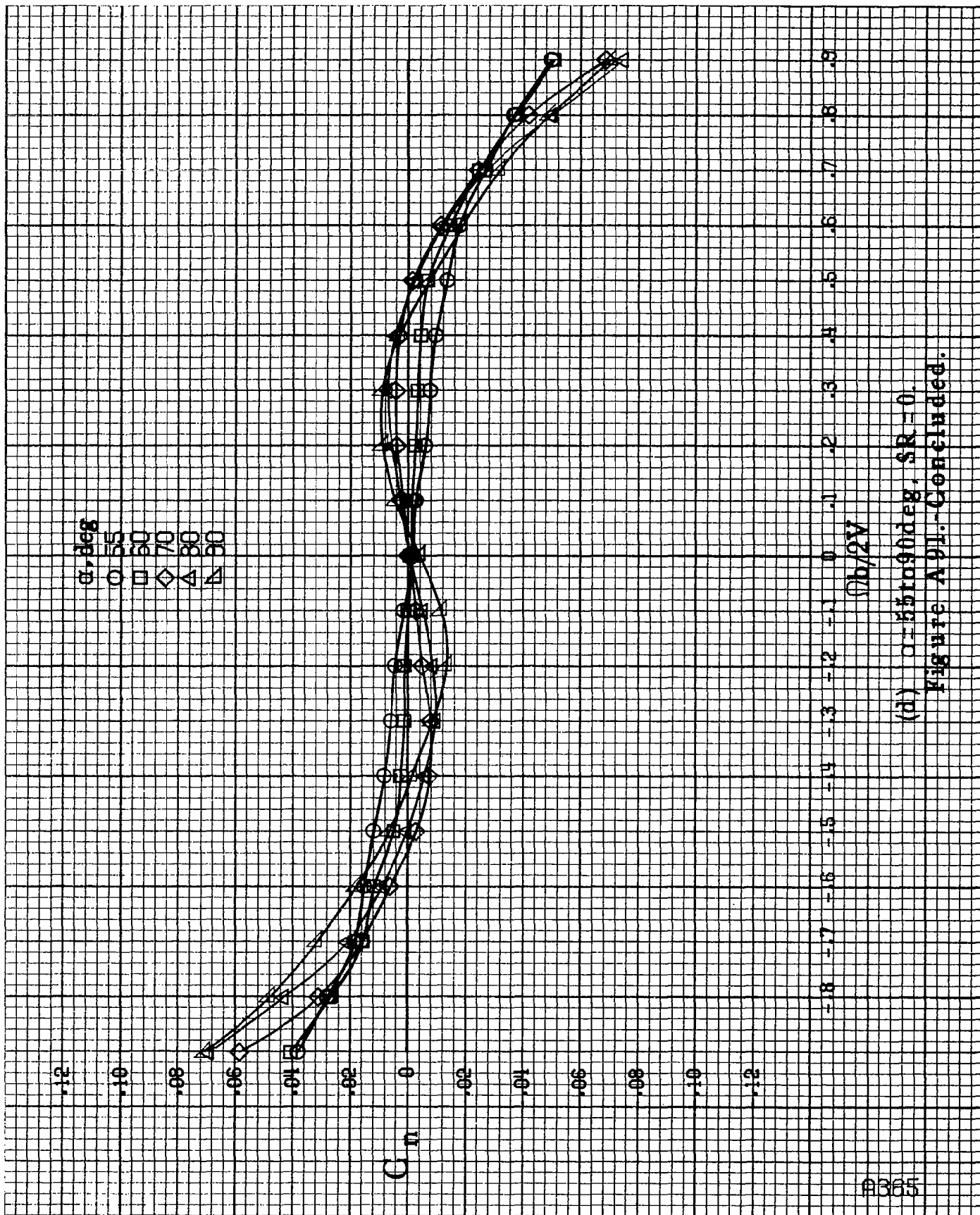
(b) $\alpha = 18$ to 35 deg, $SR = 21.4$ cm (8.6 in).

Figure A91.-Continued.

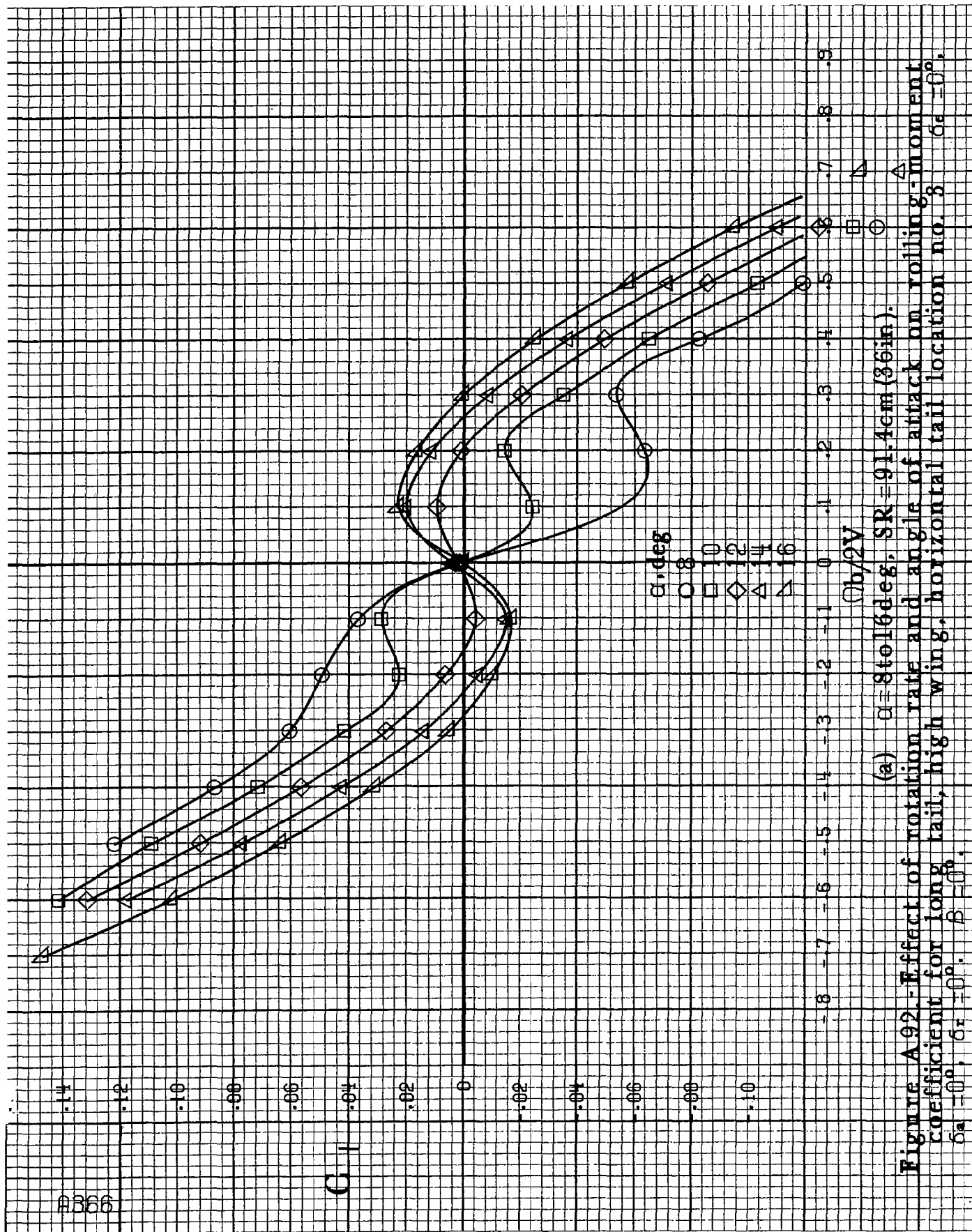
8364



(c) $\alpha=30$ to 50° , $SR=0$.
Figure A91.-Continued.

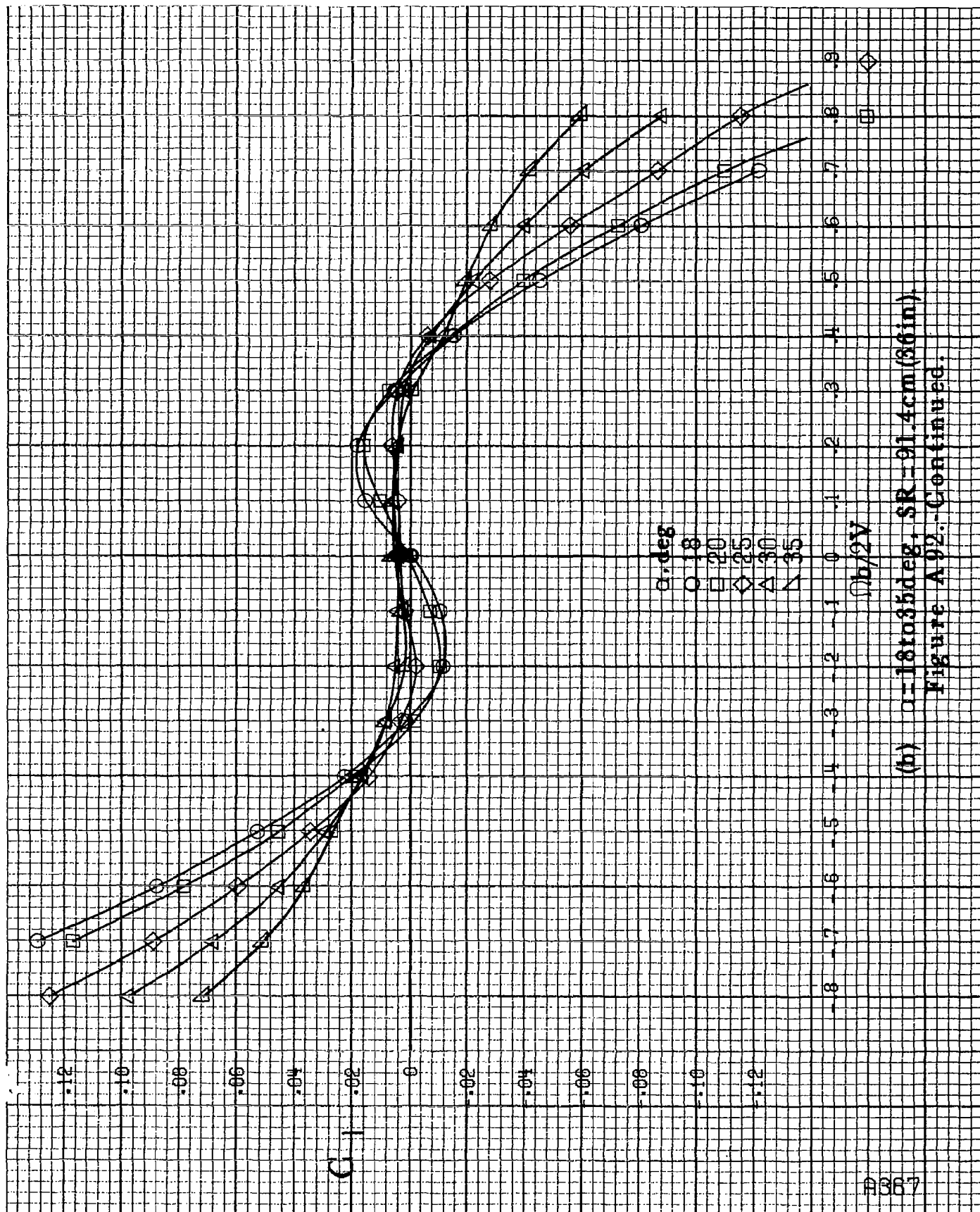


(d) $\alpha = 55$ to 90° , $SR = 0$.
Figure A91.-Concluded.



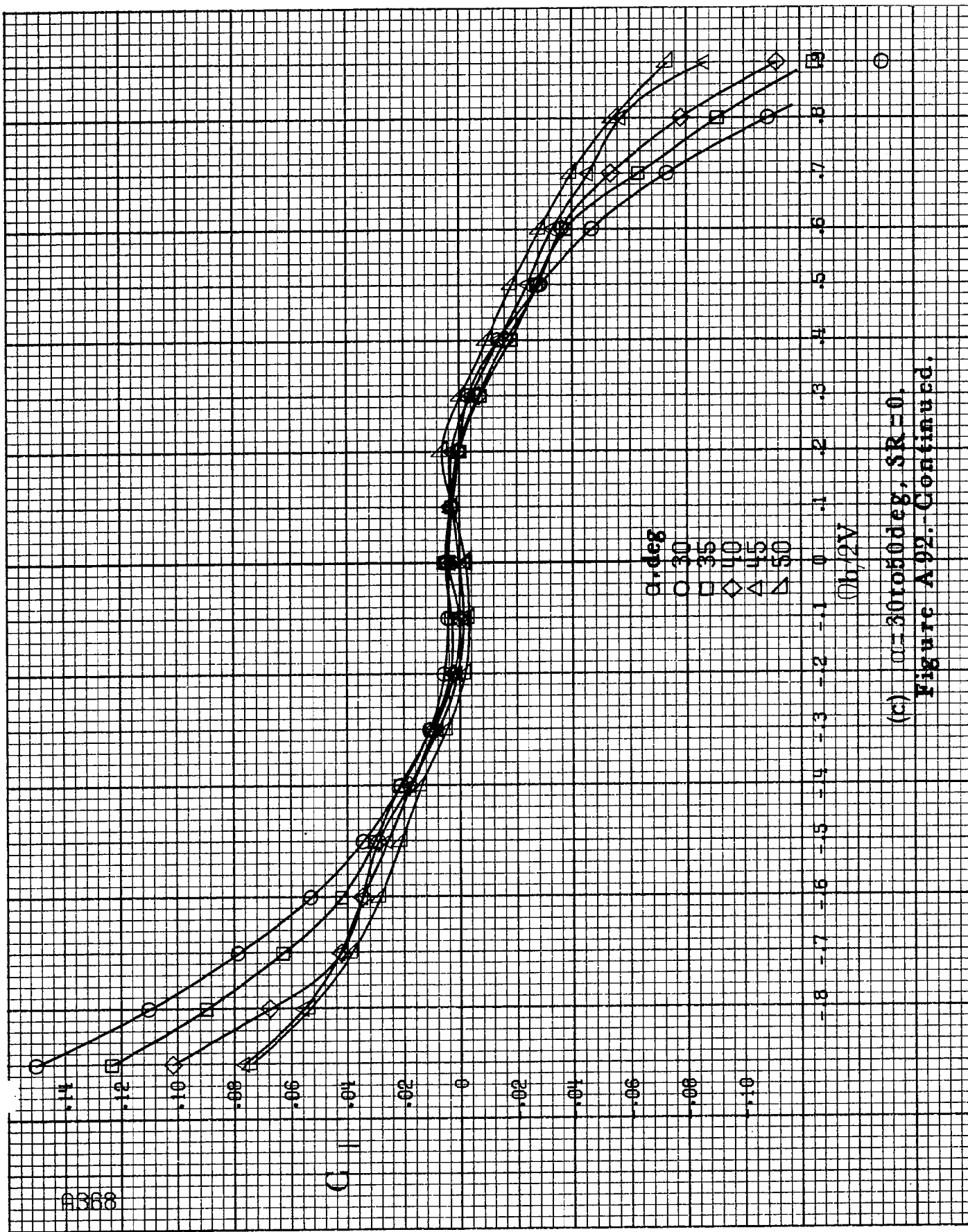
(a) $\alpha=8$ to 16° , $SR=91.4\text{cm}$ (36in).

Figure A92.-Effect of rotation rate and angle of attack on rolling-moment coefficient for long tail, high wing, horizontal tail location no. 3. $\delta_a=0^\circ$, $\delta_r=0^\circ$, $\beta=0^\circ$.

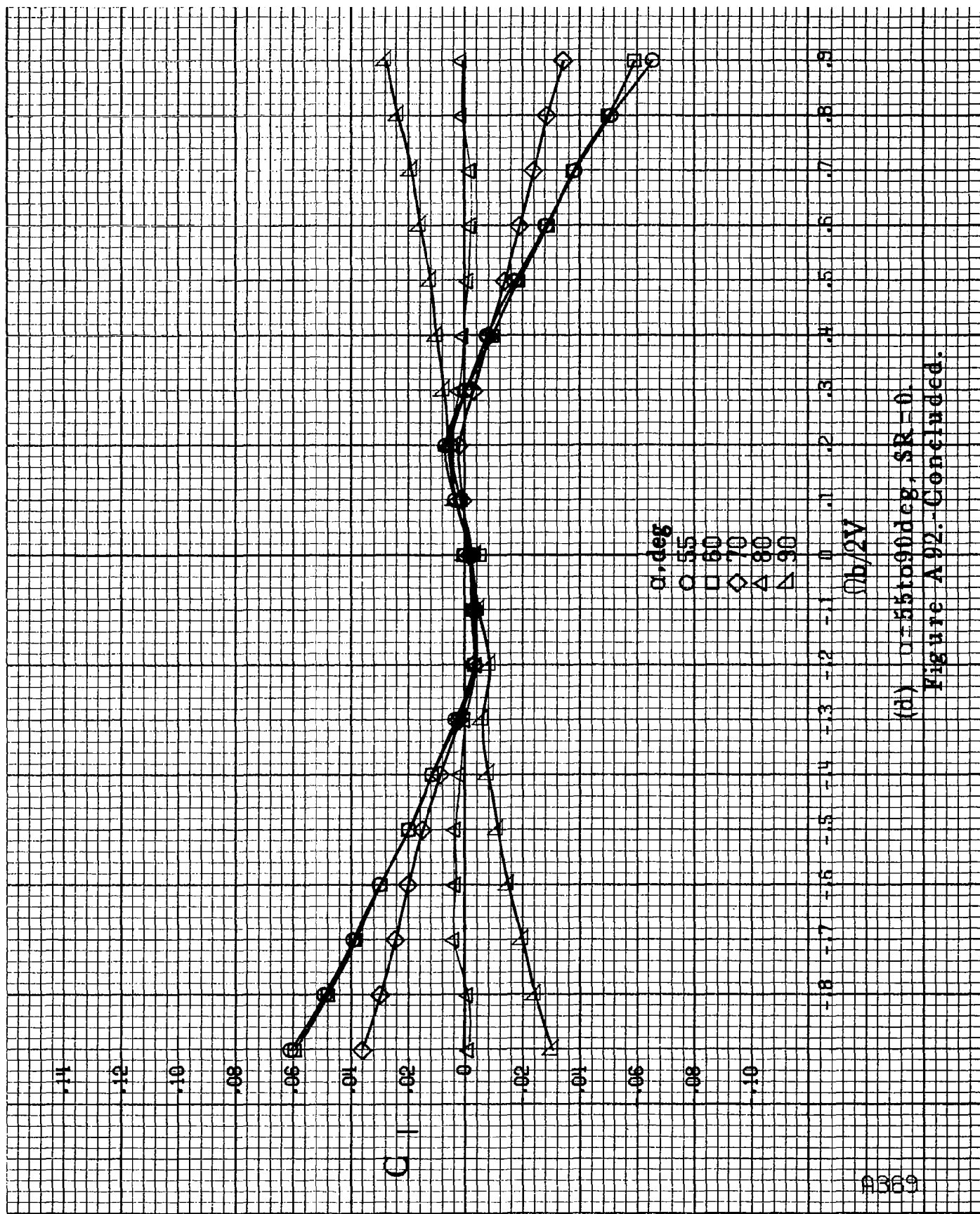


(b) $\alpha=18$ to 35 deg, $SR=91.4\text{cm}(36\text{in})$.

Figure A92.-Continued.



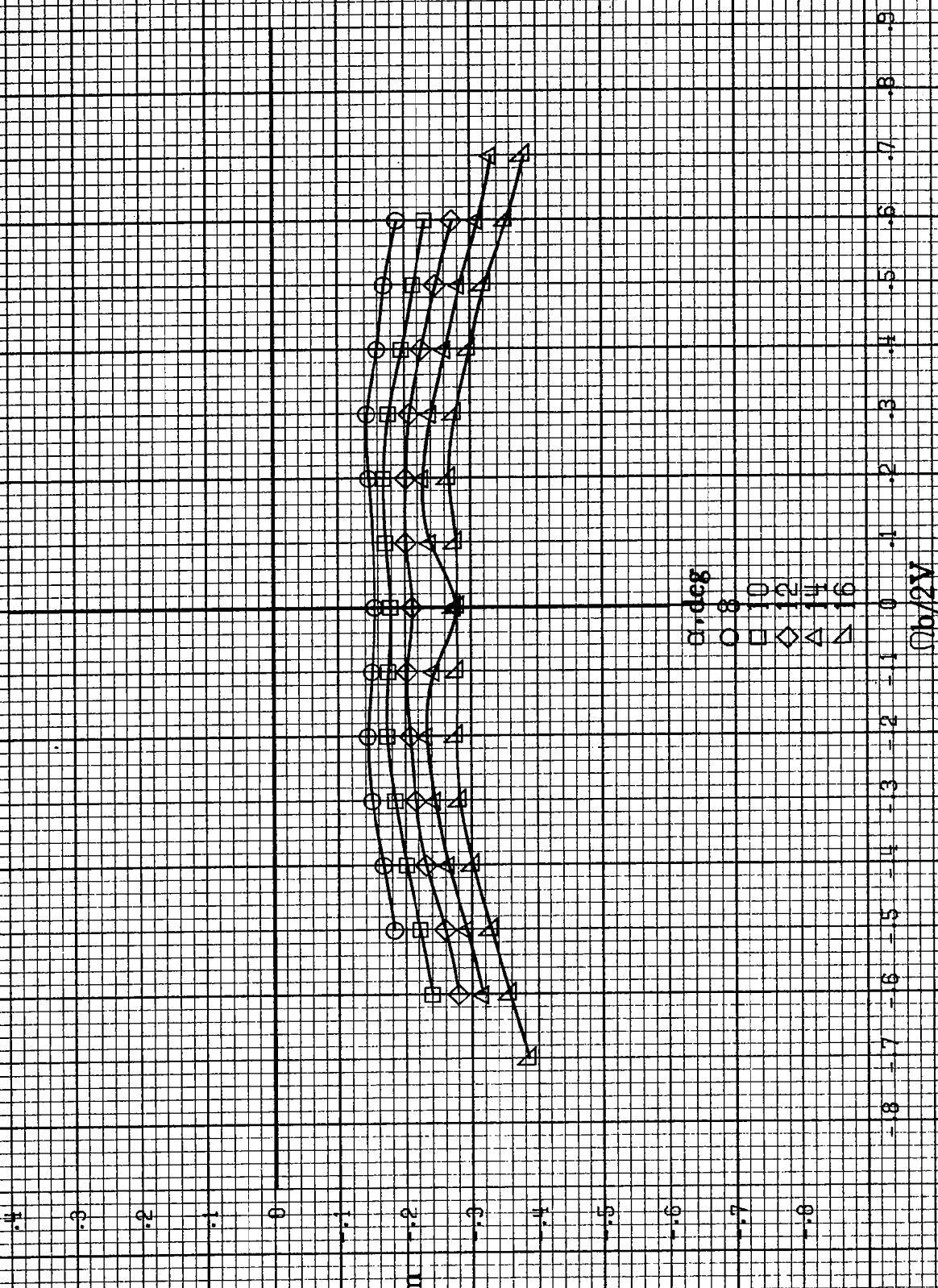
(c) $\omega=30$ to 50 deg, $SR=0$.
Figure A92. Continued.



(d) $\alpha=55$ to 90 deg, $SR=0$.
Figure A 92.-Concluded.

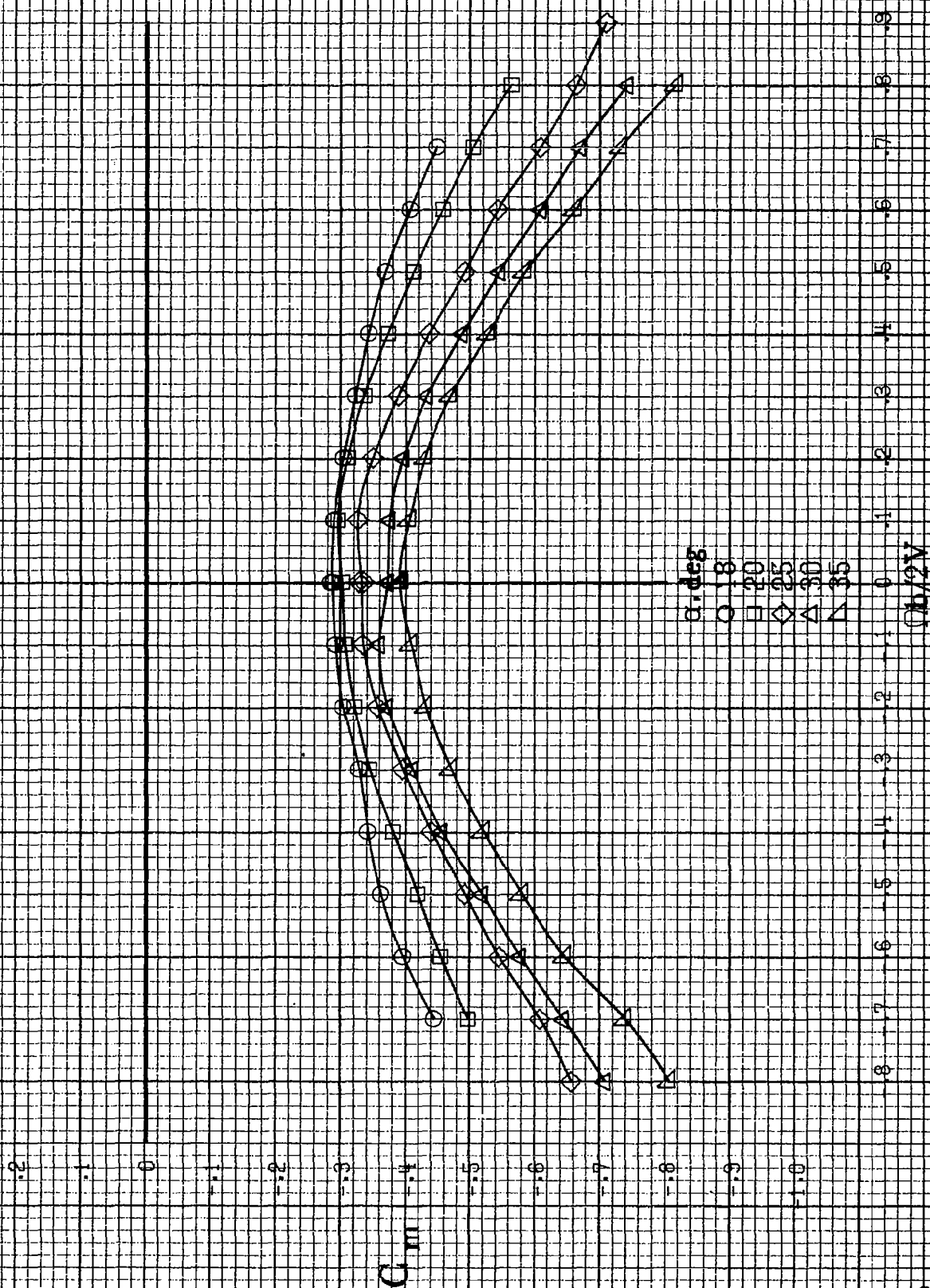
#370

C_m



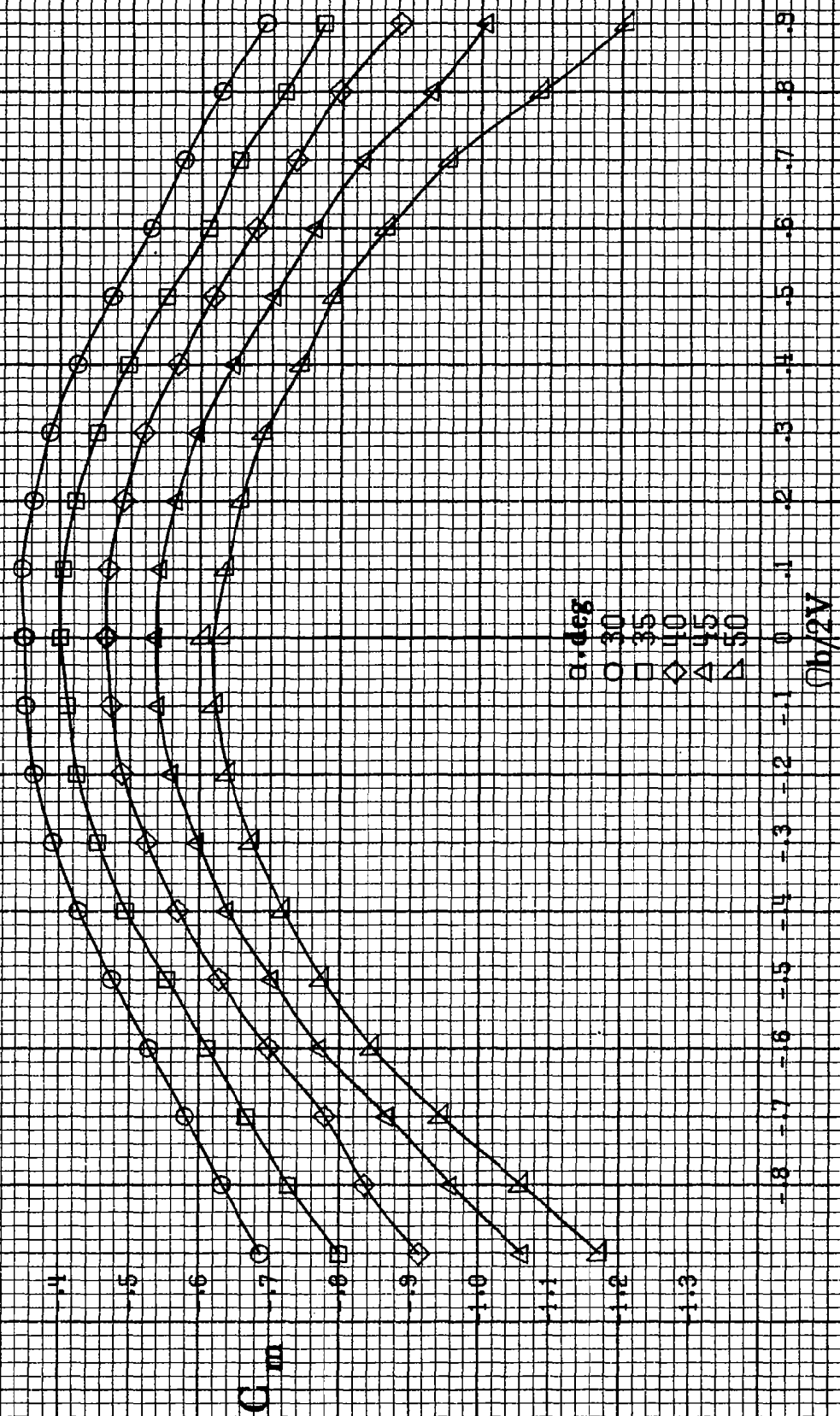
(a) $\alpha = 8$ to 16 deg, $SR = 91.4$ cm (36 in).

Figure A93.-Effect of rotation rate and angle of attack on pitching-moment coefficient for long tail, high wing, horizontal tail location no. 3. $\delta_a = 0^\circ$, $\delta_r = 0^\circ$, $\beta = 0^\circ$.

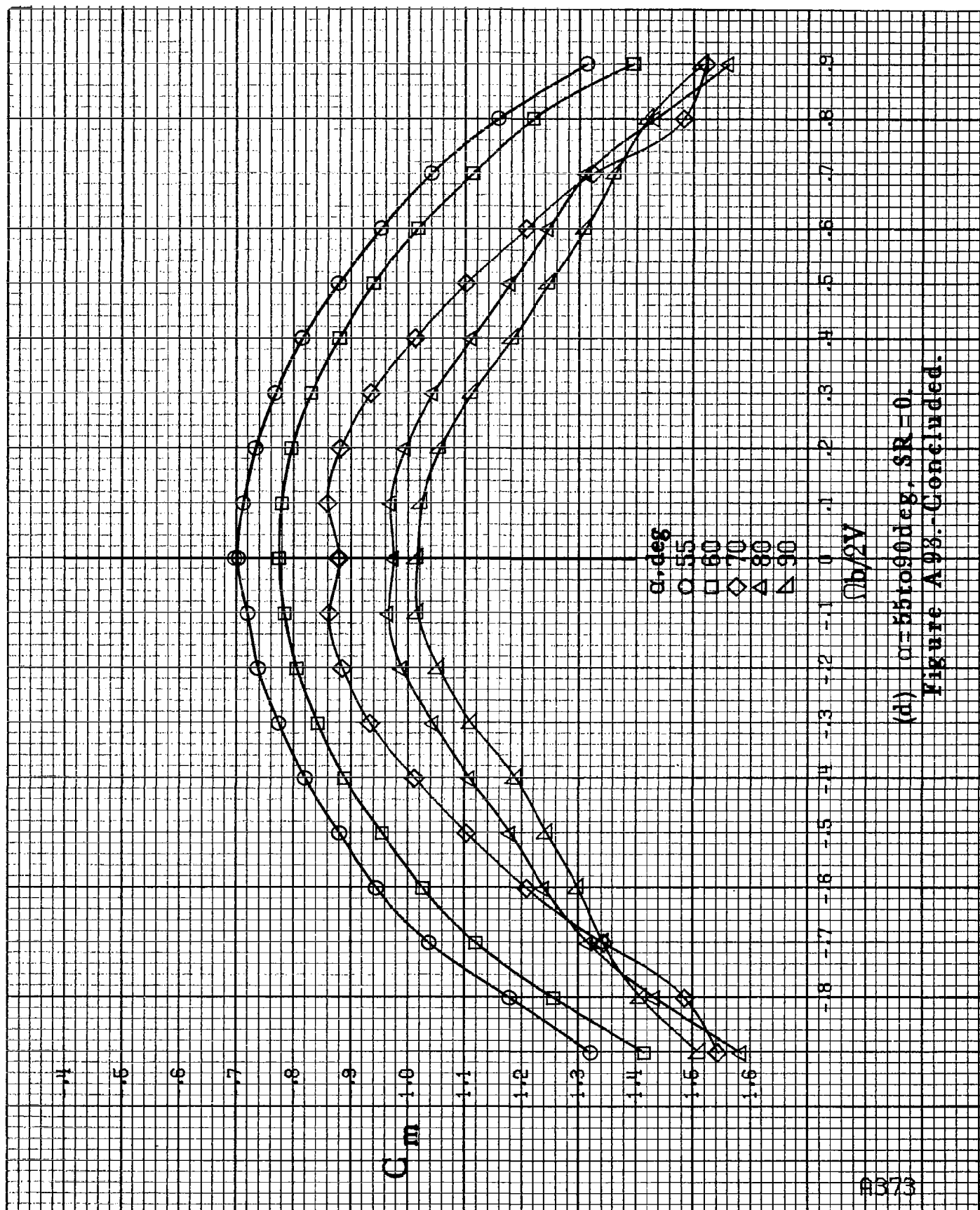


(b) $\alpha = 18$ to 35 deg, SR = 91.4 cm (36 in).
Figure A98. Continued.

#372



(a) $\alpha = 30$ to 50° , $SR = 0$.
Figure A 93.-Continued.



(d) $\alpha = 55$ to 90° , $SR = 0$.
Figure A93.-Concluded.

8374

α , deg

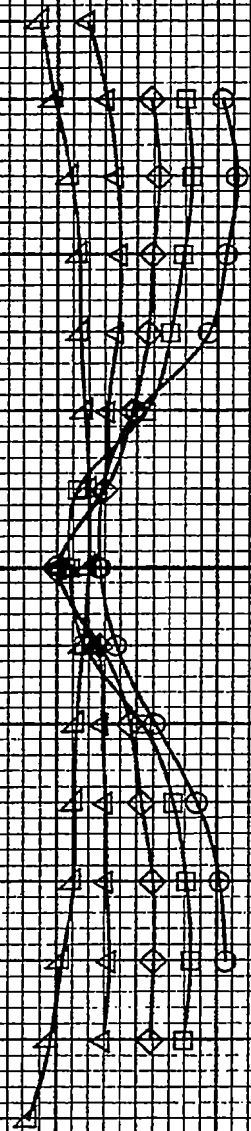
3
10
12
14
16

C_N

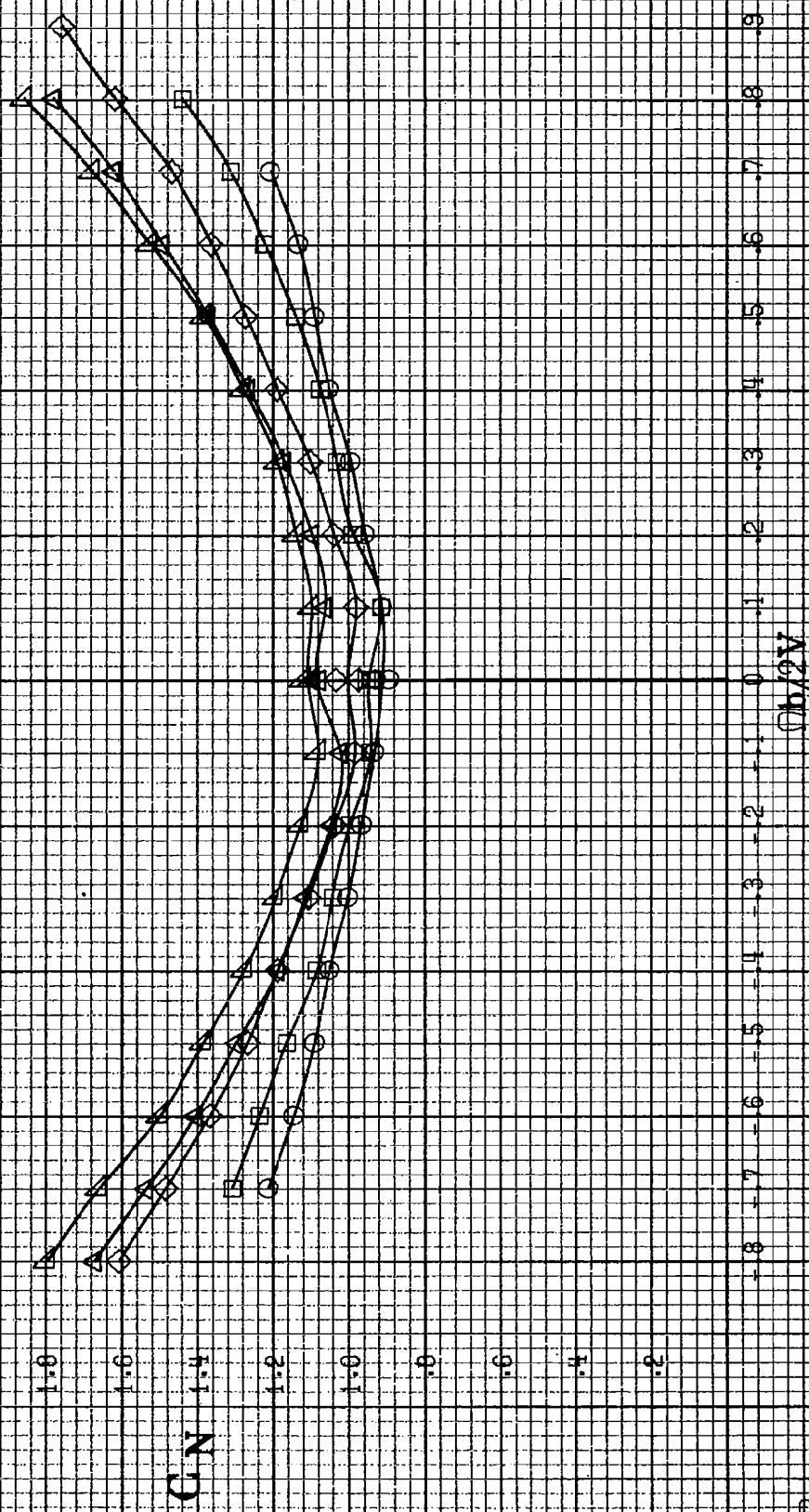
$Ch/2V$

(a) $\alpha = 8$ to 16 deg, $SR = 91.4$ cm (36 in).

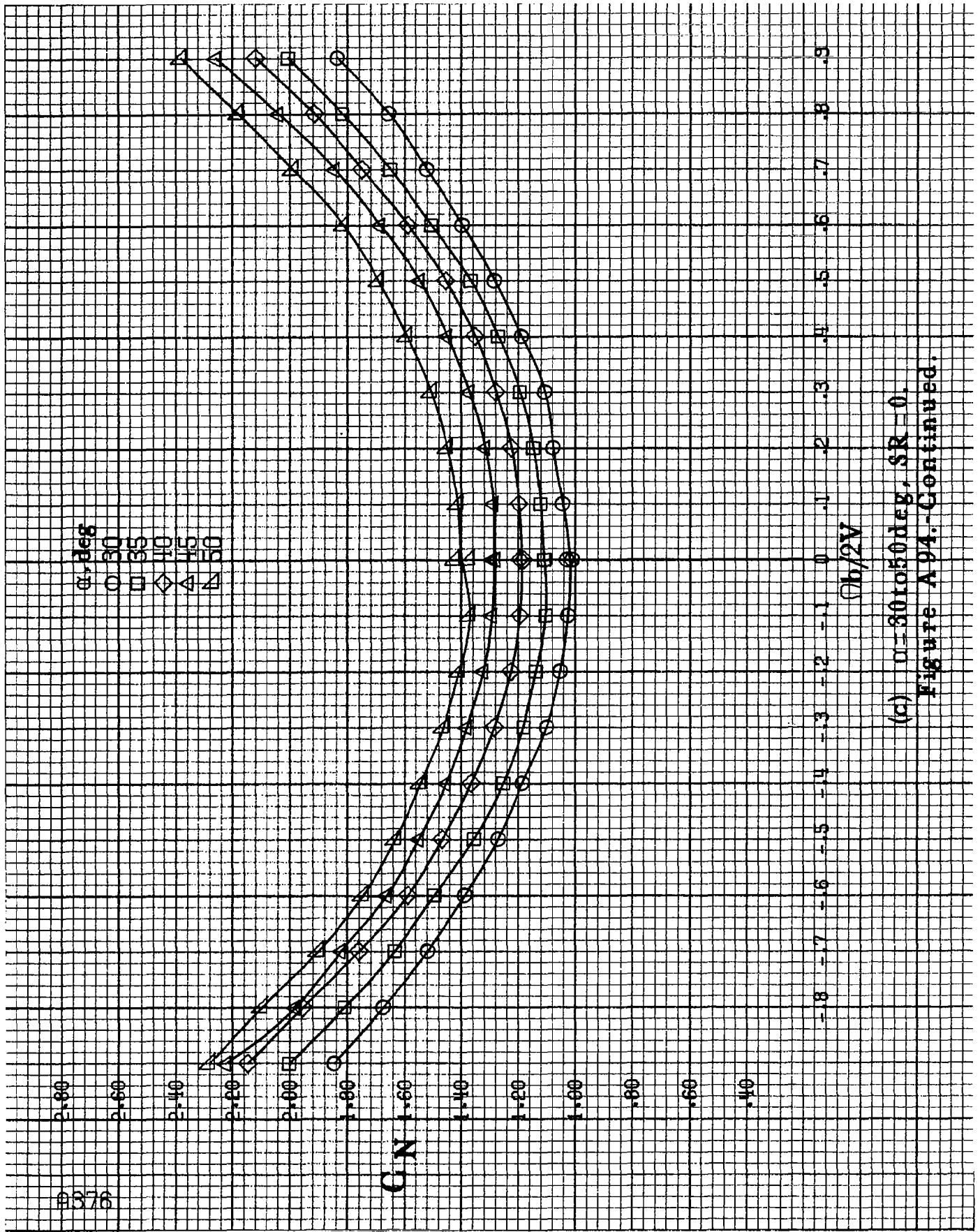
Figure A 94. Effect of rotation rate and angle of attack on normal-force coefficient for long tail, high wing, horizontal tail location no. 3. $\delta = 0^\circ$, $\delta = 10^\circ$, $\delta = 20^\circ$.



α, deg
 ○ 18
 □ 20
 ◇ 25
 △ 30
 ▴ 35



(b) $\alpha = 18$ to 35° , $SR = 91.4 \text{ cm (36 in.)}$.
 Figure A 94.-Continued.

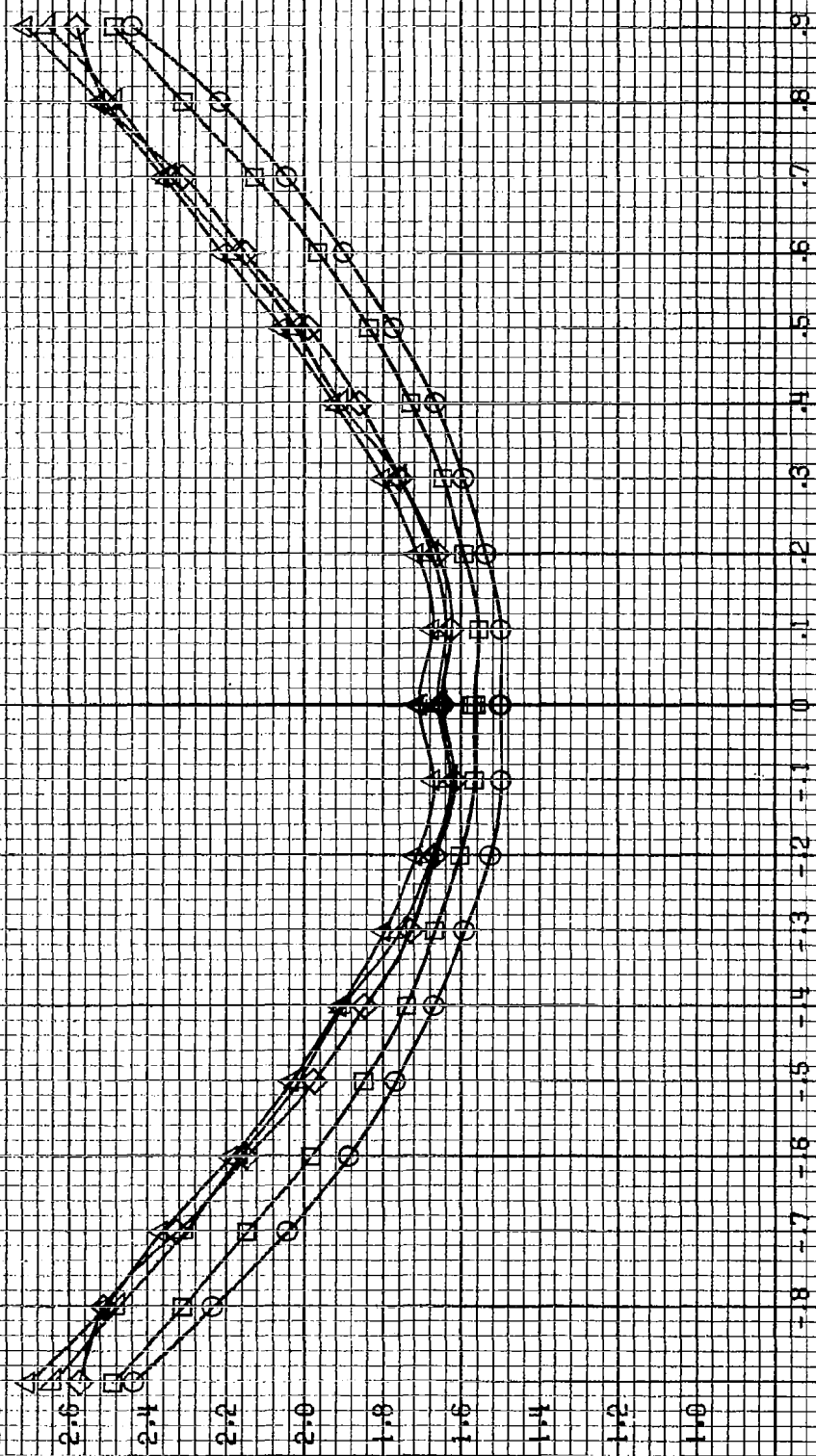


(c) $\alpha=30$ to 50 deg, $SR=0$.
Figure A94.-Continued.

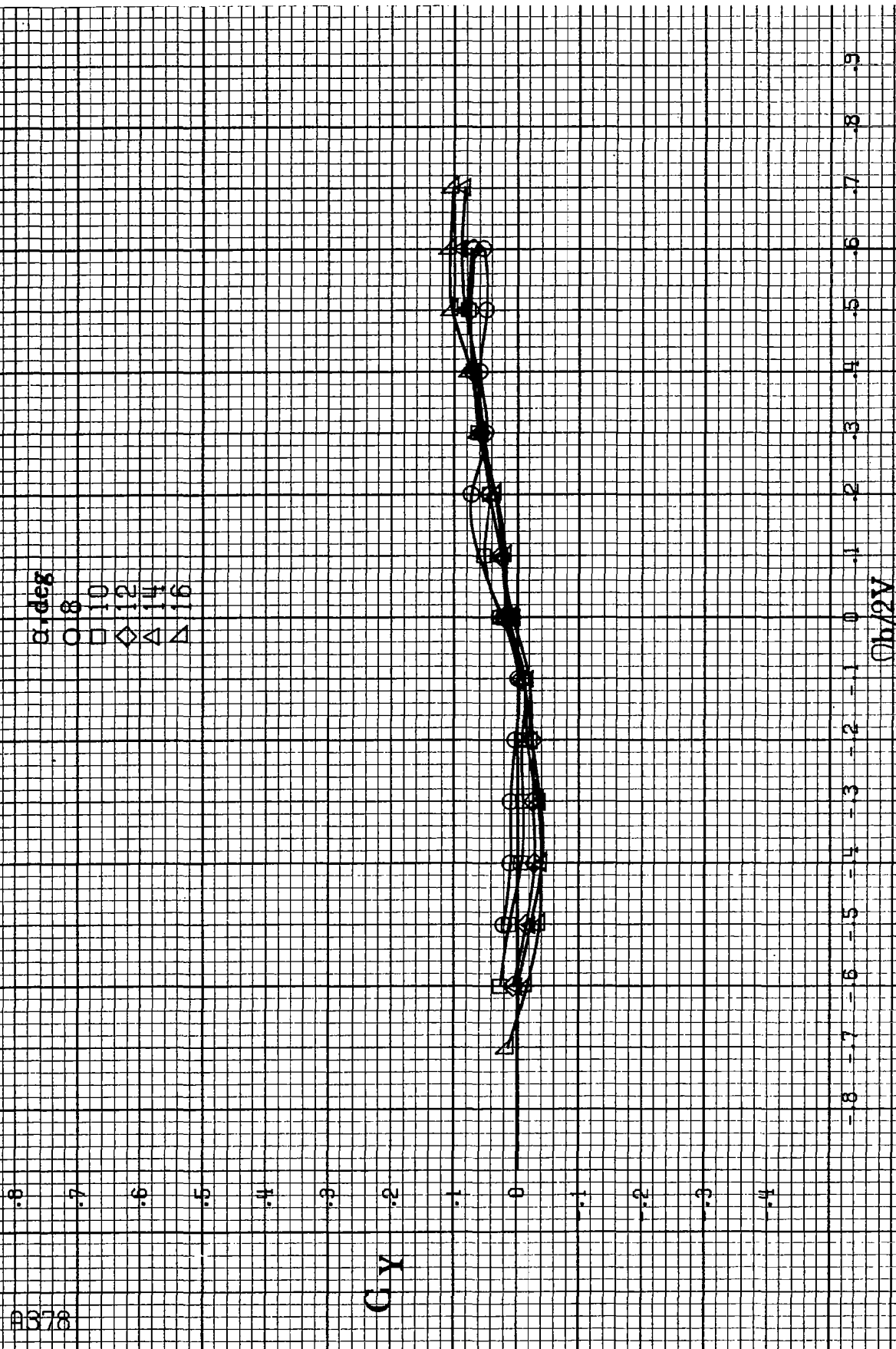
α , deg
 ○ 55
 □ 60
 ◇ 70
 △ 80
 ▴ 90

C/N

$\Omega_b/2V$



(d) $\alpha=55$ to 90 deg, $SR=0$.
 Figure A94. Concluded.



(a) $\alpha=8$ to 16° , $SR=91.4\text{cm}$ (36in).

Figure A95.-Effect of rotation rate and angle of attack on side-force coefficient for long tail, high wing, horizontal tail location no. 3. $\delta_a=0^\circ$, $\delta_r=0^\circ$, $\delta=0^\circ$.

α , deg
 O 18
 □ 20
 ◇ 25
 △ 30
 ▲ 35

Gy

$(b/2V)$

(b) $\alpha = 18$ to 35 deg, $SR = 31.4$ cm (36 in).
 Figure A 95.-Continued.

8379

A530

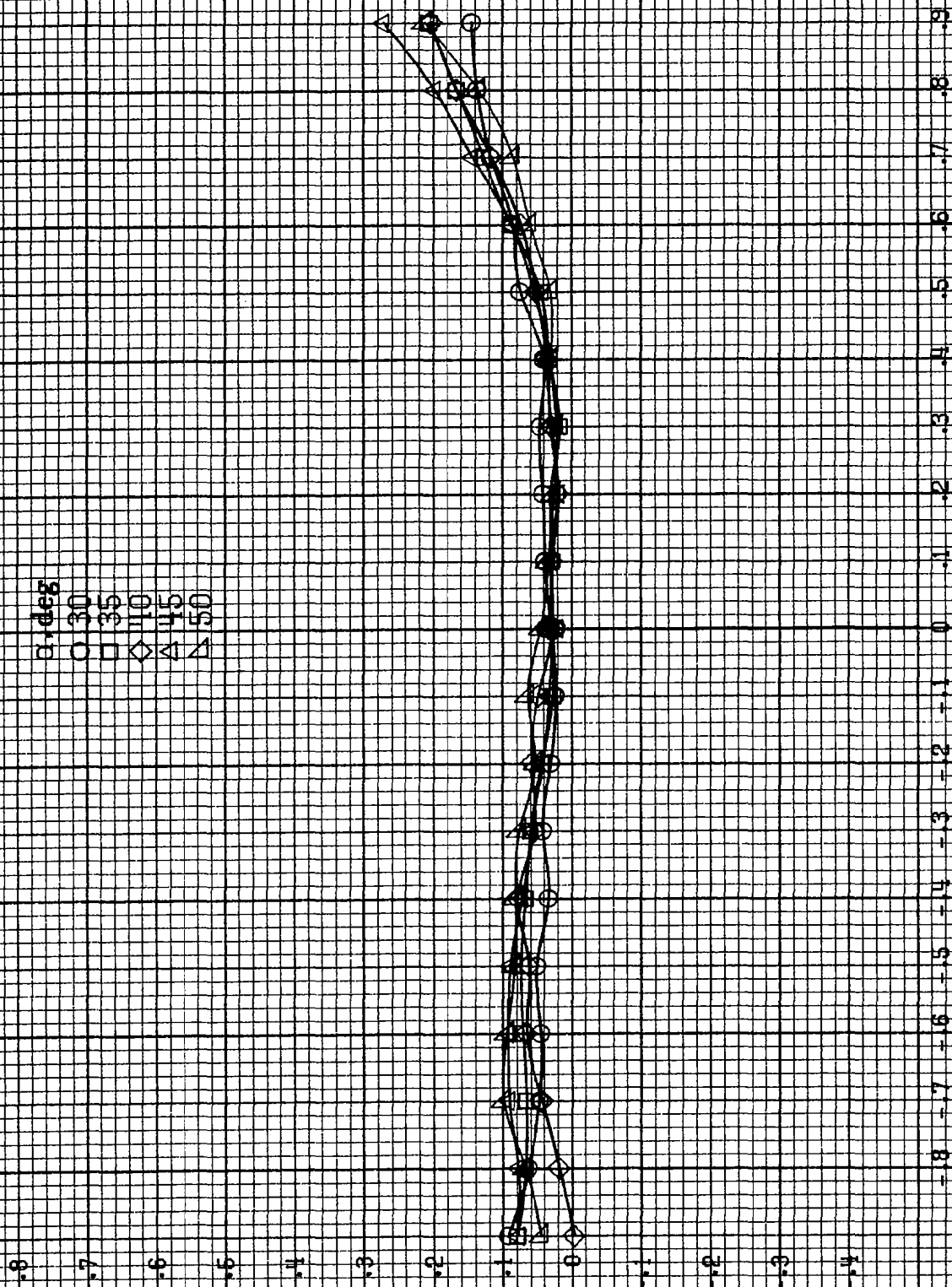
α, deg

○ 30
□ 35
◇ 40
△ 45
▽ 50

G_Y

$\phi_b/2V$

(c) $\alpha=30$ to 50 deg, $SR=0$.
Figure A95.-Continued.



α , deg
 ○ 55
 □ 60
 ◇ 70
 △ 80
 ▲ 90

0

0.1

0.2

0.3

C/V

0.4

0.5

0.6

0.7

0.8

0.9

1.0

1.1

1.2

1.3

1.4

E381

$Qb/2V$

(d) $\alpha=55$ to 90 deg, $SR=0$.

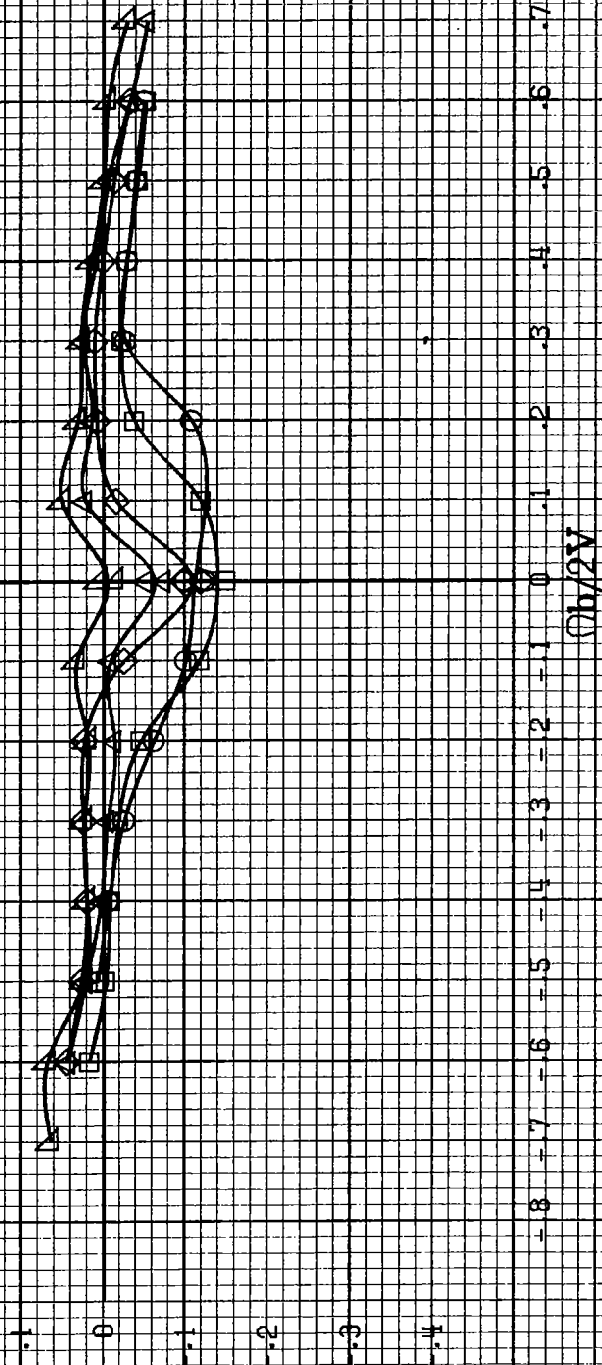
Figure A95.-Concluded.

0382

α , deg

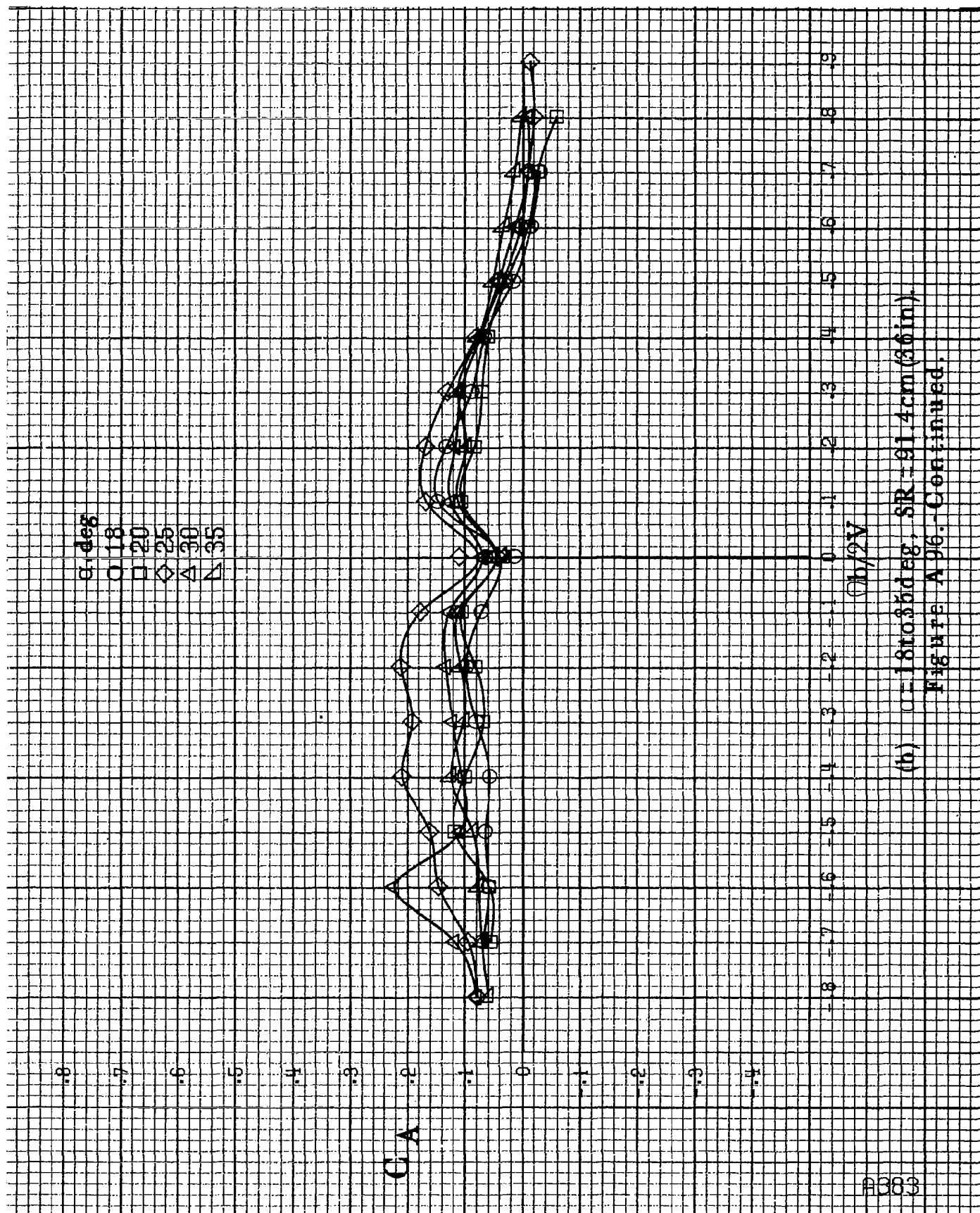
○ 8
□ 10
◇ 12
△ 14
▽ 16

C_A



(a) $\alpha = 8$ to 16 deg, $SR = 91.4$ cm (36 in).

Figure A96 - Effect of rotation rate and angle of attack on axial force coefficient for long tail, high wing, horizontal tail location no. 3. $\delta_a = 0^\circ$, $\delta_r = 0^\circ$, $\beta = 0^\circ$.



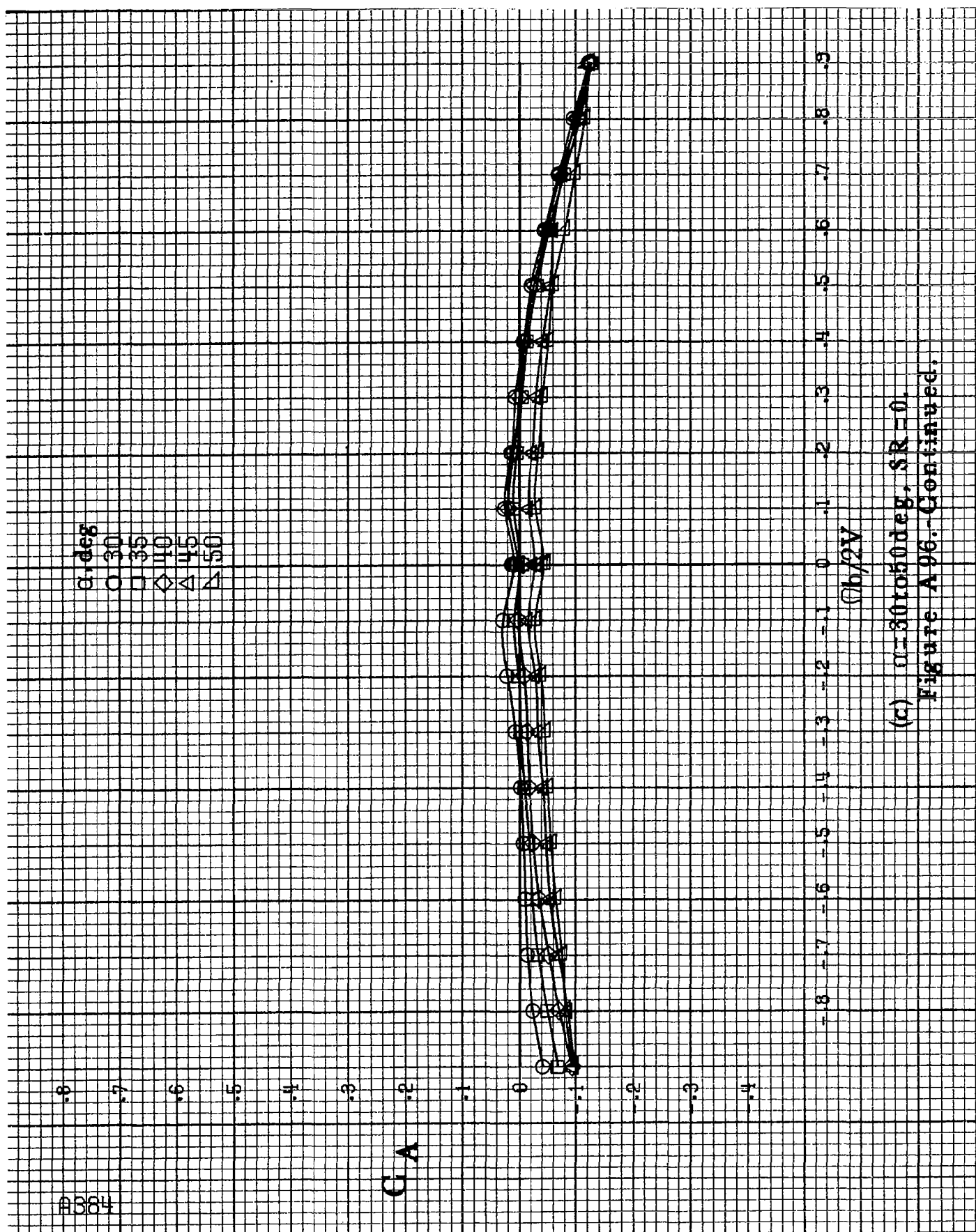
(b) $\alpha = 18$ to 35° , $SR = 91.4 \text{ cm (36 in.)}$.
Figure A 96-Continued.

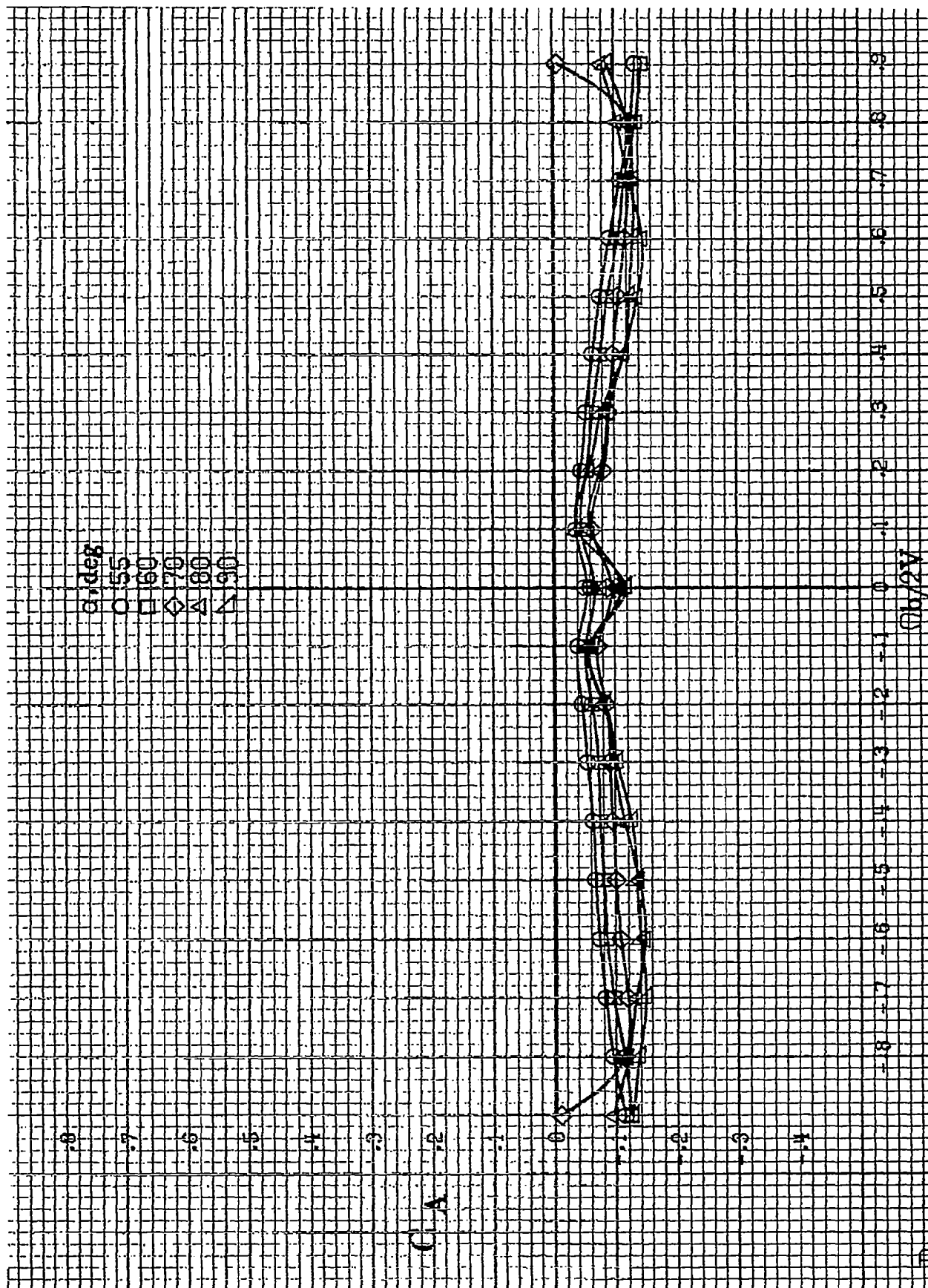
α, deg
 \circ 30
 \square 35
 \diamond 40
 \triangleleft 45
 \triangle 50

GA

$m_b/2V$

(c) $\alpha=30$ to 50 deg, $SR=0.1$
 Figure A96.-Continued.





(d) $\alpha = 55$ to 90 deg, $SR = 0$.
Figure A96. - Concluded.

1. Report No. NASA CR-3247		2. Government Accession No.		3. Recipient's Catalog No.	
4. Title and Subtitle Rotary Balance Data for a Typical Single-Engine General Aviation Design for an Angle-of-Attack Range of 8° to 90°. II - Influence of Horizontal Tail Location for Model D.				5. Report Date November 1982	
				6. Performing Organization Code	
7. Author(s) Billy Barnhart				8. Performing Organization Report No.	
				10. Work Unit No.	
9. Performing Organization Name and Address Bihrl Applied Research, Inc. 400 Jericho Turnpike Jericho, New York 11753				11. Contract or Grant No. NAS1-16205	
				13. Type of Report and Period Covered Contractor Report	
12. Sponsoring Agency Name and Address National Aeronautics and Space Administration Washington, DC 20546				14. Sponsoring Agency Code 515-10-13-06	
15. Supplementary Notes Langley Technical Monitor: James S. Bowman, Jr. Topical Report					
16. Abstract The influence of horizontal tail location on the rotational flow aerodynamics is discussed for a 1/6-scale general aviation airplane model. The model was tested using various horizontal tail positions, with both a high and a low-wing location and for each of two body lengths. Data were measured, using a rotary balance, over an angle-of-attack range of 8° to 90°, and for clockwise and counter-clockwise rotations covering an $\Omega b/2V$ range of 0 to 0.9.					
17. Key Words (Suggested by Author(s)) General Aviation Spinning Rotary Balance High angle-of-attack wind tunnel data			18. Distribution Statement Unclassified - Unlimited Subject Category 02		
19. Security Classif. (of this report) Unclassified	20. Security Classif. (of this page) Unclassified	21. No. of Pages	22. Price*		